UNIVERSITY OF SOUTHAMPTON

FACULTY OF ENGINEERING, SCIENCE AND MATHEMATICS

Institute of Sound and Vibration Research

Sound Field Reproduction

by

Filippo Maria Fazi

A thesis submitted in partial fulfillment for the
degree of Doctor of Philosophy

February 2010

UNIVERSITY OF SOUTHAMPTON

ABSTRACT

FACULTY OF ENGINEERING, SCIENCE AND MATHEMATICS
INSTITUTE OF SOUND AND VIBRATION RESEARCH

Doctor of Philosophy

SOUND FIELD REPRODUCTION

by Filippo Maria Fazi

This thesis is concerned with the problem of reproducing a desired sound field with an array of loudspeakers. A theory based on functional analysis and the theory of integral equations is developed for the study of this problem. An attempt is made to develop a mathematical framework that can be adopted as a generalized theory of sound field reproduction. The reproduction problem is formulated as an acoustical inverse problem, in which the target sound field is given on the boundary of a control volume located in the interior of the loudspeaker array, while the loudspeaker signals required for the reproduction of the desired field are to be determined. The loudspeaker array is initially modeled as a continuous distribution of secondary sources, mathematically represented by a single layer potential, whose density is to be determined. The singular value decomposition of the integral operator involved is proposed as a method for solving the inverse problem. Closed form expressions are derived for the singular system for the cases of secondary sources arranged on a sphere and on a circle. An attempt is also made to extend the calculation to unbounded geometries, such as an infinite line and a plane. The inverse problem under consideration is in general ill-posed, and the existence and uniqueness of its solution are studied in relation to sound fields of practical interest. It is shown that an exact and unique solution exists for a large family of sound fields. Strategies are proposed for overcoming the problem of nonexistence and nonuniqueness of the solution, arising in cases such as the reproduction of focused sources or when the operating frequency corresponds to one of the Dirichlet eigenvalues of the control region. An important analogy is also drawn between the problem of sound field reproduction and the theory of acoustic scattering. In a later part of this work, the assumptions of a continuous layer of secondary sources and of a single operating frequency are removed, and the resulting consequences are analyzed. The experimental validation of some of the theoretical results is described in the final part of the thesis. A large spherical loudspeaker array is used in an attempt to reproduce the sound field generated by a single virtual source, located in the exterior of the array. Experimental results are in good agreement with the theoretical results over a wide range of frequencies.

A mia nonna Alina ed a mio padre Maurizio,
dai quali non finirò mai di imparare.

[*To my grandmother Alina and to my father Maurizio,*
from whom I shall never stop learning.]

Da chimico un giorno avevo il potere
di sposare gli elementi e farli reagire,
ma gli uomini mai mi riuscì di capire
perché si combinassero attraverso l'amore
affidando ad un gioco la gioia e il dolore.

...

Primavera non bussa lei entra sicura
come il fumo lei penetra in ogni fessura
ha le labbra di carne, i capelli di grano.
Che paura, che voglia che ti prenda per mano.
Che paura, che voglia che ti porti lontano.

Ma guardate l'idrogeno tacere nel mare
guardate l'ossigeno al suo fianco dormire:
soltanto una legge che io riesco a capire
ha potuto sposarli senza farli scoppiare.
Soltanto la legge che io riesco a capire.

[*As a chemist, I once had the power*
to marry the elements and make them react,
but people I could never get to understand
why they'd combine together through love
entrusting their joy and their pain to a game.

...

Spring doesn't knock, she boldly steps in,
like smoke she diffuses through every gap.
Her lips are all fleshy, her hair is like wheat.
How scary, how tempting that she'll take your hand.
How scary, how tempting that she'll take you away.

But look at the hydrogen quiet in the sea!
look at the oxygen asleep at its side!
only a law which I comprehend
allowed them to marry and not to explode.
Only that law that I comprehend.]

(Fabrizio De André, *Un Chimico*
translated by M.Orsi, A.Simmonds,
M.Danby and F.Fazi)

Contents

Declaration of authorship

I, Filippo Maria Fazi, declare that the thesis entitled

Sound Field Reproduction

and the work presented in it are my own. I confirm that:

- this work was done wholly or mainly while in candidature for a research degree at this University;
- where any part of this thesis has previously been submitted for a degree or any other qualification at this University or any other institution, this has been clearly stated;
- where I have consulted the published work of others, this is always clearly attributed;
- where I have quoted from the work of others, the source is always given. With the exception of such quotations, this thesis is entirely my own work;
- I have acknowledged all main sources of help;
- where the thesis is based on work done by myself jointly with others, I have made clear exactly what was done by others and what I have contributed myself;
- parts of this work have been published as:

- Filippo M. Fazi and Philip A. Nelson, A theoretical study of sound field reconstruction techniques. 19th International Congress on Acoustics, Madrid, 2007.
- Filippo M. Fazi and Philip A. Nelson, Application of functional analysis to the sound field reconstruction. 23rd Conference on Reproduced Sound of the Institute of Acoustics, Newcastle, 2007.
- Filippo M. Fazi and Philip A. Nelson, The ill-conditioning problem in sound field reconstruction. 123rd International Convention of the Audio Engineering Society, New York, 2007.

- Filippo M. Fazi, Philip A. Nelson, Roland Potthast and Jeongil Seo, The study of sound field reconstruction as an inverse problem. Institute of Acoustics Spring Conference Reading, 2008.

- Filippo M. Fazi, Philip A. Nelson, Jens E. N. Christensen and Jeongil Seo, Surround System Based on Three-Dimensional Sound Field Reconstruction. 125th International Convention of the Audio Engineering Society, San Francisco, USA, 2008.

- Filippo M. Fazi, Philip A. Nelson, Roland Potthast and Jeongil Seo, An introduction to a generalised theory for sound field reproduction. 24th Conference on Reproduced Sound of the Institute of Acoustics, Brighton, 2008.

- Filippo M. Fazi, Philip A. Nelson, Roland Potthast and Jeongil Seo, Application of the theory of integral equations to the design of a multi-channel reverberation simulator. 35^o Convegno Nazionale dell'Associazione Italiana di Acustica Milano, Italy, 2008.

- Filippo M. Fazi, Philip A. Nelson and Roland Potthast, Analogies and differences between three methods for sound field reproduction. Ambisonics Symposium 2009, Graz, Austria, 2009.

Signed: .....

Date: .....

Acknowledgements

My doctoral training has been undoubtedly one of the best and most rewarding periods of my life. The first person I would like to thank for this, both on a professional and a personal level, is my supervisor Prof. Philip Nelson. He has been greatly supportive at every stage of my Ph.D. His scientific skills have been an irreplaceable guidance during my studies and his professional conduct has been a constant source of inspiration. He has always provided encouragement and has consistently motivated me to keep my scientific interests alive. Indeed, I feel very lucky for having had Prof. Nelson as my supervisor!

I would also like to thank Dr. Roland Potthast, who spent many hours working with me on the mathematics of inverse problems and integral equations. His irreplaceable guidance has helped me gain a better understanding of functional analysis thus giving a fundamental contribution to the scientific value of this thesis.

A big "thank you" to Dr. Keith Holland, whose professional expertise and guidance have been immensely valuable during the experimental part of my work.

A special acknowledgment should be awarded to Dr. Kyeongok Kang and Dr. Jeongil Seo of the Electronics and Telecommunications Research Institute (ETRI - Korea) for their consistently valuable scientific input throughout our collaboration.

I would like to thank my friends and colleagues Dr. Lara Harris, Dr. Mincheol Shin, Dr. Mun-Hum Park, Dr. Jung-Woo Choi and all the academic and administrative staff of ISVR, especially Sue Brindle, Maureen Mew and James Sturgess. They have all been very kind and helpful in the course of my Ph.D.

I am much obliged to Peter Otto, Toshiro Yamada and Suketu Kamdar, with whom I have been working during my wonderful stay at the University of California, San Diego.

Many thanks to Jack Oclee-Brown and Mark Dodd of KEF Audio for their support and for their valuable scientific contribution.

I would like to acknowledge all the contributors of the Sursound mailing list for the many enjoyable on–line discussions on Ambisonics and multi–channel audio.

Special thanks to Wikipedia, which has proven to be an extremely useful source of knowledge (which unfortunately is not citable in the list of references!).

On a more personal level, my deepest gratitude goes to my family: my father Maurizio and my *nonna* Alina (to whom this thesis is dedicated), my mother Prassede, my brother Federico and my *zia* Gianna. They have always been immensely supportive and have never doubted my ability to complete this body of work. Living far away from them during these years has been a challenge.

A huge "thank you" to Varvara for all her love, for her precious support and for never showing any signs of disappointment despite all the long hours I have dedicated to my work and to this thesis. Большое спасибо, Киса моя!

Many thanks to my housemates (Liz, Matt, Rita, Remy, Mirko, Siphiwe, Claudia and Victoria) and to all my friends in Southampton. Thank you for the wonderful time we spent together. A special thank to my "brother" Francesco, with whom I shared some of the best moments of my life, and to Chris (*Caned*), for carrying the burden of being my friend for so many years.

Thank you all! Indeed, this has been a wonderful chapter of my life.

Table of symbols

Operators and other mathematical symbols

i	imaginary unit ($i = \sqrt{-1}$)
$(\cdot)^*$	complex conjugate of a complex number or adjoint operator
$\arg(\cdot)$	argument of a complex number ($z = \|z\|e^{\arg z},\ z \in \mathbb{C}$)
$\lceil \cdot \rceil$	ceiling operator (rounding up to next integer)
$\otimes$	convolution
$\oplus$	direct sum of two sets
$\setminus$	difference of two sets ($A \setminus B = \{x : x \in A, x \notin B\}$)
$(\cdot)^\perp$	orthogonal complement
$\partial\, \cdot$	boundary of a set
$\overline{(\cdot)}$	closure of a set
$\|\cdot\|$	absolute value and Cartesian norm
$\|\|\cdot\|\|_{(D)}$	L^2 norm
$\langle \cdot \| \cdot \rangle_{(D)}$	scalar product
	(the optional subscript $_D$ refers to the domain of integration for the L^2 product)
span	span of a set of functions
$:=$	definition
$\forall$	*... for all...* (Universal quantifier)
$\in$	*...is in... / ...belongs to...*
$\subset$	*...is a subset of...*
$:$	*... such that...*
$\{x : \cdots\}$	definition of a set by stating the properties of its elements x
$\{\cdot, \cdot, \cdots\}$	definition of a set by a list of its members
$\nabla_{\mathbf{n}}$	normal derivative operator ($\nabla_{\mathbf{n}} := \hat{\mathbf{n}} \cdot \nabla$)
$\mathcal{F},\ \mathcal{F}^{-1}$	direct and inverse Fourier transform
$\mathcal{F}_t,\ \mathcal{F}_t^{-1}$	direct and inverse Fourier transform for time domain functions
$\tilde{\mathcal{F}}$	Fourier transform for both space and time
S	acoustic single layer potential (in general referred to its restriction to ∂V)
σ_n	singular values of an operator
$a_n(\cdot),\ p_n(\cdot)$	singular functions of an operator
P_D	orthogonal projection operator onto D

Sets, vectors and matrices

V	control region
Λ	reproduction region
∂V	control boundary (boundary of V)
$\partial\Lambda$	secondary source layer (boundary of Λ)
Ω_R	sphere of radius R ($\Omega_R := \{\mathbf{x} \in \mathbb{R}^m : \lvert\mathbf{x}\rvert = R\}$)
Ω	unitary sphere (sphere with $R = 1$)
B_R	ball of radius R ($B_R := \{\mathbf{x} \in \mathbb{R}^m : \lvert\mathbf{x}\rvert < R\}$)
$\mathbb{N}$	the set of the natural numbers (including zero)
$\mathbb{Z}$	the set of integer numbers
$\mathbb{Q}$	the set of rational numbers
$\mathbb{R}$	the set of real numbers
$\mathbb{R}^m$	the $m-$dimensional Euclidean space, ($\mathbb{R}^m := \{x = (x_1, x_2, \cdots, x_m) : x_1, x_2, \cdots, x_m \in \mathbb{R}\}$)
$\mathbb{C}$	the set of complex numbers
$L^2(D)$	The set of square integrable functions defined on the domain D
$\mathbf{x}$	position vector of a point on ∂V
$\mathbf{y}$	position vector of a point on $\partial\Lambda$
$\mathbf{z}$	position vector of a point in $\mathbb{R}^m$, $m = 2, 3$
$\hat{\mathbf{n}}$	unitary vector normal to a surface (usually pointing towards the exterior)
$\mathbf{q}$	location of a virtual point source
$\mathrm{diag}\{\dots\}$	diagonal matrix
$\mathbf{I}$	Identity Matrix ($I_{ij} = \delta_{ij}$)
$\mathbf{R}$	orthogonality matrix
$\mathbf{E}$	aliasing matrix

Special functions

$\delta_{(D)}(\mathbf{x} - \mathbf{y})$	Dirac delta function
δ_{nm}	Kronecker delta
$J_\nu(\cdot)$	ν-th order Bessel function of the first kind
$Y_\nu(\cdot)$	ν-th order Bessel function of the second kind (Neumann function)
$J_\nu(\cdot)$	ν-th order Bessel function
$H_\nu^{(1)}(\cdot)$	ν-th order Hankel function of the first kind (the superscript $^{(1)}$ is sometimes omitted)
$H_\nu^{(2)}(\cdot)$	ν-th order Hankel function of the second kind
$j_\nu(\cdot)$	ν-th order spherical Bessel function
$j_\nu'(\cdot)$	first derivative of the ν-th order spherical Bessel function
$h_\nu^{(1)}(\cdot)$	ν-th order spherical Hankel function of the first kind (the superscript $^{(1)}$ is sometimes omitted)
$h_\nu^{(2)}(\cdot)$	ν-th order spherical Hankel function of the second kind
$P_\nu(\cdot)$	Legendre polynomial of order ν
$P_\nu^\mu(\cdot)$	associated Legendre function
$Y_\nu^\mu(\cdot)$	spherical harmonics of order ν and mode (or degree) μ
$\mathrm{sinc}(\cdot)$	sinc function
$\mathrm{csinc}(\cdot)$	circular sinc function
$\text{Ш}(\cdot)$	comb function
$\Pi(\cdot)$	rectangular function

Other functions and physical entities

$p(\mathbf{x})$	target sound field or pressure profile [Kg m s^{-2}]
$\hat{p}(\mathbf{x})$	reproduced sound field [Kg m s^{-2}]
$a(\mathbf{y})$	secondary sources strength density [Kg s^{-2} m^{-2}] or [Kg s^{-2} m^{-1}]
$\ddot{m}$	secondary source strength [Kg s^{-2}]
$G(\mathbf{x}, \mathbf{y})$	Green function of the Helmholtz equation[m^{-1}]
$\mathbf{v}(\mathbf{z})$	particle velocity [m s^{-1}]
$\mathbf{I}(\mathbf{z})$	time averaged acoustic intensity [Kg s^{-3}]
W	acoustic power [Kg m^2 s^{-3}]
c	speed of sound propagation [m s^{-1}]
k	wave number [rad m^{-1}]
q_{vol}	volume flow [m^3 s^{-1}]
t	time [s]
ρ_0	static density of the fluid [Kg m^{-3}]
ω	angular frequency [rad s^{-1}]

Chapter 1

Introduction

1.1 Background and scientific contribution of the thesis

This thesis addresses the problem of reproducing a desired sound field with an array of loudspeakers. This problem is of relevance for many practical engineering applications. The design of multi-channel audio systems, which allow for an accurate rendering of the spatial detail of a sound scene, is probably the most obvious application. Other fields in which the reproduction of a desired acoustic field may be of relevance include the active control of sound and the design of loudspeaker or hydrophone arrays for telecommunications, public address systems, underwater arrays and sonar technologies or military applications. The general subject of multi-channel systems and array technology has received increasing interest during the last decade. This fact is probably due to the recent advancement in electronics and telecommunication technologies, which have allowed for the realization and commercial diffusion of a variety of affordable products capable of sophisticated and simultaneous real time digital processing of a large number of signals.

The main contribution of this thesis consists of the development of a rigorous theoretical study of the problem of sound field reproduction. An attempt is made to develop an analytical framework which can be adopted as a generalized theory of sound field reproduction. Other reproduction methods, such as for example Wave Field Synthesis, High Order Ambisonics and other techniques reported below, can be derived from the general theory proposed here and can be interpreted as special cases of the latter.

The starting point of this work is the mathematical formulation of the problem of sound field reproduction as an *inverse problem*. The corresponding *direct* or *forward problem* consists of the determination of the sound field generated by a given array of loudspeakers, for which the signal driving each loudspeaker is known. This problem is simply solved by creating a suitable physical model of the array. The solution of the inverse problem

requires the answer to the following question: given a desired sound field, defined within a bounded region of the space, and given a loudspeaker array, what are the loudspeaker signals which allow for the array to reproduce that desired field? In many cases, an exact answer to this question might not exist, but it is possible to give an answer, which is as accurate as possible. In other words, it is possible to compute loudspeaker signals allowing for an acoustic field to be reproduced, which is as similar as possible to the target field (later, we will see what is meant by *as similar as possible*).

The backbone of the approach developed relies on the assumption that the loudspeaker array can be modeled as a *continuous* distribution of ideal omnidirectional acoustic point sources (secondary sources). The assumption of a continuous distribution implies the use of an ideally infinite number of loudspeakers and is therefore clearly unrealistic, but this nevertheless proves extremely useful for developing a solid and rigorous theory of sound field reproduction. In Chapter 7 of this thesis, this ideal assumption is removed and the effects of the discretization of the array are studied in detail. It is clear from the outset, however, that the ideal assumption above is a good approximation to reality when the number of loudspeakers is such that the average distance between neighboring units is small in comparison to the wavelength of the sound to be reproduced. In Chapter 7, an alternative solution method is presented, which involves directly the discretization into a finite number of secondary sources of the integral operator adopted as a model of the loudspeaker array.

The assumption of a continuous distribution of secondary sources allows for the loudspeaker array to be modeled as an integral operator, and more specifically as a *single layer potential*. This crucial step leads to the fundamental connection between the problem of sound field reproduction and the branch of mathematics know as *functional analysis*, more specifically to the theory of integral equations, thus opening the door to a vast source of mathematical tools and results, which can be used to analyze and solve the inverse problem under consideration. Functional analysis has been developed mainly during the last century, and has been successfully applied to the study of a variety of problems of relevance for physics and engineering, including the study of acoustical inverse problems such as scattering of sound and acoustic holography. To the author's knowledge, the problem of sound field reproduction has not hitherto been formulated within this framework, and this is therefore believed to be a relevant scientific contribution of this thesis.

The philosophical motivation behind the effort spent developing a theory of sound field reproduction on the basis of functional analysis, apparently adding an extra layer of mathematical complexity, is probably summarized well by the following citation of E. Kreyszig, *Introductory functional analysis with applications* [Kre78, p.1]:

Mathematicians observed that problems from different fields often enjoyed related features and properties. This fact was used for an effective unifying approach towards such

problems, the unification being obtained by the omission of unessential details. Hence the advantage of such an abstract approach is that it concentrates on essential facts, so that these facts become clearly visible since the investigator's attention is not disturbed by unimportant details. In this respect the abstract method is the simplest and most economical method for treating mathematical systems. Since any such mathematical system will, in general, have various concrete realizations (concrete models), we see that the abstract method is quite versatile in its application to concrete situations. It helps to free the problem from isolation and creates relations and transitions between fields which have at first no contact with one another.

The above refers to the use, in general, of abstract mathematical models for the study of different problems, which share underlying logical properties, but suits very well the issue under consideration. In fact, the study of sound field reproduction in the framework of functional analysis not only allows for the formulation of a general theory, from which other specific approaches can be derived, but it also reveals hidden and yet enlightening analogies between the problem addressed and other apparently unrelated subjects such as acoustic scattering and Near-field Acoustical Holography, as shown in Chapter 6 of this thesis.

In the theoretical framework adopted, the acoustic fields and the functions representing the loudspeaker signals are elements of abstract spaces of functions (more specifically, Hilbert spaces). The loudspeaker array, as mentioned above, is modeled as an integral operator and the mathematical properties of this operator are analyzed. This brings to light the fact that the inverse problem under consideration is, by its very nature, an ill-posed problem, thus implying that the solution to the problem might not exist, might be non unique, or might be unstable. Existing mathematical results are deployed and new results are derived, which indicate the sound fields that can be reproduced and the degree of accuracy with which this can be accomplished. For several ideal array geometries, explicit expressions for the solution of the problem are derived, in most of cases by means of the singular value decomposition of the integral operator involved. In the cases when an exact solution of the inverse problem does not exist, approximate solutions are derived by applying regularization techniques. The validity of the results derived for ideal continuous loudspeaker arrays is then analyzed for the case of arrays including a finite number of units, and the effects due to spatial aliasing are studied in detail. The computation of the loudspeaker signals for the reproduction of sound fields with broad-band spectral content leads to the definition of digital filter design strategies. These can be implemented in digital signal processing algorithms for practical sound field reproduction systems.

Finally, an important contribution of this work, on which the last chapter of this thesis is focussed, is the experimental validation of some of the theoretical results presented. This shows that the utility of the abstract models developed is demonstrated by their application to real situations. The experiments discussed in this thesis represent an

initial step, which may pave the way to further development and practical applications of the theory.

Although no explicit connection to other branches of acoustics is made here, it is the hope of the author that some of the theoretical results developed within this work may prove useful not only for the specific subject of sound field reproduction but also for other acoustical problems such as sound radiation, acoustic source reconstruction and identification, acoustic holography, active control of sound, acoustic imaging and acoustic scattering.

It is important to emphasize that several results presented in this thesis, and especially those discussed in Chapter 7, are not novel and are reported also in the literature dedicated to other sound field reproduction techniques, such as Wave Field Synthesis and High Order Ambisonics. However, consistent with the intent of presenting a generalized theory, the deliberate choice has been made of deriving these results following the general analysis developed in this thesis, rather than introducing them by referring to other specific and established techniques. Therefore, with respect to these results, the originality of the scientific contribution lies in the fact that several results arising in different methods, are here derived within the framework of a unified general approach to the problem.

One final, yet relevant, aspect of the problem that should be considered from the very beginning is that this thesis deals with the physical reproduction of a desired sound field, rather than with the accurate rendering of its spatial attributes in terms of human perception. The relation between the accuracy of the reproduction of the physical characteristics of the desired field, such as acoustic pressure and acoustic intensity, and the human perception of the spatial attributes of the reproduced sound scene is beyond the objective of this thesis and may be the subject of future efforts.

Some of the results and concepts presented in this thesis are also reported in the following publications:

- Filippo M. Fazi and Philip A. Nelson, A theoretical study of sound field reconstruction techniques. 19th International Congress on Acoustics, Madrid, 2007 [FN07c].
- Filippo M. Fazi and Philip A. Nelson, Application of functional analysis to the sound field reconstruction. 23rd Conference on Reproduced Sound of the Institute of Acoustics, Newcastle, 2007 [FN07a].
- Filippo M. Fazi and Philip A. Nelson, The ill-conditioning problem in sound field reconstruction. 123rd International Convention of the Audio Engineering Society, New York, 2007 [FN07b].

- Filippo M. Fazi, Philip A. Nelson, Roland Potthast and Jeongil Seo, The study of sound field reconstruction as an inverse problem. Institute of Acoustics Spring Conference Reading, 2008 [FNPS08c].
- Filippo M. Fazi, Philip A. Nelson, Jens E. N. Christensen and Jeongil Seo, Surround System Based on Three-Dimensional Sound Field Reconstruction. 125th International Convention of the Audio Engineering Society, San Francisco, USA, 2008 [FNCS08].
- Filippo M. Fazi, Philip A. Nelson, Roland Potthast and Jeongil Seo, An introduction to a generalised theory for sound field reproduction. 24th Conference on Reproduced Sound of the Institute of Acoustics, Brighton, 2008 [FNPS08b].
- Filippo M. Fazi, Philip A. Nelson, Roland Potthast and Jeongil Seo, Application of the theory of integral equations to the design of a multi-channel reverberation simulator. 35^o Convegno Nazionale dell'Associazione Italiana di Acustica Milano, Italy, 2008 [FNPS08a].
- Filippo M. Fazi, Philip A. Nelson and Roland Potthast, Analogies and differences between three methods for sound field reproduction. Ambisonics Symposium 2009, Graz, Austria, 2009 [FNP09].

1.2 Brief overview of previous work

The problem of reproducing a desired sound field with an array of loudspeakers has been the subject of scientific research for many years, and several approaches have been proposed in order to provide a practical solution to this problem. Most of these methods are grounded on a solid mathematical and physical basis, and the implementation of these techniques into practical systems, especially for audio purposes, has increased progressively during the last decade. In what follows, several of these techniques are briefly described. Following this, some references are provided to work relating to the application of functional analysis and of the theory of integral equations to acoustics.

1.2.1 Wave Field Synthesis

One the most well-known sound field reproduction techniques is *Wave Field Synthesis*. This technique was initially conceived by A.J. Berkhout and presented in 1988 in a highly cited paper [Ber88]. After that, much research was undertaken, especially at the Delft University of Technology, in order to develop further this technique. Many authors contributed to this effort and a large number of scientific publications on Wave Field Synthesis is now available: [BdS97], [BDV93], [Sta97], [Ver97], [Vog93], [dV96],

[Boo04], [BVv94], [SRA08], [SR06], [Spo07], [SA09], [AS07], [CPKR08], [Cor07], [Cor06], [MLdV05] and [PRP+08] , among others.

The theory of Wave Field Synthesis is based on the well-known *Huygens-Fresnel principle*, whose first formulation appeared in 1690 in Huygens' *Traité de la lumière* (see for example [Huy66]). This principle states that each point of a propagating wave front may be regarded as a center of a new disturbance and the source of a new secondary wave, and that the principal propagating wave may be regarded as the sum of all the these secondary waves. This simple but fundamental principle laid the foundations for the so-called *Green's representation theorem* [CK83], allowing for the representation of a field p, which satisfies the homogeneous Helmholtz equation in a bounded set D, by the following integral

$$\int_{\partial D} G(\mathbf{x},\mathbf{y})\frac{\partial p(\mathbf{y})}{\partial \hat{\mathbf{n}}(\mathbf{y})} - \frac{\partial G(\mathbf{y})}{\partial \hat{\mathbf{n}}(\mathbf{y})} p(\mathbf{y})\, dS(\mathbf{y}) = \begin{cases} p(\mathbf{x}) & \text{if } \mathbf{x} \text{ is inside } D \\ p(\mathbf{x})/2 & \text{if } \mathbf{x} \text{ is on } \partial D \\ 0 & \text{if } \mathbf{x} \text{ is outside } D \end{cases}$$

where ∂D is the boundary of D, $G(\mathbf{x},\mathbf{y})$ is the Green function and $\hat{\mathbf{n}}(\mathbf{y})$ is the unitary vector orthogonal to ∂D at $\mathbf{y}$ and directed toward its exterior (see chapters 2 and 3 for more detail). In the literature on acoustics, the formula above is usually referred to as the *Kirchhoff-Helmholtz integral* (or Helmholtz integral) [Wil99].

The practical implication of this relevant result is that a given sound field can be reproduced, in the interior of a bounded region of the space, by a continuous distribution of dipole-like and monopole-like secondary sources, arranged on the boundary of this region. The strength of these secondary sources is given by the value of the acoustic pressure field and of its derivative, respectively, evaluated at the location of the secondary source under consideration. The sound field reproduced in the exterior of D is identically zero.

As will be shown in Chapter 6 of this thesis, in the special case when ∂D is an infinite plane or an infinite line, the integral representation above can be substituted by the first *Rayleigh integral* (or alternatively to the second Rayleigh integral), which reads

$$p(\mathbf{x}) = \int_{\partial D} G(\mathbf{x},\mathbf{y})\, 2\frac{\partial p(\mathbf{y})}{\partial \hat{\mathbf{n}}(\mathbf{y})}\, dS(\mathbf{y})$$

In this formulation, secondary sources of one kind only are required (monopole-like sources for the first Rayleigh integral and dipole like sources for the second). This representation formula is the basis of Wave Field Synthesis: an array of equally spaced loudspeakers is used to reproduce a desired field, and the loudspeaker signals are derived directly from the normal derivative of the desired acoustic pressure field, evaluated or measured at the location of each loudspeaker. Reproduction artifacts derived from the finite size of the array and from the discretization of the ideally continuous distribution of secondary sources are well known and are discussed in the literature. This technique

applies rigorously to planar arrays, but effective methods have been derived in order to extend it to arrays of different shape. Of special relevance is the so called *2.5 operator*, derived from a stationary phase approximation of the three dimensional free field Green function and applied to two dimensional arrays (see for example [Sta97]).

Adaptive methods have been applied to Wave Field Synthesis, as is discussed in the works, among others, of S. Spors et al. [Spo06], [SBRH07] and P.A. Gauthier et al. [GBW05], [GB06], [GB08b], [GB08a].

1.2.2 Ambisonics

Another well-known and widely used technique for sound field reproduction is *Ambisonics*. This method was invented by M.A. Gerzon and its principles were presented in a series of publications, the first of which, [Ger72], was presented in 1972. Some of these papers are: [Ger73], [Ger74], [Ger75], [Ger77c], [Ger77b], [Ger77a], [Ger80], [Ger85], [GB92], [Ger97] and [GB98]. It should be mentioned that Gerzon often refers to psychoacoustical principles in relation to the theory of Ambisonics. In [Ger80] two localization theories are mentioned, namely *Makita theory* and the *Energy vector theory*, but Gerzon also proposed his own theory of auditory localization [Ger74], [Ger92], intended as a theoretical tool for designing strategies for surround sound systems.

In spite of the fact that Gerzon's theory was valid for systems of arbitrary order, for a long period of time after its invention the practical applications of Ambisonics involved only first order systems (the *order* refers to the truncation order of the spherical harmonic series described below). The works of J.S. Bamford and J. Vanderkooy [Bam95], [BV95] and the series of publications by J. Daniel, R. Nicol and S. Moreau [Dan00], [DRP98], [Dan03], [Nic99], [NE99], [NE98], [DNM03], [Mor06] contributed to the further development of the theory and applications of Ambisonics. Much attention has been dedicated to the extension of Ambisonic systems to orders higher than the first. Some of this work emphasizes the capabilities of Ambisonics for reproducing a desired sound field. Furthermore, much effort has been dedicated to the study of analogies and differences between Ambisonics and Wave Field Synthesis. The use of the term *High Order Ambisonics* has become increasingly popular in the literature when referring to this new evolution of Ambisonics. An extensive literature is now available on the theory and applications of Ambisonics. Some of the relevant publications are, among others, [Fel75], [CG77], [Mal99], [Cot02], [Wig04], [SS06], [Sol08], [HS09], [AS08a], [AS08b], [AS08c], [SA08], [MAA07], [ZPF09], [SH01], [NMSH03], [FU98] and [HLB08]

In the work of Daniel et al. [DNM03] it is reported that Ambisonics is based on the representation of the field by means of spherical harmonics. More specifically, a given field p, satisfying the homogeneous Helmholtz equation in the interior of a sphere of

radius R, can be expressed by

$$p(\mathbf{x},\omega) = \sum_{n=0}^{\infty} i^n j_n\left(\frac{\omega}{c}\, x\right) \sum_{m=-n}^{n} Y_n^m(\hat{\mathbf{x}}) B_n^m(\omega), \quad x < R$$

where j_n are spherical Bessel functions and Y_n^m are spherical harmonics (see Chapter 2 for more detail). The coefficients $B_n^m(\omega)$ of the series constitute an infinite and countable set of complex numbers, which fully describe the sound field in the interior of the sphere of radius R. The series above is then approximated by applying a truncation to a given order N.

The so-called *Ambisonic encoding* process consist, in mathematical terms, of the determination of a given number of coefficients B_n^m (namely the coefficients with $n \leq N$ and $-n \leq m \leq n$) from the knowledge of the target field p, which is either expressed mathematically or measured. The use of the so-called *sound field microphone* is very popular for Ambisonic recordings. The set of signals generated by the encoding process are referred to as *B-format* signals and correspond to the Fourier transform, from the frequency domain (ω) to the time domain, of the coefficients $B_n^m(\omega)$.

Given an array of L loudspeakers, arranged ideally uniformly around the listener on a circle or on the surface of a sphere surrounding the listener, the *Ambisonic decoding* process generates from the B-format signals the loudspeaker signals allowing for the reproduction of the desired field. It can be shown that the reproduced sound field $\hat{p}$ can be expressed as follows

$$\begin{aligned}
\hat{p}(\mathbf{x},\omega) &= \sum_{n=0}^{\infty} i^n j_n\left(\frac{\omega}{c}\, x\right) \sum_{m=-n}^{n} Y_n^m(\hat{\mathbf{x}}) \hat{B}_n^m(k) \\
&= \sum_{\ell=1}^{L} S_\ell(\omega) \sum_{n=0}^{\infty} i^n j_n\left(\frac{\omega}{c}\, x\right) r_n\left(\frac{\omega}{c}\, y\right) \sum_{m=-n}^{n} Y_n^m(\hat{\mathbf{x}}) Y_n^m(\hat{\mathbf{y}}_\ell)^*
\end{aligned}$$

where the vectors $\mathbf{y}_\ell = y\hat{\mathbf{y}}_\ell$ indicates the position of the loudspeakers and $S_\ell(\omega)$ are the loudspeaker signals (expressed as functions of the frequency). The frequency dependent coefficients $r_n\left(\frac{\omega}{c}\, y\right)$ depend upon the chosen acoustic radiation model of the loudspeakers, and they all equal 4π if each loudspeaker is assumed to generate a single propagating plane wave. Substituting the coefficients $\hat{B}_n^m(\omega)$ with the coefficients $B_n^m(\omega)$, describing the target field, and deploying the orthogonality of the spherical harmonics (see Chapter 2), the formula above leads to the solution of the following system of linear of equations:

$$\begin{aligned}
&B_n^m(\omega) = \sum_{\ell=1}^{L} S_\ell(\omega)\; r_n\left(\frac{\omega}{c}\, y\right)\; Y_n^m(\hat{\mathbf{y}}_\ell)^*, \\
&n = 0, 1, \ldots N, \quad -n \leq m \leq n
\end{aligned}$$

The solutions of this linear system, that can be exact or approximated, provides the loudspeaker signals $S_\ell(\omega)$. If $r_n\left(\frac{\omega}{c}\, y\right)$ does not depend on the frequency, the solution

of the system above is particularly simple and the loudspeaker signals can be computed directly in the time domain by a simple linear combination of the B-format signals.

The decoding procedure discussed above is usually referred as *basic decoding*. Other decoding strategies have been proposed, such as the *in-phase decoding* or the *energy vector maximization decoding* (see for example [Dan00]). These strategies are supposed to provide better psychoacoustical performance. In terms of signal processing, these alternative strategies simply include the multiplication of the B-format signals by a set of given scaling factors before solving the linear system above.

1.2.3 Other methods for sound field reproduction

Several other methods and techniques for sound field reproduction have been proposed, especially during the last decade. New theories, which are also based on the spherical (or cylindrical) harmonic decomposition of the sound field, have been proposed by M.A. Poletti [Pol96], [Pol00], [Pol05], [Pol07], by T.D. Abhayapala, D.B. Ward, T. Betlehem and Y.J. Wu [WA01], [BA05],[WA09] and by J. Hannemann and K.D. Donohue [HD08].

P.A. Nelson, O. Kirkeby et al. [NOBH96], [KN93] proposed approaches, which rely on the numerical solution of an acoustical inverse problem. The underlying principles shares significant analogies with the theory of active control of sound (see, for example, [NE92]) and can be simplistically summarized as follows:

- A target sound field is defined on a set of given locations. These data are represented by the vector $\mathbf{p}$.
- A matrix $\mathbf{H}$ of acoustical transfer functions is computed between the elements of a given loudspeaker array and the locations above. The reproduced field at these locations is therefore given by $\hat{\mathbf{p}} = \mathbf{Ha}$, where $\mathbf{a}$ is the vector of loudspeaker signals (in practice, as discussed in Chapter 7, these are coefficients of digital filters).
- The loudspeaker signals are computed by minimizing a cost function, given by $|\mathbf{Ha} - \mathbf{p}|^2$. A modeling delay is usually included in order to preserve the causality of the digital filters. This operation typically involves the inversion of the matrix $\mathbf{H}$, which can be performed by applying various techniques, either in the time or frequency domain, and requires in general the use of regularization techniques (discussed in Chapter 6).

Other methods have been proposed, whose formulation includes the Kirchhoff-Helmholtz equation and the theory of inverse problems and acoustic holography (see, for example, [Ise99] and [CIB08]). Another relevant technique, very popular among the community of audio engineers, is the so-called *Vector Based Amplitude Panning*, proposed by V. Pulkki [Pul97]. In spite of its reduced DSP computational load (real gains applied to three

loudspeakers for reproducing a virtual source), this method features good capabilities of reproducing some physical attributes of the desired sound field. J.W. Choi's and Y.H. Kim's *acoustic contrast maximization* method [CK02] is also of relevance to the subject of sound field reproduction. This technique aims at the creation of so-called acoustically bright and dark zones with an array of loudspeakers.

Finally, several hybrid methods have been proposed: among the others, R. Nicol and M. Emerit [NE99] suggested a combination of Ambisonics and Holophony (an approach analogous to Wave Field Synthesis), while A. Farina et al. [FGAT01] suggested a combination of Ambisonics with binaural systems.

1.2.4 Functional analysis, integral equations and inverse problems in acoustics

In this thesis, mathematical concepts and techniques such as spaces of functions, integral equations and the singular value decomposition of an operator are applied to the problem of sound field reproduction. As mentioned above, these theoretical tools belong to the field of functional analysis. This branch of mathematics has been widely developed, especially during the last century, and its fundamentals are presented in a variety of texts, such as [Kre78], [Now81], [CK83], [Pot07].

Functional analysis has been successfully applied to the study of a variety of physical problems. A remarkable example is represented by quantum mechanics, but also several other branches of physics and engineering have made good use of many results from this discipline. Functional analysis has been used, for quite some time, to also tackle acoustical problems. An extensive mathematical literature exists, dedicated to the application of integral equation to direct and inverse acoustic scattering problems (see for example [CK92]). Integral equations have also been widely used in the study of acoustic radiation problems (see, for example, the work of L.G. Copley [Cop68] and of H.A. Schenck [Sch68]), and are at the basis of the *boundary element methods* (BEM) [VW04]. The singular value decomposition of integral operators has been deployed for the study of sound radiation and acoustic source reconstruction problems. In that respect, relevant contributions were given by G.V. Borgiotti et al. [Bor90], [BSWS90], [BJ93] and more recently by C. Maury et al. [ME05], [MB08].

As will become clear later, the mathematical formulation of the sound field reproduction problem as an inverse problem shares many similarities with the problem of acoustic source reconstruction and Near-Field Acoustical Holography (see, among the others, [VM89], [MWL85], [BSWS90], [Wil99], [WA79], [Sar05], [NY00], [YN00],[KN03],[WW97], [WY98], [Hal09]), Inverse Boundary Element Methods (see for example [VW04]) and active control of sound [NE92], [EF07]. All the techniques mentioned above have in common the fact that, from the knowledge of a portion of a given sound field, they aim at solving a

similar mathematical inverse problem, in order to either reconstruct the acoustic pressure and particle velocity fields near the source (acoustic holography), to identify the sources of sound generating a given field (source reconstruction) or to define the signals driving an array of secondary sources for canceling sound (active noise control) or synthesizing a given sound field (sound field reproduction).

The work presented in this thesis has been significantly inspired by the literature dedicated to all the techniques for sound field analysis and reconstruction mentioned above. It is therefore the hope of the author that the results shown here, although developed in the framework of sound field reproduction, may be also useful for further developments and comparative analysis between these techniques.

1.3 Overview of the method and summary of the thesis

In what follows an overview is given of the approach developed throughout this thesis and of the underlying assumptions. The aim is to provide the reader with a general and intuitive understanding of the subject, in order to facilitate the reading of the theoretical core of this thesis, in which the mathematical formalism may sometimes hide the physical and practical meaning of the results developed.

A preliminary chapter has been included, Chapter 2, which presents the mathematical formalism used in this thesis. Some important mathematical concepts and results are recalled, and some other less widely known concepts are reported from the literature. No effort is made in this preliminary chapter to explain the physical interpretation of the concepts introduced or their usefulness to the problem under consideration, as this is the objective of the subsequent chapters of the thesis.

Chapters 3 and 4: The inverse problem and its solution

The starting idea includes the reproduction of a sound field over a given region of space. A generic sound field can be characterized by the acoustic pressure. The latter can be mathematically represented by a *scalar field*, that is a function which describes the acoustic pressure as a function of the space and time. The sound field is therefore represented by the function $p(\mathbf{z}, t)$, where $\mathbf{z}$ is a vector representing a position in space and t is the time. For reasons which will become clear later, it is preferable to describe the acoustic field as a function of the frequency ω or equivalently of the wave number k, rather than of the time. This is simply achieved by applying the well-known Fourier transform, with respect to the variable t, to the function describing the sound field.

A region of the space is defined, over which an attempt is made to reproduce the desired field. This region is referred to as the control region, and is indicated in Figure 1.1 by

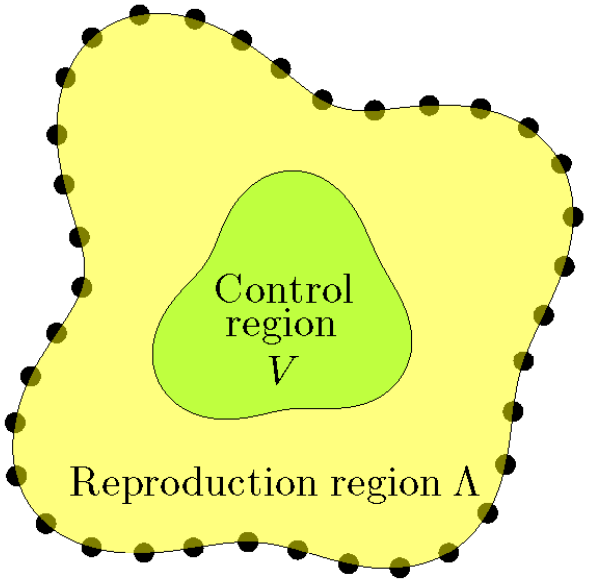

FIGURE 1.1: Two-dimensional diagrammatic representation of the control region, of the reproduction region and of the secondary sources (the black dots).

the letter V. The reproduction region can be a subset of either the three dimensional space $\mathbb{R}^3$ or of the two dimensional space $\mathbb{R}^2$. The diagram in Figure 1.1 represents a two dimensional setting, in order to simplify the visualization. It is assumed that the target sound field satisfies the homogeneous wave equation within the control region. In practical terms, this means that the control region should be free of sources of sound or scattering objects.

An attempt is made to reproduce the target acoustic field with an array of loudspeakers. The latter includes a limited number of electroacoustical transducers (represented by the black dots in Figure 1.1), which radiate sound in the space when fed by an electrical signal. Clearly, the sound fields generated by the different units of the array combine and produce a complex pattern of constructive and destructive acoustic interferences. The resulting field is referred to as the reproduced field $\hat{p}(\mathbf{z}, \omega)$. The loudspeakers of the array are also referred to as the secondary sources. These are driven by electrical signals, which are referred to as secondary source signals or secondary source strength (the difference between the two terms is clarified later). The assumption is made, that the loudspeakers are arranged on the boundary of a region of the space Λ, the reproduction region, which contains the control region V in its interior, as shown in Figure 1.1.

In order to deploy some relevant mathematical properties (more precisely, the compactness of the integral operator involved), useful to the solution of the acoustical inverse problem, the reproduction region Λ and the control region V should be *bounded* regions, meaning that they should have finite extension in the space. In spite of that, in Chapter

4 of this thesis an attempt is made to extend the approach developed also to cases when Λ and V are not bounded.

The objective is to define the secondary source signals, which allow for a reproduced field that is as similar as possible to the target field. As mentioned previously, this is the essence of the acoustical inverse problem addressed by this thesis.

A crucial step, which allows the link of the problem under consideration to the theory of integral equations, lies in the model of the loudspeaker array. The latter includes the following ideal assumptions:

- The number of loudspeakers (secondary sources) is infinite and these are continuously arranged on the boundary of Λ;
- Each loudspeaker (secondary source) radiates sound as an ideal omnidirectional point source (an acoustic monopole) for the three dimensional case, or as an ideal infinite line source (perpendicular to the plane considered) for the two dimensional case.

The first assumption is clearly unrealistic and has the drawback of completely neglecting the relevant problem know as *spatial aliasing*. This is directly related to the sampling theory and to the well-known aliasing phenomenon arising in the reproduction of a sampled function of time. This problem arises when approaches developed under the assumption of an ideally continuous distribution of loudspeakers are applied to real arrays with a finite number of transducers and has the effect of degrading the sound field reproduction performance of a system, especially at high frequencies. An extensive section of Chapter 7 is dedicated to the detailed analysis of the consequences of this assumption. For the time being, it suffices to say that the analytical results presented in what follows can be safely applied to real cases, provided that the operating wavelength is larger than the maximum distance between neighboring loudspeakers.

The second assumption is quite mild for the three dimensional problem, especially if the wave length of the sound to be reproduced is large in comparison the size of the single loudspeakers. For the two dimensional case the loudspeakers are assumed to be infinite line sources. This represents a less realistic assumption, due to the fact that traditional, compact loudspeakers exhibit a spherical spreading of acoustic energy, instead of the cylindrical decay typical of a line source. This problem is widely discussed in the literature on Wave Field Synthesis, and strategies have been developed to take this aspect into consideration (see for example [Sta97] for the 2.5 *operator* based on the stationary phase approximation). Other characteristics of real loudspeakers, such as diffraction of the loudspeaker cabinet, frequency response and non-linear distortion have also been neglected.

A further relevant assumption is made, that the loudspeakers radiate sound in the free field. In principle, this assumption could be removed and the approach developed may be extended to reverberant environments, but this would superpose, in a way, the problem of sound field reproduction with the problem of active room correction.

The ideal model of the loudspeaker array introduced above allows for the expression of the reproduced sound field at the location $\mathbf{z}$ and for a given frequency ω as an integral of the form

$$\hat{p}(\mathbf{z},\omega) = \int_{\partial\Lambda} G(\mathbf{z},\mathbf{y},\omega)a(\mathbf{y},\omega)dS(\mathbf{y})$$

where the function $G(\mathbf{z},\mathbf{y},\omega)$ represents the acoustical transfer function between the secondary source arranged at $\mathbf{y}$ and the location $\mathbf{z}$, and under the assumptions above corresponds to the so-called free field Green function. The form $a(\mathbf{y},\omega)$ is a complex valued function (having magnitude and phase), proportional to the strength of the secondary sources. The integral above is know in the literature as the *acoustic single layer potential* and is one of the fundamental mathematical entities occurring in this thesis.

The objective is now to compute a function $a(\mathbf{y},\omega)$, that is the solution of the inverse problem, such that the reproduced field is as similar as possible to the target sound field. In the ideal case, we would be able to define a source strength $a(\mathbf{y},\omega)$, such that the left hand side of the single layer potential above is the target field $p(\mathbf{z},\omega)$.

In Chapter 3, the following important concept is introduced (the uniqueness of the Dirichlet problem): if the desired sound field satisfies the homogeneous wave equation in V, the knowledge of the acoustic pressure on the *boundary* of V (and not of both the pressure and its normal derivative) *uniquely* defines the sound field in the *interior* of V. This is always valid, except for a countable set of wave numbers identified by the resonance frequencies of V. In Chapter 6 it is explained that the solution of the inverse problem involved is non unique at these frequencies, and some simple strategies are illustrated for avoiding this problem. The control of the sound field can be therefore restricted to the boundary of the control region. The function representing the restriction of the target field to this boundary is referred to as the *pressure profile*. The unknown source strength $a(\mathbf{y},\omega)$ can therefore be determined from the knowledge of the target sound field on the boundary of the control volume. Since the unknown of the problem appears as a member of the argument of an integral, an *integral equation* is involved, more specifically a Fredholm integral equation of the first kind, .

Some fundamental question arise: Does a solution of this integral equation exists? And does it exists for any desired sound field or just for some families of fields? If the solution exists, is it possible to calculate it? How? Is the solution unique or do multiple solutions exist? And if the solution does not exists, is it possible to find an approximate solution? In order to give a rigorous answer to these questions, we need to dip into the mathematics and make use of the tools and results of functional analysis. This analysis is presented in chapters 3, 4, 5 and 6 of this thesis. Fortunately, integral equations of the first kind are

well-known in the literature. Unfortunately, such equations represent so called *ill-posed problems*. This implies, in short, that no guarantee is given about the existence of a solution, and even when this exists it might not be unique, or its computation could be severely compromised by the presence of errors in the data associated with the problem.

All the concepts introduced above are presented rigorously in the first half of Chapter 3. The following logical step would be to discuss under what conditions the solution of the problem exists and is unique. However, the choice is made to assume initially that a solution exists and is unique, and to focus the attention on how to calculate this solution analytically. For this purpose, the *singular value decomposition* of a compact linear operator is introduced and applied to the integral operator in question. This powerful mathematical tool plays a crucial role in the development of most of the results derived in this thesis. It should be highlighted that the singular value decomposition of a compact linear operator is related though not identical to the singular value decomposition of a matrix, the former requiring for its derivation advanced mathematical concepts of functional analysis. One section of Chapter 2 is dedicated to the mathematical fundamentals of the singular value decomposition, while the second half of Chapter 3 illustrates the application of this technique to the specific problem under consideration.

Particular attention is given to the concepts of *secondary source modes* and *acoustic pressure modes*, which can be summarized as follows: the sound field generated by the array on the boundary of the control region (the pressure profile) can be decomposed into a usually infinite series of orthogonal functions (namely, independent from one another), referred to as the acoustic pressure modes. Each of these modes is generated by one and only one secondary source mode, that can be interpreted as a special combination of signals of the secondary sources. Each pressure mode is independent from all secondary source modes other than the one corresponding mode. The acoustic pressure modes and secondary source modes are represented in mathematical terms by the *singular functions* of the operator. The relation between the magnitude of the secondary source modes and of the corresponding acoustic pressure modes is expressed by a set of positive scalars called the *singular values* of the operator, which can be interpreted as a measure of the *modal efficiency*.

At the end of Chapter 3 a general analytical solution of the inverse problem under consideration is derived by means of the *singular system* of the operator, that is the set of all the singular functions and singular values of the integral operator. However, in spite of the generality of this solution, explicit expressions for the functions constituting the singular system depend strongly on the specific geometry of the array and of the control region, and their computation is in general non-trivial.

In Chapter 4 singular systems for some specific geometries of continuous arrays are derived, as well as explicit expressions of the secondary source strength. The case of spherical geometry is studied, and it is shown that the singular functions are strictly

related to the spherical harmonics, while the expression of the singular values includes spherical Hankel and Bessel functions, whose arguments are the wave number k and the radii of the control region and of the array. The singular system and the solution are then derived for the corresponding 2D problem, namely the circular geometry. It is shown that the singular functions are related to complex exponential functions and the singular values to Hankel and Bessel functions.

An attempt is then made to extend the approach to the case of loudspeaker arrays including a continuous distribution of secondary sources on an infinite plane or on a line. These arrangements violate the requirement of the reproduction region Λ being a bounded set. As it is mentioned at the beginning of Section 4.3, the violation of this assumption generates some mathematical difficulties (for example, the integral operator is not compact), which add several layers of complexity to the problem. However, some simplifying assumptions are made in order to go around these issues. This effort is rewarded by the finding of some interesting results: the secondary source modes are expressed by complex exponential functions, which generate either *propagating* or *evanescent* plane waves. The efficiency of each mode is put into relation with the evanescent or propagating nature of the corresponding plane wave, and in the second case also with the direction of propagation of the wave.

Chapters 5 and 6: The ill-posedness of the problem

The expressions of the singular systems derived in Chapter 4 prove to be useful for the analysis undertaken in Chapter 5. The latter is dedicated to the study of the ill-posedness of the problem under consideration. This is probably the part of this work, which is most dedicated to the underlying mathematics of the problem. The concept of ill-posedness is explained, and it is put into direct relation with the singular value decomposition of the integral operator involved. More precisely, it is shown that the ill-posedness is related to the decay of the singular values of the operator. In fact, the expression of the solution includes the inverse of the singular values, and it is clear that if one or more singular values are very small or close to zero, the amplitude of the solution will tend to infinity. This is a fundamental concept of the problem addressed here.

Attention is then focussed on the properties that the target sound field should posses in order for the solution of the inverse problem to exist. The so-called Picard theorem plays a central role in this study. The latter is introduced at the end of Chapter 2. This theorem defines two conditions, which the target sound field must satisfy in order for a solution to exist. Some theorems are presented and proved, which show firstly that the first Picard condition (relating the target field with the nullspace of the adjoint operator S^*) is satisfied for all sound fields satisfying the conditions imposed at the outset (the target field satisfies the homogeneous wave equation in V). Secondly, it is shown that the second Picard condition (relating the singular values of the operator with

the orthogonal projection of the target field onto the singular functions) is not satisfied by a restricted family of fields. It is demonstrated that the second Picard condition is satisfied by all fields generated by source of sound (or scattering objects) lying outside of the reproduction region, that is outside of the speaker array. Conversely, sound fields due to sources lying outside of the control region V but within the reproduction region Λ (see Figure 1.1) do not admit an exact solution, that is they can not be reproduced by the continuous loudspeaker array. On the other hand, it is shown that it is possible to compute solutions such that the reproduced field is an arbitrarily good approximation of the target field (this result arises from the denseness of the range of the operator S). However, the better the approximation the larger is the amplitude of the secondary source strength and the more the solution is unstable.

Subsequently, the concept of ill-conditioning and robustness of the solution against errors is addressed and again put into relation with the singular system of the operator. The uniqueness of the solution is then analyzed, and it is shown that the latter is strictly related to the so-called Dirichlet eigenvalues of V. These are introduced in Chapter 3 when discussing the uniqueness of the Dirichlet problem, and are identified by the resonance frequencies of a cavity with the shape of V and pressure release boundary conditions. It is shown that when the wave number k corresponds to one of the Dirichlet eigenvalues, the inverse problem has an infinite number of solutions allowing for an exact reproduction of the pressure profile (the field on the boundary of V), but only one of these solutions leads to an exact reproduction of the sound field in the interior of the control region.

In the remainder of Chapter 5, the concepts above are demonstrated for spherical and linear array geometries, for the case of target fields due to ideal omnidirectional point sources or line sources, respectively, which are referred to as *virtual sources*.

In Chapter 6 several strategies are presented for overcoming the different difficulties arising from the ill-posedness of the inverse problem. The concept of *regularization* is introduced and several regularization schemes are presented, such as *spectral truncation*, *spectral damping* and *Tikhonov regularization*. The method know as *time reversal mirror* is also taken into consideration as a regularization method. These techniques are discussed especially in relation with the singular system of the integral operator involved, and it is shown that their application has the effect of preventing the undesirable effects arising from the inversion of small singular values, often at the price of partially reducing the accuracy of the reproduced field. The application of regularization techniques is applied to the computation of stable and robust solutions. Special attention is dedicated to so-called focused sources. This term refers to sound fields generated by point or line sources lying in the exterior of the control region V but in the interior of the reproduction region Λ. As mentioned above, this family of sound fields does not allow for an exact solution, but the application of regularization techniques allows for the computation of approximate solutions (with bounded norm). The latter are derived

for linear, planar and spherical geometry. The first two examples are of special relevance, since they highlight the relation between the ill-posedness of the inverse problem and the attempt to reproduce the so-called *pseudo-evanescent* component of the target field. The latter is the component of the desired pressure profile, which is generated by pressure modes corresponding to evanescent waves (but does not necessarily represent the evanescent component of the target field). The interesting result arises, that the time reversal method provides an exact representation of the pseudo-propagating part of the target field, but leads to the generation of the pseudo-evanescent field due to a virtual source located at a mirrored position with respect to the linear or planar array.

In the second half of Chapter 6 the relevant analogy is drawn between the problem of sound field reproduction and the theories of scattering of sound and of Near-Field Acoustical Holography. This analogy is an important outcome of the application of functional analysis to sound field reproduction. The analysis begins with the discussion of the fact that the ill-conditioning of the problem is greatly affected by the distance between the boundary of the control volume and the boundary of the reproduction region, the latter corresponding to the layer of secondary sources. The larger this distance, the more severe are the effects of ill-conditioning of the problem. This phenomenon is well known in Near-Field Acoustical Holography, and it is shown that the ill-posed nature of acoustic holography is very similar, though not identical, to the problem of sound field reproduction, and the theories behind these two subjects benefit from some common mathematical similarities.

In light of the considerations above, the special case is considered when the control region V and the reproduction region Λ coincide, namely when the layer of secondary sources coincides with the boundary of the control region. It is shown that in this case the problem is only *mildly ill-posed* (the decay of singular values is linear rather than exponential) and can be solved by a straight-forward application of the so called *jump relation*, introduced in Chapter 2. Consequently, it is shown that the sound field reproduction problem can be reformulated in the form of an *equivalent scattering problem*. More specifically, the determination of the source strength $a(\mathbf{y})$ is equivalent to the determination of the normal particle velocity of the total field originating from the scattering of the target field by an object with the shape of the reproduction region and pressure release boundaries (also referred to as a *sound soft* object). It is shown that, in the case of planar and linear geometry, the single layer potential reduces to the well-known first Rayleigh integral formula. This important analogy allows for an explicit connection between the theory of acoustic scattering and sound field reproduction.

A relevant outcome of the above consists of the application of the so called *Kirchhoff approximation*, well-known in the study of scattering phenomena, to the solution of the reproduction problem. This approximation is typically applied when the wavelength of the sound to be reproduced is short in comparison to the characteristic dimension of the array, and allows for a simple computation of the source strength form the value of

the normal derivative of the desired field (evaluated on a portion of the boundary of the reproduction region). As mentioned at the end of the chapter, the result above allows for a rigorous interpretation of some techniques commonly used in Wave Field Synthesis and sheds light on the relation of the latter with High Order Ambisonics.

Chapters 7 and 8: Practical realization and experiments

The first section of Chapter 7 is dedicated to the study of the effects and undesired artifacts arising from the application of the result derived under the assumption of a continuous distribution of secondary sources to arrays including a finite number of elements. For this purpose, a sampling theory is discussed, in order to provide a mathematical explanation of the issues above. The phenomenon known as *spatial aliasing* is studied in detail, especially in relation to the singular system of the integral operator in question. The concepts of pre- and post-aliasing are defined and their difference explained. It is shown that the technique referred to as *spectral truncation* can be applied in order to reduce the undesired effect of pre-aliasing (but not post-aliasing!). In short, this technique involves the truncation of the series arising in the expression of the solution by means of the singular system of the integral operator. The *aliasing matrix* is defined and is used in order to provide a greater insight into the computation of the sampling reproduction error. The relevant conclusion is made that spatial aliasing always occurs (except in a few very special cases), and its effect can at most be reduced or might be negligible, but can never be completely removed.

The results above are demonstrated for the case of spherical and linear geometry, and explicit expressions for the aliasing error are derived. In the former case the effect is demonstrated of two different choices of the truncation order (representative of the number of terms included in the series expression of the solution). The case of linear geometry is studied with special attention to the case of uniform sampling and of reproduction of a plane wave. It is shown that under given conditions on the attributes of the desired plane wave, the effect of spatial aliasing can be limited to the near field of the array. If these conditions are violated, the reproduction artifacts effect also the far field. In the worse case, the reproduction of an evanescent plane wave can generate an undesired aliased plane wave which propagates to the far field.

In the second Section of Chapter 7 an alternative method for the solution of the acoustical inverse problem addressed is presented. This method involves the numerical solution of the integral equation involved, which implies the discretization of the functions representing the pressure profile and the source strength. This method can be regarded as a boundary element method. Attention is drawn to the fact that spatial aliasing can occur also from the discretization of the pressure profile. This is not the case for the other solution method presented, involving the singular value decomposition of the operator,

for which the pressure boundary is supposed to be known at all locations on the control boundary. The numerical methods involves the creation and inversion of a matrix ($\mathbf{S}$), which can be regarded as the inversion of the discretized version of the single layer potential introduced above. It is shown that the singular value decomposition of this matrix, in the limiting case when its two dimensions are both infinity and for spherical geometry, gives singular vectors and singular values, which coincide with the singular system generated by the singular value decomposition of the integral operator discussed in the previous chapters.

At the beginning of Chapter 3 the time dependency of the sound field is substituted with the dependency on the frequency ω, or equivalently on the wave number k, and the choice is made to study the problem for a single wave number. This is equivalent to the assumption that the target field is monochromatic. In the last section of Chapter 7 this hypothesis is removed and attention is focused on target sound fields with a broad band spectral content. The problem is addressed of deriving the source signals, which are required for the reproduction of such fields. Special attention is dedicated to the computation of filters, which can be applied to generate the loudspeaker signals for the reproduction of a large family of sound fields, such as those generated by a motionless, single source (either in the free field or in a reverberant environment). These filters are expressed both as functions of time and of frequency, and can be practically implemented as FIR digital filters (one filter for each loudspeaker of the array).

Results are derived for the specific cases of spherical, circular, planar and linear geometries. Much attention is dedicated to the case of spherical geometry, since this geometry is chosen for the experiments presented in Chapter 8: The filters for a single virtual source in the free field are derived, and the effects of the distance of the source and of the choice of the truncation order are illustrated. It is shown that the filters exhibit a high frequency asymptotic behavior, corresponding to a so called *panning function*. The latter can be effectively adopted as a high frequency or far field approximation of the filters, and includes simple, frequency -independent scalars, implementable as simple gains rather than complex filters. Remarkable analogies can be drawn between this panning function and elements of High Order Ambisonics theory.

For the case of linear and planar geometries, it is shown that the loudspeaker signals for a single virtual source in the free field can be computed mainly by applying a set of simple delays and gains to a pre-processed single (mono) signal, these delays and gains depending on the reciprocal location of the virtual source and of the secondary sources. The connection of this result with Wave Field Synthesis theory is highlighted.

Chapter 8 describes the design and realization of experiments for validating part of the theoretical results presented in this thesis. Firstly, the experimental arrangement is discussed. This includes a spherical array of forty loudspeakers, which was built in the large anechoic chamber of the ISVR and which was used to reproduce the field due to a

single virtual source. A translating linear array of microphones was used to measure the target and reproduced fields, the former being generated by a single loudspeaker arranged in the location of the virtual source. Secondly, the measurement procedure is presented, followed by a discussion of the design of the specific digital filters, which were used for the generation of the loudspeaker signals. The design follows the theoretical results derived in the previous chapters of the thesis, with the addition of practical solution for the specific processing of low and high frequencies (below 100 Hz and above 1.5 kHz, respectively). Finally, the experimental results are presented and their consistency with the theoretical analysis is shown.

Chapter 2

Mathematical preliminaries

In this Chapter the mathematical notation used throughout this thesis is presented, and some mathematical concepts and results relevant to this work are recalled. Special attention is dedicated to the introduction of several special functions and of some elements of set theory. The fundamentals of the Fourier series and Fourier transform are reviewed. In the final part of this chapter the mathematical fundamentals are presented of the integral representation of sound fields and of the singular value decomposition of a compact operator. The application to physical processes of these more advanced subjects, as well as their relevance to the problem under consideration, are discussed in the following chapters of this thesis.

2.1 Notation and definitions

In this thesis, lower case boldface letters are used to represent vectors and lower case italic letters generally represent scalars, functions or scalar fields. Upper case boldface letters represent matrices and upper case italic letters generally represent operators, sets or functions of time (while the related functions of frequency are represented by the corresponding lower case letters).

The superscript * represents, for a scalar, the complex conjugate and for an operator its adjoint. The symbol $i = \sqrt{-1}$ is the imaginary unit, and δ_{nm} is the Kronecker delta ($\delta_{nm} = 1$ if $n = m$, $\delta_{nm} = 0$ if $n \neq m$). The notation $x \in X$ indicates that x is in the set X, meaning that x is an element of X. The notation $x := \cdots$ has the meaning that the symbol x is defined by the given expression (for example, $x := a + b$). The symbol $\forall$ is the universal quantifier symbol. For example, the expression $\forall n \in \mathbb{N}, 2n > 0$ means that *for all* elements n of $\mathbb{N}$, $2n > 0$.

Let D be a bounded subset of the three dimensional or two dimensional space, with boundary ∂D. $\hat{\mathbf{n}}(\mathbf{z})$ is the unitary vector perpendicular to ∂D at $\mathbf{z} \in \partial D$, pointing

towards the exterior of D. When there is no risk of ambiguity, the short notation $\hat{\mathbf{n}}$ is used. The normal derivative $\nabla_{\mathbf{n}} f(\mathbf{z})$ of the function $f(\mathbf{z})$ is defined by

$$\nabla_{\mathbf{n}} f(\mathbf{z}) := \nabla f(\mathbf{z}) \cdot \hat{\mathbf{n}}(\mathbf{z}) = \frac{\partial f(\mathbf{z})}{\partial \hat{\mathbf{n}}(\mathbf{z})} \tag{2.1}$$

2.1.1 Vectors and matrices

The norm and the direction of a given vector $\mathbf{x} = [x_1, x_2, x_3]$ are respectively represented by

$$x = |\mathbf{x}| := \sqrt{\sum_{n=1}^{3} |x_n|^2}, \qquad \hat{\mathbf{x}} := \frac{\mathbf{x}}{|\mathbf{x}|} \tag{2.2}$$

The relation between Cartesian and polar co-ordinates defining the position vector $\mathbf{x}$ is

$$\mathbf{x} = [x_1,\ x_2,\ x_3] = [x \cos\phi_x \sin\theta_x,\ x \sin\phi_x \sin\theta_x,\ x \cos\theta_x] \tag{2.3}$$

Given two vectors $\mathbf{x}, \mathbf{y} \in \mathbb{R}^n$, their *scalar product* is defined by

$$\langle \mathbf{x} | \mathbf{y} \rangle = \mathbf{x} \cdot \mathbf{y} := \sum_{n=1}^{N} x_n^* y_n \tag{2.4}$$

It holds that

$$\mathbf{x} \cdot \mathbf{y} = (\mathbf{y} \cdot \mathbf{x})^* \tag{2.5}$$

The superscript $^{\mathrm{H}}$ represents the Hermitian transpose (complex conjugate transpose) of a matrix or of a vector.

2.1.2 Integrals

Given the set D, the integration of an integrable function $f(\mathbf{x})$ over the boundary ∂D is represented by

$$\int_{\partial D} f(\mathbf{x}) dS(\mathbf{x}) \tag{2.6}$$

where $dS(\mathbf{x})$ represents the infinitesimal fraction of the boundary ∂D, with the appropriate parametrization. For example: if $D = \mathbb{R}$ (the set of real numbers), then $dS(\mathbf{x}) = dx$ (in this case, $dS(\mathbf{x})$ might be substituted by dx), if D is a circle of radius R, then $dS(\mathbf{x}) = R\ d\phi$, if D is a sphere of radius R then $dS(\mathbf{x}) = R^2 \sin\theta\ d\phi\ d\theta$ and so on. In general, if D is a subset of $\mathbb{R}$ then $dS(\mathbf{x})$ is an infinitesimal line segment, while if $D \subseteq \mathbb{R}^2$, $dS(\mathbf{x})$ is an infinitesimal surface. In the case of integration over a volume, $dS(\mathbf{x})$ is an infinitesimal volume and might be substituted by $dV(\mathbf{x})$.

2.1.3 Sets

A set D is usually defined either by an explicit list of its elements, that is

$$D := \{x_1, x_2, \cdots\} \tag{2.7}$$

or by expressing the properties that its elements x must satisfies, as for example

$$D := \{x \in \mathbb{R} : x > a\} \tag{2.8}$$

(i.e. D is the set of all elements x of $\mathbb{R}$ such that x is greater than a).

The following lists some of the sets used in this thesis[1]:

$\mathbb{N}$	the set of natural numbers (including zero)
$\mathbb{Z}$	the set of integer numbers
$\mathbb{Q}$	the set of rational numbers
$\mathbb{R}$	the set of real numbers
$\mathbb{R}^m$	the m-dimensional Euclidean space, $\{x = (x_1, x_2, \cdots, x_m) : x_1, x_2, \cdots, x_m \in \mathbb{R}\}$
$\mathbb{C}$	the set of complex numbers
Ω_R	sphere of radius R, $\{\mathbf{x} \in \mathbb{R}^m : \lvert\mathbf{x}\rvert = R\}$
Ω	unitary sphere (sphere with radius $R = 1$)
B_R	ball of radius R, $\{\mathbf{x} \in \mathbb{R}^m : \lvert\mathbf{x}\rvert < R\}$
$L^2(D)$	The set of square integrable functions defined on the domain D, $\left\{f(\mathbf{x}) : \int_D \lvert f(\mathbf{x})\rvert^2 dS(\mathbf{x}) < \infty\right\}$

Given two sets A and B, the notation $A \subset B$ indicates that A is a subset of B (the notation $A \subseteq B$ indicates that A may also coincide with B). For example, we have that $\mathbb{N} \subset \mathbb{Z} \subset \mathbb{Q} \subset \mathbb{R} \subset \mathbb{C}$.

We define

$$\begin{aligned} D &= A \oplus B &&:= \{x = a + b :\ a \in A,\ b \in B\} && \text{(direct sum)} \\ D &= A \backslash B &&:= \{x \in A : x \notin B\} && \text{(subtraction)} \end{aligned} \tag{2.9}$$

For a given open set D, the symbol ∂D represents the *boundary* of D and the symbol $\overline{D}$ represents the *closure* of D, that is the union of D with its boundary (or equivalently the union of D with the set of its accumulation points [Kre78]). A given set D is said to be *closed* if it contains its boundary ($\overline{D} = D$).

[1] A more rigorous definition of L^2 includes the concept of *completion of a normed space* or *quotient space* [Kre78], which are not discussed in this thesis.

Given two square integrable functions f and g defined on D, their *scalar product* is defined by [2]

$$\langle f|g\rangle_D := \int_D f(\mathbf{x})^* g(\mathbf{x}) dS(\mathbf{x}) \tag{2.10}$$

and the L^2 norm of f is

$$||f||_D := \sqrt{\int_D |f(\mathbf{x})|^2 dS(\mathbf{x})} = \sqrt{\langle f|f\rangle_D} \tag{2.11}$$

The subscripts $_D$ can sometimes be omitted.

f is said to be *orthogonal* to g if

$$\langle f|g\rangle_D = 0 \tag{2.12}$$

Given a subspace $\Psi \subset L^2(D)$, the *orthogonal complement* of Ψ is defined by

$$\Psi^\perp := \{p_{\Psi^\perp}(\mathbf{x}) \in L^2(D) : \forall p_\Psi(\mathbf{x}) \in \Psi, \langle p_\Psi | p_{\Psi^\perp}\rangle_D = 0\} \tag{2.13}$$

Given $p(\mathbf{x}) \in L^2(D)$ and the relation

$$p(\mathbf{x}) = p_\Psi(\mathbf{x}) + p_{\Psi^\perp}(\mathbf{x}), \quad p_\Psi(\mathbf{x}) \in \Psi,\ p_{\Psi^\perp}(\mathbf{x}) \in \Psi^\perp \tag{2.14}$$

the function $p_\Psi(\mathbf{x})$ is referred to as the *orthogonal projection* of $p(\mathbf{x})$ onto the subspace Ψ. The *orthogonal projection operator* P_Ψ maps $p(\mathbf{x}) \in L^2(D)$ into its orthogonal projection onto Ψ. This means that, with reference to the equation above, $(P_\Psi p)(\mathbf{x}) = p_\Psi(\mathbf{x})$ (refer to the discussion of operator notation below).

The *span* of a set constituted by the N functions $p_n(\mathbf{x}) \in \Psi \subseteq L^2(D)$ is given by all possible linear combinations of these functions, that is

$$\text{span}\{p_n\} := \left\{ p(\mathbf{x}) : p(\mathbf{x}) = \sum_{n=1}^{N} a_n p_n(\mathbf{x}), \quad a_n \in \mathbb{C} \right\} \tag{2.15}$$

The set of functions $p_n(\mathbf{x}) \in \Psi \subseteq L^2(D)$ is said to be a *complete set* or *complete system* for Ψ if the closure of its span equals Ψ, that is

$$\overline{\text{span}\{p_n\}} = \Psi \tag{2.16}$$

In this case, $\text{span}\{p_n\}$ is said to be *dense* in Ψ.

More generally, a set $X \subseteq \Psi$ is said to be *dense* in Ψ if

$$\overline{X} = \Psi \tag{2.17}$$

[2] Formula (2.10) defines the scalar product usually adopted for L^2 spaces in connection with the L^2 norm (2.11). The reader can refer to [Kre78] for a more general definition of scalar product.

that is if for any function $p(\mathbf{x}) \in \Psi$ and for any $\epsilon > 0$, a function $p_\epsilon(\mathbf{x}) \in X$ exists, such that

$$||p - p_\epsilon|| \leq \epsilon \tag{2.18}$$

An *orthonormal set* of functions $\{p_n(\mathbf{x})\}$ is defined as a set of functions which have unitary norm and are orthogonal to one another. This implies that for any function p_n, p_m of that set, the following relation holds:

$$\langle p_n | p_m \rangle = \delta_{nm} \tag{2.19}$$

From the results presented above it follows that, if the set of the N orthonormal functions $p_n(\mathbf{x})$ is a complete set for Ψ, then any function $p(\mathbf{x}) \in \Psi$ can be expressed as the sum of its orthogonal projections $(P_n p)(\mathbf{x})$ onto the orthogonal subspaces spanned by each function $p_n(\mathbf{x})$. Therefore, in view of the definition of the scalar product (2.10), it is possible to write [3]

$$p(\mathbf{x}) = \sum_{n=1}^{N} (P_n p)(\mathbf{x}) = \sum_{n=1}^{N} \langle p_n | p \rangle_\Psi \; p_n(\mathbf{x}) \tag{2.20}$$

where N equals the dimension of the space Ψ. This might take the value of infinity or might be a finite number. The series above corresponds to a generalized Fourier series of the form (2.69) discussed below.

2.1.4 Operators

A given operator S acting between two normed spaces A and P is introduced as follows:

$$S : A \to P$$

Given two function $a(\mathbf{y}) \in A$ and $p(\mathbf{x}) \in P$, the following notation is used throughout this thesis:

$$(Sa)(\mathbf{x}) = p(\mathbf{x})$$

or equivalently

$$Sa = p \qquad \text{or} \qquad \big[Sa(\cdot)\big](\kappa) = p(\kappa)$$

This notation, widely used in the mathematics literature, is slightly different from the notation adopted in the engineering literature, in the fact that the variable appearing in the left hand side, $\mathbf{x}$, is the variable belonging to the domain of the function $p(\mathbf{x}) \in P$. For example, if the operator considered is the Fourier Transform $\mathcal{F}$ (see Section

[3] The equality is valid in the sense of the metric associated to the normed space under consideration (L^2 norm in this thesis).

2.3), which transforms the function $a(y)$ into the function $p(\kappa)$, the notation adopted is $(\mathcal{F}a)(\kappa) = p(\kappa)$, while other authors prefer the notation $\mathcal{F}[a(y)] = p(\kappa)$.

Given the operator $S : A \to P$ and two functions $a \in A$ and $p \in P$ the *adjoint operator* S^* of S, sometimes also referred to as *Hilbert adjoint* operator [Kre78], is defined to be such that

$$\langle Sa|p\rangle_{\partial V} = \langle a|S^*p\rangle_{\partial\Lambda} \tag{2.21}$$

If $S^* = S$, then S is said to be *self adjoint*.

The *range* $S(A)$ of the operator S acting from the space A into the space P is the subset of P containing all the functions, which can be generated by S acting on the functions in A. It is defined by

$$S(A) := \{p = Sa,\ a \in A\} \tag{2.22}$$

The *nullspace* $N(S)$ of the operator S acting from the space A into the space P is the subspace of A containing those functions, on which the action of S gives zero as a result. It is defined by

$$N(S) := \{a \in A : Sa = 0\} \tag{2.23}$$

2.2 Special functions and distributions

Dirac delta function

The *Dirac delta function* [4] $\delta(x)$ can be defined by the following properties [NE92, p.45]

$$\begin{aligned} \delta(x) &= 0, \quad x \neq 0' \\ \int_{-\infty}^{\infty} \delta(x)dx &= 1 \end{aligned} \tag{2.24}$$

The Dirac delta function has the following properties:

$$\int_{-\infty}^{\infty} \delta(x - x')dx = 1 \tag{2.25}$$

$$\int_{-\infty}^{\infty} f(x)\delta(x - x')dx = f(x') \quad \text{[sifting property]} \tag{2.26}$$

where the function $f(x)$ is continuous at $x = x'$. For the integration over a bounded, open interval $(-L, L)$ it holds that

$$\int_{-L}^{L} f(x)\delta(x - x')dx = f(x'), \qquad x' \in (-L, L) \tag{2.27}$$

[4] The Dirac delta function is usually regarded as a generalized function, and can be formally defined as a distribution.

It is possible to extend the definition of the Dirac delta function to a bounded or unbounded multi-dimensional domain D. It holds that

$$\int_D \delta_D(\mathbf{x}) dS(\mathbf{x}) = 1 \tag{2.28}$$

$$\int_D f(\mathbf{x})\delta_D(\mathbf{x}-\mathbf{x}')dS(\mathbf{x}) = f(\mathbf{x}'), \quad \mathbf{x}' \in D \tag{2.29}$$

where $f(\mathbf{x})$ is assumed to be continuous at $\mathbf{x} = \mathbf{x}'$. In this thesis, when no risk of confusion arises, the subscript $_D$ may be omitted.

The comb function

The comb function $\text{Ш}(x/a)$ is a series of Dirac delta functions and is defined by

$$\text{Ш}\left(\frac{x}{a}\right) := |a| \sum_{n=-\infty}^{\infty} \delta(x - na) \tag{2.30}$$

This function has the remarkable property that its Fourier transform is also a comb function [Wil99], namely

$$\int_{\mathbb{R}} \text{Ш}\left(\frac{x}{a}\right) \frac{e^{-i\kappa x}}{\sqrt{2\pi}}\, dx = \sqrt{2\pi} \sum_{n=-\infty}^{\infty} \delta\left(\kappa - n\frac{2\pi}{a}\right) \tag{2.31}$$

For this identity, it holds that $\mathcal{F}^{-1}\text{Ш} = \mathcal{F}\text{Ш}$. This equality holds only for the definition of direct and inverse Fourier transform given by equations (2.74) and(2.75), respectively.

The following relation holds [Wil99]

$$\text{Ш}\left(\frac{x}{a}\right) = \sum_{n=-\infty}^{\infty} e^{i2\pi nx/a} \tag{2.32}$$

This is often referred to as the Poisson sum formula.

Spherical Bessel and Hankel functions

The *spherical Bessel functions* of the first and second kind are defined respectively by [Wil99]

$$j_\nu(x) := \left(\frac{\pi}{2x}\right)^{1/2} J_{\nu+1/2}(x) \tag{2.33}$$

$$y_\nu(x) := \left(\frac{\pi}{2x}\right)^{1/2} Y_{\nu+1/2}(x) \tag{2.34}$$

where J_ν and Y_ν are Bessel functions of the first and second kind, respectively [GR65]. ν is an natural number. It holds that

$$\frac{\partial j_\nu(kr)}{\partial r} = k j_\nu^{'}(kr) \tag{2.35}$$

where the $j_\nu^{'}$ represents the first derivative of the corresponding Bessel function.

The *spherical Hankel functions* of first and second kind are defined respectively by [Wil99]

$$h_\nu^{(1)}(x) := j_\nu(x) + iy_\nu(x) \tag{2.36}$$
$$h_\nu^{(2)}(x) := j_\nu(x) - iy_\nu(x) \tag{2.37}$$

The following Wronskian relation holds [Wil99]

$$j_\nu(x)h_\nu'(x) - j_\nu'(x)h_\nu(x) = \frac{i}{x^2} \tag{2.38}$$

The high order approximations of the spherical Bessel and Hankel function are given by [CK92], [Wil99]

$$j_\nu(x) = \frac{x^\nu}{(2\nu+1)!!} \qquad \nu \to \infty \tag{2.39}$$
$$h_\nu^{(1)}(x) = \frac{(2\nu-1)!!}{ix^{\nu+1}} \qquad \nu \to \infty \tag{2.40}$$

where

$$(2\nu+1)!! := 1 \cdot 3 \cdot 5 \cdots (2\nu-1) \cdot (2\nu+1) \tag{2.41}$$

The large argument approximations of these functions is given by [CK92], [Wil99]

$$j_\nu(x) = \frac{1}{x}\sin\left(x - \frac{\nu\pi}{2}\right) \qquad x \to \infty \tag{2.42}$$
$$h_\nu^{(1)}(x) = (-i)^\nu h_0^{(1)}(x) = (-i)^{\nu+1}\frac{e^{ix}}{x} \qquad x \to \infty \tag{2.43}$$

Legendre polynomials and spherical harmonics

The *Legendre polynomial* P_ν of degree ν is defined by [GR65], [Wil99]

$$P_\nu(x) := \frac{1}{2^\nu \nu!}\frac{d}{dx^\nu}\left(x^2-1\right)^\nu \tag{2.44}$$

where ν is a natural number. The following orthogonality relation holds [Wil99]:

$$\int_{-1}^{1} P_\nu(x)P_{\nu'}(x)dx = \int_0^\pi P_\nu(\cos\theta)P_{\nu'}(\cos\theta)\sin\theta d\theta = \frac{2}{2\nu+1}\delta_{\nu,\nu'} \tag{2.45}$$

the completeness relation for the Legendre polynomials is given by [Wil99, p.214]

$$\sum_{\nu=0}^{\infty} \frac{2\nu+1}{2} P_\nu(x)P_\nu(y) = \delta(x-y), \quad x,y \in [-1,1] \tag{2.46}$$

The Christoffel summation formula reads as follows [GR65, p.986], formula 8.915.1:

$$\sum_{\nu=0}^{N} (2\nu+1)P_\nu(x)P_\nu(y) = (N+1)\frac{P_\nu(x)P_{\nu+1}(y) - P_\nu(y)P_{\nu+1}(x)}{y-x} \tag{2.47}$$

If $y = 1$, for $P_\nu(1) = 1, \nu \in \mathbb{N}$ we have that [Raf04]

$$\sum_{\nu=0}^{N} (2\nu+1)P_\nu(x) = (N+1)\frac{P_N(x) - P_{N+1}(x)}{1-x} \tag{2.48}$$

The *associated Legendre function* $P_\nu^\mu(x)$ is defined by [Wil99], [GR65, p.974]

$$P_\nu^\mu(x) := (-1)^\mu (1-x^2)^{\mu/2} \frac{d^\mu P_\nu(x)}{dx^\mu} \tag{2.49}$$

Where $P_\nu(x)$ is the Legendre polynomial of degree ν.

From [GR65, p.966, eq.8.737.2] we have that, when $\nu, \mu \in \mathbb{Z}$,

$$P_\nu^\mu(-x) = \cos[(\nu+\mu)\pi] P_\nu^\mu(x) \tag{2.50}$$

The *spherical harmonic* $Y_\nu^\mu(\hat{\mathbf{x}})$ is given by [Wil99]

$$Y_\nu^\mu(\hat{\mathbf{x}}) = Y_\nu^\mu(\theta_x, \phi_x) := \sqrt{\frac{(2\nu+1)(\nu-\mu)!}{4\pi(\nu+\mu)!}} P_\nu^\mu(\cos\theta_x)\, e^{i\mu\phi_x} \tag{2.51}$$

The spherical harmonics are orthonormal, that is [Wil99]

$$\begin{aligned} \int_\Omega Y_\nu^\mu(\hat{\mathbf{x}}) Y_{\nu'}^{\mu'}(\hat{\mathbf{x}}) dS(\hat{\mathbf{x}}) &= \int_0^{2\pi} d\phi_x \int_0^\pi Y_\nu^\mu(\theta_x,\phi_x) Y_{\nu'}^{\mu'}(\theta_x,\phi_x) \sin\theta_x d\theta_x = \\ &= \delta_{\nu\nu'}\delta_{\mu\mu'} \end{aligned} \tag{2.52}$$

where Ω represents the unitary sphere.

The summation formula for the spherical harmonics is [CK92, p.27]:

$$\sum_{\mu=-\nu}^{\nu} Y_\nu^\mu(\hat{\mathbf{x}}) Y_\nu^\mu(\hat{\mathbf{y}})^* = \frac{2\nu+1}{4\pi} P_\nu(\cos\varphi_{\mathbf{xy}}) \tag{2.53}$$

where $\varphi_{\mathbf{xy}}$ is the angle between the vectors $\mathbf{x}$ and $\mathbf{y}$. The following relations holds:

$$\cos\varphi_{\mathbf{xy}} = \frac{\mathbf{x}\cdot\mathbf{y}}{xy} = \sin\theta_x \sin\theta_y \cos(\phi_x - \phi_y) + \cos\theta_x \cos\theta_y \tag{2.54}$$

The following equation represents the *completeness relation* for the spherical harmonics:

$$\sum_{\nu=0}^{\infty} \sum_{\mu=-\nu}^{\nu} Y_\nu^\mu(\hat{\mathbf{x}}) Y_\nu^\mu(\hat{\mathbf{x}}')^* = \delta_\Omega(\hat{\mathbf{x}} - \hat{\mathbf{x}}') \tag{2.55}$$

The *Jacobi-Anger* expansion reads as follows [CK92, p.32]

$$\begin{aligned} e^{i\mathbf{k}\cdot\mathbf{z}} &= \sum_{\nu=0}^{\infty} i^\nu (2\nu+1) j_\nu(kz) P_\nu(\hat{\mathbf{z}}\cdot\hat{\mathbf{k}}) \\ &= \sum_{\nu=0}^{\infty} 4\pi i^\nu j_\nu(kz) \sum_{\mu=-\nu}^{\nu} Y_\nu^\mu(\hat{\mathbf{x}}) Y_\nu^\mu(\hat{\mathbf{z}})^* \end{aligned} \tag{2.56}$$

Sinc functions

The *unnormalized sinc function* is defined by

$$\operatorname{sinc}(x) := \frac{\sin(x)}{x} \tag{2.57}$$

The *circular sinc function* is defined by [Pol96]

$$\operatorname{csinc}_N(x) := \frac{\sin(Nx/2)}{\sin(x/2)} \tag{2.58}$$

The circular sinc is periodic with period 2π and its zeros are at $x = \pm 2\pi n/N,\ n = 1, 2, \ldots$

The following relation holds

$$\sum_{n=-N}^{N} e^{inx} = 2\sum_{n=0}^{N} \cos(nx) - 1 = \frac{\sin\left(\left(N+\frac{1}{2}\right)x\right)}{\sin\left(\frac{x}{2}\right)} = \operatorname{csinc}_{(2N+1)}(x) \tag{2.59}$$

where we have used equation (1.342.1) of [GR65, p.37]. In view of this result and of the Poisson sum formula (2.32), we obtain

$$\lim_{N\to\infty} \operatorname{csinc}_{(2N+1)}(ax) = \text{Ш}\left(\frac{a}{2\pi}x\right) = \frac{2\pi}{a} \sum_{n=-\infty}^{\infty} \delta\left(x - \frac{2\pi n}{a}\right), \quad a \in \mathbb{R}^+ \tag{2.60}$$

The following passages show that the circular sinc (for N odd) can be expressed as a series of sinc functions

$$\begin{aligned} \mathrm{csinc}_N(x) &= \sum_{n=-\frac{N-1}{2}}^{\frac{N-1}{2}} e^{inx} = \int_{\mathbb{R}} \left[e^{i\kappa x} \sum_{n=-\frac{N-1}{2}}^{\frac{N-1}{2}} \delta(\kappa - n) \right] d\kappa \\ &= \int_{\mathbb{R}} e^{i\kappa x} \text{Ш}(\kappa) \Pi\left(\frac{\kappa}{N}\right) d\kappa = \sum_{n=-\infty}^{\infty} \delta(x - 2\pi n) \otimes N \ \mathrm{sinc}\left(x\frac{N}{2}\right) \\ &= N \sum_{n=-\infty}^{\infty} \mathrm{sinc}\left((x - 2\pi n)\frac{N}{2}\right) \end{aligned} \tag{2.61}$$

where we have used formula (2.59), the property (2.26) of the Dirac delta function, the convolution theorem (2.93) and the properties of the comb function Ш and of the rectangle function Π, given by equations (2.31) and (2.63), respectively.

Rectangular function

The *rectangular function* $\Pi(x/a)$ is defined by

$$\Pi\left(\frac{x}{a}\right) = \begin{cases} 1, & |x| < a/2 \\ 1/2, & |x| = a/2 \\ 0, & |x| > a/2 \end{cases} \tag{2.62}$$

Its Fourier transform is given by [Wil99]

$$\int_{\mathbb{R}} \Pi\left(\frac{x}{a}\right) \frac{e^{-i\kappa x}}{\sqrt{2\pi}}\, dx = \frac{a}{\sqrt{2\pi}} \frac{\sin(\kappa a/2)}{\kappa a/2} = \frac{a}{\sqrt{2\pi}}\ \mathrm{sinc}\left(\kappa\frac{a}{2}\right) \tag{2.63}$$

Since $\Pi(x/a)$ is a real-valued, even function, we have that $\mathcal{F}^{-1}\Pi = \mathcal{F}\,\Pi$. This equality holds for the definition of direct and inverse fourier transform given respectively by equations (2.74) and(2.75), discussed below.

2.3 Fourier series and Fourier transform

2.3.1 Fourier series

Any integrable function $a(y)$, defined in the interval $(-\pi, \pi)$, can be represented by an infinite series of the form

$$a(y) = \sum_{n=-\infty}^{\infty} c_n e^{iny} \tag{2.64}$$

at any point $y \in (-\pi, \pi)$ where $a(y)$ is differentiable. The right hand side of this equation is known as *Fourier series* [Kre78, p.160]. The coefficients c_n, in general complex numbers, are referred to as *Fourier coefficients*. They can be computed with the formula

$$c_n = \frac{1}{2\pi} \int_{-\pi}^{\pi} a(y) e^{-iny} dy = \frac{\langle e^{in} | a \rangle_{(-\pi,\pi)}}{2\pi} \tag{2.65}$$

where the symbol $\langle \cdot | \cdot \rangle$ represents the scalar product defined by (2.10).

Any integrable periodic function, that is any integrable function $a(y)$ such that $a(y+\Delta) = a(y)$, can be also be expressed in the form of a Fourier series, again at any point y where $a(y)$ is differentiable. In this case, the coefficients are computed from

$$c_n = \frac{1}{2\Delta} \int_{-\Delta}^{\Delta} a(y) e^{-i\frac{ny\pi}{\Delta}} dy \tag{2.66}$$

The series (2.64) can be extended to points y where $a(y)$ is not continuous (and therefore not differentiable) but has right-hand and left-hand derivative. We have that [Dav63, p.94]

$$\sum_{n=-\infty}^{\infty} c_n e^{iny} = \lim_{h \to 0^+} \frac{1}{2} \left[a(y+h) + a(y-h) \right] \tag{2.67}$$

The meaning of the Fourier series is that the complex exponential functions e^{inx} with $-\infty < n < \infty$ represent a complete set of orthogonal functions for $L^2(-\pi, \pi)$. Therefore, in view of relation (2.20), it is possible to express any square integrable function $a(y)$ defined over $(-\pi, \pi)$ by

$$a(y) = \sum_{n=-\infty}^{\infty} \frac{\langle e^{in} | f \rangle_{(-\pi,\pi)}}{2\pi} e^{iny} \tag{2.68}$$

at any point y where $a(y)$ is continuous, otherwise the convergence holds in the sense of L^2 norm (2.11) (convergence in the *mean square*). It should be noticed that the complex exponential functions are not orthonormal, but $||e^{in}||_{(-\pi,\pi)} = \sqrt{2\pi}$. Therefore the set of functions $e^{iny}/\sqrt{2\pi}$, $-\infty < n < \infty$ defines a complete orthonormal set for $L^2(-\pi, \pi)$.

Generalized Fourier series

It is possible to extend the concept of Fourier series to other orthogonal sets of functions and to functions defined over subsets of Euclidean spaces with more than one dimension. Let the set of orthonormal functions $a_n(\mathbf{y})$ be a complete set for $L^2(D)$, with D being a bounded subset of $\mathbb{R}^m$. Then any function $a(\mathbf{y}) \in L^2(D)$ can be expressed by the following series, often referred to as *generalized Fourier series* [Now81]

$$a(\mathbf{y}) = \sum_{n=0}^{\infty} c_n a_n(\mathbf{y}) \tag{2.69}$$

where again the convergence is to be intended in the L^2 sense. The Fourier coefficients c_n are given by

$$c_n = \int_D a(\mathbf{y}) a_n(\mathbf{y})^* dS(\mathbf{y}) = \langle a | a_n \rangle_D \tag{2.70}$$

This formula is analogous to (2.66).

Parseval relation

Given the generalized Fourier series (2.69) and formula (2.70), the following relation, known as the *Parseval relation*, holds [Kre78, p.170]:

$$\sum_{n=1}^{\infty} |\langle a_n | a \rangle_D|^2 = ||a||^2 \tag{2.71}$$

Spherical spectrum

The spherical harmonics $Y_\nu^\mu(\hat{\mathbf{x}})$, defined (2.51), with $\nu = 1, 2, ...\infty$ and $|\mu| \leq \nu$, represent a complete orthonormal system for $L^2(\Omega)$ [CK92]. A given function $f(\hat{\mathbf{x}}) \in L^2(\Omega)$ can be represented by the following generalized Fourier series

$$f(\hat{\mathbf{x}}) = \sum_{\nu=0}^{\infty} \sum_{\mu=-\nu}^{\nu} \chi_{\nu\mu} Y_\nu^\mu(\hat{\mathbf{x}}) \tag{2.72}$$

at any $\hat{\mathbf{x}}$ where $f(\hat{\mathbf{x}})$ is continuous (otherwise the convergence is valid in the mean square sense). The coefficients $\chi_{\nu\mu}$ represent the *spherical spectrum* of $f(\hat{\mathbf{x}})$ and are calculated from

$$\chi_{\nu\mu} := \int_\Omega f(\hat{\mathbf{x}}) Y_\nu^\mu(\hat{\mathbf{x}})^* dS(\hat{\mathbf{x}}) \tag{2.73}$$

2.3.2 Fourier transform

The *Fourier transform* $\mathcal{F}$ of a function $a(y)$, defined for $-\infty < y < \infty$, is given by

$$(\mathcal{F}a)(\kappa) := \frac{1}{\sqrt{2\pi}} \int_{-\infty}^{\infty} e^{-i\kappa y} a(y) dy \tag{2.74}$$

The *inverse Fourier transform* $\mathcal{F}^{-1}$ is defined by

$$(\mathcal{F}^{-1}A)(y) := \frac{1}{\sqrt{2\pi}} \int_{-\infty}^{\infty} e^{i\kappa y} A(\kappa) d\kappa \tag{2.75}$$

It should be noticed that these definitions are slightly different from the conventional definitions of direct and inverse Fourier transform (see, for example, [Wil99]), in the fact

that the kernels of both integrals include here the *δ-function normalization factor* $\sqrt{2\pi}$, so that the following orthogonality relations hold:

$$\int_{\mathbb{R}} \frac{e^{i\kappa y}}{\sqrt{2\pi}} \frac{e^{-i\kappa' y}}{\sqrt{2\pi}} dy = \frac{\langle e^{i\kappa} | e^{i\kappa'} \rangle_{\mathbb{R}}}{2\pi} = \delta(\kappa - \kappa') \tag{2.76}$$

$$\int_{\mathbb{R}} \frac{e^{i\kappa y}}{\sqrt{2\pi}} \frac{e^{-i\kappa y'}}{\sqrt{2\pi}} d\kappa = \frac{\langle e^{iy} | e^{iy'} \rangle_{\mathbb{R}}}{2\pi} = \delta(y - y') \tag{2.77}$$

It can be easily shown that, for the definition above, the following relations hold true:

$$(\mathcal{F}^{-1}a)(\kappa) = (\mathcal{F}a^*)(\kappa)^* = (\mathcal{F}a)(-\kappa) = \big(\mathcal{F}a(-\,\cdot\,)\big)(\kappa) \tag{2.78}$$

Identical relations hold if the roles of the direct and inverse transforms are interchanged.

Parseval relation

As for the Fourier series, the following *Parseval relation* holds:

$$\int_{\mathbb{R}} |a(x)|^2 dx = \int_{\mathbb{R}} |(\mathcal{F}a)(\kappa)|^2 d\kappa \tag{2.79}$$

Fourier transform of the derivative of a function

Given the differentiable, square integrable function $f(x)$, we have that

$$\left(\mathcal{F}\frac{df}{dx}\right)(\kappa) = i\kappa(\mathcal{F}f)(\kappa) \tag{2.80}$$

This result is a consequence of the following relation:

$$\begin{aligned} \frac{df}{dx}(x) &= \frac{d}{dx}\left(\frac{1}{\sqrt{2\pi}}\int_{\mathbb{R}} e^{i\kappa x}(\mathcal{F}f)(\kappa)d\kappa\right) = \frac{1}{\sqrt{2\pi}}\int_{\mathbb{R}} i\kappa\, e^{i\kappa x}\,(\mathcal{F}f)(\kappa)d\kappa \\ &= \left[\mathcal{F}^{-1}\left(\,(i\,\cdot)\,\mathcal{F}f\,\right)\right](x) \end{aligned} \tag{2.81}$$

Two dimensional Fourier transform

The two dimensional Fourier transform $(\mathcal{F}a)(\boldsymbol{\kappa})$ of a function $a(\mathbf{y})$, defined over $\mathbb{R}^2$, and the inverse transform $\mathcal{F}^{-1}$ are defined by

$$(\mathcal{F}a)(\boldsymbol{\kappa}) := \frac{1}{2\pi}\int_{-\infty}^{\infty}\int_{-\infty}^{\infty} e^{-i(\kappa_1 y_1 + \kappa_2 y_2)} a(y_1, y_2) dy_1 dy_2 \tag{2.82}$$

$$(\mathcal{F}^{-1}A)(\mathbf{y}) := \frac{1}{2\pi}\int_{-\infty}^{\infty}\int_{-\infty}^{\infty} e^{i(\kappa_1 y_1 + \kappa_2 y_2)} A(\kappa_1, \kappa_2) d\kappa_1 d\kappa_2 \tag{2.83}$$

Using a more compact and general notation, the definitions above can be rewritten in the following form:

$$(\mathcal{F}a)(\boldsymbol{\kappa}) := \frac{1}{2\pi}\int_{\mathbb{R}^2} e^{-i\boldsymbol{\kappa}\cdot\mathbf{y}}a(\mathbf{y})dS(\mathbf{y}) \tag{2.84}$$

$$(\mathcal{F}^{-1}A)(\mathbf{y}) := \frac{1}{2\pi}\int_{\mathbb{R}^2} e^{i\boldsymbol{\kappa}\cdot\mathbf{y}}A(\boldsymbol{\kappa})dS(\boldsymbol{\kappa}) \tag{2.85}$$

By analogy with the one dimensional case, a δ-function normalization factor 2π has been introduced, as a consequence of the following orthogonality relations:

$$\int_{\mathbb{R}^2}\frac{e^{i\boldsymbol{\kappa}\cdot\mathbf{y}}}{2\pi}\frac{e^{-i\boldsymbol{\kappa}'\cdot\mathbf{y}}}{2\pi}dS(\mathbf{y}) = \frac{\langle e^{i\boldsymbol{\kappa}}|e^{i\boldsymbol{\kappa}'}\rangle_{\mathbb{R}^2}}{4\pi^2} = \delta(\boldsymbol{\kappa}-\boldsymbol{\kappa}') \tag{2.86}$$

$$\int_{\mathbb{R}^2}\frac{e^{i\boldsymbol{\kappa}\cdot\mathbf{y}}}{2\pi}\frac{e^{-i\boldsymbol{\kappa}\cdot\mathbf{y}'}}{2\pi}dS(\boldsymbol{\kappa}) = \frac{\langle e^{i\mathbf{y}}|e^{i\mathbf{y}'}\rangle_{\mathbb{R}^2}}{4\pi^2} = \delta(\mathbf{y}-\mathbf{y}') \tag{2.87}$$

Similarly to the Fourier series, the direct and inverse Fourier transform can be interpreted as the representation of a square integrable function $a(\mathbf{y})$ in term of the sum of its orthogonal projection onto the complete set of orthogonal functions. In fact, given the function $a(y) \in L^2(\mathbb{R}^2)$ and considering the definition of scalar product (2.10), it is possible to write for the two dimensional transforms

$$a(\mathbf{y}) = [\mathcal{F}^{-1}(\mathcal{F}a)](\mathbf{y}) = \int_{\mathbb{R}^2}\frac{e^{i\boldsymbol{\kappa}\cdot\mathbf{y}}}{2\pi}\frac{\langle e^{i\boldsymbol{\kappa}}|a\rangle_{\mathbb{R}^2}}{2\pi}dS(\boldsymbol{\kappa}) \tag{2.88}$$

at any $\mathbf{y}$ where $a(\mathbf{y})$ is continuous, otherwise the equality is valid in the mean square sense. The same holds for the one dimensional case. It can be observed that this expression is analogous to (2.20), with the relevant difference that the summation over n has been replaced by an integration over $\boldsymbol{\kappa}$.

Fourier transform in the time domain and time convention

Given a function of time $P(t)$, its temporal Fourier transform is

$$(\mathcal{F}_t P)(\omega) := \frac{1}{\sqrt{2\pi}}\int_{-\infty}^{\infty} P(t)e^{i\omega t}dt \tag{2.89}$$

It should be emphasized that the kernel of this integral is the complex conjugate of the kernel included in the definition of direct Fourier transform (2.74). The choice of the kernel $e^{-i\kappa x}$ for the *spatial* direct Fourier transform and of the kernel $e^{i\omega t}$ for the *temporal* direct Fourier transform implies that a function of the kind $e^{i(\kappa x-\omega t)}$ represents a propagating plane wave traveling in the positive x direction. This choice is defined as the *time convention* $e^{-i\omega t}$, and is frequently used in the mathematical and physical literature. This convention is adopted throughout this work. The reason for this will become clear in

Section 4.3.1: in fact, a function of the kind $e^{i(\zeta(\kappa)x-\omega t)}$ with $\zeta(\kappa) = \sqrt{k^2-\kappa^2}$ represents a propagating wave when $\kappa < k$, and an evanescent wave decaying in the positive x direction when $\kappa > k$ and therefore $i\zeta(\kappa) = -|\zeta(\kappa)|$.

Another mathematically equivalent choice, more often used in the engineering literature, is the time convention $e^{i\omega t}$ (or $e^{j\omega t}$). In this case, the kernel of the integrals (2.74) and (2.89) should be substituted with their complex conjugate, and the function $e^{i(\omega t-\kappa x)}$ represents a wave traveling in the positive x direction.

Although the direct Fourier transform in the time domain is mathematically identical to the inverse Fourier transform (2.75), in order to avoid any confusion we will use the notation $\mathcal{F}_t$ for to the transform (2.89). Analogously, we will use the symbol $\mathcal{F}_t^{-1}$ for the inverse transform. Hence it holds that

$$p(\omega) = (\mathcal{F}_t P)(\omega) \tag{2.90}$$

$$P(t) = (\mathcal{F}_t^{-1} p)(t) \tag{2.91}$$

Convolution

Let $f(x)$ and $g(x)$ be two square integrable functions defined on $\mathbb{R}$. The *convolution* of these two functions is defined by

$$f(x) \otimes g(x) := \int_{\mathbb{R}} f(x')g(x-x')dx' \tag{2.92}$$

The well-known *convolution theorem* reads as follows:

$$f(x) \otimes g(x) = \mathcal{F}^{-1}[\sqrt{2\pi}\ (\mathcal{F}f)\ (\mathcal{F}g)\ ](x) \tag{2.93}$$

Analogously, it holds that

$$\mathcal{F}(f_1 \cdot f_2 \cdots f_N)(\kappa) = (2\pi)^{-\frac{N-1}{2}} (\mathcal{F}f_1)(\kappa) \otimes (\mathcal{F}f_2)(\kappa) \otimes \cdots (\mathcal{F}f_N)(\kappa) \tag{2.94}$$

2.4 Integral representation of wave fields

In this section some integral formulae are introduced, which are of relevance to this work. These formulae are presented following the material reported in [CK83], [CK92], [Pot07] and [Wil99].

It is recalled that a function $u(\mathbf{z})$ is said to satisfy the homogeneous Helmholtz equation in the domain D if

$$\nabla^2 u(\mathbf{z}) + k^2 u(\mathbf{z}) = 0, \quad \mathbf{z} \in D \tag{2.95}$$

2.4.1 Single layer potential

Given the bounded domain Λ [5] and the integrable function $a(\mathbf{y})$, the integral

$$u(\mathbf{z}) := \int_{\partial\Lambda} G(\mathbf{z},\mathbf{y})a(\mathbf{y})dS(\mathbf{y}), \quad \mathbf{z} \in \mathbb{R}^m \backslash \partial\Lambda, \quad m = 2,3 \tag{2.96}$$

is called *acoustic single layer potential* with density a (not to be confused with the acoustic energy density function). $G(\mathbf{z},\mathbf{y})$ is the fundamental solution of the Helmholtz equation, that will be introduced in Chapter 3 and which is given by (3.6) and (3.7) for the three-dimensional and one-dimensional case, respectively.

Having defined

$$u_+(\mathbf{z}) := u(\mathbf{z}) \quad \mathbf{z} \in \mathbb{R}^m \backslash \overline{\Lambda} \tag{2.97}$$

$$u_-(\mathbf{z}) := u(\mathbf{z}) \quad \mathbf{z} \in \Lambda \tag{2.98}$$

we have that both $u_+(\mathbf{z})$ and $u_-(\mathbf{z})$ satisfies the homogeneous Helmholtz equation in the exterior and in the interior of Λ, respectively.

If the function $a(\mathbf{y})$ is continuous, then the acoustic single layer potential is continuous throughout $\mathbb{R}^m$. We have that

$$u(\mathbf{z}) = \int_{\partial\Lambda} G(\mathbf{z},\mathbf{y})a(\mathbf{y})dS(\mathbf{y}), \quad \mathbf{z} \in \partial\Lambda \tag{2.99}$$

Given the unitary vector $\hat{\mathbf{n}}(\mathbf{x})$, normal to $\partial\Lambda$ at $\mathbf{z}$ and directed towards the exterior of Λ, we define the right and left derivative of the single layer potential as:

$$\begin{aligned} \nabla_{\mathbf{n}} u_+(\mathbf{z}) &:= \lim_{h\to+0} \hat{\mathbf{n}}(\mathbf{z}) \cdot \nabla(\mathbf{z} + h\hat{\mathbf{n}}) \\ \nabla_{\mathbf{n}} u_-(\mathbf{z}) &:= \lim_{h\to+0} \hat{\mathbf{n}}(\mathbf{z}) \cdot \nabla(\mathbf{z} - h\hat{\mathbf{n}}) \end{aligned} \tag{2.100}$$

The normal derivative of the single layer potential is discontinuous at the boundary. Considering the right and left derivatives introduced above, the following relevant relation holds (see, for example, [CK92, p.39]):

$$\nabla u_\pm(\mathbf{y}) = \int_{\partial\Lambda} \frac{\partial G(\mathbf{x},\mathbf{y})}{\partial \hat{\mathbf{n}}(\mathbf{y})}\, a(\mathbf{x})\, dS(\mathbf{x}) \mp \frac{1}{2} a(\mathbf{y}), \quad \mathbf{y} \in \partial\Lambda \tag{2.101}$$

This results leads to:

$$\nabla_{\mathbf{n}} u_-(\mathbf{y}) - \nabla_{\mathbf{n}} u_+(\mathbf{y}) = a(\mathbf{y}) \quad \mathbf{y} \in \partial\Lambda \tag{2.102}$$

[5] The set Λ must have boundary $\partial\Lambda$ of class C^2 (two times differentiable with continuous second derivative) and simply connected exterior.

These formulae are referred to as the *jump relation* for the acoustic single layer potential, and have the relevant meaning that the density of the potential is given by the difference (*jump*) between its left and right normal derivative on the boundary $\partial\Lambda$.

We have $u_+(\mathbf{z})$ and $u_-(\mathbf{z})$ are both solutions of the homogeneous Helmholtz equation in the respective domains, they are continuous on $\partial\Lambda$ (if the density is continuous) but their normal derivatives have a discontinuity on $\partial\Lambda$. Hence $u_+(\mathbf{z})$ and $u_-(\mathbf{z})$ can be understood as two different sound fields, representing the solutions of an exterior and interior Dirichlet problem, respectively (see Section 3.18). From these considerations, given two sound fields $p_+(\mathbf{z})$ and $p_-(\mathbf{z})$, that are solutions of the homogeneous Helmholtz equation in the exterior and interior of Λ, respectively, they can be represented by

$$p(\mathbf{z})_\pm = \int_{\partial\Lambda} G(\mathbf{x},\mathbf{y})(\nabla_\mathbf{n} p_-(\mathbf{y}) - \nabla_\mathbf{n} p_+(\mathbf{y}))dS(\mathbf{y}) = \begin{cases} p_+(\mathbf{z}) & \mathbf{z} \in \mathbb{R}^m \backslash \Lambda \\ p_-(\mathbf{z}) & \mathbf{z} \in \overline{\Lambda} \end{cases} \tag{2.103}$$

it is clear that $p_+(\mathbf{z}) = p_-(\mathbf{z}),\ \mathbf{y} \in \partial\Lambda$. This result is often referred to as the *Simple Source Formulation* [Wil99, p.267] [6].

2.4.2 Green's second theorem and the Kirchhoff-Helmholtz integral

Given two functions $u(\mathbf{z})$ and $v(\mathbf{z})$, which are of class C^2 on Λ (two times differentiable with continuous second derivative) and continuous on $\partial\Lambda$, it holds that

$$\int_\Lambda u(\mathbf{z})\nabla^2 v(\mathbf{z}) - v(\mathbf{z})\nabla^2 u(\mathbf{z})dV(\mathbf{z}) = \int_{\partial\Lambda} u(\mathbf{y})\nabla_\mathbf{n} v(\mathbf{y}) - v(\mathbf{y})\nabla_\mathbf{n} u(\mathbf{y})dS(\mathbf{y}) \tag{2.104}$$

This result is often referred to as the *second Green's theorem* [CK83, p.68].

If the field $p_-(\mathbf{z})$ satisfies the homogeneous Helmholtz equation in any open and bounded set that contains Λ and its boundary $\partial\Lambda$, then it holds that [Wil99, p.256]

$$\int_{\partial\Lambda} G(\mathbf{z},\mathbf{y})\nabla_\mathbf{n} p_-(\mathbf{y}) - \nabla_\mathbf{n} G(\mathbf{z},\mathbf{y}) p_-(\mathbf{y})dS(\mathbf{y}) = \begin{cases} p_-(\mathbf{z}) & \mathbf{z} \in \Lambda \\ p_-(\mathbf{z})/2 & \mathbf{z} \in \partial\Lambda \\ 0 & \mathbf{z} \in \mathbb{R}^m \backslash \overline{\Lambda} \end{cases} \tag{2.105}$$

where

$$\nabla_\mathbf{n} G(\mathbf{z},\mathbf{y}) := \frac{\partial G(\mathbf{z},\mathbf{y})}{\partial \hat{\mathbf{n}}(\mathbf{y})} \tag{2.106}$$

A function $p(\mathbf{z})$ is said to satisfy the *Sommerfeld radiation condition* [Wil99, p.261] if

$$\lim_{z\to\infty} z\left(\frac{\partial p(\mathbf{z})}{\partial z} - ikp(\mathbf{z})\right) = 0 \tag{2.107}$$

[6] In [Wil99] the role of the left and right derivatives in equation (2.103) is exchanged. This is due to the vector $\hat{\mathbf{n}}$ pointing towards the interior of Λ.

This condition implies that the sound field $p(\mathbf{z})$ vanishes when $|\mathbf{z}|$ tends to infinity.

If the sound field $p_+(\mathbf{z})$ is a solution of the homogeneous Helmholtz equation in the smallest open set containing the exterior of Λ and the boundary $\partial\Lambda$, and if $p_+(\mathbf{z})$ satisfies the Sommerfeld radiation condition, then the following result, similar to equation (2.105), holds [Wil99, p.261]:

$$\int_{\partial\Lambda} \nabla_{\mathbf{n}} G(\mathbf{z},\mathbf{y}) p_+(\mathbf{y}) - G(\mathbf{z},\mathbf{y}) \nabla_{\mathbf{n}} p_+(\mathbf{y}) dS(\mathbf{y}) = \begin{cases} 0 & \mathbf{z} \in \Lambda \\ p_+(\mathbf{z})/2 & \mathbf{z} \in \partial\Lambda \\ p_+(\mathbf{z}) & \mathbf{z} \in \mathbb{R}^m \backslash \overline{\Lambda} \end{cases} \tag{2.108}$$

Equations (2.105) and (2.108) are usually referred to as the *Helmholtz integral* or as the *Kirchhoff-Helmholtz integral*. They represent a powerful tool for the representation of sound fields, which are solutions of an interior or an exterior problem, respectively.

A relevant difference between the Simple Source Formulation (2.103) and the Kirchhoff-Helmholtz integral is that in the former the density of the potential is given as a function of the normal derivatives on $\partial\Lambda$ of *both* the exterior *and* interior fields $p_+(\mathbf{z})$ and $p_-(\mathbf{z})$, while equations (2.105) and (2.108) require the knowledge of *either* the interior sound field $p_-(\mathbf{z})$ *or* of the exterior field $p_+(\mathbf{z})$, respectively, but *both* the value of the considered field *and* its normal derivative on $\partial\Lambda$ must be known.

2.5 Spectral decomposition and SVD

The mathematical derivation of the singular value decomposition (SVD) of the operator S is briefly reported here, following a procedure analogous to that described in [CK92] and [Pot07].

2.5.1 Spectral theorem for a self adjoined, compact linear operator

Let S be a linear compact[7] operator, acting between two normed spaces A and P. Its adjoint operator S^* is also compact and the composite operator S^*S is compact and self adjoined ([Kre78]).

The eigenfunctions $a_n(\mathbf{y})$ and the eigenvalues μ_n of S^*S are given by the solutions of the eigenvalue problem

$$(S^*Sa_n)(\mathbf{y}) = \lambda_n a_n(\mathbf{y}) \tag{2.109}$$

They have the following properties see [Kre78, p.420 and p.461]:

[7] The discussion of the concept of compactness of an operator is beyond the scope of this work. The reader can refer to [Kre78, p.405] for an introduction to this subject

- The eigenvalues λ_n are real (from S self-adjoined);
- The eigenvalues λ_n are countable (from S compact);
- The only possible accumulation point for the eigenvalues is 0 (from S self-adjoined);
- Eigenfunctions associated with different eigenvalues are orthogonal (from S self-adjoined);
- The dimension of the eigenspace associated to any non-zero eigenvalue is finite (from S compact).

All non-zero eigenvalues are ordered as

$$|\lambda_1| \geq |\lambda_2| \geq |\lambda_3| \geq \cdots \geq |\lambda_N| \tag{2.110}$$

where each eigenvalue is repeated according to its multiplicity. N, the total number of eigenvalues, can be either finite or infinite. In what follows, we will assume that $N = \infty$. The eigenfunctions $a_n(\mathbf{y})$ can be chosen to be such that $||a_n|| = 1$. This property, together with the orthogonality relation, implies that the eigenfunctions are orthonormal (see (2.19)), that is

$$\langle a_n | a_m \rangle_{\partial\Lambda} = \delta_{n,m} \quad \forall n, m = 1, 2, 3... \tag{2.111}$$

The determination of the eigenfunctions is in general not unique, due to the possible presence of one or more *degenerate eigenvalues*. Such an eigenvalue has multiplicity [8] $\mu > 1$, and is associated to an eigenspace with the same dimension. The set of eigenfunctions, which span this eigenspace, are not uniquely defined.

The hearth of the SVD is the application *spectral theorem for compact and self adjoined linear operators* to S^*S. The derivation and discussion of this powerful theorem is beyond the scope of this thesis, and the reader can refer to standard textbooks on functional analysis such as [Kre78], [Pot07] and [Kre99] for a better insight. The main results of this theorem, for the case of the operator S^*S, is that

- any function $a(\mathbf{y}) \in L^2(\partial\Lambda)$ can be expressed as

$$a(\mathbf{y}) = \sum_{n=1}^{\infty} a_n(\mathbf{y}) \langle a_n | a \rangle + (P_{N(S^*S)} a)(\mathbf{y}) \tag{2.112}$$

  where the operator $P_{N(S^*S)}$ represents the orthogonal projection onto $N(S^*S)$, the nullspace of S^*S. The latter equals $N(S)$ [CK92, p.91] and is defined by (2.23).

[8] The algebraic and numeric multiplicity of the eigenvalue are assumed to be equal.

- The action of S^*S on $a(\mathbf{y})$ can be expressed as

$$(S^*Sa)(\mathbf{y}) = \sum_{n=1}^{\infty} a_n(\mathbf{y})\lambda_n\langle a_n|a\rangle \tag{2.113}$$

If S is injective, that is if

$$\forall f(\mathbf{y}), g(\mathbf{y}) \in L^2(\partial\Lambda), \qquad f(\mathbf{y}) \neq g(\mathbf{y}) \rightarrow (Sf)(\mathbf{x}) \neq (Sg)(\mathbf{x}) \tag{2.114}$$

then the set of orthogonal functions $a_n(\mathbf{y})$ is a complete set for $L^2(\partial\Lambda)$. This means (see (2.15)) that any function $a(\mathbf{y}) \in L^2(\partial\Lambda)$ can be expressed by a series of the eigenfunctions $a_n(\mathbf{y})$.

The meaning of equation (2.113) is that a self adjoined and compact linear operator can be diagonalized following a procedure analogous to the eigenvalue decomposition of a normal matrix, although for the analogy to hold the matrix must have infinite dimensions.

2.5.2 Singular Value Decomposition of a compact linear operator

The singular values σ_n of the compact operator S are defined as the square roots of the non-zero eigenvalues λ_n of S^*S, ordered with decreasing magnitude.

The functions $p_n(\mathbf{x})$ are generated by letting the operator S act on the different functions $a_n(\mathbf{y})$:

$$p_n(\mathbf{x}) = \frac{1}{\sigma_n}(Sa_n)(\mathbf{x}) \tag{2.115}$$

In view of the orthogonality of the functions $a_n(\mathbf{y})$ and of the definition of the adjoint operator (2.21), it can be easily proven that the functions $p_n(\mathbf{x})$ are mutually orthogonal and of unitary L^2 norm, namely

$$\begin{aligned} \langle p_n|p_m\rangle_{\partial V} &= \frac{1}{\sigma_n\sigma_m}\langle Sa_n|Sa_m\rangle_{\partial V} = \frac{1}{\sigma_n\sigma_m}\langle a_n|S^*Sa_m\rangle_{\partial\Lambda} \\ &= \frac{\sigma_m^2}{\sigma_n\sigma_m}\langle a_n|a_m\rangle_{\partial\Lambda} = \delta_{n,m} \end{aligned} \tag{2.116}$$

The functions $p_n(\mathbf{x})$ and $a_n(\mathbf{y})$ are called the left and right singular functions of S, respectively, and together with the singular values σ_n constitute a singular system of the operator S. As in the case of the determination of the eigenfunctions of S^*S, the choice of the singular system is not unique, due to the potential degeneracy of the singular values.

The singular system $\{\sigma_n, a_n(\mathbf{y}), p_n(\mathbf{x})\}$ has the following properties [Pot07], [CK92]:

$$(Sa_n)(\mathbf{x}) = \sigma_n p_n(\mathbf{x}) \tag{2.117}$$
$$(S^* p_n)(\mathbf{y}) = \sigma_n a_n(\mathbf{y}) \tag{2.118}$$
$$(S^* S a_n)(\mathbf{y}) = \sigma_n^2 a_n(\mathbf{y}) \tag{2.119}$$

The action of the operators S, S^* and S^*S can be expressed as:

$$(Sa)(\mathbf{x}) = \sum_{n=1}^{\infty} p_n(\mathbf{x}) \sigma_n \langle a_n | a \rangle_{\partial\Lambda} \tag{2.120}$$
$$(S^* p)(\mathbf{y}) = \sum_{n=1}^{\infty} a_n(\mathbf{y}) \sigma_n \langle p_n | p \rangle_{\partial V} \tag{2.121}$$
$$(S^* S a)(\mathbf{y}) = \sum_{n=1}^{\infty} a_n(\mathbf{y}) \sigma_n^2 \langle a_n | a \rangle_{\partial\Lambda} \tag{2.122}$$

Each function $p(\mathbf{x}) \in L^2(\partial V)$ can be expressed as

$$p(\mathbf{x}) = \sum_{n=1}^{\infty} p_n(\mathbf{x}) \langle p_n | p \rangle_{\partial V} + (P_{N(S^*)} p)(\mathbf{x}) \tag{2.123}$$

where the operator $P_{N(S^*)}$ represents the orthogonal projection onto the nullspace of S^*. Note that the series $p(\mathbf{x})$ is an orthonormal and complete system for $L^2(\partial V)$ only if the nullspace of S^* is trivial (namely, if $S^* p = 0$ implies that $p = 0$).

2.5.3 On the existence, uniqueness and expression of the solution

Let S be a linear compact operator acting between two normed spaces A and P. Following [CK92, p.89], it can be shown that the nullspace of S^* is the orthogonal complement of the range of S, and that the closure of the range of S equals the orthogonal complement of the null-space of its adjoint. This means that

$$N(S^*) = S(L^2(\partial\Lambda))^{\perp} \tag{2.124}$$
$$\overline{S(L^2(\partial\Lambda))} = N(S^*)^{\perp} \tag{2.125}$$

The following inverse problem is addressed:

$$p(\mathbf{x}) = (Sa)(\mathbf{x}) \tag{2.126}$$

where the function $p(\mathbf{x}) \in P$ is given and the function $a(\mathbf{y}) \in A$ has to be determined, when this is possible.

Theorem 2.1. ***Picard theorem*** *[CK92, p.91] Given the problem $p(\mathbf{x}) = (Sa)(\mathbf{x})$ described above, the solution $a(\mathbf{y})$ exists if and only if the following two conditions hold:*

$$p(\mathbf{x}) \in N(S^*)^{\perp} \tag{2.127}$$

$$\sum_{n=1}^{\infty} \frac{|\langle p_n|p\rangle|^2}{\sigma_n^2} < \infty \tag{2.128}$$

In order to seek a solution of the integral equation (3.19), which has the same form of (2.126) and will be introduced in Chapter 3, the following results are applied:

$$\begin{aligned} &p(\mathbf{x}) = (Sa)(\mathbf{x}) \\ &\langle p_n|p\rangle = \langle p_n|Sa\rangle = \langle S^* p_n|a\rangle = \sigma_n \langle a_n|a\rangle \\ &\langle a_n|a\rangle = \frac{1}{\sigma_n}\langle p_n|p\rangle \end{aligned} \tag{2.129}$$

As a consequence of this result and using the relation (2.112), if one solution $a(\mathbf{y})$ exists, this is given by

$$a(\mathbf{y}) = \sum_{n=1}^{\infty} a_n(\mathbf{y}) \frac{1}{\sigma_n} \langle p_n|p\rangle \tag{2.130}$$

This solution is, in general, not unique. In fact, if $a(\mathbf{y})$ given by (2.130) is a solution for $Sa = p$ and if the nullspace of S is non trivial, then any function $a(\mathbf{y}) + \tilde{a}(\mathbf{y})$ with $\tilde{a}(\mathbf{y}) \in N(S)$ is also a solution.

It can be observed that, because of the definition of nullspace, any function $\tilde{a}(\mathbf{x}) \in N(S)$ does not contribute to generating $p(\mathbf{x})$.

Note that condition (2.128) implies that the solution $a(\mathbf{y})$ must have finite norm. In fact, considering equations (2.113) and (2.115), the orthogonality of $a_n(\mathbf{y})$, the definition of σ_n and the Parseval relation (2.71), it holds that

$$\begin{aligned} \infty \;&>\; \sum_{n=1}^{\infty} \frac{|\langle p_n|p\rangle|^2}{\sigma_n^2} = \sum_{n=1}^{\infty} \frac{|\langle Sa_n|Sa\rangle|^2}{\sigma_n^2} = \\ &= \sum_{n=1}^{\infty} \frac{|\langle S^* Sa_n|a\rangle|^2}{\sigma_n^2} = \sum_{n=1}^{\infty} \frac{\lambda_n}{\sigma_n^2} |\langle a_n|a\rangle|^2 = ||a||^2 \end{aligned} \tag{2.131}$$

Chapter 3

Sound field reproduction as an inverse problem

In this chapter the problem of sound field reproduction is mathematically formulated in the form of an acoustical inverse problem. Firstly, the main assumption and the general framework of the problem are formulated, starting from the wave equation. Secondly, mathematical entities and results such as the acoustic single layer potential and the Dirichlet problem, relevant to this work, are introduced. The acoustical inverse problem under consideration is then formulated as an integral equation of the first kind. Consequently, the singular value decomposition of the integral operator is introduced and used as a tool for solving the integral equation. These concepts represent the theoretical basis of the entire thesis, and are crucial for the development of the results presented in the rest of this work. An effort has been made to provide a physical interpretation, in the framework of the acoustical problem considered, of the mathematical concepts introduced. Special attention is dedicated to the physical interpretation of the singular system of the integral operator arising in the formulation of the problem.

3.1 Mathematical formulation of the problem

Let V and Λ be two simply connected subsets of the three dimensional space, such that $V \subseteq \Lambda \subset \mathbb{R}^m$, $m = 2, 3$ and that their boundaries ∂V and $\partial \Lambda$ are smooth (of class C^2).

Most of the arguments presented here hold for both two-dimensional and three-dimensional problems. Hence, unless differently specified, $\mathbb{R}^m$ is either $\mathbb{R}^2$ or $\mathbb{R}^3$, respectively, depending on the problem considered. In what follows, V and Λ are referred to as the *control region* and the *reproduction region*, respectively, while ∂V is referred to as the *control boundary*. A given choice of V and Λ defines a *geometrical arrangement*. Figure 3.1 shows an example of a generic geometrical arrangement. For the sake of clarity we use

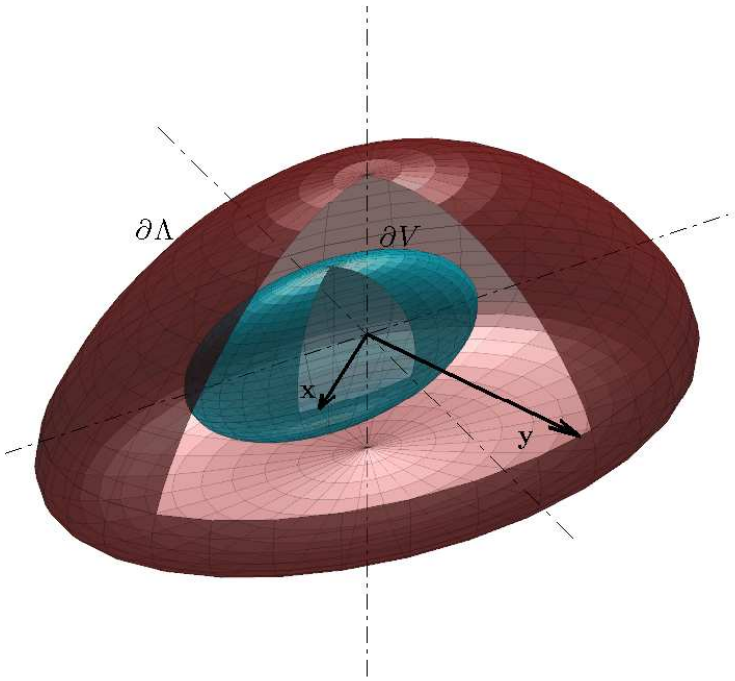

FIGURE 3.1: Generic three dimensional geometrical arrangement.

the notation $\mathbf{z}$ for any vector identifying a location in $\mathbb{R}^m$, while the vectors $\mathbf{x}$ and $\mathbf{y}$ identify locations in ∂V and $\partial\Lambda$, respectively.

It is assumed that a sound field $p(\mathbf{z}, t)$, hereafter referred to as the target sound field, is defined over $\overline{V}$ (namely over the closure of V) and satisfies the homogeneous wave equation [1]

$$\nabla^2 p(\mathbf{z}, t) - \frac{1}{c^2}\frac{\partial p(\mathbf{z}, t)}{\partial t} = 0, \quad \mathbf{z} \in \overline{V} \tag{3.1}$$

where c is the speed of sound. The fact that this equation is homogeneous, that is that the right-end side of the equation is zero, implies that no sources of sound and no scattering objects are contained in V. Hence, $p(\mathbf{x})$ can represent a physical sound field generated by sources located in the exterior of V (but not necessarily in the exterior of Λ). The one dimensional Fourier transform (2.89) with respect to the time variable t is applied to the right side of equation (3.2). As a result the latter reduces, for a given frequency ω, to the homogeneous Helmholtz equation

$$\nabla^2 p(\mathbf{z}, k) + k^2 p(\mathbf{z}, k) = 0, \quad \mathbf{z} \in \overline{V} \tag{3.2}$$

where $k = \omega/c$ is the wave number and the time convention $e^{-i\omega t}$ has been chosen. It is assumed that the sound propagates in a non dispersive and homogeneous medium (c is independent of $\mathbf{z}$ and ω). In the following passages the operating frequency ω is assumed to be fixed, and the dependence of p and other functions from k is omitted for brevity.

[1] The assumption is made that $\nabla^2 p$ exists on the boundary ∂V. More rigorously, it can be said that equations (3.1) and (3.2) are satisfied in the smallest open set containing $\overline{V}$.

The function $p(\mathbf{x})$, $\mathbf{x} \in \partial V$, is the restriction of the sound field $p(\mathbf{z})$ to the control boundary ∂V, and is hereafter referred to as the *pressure profile*.

The set Ψ_V is now defined as the set of all pressure profiles $p(\mathbf{x})$, which are of interest for the sound field reproduction problem addressed here. These are the restrictions to ∂V of all target sound fields satisfying equation (3.2). Formally

$$\Psi_V := \{p(\mathbf{x})|_{\partial V} : \nabla^2 p(\mathbf{z}) + k^2 p(\mathbf{z}) = 0, \quad \mathbf{z} \in \overline{V}\} \tag{3.3}$$

3.2 Acoustic single layer potential and the inverse problem

The assumption is made now that a continuous distribution of monopole-like sources is arranged on the boundary $\partial\Lambda$. These sources are referred to as *secondary sources* and $\partial\Lambda$ is therefore referred to as *secondary source layer*.

The sound field $p_{\mathbf{y}}(\mathbf{z})$ due to a single secondary source, located at $\mathbf{y} \in \partial\Lambda$, is assumed to satisfy the inhomogeneous Helmholtz equation [KF62]:

$$\nabla^2 p_{\mathbf{y}}(\mathbf{z}) + k^2 p_{\mathbf{y}}(\mathbf{z}) = i\omega\rho_0 q_{vol} \;\; \delta(\mathbf{z}-\mathbf{y}), \quad \mathbf{z} \in \Lambda \tag{3.4}$$

where ρ_0 is the static density of the fluid and q_{vol} is the *volume flow* generated by the secondary source. This implies that the secondary sources radiate sound as an ideal monopoles for the three dimensional problem and as an ideal infinite line sources, perpendicular to the plane considered, for the two dimensional problem.

We define

$$\ddot{m} = -i\omega\rho_0 q_{vol} \tag{3.5}$$

This can be interpreted as the *volume acceleration* of the secondary source, multiplied by the static density ρ_0 of the fluid [KN93]. This product can in turn be interpreted as the *time derivative of the mass flow* due to the secondary source considered. In this sense, each secondary source can be interpreted either as a simple source which pulsates (alters its volume) with an acceleration of $\ddot{m}/\rho_0$, or equivalently as a device which locally injects and subtract mass into and from the system, and $\ddot{m}$ represents the second time derivative of this mass variation process. $\ddot{m}$ is hereafter referred to as the *source strength* [2] and has dimensions of $[Kg\ s^{-2}]$.

The solution of the inhomogeneous Helmholtz equation (3.4) with $\ddot{m} = 1$ is given by the Green function $G(\mathbf{z}, \mathbf{y})$, and the field given by the secondary source located at $\mathbf{y}$ is therefore given by $p_{\mathbf{y}}(\mathbf{z}) = \ddot{m}G(\mathbf{z}, \mathbf{y})$. The assumption is made that the sound propagates

[2] In the literature [Wil99],[KF62], the term source strength is usually referred to the volume velocity q_{vol}, as the inhomogeneous wave equation is solved for the velocity potential $\Phi = p/(i\omega\rho_0)$ rather than for the acoustic pressure p.

in the free field, then $G(\mathbf{z}, \mathbf{y})$ satisfies the Sommerfeld radiation condition (2.107) and corresponds to the free field Green function [Wil99], [CK92]

$$G(\mathbf{z}, \mathbf{y}) = \frac{e^{ik|\mathbf{z}-\mathbf{y}|}}{4\pi|\mathbf{z}-\mathbf{y}|}, \qquad \mathbf{z} \neq \mathbf{y} \quad \text{if } \Lambda \subset \mathbb{R}^3 \tag{3.6}$$

$$G(\mathbf{z}, \mathbf{y}) = \frac{i}{4} H_0^{(1)}\left(k|\mathbf{z}-\mathbf{y}|\right), \qquad \mathbf{z} \neq \mathbf{y} \quad \text{if } \Lambda \subset \mathbb{R}^2 \tag{3.7}$$

$H_0^{(1)}(\cdot)$ is the zero order Hankel function of the first kind. If the assumption of free field propagation is removed, as for the case of a reverberant environment, most of the results presented in this work will still hold, but all of the equations involving or derived from a series or integral representation of the free field Green function (as for example in Chapter 4) will need to be calculated again using a different (and not always simple) representation of the Green function.

The relation between pressure p and particle velocity $\mathbf{v}$ of the field is given by Euler's equation [Wil99]

$$-\nabla p(\mathbf{z}) = \rho_0 \frac{\partial \mathbf{v}(\mathbf{z}))}{\partial t} \tag{3.8}$$

which for fixed frequency ω reduces to

$$\nabla p(\mathbf{z}) = i\omega\rho_0 \mathbf{v}(\mathbf{z}) \tag{3.9}$$

For the case of a secondary source radiating sound as an acoustic monopole, we observe that $\nabla p(\mathbf{z}) = \hat{\mathbf{z}}\partial p(\mathbf{z})/\partial z$. Consequently, for the free field case, we have the following expression for the pressure p, particle velocity $\mathbf{v}$ and (time averaged) intensity $\mathbf{I}$ of the acoustic field due to a secondary source and of the acoustic power W generated by it [Wil99]:

$$p(\mathbf{z}) = \ddot{m}\frac{e^{ikz}}{4\pi z} \tag{3.10}$$

$$\mathbf{v}(\mathbf{z}) = \ddot{m}\frac{1}{\rho_0 c}\frac{e^{ikz}}{4\pi z}\left(1 + \frac{i}{kz}\right)\hat{\mathbf{z}} = \frac{p(\mathbf{z})}{\rho_0 c}\left(1 + \frac{i}{kz}\right)\hat{\mathbf{z}} \tag{3.11}$$

$$\mathbf{I}(\mathbf{z}) = \frac{1}{2}\mathrm{Re}\left[p(\mathbf{z})\mathbf{v}(\mathbf{z})^*\right] = \frac{\ddot{m}^2}{32\pi^2 z^2 \rho_0 c}\hat{\mathbf{z}} = \frac{|p(\mathbf{z})|^2}{2\rho_0 c}\hat{\mathbf{z}} \tag{3.12}$$

$$W = \frac{\ddot{m}^2}{8\pi\rho_0 c} = \frac{|p(\mathbf{z})|^2}{2\rho_0 c} 4\pi z^2 \tag{3.13}$$

The last expression highlights the fact that the acoustic power generated by a secondary source is proportional to the square of $\ddot{m}$.

Given a continuous distribution of secondary sources on $\partial\Lambda$, the source strength can be substituted by the source strength *density* $a(\mathbf{y})$, which represents the strength $\ddot{m}$ per unit of area (or unit of length for the two dimensional problem), thus given by

$$a := \frac{d\ddot{m}}{dS} \tag{3.14}$$

Clearly, $a(\mathbf{y})$ has the dimensions of $[Kg\ s^{-2}\ \mathrm{m}^{-2}]$ (for the 3D problem). In what follows, when there is no risk of confusion, we will for simplicity refer to $a(\mathbf{y})$ as source strength, omitting the word density. It should be clear, however, that the term source strength is referred to $\ddot{m}$.

Let $\hat{p}(\mathbf{z})$ be the sound field generated by the continuous distribution of secondary sources mentioned above. The pressure field $\hat{p}(\mathbf{z})$ is hereafter referred to as the reproduced sound field and it is due to the linear superposition of the fields generated by the layer of secondary sources. It can be described by the following integral:

$$\hat{p}(\mathbf{z}) = \int_{\partial\Lambda} G(\mathbf{z},\mathbf{y})a(\mathbf{y})dS(\mathbf{y}), \quad \mathbf{z} \in \mathbb{R}^m, \ \ m = 2,3 \tag{3.15}$$

This integral is called the acoustic *single layer potential* [CK83, p.46]. The function $a(\mathbf{y})$ is also referred to as the density of the potential [CK92] and represents, as discussed above, the strength of the secondary sources per unit of area or unit of length.

We define [3] also the operator S as the restriction of the single layer potential (3.15) to the boundary ∂V:

$$(Sa)(\mathbf{x}) := \int_{\partial\Lambda} G(\mathbf{x},\mathbf{y})a(\mathbf{y})dS(\mathbf{y}), \quad \mathbf{x} \in \partial V \tag{3.16}$$

For compactness of notation, the symbol S is used in the rest of this work also for the restriction of the single layer potential (3.15) to a different domain, provided that the latter is clearly specified. For example, the notation $(Sa)(\mathbf{z})$, $\mathbf{z} \in V$ defines the restriction of (3.15) to the interior of V, while the notation $(Sa)(\mathbf{z})$, $\mathbf{z} \in R^m$ identifies the single layer potential defined by (3.15).

The operator S defined here should not be confused with the integral (2.103) involved in the *Simple Source Formulation* [Wil99], for which the control region V and the reproduction region Λ coincide.

The sound field reproduction problem addressed in this work consists of determining the density $a(\mathbf{y})$, such that the reproduced sound field $\hat{p}(\mathbf{z})$ is the best approximation, in an L^2 sense, of the target field $p(\mathbf{z})$ in V. In other words, the aim is to determine the density $a(\mathbf{y})$ which minimizes the norm

$$\left|\left| \int_{\partial\Lambda} G(\cdot,\mathbf{y})a(\mathbf{y})dS(\mathbf{y}) - p \right|\right|_V \tag{3.17}$$

[3] Note that the definition of the operator S provided here differs from that often used in the literature [CK83], [CK92], [Pot07] for a factor 2 and in the fact that the boundaries $\partial\Lambda$ and ∂V usually coincide

3.3 The Dirichlet problem

A relevant aspect of the problem under consideration is that, under given conditions, the target sound field $p(\mathbf{z})$ in the interior of V is uniquely determined from a knowledge of its value on the boundary of the control region, that is from the knowledge of the pressure profile.

In order to illustrate this concept, we proceed as follows: given the continuous function $f(\mathbf{x})$ defined on ∂V, representing the pressure profile, we seek the solution of the so called Dirichlet problem

$$\begin{cases} \nabla^2 p(\mathbf{z}) + k^2 p(\mathbf{z}) = 0, & \mathbf{z} \in V \\ p(\mathbf{x}) = f(\mathbf{x}), & \mathbf{x} \in \partial V \end{cases} \tag{3.18}$$

where the second equation represents the Dirichlet boundary condition. This is a well known mathematical problem and in [CK83] and [CK92] is shown that it has a unique solution, apart from the case when k is one of the so called Dirichlet eigenvalues. These are defined as the set of wave numbers k_n such that the problem (3.18) with homogenous Dirichlet boundary condition $f(\mathbf{x}) = 0$ admits at least one non-trivial solution $p_n(\mathbf{z})$. In the case of V being a bounded set, it can be shown that the negative Laplacian is a compact linear operator and for this reason the set of the Dirichlet eigenvalues k_n constitutes an infinite but countable set. In physical terms, the problem (3.18) corresponds to the modal decomposition of the sound field in a cavity with the geometrical shape of V and pressure release boundary conditions ($p(\mathbf{x}) = 0$, $\mathbf{x} \in \partial V$), and the set of wave numbers k_n correspond to the infinite number of resonance frequencies of that cavity.

In the case of k being one of the Dirichlet eigenvalues, the solution of (3.18) is not unique. This can be easily proven: assume that $k = k_n$ and $p_n(\mathbf{z})$ is the corresponding eigenfunction (the eigenvalue is assumed to be non degenerate). Given a solution $p(\mathbf{z})$ of (3.18), the function $\tilde{p}(\mathbf{z}) = p(\mathbf{z}) + m p_n(\mathbf{z}), m \in \mathbb{R}$ is also a solution. In this case only the Dirichlet boundary condition is not sufficient for solving (3.18), but it is necessary to impose boundary conditions both on the field and on its gradient (a Cauchy boundary condition). In Section 5.5, we will see that this nonuniqueness problem of the interior Dirichlet problem has some consequences for the uniqueness of the sound field reproduction problem.

In what follows, unless specified differently, the assumption is made that $k \neq k_n$. Under this condition, what has been discussed proves that the sound field $p(\mathbf{z})$ in V is uniquely defined by its value on ∂V, and this also implies that if the target sound field is reproduced exactly on ∂V, then it is reproduced exactly also in V.

Using arguments related to the analytical continuation of $\hat{p}(\mathbf{z})$, it can be shown that the condition $\hat{p}(\mathbf{x}) = p(\mathbf{x})$ on ∂V implies that the field is accurately reconstructed also in the region of the space belonging to the interior of Λ and to the exterior of V (namely

in $\Lambda \backslash \overline{V}$), provided that $p(\mathbf{z})$ still satisfies the homogeneous Helmholtz equation in that region.

3.4 The integral equation

The discussion above leads to the conclusion that, under the conditions described above, the sound field reproduction problem can be reformulated in terms of the reconstruction of the pressure profile on ∂V, at frequencies other than those identified by the Dirichlet eigenvalues k_n. Consequently, the optimal reconstruction (always in terms of the L^2 norm) of the target sound field is given by a potential Sa, whose density $a(\mathbf{y})$ is the solution of

$$p(\mathbf{x}) = (Sa)(\mathbf{x}) = \int_{\partial\Lambda} G(\mathbf{x}, \mathbf{y}) a(\mathbf{y}) dS(\mathbf{y}), \quad \mathbf{x} \in \partial V \tag{3.19}$$

The latter is an integral equation of the first kind [Pot07], [Pot01], [Kre99] (sometimes referred to as Fredholm equation of the first kind [Kre78]), and is one of the central concepts of this work. For a thorough presentation of the subject of integral equations, the reader can refer to the extensive literature dedicated to this wide topic (see, for example, [Kre78], [CK83] or [Pot07]).

It is important to underline that the left hand side of equation (3.19) differs from the function $\hat{p}(\mathbf{z})$ in equation (3.15), the former being the pressure profile, defined on ∂V, the latter the reproduced sound field in the entire space $\mathbb{R}^m$, $m = 2, 3$. In fact, (3.15) defines the acoustic single layer potential, while (3.19) is an integral equation with unknown function $a(\mathbf{y})$.

As will become clear later, equation (3.19) represents an inverse problem, and because of its nature of an integral equation of the first kind, it represents an ill-posed problem. This implies that the solution of (3.19) could either not exist, be non-unique or be unstable (does not depend continuously on the data). These concepts are discussed further in Chapter 5, that is dedicated to the problem of ill-conditioning.

It is therefore not possible, in general, to compute an exact solution of an ill-posed problem. However, as it is shown later, it is usually possible to compute an approximate solution by using a regularization scheme.

3.5 Singular Value Decomposition

The inverse problem (3.19) can be tackled with different methods (see, for example, [CK92] for other solution methods). Some of these include the singular value decomposition (SVD) of the operator S. This powerful method is discussed in what follows and provides considerable insight into the physical problem of sound field reproduction.

The analytical SVD used here, involving a compact linear operator acting on a function, can be simplistically understood as an extension of the more popular *discrete* SVD, performed on a matrix acting on a vector, to the more general case of abstract spaces of functions such as, for example, Hilbert spaces [Kre78]. The *discrete* SVD has been widely used in acoustical problems related to analysis and control of sound fields and source reconstruction (see for example [VM89], [NY00],[KN03], [WHH03], [Spo06], [SS06], [GBW05], [GB08b]). A simple explanation of the discrete SVD and its interpretation in the context of sound field reproduction is reported in Appendix A (the reader can also refer to [FN07b]). The extension of the SVD to operators is probably due to E. Schmidt ([Sch07], published in 1907), who introduced the infinite dimensional analogous of the SVD, and used it to approximate operators [Ste93]. The use of the SVD of operators for radiation problems was proposed by W.A. Veronesi and J.D. Maynard [VM89] for the case of planar geometry. G.V. Borgiotti et al. also used this technique in the for conformal holography and acoustic radiation [Bor90], [BSWS90], [BJ93], and C. Maury, S.J. Elliott and T. Bravo [ME05], [MB08] recently proposed some analytical formulation of the singular system of the radiation operator in terms of prolate spheroidal wave functions [ME05]. The SVD of an integral operator is also frequently used in acoustic scattering problems (see, for example, [CK92]).

A short review of the main mathematical passages involved in the derivation of the SVD and some of its relevant properties are reported in Section 2.5. A better insight into the mathematics of the SVD can be found, for example, in [CK92] and [Pot07]. Some of the properties of the operator S and its adjoint operator, which will be useful later in this paper, are briefly discussed here. An important property is the *compactness* of S. Despite the relevance of this concept in respect to the SVD, an exhaustive presentation of this subject is not brief and no attempt has been made to describe the details here. The reader is referred to [Kre78] or [Pot07] for more detail.

3.5.1 The compactness of S, the adjoint operator S^* and the composite operator S^*S

The compactness of S is crucial to the validity of the following arguments. We are not concerned here with the physical interpretation of compactness of an operator, but we need to make sure that the operator S is compact in order to apply some relevant properties that compact operators possess. In [CK83, p.5] (among others) the proof is given that under the assumptions introduced above, S is a linear and compact operator, since its kernel is continuous (or weakly singular if $\Lambda = V$) and since the domain of integration ∂V is bounded. It should be noticed that if the domain of integration ∂V is not bounded, then S is not compact. This case is considered in Section 4.3.

Considering the definition of an adjoint operator (2.21), it can be easily seen that $S \neq S^*$, that is S is not self adjoined. The adjoint operator S^* is

$$(S^*p)(\mathbf{y}) = \int_{\partial V} G(\mathbf{y},\mathbf{x})^* p(\mathbf{x}) dS(\mathbf{x}), \quad \mathbf{y} \in \partial\Lambda \tag{3.20}$$

The operator S^* does not have a real physical meaning, but it could be interpreted as a *time reversed* single layer potential. We can imagine that a continuous distribution of monopole-like sources, with source strength equal to $p(\mathbf{x})$, is arranged on ∂V. The sound field generated by this source layer is reversed in time; this arises from the fact that the kernel of S^* is the complex conjugate of $G(\mathbf{y},\mathbf{x})$ and considering that $(\mathcal{F}_t^{-1}p^*)(t) = (\mathcal{F}_t^{-1}p)(-t)^*$ (see formula (2.78)). Equivalently, the sources on ∂V could be interpreted as *sources of incoming sound*, which have of course no reasonable physical meaning. $(S^*p)(\mathbf{y})$ is actually this time reversed field measured on $\partial\Lambda$. A similar interpretation was suggested by Tanter et al. [TAG+01].

As shown in [Kre78, p.416], if S is compact then S^* is also compact. The composed operator S^*S is expressed by

$$(S^*Sa)(\mathbf{y}) = \int_{\partial V} G(\mathbf{y},\mathbf{x})^* \left(\int_{\partial\Lambda} G(\mathbf{x},\hat{\mathbf{y}}) a(\hat{\mathbf{y}}) dS(\hat{\mathbf{y}}) \right) dS(\mathbf{x}), \quad \mathbf{y} \in \partial\Lambda \tag{3.21}$$

This operator is compact and self adjoined. As explained in Section 2.5, these two properties imply relevant consequences for the spectral decomposition of the operator S^*S, on which the SVD of S is grounded.

Following the interpretation of S^* proposed above, the composite operator S^*S could be figuratively understood as follows: an acoustic field is generated by the secondary sources on $\partial\Lambda$ with strength $a(\mathbf{y})$. This field, $(Sa)(\mathbf{x})$, is measured on ∂V and the pressure profile $p(\mathbf{x})$ is used to define the strength of a second layer of sources, this time arranged on ∂V. These sources generate a second field, which is time reversed and measured on $\partial\Lambda$. The function describing the acoustic pressure of this time reversed field on $\partial\Lambda$ is $(S^*Sa)(\mathbf{y})$.

3.5.2 Singular system and SVD of S

Following the passages reported in Section 2.5, it is possible to compute a singular system $\{\sigma_n, a_n(\mathbf{y}), p_n(\mathbf{x})\}$, where σ_n are the singular values of S, while $p_n(\mathbf{x})$ and $a_n(\mathbf{y})$ are respectively its left and right singular functions. The latter represent two sets of orthonormal functions, defined on ∂V and $\partial\Lambda$, respectively, and are analogous to the singular vectors in the case of the SVD of a matrix. One of the most powerful features of the SVD is that any function $a(\mathbf{y}) \in L^2(\partial\Lambda)$ and any function $p(\mathbf{x}) \in L^2(\partial V)$ can be expressed by

$$a(\mathbf{y}) = \sum_{n=1}^{\infty} a_n(\mathbf{x})\langle a_n|a\rangle_{\partial\Lambda} + \left(P_{N(S)}a\right)(\mathbf{y}) \tag{3.22}$$

$$p(\mathbf{x}) = \sum_{n=1}^{\infty} p_n(\mathbf{x})\langle p_n|p\rangle_{\partial V} + \left(P_{N(S^*)}p\right)(\mathbf{x}) \tag{3.23}$$

$P_{N(S)}$ and $P_{N(S^*)}$ are the orthogonal projection operators onto the nullspace of S and S^* respectively (see (2.14) for the definition of orthogonal projection operator). If S is injective [4] , its nullspace is trivial (contains only 0), and the functions $a_n(\mathbf{y})$ are a *complete* set of functions for $L^2(\partial\Lambda)$ (see Section 2.5). The same holds for S^*, and the set of functions $p_n(\mathbf{x})$ in $L^2(\partial V)$, respectively.

The equalities above are valid only at points where the functions are continuous. It should be noticed, however, that the presence of removable or jump discontinuities is not relevant for the physical problem under consideration. In fact, since $p(\mathbf{x})$ is solution of the homogeneous Helmholtz equation (3.2), it is differentiable and is therefore continuous. On the other hand, given the functions $a(\mathbf{y})$ and $a'(\mathbf{y})$ that are identical apart from a countable set of points where $a'(\mathbf{y})$ is discontinuous. we observe that $Sa = Sa'$. As a matter of fact, in an L^2 sense, the two functions are identified.

The result above implies that (in the case of S and S^* injective) any square integrable function $p(\mathbf{x})$, representing the sound field on ∂V, can be expressed as a series of the singular functions $p_n(\mathbf{x})$. Analogously, any square integrable function $a(\mathbf{y})$ defining the source strength on $\partial\Lambda$ can be expressed as a series of $a_n(\mathbf{y})$. In this setting, equations (3.22) and (3.23) can be interpreted as a *generalized Fourier series* for $a(\mathbf{y})$ and $p(\mathbf{x})$ respectively, with $\langle a_n|a\rangle_{\partial\Lambda}$ and $\langle p_n|p\rangle_{\partial V}$ being the Fourier coefficients. From a slightly different perspective, equations (3.22) and (3.23) could be interpreted as the *modal decomposition* of the source strength $a(\mathbf{y})$ and of the pressure profile $p(\mathbf{x})$, respectively. The scalar product $\langle a_n|a\rangle_{\partial\Lambda}$ can be interpreted as the component of the source strength with respect to the *modal function* or *modal shape* $a_n(\mathbf{y})$ (and analogously for $\langle p_n|p\rangle_{\partial V}$).

The action of the operator S on $a(\mathbf{y})$ can be expressed by

$$(Sa)(\mathbf{x}) = \sum_{n=1}^{\infty} p_n(\mathbf{x})\sigma_n\langle a_n|a\rangle_{\partial\Lambda} \tag{3.24}$$

This result represents the SVD of S, and has as the following meaning: given the source strength $a(\mathbf{y})$, the reproduced sound field can be computed by

[4] An operator $S : A \to \Psi$ is injective if any two distinct element a and a' of A are associated with two distinct elements p and p' of Ψ, such that $Sa = p$ and $Sa' = p'$.

1. Calculating the set of scalars $\langle a_n|a\rangle_{\partial\Lambda}$ obtained from the scalar product of the source strength $a(\mathbf{y})$ with the singular functions $a_n(\mathbf{y})$ (this operation is analogous to the computation of the coefficients of a Fourier series);
2. Multiplying each coefficient $\langle a_n|a\rangle_{\partial\Lambda}$ by the corresponding singular value σ_n;
3. Modulating the singular functions $p_n(\mathbf{x})$ by the coefficients obtained in the previous passage. This operation gives an infinite set of scaled orthogonal functions;
4. Synthesizing the target sound field by summing the scaled orthogonal functions.

It is interesting to observe that, even if the problem formulation includes an integral operator (instead of a matrix), the singular functions and singular values are countable, that is they can be associated with natural numbers $n = 1, 2, ...$ This property is a consequence of the compactness of S (see Section 2.5). If this was not the case, the series in (3.22),(3.23) and (3.24) would become integrals, and the series of singular values a function (the spectrum of S). An analogous argument can be used to interpret the difference between a Fourier series and a Fourier integral.

It can be noticed that, in the special case when the set of left and right singular functions are the same, the passages described above define a convolution operation. Original approaches to the sound field reproduction in terms of spatial convolutions, which share some analogies with the approach discussed here, have been proposed by Nicol and Emerit [NE99] and by Ahrens and Spors [AS08d], [AS08a].

Another possible understanding of the SVD is the so called *mode matching* approach, as proposed by Poletti [Pol05],[Pol00]. In this interpretation, every *mode* $p_n(\mathbf{x})$ of the pressure profile is matched to one *mode* $a_n(\mathbf{y})$ of the source strength. The latter could be described as a given combination of strengths of the secondary sources. One example of *source mode* is the typical case of all secondary sources acting in-phase (very often corresponding to the first mode $a_1(\mathbf{y})$). Consistently with this interpretation, the singular functions $p_n(\mathbf{x})$ and $a_n(\mathbf{y})$ are hereafter also referred to as *acoustic pressure modes* and *secondary source modes* (or *array modes*), respectively.

It is important to emphasize that, as a consequence of the orthogonality of the singular functions, each pressure mode $p_n(\mathbf{x})$ is controlled by one and only one secondary source mode $a_n(\mathbf{y})$. Furthermore, the amount of energy transferred between one mode $a_n(\mathbf{y})$ and one mode $p_n(\mathbf{x})$ is related to the corresponding singular value σ_n, which is always a positive value. In other terms, from (3.24) and from the orthonormality of the singular functions we can easily derive the relation

$$\sigma_n = \frac{|\langle p_n|\hat{p}\rangle|}{||a_n||} = \frac{||Sa_n||}{||a_n||} \tag{3.25}$$

This means that the singular values are representative of the efficiency (in energetic terms) of the secondary source modes. In this sense, if a given amount of energy is

required for the mode $p_n(\mathbf{x})$ of the reproduced pressure profile, the corresponding secondary source mode $a_n(\mathbf{y})$ must be driven with a small amount of energy if σ_n is large, or oppositely with a large amount of energy (sometimes very large!) if σ_n is small. As will become clear in Chapter 5, this phenomenon is one of the main reasons for the ill conditioning of the inverse problem (3.19). In view of this interpretation, the singular values are also referred to here as *modal efficiency*.

The actions of the operators S^* and S^*S can be expressed analogously to the case of S in equation (3.24):

$$(S^*p)(\mathbf{y}) = \sum_{n=1}^{\infty} a_n(\mathbf{y})\sigma_n\langle p_n|p\rangle_{\partial V} \tag{3.26}$$

$$(S^*Sa)(\mathbf{y}) = \sum_{n=1}^{\infty} a_n(\mathbf{x})\sigma_n^2\langle a_n|a\rangle_{\partial\Lambda} \tag{3.27}$$

As will become clear in Chapter 4, the integral operator S acts as a *spatial low-pass filter*, which has in general the effect of smoothing out the rapid spatial variations when transforming $a(\mathbf{y})$ into $p(\mathbf{x})$. This can be intuitively interpreted with the fact that the low efficiency modes are generally associated with rapid spatial variations of the pressure profile, which are therefore hard to reproduce. This concept is demonstrated more rigorously in Section 4.1.

3.5.3 Separable geometries and representation of the single layer potential

It must be emphasized that the expression (3.24) of the operator S by means of its singular system $\{\sigma_n, a_n(\mathbf{y}), p_n(\mathbf{x})\}$ provides an expression for the single layer potential (3.15) only on the boundary ∂V of the control region, but generally not in its interior or in Λ. The singular system of S is clearly determined by the choice of both Λ and V, and if one of these two sets varies, the functions $\sigma_n, a_n(\mathbf{y}), p_n(\mathbf{x})$ will be different.

However, in the special case when $\partial\Lambda$ and ∂V represent the separation surfaces [MF53] of geometries in which the Helmholtz equation can be solved by separation of variables (such as spheres, circles, planes, etc.), it will be shown that simple analytical relations exist between the singular system of S defined for different ∂V and $\partial\Lambda$ corresponding to different separation surfaces. Consequently, the representation of S by means of its singular system can be extended to the single layer potential in the interior of Λ (and by applying further analytical relations, also to its exterior). This concept will become clear in Chapter 4, where the formulation of the singular systems of S for some separable geometries is presented.

3.5.4 Solution of the inverse problem

If an exact solution to the integral equation (3.19) exists, this is given by (see Section 2.5)

$$a(\mathbf{y}) = \sum_{n=1}^{\infty} a_n(\mathbf{y}) \frac{1}{\sigma_n} \langle p_n | p \rangle_{\partial V} \tag{3.28}$$

This meaningful result provides an expression of the source strength function $a(\mathbf{y})$ in terms of singular functions and singular values of S. Assuming that these are known, the SVD gives the following important insight into the problem of sound field reproduction:

- The scalar product $\langle p_n | p \rangle$ reveals *how much* of a given mode $p_n(\mathbf{x})$ is present in the target pressure profile $p(\mathbf{x})$. It must be remembered that this analysis is performed on the boundary ∂V of the control region.
- Each singular function $a_n(\mathbf{y})$ describes what combination of strength of the secondary sources is required to generate a given mode $p_n(\mathbf{x})$ of the target pressure profile
- The singular values σ_n indicate *how efficiently* each source mode $a_n(\mathbf{y})$ transfers the acoustic energy to the related acoustic pressure mode $p_n(\mathbf{x})$. It should be emphasized that the singular values σ_n depend only on the operator S, and not on the target sound field. In other words, the singular values are influenced only by the geometry of the secondary source layer $\partial\Lambda$ and of the control region V, and by the function $G(\mathbf{x}, \mathbf{y})$, representing the acoustical transfer function between the secondary sources and any point on ∂V.
- The factor $\langle p_n | p \rangle / \sigma_n$ defines *how much* of each secondary source mode $a_n(\mathbf{y})$ is required for the reproduction of the pressure profile $p(\mathbf{x})$. This factor depends on both the system configuration (Λ,V and $G(\mathbf{x}, \mathbf{y})$) and on the characteristics of $p(\mathbf{x})$.

From (3.28) and in view of the Parseval relation (2.71), the following relation can be easily derived :

$$||a||^2 = \sum_{n=1}^{\infty} \frac{|\langle p_n | p \rangle|^2}{\sigma_n^2} \tag{3.29}$$

This equation defines the relation between the norm of the source strength function $a(\mathbf{y})$, proportional to the total amount of acoustic energy generated by the secondary sources, the contribution of each single mode $p_n(\mathbf{x})$ to the target pressure profile and the related efficiency σ_n. As discussed in Section 5.3, the first Picard condition (5.2) for the existence of the solution $a(\mathbf{y})$ imposes that the series in (3.29), and hence the total energy $||a||^2$, must be less than infinity.

If we assume that the expression of the target pressure profile includes a single *low efficiency mode* p_n, associated to a small singular value σ_n, then the total amount of

energy generated by the secondary sources (proportional to $|\langle p_n|p\rangle|^2/\sigma_n^2$) will largely exceed the total energy of the acoustic field on ∂V (proportional to $|\langle p_n|p\rangle|^2$). The main physical reason behind the small efficiency of a mode is given by the fact that the fields generated by the different secondary sources interfere destructively on ∂V.

But the small singular value σ_n does not give any information about the acoustic energy of the sound field in other regions of the space, different from ∂V. This energy is likely to be also very large if $||a||$ is large.

It has been shown that equation (3.28) provides a powerful method for the computation of a solution to the inverse problem (3.19). However, some optimistic assumptions have been made: the solution exist and is unique and the singular system $\{\sigma_n, a_n(\mathbf{y}), p_n(\mathbf{x})\}$ for the given operator S is known. However, the existence and uniqueness of the solution need to be verified, and the singular system of S must be calculated, depending on the geometry Λ, V and on $G(\mathbf{x}, \mathbf{y})$. The next two chapters are dedicated to these subjects.

Chapter 4

Solution for special geometries

The computation of the singular functions $p_n(\mathbf{x})$ and $a_n(\mathbf{y})$ and of the singular values σ_n is in general not a simple task. Their determination in a closed analytical form is relatively simple for some special geometries of Λ and V, while for arbitrary geometries a numerical approach is often the only option. In this chapter, some singular systems are studied in the case of some specific but important geometries. The assumption of free field propagation holds for all the cases dealt with here.

The cases are studied where $\partial\Lambda$ and ∂V are concentric spheres and concentric circles, respectively. The analysis is then extended to the case of $\partial\Lambda$ and ∂V being infinite parallel planes and parallel lines, respectively. The study of the latter two geometries requires some further mathematical assumptions, since the operator involved is no longer compact. This additional effort is justified by the fact that the functions arising from the decomposition of the integral operator can be simply interpreted as propagating and evanescent plane waves, and a greater insight is provided into the problem under consideration and into the solution technique adopted.

The results presented in this chapter show very clearly the relation of the sound field reproduction problem to Acoustical Holography (discussed in more detail in Section 6.4.1) and, more generally, to other acoustical inverse problems.

All the derivations begin from the expansion of the free field Green function, given by equation (3.6) and (3.7), in terms of orthogonal functions which suit the given geometry.

The notation used in the following derivations is recalled here. Thus, with respect to the vector $\mathbf{x}$

$$\begin{aligned} &x := |\mathbf{x}| \quad \hat{\mathbf{x}} := \mathbf{x}/x \\ &\mathbf{x} = [x\cos\phi_x \sin\theta_x,\ x\sin\phi_x \sin\theta_x,\ x\cos\theta_x] \end{aligned} \tag{4.1}$$

and the spherical harmonics are written as

$$Y_n^m(\hat{\mathbf{x}}) = Y_n^m(\theta_x, \phi_x)$$

Analogous relations hold for the position vector $\mathbf{y}$. The symbol $\lceil \cdot \rceil$ denotes rounding up to the next integer.

4.1 Concentric spheres

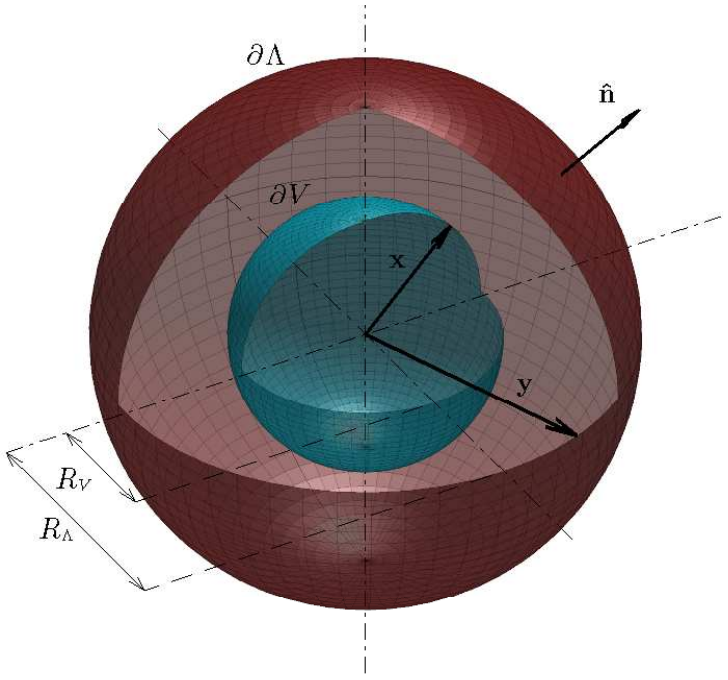

FIGURE 4.1: Geometrical arrangement with concentric spheres.

The case is considered where Λ and V are two concentric spheres with radius R_Λ and R_V, respectively. The condition $V \subseteq \Lambda$ is simply satisfied by imposing $R_V \leq R_\Lambda$. It follows that $|\mathbf{x}| = R_V$, $\mathbf{x} \in \partial V$ and $|\mathbf{y}| = R_\Lambda$, $\mathbf{y} \in \partial\Lambda$.

The free field Green function (3.6) can be expressed by [Wil99]

$$\frac{e^{ik|\mathbf{x}-\mathbf{y}|}}{4\pi|\mathbf{x}-\mathbf{y}|} = \sum_{\nu=0}^{\infty} ikh_\nu^{(1)}(ky) j_\nu(kx) \sum_{\mu=-\nu}^{\nu} Y_\nu^\mu(\hat{\mathbf{x}}) Y_\nu^\mu(\hat{\mathbf{y}})^*, \quad y > x \tag{4.2}$$

The following orthogonality relations follow from the orthonormality of the spherical harmonics (2.52)

$$\begin{aligned} \int_{\partial V} Y_\nu^\mu(\hat{\mathbf{x}}) Y_{\nu'}^{\mu'}(\hat{\mathbf{x}}) dS(\mathbf{x}) &= R_V^2 \delta_{\nu\nu'} \delta_{\mu\mu'} \\ \int_{\partial\Lambda} Y_\nu^\mu(\hat{\mathbf{y}}) Y_{\nu'}^{\mu'}(\hat{\mathbf{y}}) dS(\mathbf{y}) &= R_\Lambda^2 \delta_{\nu\nu'} \delta_{\mu\mu'} \end{aligned} \tag{4.3}$$

For this geometry, we have that $dS(\mathbf{x}) = R_V^2 \cos(\theta_x) d\phi_x d\theta_x$ and $dS(\mathbf{y}) = R_\Lambda^2 \cos(\theta_y) d\phi_y d\theta_y$. The factors R_V^2 and R_Λ^2 on the right hand sides of these equations result from performing the integrations on ∂V and $\partial\Lambda$, respectively, instead of on the unitary sphere as in (2.52).

In view of these orthogonality relation, it is possible to substitute the kernel of the integrals (3.19), (3.20) and (3.21) with equation (4.2) and rearrange the order of summation and integration in order to obtain

$$(Sa)(\mathbf{x}) = \sum_{\nu=0}^{\infty} iR_V R_\Lambda k h_\nu^{(1)}(kR_\Lambda) j_\nu(kR_V) \sum_{\mu=-\nu}^{\nu} \frac{Y_\nu^\mu(\hat{\mathbf{x}})}{R_V} \frac{\langle Y_\nu^\mu | a \rangle_{\partial\Lambda}}{R_\Lambda} \tag{4.4}$$

$$(S^* p)(\mathbf{y}) = \sum_{\nu=0}^{\infty} -iR_V R_\Lambda k h_\nu^{(2)}(kR_\Lambda) j_\nu(kR_V) \sum_{\mu=-\nu}^{\nu} \frac{Y_\nu^\mu(\hat{\mathbf{y}})}{R_\Lambda} \frac{\langle Y_\nu^\mu | p \rangle_{\partial V}}{R_V} \tag{4.5}$$

$$(S^* Sa)(\mathbf{y}) = \sum_{\nu=0}^{\infty} R_V^2 R_\Lambda^2 k^2 |h_\nu(kR_\Lambda) j_\nu(kR_V)| \sum_{\mu=-\nu}^{\nu} \frac{Y_\nu^\mu(\hat{\mathbf{y}})}{R_\Lambda} \frac{\langle Y_\nu^\mu | a \rangle_{\partial\Lambda}}{R_\Lambda} \tag{4.6}$$

Note that $\langle \cdot | \cdot \rangle_{\partial\Lambda} = \langle \cdot | \cdot \rangle_\Omega R_\Lambda^2$ and $\langle \cdot | \cdot \rangle_{\partial V} = \langle \cdot | \cdot \rangle_\Omega R_V^2$, where Ω is the unitary sphere. Comparing these results with equations (3.24), (3.26) and (3.27), expressing the actions of the three integral operators above in terms of elements of the singular system $\{\sigma_n, a_n(\mathbf{y}), p_n(\mathbf{x})\}$ of S, the following choices can be made

$$\sigma_n = kR_V R_\Lambda |h_\nu(kR_\Lambda) j_\nu(kR_V)| \tag{4.7}$$

$$a_n(\mathbf{y}) = \frac{1}{R_\Lambda} Y_\nu^\mu(\hat{\mathbf{y}}) \tag{4.8}$$

$$p_n(\mathbf{x}) = \frac{\gamma_\nu}{R_V} Y_\nu^\mu(\hat{\mathbf{x}}) \tag{4.9}$$

$$\gamma_\nu = \exp\left[i \left(\arg\left(h_\nu(kR_\Lambda) j_\nu(kR_V) \right) + \frac{\pi}{2} \right) \right] \tag{4.10}$$

$$\nu = \lceil \sqrt{n} - 1 \rceil, \qquad \mu = n - 1 - \nu - \nu^2 \tag{4.11}$$

From equations (4.4),(4.5) and (4.6) it follows that this singular system satisfies the relations (2.120), (2.121) and (2.122) reported in Section 2.5.

The factor γ_ν is a complex scalar of unitary norm, and represents the change of phase experienced by the corresponding modes in the propagation from $\partial\Lambda$ to ∂V. It has been introduced into the formulation of $p_n(\mathbf{x})$ since the singular values are constrained to be real by definition.

The two indices ν and μ, playing the role of the single index n, are due to the degeneracy of the singular values, often arising in eigenvalue problems in which symmetrical geometries such as cylinders or spheres are involved. In fact, a singular value related to a given coefficient ν has multiplicity of $2\nu + 1$, and is associated with $2\nu + 1$ singular vectors $a_n(\mathbf{y})$ and with $2\nu + 1$ singular vectors $p_n(\mathbf{x})$. The relation between n and ν, μ is given by (4.11) and is shown in Table 4.1.

n	1	2	3	4	5	6	7	8	9	10	$\cdots$
ν	0	1	1	1	2	2	2	2	2	3	$\cdots$
μ	0	-1	0	1	-2	-1	0	1	2	-3	$\cdots$

TABLE 4.1: Relation between the index n of the elements of the singular system $\{\sigma_n,\ a_n(\mathbf{y}),\ p_n(\mathbf{x})\}$ and the spherical harmonic and Hankel function indices ν and μ.

However, this indexing method might not be adequate, since the singular values are by definition ordered by decreasing magnitude (see section 2.5), and therefore they might need to be re-ordered (and accordingly the singular functions).

The constant factors R_V and R_Λ have been introduced into the formulation of the singular values and of the singular functions in order for $p_n(\mathbf{x})$ and $a_n(\mathbf{y})$ to have unitary norm, with respect to the integrations (4.3), since these are performed on the non-unitary spheres ∂V and $\partial\Lambda$, respectively.

Summarizing, it can be stated that for the case of two concentric spheres, the singular values are functions of the wave number k (and hence of the frequency) and of the radii of the two spheres. Their expression includes the absolute value of a combination of spherical Hankel and Bessel functions, with arguments kR_Λ and kR_V, respectively.

4.1.1 Properties of the singular system

Figure 4.2 and Figure 4.3 represents the spherical Bessel and Hankel functions, respectively. It is very important to notice that absolute value of the Hankel functions is always larger than zero, while this is not true for the Bessel functions. As a consequence, the singular values given by (4.7) can theoretically equal zero for given values of the product kR_V (in which case they would no longer be regarded as singular values, by definition). As shown in Appendix C, the frequencies ω_n such that $j_n(R_V\omega_n/c) = 0$ identify the resonance frequencies of a sphere with radius R_V and pressure release boundaries, and the corresponding wave numbers k_n are the Dirichlet eigenvalues for the domain V (see Section 3.3). As will be explained in Chapter 5, the Dirichlet eigenvalues of Λ do not play any role here.

It can be observed that, for small arguments and high orders, the Hankel functions tend to diverge, while the Bessel functions tend to zero (apart from the order $\nu = 0$). The high order approximations of the spherical Bessel and Hankel function are given by equations (2.39) and (2.40), respectively, which are reported below

$$j_\nu(x) = \frac{x^\nu}{(2\nu+1)!!} \qquad \nu \to \infty \tag{4.12}$$

$$h_\nu^{(1)}(x) = \frac{(2\nu-1)!!}{ix^{\nu+1}} \qquad \nu \to \infty \tag{4.13}$$

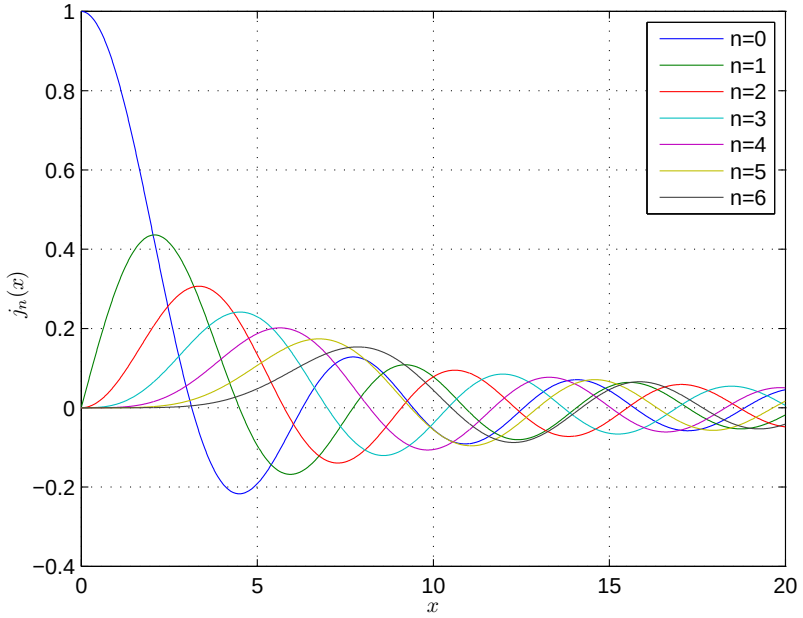

FIGURE 4.2: Spherical Bessel functions of order $n = 0$ to $n = 6$).

where

$$(2\nu + 1)!! := 1 \cdot 3 \cdot 5 \cdots (2\nu - 1) \cdot (2\nu + 1) \tag{4.14}$$

The high order approximation of the singular values is therefore

$$\sigma_n = \frac{R_V}{2\nu + 1} \left(\frac{R_V}{R_\Lambda} \right)^\nu \quad n \to \infty \tag{4.15}$$

This result is a consequence of the behavior of the Bessel and Hankel functions for high order or small arguments. Since it has been assumed that $R_V \leq R_\Lambda$, it is clear that the asymptotic expression above tends to zero as n (and thus ν) tends to infinity.

Decay of the singular values Figure 4.4 shows the singular values of S as expressed by equation (4.7), with $k = 15R_\Lambda$, $0 \leq \nu \leq 40$ and different values of R_V. The degenerate singular values are not repeated according to their multiplicity. The continuous line represents the asymptotic decay given by equation (4.15). It can be observed that, if $R_V < R_\Lambda$, the asymptotic decay of the singular values for $n \to \infty$ is dominated by the term $(R_V/R_\Lambda)^\nu$. This decay becomes steeper as the difference becomes larger between the radii of the two concentric spheres. As a consequence of this exponential decay, the inverse problem addressed is said to be *severely ill-posed*. In the limiting case when $R_V = R_\Lambda$, the asymptotic decay of the singular values is dominated by the term $R_V/(2\nu + 1)$. In this case, the singular values exhibit a linear decay, the slope of which does not depend on the geometrical arrangement. The linear decay of σ_n implies that the inverse problem is *mildly ill-posed* [CK92, p.92].

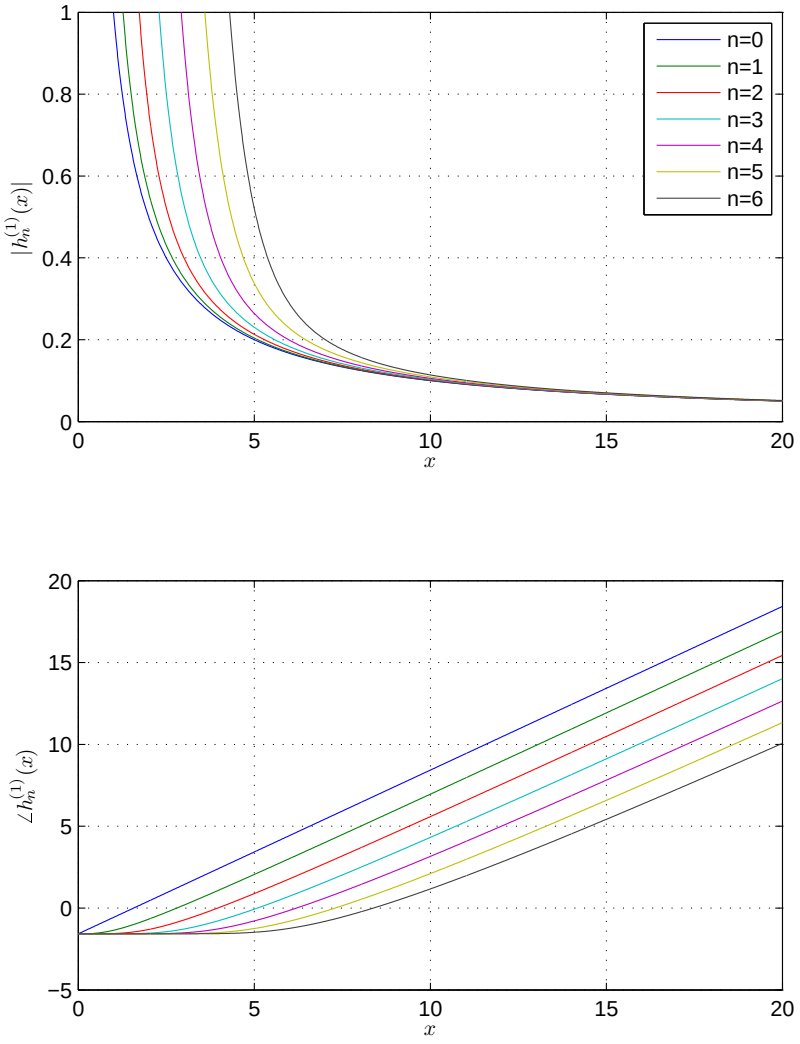

FIGURE 4.3: The magnitude and phase of the spherical Hankel functions of the first kind of order $n = 0$ to $n = 6$.

The large argument approximation of these functions are given respectively by equations (2.42) and (2.43), reported here

$$j_\nu(x) = \frac{1}{x}\sin\left(x - \frac{\nu\pi}{2}\right) \qquad x \to \infty \tag{4.16}$$

$$h_\nu^{(1)}(x) = (-i)^\nu h_0^{(1)}(x) = (-i)^{\nu+1}\frac{e^{ix}}{x} \qquad x \to \infty \tag{4.17}$$

Consequently, the high frequency or large wave number approximation of the singular values σ_n defined by (4.7) is given by

$$\sigma_n = \frac{1}{k}\sin\left(kR_V - \frac{\nu\pi}{2}\right) \quad k \to \infty \tag{4.18}$$

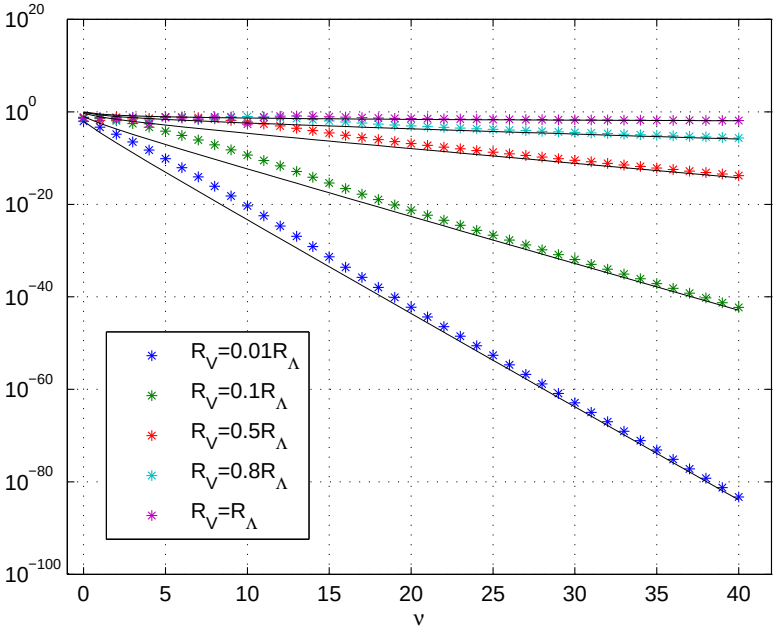

FIGURE 4.4: Singular values σ_n, computed with $k = 15R_\Lambda$ and a range of values of R_V. The degenerate singular values are not repeated according to their multiplicity. The continuous line shown represents the asymptotic decay given by the high order expansion of the Bessel and Hankel functions.

This means that the high frequency approximations of the singular values correspond to a $1/k$ factor with a sinusoidal modulation. It is relevant to note that the radius of $\partial\Lambda$ does not contribute to the expression above.

The left and right singular functions $a_n(\mathbf{y})$ and $p_n(\mathbf{x})$ are identical, apart from a constant factor, and are represented by spherical harmonics. These have the relevant property of being independent of the frequency ω. It can also be observed that the representation of the operator S given by (4.4) can be extended to the expression of the single layer potential (3.15) in all the reproduction region Λ. This can be simply achieved by substituting $\mathbf{x} \in \partial V$ with $\mathbf{z} \in \Lambda$ in equation (4.4) and in the expression of the singular system, equations (4.7)-(4.11). The functions $(Sa_n)(\mathbf{z})$, $\mathbf{z} \in \Lambda$ can be interpreted as standing spherical waves in the interior of Λ. Figures 4.5-4.10 show the horizontal cross-section of the acoustic field due to several secondary source modes, corresponding to different spherical harmonics Y_ν^μ, and for different values of k. On the right hand side of each figure, a plot of the real part of the corresponding spherical harmonic is illustrated (the red and blue color correspond to positive and negative sign, respectively, while the radial coordinate represents the absolute value of the real part of the function).

Each spherical wave $(Sa_n)(\mathbf{z})$ is characterized, in the interior of Λ, by nodal surfaces defined by spheres of radius R_n such that $j_\nu(kR_n) = 0$. It is clear that if ∂V corresponds to one of these nodal surfaces, that is if $R_V = R_n$ for a given n, then the corresponding singular function $(Sa_n)(\mathbf{x}) = 0, \quad \mathbf{x} \in \partial V$. This implies that all function identified by the

spherical harmonics $Y_\nu^\mu(\mathbf{y})$, corresponding to the given order n, are in the nullspace of S, defined by (2.23). Strictly speaking, these spherical harmonics do not define singular functions. However, they might be interpreted as secondary source modes with zero efficiency. It should be emphasized that if $(Sa_n)(\mathbf{x}) = 0$ for all $\mathbf{x}$ in ∂V, this definitely does not imply that $(Sa_n)(\mathbf{z}) = 0$ for all points $\mathbf{z} \in \Lambda \backslash \partial V$. This fact is associated with the problem of nonuniqueness of the solution discussed in Chapter 5.

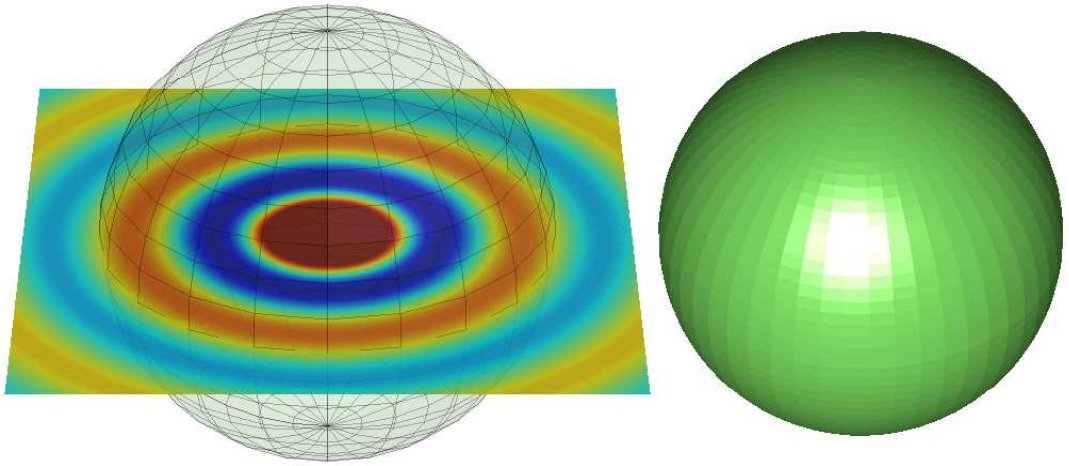

FIGURE 4.5: Acoustic field due to the secondary source mode $Y_0^0(\hat{\mathbf{y}})/R_\Lambda$, for $k = 9/R_\Lambda$.

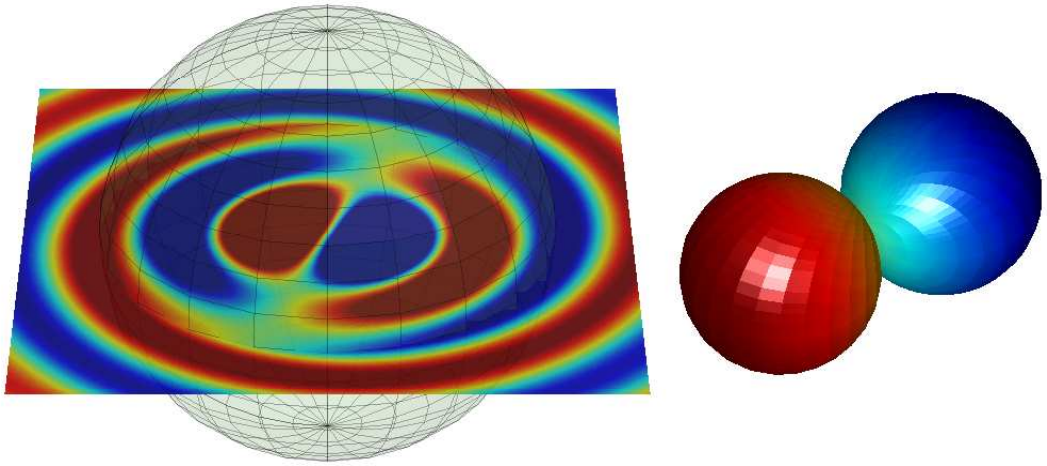

FIGURE 4.6: Acoustic field due to the secondary source mode $Y_1^1(\hat{\mathbf{y}})/R_\Lambda$, for $k = 9/R_\Lambda$.

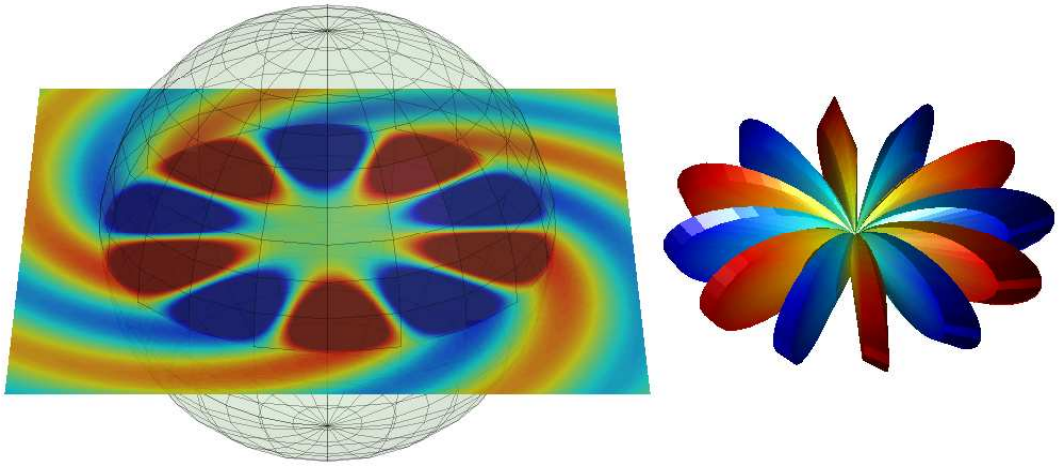

FIGURE 4.7: Acoustic field due to the secondary source mode $Y_6^{-6}(\hat{\mathbf{y}})/R_\Lambda$, for $k = 9/R_\Lambda$.

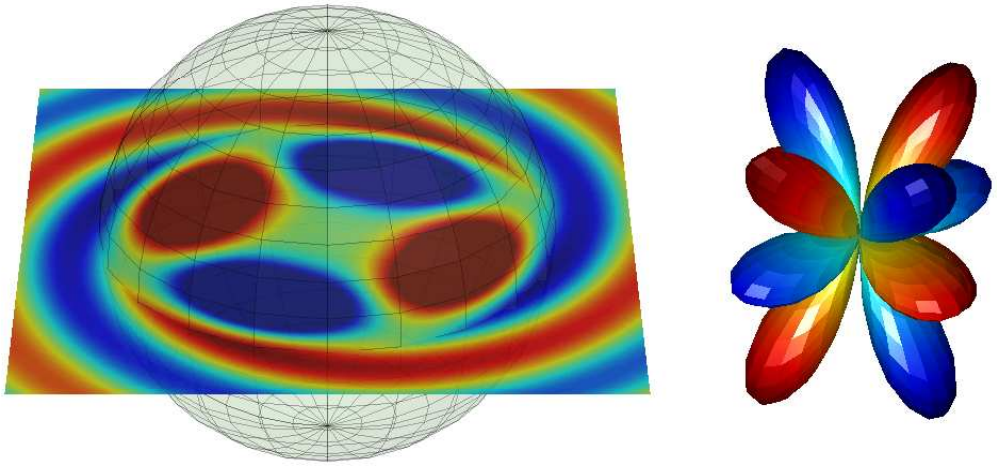

FIGURE 4.8: Acoustic field due to the secondary source mode $Y_4^2(\hat{\mathbf{y}})/R_\Lambda$, for $k = 9/R_\Lambda$.

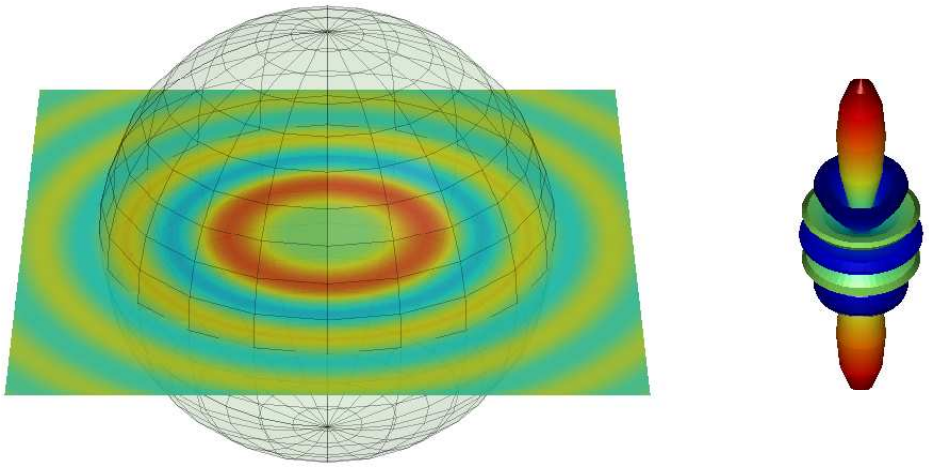

FIGURE 4.9: Acoustic field due to the secondary source mode $Y_6^0(\hat{\mathbf{y}})/R_\Lambda$, for $k = 18/R_\Lambda$.

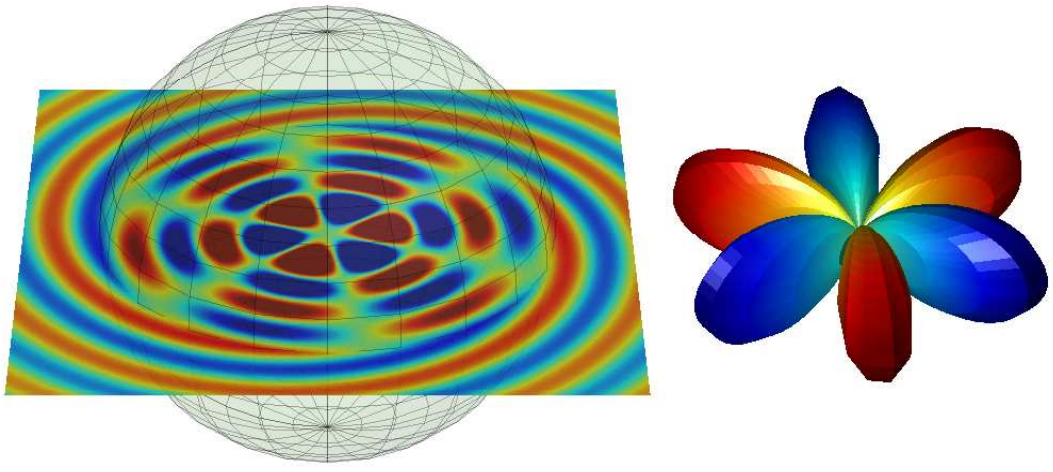

FIGURE 4.10: Acoustic field due to the secondary source mode $Y_3^{-3}(\hat{\mathbf{y}})/R_\Lambda$, for $k = 18/R_\Lambda$.

The analytical SVD of S for this geometrical arrangement can be compared with the traditional *discrete* version (expressing any matrix $\mathbf{H} = \mathbf{U}\mathbf{\Sigma}\mathbf{V}^{\mathrm{H}}$). It can be argued that the role of the unitary matrices $\mathbf{U}$ and $\mathbf{V}^{\mathrm{H}}$ is here played by a generalized Fourier series (2.69) and by the determination of the Fourier coefficients (2.70), respectively. The orthonormal functions of the generalized Fourier series are closely related to spherical harmonics. The diagonal matrix $\mathbf{\Sigma}$ corresponds here to the set of singular values σ_n.

4.1.2 Solution

The solution of the integral equation (3.19) is given, if it exists and is unique, by equation (3.28) in combination with the results shown above. This leads to

$$a(\mathbf{y}) = \sum_{\nu=0}^{\infty} \sum_{\mu=-\nu}^{\nu} \frac{Y_\nu^\mu(\hat{\mathbf{y}})}{ikR_V^2 R_\Lambda^2 h_\nu^{(1)}(kR_\Lambda) j_\nu(kR_V)} \langle Y_\nu^\mu | p \rangle_{\partial V} \tag{4.19}$$

The assumption has been made, that $j_\nu(kR_V) \neq 0 \quad \forall \nu = 0, 1, ...\infty$. If this is not the case, the expression given above represents one of the infinite possible solutions to (3.19). This special case is discussed in detail in Chapter 5.

Not surprisingly, results analogous to the above arise in the literature dedicated to spherical microphone arrays [Raf04], [Raf05] and High Order Ambisonics [DNM03], [AS08a].

Equation (4.19) can also be obtained as follows. Equation (3.19) is rewritten by substituting the kernel of the integral with the series (4.2), thus obtaining

$$p(\mathbf{x}) = \sum_{\nu=0}^{\infty} ikh_\nu^{(1)}(ky) j_\nu(kx) \sum_{\mu=-\nu}^{\nu} Y_\nu^\mu(\hat{\mathbf{x}}) \langle Y_\nu^\mu | a \rangle_{\partial\Lambda}, \quad \mathbf{x} \in V \tag{4.20}$$

Both sides of the equation above are multiplied by $Y_{\nu'}^{\mu'}(\hat{\mathbf{x}})^*/R_V$ and integrated over ∂V. Rearranging the order of integration we obtain

$$\begin{aligned} \int_{\partial V} p(\mathbf{x}) \frac{Y_{\nu'}^{\mu'}(\hat{\mathbf{x}})^*}{R_V} dS(\mathbf{x}) &= \sum_{\nu=0}^{\infty} iR_V R_\Lambda k h_\nu^{(1)}(ky) j_\nu(kx) \\ &\times \sum_{\mu=-\nu}^{\nu} \int_{\partial V} \frac{Y_\nu^\mu(\hat{\mathbf{x}})}{R_V} \frac{Y_{\nu'}^{\mu'}(\hat{\mathbf{x}})^*}{R_V} dS(\mathbf{x}) \frac{\langle Y_\nu^\mu | a \rangle_{\partial\Lambda}}{R_\Lambda} \end{aligned} \tag{4.21}$$

In view of the definition of scalar product (2.10) and of the orthogonality relation (4.3) the equation above can be rewritten as

$$\frac{\langle Y_{\nu'}^{\mu'} | p \rangle_{\partial V}}{R_V} = \sum_{\nu=0}^{\infty} iR_V R_\Lambda k h_\nu^{(1)}(ky) j_\nu(kx) \sum_{\mu=-\nu}^{\nu} \delta_{\nu\nu'} \delta_{\mu\mu'} \frac{\langle Y_\nu^\mu | a \rangle_{\partial\Lambda}}{R_\Lambda} \tag{4.22}$$

This, after substituting the dummy variables ν' and μ' with ν and μ, leads to

$$\frac{\langle Y_\nu^\mu|p\rangle_{\partial V}}{R_V} = iR_V R_\Lambda k h_\nu^{(1)}(ky) j_\nu(kx) \frac{\langle Y_\nu^\mu|a\rangle_{\partial\Lambda}}{R_\Lambda} \tag{4.23}$$

Assuming that $j_\nu(kx) \neq 0$ it is possible to write

$$\frac{1}{iR_V R_\Lambda k h_\nu^{(1)}(ky) j_\nu(kx)} \frac{\langle Y_\nu^\mu|p\rangle_{\partial V}}{R_V} = \frac{\langle Y_\nu^\mu|a\rangle_{\partial\Lambda}}{R_\Lambda} \tag{4.24}$$

The spherical harmonics $Y_\nu^\mu(\mathbf{y})$ constitute a complete set of functions for $L^2(\partial\Lambda)$ [CK92, p.24]. That is, any square integrable function $a(\mathbf{y})$ defined on $\partial\Lambda$ can be represented, at any point where this function is continuous, by a linear combination of spherical harmonics. As a consequence it is possible to compute the solution $a(\mathbf{y})$ to (3.19), if this exists, in the form of

$$a(\mathbf{y}) = \sum_{\nu=0}^{\infty} \sum_{\mu=-\nu}^{\nu} \frac{Y_\nu^\mu(\mathbf{y})}{R_\Lambda} \frac{\langle Y_\nu^\mu|a\rangle_{\partial\Lambda}}{R_\Lambda} \tag{4.25}$$

In view of this result, and if both sides of equation (4.24) are multiplied by $Y_\nu^\mu(\mathbf{y})/(R_\Lambda)$ and summing over ν, μ, one obtains

$$\sum_{\nu=0}^{\infty} \sum_{\mu=-\nu}^{\nu} \frac{Y_\nu^\mu(\mathbf{y})}{iR_V^2 R_\Lambda^2 k h_\nu^{(1)}(ky) j_\nu(kx)} \langle Y_\nu^\mu|p\rangle_{\partial V} = a(\mathbf{y}) \tag{4.26}$$

This result is identical to (4.19), as expected.

An example of solution for the target field due to a virtual point source is presented in Section 5.6.1.

4.1.3 The integral operator as a low-pass spatial filter

We have seen that both $p(\mathbf{x})$ and $a(\mathbf{y})$, assuming that they are square integrable functions, can be represented by a generalized Fourier series of the form (2.73), at any point where they are continuous (otherwise the equality holed as mean square). The Fourier coefficients are given by the spherical spectrum (2.73) and, if the nullspaces of S and S^* are trivial, it holds that

$$a(\mathbf{y}) = \sum_n^{\infty} \chi_{\nu,\mu}^a Y_\nu^\mu(\hat{\mathbf{y}}) = \sum_{\nu,\mu}^{\infty} \frac{\langle a_n|a\rangle_{\partial\Lambda}}{R_\Lambda} Y_\nu^\mu(\hat{\mathbf{y}}) \tag{4.27}$$

$$p(\mathbf{x}) = \sum_n^{\infty} \chi_{\nu,\mu}^p Y_\nu^\mu(\hat{\mathbf{x}}) = \sum_{\nu,\mu}^{\infty} \gamma_\nu \frac{\langle p_n|p\rangle_{\partial V}}{R_V} Y_\nu^\mu(\hat{\mathbf{x}}) \tag{4.28}$$

These formulae clearly show that the spherical spectra of $a(\mathbf{y})$ and $p(\mathbf{x})$ are equal to the scalar products $\langle a_n|a\rangle$ and $\langle p_n|p\rangle$, apart from the constants R_Λ and R_V and the phase factor γ_ν.

Equation (3.28) shows that the spherical spectrum of $a(\mathbf{y})$ is related to that of $p(\mathbf{x})$ by the relation

$$\chi^p_{\nu,\mu} = \left[\sigma_n \gamma_n \frac{R_\Lambda}{R_V}\right] \chi^a_{\nu,\mu} = \left[ikh_\nu(kR_\Lambda) j_\nu(kR_V) R_\Lambda^2\right] \chi^a_{\nu,\mu} \tag{4.29}$$

The function within the square brackets in the equation above can be interpreted as a *spatial filter*, which transforms $a(\mathbf{y})$ into $p(\mathbf{x})$ and provides an alternative representation of the action of the operator S.

Equation (4.15) shows that the singular values exhibit an exponential decay, governed by the ratio R_V/R_Λ. This decay can be interpreted as a *spatial low-pass filtering* that the spherical spectrum of $a(\mathbf{y})$ undergoes after the action of the operator S. As a consequence, $p(\mathbf{x})$ will be in general *smoother* than $a(\mathbf{y})$, and this is not surprising as the former is obtained after an integration (which is generally associated with a low-pass filter). It is clear that the inverse problem is associated with a spatial filter which boosts the high orders of the spherical spectrum of $p(\mathbf{x})$.

What has been discussed justifies what has been qualitatively discussed in Section 3.5: the low efficiency modes are associated with rapid spatial variations (here with respect of angular coordinates) of the pressure profile $p(\mathbf{x})$ and of the source strength $a(\mathbf{y})$. This leads to the consequence that the reproduction of pressure profiles with very rapid angular variations is problematic, and can lead to instability of the system. This will be discussed in more detail in Chapter 5.

4.2 Concentric circles

We consider the two dimensional case of Λ and V being two concentric circles, with radius R_Λ and R_V, respectively ($R_V \leq R_\Lambda$). This geometrical arrangement is shown in Figure 4.11. The starting point of the analysis is the following translation (or summation) theorem [CK92, p.66]:

$$H_0^{(1)}(k|\mathbf{x}-\mathbf{y}|) = H_0^{(1)}(ky) J_0(kx) + 2\sum_{n=1}^{\infty} H_n^{(1)}(ky) J_n(kx) \cos\left(n(\phi_x - \phi_y)\right) \tag{4.30}$$

The two dimensional free field Green function (3.7) can therefore be expressed by

$$G(\mathbf{x},\mathbf{y}) = \frac{i}{4} \sum_{n=-\infty}^{\infty} H_{|n|}^{(1)}(ky) J_{|n|}(kx) e^{in(\phi_x - \phi_y)}, \quad y > x \tag{4.31}$$

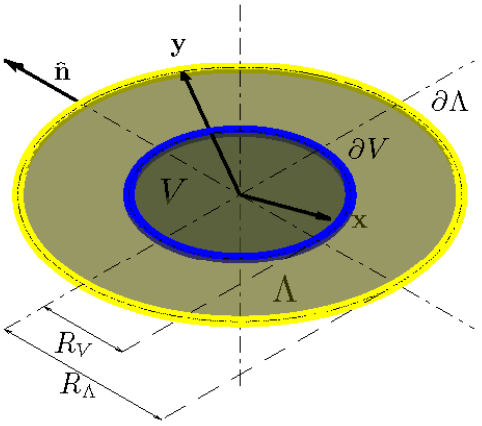

FIGURE 4.11: Geometrical arrangement with concentric circles.

the following orthogonality relations hold

$$\int_{\partial V} e^{in\hat{\mathbf{x}}} e^{in'\hat{\mathbf{x}}} dS(\mathbf{x}) = 2\pi R_V \delta_{nn'} \tag{4.32}$$

$$\int_{\partial \Lambda} e^{in\hat{\mathbf{y}}} e^{in'\hat{\mathbf{y}}} dS(\mathbf{y}) = 2\pi R_\Lambda \delta_{nn'} \tag{4.33}$$

where $dS(\mathbf{x}) = R_V d\phi_x$ and $dS(\mathbf{y}) = R_\Lambda d\phi_y$.

Equation (4.31) is used to express the kernel of the integrals (3.19), (3.20) and (3.21). After rearranging the order of integration and summation the following results can be obtained:

$$(Sa)(\mathbf{x}) = \frac{i\pi\sqrt{R_V R_\Lambda}}{2} \sum_{n=-\infty}^{\infty} H^{(1)}_{|n|}(kR_\Lambda) J_{|n|}(kR_V) \frac{e^{in\hat{\mathbf{x}}}}{\sqrt{2\pi R_V}} \frac{\langle e^{-in\hat{\mathbf{y}}} | a \rangle_{\partial\Lambda}}{\sqrt{2\pi R_\Lambda}} \tag{4.34}$$

$$(S^* p)(\mathbf{y}) = \frac{-i\pi\sqrt{R_V R_\Lambda}}{2} \sum_{n=-\infty}^{\infty} H^{(2)}_{|n|}(kR_\Lambda) J_{|n|}(kR_V) \frac{e^{in\hat{\mathbf{y}}}}{\sqrt{2\pi R_\Lambda}} \frac{\langle e^{-in\hat{\mathbf{x}}} | p \rangle_{\partial V}}{\sqrt{2\pi R_V}} \tag{4.35}$$

$$(S^* Sa)(\mathbf{y}) = \frac{\pi^2 R_V R_\Lambda}{4} \sum_{n=-\infty}^{\infty} \left| H^{(1)}_{|n|}(kR_\Lambda) J_{|n|}(kR_V) \right| \frac{e^{in\hat{\mathbf{y}}}}{\sqrt{2\pi R_\Lambda}} \frac{\langle e^{-in\hat{\mathbf{y}}} | a \rangle_{\partial\Lambda}}{\sqrt{2\pi R_\Lambda}} \tag{4.36}$$

n	1	2	3	4	5	6	$\cdots$
ν	0	-1	1	-2	2	-3	$\cdots$

TABLE 4.2: Relation between the index n of the elements of the singular system $\{\sigma_n,\ a_n(\mathbf{y}),\ p_n(\mathbf{x})\}$ and the number ν.

Comparing these results with equations (3.24), (3.26) and (3.27), a singular system $\{\sigma_n, a_n(\mathbf{y}), p_n(\mathbf{x})\}$ can be defined by

$$\sigma_n = \frac{\pi}{2}\sqrt{R_V R_\Lambda}\left|H^{(1)}_{|\nu|}(kR_\Lambda)J_{|\nu|}(kR_V)\right| \tag{4.37}$$

$$a_n(\mathbf{y}) = \frac{1}{\sqrt{2\pi R_\Lambda}}e^{i\nu\hat{\mathbf{y}}} \tag{4.38}$$

$$p_n(\mathbf{x}) = \frac{\gamma_\nu}{\sqrt{2\pi R_V}}e^{i\nu\hat{\mathbf{x}}} \tag{4.39}$$

$$\gamma_\nu = \exp\left[i\left(\arg\left(H^{(1)}_{|\nu|}(kR_\Lambda)J_{|\nu|}(kR_V)\right)+\frac{\pi}{2}\right)\right] \tag{4.40}$$

$$\nu = (-1)^{(n-1)}\left\lceil\frac{n-1}{2}\right\rceil \tag{4.41}$$

It can be easily proven that this singular system satisfies the relations (2.120), (2.121) and (2.122).

The index ν takes into account the double multiplicity of all singular values σ_n, $n > 1$. The relation (4.41) is shown in Table 4.2. The singular values might need to be re-ordered with decreasing value.

As in the case of the concentric spheres, the constant $\sqrt{2\pi R}$ has been introduce for the normalization of the singular functions and the complex factor γ_n is required for the singular values to be real.

As for the previous geometrical configuration, the singular values depend on the wave number k and on the two radii, and include a combination of Hankel and Bessel functions (but in this case not *spherical* Hankel and Bessel functions). The left and right singular functions are frequency independent and are closely related to complex exponentials, apart from a constant normalization factor. The properties of the singular system are analogous (although not identical) to those of discussed in the case of the concentric spheres.

If the comparison is made with the discrete SVD, the role of the unitary matrices $\mathbf{U}$ and $\mathbf{V}^{\mathrm{H}}$ is played this time by the traditional Fourier series (2.64) and by the determination of the Fourier coefficients (2.65), respectively.

If a solution to the integral equation (3.19) exists, this is given by

$$a(\mathbf{y}) = \sum_{\nu=-\infty}^{\infty}\frac{e^{i\nu\hat{\mathbf{y}}}}{i\pi^2 R_V R_\Lambda H^{(1)}_{|\nu|}(kR_\Lambda)J_{|\nu|}(kR_V)}\langle e^{i\nu\hat{\mathbf{x}}}|p\rangle_{\partial V} \tag{4.42}$$

as a consequence of equation (3.28). Analogously to (4.19), it has been assumed that $J_\nu(kR_V) \neq 0 \; \forall \nu = 0, 1, ...\infty$.

An alternative way to arrive at the same result is to perform mathematical operations analogous to those described for the case of concentric spheres.

4.3 Parallel infinite planes

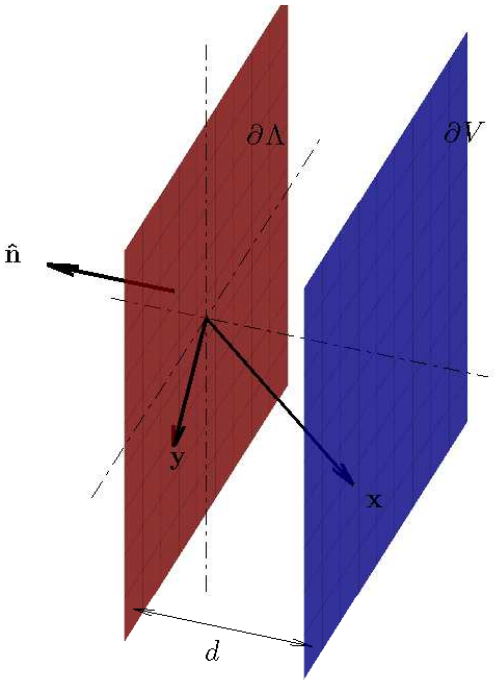

FIGURE 4.12: Geometrical arrangement with parallel planes.

Attention is now focused on the special case that occurs when $\partial\Lambda$ and ∂V correspond to two parallel infinite planes, separated by a distance d, as shown by Figure 4.12. In this case, Λ and V correspond to two half-spaces, with $V \subseteq \Lambda$. It is assumed that the origin of the co-ordinate system is on $\partial\Lambda$.

This geometrical arrangement can be interpreted as a degeneration of the case when Λ and V are two hemispheres with an ideally infinite radius (a similar philosophy is used in the theory of Wave Field Synthesis for the domain of integration of the Kirchhoff-Helmholtz integral [Sta97]).

This special geometry implies some severe mathematical difficulties related to the integral operator (3.16), whose definition now includes two unbounded sets. These issues have been already observed and studied, in relation also to acoustic scattering problems, as reported for example in [CWHP06]. In this publication it is argued that two main difficulties arise: the first is due to the unboundedness of S, caused by the *slow decay* at

infinity of the kernel (3.6) (the 3D free field Green function). This implies that $(Sa)(\mathbf{x})$ is not well defined for all densities $a(\mathbf{y}) \in L^2(\partial\Lambda)$. The second difficulty is related to the *loss of compactness* of S and S^*, due to $\partial\Lambda$ and ∂V being unbounded. This implies that S does not have the useful properties of compact operators described in Section 2.5 and this problem is a severe barrier to establishing the existence of the solution of the integral equation considered. Furthermore, the singular value decomposition of compact operators discussed in Section 2.5 should be revisited in view of the spectral decomposition of linear *non-compact* operators, which involves a more complex theory (see for example [Kre78]). One of the relevant consequences of S not being compact is that its eigenvalues are, in general, not countable.

A thorough discussion of these two issues and the formulation of techniques to overcome them is the subject of ongoing mathematical research and is far beyond the scope of this work.

It can be briefly mentioned, without going into the detail, that an elegant way to overcome the first difficulty described above consists in adding a small imaginary part to the wave number k, that is $k = (1 + i\epsilon)\omega/c$. The imaginary part mimics the physical decay with distance of any radiating acoustic wave, due to viscous losses occurring during the propagation of the wave in the medium. This is closely related to the *minimum absorption principle* mentioned in [CWHP06]. As explained by Maury and Bravo [MB08], the factor $e^{ikx} = e^{-x\epsilon\omega/c}e^{ix\omega/c}$ determines an exponential decay of the fundamental solution (3.6), which allows for S being bounded.

Despite the mathematical difficulties mentioned above, the case of two parallel infinite plane (and lines in the next section) is worth of consideration since it has some interesting peculiarities that provide further insight into the sound field reconstruction problem. More specifically, we will see that the kernel of the operator S can be decomposed into evanescent and propagating waves. The resulting expression of S is believed to provide a better understanding of the problem of ill-conditioning, and especially of its physical interpretation. This subject is discussed in Chapter 5. This special case also serves to emphasize the strong relation between sound field reproduction and Near-Field Acoustical Holography, especially with the well-established planar holography. This subject is discussed further in Section 6.4.1.

In order to go around the two issues above, the very strong assumptions are made that the solution $a(\mathbf{y})$ of the inverse problem S exists and is such that S is bounded. With this premise, intended to justify a possible lack of mathematical rigor for the sake of a better understanding of the problem, we begin the analysis.

4.3.1 Propagating and evanescent plane waves

A *propagating plane wave* of frequency $\omega = ck$ and unitary amplitude, traveling in the direction $\hat{\mathbf{r}}$, can be described by the expression [Wil99],[WA01]

$$p_{p.p.w.}(\mathbf{z}) = e^{i(\mathbf{z}\cdot\hat{\mathbf{r}}k+\varphi)} = e^{i(\mathbf{z}\cdot\mathbf{k}+\varphi)}, \quad \mathbf{z} \in \mathbb{R}^3 \tag{4.43}$$

where φ is an arbitrary phase and $\mathbf{k}$ is referred to as the wave vector. It has the magnitude of k and the direction of the propagating plane wave, and is defined by

$$\mathbf{k} := k\hat{\mathbf{r}} = [k_1,\ k_2,\ k_3] \tag{4.44}$$

Given the usual unitary vector $\hat{\mathbf{n}}$, perpendicular to $\partial\Lambda$ and directed as shown in Figure 4.12, it is possible to express the wave vector $\mathbf{k}$ as the sum of two orthogonal vectors $\boldsymbol{\kappa}$ and $\mathbf{k}_n$ defined by:

$$\mathbf{k_n} := (\hat{\mathbf{n}}\cdot\mathbf{k})\hat{\mathbf{n}} \tag{4.45}$$

$$\boldsymbol{\kappa} := \mathbf{k} - \mathbf{k_n} \tag{4.46}$$

The term $\zeta(\kappa)$ is now defined as the component of $\mathbf{k}$ in the direction identified by $-\hat{\mathbf{n}}$. This is given by

$$\zeta(\kappa) := -\hat{\mathbf{n}}\cdot\mathbf{k} \tag{4.47}$$

It can be observed that the dependance of ζ on κ is expressed by the following relation:

$$\zeta(\kappa) = \pm\sqrt{k^2 - \kappa^2}, \quad \kappa \leq k \tag{4.48}$$

$\zeta(\kappa)$ is positive if the acoustic energy carried by the plane wave flows from the half plane $\mathbb{R}^3\backslash\overline{\Lambda}$ into the half plane Λ, that is if the plane wave is traveling from $\mathbb{R}^3\backslash\overline{\Lambda}$ to Λ (this is the case considered in what follows).

The notation introduced above allows also for the description of evanescent waves [Wil99] in the half space identified by Λ. An *evanescent plane wave* [1] decaying in the direction $-\hat{\mathbf{n}}$, that is when moving away from the surface $\partial\Lambda$, and traveling in a direction parallel to $\partial\Lambda$, can be represented by (4.43), with the only difference that $\zeta(\kappa)$ is a positive imaginary number (or analogously that the component of $\hat{\mathbf{r}}$ in the direction identified by $-\hat{\mathbf{n}}$ is a positive imaginary number).

From (4.45) and (4.47), it is obvious that $\mathbf{k_n} = -\zeta(\kappa)\hat{\mathbf{n}}$. As the origin of the co-ordinate system has been assumed to lie on $\partial\Lambda$, the product $(\mathbf{z}\cdot\hat{\mathbf{n}})$ is always negative if $\mathbf{z} \in \Lambda$. Hence, for an evanescent wave, the product $i(\mathbf{z}\cdot\mathbf{k_n}) = -i\zeta(\kappa)(\mathbf{z}\cdot\hat{\mathbf{n}})$ is real and negative.

[1] Often in the literature [Wil99], the term *plane* is referred to propagating waves only.

An evanescent wave can therefore be described by the expression

$$p_{e.p.w.}(\mathbf{z}) = e^{i(\mathbf{z}\cdot\mathbf{k}+\varphi)} = e^{i(\mathbf{z}\cdot\mathbf{k_n}+\mathbf{z}\cdot\boldsymbol{\kappa}+\varphi)} = e^{-|\zeta(\kappa)\mathbf{z}\cdot\hat{\mathbf{n}}|}e^{i(\mathbf{z}\cdot\boldsymbol{\kappa}+\varphi)}, \qquad \mathbf{z}\in\mathbb{R}^3 \tag{4.49}$$

Here $\zeta(\kappa)$ is given here by equation (4.47) modified for the particular case of an evanescent wave:

$$\zeta(\kappa) = \sqrt{k^2-\kappa^2} = i\sqrt{\kappa^2-k^2}, \quad \kappa > k \tag{4.50}$$

The value $-i\sqrt{\kappa^2-k^2}$ does not have any physical meaning for $\zeta(\kappa)$, as it represents a wave whose amplitude increases exponentially with distance from $\partial\Lambda$ [Wil99].

It can be observed that any restriction of a plane wave to the plane $\partial\Lambda$ can be expressed by $e^{i\boldsymbol{\kappa}\cdot\mathbf{x}}$, $\mathbf{x}\in\partial\Lambda$, and corresponds to a wave propagating in Λ if $\kappa < k$ and $\zeta(\kappa)$ is real and positive. On the contrary, if $\kappa > k$ and $\zeta(\kappa)$ is purely imaginary, the exponential form corresponds to an evanescent wave decaying in Λ with increasing distance from $\partial\Lambda$. The special case of $\kappa = k$ defines a plane wave propagating in a direction parallel to $\partial\Lambda$.

A better understanding of the notation introduced above is given by the special case when $\partial\Lambda = \{\mathbf{z} : z_3 = 0\}$ and $\hat{\mathbf{n}} = [0,\ 0,\ -1]$. In this case Equations (4.43) and (4.49) become

$$p_{p.p.w.}(\mathbf{z}) = e^{i(z_1k_1+z_2k_2+z_3k_3+\varphi)}, \quad \mathbf{z}\in\mathbb{R}^3 \tag{4.51}$$

$$p_{e.p.w.}(\mathbf{z}) = e^{-|k_3|z_3}e^{i(z_1k_1+z_2k_2+\varphi)}, \quad \mathbf{z}\in\mathbb{R}^3 \tag{4.52}$$

respectively.

Figure 4.13 and Figure 4.14 represent the acoustic fields due to a propagating plane wave and to an evanescent plane wave, respectively.

4.3.2 Derivation of $\sigma_\kappa,\ a_{\boldsymbol{\kappa}}(\mathbf{y}),\ p_{\boldsymbol{\kappa}}(\mathbf{x})$

The so called Weyl integral [2] [Wil99, p.35], [MW95, p.120-124] expresses the free field Green function (3.6) as a superposition of plane waves, both propagating and evanescent:

$$\frac{e^{ik|\mathbf{x}-\mathbf{y}|}}{4\pi|\mathbf{x}-\mathbf{y}|} = \frac{i}{8\pi^2}\int_{-\infty}^{\infty}\int_{-\infty}^{\infty} e^{i[k_1(x_1-y_1)+k_2(x_2-y_2)]}\frac{e^{ik_3|x_3-y_3|}}{k_3}dk_1dk_2 \tag{4.53}$$

This can be rewritten in the following more generic formulation:

$$\frac{e^{ik|\mathbf{x}-\mathbf{y}|}}{4\pi|\mathbf{x}-\mathbf{y}|} = \frac{i}{8\pi^2}\int_{\mathbb{R}^2}\frac{e^{i\zeta(\kappa)|(\mathbf{x}-\mathbf{y})\cdot\hat{\mathbf{n}}|}}{\zeta(\kappa)}e^{i\boldsymbol{\kappa}\cdot(\mathbf{x}-\mathbf{y})}dS(\boldsymbol{\kappa}) \tag{4.54}$$

[2] See also [CWHP06] for an elegant derivation of an analogous result in terms of the *Funk-Hecke formulae*

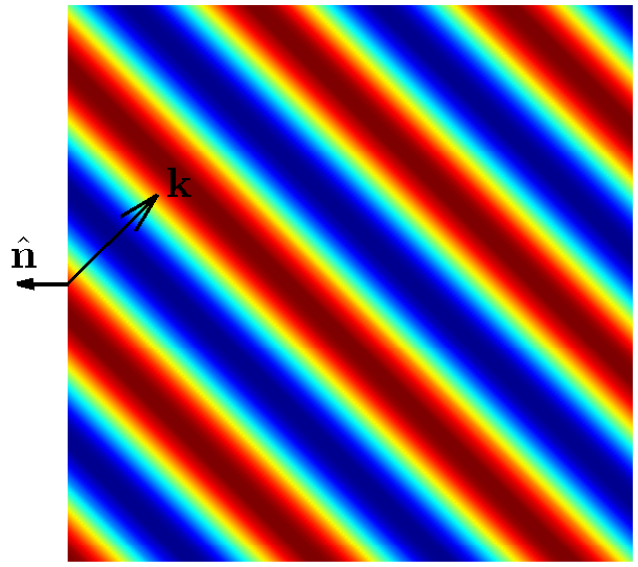

FIGURE 4.13: Acoustic field due to a propagating plane wave, with $\kappa = k/2$.

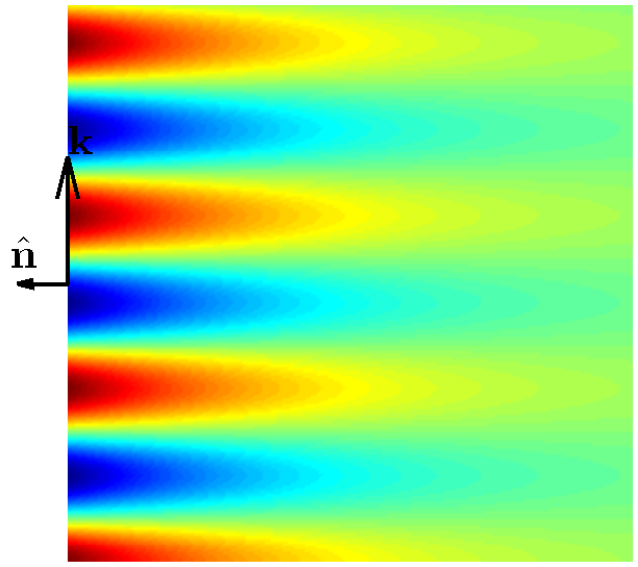

FIGURE 4.14: Acoustic field due to an evanescent plane wave, with $\kappa = 1.1k$. The imaginary component of $\mathbf{k}$ is not represented.

With reference to Figure 4.12, it is recalled that $\mathbf{x} \in \partial V$ and $\mathbf{y} \in \partial\Lambda$, and that the origin of the coordinate system is on $\partial\Lambda$. It is clear that $|(\mathbf{x}-\mathbf{y})\cdot\hat{\mathbf{n}}| = d$. This leads to

$$\frac{e^{ik|\mathbf{x}-\mathbf{y}|}}{4\pi|\mathbf{x}-\mathbf{y}|} = \int_{\mathbb{R}^2} \frac{ie^{i\zeta(\kappa)d}}{2\zeta(\kappa)} \frac{e^{i\boldsymbol{\kappa}\cdot\mathbf{x}}}{2\pi} \frac{e^{-i\boldsymbol{\kappa}\cdot\mathbf{y}}}{2\pi} dS(\boldsymbol{\kappa}) \tag{4.55}$$

It is recalled that $\zeta(\kappa)$ is either real and positive if $\kappa < k$, and the acoustic energy is flowing from $\mathbf{y}$ to $\mathbf{x}$, or purely imaginary with positive imaginary part if $\kappa > k$. The integrand in (4.55) has a singularity for $\kappa = k$, which is anyway integrable except for $|\mathbf{x}-\mathbf{y}| = 0$ [MW95] (for which the Green function (3.6) is not defined). [3]

The first fraction in the integral above can be expressed as the product of a real, non negative function σ_κ and of a complex function γ_κ of unitary absolute value. Thus

$$\frac{ie^{i\zeta(\kappa)d}}{2\zeta(\kappa)} = \sigma_\kappa\gamma_\kappa \tag{4.56}$$

$$\sigma_\kappa = \frac{e^{-\mathrm{Im}(\zeta(\kappa))d}}{2|\zeta(\kappa)|} \tag{4.57}$$

$$\gamma_\kappa = \exp\left[i\left(\mathrm{Re}(\zeta(\kappa))d - \arg(\zeta(\kappa)) + \frac{\pi}{2}\right)\right] \tag{4.58}$$

Inserting equation (4.55) in the definition (3.16) of S and considering the definition (2.10) of the scalar product we obtain the following expression for the operator S:

$$\left(Sa\right)(\mathbf{x}) = \int_{\mathbb{R}^2} \sigma_\kappa\gamma_\kappa \frac{e^{i\boldsymbol{\kappa}\cdot\mathbf{x}}}{2\pi} \frac{\langle e^{i\boldsymbol{\kappa}}|a\rangle_{\partial\Lambda}}{2\pi} dS(\boldsymbol{\kappa}), \quad \mathbf{x} \in \partial V \tag{4.59}$$

It can be observed that the value of σ_κ tends to infinity for $\kappa \to k$. This is a consequence of the integrable singularity arising in the Weyl integral and is in turn strictly related to the fact that S is not well defined for all $a(\mathbf{y}) \in L^2(\partial\Lambda)$, as it has been discussed at the beginning of this section. As shown in [CWHP06], if the free field Green function $G(\mathbf{x},\mathbf{y})$ is integrated over a disk $B_{\mathbf{y}}(R)$ defined by

$$B_{\mathbf{y}}(R) := \{\mathbf{x} \in \partial V : (x_1-y_1)^2 + (x_2-y_2)^2 < R^2\}$$

and we let the radius R tend to infinity, we have that

$$\lim_{R\to\infty} \int_{B_{\mathbf{y}}(R)} |G(\mathbf{x},\mathbf{y})|^2 dS(\mathbf{x}) = \lim_{R\to\infty} \int_0^{2\pi} d\phi \int_0^R \frac{1}{16\pi^2(r^2+d^2)}\, r\, dr \tag{4.60}$$

$$= \lim_{R\to\infty} \frac{1}{16\pi} \ln\left(\frac{R^2+d^2}{d^2}\right) = \infty$$

where $r := \sqrt{(y_1-x_1)^2 + (y_2-x_2)^2}$.

[3] The author would like to acknowledge Dr. Earl Williams for having stimulated the study of the singularity arising in the Weyl integral in relation to the unboundedness of the integral operator S.

However, if as discussed above the wave number is such that $k = (1 + i\epsilon)\omega/c$ and $r \geq 0, d \neq 0$, we see that

$$0 \leq \frac{e^{-2\frac{\omega}{c}\epsilon\sqrt{r^2+d^2}}}{r^2+d^2} r \leq \frac{e^{-2\frac{\omega}{c}\epsilon r}}{d^2} r, \quad r \geq 0 \tag{4.61}$$

Therefore, applying a simple comparison test, we can prove that $G(\mathbf{x}, \mathbf{y})$ with modified k is square integrable on $B_{\mathbf{y}}(R)$:

$$\lim_{R\to\infty} \int_{B_{\mathbf{y}}(R)} |G(\mathbf{x}, \mathbf{y})|^2 dS(\mathbf{x}) = \lim_{R\to\infty} \int_0^{2\pi} d\phi \int_0^R \frac{e^{-2\frac{\omega}{c}\epsilon\sqrt{r^2+d^2}}}{16\pi^2(r^2+d^2)}\, r\, dr \tag{4.62}$$

$$\leq \lim_{R\to\infty} \frac{1}{8\pi} \int_0^R \frac{e^{-2\frac{\omega}{c}\epsilon r}}{d^2}\, r dr = \frac{1}{8\pi d^2} \frac{1}{\left(2\frac{\omega}{c}\epsilon\right)^2} < \infty \tag{4.63}$$

Some attention should be paid for the case when $d = 0$. In this case the integral above diverges, but this is due to the pole-like singularity of the Green function at $\mathbf{x} = \mathbf{y}$ rather than to the slow decay of $G(\mathbf{x}, \mathbf{y})$ at infinity.

From equation (4.55) it is possible to compute the complex conjugate of the free field Green function (3.6). This is given by

$$\begin{aligned} \left(\frac{e^{ik|\mathbf{x}-\mathbf{y}|}}{4\pi|\mathbf{x}-\mathbf{y}|}\right)^* &= \int_{\mathbb{R}^2} \frac{-ie^{-i\zeta(\kappa)^* d}}{2\zeta(\kappa)^*} \frac{e^{i\boldsymbol{\kappa}\cdot\mathbf{y}}}{2\pi} \frac{e^{-i\boldsymbol{\kappa}\cdot\mathbf{x}}}{2\pi} dS(\boldsymbol{\kappa}) \\ &= \int_{\mathbb{R}^2} \sigma_\kappa \gamma_\kappa^* \frac{e^{i\boldsymbol{\kappa}\cdot\mathbf{y}}}{2\pi} \frac{e^{-i\boldsymbol{\kappa}\cdot\mathbf{x}}}{2\pi} dS(\boldsymbol{\kappa}) \end{aligned} \tag{4.64}$$

In view of this result the following expression for the adjoint operator S^* can be derived:

$$\left(S^* p\right)(\mathbf{y}) = \int_{\mathbb{R}^2} \sigma_\kappa \gamma_\kappa^* \frac{e^{i\boldsymbol{\kappa}\cdot\mathbf{y}}}{2\pi} \frac{\langle e^{i\boldsymbol{\kappa}} | p \rangle_{\partial V}}{2\pi} dS(\boldsymbol{\kappa}), \quad \mathbf{y} \in \partial\Lambda \tag{4.65}$$

Combining these results it is possible to apply the following steps:

$$\begin{aligned} &\left(S^* S a\right)(\mathbf{y}) \\ &= \int_{\mathbb{R}^2} \sigma_\kappa \gamma_\kappa^* \frac{e^{i\boldsymbol{\kappa}\cdot\mathbf{y}}}{2\pi} \left[\int_{\partial V} \frac{e^{i\boldsymbol{\kappa}\cdot\mathbf{x}}}{2\pi} \left(\int_{\mathbb{R}^2} \sigma_{\boldsymbol{\kappa}'} \gamma_{\boldsymbol{\kappa}'} \frac{e^{i\boldsymbol{\kappa}'\cdot\mathbf{x}}}{2\pi} \frac{\langle e^{i\boldsymbol{\kappa}'} | a \rangle_{\partial\Lambda}}{2\pi} dS(\boldsymbol{\kappa}')\right) dS(\mathbf{x})\right] dS(\boldsymbol{\kappa}) \end{aligned} \tag{4.66}$$

We rearrange the order of integration and use the orthogonality relation (2.86) to give

$$\begin{aligned} &\left(S^* S a\right)(\mathbf{y}) \\ &= \int_{\mathbb{R}^2} \sigma_\kappa \gamma_\kappa^* \frac{e^{i\boldsymbol{\kappa}\cdot\mathbf{y}}}{2\pi} \left(\int_{\mathbb{R}^2} \delta(\boldsymbol{\kappa} - \boldsymbol{\kappa}') \sigma_{\boldsymbol{\kappa}'} \gamma_{\boldsymbol{\kappa}'} \frac{\langle e^{i\boldsymbol{\kappa}'} | a \rangle_{\partial\Lambda}}{2\pi} dS(\boldsymbol{\kappa}')\right) dS(\boldsymbol{\kappa}) \end{aligned} \tag{4.67}$$

In view of the property of the Dirac delta function (2.29) and observing that $\gamma_\kappa \gamma_\kappa^* = 1$, $\forall \boldsymbol{\kappa} \in \mathbb{R}^2$, we obtain the following expression for the composite operator S^*S

$$\left(S^*Sa\right)(\mathbf{y}) = \int_{\mathbb{R}^2} \sigma_\kappa^2 \frac{e^{i\boldsymbol{\kappa}\cdot\mathbf{y}}}{2\pi} \frac{\langle e^{i\boldsymbol{\kappa}} | a \rangle_{\partial\Lambda}}{2\pi} dS(\boldsymbol{\kappa}) \tag{4.68}$$

All the results above can be rewritten in terms of Fourier transforms, such that

$$\begin{aligned}
(Sa)(\mathbf{x}) &= \left[\mathcal{F}^{-1}\left(\sigma_\kappa \gamma_\kappa (\mathcal{F}a)\right)\right](\mathbf{x}) && (4.69)\\
(S^*p)(\mathbf{y}) &= \left[\mathcal{F}^{-1}\left(\sigma_\kappa \gamma_\kappa^* (\mathcal{F}p)\right)\right](\mathbf{y}) && (4.70)\\
\left(S^*Sa\right)(\mathbf{y}) &= \left[\mathcal{F}^{-1}\left(\sigma_\kappa^2 (\mathcal{F}a)\right)\right](\mathbf{y}) && (4.71)
\end{aligned}$$

We define now the following orthogonal functions

$$\begin{aligned}
a_{\boldsymbol{\kappa}}(\mathbf{y}) &= \frac{1}{2\pi} e^{i\boldsymbol{\kappa}\cdot\mathbf{y}}, \quad \mathbf{y} \in \partial\Lambda && (4.72)\\
p_{\boldsymbol{\kappa}}(\mathbf{x}) &= \frac{\gamma_\kappa}{2\pi} e^{i\boldsymbol{\kappa}\cdot\mathbf{x}}, \quad \mathbf{x} \in \partial V && (4.73)
\end{aligned}$$

From an analogy with the previous geometrical arrangements considered, these functions might be regarded as secondary source modes and pressure modes, respectively (although these functions are not countable). Note that these functions are not orthonormal, since $\langle p_{\boldsymbol{\kappa}} | p_{\boldsymbol{\kappa}} \rangle = \langle a_{\boldsymbol{\kappa}} | a_{\boldsymbol{\kappa}} \rangle = \delta(\boldsymbol{\kappa})$ and their norm is therefore is unbounded (strictly, these functions do not belong to $L^2(\mathbb{R}^2)$), but they can be regarded as *δ-function normalized*.

The results presented above and the orthogonality relations (2.86) lead to the following relations:

$$\begin{aligned}
\left(Sa_{\boldsymbol{\kappa}}\right)(\mathbf{x}) &= \sigma_\kappa p_{\boldsymbol{\kappa}}(\mathbf{x}), \quad \mathbf{x} \in \partial V && (4.74)\\
\left(S^*p_{\boldsymbol{\kappa}}\right)(\mathbf{y}) &= \sigma_\kappa a_{\boldsymbol{\kappa}}(\mathbf{y}), \quad \mathbf{y} \in \partial\Lambda && (4.75)\\
\left(S^*Sa_{\boldsymbol{\kappa}}\right)(\mathbf{y}) &= \sigma_\kappa^2 a_{\boldsymbol{\kappa}}(\mathbf{y}), \quad \mathbf{y} \in \partial\Lambda && (4.76)
\end{aligned}$$

where σ_κ is given by formula (4.57).

It can be observed that the set of functions $\sigma_\kappa, a_{\boldsymbol{\kappa}}(\mathbf{y}), p_{\boldsymbol{\kappa}}(\mathbf{x})$ have the same properties of the singular system described in Section 2.5, apart from $a_{\boldsymbol{\kappa}}(\mathbf{y})$ and $p_{\boldsymbol{\kappa}}(\mathbf{x})$ being δ-function normalized and orthogonal instead of orthonormal. However, it has been said that for this special geometrical arrangement the operator S is not compact and is not well defined for all densities $a(\mathbf{y}) \in L^2(\mathbb{R}^2)$. As a consequence, the set of functions $\sigma_\kappa, a_{\boldsymbol{\kappa}}(\mathbf{y}), p_{\boldsymbol{\kappa}}(\mathbf{x})$ can not be rigorously defined as a singular system.

One of the main differences is that σ_κ is a function, and not a countable set of numbers as in the cases discussed above. This is due to the fact that the eigenvalues of S^*S, and hence the singular values of S, are countable when S is compact (see Section 2.5). We

will not discuss this issue any further, but the reader can consider the relevant analogy between the Fourier series and the Fourier transform of a function $f(x)$ defined over $D \subseteq \mathbb{R}$. When D is bounded, it is possible to express $f(x)$ by the Fourier series (2.64), and the Fourier coefficients define a countable set. On the contrary, if D is unbounded, $f(x)$ can be expressed in the form of the integral (2.88) instead of a series, and the countable set of Fourier coefficients is substituted by the function $(\mathcal{F}f)(\kappa)$.

4.3.3 Properties of $\sigma_\kappa,\ a_{\boldsymbol{\kappa}}(\mathbf{y}),\ p_{\boldsymbol{\kappa}}(\mathbf{x})$

We discuss now some of the properties of the functions $\sigma_\kappa, a_{\boldsymbol{\kappa}}(\mathbf{y}), p_{\boldsymbol{\kappa}}(\mathbf{x})$. Firstly, it can be easily observed that the functions $a_{\boldsymbol{\kappa}}(\mathbf{y})$ and $p_{\boldsymbol{\kappa}}(\mathbf{x})$ represent two-dimensional plane waves defined on $\partial\Lambda$ and on ∂V, respectively.

Secondly, it can be noticed that σ_κ and γ_κ assume different forms depending whether $\kappa < k$ or $\kappa > k$. In fact

$$\sigma_\kappa = \frac{1}{2|\zeta(\kappa)|}, \quad \gamma_\kappa = ie^{i|\zeta(\kappa)|d}, \quad \kappa < k \tag{4.77}$$

$$\sigma_\kappa = \frac{1}{2|\zeta(\kappa)|}e^{-|\zeta(\kappa)|d}, \quad \gamma_\kappa = 1, \quad \kappa > k \tag{4.78}$$

Figure 4.15 shows the value of σ_κ and of the phase of γ_κ as a function of $|\kappa|/k$ and for different values of d. It can be noticed that $\sigma_\kappa = 1/2$ (-6.0206 dB) for $\kappa = 0$ and that σ_κ tends to infinity for $\kappa = k$. The jump discontinuity of γ_κ at $\kappa = k$ (from $\pi/2$ to 0) is due to $\sigma_\kappa\gamma_\kappa$ changing from a purely imaginary value to a purely real value. As we will see soon, this jump identifies the passage from the propagating mode region to the evanescent mode region.

As in the case of the spherical geometry, the expressions (4.59) and (4.69) of the integral operator S can be extended to the expression for the single layer potential in all $\mathbb{R}^3$ by simply substituting d with $|(\mathbf{z}\cdot\hat{\mathbf{n}})|$ into the definitions of $\sigma_\kappa,\ \gamma_\kappa$, equations (4.56)-(4.58), and $\mathbf{x} \in \partial V$ with $\mathbf{z} \in \mathbb{R}^3$ in equations (4.59) and (4.73).

The argument of the exponential $e^{i\zeta(\kappa)}$ highlights the difference between propagating and evanescent modes $a_{\boldsymbol{\kappa}}, p_{\boldsymbol{\kappa}}$. In fact when $\kappa > k$ the corresponding function $(Sa_{\boldsymbol{\kappa}})(\mathbf{z}),\ \mathbf{z} \in \Lambda$ represents a propagating wave in Λ. The factor γ_κ, included in the definition of $p_{\boldsymbol{\kappa}}(\mathbf{x})$, represents the change in phase that the plane wave undergoes in the propagation from the surface $\partial\Lambda$ to the surface ∂V. This depends on the distance d between the two planes and on the direction of propagation of the plane wave $(Sa_{\boldsymbol{\kappa}})(\mathbf{z}),\ \mathbf{z} \in \Lambda$, identified by the vector $\hat{\mathbf{r}}_{\boldsymbol{\kappa}}$. The function $\zeta(\kappa)$ can be directly related to the angle between the normal vectors $\hat{\mathbf{n}}$ and $\hat{\mathbf{r}}_{\boldsymbol{\kappa}}$. Considering the expressions (4.45), (4.46), (4.47) and (4.50) it holds that

$$-\hat{\mathbf{n}}\cdot\hat{\mathbf{r}}_{\boldsymbol{\kappa}} = \frac{\zeta(\kappa)}{k}, \quad \kappa < k \tag{4.79}$$

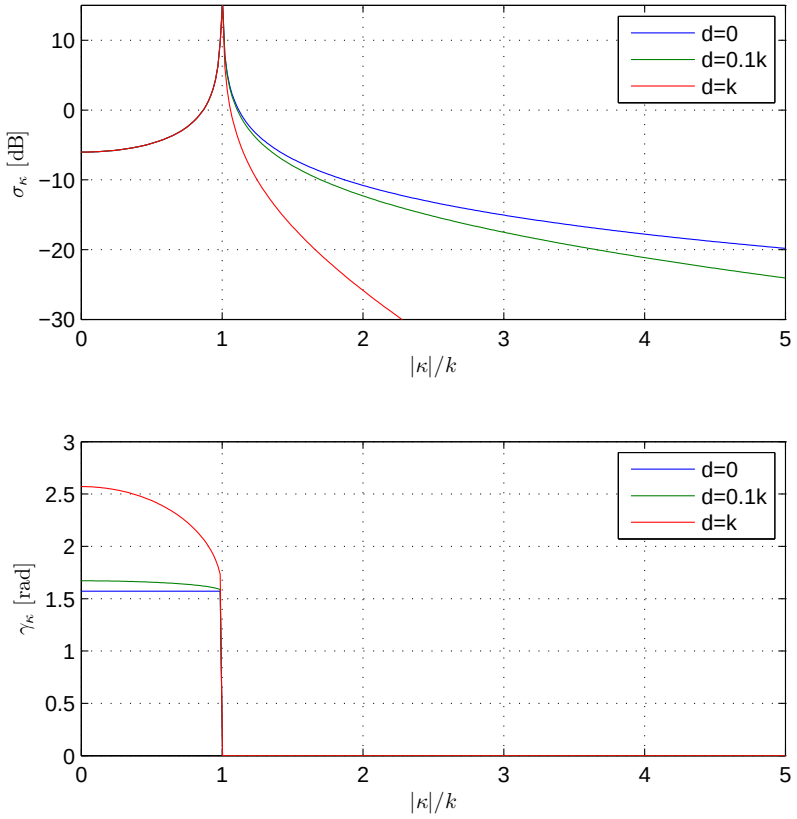

FIGURE 4.15: Values of σ_κ (dB scale) and phase of γ_κ as a function of $|\kappa|/k$.

This scalar product obviously corresponds to the cosine of the angle between the two vectors considered. The case of $\kappa = 0$ corresponds to $(Sa_{\boldsymbol{\kappa}})(\mathbf{z})$, $\mathbf{z} \in \Lambda$ being a plane wave propagating in the direction $-\hat{\mathbf{n}}$, while the limiting case of $\kappa = k$ defines a wave propagating in a direction parallel to $\partial\Lambda$.

On the contrary, when $\kappa > k$, then $(Sa_{\boldsymbol{\kappa}})(\mathbf{z})$, $\mathbf{z} \in \Lambda$ represents an evanescent wave, decaying exponentially in the direction $-\hat{\mathbf{n}}$. The complex exponential $e^{i\zeta(\kappa)d}$ represents now a positive real number smaller than unity, which is proportional to the decrease in amplitude of the evanescent wave on the plane ∂V with respect to its amplitude on $\partial\Lambda$.

Figures 4.16-4.20 show the horizontal cross-section of the fields $(Sa_{\boldsymbol{\kappa}})(\mathbf{z})$ for different values of $\boldsymbol{\kappa}$. The comparison of these figures with figures 4.13 and 4.14 can help make the analogy with propagating and evanescent waves more clear. It can be observed that for $|\kappa| < k$ (figures 4.16 to 4.18) the amplitude of the field increases with increasing $|\kappa|$, as a consequence of the factor $1/\zeta(\kappa)$. This phenomenon is reversed for $|\kappa| > k$ (figures 4.19 and 4.20) but it is not evident, for the amplitude of the field is dominated by the exponential energy decay.

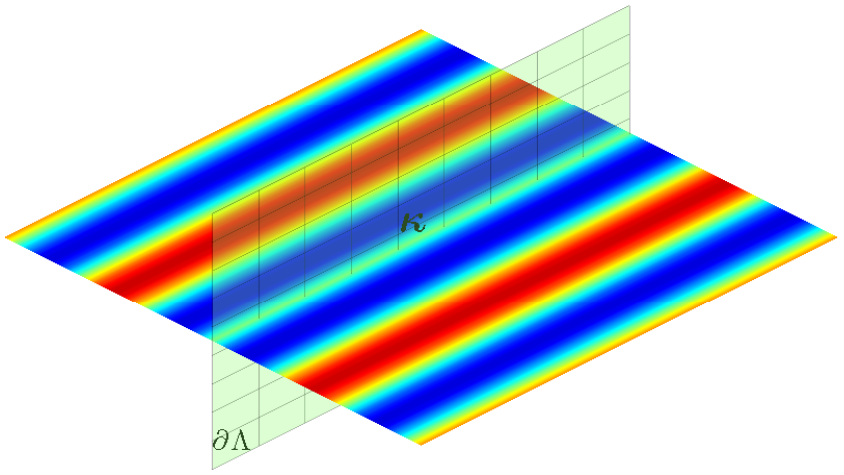

FIGURE 4.16: Horizontal cross-section of the acoustic field due to $(Sa_{\boldsymbol{\kappa}})(\mathbf{z})$, with $\boldsymbol{\kappa} = [\,0,\ 0]$.

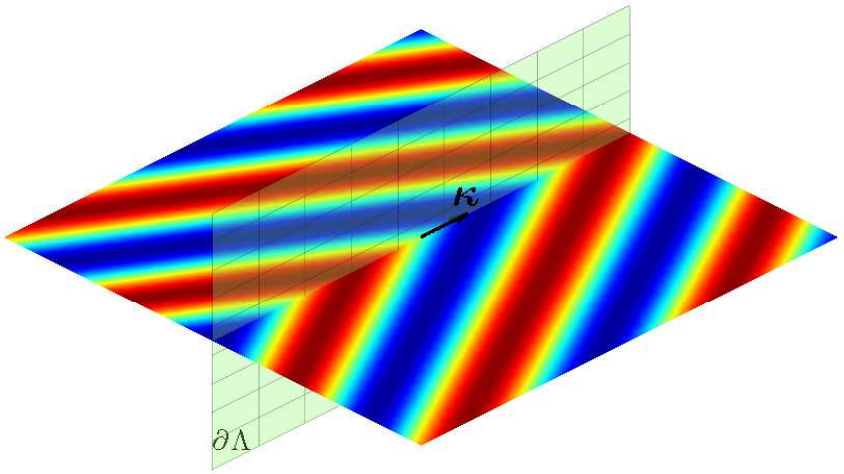

FIGURE 4.17: Horizontal cross-section of the acoustic field due to $(Sa_{\boldsymbol{\kappa}})(\mathbf{z})$, with $\boldsymbol{\kappa} = [0.5k,\ 0]$.

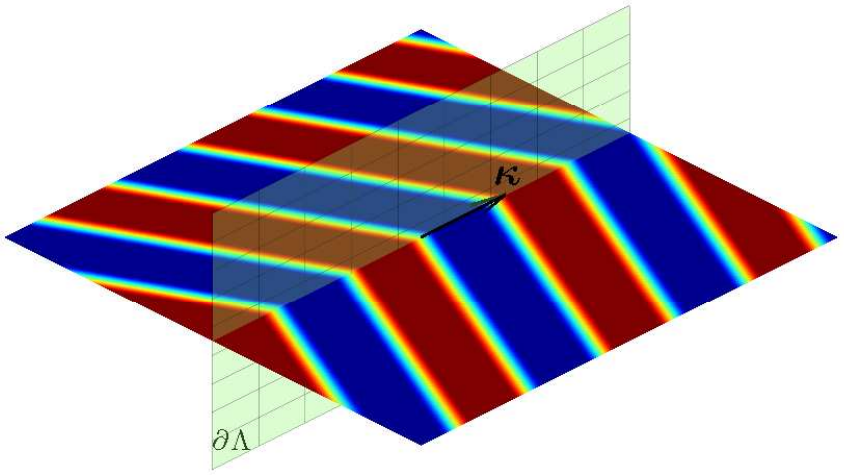

FIGURE 4.18: Horizontal cross-section of the acoustic field due to $(Sa_{\boldsymbol{\kappa}})(\mathbf{z})$, with $\boldsymbol{\kappa} = [0.9k,\ 0]$.

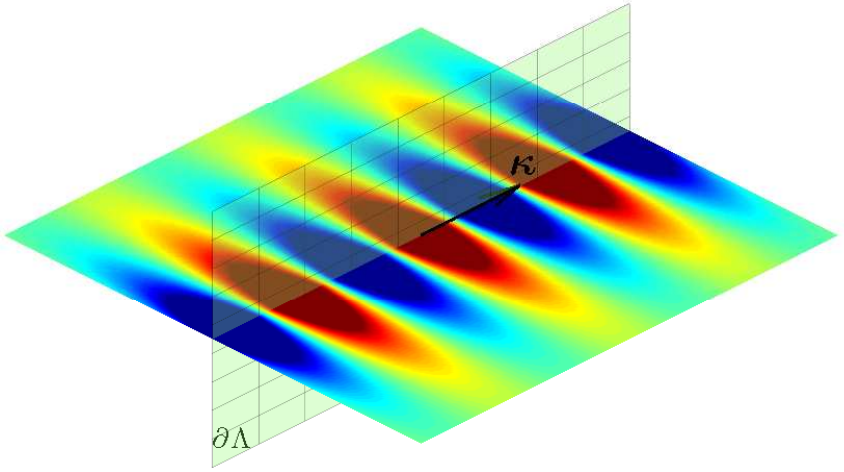

FIGURE 4.19: Horizontal cross-section of the acoustic field due to $(Sa_{\boldsymbol{\kappa}})(\mathbf{z})$, with $\boldsymbol{\kappa} = [1.05k,\ 0]$.

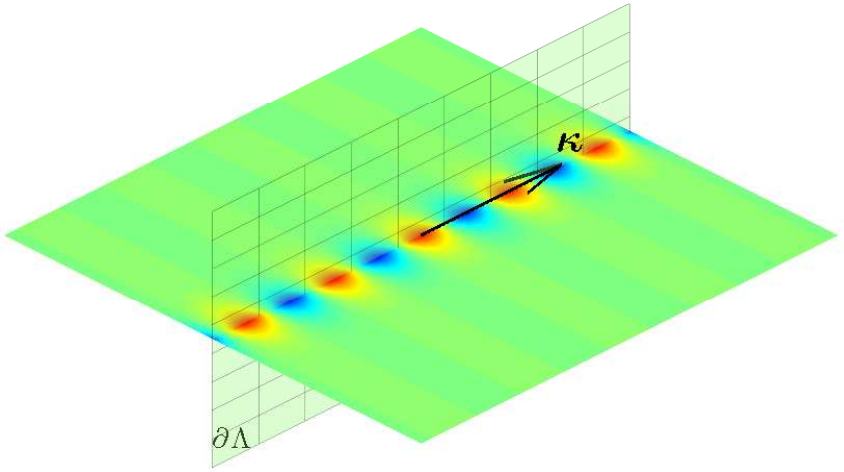

FIGURE 4.20: Horizontal cross-section of the acoustic field due to $(Sa_{\boldsymbol{\kappa}})(\mathbf{z})$, with $\boldsymbol{\kappa} = [1.5k,\ 0]$.

In Section 2.5 the concept of degenerate eigenvalues has been mentioned, in the case when S is compact. A singular value is said to be degenerate when more than one singular function is associated with it, and these singular functions span a space of functions with dimension equal to the geometrical multiplicity of that eigenvalue. In the special case described here, a single pair of $a_{\boldsymbol{\kappa}'}(\mathbf{y})$ and $p_{\boldsymbol{\kappa}'}(\mathbf{x})$ is associated with a given vector $\boldsymbol{\kappa}'$, but an infinite number of modes are associated with the same value of $\sigma_{\kappa'}$. Figure 4.21 shows a colored plot of values of σ_κ in a so-called k-space diagram [Wil99]. The latter is constituted by a plane representing all the values that $\boldsymbol{\kappa}$ can assume. All functions $a_{\boldsymbol{\kappa}}(\mathbf{y})$ and $p_{\boldsymbol{\kappa}}(\mathbf{x})$ are identified by one point in this plane. In the figure, the five blue crosses identify the five modes illustrated by figures 4.16-4.20. It can be understood that the points representing all functions $a_{\boldsymbol{\kappa}'}(\mathbf{y})$ and $p_{\boldsymbol{\kappa}'}(\mathbf{x})$ associated with the same value of $\sigma_{\kappa'}$ define a circle with radius κ'. The circle with radius k (the dashed line in the figure) is the so called *radiation circle*. In fact, all functions corresponding to propagating modes in Λ are represented on the k-space diagram by points lying within this circle. All points in its exterior are associated with evanescent modes. Many of these considerations are well known in other branches of physics and engineering such as optics and Near-Field Acoustical Holography (see, for example, [MW95] and [Wil99]). The arguments presented here show the meaningful link of the problem of sound field reproduction to these other disciplines.

It can be observed that, both for the case of propagating and evanescent modes, the magnitude of $(Sa_{\boldsymbol{\kappa}})(\mathbf{x})$ reduces by a factor $1/(2|\zeta(\kappa)|)$. This factor depends only on κ and is not related to the distance between the two planes $\partial\Lambda$ and ∂V. As will be shown

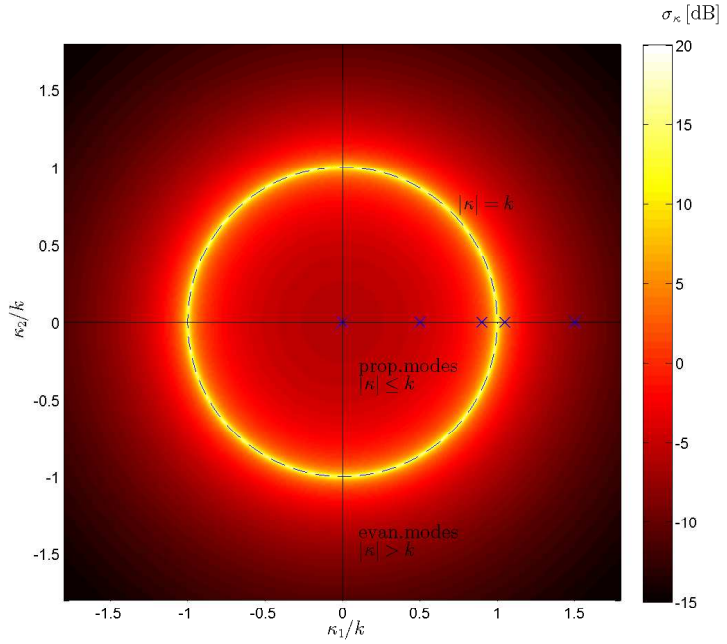

FIGURE 4.21: Representation of the value of σ_κ in the k-space, with $d = 0.1k$. The dashed line represents the radiation circle, while the five blue crosses identify the modes illustrated in the figures 4.16-4.20.

in Section 6.4, this is related to the fact that the determination of $a(\mathbf{y})$ is implicitly connected to an operation of partial derivation of the field in the direction $-\hat{\mathbf{n}}$, which is in turn related to a multiplication by a factor $i\zeta(\kappa)$.

Decay of σ_κ In light of what has been discussed, if $d \neq 0$ the asymptotic behavior of the function σ_κ for $\kappa \to \pm\infty$ is dominated by the factor $e^{-|\zeta(\kappa)|d}$, as illustrated by Figure 4.15. If an analogy is drawn with the cases of the other geometrical arrangements described above, this behavior of σ_κ could be interpreted as an exponential decay of the efficiency of the source modes $a_{\boldsymbol{\kappa}}(\mathbf{y})$. It is recalled, however, that S is not compact and consequently σ_κ is not a countable set. Henceforth, the definition of $a_{\boldsymbol{\kappa}}(\mathbf{y})$ and $p_{\boldsymbol{\kappa}}(\mathbf{x})$ as *modes* is probably not rigorous. As for the case of the concentric spheres, the decay of σ_κ becomes steeper as d becomes larger, which represents the distance between $\partial\Lambda$ and ∂V. For what has been said, the inverse problem addressed can be referred to as being *severely ill-posed*. In the limiting case of $d = 0$, it can be noticed that the asymptotic behavior of σ_κ is dominated by the factor $1/(2|\zeta(\kappa)|$, which determines a linear decay. This implies that the inverse problem in that case is *mildly ill-posed*.

4.3.4 Solution

We seek now a solution of the integral equation (3.19). The latter can be expressed in the form (4.59), substituting the left hand side $(Sa)(\mathbf{x})$ with the target pressure profile

$p(\mathbf{x})$. We multiply both sides of the equation by $e^{-i\boldsymbol{\kappa}'\mathbf{x}}/(2\pi)$ and integrate over ∂V. After having rearranged the order of integration of the right hand side we obtain:

$$\int_{\partial V} p(\mathbf{x}) \frac{e^{-i\boldsymbol{\kappa}'\cdot\mathbf{x}}}{2\pi} dS(\mathbf{x}) = \int_{\mathbb{R}^2} \sigma_\kappa \gamma_\kappa \left(\int \frac{e^{i\boldsymbol{\kappa}\cdot\mathbf{x}}}{2\pi} \frac{e^{-i\boldsymbol{\kappa}'\cdot\mathbf{x}}}{2\pi} dS(\mathbf{x}) \right) \frac{\langle e^{i\boldsymbol{\kappa}} | a \rangle_{\partial\Lambda}}{2\pi} dS(\boldsymbol{\kappa}) \tag{4.80}$$

We apply the orthogonality property (2.86) and the property of the Dirac delta function (2.26), and in view of the definition of the scalar product (2.10) we obtain

$$\frac{\langle e^{i\boldsymbol{\kappa}} | p \rangle_{\partial V}}{2\pi} = \sigma_\kappa \gamma_\kappa \frac{\langle e^{i\boldsymbol{\kappa}} | a \rangle_{\partial\Lambda}}{2\pi} \tag{4.81}$$

where the dummy variable κ' has been renamed in terms of κ. This equation corresponds to a *mode matching* method, where the secondary source modes and the acoustic pressure modes are two-dimensional plane waves on $\partial\Lambda$ and on ∂V, respectively.

Assuming that $\sigma_\kappa \neq 0$, it is possible to divide both sides by $\sigma_\kappa \gamma_\kappa$, multiply by $e^{i\boldsymbol{\kappa}\cdot\mathbf{y}}/(2\pi)$ and integrate over $\mathbb{R}^2$. This leads to

$$\int_{\mathbb{R}^2} \frac{\gamma_\kappa^*}{\sigma_\kappa} \frac{e^{i\boldsymbol{\kappa}\cdot\mathbf{y}}}{2\pi} \frac{\langle e^{i\boldsymbol{\kappa}} | p \rangle_{\partial V}}{2\pi} dS(\boldsymbol{\kappa}) = \int_{\mathbb{R}^2} \int_{\partial\Lambda} \frac{e^{i\boldsymbol{\kappa}\cdot\mathbf{y}}}{2\pi} \frac{e^{i\boldsymbol{\kappa}\cdot\mathbf{y}'}}{2\pi} a(\mathbf{y}') dS(\mathbf{y}') dS(\boldsymbol{\kappa}) \tag{4.82}$$

The scalar product $\langle e^{i\boldsymbol{\kappa}} | a \rangle_{\partial\Lambda}$ has been re-expanded and $e^{i\boldsymbol{\kappa}\cdot\mathbf{y}'}$ has been brought inside the second integral. We now rearrange the order of integration on the right hand side, apply the orthogonality relation (2.87) and the property of the Dirac delta function (2.26). This operation allows the two integrals on the right hand side to vanish. Finally, we obtain the following expression for the solution $a(\mathbf{y})$, which is given by:

$$a(\mathbf{y}) = \int_{\mathbb{R}^2} \frac{1}{\sigma_\kappa} \frac{e^{i\boldsymbol{\kappa}\cdot\mathbf{y}}}{2\pi} \frac{\langle \gamma_\kappa e^{i\boldsymbol{\kappa}} | p \rangle_{\partial V}}{2\pi} = \int_{\mathbb{R}^2} \frac{-i\zeta(\kappa)}{e^{i\zeta(\kappa)d}} \frac{e^{i\boldsymbol{\kappa}\cdot\mathbf{y}}}{2\pi^2} \langle e^{i\boldsymbol{\kappa}} | p \rangle_{\partial V} dS(\boldsymbol{\kappa}) \tag{4.83}$$

It should be emphasized that no proof has been derived of the existence of the solution, and it might be the case that the expression above does not give a bounded function (this is the case for example of a *focused source*, introduced in Chapter 6). However, if a bounded solution exists, this can be computed with the expression above.

Considering the definitions of $a_{\boldsymbol{\kappa}}(\mathbf{y})$ and $p_{\boldsymbol{\kappa}}(\mathbf{x})$, the result above can be rewritten as

$$a(\mathbf{y}) = \int_{\mathbb{R}^2} \frac{a_{\boldsymbol{\kappa}}(\mathbf{y})}{\sigma_\kappa} \langle p_{\boldsymbol{\kappa}} | p \rangle_{\partial V} dS(\boldsymbol{\kappa}) \tag{4.84}$$

This expression is analogous to equation (3.28), which gives the solution of the integral equation considered in terms of a singular system of the operator S. The difference is, again, that the series in (3.28) is substituted here by an integral.

Finally, the same result can be expressed by means of direct and inverse Fourier transforms, namely

$$a(\mathbf{y}) = \mathcal{F}^{-1}\left[\frac{(\mathcal{F}p)}{\sigma_\kappa \gamma_\kappa}\right](\mathbf{y}) \tag{4.85}$$

4.4 Infinite parallel lines

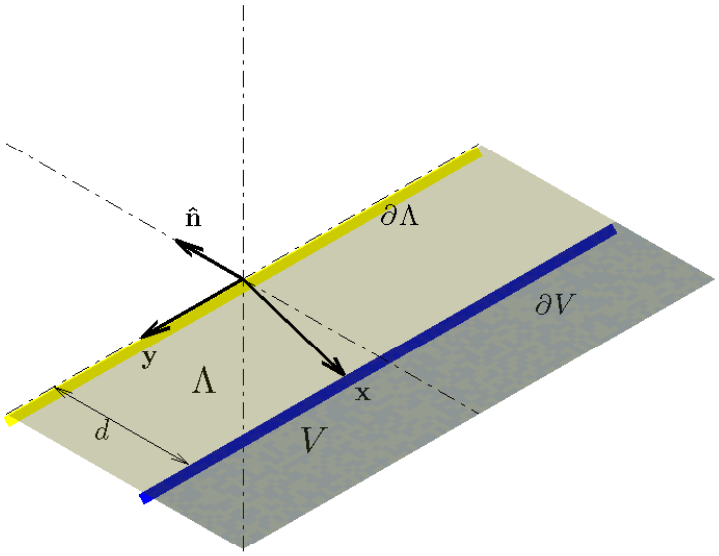

FIGURE 4.22: Geometrical arrangement with parallel lines.

The two-dimensional case is now considered in which $\partial\Lambda$ and ∂V are two infinite lines with distance d, as illustrated by Figure 4.22. This is analogous to the previous case of two parallel planes, with the difference that the kernel of S is now the two dimensional Green function (3.7).

As in the previous case, Λ and V are unbounded sets. This implies that the S is not compact, with all of the same implications discussed above. The problem of S being unbounded holds here too, due to the slow decay of the kernel of S. For the sake of completeness, it can be mentioned that this problem is less severe than for the previous three-dimensional case, as discussed in [CWHP06]. However, we will not discuss these problems any further here.

We start as before with the expansion of the free field Green function in terms of plane waves. In order to keep the notation simple, we assume that

$$\partial\Lambda := \{\mathbf{y} \in \mathbb{R}^3 : y_2 = 0,\ y_3 = 0\} \tag{4.86}$$

$$\partial V := \{\mathbf{x} \in \mathbb{R}^3 : x_2 = 0,\ x_3 = d\} \tag{4.87}$$

The two-dimensional free field Green function (3.7) corresponds to an infinite line source. This can be expressed as an infinite distribution of point sources arranged on a straight line, perpendicular to the plane where $\partial\Lambda$ and ∂V lie. This is expressed mathematically by the following integral [GR65, p.915 equation 8.421.11]

$$\frac{i}{4}H_0^{(1)}(kx) = \int_{-\infty}^{\infty} \frac{e^{ik\sqrt{x^2+y^2}}}{4\pi\sqrt{x^2+y^2}}dy \tag{4.88}$$

This result can be combined with the Weyl integral (4.53) with $x_2 = 0$ in order to obtain

$$\frac{i}{4}H_0^{(1)}(k|\mathbf{x}-\mathbf{y}|) = \frac{i}{8\pi^2}\int_{-\infty}^{\infty}\int_{-\infty}^{\infty}\left(\int_{-\infty}^{\infty} e^{-ik_2y_2}dy_2\right)e^{i[k_1(x_1-y_1)]}\frac{e^{ik_3|x_3-y_3|}}{k_3}dk_1dk_2 \tag{4.89}$$

where the order of integration has been rearranged. The integral within brackets equals $2\pi\delta(k_2)$ [Wil99]. Integrating with respect to k_2 and applying the property (2.25) of the Dirac delta function leads to the plane wave expansion of the two-dimensional free field Green function. This is given by

$$\frac{i}{4}H_0^{(1)}(k|\mathbf{x}-\mathbf{y}|) = \frac{i}{4\pi}\int_{-\infty}^{\infty} e^{ik_1(x_1-y_1)}\frac{e^{ik_3|x_3-y_3|}}{k_3}dk_1 \tag{4.90}$$

In order to use a notation consistent with that used in the previous section, we define

$$\kappa = k_1 \tag{4.91}$$

$$\zeta(\kappa) = \sqrt{k^2-\kappa^2} \tag{4.92}$$

and we rewrite equation (4.90) in the following form:

$$\frac{i}{4}H_0^{(1)}(k|\mathbf{x}-\mathbf{y}|) = \int_{\mathbb{R}} \frac{e^{i\kappa(x_1-y_1)}}{2\pi}\frac{ie^{i\zeta(\kappa)d}}{2\zeta(\kappa)}d\kappa \tag{4.93}$$

An alternative derivation of this result can be obtained by performing the Fourier transform of $H_0(k|\mathbf{x}-\mathbf{y}|)$ and considering equations 6.677.1 and 6.677.2 in [GR65, p.722]. It should also be understood that the Fourier transform of $H_0(k|\mathbf{x}-\mathbf{y}|)$ is not defined for $\kappa = k$.

We define σ_κ and γ_κ and the orthogonal functions $a_\kappa(\mathbf{y})$ and $p_\kappa(\mathbf{x})$ as follows:

$$\sigma_\kappa = \frac{e^{-\mathrm{Im}(\zeta(\kappa))d}}{2|\zeta(\kappa)|} \tag{4.94}$$

$$\gamma_\kappa = \exp\left[i\left(\mathrm{Re}(\zeta(\kappa))d - \arg(\zeta(\kappa)) + \frac{\pi}{2}\right)\right] \tag{4.95}$$

$$a_\kappa(\mathbf{y}) = \frac{1}{\sqrt{2\pi}}e^{i\kappa y_1} \tag{4.96}$$

$$p_\kappa(\mathbf{x}) = \frac{\gamma(\kappa)}{\sqrt{2\pi}}e^{i\kappa x_1} \tag{4.97}$$

The definition σ_κ and γ_κ above is identical to the case of parallel planes, equations (4.57) and (4.58), while the definition of $a_\kappa(\mathbf{y})$ and $p_\kappa(\mathbf{x})$ is analogous to equations (4.72) and (4.73), respectively. The properties of these functions are therefore analogous to those described in Section 4.3.

Equation (4.93) can be substituted into the integral equation (3.19) and, performing operations identical to those described above, we obtain the following results:

$$(Sa)(\mathbf{x}) = \int_{\mathbb{R}} \sigma_\kappa p_\kappa(\mathbf{x}) \langle a_\kappa | a \rangle_{\partial\Lambda} d\kappa, \quad \mathbf{x} \in \partial V \tag{4.98}$$

$$(S^* p)(\mathbf{y}) = \int_{\mathbb{R}} \sigma_\kappa a_\kappa(\mathbf{y}) \langle p_\kappa | p \rangle_{\partial V} d\kappa, \quad \mathbf{y} \in \partial\Lambda \tag{4.99}$$

$$(S^* S a)(\mathbf{y}) = \int_{\mathbb{R}} \sigma_\kappa^2 a_\kappa(\mathbf{y}) \langle a_\kappa | a \rangle_{\partial\Lambda} d\kappa, \quad \mathbf{y} \in \partial\Lambda \tag{4.100}$$

As for the case of two parallel planes, these results can be expressed by means of direct and inverse Fourier transforms (see (4.69),(4.70) and (4.71)).

If a solution $a(\mathbf{y})$ to the integral equation (3.19) exists, this is given by

$$a(\mathbf{y}) = \int_{\mathbb{R}} \frac{-i2\zeta(\kappa)}{e^{i\zeta(\kappa)d}} \frac{e^{i\kappa y_1}}{2\pi} \langle e^{i\kappa x_1} | p \rangle_{\partial V} d\kappa \tag{4.101}$$

As for the case of the parallel planes, this result can be expressed also by the following formulae:

$$a(\mathbf{y}) = \int_{\mathbb{R}} \frac{a_\kappa(\mathbf{y})}{\sigma_\kappa \gamma_\kappa} \langle p_\kappa | p \rangle_{\partial V} d\kappa \tag{4.102}$$

$$a(\mathbf{y}) = \mathcal{F}^{-1}\left[\frac{(\mathcal{F}p)}{\sigma_\kappa \gamma_\kappa}\right](\mathbf{y}) \tag{4.103}$$

These results are almost identical to equations (4.83),(4.84) and (4.85) and were obtained with the same procedure. The main difference in that the integrals on the right hand side of (4.101) and (4.102) are performed over $\mathbb{R}$ instead of $\mathbb{R}^2$. Consequently, the Fourier transform in (4.103) is one dimensional.

An example of solution for the target field due to a virtual point source is presented in Section 5.6.2.

Chapter 5

The ill-posedness of the inverse problem

In the previous chapters expressions have been derived for the solution of the integral equation (3.19), under the relevant assumption that this solution exists and is unique. But this assumption is not valid for a general case. In Section 3.4 it was briefly mentioned that equation (3.19) is an integral equation of the first kind. The so called *Fredholm alternative*, described in [Kre78] and [CK83] provides powerful mathematical tools to prove the solvability of integral equations of the second kind and these are of great relevance to the solution of many inverse problems. However, this theoretical approach does not apply to integral equations of the first kind, such as that arising in the sound field reproduction problem addressed here. The inverse problem represented by equation (3.19) is actually ill-posed, and is therefore generally not solvable.

The reader might find it strange that some effort has been dedicated to deriving expressions for a solution, whose existence was taken for granted, when we now state that this solution does in general not exist. The subject of this chapter is to provide a detailed mathematical analysis of the solvability of the integral equation (3.19). In view of this analysis we will be able to define those assumption regarding the target sound field and the geometrical arrangement for which an exact solution exists, and if this solution is or is not unique. We will see that a large category of sound fields of practical interest allow for the computation of an exact solution. In this sense, things are not as bad as the nature of the inverse problem addressed would suggest on first examination.

It will be shown that even when the solution exists it may not be stable and the reproduced field can be severely affected by the presence of small errors. If this is the case, or if the inverse problem is not solvable, it is always possible to compute an approximate solution, which can be effective for practical purposes. This is the subject of the next chapter.

The concept of ill-posedness of a problem is discussed in detail in what follows. The mathematical concept of ill-posedness is presented, and then the causes of this problem are analyzed. The solvability of the inverse problem is studied in relation to the characteristics of the target sound field considered. The results obtained in the previous chapters are used to clarify these arguments with specific examples.

The arguments presented in this chapter lead to the important consideration that while the existence of the solution depends on the secondary source layer $\partial\Lambda$ and on the target field, the uniqueness of the problem depends on the control boundary and on the operating frequency of the target field.

5.1 The definition of an ill-posed problem

The mathematical analysis of an ill-posed problem presented here follows the definition introduced by Hadamard [Had23], [CK92]. An elegant link between this theory and its meaning in relation to engineering applications is described by Deschamp and Cabayan [DC72].

Given an operator S from a normed space A into a normed space Ψ, (such as for example $L^2(\partial\Lambda)$ and $L^2(\partial V)$ introduced above), an equation of the form $Sa = p$ is said to be well-posed or properly posed if S is bijective[1] and if its inverse S^{-1} is continuous. This means that, for any function $p \in \Psi$ one and only one function $a \in A$ exists, such that $Sa = p$, and this solution depends continuously on the data p. If one of these conditions does not hold, then the problem $Sa = p$ is said to be ill-posed or improperly posed.

Three different kind of ill-posedness are possible, corresponding to the cases where, for at least one function $p \in \Psi$,

1. no function $a \in A$ exist, such that $Sa = p$ (*nonexistence*);
2. more than one function $a \in A$ exists, such that $Sa = p$ (*nonuniqueness*);
3. the solution $a \in A$ does not depend continuously on the data p (*instability*).

In the framework of sound field reproduction, the ill-posedness of the problem involved can be interpreted as follows. We firstly choose A to be the set of square integrable functions on $\partial\Lambda$. This choice is maintained throughout this work. We define then a geometrical arrangement and a given set Ψ of target pressure profiles defined on the control boundary ∂V. We then pose the following question: Is it possible, for *any* pressure profile $p(\mathbf{x}) \in \Psi$, to calculate the strength of the secondary sources $a(\mathbf{y}) \in A$, such that the operator $(Sa)(\mathbf{x})$ allows the reproduction of the target pressure profile? If

[1] An operator $S : A \to \Psi$ is bijective if every element p of Ψ is associated with one and only one element a of A, such that $Sa = p$.

the answer to this question is negative, then we are in the presence of the first kind of ill-posedness.

Furthermore, if $a(\mathbf{y})$ exists, can it be defined uniquely or does more than one source strength exist, such that $Sa = p$ on ∂V? If the answer is the latter, then we are faced with the second kind of ill-posedness. It must be clearly emphasized that even if we have multiple possible choices for the source strength a, such that Sa gives an exact reproduction of the pressure profile, that is of the sound field on the control *boundary* ∂V, this does not imply that all these possible choices of source strength provide an accurate reproduction of the target field in the *interior* of the control region V (and possibly in the rest of the reproduction region Λ). On the contrary, there is in general only one exact choice of $a(\mathbf{y})$, which allows for an accurate reproduction of the field in all V. As shown below, this fact is directly related to the non-uniqueness of the Dirichlet problem, discussed in Section 3.3.

Finally, it is also possible that even if an exact solution $a(\mathbf{y})$ exists, this might lead to a system which is *not stable*. This means that the presence of very small errors, such as a small amount of noise in the data describing the target pressure profile, might result in a disastrous degradation of the reproduced sound field. In this case, $a(\mathbf{y})$ can be classified as an *unstable* solution. This is the third kind of ill-posedness, which is sometimes also known in numerical analysis as the problem of *ill-conditioning*.

In general, for a given operator S and sets A and Ψ, the three kind off ill-posedness co-exist. For example, if the attempt is made to solve the ill-posed inverse problem discussed above for all possible functions $p(\mathbf{x}) \in L^2(\partial V)$, we should expect that for some target functions $p(\mathbf{x})$ the problem has no solution, and for some other functions the solution is either non-unique, unstable or both.

As explained in [CK92], the ill-posedness of a problem does not depend only on the operator involved, but also on the spaces A and Ψ.[2] This suggests that, if a problem is ill-posed for a given data space Ψ, it might be possible to restore stability by limiting the data space to a subset $\Psi' \subset \Psi$. It could also be possible, in principle, to define for which subset $\Psi \subseteq L^2(\partial V)$ the problem is solvable, and for which subsets the solution is non-unique or unstable.

It is also of considerable relevance, especially for practical purposes, to identify those physical parameters of the given problem which determine its ill-posedness. For example, it is important to understand if a way around the problem of ill-posedness could be found by modifying the shape of the control region or of the control volume or both. Later in this chapter, we will assume that the target sound field is due to a monopole-like source, and we will study how the location of this point source can affect the solvability of the problem.

[2] The ill-posedness of S depends also on the norms defined on the spaces A, and Ψ, here chosen to be the L^2 norm (2.11).

In what follows, the three type of ill-posedness are studied separately, and the causes by which they are determined are analyzed.

5.2 Picard first condition and the denseness of the range of S

The first type of ill-posedness relates to the existence of the solution of the integral equation (3.19), which is repeated here:

$$(Sa)(\mathbf{x}) = p(\mathbf{x}), \quad \mathbf{x} \in \partial V$$

One can expect that a condition for the solution $a(\mathbf{y})$ to exists is that the function $p(\mathbf{x})$ is in the *range* of S (see definition (2.22)). In other words, one can expect that a solution exists if the target profile $p(\mathbf{x})$ belongs to the set of functions obtained by letting S act on all functions $a(\mathbf{y}) \in L^2(\partial\Lambda)$.

This intuitive concept is expressed more rigorously by the Picard theorem (2.1). This states that a solution $a(\mathbf{y})$ exists if and only if

$$p(\mathbf{x}) \in N(S^*)^\perp \tag{5.1}$$

$$\sum_{n=1}^{\infty} \frac{|\langle p_n | p \rangle|^2}{\sigma_n^2} < \infty \tag{5.2}$$

The first of the two conditions above requires the function $p(\mathbf{x})$ to be in the closure of the range of S. In fact, the result expressed by equation (2.125) states that $\overline{S(L^2(\partial\Lambda))} = N(S^*)^\perp$, that is the closure of the range of S corresponds to the orthogonal complement to the nullspace of S^*.

It is useful to underline that conditions (5.1) requires that $p(\mathbf{x})$ is in the *closure* of the range of S, and not strictly in its range. Hence, the first Picard condition alone does not guarantee the solvability of the integral equation. We will come back to this important point later in this chapter.

Recalling the definition (2.115) of the singular functions $p_n(\mathbf{x})$, we repeat here equation (3.23)

$$p(\mathbf{x}) = \sum_{n=1}^{\infty} p_n(\mathbf{x}) \langle p_n | p \rangle_{\partial V} + \left(P_{N(S^*)} p\right)(\mathbf{x})$$

which implies that the target pressure profile $p(\mathbf{x})$ can be expressed as a series of singular functions plus a function belonging to the nullspace of S^*. This concept can be reformulated as follows

$$\Psi_V \subseteq \overline{\text{span}\{p_n\}} \oplus N(S^*) = \overline{S(L^2(\partial V))} \oplus N(S^*) \tag{5.3}$$

It can be noticed that the two expressions above are consistent with condition (5.1). The implication of (5.3) is that if $p(\mathbf{x})$ has a non-zero orthogonal projection on the nullspace of S^*, then this target pressure profile can not be reproduced by the operator S. More specifically, the component of the target pressure profile which belongs to the nullspace of S^* can not be generated by S.

An intuitive explanation of the nullspace of S^*, can be provided following the figurative interpretation of S^* given in Section 3.5.1. If a continuous distribution of monopole-like sources with strength $p(\mathbf{x})$ is arranged on ∂V, and S^*p is the time reversed[3] field generated by these sources, then $N(S^*)$ is the set of the functions $p_{N(S^*)}(\mathbf{x})$ such that $(S^*p_{N(S^*)})(\mathbf{y}) = 0,\ \mathbf{y} \in \partial\Lambda$.

We will study now under what circumstances the pressure profiles $p(\mathbf{x}) \in \Psi_V$ satisfy the first Picard condition (5.1). The reader familiar with radiation problems might have already understood that if $S^*p_{N(S^*)}$ vanishes on $\partial\Lambda$, then the corresponding potential $\int_{\partial V} G(\mathbf{y},\mathbf{x})^* p_{N(S^*)}(\mathbf{x}) dS(\mathbf{x})$ equals zero on all $R^m \backslash V,\ m = 2,3$ (the exterior of V), including the boundary ∂V. As shown in Appendix B, this is derived from the uniqueness of the exterior Dirichlet problem. However, this fact does not imply that the field is zero also in the interior of V. This arises from the non-uniqueness of the interior Dirichlet problem, and suggests that there might be a relation between the nullspace of S^* (and hence the range of S) and the solutions of the Dirichlet problem (3.18) with homogeneous boundary conditions. The latter defines a field equal to zero on ∂V, but not zero in V. This is formally proven in what follows.

Let D_V be the linear space defined by [4]

$$D_V := \left\{ \nabla_{\mathbf{n}} u(\mathbf{x})|_{\partial V} : \nabla^2 u(\mathbf{z}) + k^2 u(\mathbf{z}) = 0 \quad \mathbf{z} \in V, \quad u(\mathbf{x}) = 0 \ \ \mathbf{x} \in \partial V \right\} \tag{5.4}$$

This means that D_V contains the normal derivative of any function $u(\mathbf{z})$ that is a solution of the homogeneous interior Dirichlet problem in V and that is restricted to ∂V.

Theorem 5.1. *The nullspace of the operator S^* coincides with the set D_V, that is*

$$N(S^*) = D_V \tag{5.5}$$

The proof of this theorem is given in Appendix B and is based on arguments inspired by the discussion on the solvability of the Dirichlet and Neumann problems presented in [CK83].

The theorem above, equation (2.125) and the definition of orthogonal projection (2.14) lead to the following result

[3] The concept of time reversal is not relevant for the definition of $N(S^*)$ as $(S^*p_{N(S^*)})(\mathbf{y}) = (S^*p^*_{N(S^*)})(\mathbf{y})^* = 0$ and both $p_{N(S^*)}(\mathbf{x})$ and $p_{N(S^*)}(\mathbf{x})^*$ belong to $N(S^*)$

[4] The assumption is made that the normal derivative of $\nabla_{\hat{\mathbf{n}}} u$ exists on ∂V, in the sense described by [CK83, p.68]

Corollary 5.2. *A function $p(\mathbf{x}) \in L^2(\partial V)$ is in the closure of the range of S if and only if*

$$\langle \nabla_{\mathbf{n}} u | p \rangle_{\partial V} = 0 \tag{5.6}$$

for all functions $\nabla_{\mathbf{n}} u(\mathbf{x}) \in D_V$, where D_V is defined by (5.4).

This important result states that any function $p(\mathbf{x})$, which has zero orthogonal projection on the set D_V, is in the closure of the range of S. When $k \neq k_n$, where k_n is one of the Dirichlet eigenvalues introduced in Section 3.3, the homogeneous interior Dirichlet problem is solved only by the function $p(\mathbf{z}) = 0$, $\forall \mathbf{z} \in \overline{V}$. As a consequence, D_V contains only the function identically equal to zero and the condition (5.6) is trivially satisfied for all $p(\mathbf{x}) \in \Psi_V$. This leads to the following result:

Corollary 5.3. *If the wave number k is not one of the Dirichlet eigenvalues for V, then any function $p(\mathbf{x}) \in \Psi_V$ is in the closure of the range of S.*

The existence of the solution also for the case of $k = k_n$ is a direct consequence of the following theorem:

Theorem 5.4. *Any function $p(\mathbf{x}) \in \Psi_V$ is in the closure of the range of S.*

The proof is given in Appendix B. This important result indicates that all the target pressure profiles of interest for the sound field reproduction problem addressed here have zero projection on the nullspace of S^*, including the case when $k = k_n$.

What has been discussed in this section means that any pressure profile $p(\mathbf{x})$ of interest for the sound field reproduction problem considered here is in the closure of the range of S. Consequently, equations (3.23) and (5.3) can be respectively reformulated as follows:

$$p(\mathbf{x}) = \sum_{n=1}^{\infty} p_n(\mathbf{x}) \langle p_n | p \rangle_{\partial V} \tag{5.7}$$

$$\Psi_V \subseteq \overline{\text{span}\{p_n\}} = \overline{S(L^2(\partial\Lambda))} \tag{5.8}$$

Equation (5.8) indicates that the range of S is *dense* in Ψ_V (see definition (2.16) of a dense set). In other words, given any target pressure profile $p(\mathbf{x}) \in \Psi_V$ and any $\epsilon > 0$, a source strength $a_\epsilon(\mathbf{y})$ exists such that

$$||S a_\epsilon - p||_{\partial V} \leq \epsilon \tag{5.9}$$

This means that any pressure profile in Ψ_V can be reproduced by the secondary source layer with *arbitrary accuracy*.

5.3 Picard second condition and the nonexistence of the solution

It can be noticed that the existence of a solution of the inverse problem $Sa = p,\ p \in \Psi_V$ implies that the inequality (5.9) is substituted by

$$||Sa - p||_{\partial V} = 0 \tag{5.10}$$

If this is the case, the statement that $S(L^2(\partial\Lambda))$ is dense in Ψ_V is substituted by the stronger proposition $\Psi_V \subseteq S(L^2(\partial\Lambda))$. In other words, all elements of Ψ_V are in the range of the operator S.

Two cases can be now analyzed: the case when the target pressure profile belongs to the range of S, and the case when $p(\mathbf{x})$ does not belong to $S(L^2(\partial\Lambda))$ but belongs to its closure. In the first case, an exact solution $a(\mathbf{y})$ of the inverse problem (3.19) exists, while this is not true for the second case.

As described above, if the two Picard conditions (5.1) and (5.2) are satisfied, then the solution $a(\mathbf{y})$ exists. It has been shown that the first Picard condition (5.1) holds if p is in the *closure* of the range of S and is always satisfied by any pressure profile of interest. The addition of the second condition (5.2) corresponds to the requirement of $p(\mathbf{x})$ being in the range of S, and not simply in its closure. In order to provide a more intuitive explanation of this concept, we proceed as follows. Equations (5.7) and (5.8) denote that any pressure profile $p(\mathbf{x}) \in \Psi_V$ can be expressed as a linear superposition of sound pressure modes $p_n(\mathbf{x})$. As we have seen, this is a consequence of $p(\mathbf{x})$ being in the *closure* of the range of S. The indication of *how much* a given pressure mode contributes to the target pressure profile is given by the scalar product $\langle p_n|p\rangle_{\partial V}$. In Section 3.5 it is explained that a given pressure mode is related to one and only one secondary source mode $a_n(\mathbf{y})$ and to a modal efficiency σ_n by the relation

$$\langle p_n|p\rangle_{\partial V} = \sigma_n \langle a_n|a\rangle_{\partial\Lambda},\quad n = 1, 2, ...N$$

It is clear that, given the n-th Fourier coefficient $\langle p_n|p\rangle$ of the target pressure profile, the required energy of the corresponding secondary source mode $a_n(\mathbf{y})$ is given by

$$|\langle a_n|a\rangle|^2 = \frac{|\langle p_n|p\rangle|^2}{\sigma_n^2} \tag{5.11}$$

From this formula, it is obvious that this modal energy is larger the smaller is the modal efficiency σ_n^2. In Section 2.5 it is reported that the eigenvalues of S^*S, and hence the singular values σ_n of S, accumulate at zero. As an example, it is possible to consider the high order approximation of the singular values in the spherical geometrical arrangement expressed by equation (4.15). It is clear that the singular values decay exponentially (if $R_\Lambda > R_V$) and accumulate at zero. The decay of the singular values implies that the

high order modes are characterized by decreasing efficiency. Consequently, the larger is the contribution of high order pressure modes to the target pressure profile, the larger is the energy of the signal driving the secondary sources for reconstructing the target pressure profile. The total energy generated by the secondary sources is given by $||a||^2$. The latter, in view of the orthogonality of the source modes and of equation (5.11), is given by

$$||a||^2 = \lim_{N\to\infty} \sum_{n=1}^{N} \frac{|\langle p_n|p\rangle|^2}{\sigma_n^2} \tag{5.12}$$

The series above must converge in order for a bounded solution $a(\mathbf{y})$ to exists. It can be observed that the absolute value of the Fourier coefficients $\langle p_n|p\rangle$ should decay to zero *much more rapidly* than the singular values σ_n in order for the total source energy to be finite. This condition is actually represented by the second Picard condition (5.2). For example, if the singular values of S exhibit the asymptotic decay α^{-n}, $n \to \infty$, $\alpha \in \mathbb{R}^+$, then the Fourier coefficients $\langle p_n|p\rangle$ should exhibit a steeper asymptotic decay β^{-n}, with $\beta > \alpha$, in order for the geometric series $\sum(\alpha^2/\beta^2)^n$ to converge.

If the target pressure profile $p(\mathbf{x}) \in \Psi_V$ does not satisfy the second Picard condition (5.2), but satisfies the first condition (5.1) discussed in the previous section, then the given pressure profile does not belong the range of S (just to its closure), and an exact solution to the inverse problem (3.19) does not exist. This case corresponds to the first kind of ill-posedness.

A topological analysis of the latter case shows that if p is not in the range of S but is in its closure, then p is a *limit point* for $S(L^2(\partial\Lambda))$ (the converse implication is not true). This means that, for any $\epsilon > 0$, there is at least one point $p' \in S(L^2(\partial\Lambda))$ such that $||p - p'|| < \epsilon$. This is analogous to the concept of denseness discussed above, and implies that even if the desired pressure profile can not be generated by the single layer potential S, it is possible to generate a profile which is arbitrarily *close* to it (in the sense of L^2 distance).

In order to make this concept more clear, an intuitive example is provided: assume that the target profile p is the one-dimensional Dirac function (2.24), and that the operator S is a low-pass filter, which attenuates high frequencies with constant roll-off. We want to define the signal a which, after the low-pass filtering due to S, corresponds to a Dirac delta function. It is clear that the latter has a spectrum, that exhibits the same energy for all frequencies. On the other side, the operator S is responsible of the attenuation of high frequencies. Therefore, in order to compensate for this attenuation, the function a should have an ideally infinite amount of energy at high frequencies. This is equivalent to the fact that the *inverse filter* of the low-pass filter S, that is the inverse operator S^{-1}, should cause an infinite high frequency boost. For this reason, it is clear that no bounded function a exists, such that $Sa = p$. It is however possible to compute a function $\tilde{a}$ with finite amount of energy at high frequencies, which generates after the low-pass filtering S a reasonable approximation of the Dirac delta function. This is equivalent to

a regularization scheme, discussed in the next chapter. It can be seen that the larger the high frequencies content of $\tilde{a}$, the better the approximation of p.

This conceptual analysis can be applied, with the required modifications, to the sound field reproduction addressed here. In fact, in view of equation (2.120), we see that the decay of the singular values of the single layer potential acts as a low-pass filter for the generalized Fourier series representing the density a. In other words, S generates a function which is *smoother* than the potential a. The second Picard condition (5.2) actually requires that the Fourier coefficients representing p exhibit a steeper decay than the decay of the singular values σ_N. If this was not the case, an infinite amount of energy would be required for the higher orders of the Fourier series representation of a in order to generate p. In Section 6.2 we will see that, even when an exact solution does not exist, it is possible to determine an approximate solution, which allows to some extent an accurate reproduction of the target field.

5.4 Ill-conditioning

We move now to the case when the target pressure profile belongs to the range of S (both Picard conditions are satisfied) and therefore an exact solution $a(\mathbf{y})$ to the inverse problem considered exists . In Section 3.5 it has been shown that the solution is of the form given by equation (3.28), which is again reported here:

$$a(\mathbf{y}) = \sum_{n=1}^{\infty} a_n(\mathbf{y}) \frac{1}{\sigma_n} \langle p_n | p \rangle_{\partial V}$$

In the previous section, it has been argued that the decay of the singular values of S is responsible for very large values of $||a||$, which might lead to the nonexistence of the solution for some pressure profiles. It is shown here that this behavior of the singular values is responsible also for the third kind of ill-posedness. In order to do that, we first generate a perturbed version of the pressure profile defined by

$$\tilde{p}(\mathbf{x}) = p(\mathbf{x}) + \delta p(\mathbf{x}) \tag{5.13}$$

where the perturbation $\delta p(\mathbf{x})$ is a function representing, for example, small errors in the data describing the target pressure profile. For simplicity, we assume that the perturbation can be described by one pressure mode only, that is $\delta p(\mathbf{x}) = ||\delta p|| p_n(\mathbf{x})$. We also assume that the perturbation is small in respect to the pressure profile, that is $||\delta p|| \ll ||p||$. Since the problem is linear, the solution with perturbed data is given by

$$\tilde{a}(\mathbf{y}) = a(\mathbf{y}) + \frac{||\delta p||}{\sigma_n} a_n(\mathbf{y}) \tag{5.14}$$

From this expression it can be deduced that if the mode $p_n(\mathbf{x})$ is a high order mode, associated with a very small singular value $\sigma_n \ll ||\delta p||$, then the effect of the perturbation is significantly amplified. This might lead to a very large $||a||$, corresponding to an unreasonably large amount of energy generated by the secondary sources. This *error amplification* corresponds to the third kind of ill-posedness, also known as *ill-conditioning*. In mathematical terms, it is said that the solution $a(\mathbf{y})$ does not depend continuously on the data. In fact, as we have seen, a very small variation δp of the data, which has a non zero orthogonal projection onto high order modes, might lead to a meaningless solution.

The discussion above suggests also that, for engineering purposes, the line defining the existence of the solution is not so well defined, or equivalently that the problems of nonexistence and ill-conditioning are closely related. The singular functions $p_n(\mathbf{x})$ and $a_n(\mathbf{y})$ associated with very small singular values could be considered, in practical terms, as belonging to the nullspace of S^* and S, respectively. In mathematical terms, given a small $\epsilon > 0$ and recalling that $||a_n|| = ||p_n|| = 1$, we see (with some lack of rigor) that

$$\epsilon \geq \sigma_n \approx 0 \rightarrow \epsilon \geq ||\sigma_n a_n(\mathbf{y})|| = ||(S^* p_n)(\mathbf{y})|| \approx 0 \rightarrow p_n \in N^*(S) \tag{5.15}$$

This implies that the pressure mode $p_n(\mathbf{x})$ can not be reproduced and an exact solution for the inverse problem addressed does not exist if the pressure profile has a non-zero orthogonal projection on that mode.

In numerical calculations, the parameter ϵ in the expression above is imposed by the numerical resolution limit, while if the data describing the pressure profile are acquired with measurement, ϵ is given by the measurement error and noise and by the dynamic range of the system, and can be quite large (in comparison with the largest singular value σ_1) if the measurement system is not adequate. The measurements are the most critical and delicate link in the chain, as far as the ill-conditioning problem is concerned. Measurement noise from different microphones is generally uncorrelated, and the function $\delta p(\mathbf{x})$ describing this noise potentially has a large orthogonal projection on high orders $p_n(\mathbf{x})$, thus leading to large error amplification.

On the reproduction side (that is to say if no error is made in the determination of $\langle p_n|p\rangle$) the effect of a non-robust solution might arise, for example, from inaccurate positioning of the secondary sources or variation of the speed of sound. It can be observed that this effect is largely dependent on the energy distribution of the Fourier coefficients $\langle p_n|p\rangle_{\partial V}$ of the pressure profile, and therefore on the sound field to be reproduced. If most of the energy of the pressure profile $p(\mathbf{x})$ is concentrated in the low orders, the solution tends to be well-behaved. On the other hand, if much energy is contained in the high order coefficients, the norm of $a(\mathbf{y})$ becomes large and relevant destructive interference phenomena occurs between the pressure fields generated by the secondary sources. This obviously amplifies the effects caused by the presence of errors and the solution $a(\mathbf{y})$

tends to instability. If too much energy is contained in the high orders, then the second Picard condition (5.2) is not satisfied and the solution does not exist.

5.5 Uniqueness of the solution and Dirichlet eigenvalues

In the previous sections the study of the existence of the solution of the inverse problem (3.19) has been addressed, but no discussion has been presented on whether the solution is unique or more than one solution exists. It is shown in this section that the solution of the inverse problem, assuming it exists, is unique if the wave number k is not one of the Dirichlet eigenvalues k_n. On the contrary, if $k = k_n$, the solution of the integral equation is not unique. This subject completes the study of the integral equation (3.19).

The proof of the uniqueness of the solution of (3.19) is equivalent to the proof of the injectivity of S, that is for any two functions $a(\mathbf{y}), a'(\mathbf{y}) \in L^2(\partial\Lambda)$ with $||a-a'|| = 0$ (they are equal in L^2 sense), we have that $Sa \neq Sa'$ [Kre78, p.614]. This is in turn equivalent to the proof that the nullspace of S is trivial, that is $(Sa)(\mathbf{x}) = 0 \rightarrow a(\mathbf{y}) = 0$. This second equivalence can be simply justified as follows: since S is a linear operator, if its nullspace is non-trivial, that is to say if the non-trivial function $a_0(\mathbf{y}) \in L^2(\partial\Lambda)$ exists such that $(Sa_0)(\mathbf{x}) = 0$, then for any function $a(\mathbf{y}) \in L^2(\partial\Lambda)$ it holds that $Sa = S(a + a_0)$, hence S is not injective. Similarly, if S is not injective then two functions $a', a \in L^2(\partial\Lambda)$, $||a - a'|| \neq 0$ exist such that $(Sa)(\mathbf{x}) = (Sa')(\mathbf{x})$. Consequently, $\big(S(a - a')\big)(\mathbf{x}) = 0$, which implies that the non-trivial function $(a - a')(\mathbf{y})$ belongs to the nullspace of S.

Theorem 5.5. *Given $p(\mathbf{x}) \in \Psi_V$, where ψ_V is defined by (3.3), if the wave number k is not one of the Dirichlet eigenvalues for V, then the solution $a(\mathbf{y})$ of the inverse problem $Sa = p$ is unique.*

The proof is given again in Appendix B.

The theorem above also implies that if k is one of the Dirichlet eigenvalues for V, then the solution $a(\mathbf{y})$ is in general not unique. In fact, given the solution (3.28) in terms of a singular system of S, any solution of the form $a(\mathbf{y}) + a_0(\mathbf{y})$, where $a_0 \in N(S)$, is also a solution. This case corresponds to the second type of ill-posedness.

Recalling what has been discussed in Section 3.3, if $k = k_n$ the Dirichlet problem (3.18) is not uniquely solvable and the knowledge of the pressure profile $p(\mathbf{x})$, $\mathbf{x} \in \partial V$ alone is not enough to determine the field in the interior of V. This suggests that even if the solution of the integral equation (3.19) is not unique, only one of these solutions is such that $(Sa)(\mathbf{z}) = p(\mathbf{z})$, $\forall \mathbf{z} \in V$. In other words, even if the integral equation has an infinite number of exact solutions, only one of these solutions allows for the exact reproduction of the target field in the interior (and possibly in the exterior) of the control region. In the next chapter some techniques are presented for overcoming this nonuniqueness problem.

Assuming that this concept could be extended also to the case when ∂V is unbounded, as in the cases described in sections 4.3 and 4.4, it can be deduced that the problem of nonuniqueness does not arise as the homogeneous Dirichlet problem has only the trivial solution (intuitively, an open space does not have acoustic resonance frequencies).

5.5.1 Dirichlet eigenvalues of Λ

It is interesting to note that the Dirichlet (and Neumann) eigenvalues $k_n^{'}$ for the reproduction region Λ do not play any role with respect to the solvability and uniqueness of this inverse problem. It is useful however to notice that the reproduced sound field has the following interesting peculiarity when the wave number is one of the Dirichlet eigenvalues for Λ. Let D_Λ be the linear space of the normal derivatives of the solution of the homogeneous Dirichlet problem for Λ, restricted to $\partial\Lambda$. D_Λ is defined analogously to D_V by

$$D_\Lambda := \left\{ \nabla_{\mathbf{n}} u(\mathbf{y})|_{\partial\Lambda} : \nabla^2 u(\mathbf{z}) + k^2 u(\mathbf{z}) = 0, \quad \mathbf{z} \in \Lambda, \quad u(\mathbf{y}) = 0, \quad \mathbf{y} \in \partial\Lambda \right\} \tag{5.16}$$

If the secondary sources are driven by a source mode $a_n(\mathbf{y})$, which lies completely on D_Λ, then we have that

$$(Sa_n)(\mathbf{z}) = 0, \quad \mathbf{z} \in \mathbb{R}^m \backslash \Lambda, \quad a_n(\mathbf{y}) \in D_\Lambda \tag{5.17}$$

which means that the acoustic field generated by Sa_n vanishes in the exterior of Λ. This can be shown using the same arguments used with respect to the uniqueness of the exterior Dirichlet problem, which are presented in Appendix B. Figure 5.1 shows the reproduction of the mode $Y_5^{-3}(\mathbf{y})/R_\Lambda$ by a continuous distribution of sources on the sphere $\partial\Lambda = \Omega_{R_\Lambda}$. The wave number k considered is one of the Dirichlet eigenvalues for Λ, more specifically $j_5(kR_\Lambda) = 0$. It can be observed that the field in the exterior of the sphere is zero, while this in not the case for the field in the interior.

The result shown above can be extended to any general source strength $a(\mathbf{y})$: the field generated by the orthogonal projection of $a(\mathbf{y})$ onto D_V is zero in the exterior of the reproduction region.

5.6 Examples with spherical and linear geometry

The results discussed in the previous sections of this chapter are now illustrated with some examples. A representative and didactically interesting case is given by the three-dimensional target sound field due to a single monopole-like source, hereafter referred to as *virtual source*. In fact, any sound field of practical interest, which is due to sources contained in a bounded region, can be represented by the linear superposition of the

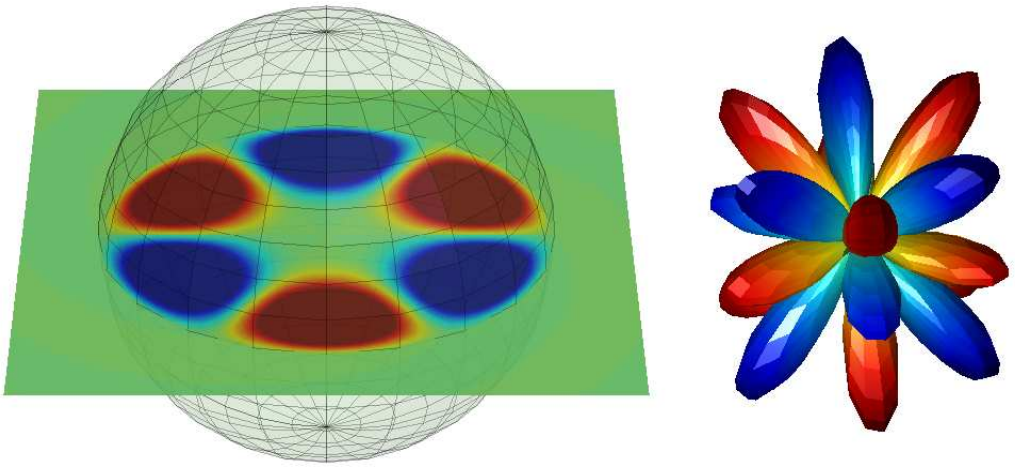

FIGURE 5.1: Sound field generated by a continuous distribution of sources on the sphere $\partial\Lambda$. The secondary source strength $a(\mathbf{y})$ is given by the function $Y_5^{-3}(\mathbf{y})/R_\Lambda$, and $j_5(k_n^{'}R_\Lambda) = 0$ ($k_n^{'}$ is one of the Dirichlet eigenvalues of Λ).

fields generated by a finite or infinite number of monopole-like sources. The equivalent of such a source for a two dimensional problem is the line source. In this section the problems are addressed of the reproduction of the three-dimensional sound field due to a monopole source with secondary sources arranged on a sphere and the reproduction of the field due to a line source with secondary sources on a line.

5.6.1 Monopole source and concentric sphere arrangement

The field generated by a monopole source with unitary strength $\ddot{m}$, that is with volume velocity $q_{vol} = (-i\rho_0 ck)^{-1}$, was discussed in Section 3.2 and can be described by the free field Green function (3.6). This equation can be expressed in the form given by equation (4.2). It is assumed that the monopole generating the target field is located at $\mathbf{q} \in \mathbb{R}^3 \backslash \overline{V}$. The pressure profile due to that monopole is hence given by

$$p(\mathbf{x}) = \frac{e^{ik|\mathbf{x}-\mathbf{q}|}}{4\pi|\mathbf{x}-\mathbf{q}|} = \sum_{\nu=0}^{\infty} ikh_\nu^{(1)}(kq) j_\nu(kR_V) \sum_{\mu=-\nu}^{\nu} Y_\nu^\mu(\hat{\mathbf{x}}) Y_\nu^\mu(\hat{\mathbf{q}})^*, \quad \mathbf{x} \in \partial V \tag{5.18}$$

In view of the orthogonality relation for the spherical harmonics (4.3), we have that

$$\langle Y_\nu^\mu | p \rangle_{\partial V} = R_V^2 ikh_\nu(kq) j_\nu(kR_V) Y_\nu^\mu(\hat{\mathbf{q}})^* \tag{5.19}$$

The representations (4.4) and (4.5) of S and S^*, respectively, are given by

$$\begin{aligned}(Sa)(\mathbf{x}) &= \sum_{\nu=0}^{\infty} iR_V R_\Lambda k h_\nu^{(1)}(ky) j_\nu(kx) \sum_{\mu=-\nu}^{\nu} \frac{Y_\nu^\mu(\hat{\mathbf{x}})}{R_V} \frac{\langle Y_\nu^\mu | a \rangle_{\partial\Lambda}}{R_\Lambda} \\ (S^*p)(\mathbf{y}) &= \sum_{\nu=0}^{\infty} -iR_V R_\Lambda k h_\nu^{(2)}(ky) j_\nu(kx) \sum_{\mu=-\nu}^{\nu} \frac{Y_\nu^\mu(\hat{\mathbf{y}})}{R_\Lambda} \frac{\langle Y_\nu^\mu | p \rangle_{\partial V}}{R_V}\end{aligned}$$

5.6.1.1 Existence of the solution - first Picard condition

Given the wave number k_n such that $j_n(k_n R_V) = 0$, it can be observed that all functions of the kind

$$\nabla_{\mathbf{n}} u_n(\mathbf{z}) = a k j_n'(k_n R_V) Y_n^m(\hat{\mathbf{x}}), \quad |m| \leq n, \;\; a \in \mathbb{R}, \;\; \mathbf{x} \in \partial V \tag{5.20}$$

are in the nullspace of S^*. In fact, it holds that

$$\begin{aligned}(S^* u_n)(\mathbf{y}) &= \sum_{\nu=0}^{\infty} -iR_V R_\Lambda k_n h_\nu^{(2)}(k_n R_\Lambda) j_\nu(k_n R_V) \\ &\times \sum_{\mu=-\nu}^{\nu} \frac{Y_n^m(\hat{\mathbf{y}})}{R_\Lambda} (\delta_{n\nu}\delta_{m\mu} k_n j_n'(k_n R_V) R_V) = 0\end{aligned} \tag{5.21}$$

Comparing equation (5.20) with the solution of the homogeneous interior Dirichlet problem for a sphere given by equation (C.2), it can be noticed that $\overline{\text{span}\{\nabla_{\mathbf{n}} u_n\}}$, that is the linear space spanned by all functions $\nabla_{\mathbf{n}} u_n(\mathbf{x})$, corresponds to the set D_V defined by equation (5.4).

It can be also observed that, given the wave number k_n and the function $\nabla_{\mathbf{n}} u_n(\mathbf{x}) \in D_V$, the orthogonal projection pressure of the profile (5.18) onto the subspace D_V is always zero. It holds that

$$\langle u_n | p \rangle_{\partial V} = \sum_{\nu=0}^{\infty} ik_n h_\nu^{(1)}(k_n q) j_\nu(k_n R_V) \sum_{\mu=-\nu}^{\nu} Y_\nu^\mu(\hat{\mathbf{q}})^* j_n'(k_n R_V) \langle Y_n^m | Y_\nu^\mu \rangle_{\partial V} = 0 \tag{5.22}$$

for any function $u_n \in D_V$. Hence the pressure profile due to a monopole source located at *any* position $\mathbf{q} \in R^3 \backslash \overline{V}$ is in the closure of the range of S. These results are consistent with what has been discussed in Section 5.2.

5.6.1.2 Existence of the solution - second Picard condition

We consider the singular system given by equations (4.7) to (4.11). Recall that the expressions of the singular values σ_n and of the singular functions $p_n(\mathbf{x})$ are given by

$$\begin{aligned} \sigma_n &= kR_V R_\Lambda |h_\nu(kR_\Lambda) j_\nu(kR_V)| \\ p_n(\mathbf{x}) &= \frac{\gamma_\nu}{R_V} Y_\nu^\mu(\hat{\mathbf{x}}) \end{aligned}$$

It is now possible to obtain the following expression for the second Picard condition (2.128)

$$\sum_{n=1}^{N} \frac{|\langle p_n|p\rangle_{\partial V}|^2}{\sigma_n^2} = \frac{1}{R_\Lambda^2} \sum_{\nu=0}^{\infty} \left| \frac{h_\nu(kq)}{h_\nu(kR_\Lambda)} \right|^2 \sum_{\mu=-\nu}^{\nu} |Y_\nu^\mu(\hat{\mathbf{q}})|^2 < \infty \tag{5.23}$$

This series must converge in order for the second Picard condition to be satisfied.

Considering that $|Y_\nu^\mu(\hat{\mathbf{q}})|^2 = Y_\nu^\mu(\hat{\mathbf{q}}) Y_\nu^\mu(\hat{\mathbf{q}})^*$, from the spherical harmonic summation formula (2.53) we obtain

$$\sum_{\mu=-\nu}^{\nu} |Y_\nu^\mu(\hat{\mathbf{q}})|^2 = \left| \frac{2\nu+1}{4\pi} P_\nu(1) \right| = \frac{2\nu+1}{4\pi} \tag{5.24}$$

The last equality is due to the fact that $P_\nu(1) = 1,\ \nu = 1, 2, ...$ [Wil99, p.187]. The high order asymptotic approximation of the Hankel functions (2.40) leads to

$$\lim_{\nu\to\infty} \frac{h_\nu(kq)}{h_\nu(kR_\Lambda)} = \left(\frac{R_\Lambda}{q} \right)^{\nu+1} \tag{5.25}$$

Hence we have that

$$\lim_{n\to\infty} \frac{|\langle p_n|p\rangle_{\partial V}|^2}{\sigma_n^2} = \frac{2\nu+1}{4\pi q^2} \left(\frac{R_\Lambda}{q} \right)^{2\nu} \tag{5.26}$$

Given a generic series $\sum a_n$, the ratio test for the convergence of a series [WW27] states that if the limit

$$R := \lim_{n\to\infty} \frac{a_{n+1}}{a_n} \tag{5.27}$$

exists, then the series above converges if $R < 1$ and diverges if $R > 1$. We observe that

$$\lim_{n\to\infty} \frac{|\langle p_{n+1}|p\rangle_{\partial V}|^2}{\sigma_{n+1}^2} \frac{\sigma_n^2}{|\langle p_n|p\rangle_{\partial V}|^2} = \lim_{\nu\to\infty} \frac{2(\nu+1)+1}{2\nu+1} \left(\frac{R_\Lambda}{q} \right)^2 = \left(\frac{R_\Lambda}{q} \right)^2 \tag{5.28}$$

and the ratio test indicates that the series 5.24 converges if $q > R_\Lambda$, and it diverges if $q < R_\Lambda$.

This very important result indicates that the sound field due to a monopole source can be reproduced by the layer of secondary sources on $\partial\Lambda$ only if the virtual monopole source is located in the *exterior* of Λ. If the virtual source is located in the exterior of V but in the *interior* of Λ, then the pressure profile $p(\mathbf{x})$ is still in the *closure* of the range of

S, but the series (4.19), which should represent the strength of the secondary sources, diverges. It is clear that in the special case when the virtual source is on the boundary of Λ, that is if $\mathbf{q} \in \partial\Lambda$, we have that $a(\mathbf{y}) = \delta_{\partial\Lambda}(\mathbf{y} - \mathbf{q})$.

5.6.1.3 Analytical expression of the solution

The combination of equation (5.19) with equation (4.19) leads to the following expression for the source strength:

$$a(\mathbf{y}) = \sum_{\nu=0}^{\infty} \frac{h_\nu(kq)}{R_\Lambda^2 h_\nu(kR_\Lambda)} \sum_{\mu=-\nu}^{\nu} Y_\nu^\mu(\hat{\mathbf{y}}) Y_\nu^\mu(\hat{\mathbf{q}})^* \tag{5.29}$$

Applying the summation formula of the spherical harmonics (2.53) we obtain

$$a(\mathbf{y}) = \sum_{\nu=0}^{\infty} \frac{2\nu+1}{4\pi R_\Lambda^2} \frac{h_\nu(kq)}{h_\nu(kR_\Lambda)} P_\nu(\cos\varphi_{\mathbf{qy}}) \tag{5.30}$$

where $\cos\varphi_{\mathbf{zy}} = \hat{\mathbf{q}} \cdot \hat{\mathbf{y}}$ is the cosine of the angle between the vectors $\mathbf{q}$ and $\mathbf{y}$ and can be calculated using equation (2.54). If one of these expression of $a(\mathbf{y})$ is inserted in the expression (4.4) of S, we obtain the equation (5.18), which represents the target field. This confirms that the solution is correct and that $(Sa)(\mathbf{x}) = p(\mathbf{x})$.

The fact should be highlighted that the control volume V does not appear in the expression of the solution. This is due the fact that the latter is computed from the analytic description of the target field, rather than from data on ∂V.

Figure 5.2 represents the horizontal cross-section of the sound field $p(\mathbf{z})$ generated by an omnidirectional point source (an acoustic monopole), located at $[r_q, \theta_q, \phi_q] = [2.5\text{ m}, 80°, 140°]$ and with the wave number $k = 6$ rad/m. Figure 5.3 shows the reproduced field $\hat{p}(\mathbf{z})$ for a virtual source at the same location, with a secondary source layer $\partial\Lambda$ corresponding to a sphere of radius $R_\Lambda = 1.5$ m. The reproduced field $\hat{p}$ has been calculated from the expression (4.4) of S, with the density $a(\mathbf{y})$ given by the series (5.29), truncated to the order $N = 13$. Figure 5.4 represents the *normalized reproduction error* $\epsilon_N(\mathbf{z})$, defined as follows:

$$\epsilon_N(\mathbf{z}) := \frac{|p(\mathbf{z}) - \hat{p}(\mathbf{z})|^2}{|p(\mathbf{z})|^2} 100 \tag{5.31}$$

It can be appreciated that the normalized reproduction error is close to zero (apart from the approximation due to the truncation of (5.29)) in the entire reproduction region Λ.

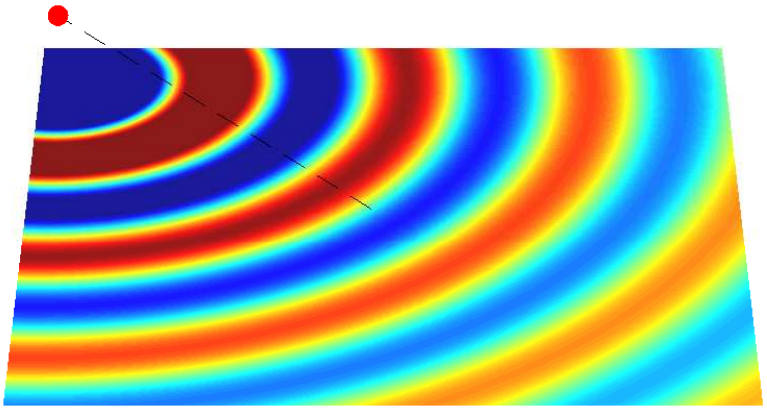

FIGURE 5.2: Horizontal cross-section of the sound field due to an omnidirectional point source (red dot) located at $[r_q, \theta_q, \phi_q] = [2.5\text{ m}, 80°, 140°]$. The wave number is $k = 6$ rad/m.

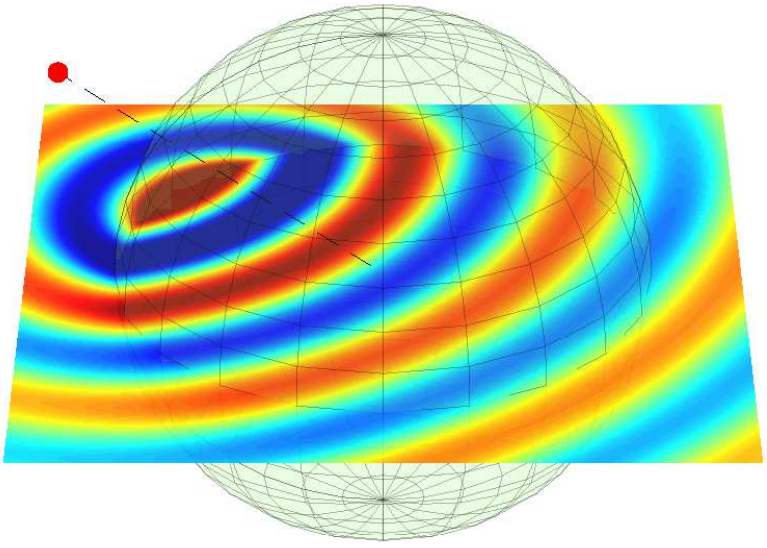

FIGURE 5.3: Horizontal cross-section of the reproduced sound field for a virtual source (red dot) located at $[r_q, \theta_q, \phi_q] = [2.5\text{ m}, 80°, 140°]$. The wave number is $k = 6$ rad/m and the radius of the sphere is $R_\Lambda = 1.5$ m.

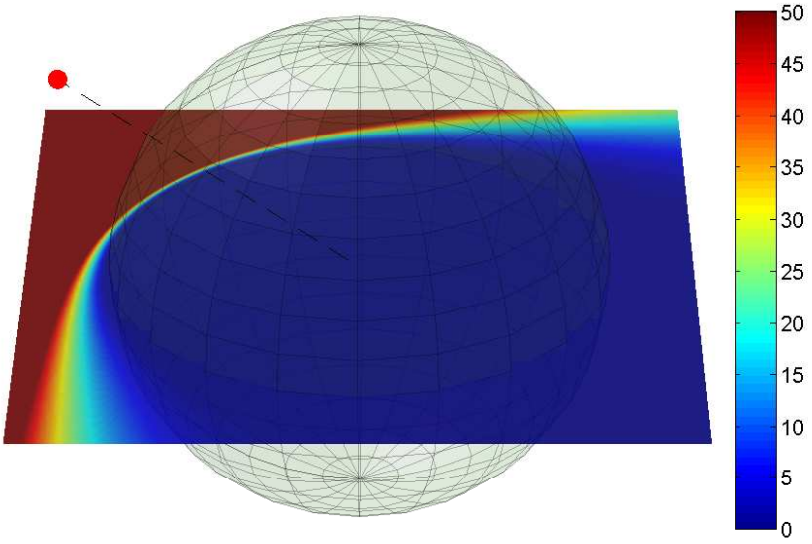

FIGURE 5.4: Horizontal cross-section of normalized reproduction error (%) for a virtual source (red dot) located at $[r_q, \theta_q, \phi_q] = [2.5\text{ m}, 80°, 140°]$. The wave number is $k = 6$ rad/m and the radius of the sphere is $R_\Lambda = 1.5$ m.

We have seen that in the case of $q < R_\Lambda$ the series given above diverges. This fact has the physical meaning that if an attempt is made to generate a sound field with a singularity at $\mathbf{q}$, in the interior of the reproduction region Λ, then the secondary sources should generate an infinite amount of energy. The sound field generated by these would interact destructively in order to generate the target pressure profile $p(\mathbf{x})$, represented by a bounded function.

In the limiting case when $\mathbf{q} \in \partial\Lambda$, the ratio of Hankel functions in equations (5.29) and (5.30) equals unity. Hence, for the completeness relation of the spherical harmonics (2.55), we obtain

$$a(\mathbf{y}) = \sum_{\nu=0}^{\infty} \frac{1}{R_\Lambda^2} \sum_{\mu=-\nu}^{\nu} Y_\nu^\mu(\hat{\mathbf{y}}) Y_\nu^\mu(\hat{\mathbf{q}})^* = \frac{\delta_\Omega(\hat{\mathbf{y}} - \hat{\mathbf{q}})}{R_\Lambda^2} \tag{5.32}$$

Given an arbitrary square integrable function $f(\hat{\mathbf{y}})$ defined on the spherical surface $\partial\Lambda$, the property (2.26) of the Dirac delta function can be rewritten in this case as

$$\int_{\partial\Lambda} f(\hat{\mathbf{y}}) \frac{\delta_\Omega(\hat{\mathbf{y}} - \hat{\mathbf{q}})}{R_\Lambda^2} dS(\mathbf{y}) = \int_\Omega f(\hat{\mathbf{y}}) \frac{\delta_\Omega(\hat{\mathbf{y}} - \hat{\mathbf{q}})}{R_\Lambda^2} R_\Lambda^2 dS(\hat{\mathbf{y}}) = f(\hat{\mathbf{z}}) \tag{5.33}$$

where $f(\hat{\mathbf{y}})$ is assumed to be continuous at $\hat{\mathbf{y}} = \hat{\mathbf{z}}$. This shows that $\delta_{\partial\Lambda}(\mathbf{y} - \mathbf{q}) = \delta_\Omega(\hat{\mathbf{y}} - \hat{\mathbf{q}})/R_\Lambda^2$. Hence we observe that, consistently with what was argued above, when $\mathbf{q} \in \partial\Lambda$ we have that $a(\mathbf{y}) = \delta_{\partial\Lambda}(\mathbf{y} - \mathbf{q})$

Equation (5.29) could be regarded as a *low-pass filtered* spherical Dirac delta function. It has been shown that

$$\delta_{\partial\Lambda}(\mathbf{y}-\mathbf{q}) = \frac{1}{R_\Lambda^2}\sum_{\nu=0}^{\infty}\sum_{\mu=-\nu}^{\nu} Y_\nu^\mu(\hat{\mathbf{y}})Y_\nu^\mu(\hat{\mathbf{q}})^* \tag{5.34}$$

This expression can be interpreted as a generalized Fourier series for the Dirac delta function. The spatial filter Ξ_ν is defined by

$$\Xi_\nu = \frac{h_\nu(kq)}{h_\nu(kR_\Lambda)} \tag{5.35}$$

Equation (5.29) can be therefore rewritten as follows:

$$a(\mathbf{y}) = \frac{1}{R_\Lambda^2}\sum_{\nu=0}^{\infty}\Xi_\nu\sum_{\mu=-\nu}^{\nu} Y_\nu^\mu(\hat{\mathbf{y}})Y_\nu^\mu(\hat{\mathbf{q}})^* \tag{5.36}$$

This illustrates that $a(\mathbf{y})$ is obtained by modulating the Fourier coefficients of $\delta_{\partial\Lambda}(\mathbf{y}-\mathbf{q})$ by the filter coefficients Ξ_ν.

Figure 5.6 represents the absolute values of Ξ_ν for different distances q of the virtual source and $R_\Lambda = 1$ m, k = 1 rad/m.

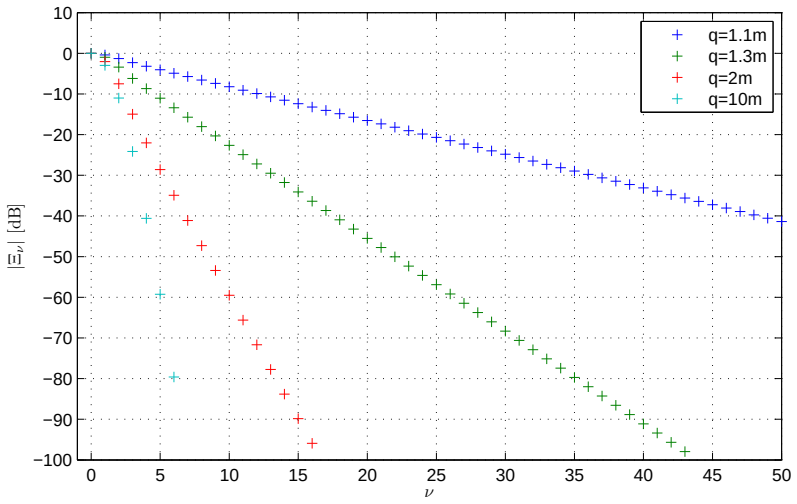

FIGURE 5.5: Magnitude of the coefficients of the spatial filter Ξ_ν (spherical arrangement) for different distances q and $R_\Lambda = 1$ m, $k = 1$ rad/m

In the case of $q > R_\Lambda$, the high order terms of the series are *damped* by Ξ_ν. The function $a(\mathbf{y})$ is smoother the steeper is the decay of the magnitude of its Fourier coefficients. This implies that the *main lobe* of the source strength function $a(\mathbf{y})$, which is infinitely narrow for the case when $q = R_\Lambda$, becomes broader the further away the virtual source is from the reproduction region. The limiting case is when q tends to infinity. In this case, considering the large argument asymptotic approximation (2.43) of the Hankel functions,

we have that

$$\Xi_\nu = \lim_{q\to\infty} (-i)^\nu \frac{h_0(kq)}{h_\nu(kR_\Lambda)} \tag{5.37}$$

If the magnitude decay and change of phase are compensated for by multiplying by a factor $4\pi q e^{-ikq}$ the target field, the latter corresponds to a plane wave and the spatial filter above becomes

$$\Xi_\nu = \frac{4\pi(-i)^\nu}{ikh_\nu(kR_\Lambda)} \tag{5.38}$$

What has been discussed is demonstrated by Figure 5.6, which shows the absolute value and phase of $a(\mathbf{y})$ (computed with series (5.30) truncated at the order $N = 100$) as a function of the angle $\varphi_{\mathbf{qy}}$, for different distance q of the virtual source and $R_\Lambda = 1$ m, $k = 1$ rad/m.

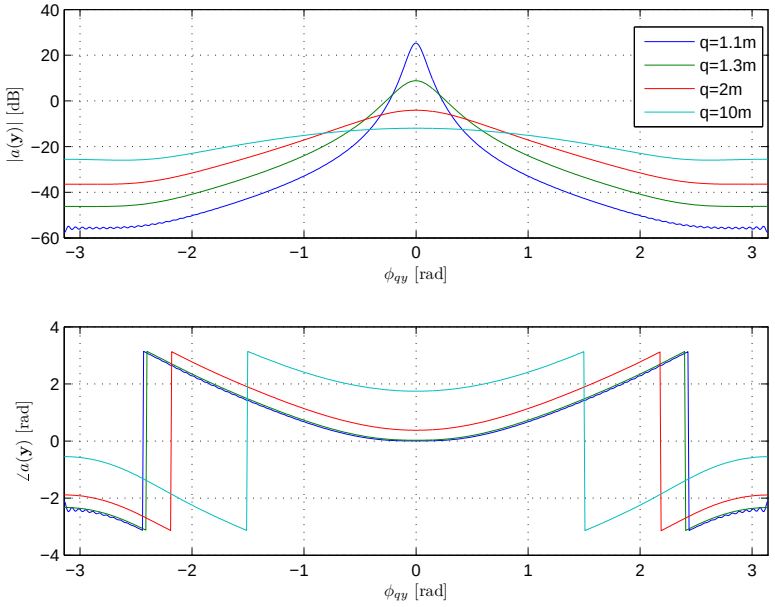

FIGURE 5.6: Magnitude and phase of the density $a(\mathbf{y})$ (spherical arrangement) for different distances q and $R_\Lambda = 1$ m, $k = 1$ rad/m.

This has the meaningful consequence that the closer is the virtual source to $\partial\Lambda$, the more the majority of the energy $||a||^2$ is concentrated in the vicinity of the location identified by the direction $\hat{\mathbf{q}}$ on $\partial\Lambda$.

5.6.1.4 Uniqueness of the solution

Applying the operator S, represented by (4.4), to the solution (5.29), it can be observed that the target sound field is reproduced exactly in the entire reproduction region, that is

$(Sa)(\mathbf{z}) = p(\mathbf{z}),\ \mathbf{z} \in \Lambda$. As discussed above, this holds as long as $\mathbf{q} \notin \Lambda$. Equation (5.29) determines a *unique* solution, which allows for the exact reproduction of the target field in the entire volume Λ. The expression of this solution is completely independent of the control region V.

It has been mentioned that, in the case under consideration, the calculation of the solution has been computed from the analytical expression (5.18) for the target pressure profile. In the more general case, however, the calculation of (4.19) is computed from a set of data describing the acoustic pressure on the control boundary ∂V. This might lead to a nonuniqueness problem. In order to demonstrate this, we assume that the wave number is one of the Dirichlet eigenvalues k_n for the domain V. As shown in Appendix C, this implies that $j_n(k_n R_V) = 0$ for a given n. In this case the functions $Y_n^m(\hat{\mathbf{y}})/R_\Lambda,\ |m| \leq n$ could be interpreted as *zero efficiency modes*. They are *not* singular functions of S, they span its nullspace. This implies that the series (4.19), representing the general solution, does not include the terms with $\nu = n$. Therefore equation (4.19) represents in this case one of the exact solutions to the integral equation (3.19), but all solutions of the form

$$a(\mathbf{y}) = \sum_{\substack{\nu=0 \\ n\neq\nu}}^{\infty} \sum_{\mu=-\nu}^{\nu} \frac{Y_\nu^\mu(\hat{\mathbf{y}})}{ikR_V^2 R_\Lambda^2 h_\nu^{(1)}(kR_\Lambda) j_\nu(kR_V)} \langle Y_\nu^\mu | p \rangle_{\partial V} + \sum_{m=-n}^{n} \alpha_m Y_n^m(\hat{\mathbf{y}}),\ \alpha_m \in \mathbb{C}$$

are also correct solutions. It can be noticed that the last sum represents an element in the nullspace of S.

Formula (4.19) does not give in this case the correct source strength for the reproduction of the target field *in the interior of* V, but only on its boundary. It can be actually seen that (4.19) does not allow for the computation of the term

$$\frac{2n+1}{4\pi R_\Lambda^2} \frac{h_n(k_n q)}{h_n(k_n R_\Lambda)} P_n(\cos\varphi_{\mathbf{qy}})$$

in the series (5.30) for the given n, which identifies the Dirichlet eigenvalue k_n.

It is important to emphasize that this nonuniqueness problem is due only to an *unlucky* combination of the radius R_V and the wave number. Assuming that the operating frequency is given, only the size of the control region V is *responsible* for this problem. These relevant considerations are in perfect agreement with the results presented in Section 5.5.

As an example, we assume that the target field, generated by a monopole source in $\mathbf{q}$, is measured on the sphere ∂V with radius R_V such that $j_0(kR_V) = 0$ ($k = 4$ rad/m, $\mathrm{R_V} = 0.7854$ m). This arrangement is illustrated in Figure 5.7. The pressure profile is given by the usual expansion (5.18). We observe that the first term of the series, $\nu = 0$, equals zero: this implies that the function $Y_0^0(\mathbf{y}),\ \mathbf{y} \in \partial\Lambda$ is in the nullspace of S, and is not one of its singular functions. Figure 5.8 shows the field (amplified by a factor 4 for better

visualization) given only by the term $\nu = 0$ of series (5.18), that is

$$p_0(\mathbf{z}) = ikh_0(kq)j_0(kz)Y_0^0(\hat{\mathbf{x}})Y_0^0(\hat{\mathbf{q}})^*, \quad \mathbf{z} \in \mathbb{R}^3,\ z < q \tag{5.39}$$

It can be noticed that ∂V corresponds to a nodal surface of the field, namely $p_0(\mathbf{x}) = 0,\ \mathbf{x} \in \partial V$. Nevertheless $p_0(\mathbf{z}) \neq 0$ in most of the other locations in Λ. A solution $a(\mathbf{y})$ is computed from equation (4.19) (truncated to the order $N = 7$). Clearly, the series does not include the first term. The orthogonal projections $\langle p_n|p\rangle_{\partial V}$ have been computed via numerical integration on the sphere V. The latter is performed as described in Chapter 7. V is divided into 144 Dirichlet cells, following the sampling scheme proposed by Fliege [Fli], [FM96]. The field $(Sa)(\mathbf{z})$ and the normalized reproduction error are shown in figures 5.9 and 5.10, respectively. Not surprisingly, the error approaches zero in the vicinity of ∂V, but it is large in the rest of Λ.

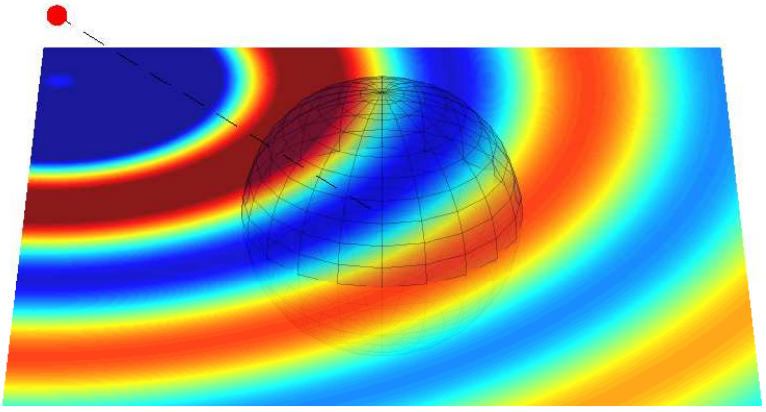

FIGURE 5.7: Horizontal cross-section of the field generated by an omnidirectional point source (red dot) located at $[r_q, \theta_q, \phi_q] = [2.5\text{ m}, 80°, 140°]$. The sphere represents the control boundary ∂V. The wave number is $k = 4$ rad/m and the radius of the sphere is $R_V = 0.7854$ m.

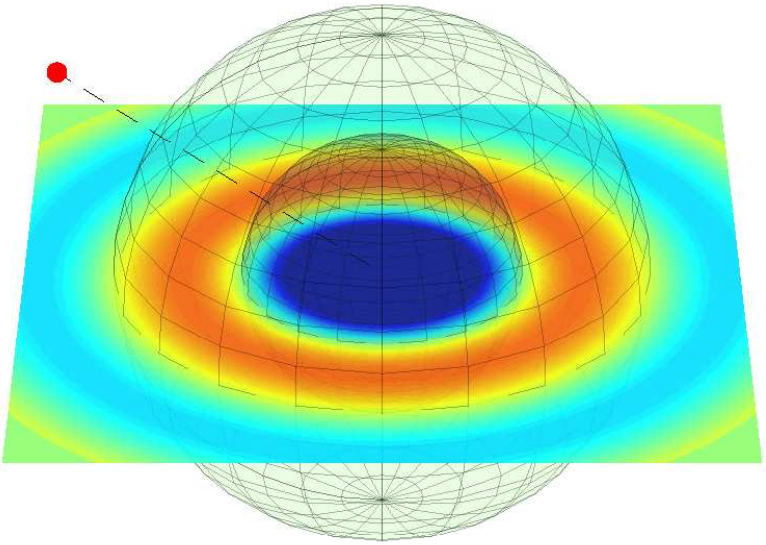

FIGURE 5.8: Horizontal cross-section of the field $(SY_0^0)(\mathbf{z})$. The two spheres represent the control boundary ∂V (smaller sphere) and the secondary source layer $\partial\Lambda$. The wave number is $k = 4$ rad/m and the radii of the spheres are $R_V = 0.7854$ m and $R_\Lambda = 1.5$ m, respectively.

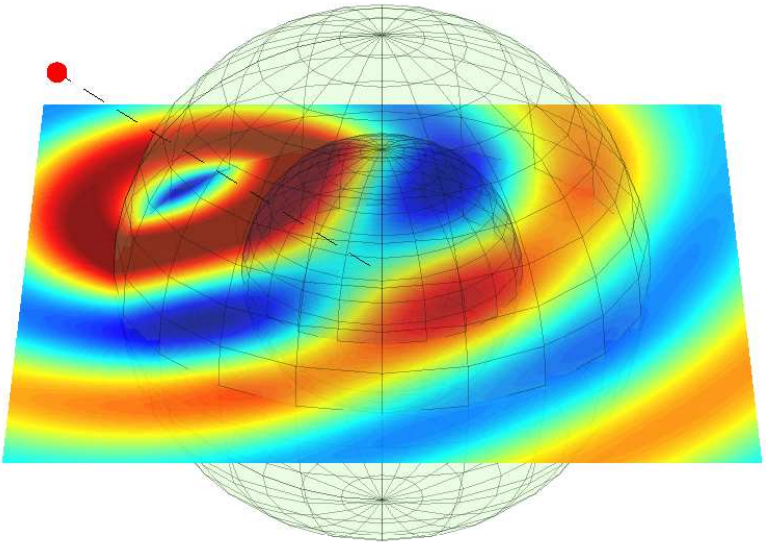

FIGURE 5.9: Horizontal cross-section of the reproduced field for a virtual source located at $[r_q, \theta_q, \phi_q] = [2.5\text{ m}, 80°, 140°]$. The density $a(\mathbf{y})$ was computed with series (4.19), without the terms with $\nu = 0$. The two spheres represent the control boundary ∂V (smaller sphere) and the secondary source layer $\partial\Lambda$. The wave number is $k = 4$ rad/m and the radii of the spheres are $R_V = 0.7854$ m and $R_\Lambda = 1.5$ m, respectively.

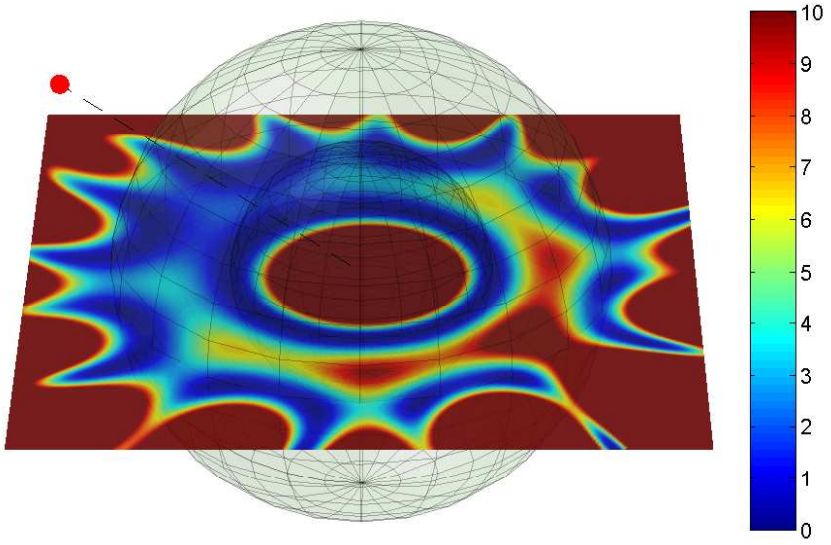

FIGURE 5.10: Horizontal cross-section of normalized reproduction error (%) for a virtual source (red dot) located at $[r_q, \theta_q, \phi_q] = [2.5\text{ m}, 80°, 140°]$. For better visualization, the color scale is clipped at 10% and is different from that used in Figure 5.4. The two spheres represent the control boundary ∂V (smaller sphere) and the secondary source layer $\partial\Lambda$. The wave number is $k = 4$ rad/m and the radii of the spheres are $R_V = 0.7854$ m and $R_\Lambda = 1.5$ m, respectively.

5.6.2 Line source and parallel line arrangement

The case is now considered when the secondary sources are arranged on an infinite line $\partial\Lambda \in \mathbb{R}^2$, as shown in Figure 4.22, and it is assumed that the virtual source is a line source with unitary amplitude, located at $\mathbf{q} = [q_1,\ 0,\ q_3]$ and perpendicular to the plane identified by $\partial\Lambda$ and ∂V, as shown in Figure 5.13. The pressure profile due to a line source is described by equation (3.7). This equation can be expressed in the following form, analogous to equation (4.93):

$$p(\mathbf{x}) = \frac{i}{4} H_0^{(1)}(k|\mathbf{x} - \mathbf{q}|) = \int_{\mathbb{R}} \frac{e^{i\kappa(x_1 - q_1)}}{2\pi} \frac{i e^{i\zeta(\kappa) d_0}}{2\zeta(\kappa)} d\kappa, \quad \mathbf{x} \in \partial V \tag{5.40}$$

where d_0 is the distance between $\mathbf{q}$ and the line ∂V. As discussed in Chapter 4, the expression above gives the representation of the field due to a line source by means of propagating and evanescent plane waves. In this case, the operator S is not a compact operator, as Λ and V are unbounded domains. We can not therefore apply the criteria introduced in this chapter for solving the integral equation considered. We can however provide an expression for the solution in the form of equation (4.102), and then discuss

this result. We firstly recall the following expressions from Section 4.4:

$$\begin{aligned} a(\mathbf{y}) &= \mathcal{F}^{-1}\left[\frac{(\mathcal{F}p)}{\sigma_\kappa \gamma_\kappa}\right](\mathbf{y}) \\ \sigma_\kappa \gamma_\kappa &= \frac{i e^{i\zeta(\kappa)d}}{2\zeta(\kappa)} \\ \zeta(\kappa) &= \sqrt{k^2 - \kappa^2} \end{aligned}$$

It can be observed that, in view of the orthogonality relation (2.76) and of the property of the Dirac delta function (2.26), the following equation holds:

$$(\mathcal{F}p)(\kappa) = \frac{i e^{i\zeta(\kappa)d_0}}{2\zeta(\kappa)} \frac{e^{-i\kappa q_1}}{\sqrt{2\pi}} \tag{5.41}$$

Inserting this result into the expressions for $a(\mathbf{y})$ and $\sigma_\kappa \gamma_\kappa$ given above, and considering that $d_0 - d = -q_3$, we obtain

$$a(\mathbf{y}) = \left[\mathcal{F}^{-1}\left(\frac{e^{i[-\zeta(\kappa)q_3 - \kappa q_1]}}{\sqrt{2\pi}}\right)\right](\mathbf{y}) \tag{5.42}$$

This solution can be expressed explicitly as follows

$$a(\mathbf{y}) = \int_{\mathbb{R}} e^{-i\zeta(\kappa)q_3} \frac{e^{i\kappa(y_1 - q_1)}}{2\pi} d\kappa \tag{5.43}$$

As for the case of the spherical geometry, the solution does not depend on the control boundary ∂V, since $a(\mathbf{y})$ has been computed from the analytical expression of the target field.

Alternatively, the solution can be computed using a convolution approach, and defining the spatial filter

$$\Xi(\kappa) := e^{i\zeta(\kappa)(d_0 - d)} \tag{5.44}$$

$$\tag{5.45}$$

one obtains

$$a(\mathbf{y}) = (\mathcal{F}^{-1}\Xi)(\mathbf{y}) \otimes \frac{\delta(y_1 - q_1)}{\sqrt{2\pi}} \tag{5.46}$$

The spatial filter $\Xi(\kappa)$ is a complex exponential with unitary absolute value for $|\kappa| < k$ and is an exponential with real argument when $|\kappa| > k$. If $d_0 > d$, that is if the virtual source is more distant from ∂V than $\partial \Lambda$, then the spatial filter decays exponentially with increasing κ. Conversely $\Xi(\kappa)$ increases exponentially if $d_0 < d$. In the limiting case when $d_0 = d$, we have that $\Xi(\kappa) = 1$ and $a(\mathbf{y}) = \delta(y_1 - q_1)$.

Figure 5.11 shows the absolute value and the phase of the spatial filter $\Xi(\kappa)$ for different values of $d_0 - d = -q_3$ and $k = 1$ rad/m. It can be observed that, as discussed in section 4.3.1, the values for $|\kappa/k| < 1$ corresponds to propagating plane waves (in two dimensions), characterized by zero magnitude and non-zero phase. Conversely, the values for $|\kappa/k| > 1$ correspond to evanescent waves, with zero phase and exponentially decreasing magnitude.

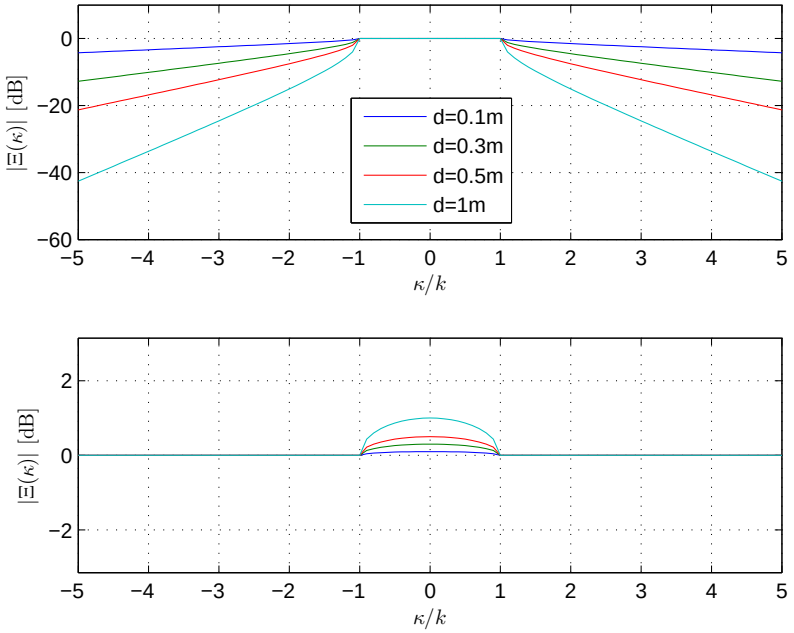

FIGURE 5.11: Magnitude and phase of the spatial filter $\Xi(\kappa)$ (linear geometry), for different values of $-q_3 = d_0 - d$

Figure 5.11 shows a plot of magnitude and phase of $a(\mathbf{y})$, computed with equation (5.43) for different values of $d_0 - d = -q_3$ and $k = 1$ rad/m. The integration was performed $-100k < \kappa < 100k$ and $d\kappa = 0.1k$.

What has been shown here is analogous to the case of the spherical geometry discussed above. In fact, the source strength function can be interpreted as a spatially filtered Dirac delta function. If $d_0 > d$, the spatial spectrum of the solution $a(\mathbf{y})$ exhibits the decay imposed by the exponentially decaying spatial filter $\Xi(\kappa)$. Henceforth, $a(\mathbf{y})$ is smoother the further away the virtual source is from $\partial\Lambda$ and its main lobe gets broader. If $\mathbf{q} \in \partial\Lambda$, then $a(\mathbf{y})$ corresponds to a Dirac delta function and its spatial spectrum is flat. If $d_0 < d$, that is if $\mathbf{q} \in \Lambda \backslash \overline{V}$, the spatial filter $\Xi(\kappa)$ increases exponentially with κ, thus leading to a divergent solution. It can be therefore deduced, that the inverse problem addressed is not solvable for $d_0 < d$.

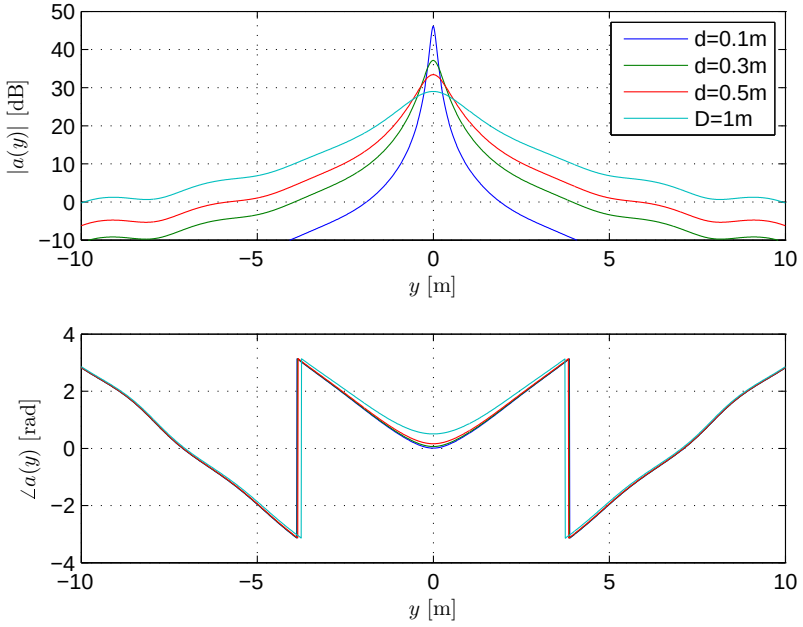

FIGURE 5.12: Magnitude and phase of the density $a(\mathbf{y})$ (linear geometry) for different values of $-q_3 = d_0 - d$

In view of the orthogonality relation (2.76) and of the property of the Dirac delta function (2.26) we can observe that

$$\begin{aligned} \langle a_\kappa | a \rangle_{\partial\Lambda} &= \int_{\partial\Lambda} \frac{1}{\sqrt{2\pi}} e^{-i\kappa y_1} \int_{\mathbb{R}} e^{i\zeta(\kappa')(d_0-d)} \frac{e^{i\kappa'(y_1-q_1)}}{2\pi} d\kappa' \, dy_1 \\ &= \int_{\mathbb{R}} e^{i\zeta(\kappa')(d_0-d)} \frac{e^{-i\kappa' q_1}}{\sqrt{2\pi}} \left(\int_{\partial\Lambda} \frac{1}{2\pi} e^{i(\kappa'-\kappa)y_1} dy_1 \right) d\kappa' \\ &= e^{i\zeta(\kappa)(d_0-d)} \frac{e^{-i\kappa q_1}}{\sqrt{2\pi}} \end{aligned} \tag{5.47}$$

Substituting this result into the expression (4.98) for the operator S, we obtain

$$\begin{aligned} (Sa)(\mathbf{x}) &= \int_{\mathbb{R}} \sigma_\kappa p_\kappa(\mathbf{x}) \langle a_\kappa | a \rangle_{\partial\Lambda} d\kappa = \int_{\mathbb{R}} \sigma_\kappa p_\kappa(\mathbf{x}) e^{i\zeta(\kappa)(d_0-d)} \frac{e^{-i\kappa q_1}}{\sqrt{2\pi}} \\ &= \int_{\mathbb{R}} \frac{i e^{i\zeta(\kappa) d_0}}{2\zeta(\kappa)} \frac{e^{i\kappa(x_1-q_1)}}{2\pi} = \frac{i}{4} H_0^{(1)}(k|\mathbf{x}-\mathbf{q}|), \quad \mathbf{x} \in \partial V \end{aligned} \tag{5.48}$$

where the last equality follows from equation (4.93). This shows that the expression (5.43) for $a(\mathbf{y})$ gives the correct solution of the inverse problem under consideration. This equation can be extended to any $\mathbf{z} \in \mathbb{R}^2$ by simply substituting $d_0 = x_3 - q_3$ with $|z_3| - q_3$.

Figure 5.13 shows the field due to a line source located at $[q_1, q_3] = [\,0\text{ m}, -0.5\text{ m}]$. The wave number is $k = 10\,\text{rad/m}$. Figure 5.14 shows the reproduced field for a virtual source at eh same location, with secondary sources continuously arranged on the infinite

line $\partial\Lambda$. The field has been computed using the definition of single layer potential (3.15) with the 2D kernel (3.7). The infinite line has been approximated by a 20 m long segment (the plotting area is 16 m^2), discretized into 128 secondary sources with 0.1571 m spacing. The source strength $a(\mathbf{y})$ has been computed by applying equation (5.43). The integral over $\mathbb{R}$ has been approximated by a finite integral from $\kappa = 10k$ to $\kappa = -10k$, and computed using a quadrature with uniform sampling with $(d\kappa = 0.01k$. Figure 5.15 reports a plot of the normalized reproduction error $\epsilon_N(\mathbf{z})$ (%), defined by equation (5.31). It can be observed that the reproduced field is symmetric with respect to $\partial\Lambda$, and that it reproduced perfectly (apart from approximation errors) the target pressure profile in the entire Λ.

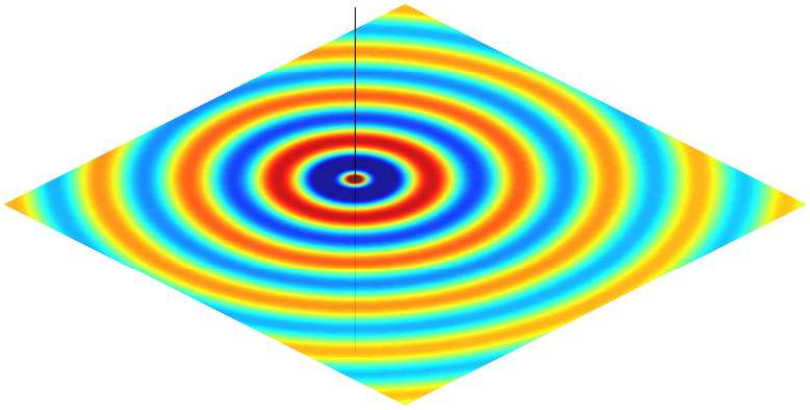

FIGURE 5.13: Pressure field generated by a line source (vertical black line) located at $[q_1, q_3] = [\ 0\ \text{m}, -0.5\ \text{m}]$. The wave number is $k = 10$ rad/m

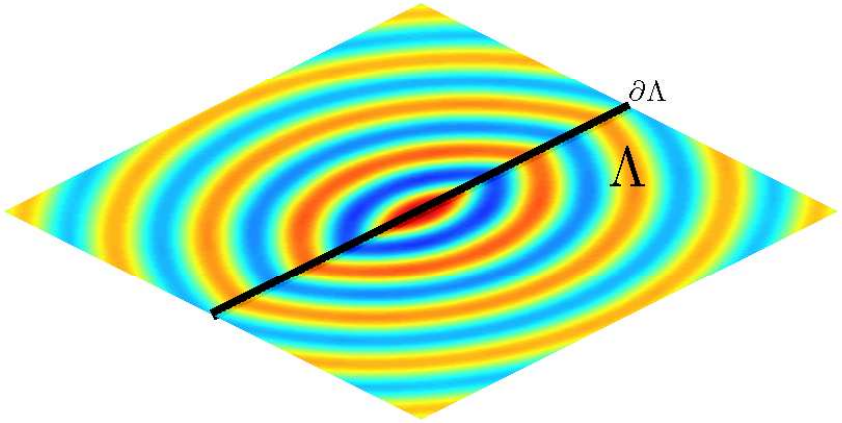

FIGURE 5.14: Reproduced field for a virtual source located at $[q_1, q_3] = [\ 0\ \text{m}, -0.5\ \text{m}]$. The wave number is $k = 10$ rad/m

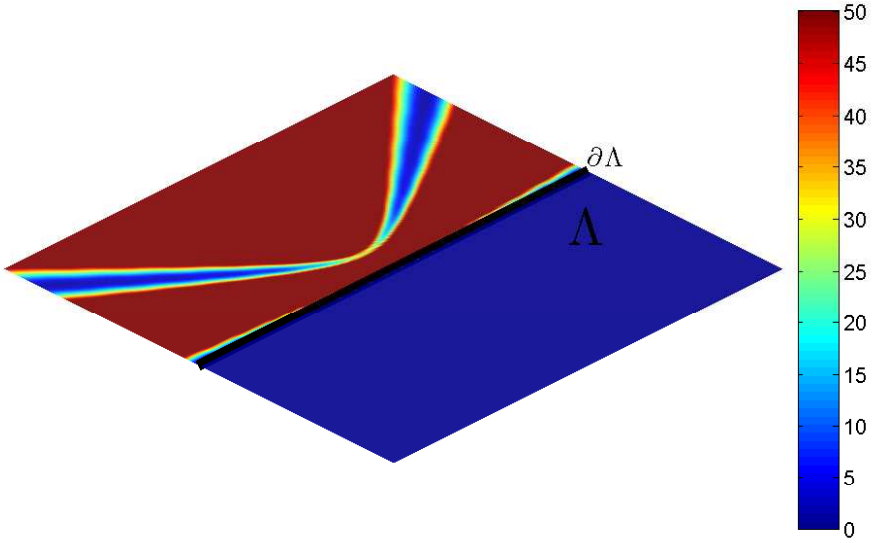

FIGURE 5.15: Normalized reproduction error (%) for a virtual source located at $[q_1, q_3] = [\ 0\ \text{m}, -0.5\ \text{m}]$. The wave number is $k = 10$ rad/m

5.7 Summary of parameters affecting the ill-posedness of the problem

The ill-posedness of the inverse problem given by the integral equation (3.19) is a mathematical property of the operator S and of the normed spaces between which it is acting (here $L^2(\partial\Lambda)$ and Ψ_V), and represents a sever barrier to the determination of a sensible solution. We have seen that the effect of the three different types of ill-posedness arises for different typologies of sound fields to be reproduced and of the geometrical arrangement of the problem. More precisely, we have shown that:

- when the desired sound field is given by a virtual source located in the region $\Lambda\backslash V$, in the exterior of the control region but within the reproduction area, an exact and bounded solution $a(\mathbf{y})$ does not exist (nonexistence);
- when the operating frequency of the desired sound field corresponds to one of those identified by k_n, the Dirichlet eigenvalues of V, the solution of the inverse problem is not unique, but only one of the solutions allows an accurate reproduction in the *interior* of V (nonuniqueness);
- if the data describing the target field are contaminated by errors, these might severely compromise the determination of an accurate solution of the inverse problem, leading to very large errors in the reproduced field (instability).

It is important to emphasize the fact that these effects of ill-posedness of the inverse problem depend mainly on the relation between the sound field to be reproduced *and* the sets Λ and V.

The theorems proving the existence of the solution can be simply reformulated by the following intuitive proposition:

A sound field due to a virtual source in the exterior of the reproduction area Λ can be perfectly reproduced by an array with an infinite number of secondary sources, independently of the operating frequency ω

or equivalently, the sound field can be represented by the single layer potential (3.15) in Λ. This implies that the feasibility of the field reproduction depends only on the geometry of the array and on the location of the virtual source, but it does not depend on the geometry of the control region V. This is confirmed by the analytical expressions (5.30) and (5.43) of the secondary source strength $a(\mathbf{y})$ for a monopole-like virtual source. These expressions do not include any reference to the control region. In other words, if we have complete knowledge of the target sound field, the latter can be reproduced under the condition above.

A different matter is the determination of the strength of the secondary sources $a(\mathbf{y})$, provided that we are sure of its existence. When the target pressure profile is described by data, this process is strongly dependent on the geometry of the control region V and on its location in respect to Λ. We have seen in Section 4 that the asymptotic exponential decay of the singular values of the integral operator S, responsible of the amplification of errors, is controlled by the distance between the boundaries $\partial\Lambda$ and ∂V, for all geometrical arrangements considered. This is analogous to a Near-Field Acoustical Holography problem, as we need to *back-propagate* the sound field from V to $\partial\Lambda$. In the limiting case when $V = \Lambda$, the problem is mildly ill-posed (the linear decay of the singular values is due to an operation of derivation).

We have also seen in Section 5.4 that the problem of ill-conditioning is related to the presence of large amount of energy in the high order components of the Fourier series $\langle p_n|p\rangle_{\partial V}$ representing the pressure profile. In view of the results presented in Section 5.6, we see that the effect of ill-conditioning on the reproduction side is larger, the closer the virtual source is to Λ (the best case, in that sense, is represented by a plane wave).

The considerations above can be summarized by the following proposition:

The stability of the solution is governed by the distance between the boundaries ∂V and $\partial\Lambda$ and by the decay of the Fourier coefficients $\langle p_n|p\rangle_{\partial V}$ representing the pressure profile.

In Section 5.5 it has been shown that the uniqueness of the solution is determined by the Dirichlet eigenvalues k_n of V (hence the solution is unique for unbounded V), and not by the Neumann or Dirichlet eigenvalues of Λ. Therefore it can be stated that

The nonuniqueness of the solution depends only on the geometry of the control region V and on the operating frequency ω. The problem arises only for bounded control regions and at an infinite but countable number of frequencies.

In the cases considered in Section 5.6, we have seen that when the solution can be computed analytically from the explicit expression of the target field, the nonuniqueness problem does not arise. In these circumstances, the parameters related to the control region V are not included in the expression of the solution. Henceforth its stability does not depend on V.

Chapter 6

Methods for dealing with the ill-posedness

In the previous chapter, the ill-posedness of the inverse problem represented by the integral equation (3.19) has been thoroughly studied. This analysis has clarified that, although an exact solution exists for the majority of the cases of interest, the solution of the inverse problem can be severely affected by the problem of ill-conditioning and can be therefore unstable.

We have also seen that there is a category of sound field of practical interest, for which an exact solution does not exist. This is the case for sound fields generated by a source located within the reproduction region. A virtual source lying within this region is usually referred as a *focused sources* [AS08c], [Men09].

In all of these circumstances, it is possible to use some strategies to minimize the effect of the problems described above (instability and nonexistence), at the price of achieving an approximate reproduction of the desired field. These strategies usually include the modification of the operator S or of the target field (these operation provide in many cases equivalent results). More specifically, some actions are undertaken in order to avoid or limit the attempt to reproduce those modes $p_n(\mathbf{x})$ of the pressure profile, which are related to small singular values σ_n. These high order modes have been shown to be responsible for both the problem of nonexistence and of instability. The first part of this chapter introduces these strategies, many of which are well known regularization methods. Their application is discussed in relation to the sound field reproduction problem addressed here, concentrating initially on the problem of instability and then on that of nonuniqueness and focused sources. Examples are provided for different geometries of secondary source layer.

The second part of this chapter is focussed on a remarkable analogy, which links the problem of sound field reproduction to an equivalent acoustic scattering problem. This

analogy arises from the specific circumstance, in which the control and reproduction region coincide ($V = \Lambda$). This case has been demonstrated in the previous chapters to correspond to a mildly ill-posed problem. The solution of the equivalent scattering problem defines an alternative method, although equivalent, for computing a solution to the field reproduction problem, reducing at the same time the potential effect of ill-conditioning to its minimum (hence the motivation for including this subject in this chapter). The relevant analogy to Near-Field Acoustical Holography, which we have begun to draw in the course of the previous chapters, is also discussed here.

6.1 Regularization methods

We have seen in Section 5.4 that the reason for the ill-conditioning of the inverse problem addressed is mathematically represented by the inversion of very small singular values, which correspond to non-efficient array modes and which determine the amplification of errors in the data. One might therefore arbitrarily decide non to attempt the reproduction of these low-efficiency pressure modes. This choice might on one hand degrade the accuracy of the reproduced field for an ideal error-free case, but on the other hand it makes the solution robust with respect to the effect of data errors.

The strategy discussed above is mathematically described by the *spectral cut-off* of the operator S. This technique corresponds to the truncation of the series (3.28), giving an expression for the solution, to a given order N. The approximate solution $\tilde{a}_{s.t.}(\mathbf{y})$ is therefore given by

$$\tilde{a}_{s.t.}(\mathbf{y}) = \sum_{n=1}^{N} a_n(\mathbf{y}) \frac{1}{\sigma_n} \langle p_n | p \rangle_{\partial V} \tag{6.1}$$

It is recalled that the singular values are ordered with decreasing magnitude. The smaller singular values are therefore excluded from the computation of the series above, thus avoiding the error amplification associated with their inversion.

The spectral cut-off is one of the regularization schemes that are often used in the solution of inverse problems. This technique is to some extent applied automatically when the computation of the series is performed numerically (as its order must be finite), and is often adopted as a consequence of the discretization of the single layer potential into an array including a finite number of secondary sources. In fact, as will be discussed in Section 7.1, it is reasonable (although not mandatory) to truncate the series to an order N which is less or equal to the number of secondary sources included in the array.

We have seen that the inversion of the small singular values might be responsible for large values of $||a(\mathbf{y})||$ (related to the acoustic energy generated by the secondary sources), as a consequence of the attempt to reproduce low efficiency modes. The spectral cut-off, as well as other regularization methods, has therefore the effect of reducing the total

acoustic energy generated by the array. This is obviously beneficial with respect to the robustness of the system and to its performance in non-anechoic environments.

The sharp spectral cut-off described above could be smoothed by applying to the singular values of S a tapering window w_n , such as

$$w_n = \begin{cases} 1, & n \leq N \\ a_n, & N < n < N + N' \\ 0, & n \geq N + N' \end{cases} \tag{6.2}$$

where a_n is a monotonically decreasing sequence with $0 < a_n < 1$ and N' is an arbitrary integer. Clearly the case of $a_n = 0$ corresponds to the sharp spectral cut-off described above. The series (3.28) could be therefore approximated by

$$\tilde{a}_{s.d.}(\mathbf{y}) = \sum_{n=1}^{\infty} a_n(\mathbf{y}) \frac{w_n}{\sigma_n} \langle p_n | p \rangle_{\partial V} \tag{6.3}$$

The tapering window above is one of the many possible choices. Different kind of windows and their properties have been widely studied (see for example [CBG10, p.281-303] and [Har78]). In the case of spherical geometry, this smooth damping technique corresponds in some measure to the different decoding criteria for High Order Ambisonics (such as the *Max* r_E or the *In-phase* criterion), although the derivation is very different. As shown for example in [DRP98], these criteria include the use of weights applied to the encoded signals, in a similar fashion to the weights w_n that might be applied to the Fourier coefficients $\langle p_n | p \rangle$.

The spectral cut-off and damping techniques introduced above are two of the various regularization techniques, which are extensively discussed in the scientific literature. A very good tutorial explanation of the link between the mathematical and physical meaning of the regularization is given by Deschamp and Cabayan in [DC72].

We mention here what is probably the most widely used regularization technique, known as *Tikhonov regularization* (see, for example, [KNHOB98], [CK92] and [DC72]), named after the Russian mathematician Andrey N. Tikhonov. This method can be explained with respect to the reformulation of the inverse problem in terms of the minimization of the following function:

$$||Sa - p||^2 + \beta ||a||^2 \tag{6.4}$$

where β is referred to as the regularization parameter. This approach attempts to minimize the L^2 distance $||Sa - p||$ between the target and reproduced field, requiring at the same time the solution $a(\mathbf{y})$ to have a small norm. This will in turn have a bounding effect on the inversion of the singular values. In fact, the solution of the minimization

problem leads to the following modification of series (3.28) [CK92]:

$$\tilde{a}_{T.}(\mathbf{y}) = \sum_{n=1}^{\infty} a_n(\mathbf{y}) \frac{\sigma_n}{\beta + \sigma_n^2} \langle p_n | p \rangle_{\partial V} \tag{6.5}$$

Instead of completely avoiding the reproduction of the low efficiency modes, as in the case of the spectral cut-off, a reduced energy version of the latter is generated by the array. The Tikhonov regularization technique has the disadvantage of affecting the reproduction of all pressure modes, as the regularization parameter β is added to all singular values. However, if the choice of β is made wisely, the effect of the regularization parameter on the reproduction of the high efficiency modes is negligible.

The regularization techniques described here can be used in order to reduce the effect of ill-conditioning, by finding an approximate solution, which is more stable and robust with respect to errors and noise, even though an exact solution might exist in ideal error-free conditions.

Figure 6.1 shows the horizontal cross-section of the sound field due to an acoustic monopole located at $[r_q, \theta_q, \phi_q] = [2.5\text{ m}, 80°, 140°]$ and with $k = 6$ rad/m. The field is virtually measured on $\partial\Lambda$, a sphere of radius $R_V = 0.5$ m. The measured values have been perturbed with uncorrelated noise, with mean magnitude equal to 10% of the maximum of the magnitudes of the measured values. A solution $a(\mathbf{y})$ of the inverse problem has been computed by applying equation 4.19 (the series is truncated to the order $N = 10$). The orthogonal projections $\langle p_n | p \rangle_{\partial V}$ have been computed as described in sections 5.6.1.4 and 7.1.2 (V is uniformly sampled at 144 locations [Fli], [FM96] and the integral is solved numerically using a quadrature method). Figures 6.2 and 6.3 represent the reproduced field and the normalized reproduction error defined by (5.31). The secondary source layer is represented by the larger sphere, having a radius $R_\Lambda = 1.5$ m. It can be observed that the secondary sources generate a large amount of acoustic energy, and their fields interfere mainly destructively in order to reproduce the target field, which is accurate only in the vicinity of the center of the array.

A second solution was computed applying the Tikhonov regularization scheme, described by equation (6.5). The regularization parameter chosen is $\beta = 10^{-5} \approx 10^{-4}\sigma_1$. The reproduced field generated by the regularized solution and the related normalized reproduction error are shown in Figure 6.4 and Figure 6.5, respectively. As a consequence of the regularization, the effect of ill-conditioning has been reduced: not only has the region characterized by a small reproduction error become larger, but also the acoustic energy generated by the secondary sources and the amplitude of the field in the exterior of Λ are much smaller when compared to the non-regularized case.

As discussed in Section 6.2, a regularization scheme may be used also for finding an approximate reproduction of a sound field, for which an exact solution does not exist.

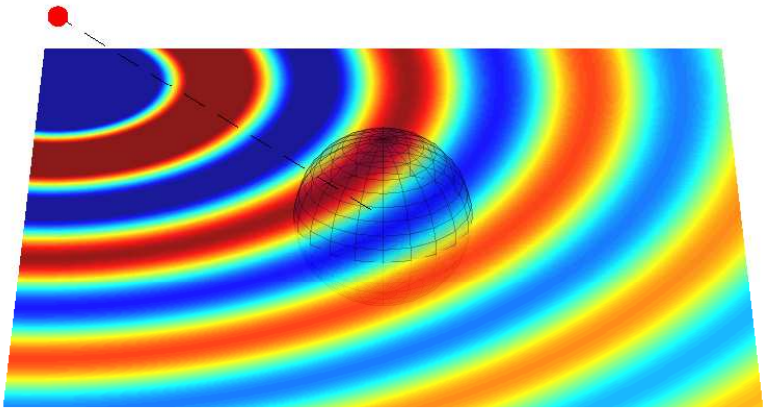

FIGURE 6.1: Horizontal cross-section of the field generated by an omnidirectional point source (red dot) located at $[r_q, \theta_q, \phi_q] = [2.5\text{ m}, 80°, 140°]$. The sphere represents the control boundary ∂V.

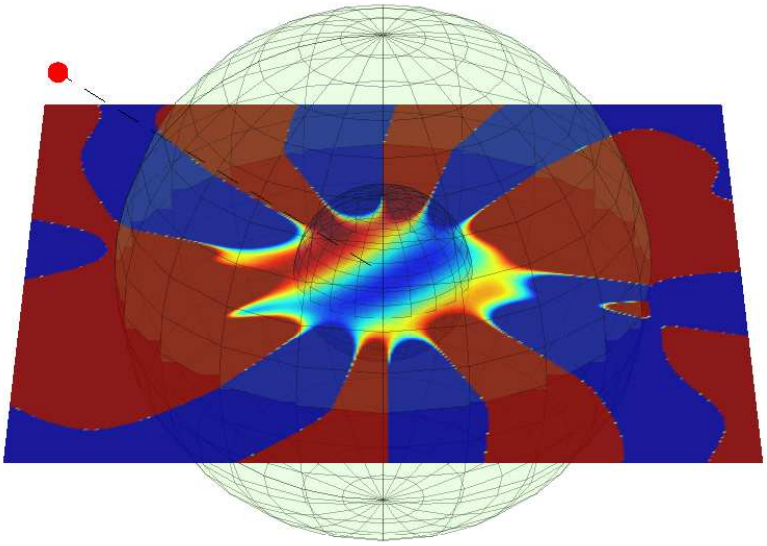

FIGURE 6.2: Horizontal cross-section of the reproduced field for a virtual source located at $[r_q, \theta_q, \phi_q] = [2.5\text{ m}, 80°, 140°]$. The density $a(\mathbf{y})$ was computed with series (4.19), without applying any regularization. The two spheres represent the control boundary ∂V (smaller sphere) and the secondary source layer $\partial\Lambda$.

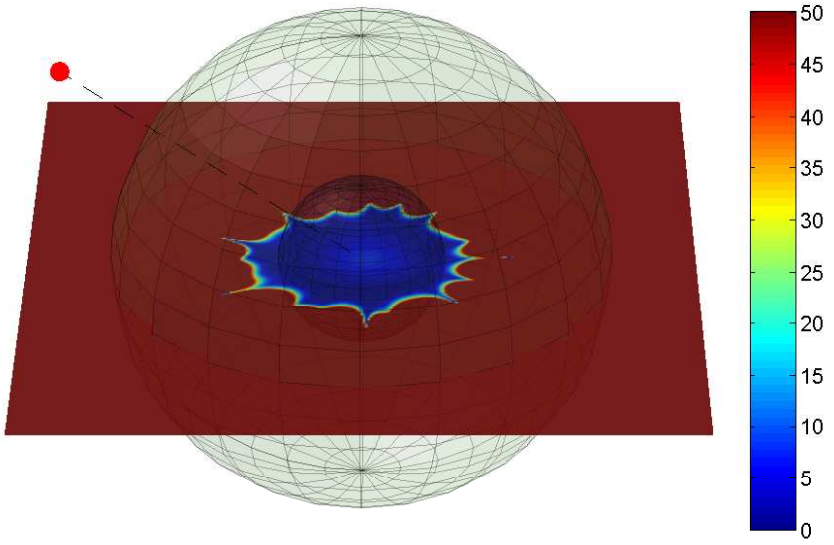

FIGURE 6.3: Horizontal cross-section of normalized reproduction error (%) for a virtual source located at $[r_q, \theta_q, \phi_q] = [2.5\text{ m}, 80°, 140°]$, and for a non-regularized solution. The two spheres represent the control boundary ∂V (smaller sphere) and the secondary source layer $\partial\Lambda$.

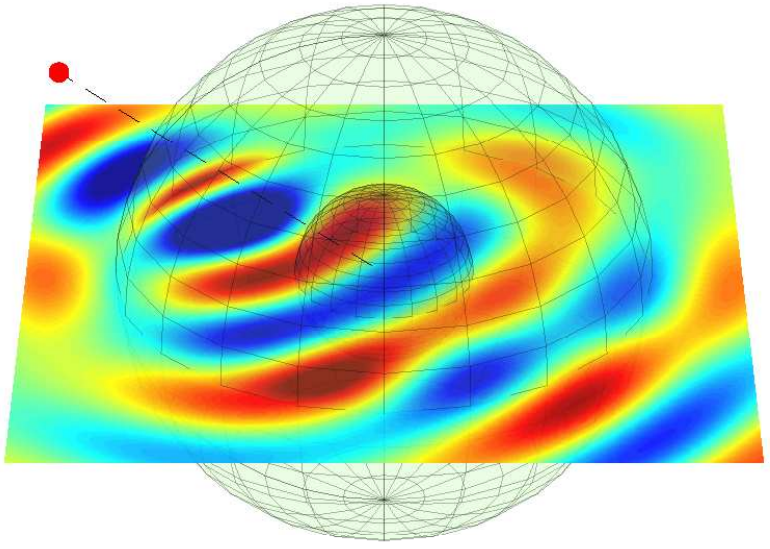

FIGURE 6.4: Horizontal cross-section of the reproduced field for a virtual source located at $[r_q, \theta_q, \phi_q] = [2.5\text{ m}, 80°, 140°]$. The density $a(\mathbf{y})$ was computed applying the Tikhonov regularization,equation (6.5), with $\beta = 10^{-5}$. The two spheres represent the control boundary ∂V (smaller sphere) and the secondary source layer $\partial\Lambda$.

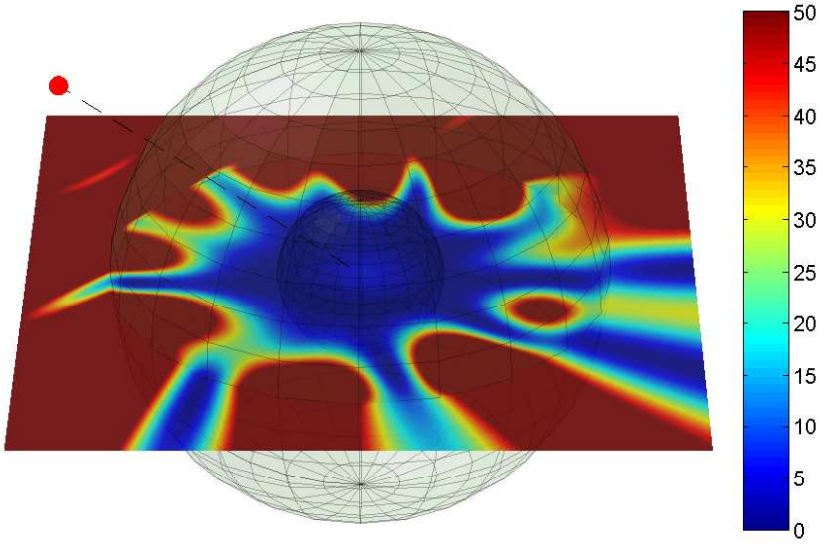

FIGURE 6.5: Horizontal cross-section of normalized reproduction error (%) for a virtual source (red dot) located at $[r_q, \theta_q, \phi_q] = [2.5\text{ m}, 80°, 140°]$, and regularized solution. The two spheres represent the control boundary ∂V (smaller sphere) and the secondary source layer $\partial\Lambda$.

6.2 Focused sources

The inverse problem (3.19) involving the reproduction of a sound field due to a virtual source located within the reproduction region has been proven not to have a solution. It is however possible to come to a compromise and attempt an approximate reproduction. This objective can be achieved in different ways, some of which are illustrated in what follows. Although the strategies presented can be regarded as regularization schemes, they are not applied directly to the operator and to its singular values, but rather act on the target sound field, transforming it into a similar field, for which a solution of the inverse problem exists.

As previously mentioned, the (approximate) reproduction of the field due to a virtual source located within the reproduction region is referred to as *focused source* in the literature on Wave Field Synthesis [AS08c].

In Section 5.3 it has been shown that the nonexistence of the solution is related to the decay of the Fourier coefficients $\langle p_n | p \rangle_{\partial V}$, which must be steeper than the decay of the singular values σ_n. When this is not the case, the series (3.28) diverges. An intuitive strategy to prevent this happening is to truncate or damp the series, as illustrated by the regularization techniques discussed in the previous section.

With reference to equations (6.1), (6.2) and (6.3), we see that the reproduced sound field is given by

$$\tilde{p}_{s.d.}(\mathbf{x}) = \sum_{n=1}^{\infty} w_n p_n(\mathbf{x}) \langle p_n | p \rangle_{\partial V} \tag{6.6}$$

and the reproduction error on ∂V (not necessarily in its interior) is therefore

$$\epsilon_{s.d.}(\mathbf{x}) = \sum_{n=1}^{\infty} (1 - w_n) p_n(\mathbf{x}) \langle p_n | p \rangle_{\partial V} \tag{6.7}$$

which becomes, in the special case of sharp spectral cut-off ($w_n = 1$ if $n \leq N$ and $w_n = 0$ if $n > N$)

$$\epsilon_{s.t.}(\mathbf{x}) = \sum_{n=N+1}^{\infty} p_n(\mathbf{x}) \langle p_n | p \rangle_{\partial V} \tag{6.8}$$

It is now shown how these and other related strategies can be applied to some of the specific geometrical arrangements introduced in the previous chapters.

6.2.1 Parallel line geometry

We consider the extension of the spectral damping method to the case of linear unbounded domains Λ and V, as described in Sections 4.4. Analogous conclusions can be drawn for the case of planar geometrical arrangement described in Section 4.3. For simplicity, we report here equations (4.56), (4.98) (extended to $\mathbb{R}^2$) and (5.43) representing, for the linear geometry, the function σ_κ (analogous to the singular values for S compact), the representation of S and the expression of the solution for a virtual point source. These are respectively given by

$$\sigma_\kappa = \frac{e^{-\mathrm{Im}(\zeta(\kappa))d}}{2|\zeta(\kappa)|} \tag{6.9}$$

$$(Sa)(\mathbf{z}) = \frac{i}{2\pi} \int_{\mathbb{R}} \frac{e^{i\zeta(\kappa)|z_3|}}{2\zeta(\kappa)} e^{i\kappa z_1} \langle e^{i\kappa} | a \rangle_{\partial\Lambda} d\kappa, \ \mathbf{z} \in \mathbb{R}^2 \tag{6.10}$$

$$a(\mathbf{y}) = \int_{\mathbb{R}} e^{-i\zeta(\kappa)q_3} \frac{e^{i\kappa(y_1 - q_1)}}{2\pi} d\kappa \tag{6.11}$$

The integral (6.10), evaluated at $\mathbf{z} = \mathbf{x} \in \partial V$, can be split into one part, $S_{prop.}$, representing a superposition of propagating waves ($|\kappa|/k \leq 1$ and $\mathrm{Im}(\zeta(\kappa)) = 0$), and a second part, $S_{evan.}$,representing a superposition of evanescent waves ($|\kappa|/k > 1$ and

$\mathrm{Re}(\zeta(\kappa)) = 0$). This concept is expressed by the following relations:

$$
\begin{aligned}
(Sa)(\mathbf{x}) &= (S_{prop.}a)(\mathbf{x}) + (S_{evan.}a)(\mathbf{x}) && (6.12)\\
(S_{prop.}a)(\mathbf{x}) &:= \frac{i}{2\pi}\int_{-k}^{k} \frac{e^{i|\zeta(\kappa)|d}}{2|\zeta(\kappa)|} e^{i\kappa x_1} \langle e^{i\kappa}|a\rangle_{\partial\Lambda} d\kappa && (6.13)\\
(S_{evan.}a)(\mathbf{x}) &:= \frac{1}{2\pi}\int_{k}^{\infty} \frac{e^{-|\zeta(\kappa)|d}}{2|\zeta(\kappa)|} e^{i\kappa x_1} \langle e^{i\kappa}|a\rangle_{\partial\Lambda} d\kappa && (6.14)\\
&+ \frac{1}{2\pi}\int_{-\infty}^{-k} \frac{e^{-|\zeta(\kappa)|d}}{2|\zeta(\kappa)|} e^{i\kappa x_1} \langle e^{i\kappa}|a\rangle_{\partial\Lambda} d\kappa
\end{aligned}
$$

Considering the results and the discussions reported in sections 4.4 and 4.3, it can be observed that the inverse operator of $S_{prop.}$ is always bounded, as $||e^{i|\zeta(\kappa)|d}/|\zeta(\kappa)|||^{-1} = |\zeta(\kappa)|$ is finite for $-k < \kappa < k$.

It is now possible to deliberately choose to attempt the reproduction of just that component $p_{prop.}(\mathbf{x})$ of the pressure profile $p(\mathbf{x})$, which has an orthogonal projection on the subspace spanned by $e^{i\kappa x_1}$, $|\kappa| \leq k$, that is the component of $p(\mathbf{x})$, which can be represented by the integral (6.13).

The corresponding source strength $\tilde{a}_{s.t.}(\mathbf{y})$ (assuming again that the origin of the coordinate system lies on $\partial\Lambda$) can be expressed similarly to equation (4.101) by

$$
\tilde{a}_{s.t.}(\mathbf{y}) = \int_{-k}^{k} \frac{-i2\zeta(\kappa)}{e^{i\zeta(\kappa)d}} \frac{e^{i\kappa y_1}}{2\pi} \langle e^{i\kappa}|p\rangle_{\partial V} d\kappa \tag{6.15}
$$

Inserting this result in equation (6.10) and considering the orthogonality relation (2.76) it can be easily seen that the reproduced field is

$$
(S\tilde{a}_{s.t.})(\mathbf{z}) = p_{prop.}(\mathbf{z}) = \frac{1}{2\pi}\int_{-k}^{k} e^{i[\kappa z_1 + \zeta(\kappa)(|z_3|-d)]} \langle e^{i\kappa}|p\rangle_{\partial V} d\kappa, \quad \mathbf{z} \in \mathbb{R}^2 \tag{6.16}
$$

Note that this solution is also valid for the half space $z_3 < 0$, as $(Sa)(z_1, z_3) = (Sa)(z_1, -z_3)$ for this special geometrical arrangement.

Analogously, the reproduction error is given by

$$
\begin{aligned}
\epsilon_{s.t.}(\mathbf{z}) = p_{evan.}(\mathbf{x}) &= \frac{1}{2\pi}\int_{k}^{\infty} e^{-|\zeta(\kappa)|(z_3-d)} e^{i\kappa z_1} \langle e^{i\kappa}|p\rangle_{\partial V} d\kappa && (6.17)\\
&+ \frac{1}{2\pi}\int_{-\infty}^{-k} e^{-|\zeta(\kappa)|(z_3-d)} e^{i\kappa z_1} \langle e^{i\kappa}|p\rangle_{\partial V} d\kappa, \quad \mathbf{z} \in V
\end{aligned}
$$

Pseudo-evanescent and pseudo-propagating fields. [1] It is important to clarify that $p_{prop.}$ does not physically represent the propagating part of the desired sound field, it rather represents the component of the target field, which can be represented by a

[1] The author would like to acknowledge Dr. Dylan Menzies for having brought up this important point in the course of a private conversation.

linear superposition of plane waves in the half space defined by $z_3 \geq q_3$. Similarly, $p_{evan.}$ does not represent the physical evanescent or non-propagating component of the target field, but instead it gives the component of p, which can be expressed, in the same half space $z_3 \geq q_3$, by a superposition of evanescent waves. A clarifying example is given by the Weyl integral representation of a monopole field, equation (4.54): although the field of a monopole does *not* have any evanescent component, its Weyl integral representation includes both propagating and evanescent waves. In order to avoid any confusion, we will refer to $p_{prop.}(\mathbf{z})$ and $p_{prop.}(\mathbf{z})$ as the *pseudo-propagating* and *pseudo-evanescent* fields, respectively.

Equations (6.15) and (6.16) can also be obtained with a κ-*space* filtering process: $\tilde{a}_{s.t.}(\mathbf{y})$ and $p_{prop.}(\mathbf{x})$ can be computed by convolving $a(\mathbf{y})$ (when this is bounded) and $p(\mathbf{x})$, respectively, by a spatial filter, representing a rectangular window $\Pi(\kappa/(2k))$ in the κ domain. The expression of the rectangular function $\Pi(\cdot)$ and of its Fourier transform are given by equation (2.62) and (2.63), and are reported here:

$$\Pi\left(\frac{\kappa}{2k}\right) = \begin{cases} 1, & |\kappa| < k \\ 1/2, & |\kappa| = k \\ 0, & |\kappa| > k \end{cases} \tag{6.18}$$

$$\left(\mathcal{F}^{-1}\Pi\left(\frac{\cdot}{2k}\right)\right)(x_1) = \frac{2k}{\sqrt{2\pi}}\frac{\sin(kx_1)}{kx_1} = \frac{2k}{\sqrt{2\pi}}\ \mathrm{sinc}\,(kx_1) \tag{6.19}$$

Therefore, from the convolution theorem (2.94), we have that

$$\tilde{a}_{s.t.}(\mathbf{y}) = a(y_1, 0) \otimes \frac{k}{\pi}\ \mathrm{sinc}\,(ky_1) \tag{6.20}$$

$$p_{prop.}(\mathbf{x}) = p(x_1, x_3) \otimes \frac{k}{\pi}\ \mathrm{sinc}\,(kx_1) \tag{6.21}$$

We consider now the case of a focused virtual source, located at $\mathbf{z} \in (\Lambda \backslash V)$, at a distance $q_3 < d$ from $\partial\Lambda$. In view of equation (6.11), the approximate solution $\tilde{a}(\mathbf{y})_{s.t.}$ is given by

$$\tilde{a}_{s.t.}(\mathbf{y}) = \int_{-k}^{k} e^{-i\zeta(\kappa)q_3}\frac{e^{i\kappa(y_1-q_1)}}{2\pi}d\kappa \tag{6.22}$$

For the case of a focused source, the following relations hold for the reproduced and error field:

$$(S\tilde{a}_{s.t.})(\mathbf{z}) = p_{prop.}(\mathbf{z}) = \frac{i}{2\pi}\int_{-k}^{k}\frac{e^{i\zeta(\kappa)(|z_3|-q_3)}}{2\zeta(\kappa)}e^{i\kappa(z_1-q_1)}d\kappa,\ \mathbf{z} \in \mathbb{R}^2 \tag{6.23}$$

$$\begin{aligned} \epsilon_{s.t.}(\mathbf{z}) = p_{evan.}(\mathbf{z}) &= \frac{1}{2\pi}\int_{-\infty}^{-k}\frac{e^{-|\zeta(\kappa)|(z_3-q_3)}}{2|\zeta(\kappa)|}e^{i\kappa(z_1-q_1)}d\kappa \\ &+ \frac{1}{2\pi}\int_{k}^{\infty}\frac{e^{-|\zeta(\kappa)|(z_3-q_3)}}{2|\zeta(\kappa)|}e^{i\kappa(z_1-q_1)}d\kappa,\ \mathbf{z} \in V \end{aligned} \tag{6.24}$$

The sum of the reproduced field and of the error clearly gives the field due to a line source at $\mathbf{q}$, as expressed by equation (4.90).

Figure 6.6 shows the sound field generated by a line source located at $[q_1, q_3] = [\ 0\ \text{m}, 0.5\ \text{m}]$, in the interior of Λ. The wave number is $k = 10\ \text{rad/m}$ and the distance between $\partial\Lambda$ and ∂V is $d = 1\ \text{m}$. Figures 6.7 and 6.8 represent the reproduced field and the normalized reproduction error, defined by (5.31). The source strength was computed with equation (6.15). The integral was solved numerically, applying a uniform discretization ($d\kappa = 0.010002$) of the domain of integration $[-k, k]$ and a quadrature formula. The field has been computed using the definition of single layer potential (3.15) with the 2D kernel (3.7). The infinite line has been approximated by a 40 m long segment (the plotting area is 16 m^2), discretized into 255 secondary sources with 0.1572 m spacing. It can be observed that the reproduction error decreases with distance from $\partial\Lambda$. A comparison with Figure 4.14 highlights the fact that the error is due to the pseudo-evanescent field, as indicated by equation (6.24).

The method presented here is analogous to the spectral cut-off described in the previous section. It is also possible to attempt an approximate reproduction of the target field, by applying a regularization method such as the smooth spectral damping or the Tikhonov scheme to the expression (5.43) of the solution. It is recalled that, without the use of a regularization technique, this integral would diverge for a focused virtual source. The application of these techniques (spectral damping and Tikhonov regularization) leads to the following expression for the approximate solution:

$$\tilde{a}_{s.d.}(\mathbf{y}) = \int_{\mathbb{R}} w(\kappa) e^{-i\zeta(\kappa)q_3} \frac{e^{i\kappa(y_1-q_1)}}{2\pi} d\kappa \tag{6.25}$$

$$\tilde{a}_{T.}(\mathbf{y}) = \int_{\mathbb{R}} \frac{e^{-i\zeta(\kappa)q_3}}{1+\beta 4|\zeta(\kappa)|^2 e^{\text{Im}(\zeta(\kappa))d_0}} \frac{e^{i\kappa(y_1-q_1)}}{2\pi} d\kappa \tag{6.26}$$

$$\tag{6.27}$$

where $\beta > 0$ is the regularization parameter and $w(\kappa)$ is a smooth tapering window with $w(\kappa) = 1$ for $|\kappa| < k$, $0 \leq w(\kappa) \leq 1$ for $k \leq |\kappa| \leq k_N$ and $w(\kappa) = 0$ for $|\kappa| > k_N > k$.

6.2.1.1 Time Reversal Mirror

A technique widely used for the reproduction of a field generated by a focused sound sources is represented by the so called *Time Reversal mirror*. This technique was initially developed in the framework of ultrasonic imaging by Fink et al. [Fin92], [WTF92], [TAG+01] and its use has been later extended to audio engineering purposes [YTF03b], [YTF03a], [Ver97].

The basis of this technique consists of driving the secondary sources with the time reversed version of the normal derivative of the target field (or sometimes the field itself),

measured on $\partial\Lambda$ [Ver97]. We study in what follows the detail of this technique for the case of linear geometrical arrangement.

First, we rewrite equation (4.90) for a point source located at $\mathbf{q}$ and for the case of $\mathbf{y} \in \partial\Lambda$ and

$$\frac{i}{4}H_0^{(1)}(k|\mathbf{y}-\mathbf{q}|) = \frac{i}{4\pi}\int_{-\infty}^{\infty}\frac{e^{i\kappa(y_1-q_1)}}{\zeta(\kappa)}\frac{e^{i\zeta(\kappa)|q_3-y_3|}}{dn}d\kappa \tag{6.28}$$

We see that $q_3 < 0$ if $\mathbf{q} \notin \Lambda$, and $q_3 > 0$ if $\mathbf{q} \in \Lambda\backslash V$, the latter being the case considered here. It is reminded that $k = \omega/c$ for the dispersion relation. Considering that we have assumed that $\hat{\mathbf{n}} = [0, 0, -1]$, $y_3 = 0$ and $q_3 > 0$, the approximate solution $\tilde{a}_{t.r.}(\mathbf{y})$ computed with the Time Reversal mirror technique is given by

$$\begin{aligned}
\tilde{a}_{t.r.}(\mathbf{y}) &:= 2\left[\frac{d}{d\hat{\mathbf{n}}(\mathbf{y})}\left(\frac{i}{4}H_0^{(1)}(k|\mathbf{y}-\mathbf{q}|)\right)\right]^* \qquad (6.29)\\
&= \left[\frac{i}{2\pi}\int_{-\infty}^{\infty}e^{i\kappa(y_1-q_1)}\frac{1}{\zeta(\kappa)}\lim_{dn=0}\frac{e^{i\zeta(\kappa)(q_3-dn)}-e^{i\zeta(\kappa)q_3}}{dn}d\kappa\right]^*\\
&= \left[\frac{i}{2\pi}\int_{-\infty}^{\infty}e^{i\kappa(y_1-q_1)}\frac{e^{i\zeta(\kappa)q_3}}{\zeta(\kappa)}\frac{(1-i\zeta(\kappa)dn)-1}{dn}d\kappa\right]^*\\
&= \frac{1}{2\pi}\int_{-\infty}^{\infty}e^{-i\kappa(y_1-q_1)}e^{-i\zeta(\kappa)^*q_3}d\kappa
\end{aligned}$$

Using the usual orthogonality relation (2.76) and the property of the Dirac delta function (2.26) and considering that $\zeta(-\kappa) = \zeta(\kappa)$, we obtain

$$\begin{aligned}
\langle e^{i\kappa}|\tilde{a}_{t.r.}\rangle_{\partial\Lambda} &= \frac{1}{2\pi}\int_{-\infty}^{\infty}\left[\int_{-\infty}^{\infty}e^{-i\kappa y_1}e^{-i\tilde{\kappa}y_1}dy_1\right]e^{i\tilde{\kappa}q_1}e^{-i\zeta(\tilde{\kappa})^*q_3}d\tilde{\kappa} \qquad (6.30)\\
&= \int_{-\infty}^{\infty}\delta(\tilde{\kappa}+\kappa)e^{i\tilde{\kappa}q_1}e^{-i\zeta(\tilde{\kappa})^*q_3}d\tilde{\kappa} = e^{-i\kappa q_1}e^{-i\zeta(\kappa)^*q_3}
\end{aligned}$$

In view of this result, substituting this expression to the density in equation (6.10) leads to the following result

$$(S\tilde{a}_{t.r.})(\mathbf{z}) = \frac{i}{2\pi}\int_{\mathbb{R}}\frac{e^{i[\zeta(\kappa)|z_3|-\zeta(\kappa)^*q_3]}}{2\zeta(\kappa)}e^{i\kappa(z_1-q_1)}d\kappa, \quad \mathbf{z} \in \mathbb{R}^2 \tag{6.31}$$

As discussed in the previous section, we can split this integral in two parts

$$\begin{aligned}
(S\tilde{a}_{t.r.})(\mathbf{z}) &= p_{prop.t.r.}(\mathbf{z}) + p_{evan.t.r.}(\mathbf{z}) \qquad (6.32)\\
p_{prop.t.r.}(\mathbf{z}) &= \frac{i}{2\pi}\int_{-k}^{k}\frac{e^{i\zeta(\kappa)(|z_3|-q_3)}}{2\zeta(\kappa)}e^{i\kappa(z_1-q_1)}d\kappa, \ \mathbf{z} \in \mathbb{R}^2 \qquad (6.33)\\
p_{evan.t.r.}(\mathbf{z}) &= \frac{1}{2\pi}\int_{-\infty}^{-k}\frac{e^{-|\zeta(\kappa)|(|z_3|+q_3)}}{2|\zeta(\kappa)|}e^{i\kappa(z_1-q_1)}d\kappa \qquad (6.34)\\
&+ \frac{1}{2\pi}\int_{k}^{\infty}\frac{e^{-|\zeta(\kappa)|(|z_3|+q_3)}}{2|\zeta(\kappa)|}e^{i\kappa(z_1-q_1)}d\kappa, \ \mathbf{z} \in \mathbb{R}^2
\end{aligned}$$

A comparison of these results with equations (6.23) and (6.24) shows that the reproduced field $(S\tilde{a}_{t.r.})(\mathbf{z})$ is the sum of a first field $p_{prop.t.r.}(\mathbf{z})$, which is the pseudo-propagating component of the desired field, generated by a line source at $\mathbf{q}$, and of a second field $p_{evan.t.r.}(\mathbf{z})$, which is not the pseudo-evanescent component of the desired field, but it is the pseudo-evanescent field of a virtual *mirrored-source* in respect to the line $\partial\Lambda$ (namely located at $\mathbf{q}_{mirr} = [q_1, q_2, -q_3]$). This is quite a remarkable result, which sheds some light on the reproduction error given by the time reversal technique for focused sources. This method allows a simpler calculation of the driving function relative to the method described in the previous section, and could be also regarded as a regularization method. Analogous results can be derived with similar passages for the three dimensional problem and a geometrical arrangement with infinite planes.

Figures 6.9 and 6.10 report the reproduced field and the normalized reproduction error, respectively, for a focused source in the location $[q_1, q_3] = [\ 0\ \text{m}, 0.5\ \text{m}]$, in the interior of Λ. The wave number is $k = 10$ rad/m and the distance between $\partial\Lambda$ and ∂V is $d = 1$ m. The source strength was computed with equation (6.29). The numerical integrations for the computing $a(\mathbf{y})$ and $\hat{p}(\mathbf{z})$ have been performed with the same method used for Figure 6.7.

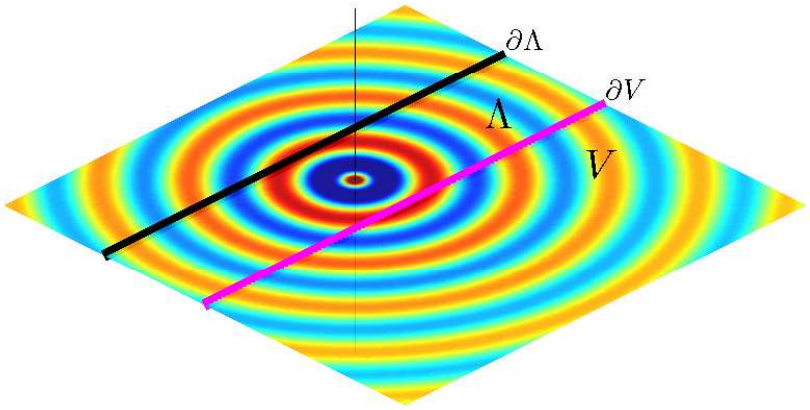

FIGURE 6.6: Pressure field generated by a line source (vertical black line) located at $[q_1, q_3] = [\ 0\ \text{m}, 0.5\ \text{m}]$. The wave number is $k = 10$ rad/m

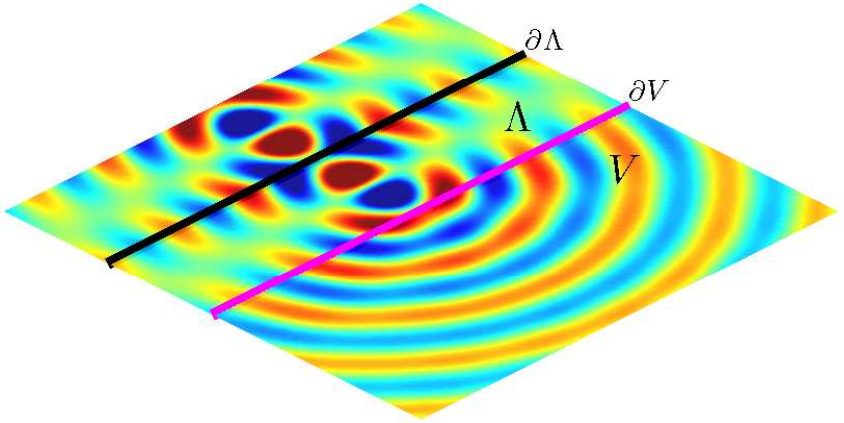

FIGURE 6.7: Reproduced field for a focused source located at $[q_1, q_3] = [\ 0\ \text{m}, 0.5\ \text{m}]$. The wave number is $k = 10\ \text{rad/m}$ and the distance between $\partial\Lambda$ and ∂V is $d = 1\ \text{m}$. The source strength was computed with equation (6.15).

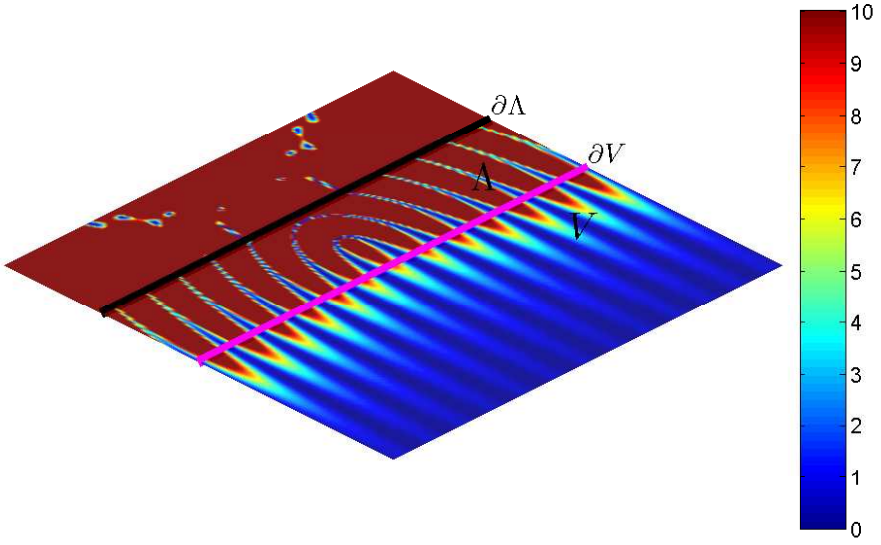

FIGURE 6.8: Normalized reproduction error (%, clipped at 10%) for a line source located at $[q_1, q_3] = [\ 0\ \text{m}, 0.5\ \text{m}]$. The wave number is $k = 10\ \text{rad/m}$ and ∂V is $d = 1\ \text{m}$. The source strength was computed with equation (6.15).

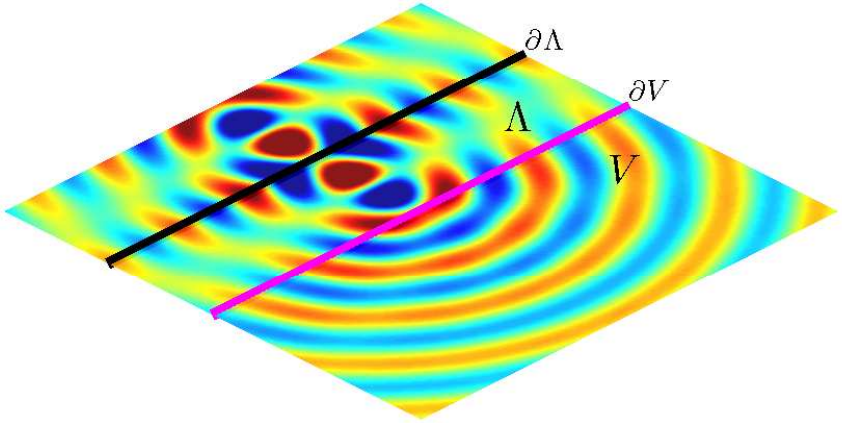

FIGURE 6.9: Reproduced field for a focused source located at $[q_1, q_3] = [\ 0\ \text{m}, 0.5\ \text{m}]$. The wave number is $k = 10$ rad/m and the distance between $\partial\Lambda$ and ∂V is $d = 1$ m. The source strength was computed with the time reversal technique, equation (6.29).

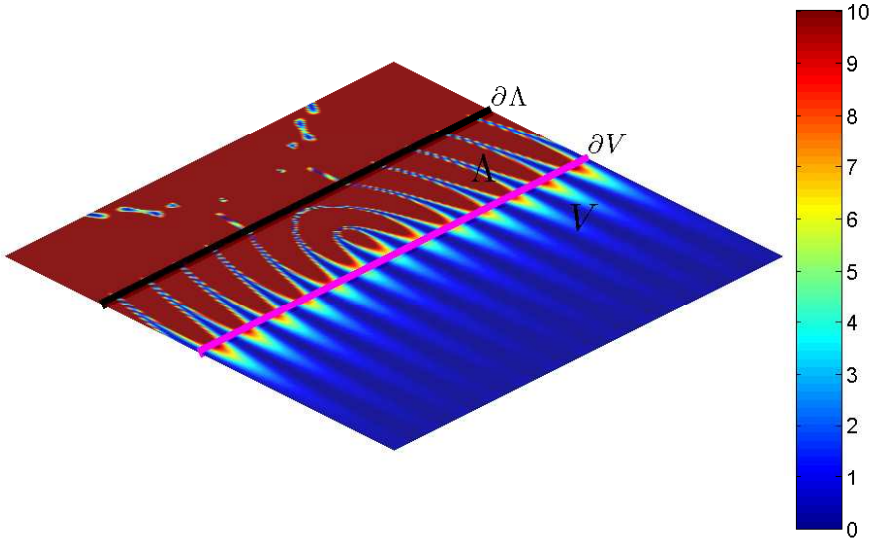

FIGURE 6.10: Normalized reproduction error (%, clipped at 10%) for a line source located at $[q_1, q_3] = [\ 0\ \text{m}, 0.5\ \text{m}]$. The wave number is $k = 10$ rad/m and ∂V is $d = 1$ m. The source strength was computed with the time reversal technique, equation (6.29).

6.2.2 Parallel plane geometry

Results analogous to those presented for the parallel line geometry can be obtained for the three dimensional case, with the infinite plane geometry introduced in Section 4.3. The most relevant difference is that the integral (4.84), which gives the solution, should be limited to the disk $B_k := \{\boldsymbol{\kappa} \in \mathbb{R}^2 : |\boldsymbol{\kappa}| < k\}$ rather than to the interval $[-k, k]$. With mathematical passages analogous to the case of the linear geometry, we derive the following solution for a focused virtual source in 3D:

$$\tilde{a}_{s.t.}(\mathbf{y}) = \int_{B_k} e^{-i\zeta(\kappa)q_3} \frac{e^{i\boldsymbol{\kappa}\cdot(\mathbf{y}-\mathbf{q})}}{4\pi^2} dS(\boldsymbol{\kappa}) \tag{6.35}$$

where the simplifying assumption has been made that $\partial\Lambda = \{\mathbf{y} \in \mathbb{R}^3 : y_3 = 0\}$. The reproduced field is given by inserting this equation into expression (4.59) for S, thus obtaining

$$\left(S\tilde{a}_{s.t.}\right)(\mathbf{z}) \quad = \quad \frac{i}{8\pi^2} \int_{B_k} \frac{e^{i\zeta(\kappa)(|z_3|-q_3)}}{\zeta(\kappa)} e^{i[\kappa_1(z_1-q_1)+\kappa_2(z_2-q_2)]} dS(\boldsymbol{\kappa}), \quad \mathbf{z} \in \mathbb{R}^3 \tag{6.36}$$

This expression clearly resembles the Weyl integral (4.53), with the relevant difference that the integration is now limited to $|\kappa| < k$.

Figure 6.11 represents the sound field due to a monopole source at the location $[q_1, q_2, q_3] = [0,\ 0,\ 0.5\ \text{m}]$. The square plotting area has a side length of 2 m and the distance between $\partial\Lambda$ and ∂V (the latter drawn for reference only) is $d = 2$ m. The wave number is $k = 12$ rad/m. Figures 6.12 and 6.13 show the reproduced field and the normalized reproduction error (5.31), respectively, for a focused virtual source in the same location $\mathbf{q}$. The density $\tilde{a}_{s.t.}(\mathbf{y})$ was computed from equation (6.35). The integration was limited to the ball $|\kappa| \leq k - 0.10002$ (in order to avoid the singularity at $|\kappa| = 0$), and performed by applying a quadrature formula, with a regular sampling of $d\kappa_1 = d\kappa_2 = 0.10002$. The field has been computed using the definition of the single layer potential, equation (3.15), having limited the integration to the square of size $[-5\ \text{m}, 5\ \text{m}] \times [-5\ \text{m}, 5\ \text{m}]$ and applied a discretization $dy_1 = dy_2 = 0.176$ m.

A comparison of the reproduction error in Figure 6.13 with the analogous plot for a linear geometry, Figure 6.8, highlights the presence in the former field of an elongated area of inaccurate reproduction, perpendicular to $\partial\Lambda$ and directed towards $\mathbf{q}$. This error was absent in the 2D case. In fact, the reproduction error is given by

$$\epsilon_{s.t.}(\mathbf{z}) \quad = \quad \frac{i}{8\pi^2} \int_{|\boldsymbol{\kappa}|>k} \frac{e^{i\zeta(\kappa)(|z_3|-q_3)}}{\zeta(\kappa)} e^{i[\kappa_1(z_1-q_1)+\kappa_2(z_2-q_2)]} dS(\boldsymbol{\kappa}), \quad \mathbf{z} \in \Lambda \tag{6.37}$$

The error along the half line $\ell := \{\mathbf{z} \in \mathbb{R}^3 : z_1 = q_1, z_2 = q_2, z_3 \geq q_3\}$, orthogonal to $\partial\Lambda$ directed towards $\mathbf{q}$, can be expressed applying to the integral above the substitution

$$\begin{aligned} -i\zeta(\kappa) &= -i\sqrt{k^2 - \kappa^2} = t, \\ \kappa &= \sqrt{k^2 + t^2}, \\ \kappa\, d\kappa &= t\, dt, \\ dS(\kappa) &= \kappa \frac{d\kappa}{dt}\, dt\, d\phi_\kappa = t\, dt\, d\phi_\kappa \end{aligned}$$

leading to

$$\begin{aligned} \epsilon_{s.t.}(\mathbf{z}) &= \frac{1}{8\pi^2} \int_0^{2\pi} d\phi_\kappa \int_0^\infty e^{-t(|z_3| - q_3)} dt \\ &= -\frac{1}{4\pi} \frac{e^{-t(|z_3| - q_3)}}{|z_3| - q_3} \Bigg|_0^\infty = \frac{1}{4\pi(|z_3| - q_3)}, \quad \mathbf{z} \in \ell \end{aligned} \tag{6.38}$$

This result was derived by Menzies [Men09], who also pointed out that this error has the same decay with distance $(1/r)$ of the fundamental solution. Therefore, unlike the two dimensional case, the error can not be regarded as being limited to the near-field of the secondary sources. The analysis of the error on ℓ shows that the latter may be reduced by increasing the radius of the integration disk B_k, thus including some evanescent modes in the computation of $a(\mathbf{y})$.

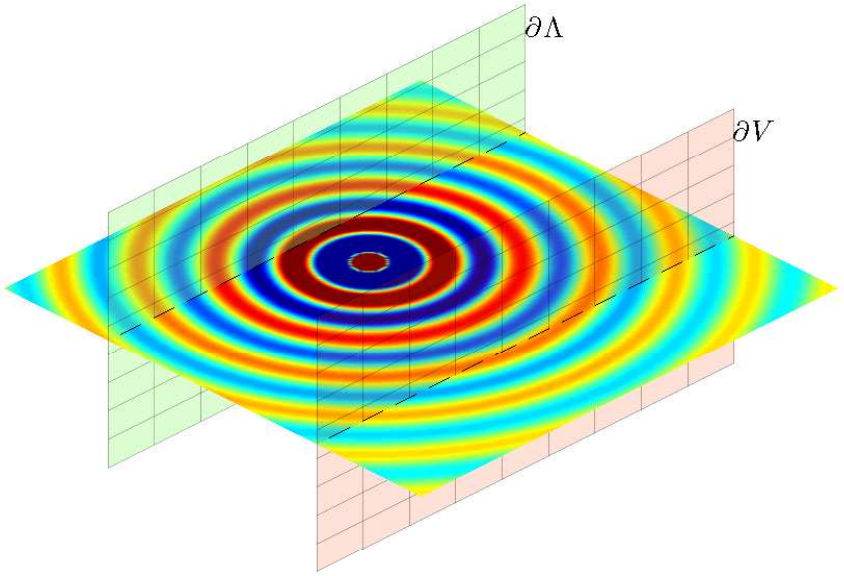

FIGURE 6.11: Pressure field generated by an omnidirectional point source located at $[q_1, q_2, q_3] = [\ 0\ \text{m},\ 0\ \text{m}, 0.5\ \text{m}]$. The wave number is $k = 12$ rad/m

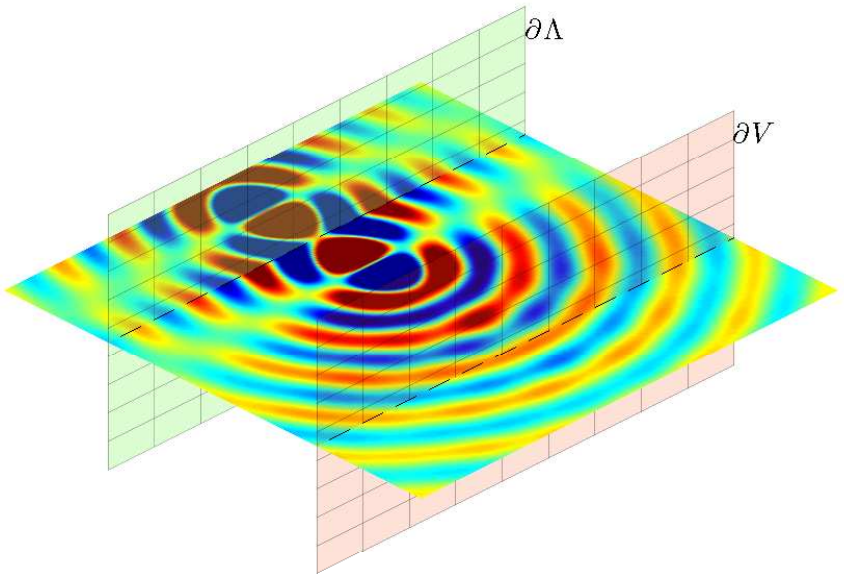

FIGURE 6.12: Reproduced field for a focused source located at $[q_1, q_2, q_3] = [\ 0\ \text{m},\ 0\ \text{m}, 0.5\ \text{m}]$. The wave number is $k = 12$ rad/m and the distance between $\partial\Lambda$ and ∂V is $d = 2$ m. The source strength was computed with equation (6.35).

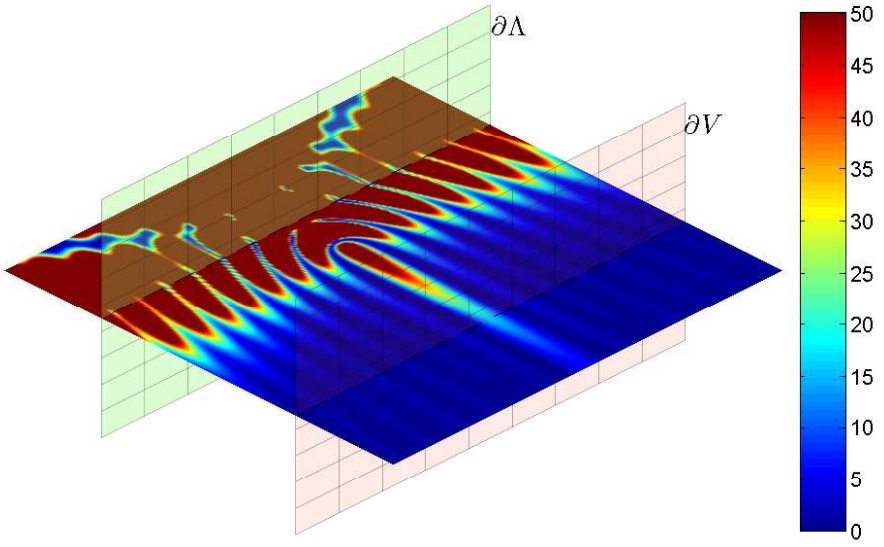

FIGURE 6.13: Normalized reproduction error (%, clipped at 50%) for a focused source located at $[q_1, q_2, q_3] = [\ 0\ \text{m},\ 0\ \text{m}, 0.5\ \text{m}]$. The wave number is $k = 12$ rad/m and ∂V is $d = 2$ m. The source strength was computed with equation (6.35).

6.2.3 Concentric sphere geometry

The case is now considered of a focused source for the arrangement of concentric spheres discussed in Section 4.1. We consider the target sound field due to a virtual point source located at $\mathbf{q} \in \Lambda \backslash V$. As mentioned previously, no exact solution exists for this target field, but it is possible to seek an approximate solution. One attempt can be made by applying the spectral cut-off described by equation (6.1). In this case, considering the results shown in Section 5.6.1, the approximate solution $\tilde{a}$, the reproduced field $(S\tilde{a})(\mathbf{z})$ and the error $e(\mathbf{z})$ are given respectively by

$$\tilde{a}_{s.t.}(\mathbf{y}) = \sum_{\nu=0}^{N} \frac{h_\nu(kq)}{R_\Lambda^2 h_\nu(kR_\Lambda)} \frac{2\nu+1}{4\pi} P_\nu(\hat{\mathbf{y}} \cdot \hat{\mathbf{q}}) \tag{6.39}$$

$$(S\tilde{a}_{s.t.})(\mathbf{z}) = \sum_{\nu=0}^{N} ikh_\nu(kq) j_\nu(kz) \frac{2\nu+1}{4\pi} P_\nu(\hat{\mathbf{z}} \cdot \hat{\mathbf{q}}), \quad \mathbf{z} \in \Lambda \tag{6.40}$$

$$\epsilon_{s.t.}(\mathbf{z}) = \sum_{\nu=N+1}^{\infty} ikh_\nu(kq) j_\nu(kz) \frac{2\nu+1}{4\pi} P_\nu(\hat{\mathbf{z}} \cdot \hat{\mathbf{q}}), \quad \mathbf{z} \in \Lambda,\ z < q \tag{6.41}$$

This technique is implicitly used in High Order Ambisonics, since the order of the series above is finite. It is not always well understood that the nonexistence of the solution and to the second Picard condition are actually related to what is sometimes referred to as the *bass boost* effect for focused sources. This phenomenon corresponds to a large amount of energy generated by the secondary sources at low frequencies and to severe reproduction artifacts in the region $\Lambda \backslash V$ (see figures 6.16 and 6.17). The denseness of the range of S, discussed in Section 5.2, ensures the fact that an arbitrary small error can be achieved on ∂V (and consequently in its interior, but not in its exterior) by letting the order N become arbitrarily large. This has the side effect of increasing the norm of $a(\mathbf{y})$ and making the system more and more unstable, with serious reproduction artifacts in the exterior of V.

A similar method includes the smooth damping of the spectrum of the operator, as shown by equation 6.3. This leads to

$$\tilde{a}_{s.t.}(\mathbf{y}) = \sum_{\nu=0}^{\infty} w_\nu \frac{h_\nu(kq)}{R_\Lambda^2 h_\nu(kR_\Lambda)} \frac{2\nu+1}{4\pi} P_\nu(\hat{\mathbf{y}} \cdot \hat{\mathbf{q}}) \tag{6.42}$$

$$(S\tilde{a}_{s.t.})(\mathbf{z}) = \sum_{\nu=0}^{\infty} w_\nu ikh_\nu(kq) j_\nu(kz) \frac{2\nu+1}{4\pi} P_\nu(\hat{\mathbf{z}} \cdot \hat{\mathbf{q}}), \quad \mathbf{z} \in \Lambda \tag{6.43}$$

$$\epsilon_{s.t.}(\mathbf{z}) = \sum_{\nu=0}^{\infty} (1-w_\nu) ikh_\nu(kq) j_\nu(kz) \frac{2\nu+1}{4\pi} P_\nu(\hat{\mathbf{z}} \cdot \hat{\mathbf{q}}), \quad \mathbf{z} \in \Lambda,\ z < q \tag{6.44}$$

As already mentioned, the smooth spectral damping technique is widely used in Ambisonics, although the use of this technique for focused sources has been suggested only recently by Adriaensen, in the form of private communications.

Results analogous to equations (6.39)-(6.44) can be obtained from the equations shown in Section 4.2 for the concentric circle geometry.

Figures 6.18 and 6.19 show the reproduced field for a focused virtual source, located at $[r_q, \theta_q, \phi_q] = [1\text{ m}, 90°, 0°]$. The boundary $\partial\Lambda$ is a sphere of radius $R_\Lambda = 1.5$ m and the wave number is $k = 12$ rad/m. The density of the potential was computed with equation (6.42) and a tapering window w_ν such that

$$w_\nu = \begin{cases} 1, & \nu < 5 \\ \frac{1}{5}(10 - \nu), & 5 \leq \nu \leq 10 \\ 0, & \nu > 10 \end{cases} \tag{6.45}$$

A different method for calculating an approximate solution can be obtained from the expression of the field due to a monopole-like source given by the Weyl integral 4.54, with the integration domain limited to $|\kappa| \leq k$, similarly to the linear geometry shown above. An analogous idea was recently developed by Ahrens and Spors [AS08c] for the circular array geometry. The extension is shown here to the case of spherical arrays. Results analogous to those presented here can be found in a recent work by Menzies [Men09], which has been of significant inspiration in the derivation of what is presented here.

We consider a source located at $\mathbf{q} = [0, 0, -d]$ and the half space $\Gamma_{-d} := \{\mathbf{z} \in \mathbb{R}^3 : z_3 \geq -d\}$, as illustrated by Figure 6.14.

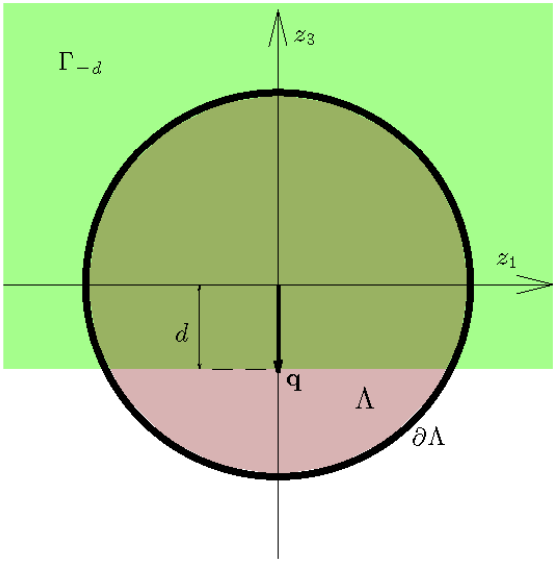

FIGURE 6.14: Horizontal cross-section of Λ, illustrating the source location $\mathbf{q}$ and the half space Γ_{-d}.

We have seen that the field due to a point source can be expressed in Γ_{-d} by the Weyl integral 4.54, reported below for clarity

$$G(\mathbf{z},\mathbf{q}) = \frac{e^{ik|\mathbf{z}-\mathbf{q}|}}{4\pi|\mathbf{z}-\mathbf{q}|} = \frac{i}{8\pi^2}\int_{\mathbb{R}^2} \frac{e^{i\zeta(\kappa)(z_3+d)}}{\zeta(\kappa)} e^{i\boldsymbol{\kappa}\cdot\mathbf{z}} dS(\boldsymbol{\kappa}), \quad z_3 \geq -d \tag{6.46}$$

The domain of integration is now limited to the disc

$$B_k := \{\boldsymbol{\kappa} \in \mathbb{R}^2 : |\boldsymbol{\kappa}| < k\} \tag{6.47}$$

thus obtaining

$$\tilde{G}(\mathbf{z},\mathbf{q}) = \frac{i}{8\pi^2}\int_{B_k} \frac{e^{i\zeta(\kappa)(z_3+d)}}{\zeta(\kappa)} e^{i\boldsymbol{\kappa}\cdot\mathbf{z}} dS(\boldsymbol{\kappa}), \quad \mathbf{z} \in \mathbb{R}^3 \tag{6.48}$$

As observed above, this field is due to a superposition of propagating plane waves, and this is the field we want to reproduce. $\tilde{G}(\mathbf{z},\mathbf{q})$ is defined in all $\mathbb{R}^3$, but it gives an approximation on Γ_{-d} of the field due to a monopole source at $\mathbf{q}$. Following the passages illustrated in Appendix D, we obtain the exact solution $a_{\tilde{G}}(\mathbf{y})$ for the inverse problem (3.19) with $\tilde{G}(\mathbf{z},\mathbf{q})$ as the target field. This is given by

$$a_{\tilde{G}}(\mathbf{y}) = \sum_{\nu=0}^{\infty}\left(\frac{ik}{4\pi}\sum_{n=0}^{\infty} i^n j_n(kd)(2n+1)\breve{P}_{n\nu}\right)\frac{i^\nu(2\nu+1)}{ikR_\Lambda^2 h_\nu(kR_\Lambda)}P_\nu(\cos\theta_y) \tag{6.49}$$

where

$$\breve{P}_{n\nu} := \int_0^1 P_\nu(\alpha)P_n(\alpha)d\alpha = \begin{cases} \frac{1}{2\nu+1} & [\nu = n] \\ 0 & [\nu - n \text{ is even}, \nu \neq \text{n}] \\ \frac{(-1)^{\frac{1}{2}(\nu+n-1)}\nu!n!}{2^{\nu+n-1}(\nu-n)(n+\nu+1)\left[\left(\frac{n}{2}\right)!\left(\frac{\nu-1}{2}\right)!\right]^2} & [n \text{ even}, \nu \text{ odd}] \end{cases} \tag{6.50}$$

or equivalently (see Appendix D)

$$a_{\tilde{G}}(\mathbf{y}) = \sum_{\nu=0}^{\infty}\left(\frac{ik}{4\pi}\int_0^1 e^{ikdx}P_\nu(x)dx\right)\frac{i^\nu(2\nu+1)}{ikR_\Lambda^2 h_\nu(kR_\Lambda)}P_\nu(\cos\theta_y) \tag{6.51}$$

This solution has been derived for $r_q = d$, $\theta_q = \pi$, but it can be extended to any other virtual source location by substituting $P_\nu(\cos\theta_y)$ with $P_\nu(-\hat{\mathbf{y}}\cdot\hat{\mathbf{q}})$ and $j_n(kd)$ with $j_n(kq)$. This leads to

$$a_{\tilde{G}}(\mathbf{y}) = \sum_{\nu=0}^{\infty}\left(\frac{ik}{4\pi}\sum_{n=0}^{\infty} i^n j_n(kq)(2n+1)\breve{P}_{n\nu}\right)\frac{i^\nu(2\nu+1)}{ikR_\Lambda^2 h_\nu(kR_\Lambda)}P_\nu(-\hat{\mathbf{q}}\cdot\hat{\mathbf{y}}) \tag{6.52}$$

A comparison of this result with expression (6.42), giving the approximate solution obtained with the smooth spectral damping technique, shows that $a_{\tilde{G}}$ could be also interpreted as an approximate solution obtained with the same technique and a *distance*

dependent tapering window $w_\nu(d)$ given by

$$w_\nu(d) := \frac{1}{i^\nu h_\nu(kd)} \sum_{n=0}^{\infty} i^n j_n(kd)(2n+1)\breve{P}_{n\nu} \tag{6.53}$$

In view of the spherical harmonic summation formula (2.53), we observe that

$$\begin{aligned} \langle Y_\nu^\mu | a_{\tilde{G}} \rangle_{\partial\Lambda} &= \left(\frac{ik}{4\pi} \sum_{n=0}^{\infty} i^n j_n(kd)(2n+1)\breve{P}_{n\nu} \right) \frac{4\pi i^\nu Y_\nu^\mu(-\hat{\mathbf{q}})^*}{ikh_\nu(kR_\Lambda)} \\ &= \left(\frac{ik}{4\pi} \int_0^1 e^{ikdx} P_\nu(x) dx \right) \frac{4\pi i^\nu Y_\nu^\mu(-\hat{\mathbf{q}})^*}{ikh_\nu(kR_\Lambda)} \end{aligned} \tag{6.54}$$

Note that from the Jacobi-Anger expansion (2.56) we have that

$$4\pi i^\nu Y_\nu^\mu(-\hat{\mathbf{q}})^* j_\nu(k) = \langle Y_\nu^\mu | e^{ik\hat{\mathbf{q}}\cdot\mathbf{x}} \rangle_\Omega \tag{6.55}$$

which corresponds to the coefficients of a plane wave traveling in the direction $\hat{\mathbf{q}}$. From this result and from expression (4.4) of S, we obtain

$$\begin{aligned} (Sa_{\tilde{G}})(\mathbf{z}) &= \sum_{\nu=0}^{\infty} ikh_\nu^{(1)}(kR_\Lambda) j_\nu(kz) \sum_{\mu=-\nu}^{\nu} Y_\nu^\mu(\hat{\mathbf{z}}) \langle Y_\nu^\mu | a_{\tilde{G}} \rangle_{\partial\Lambda} \\ &= \sum_{\nu=0}^{\infty} \left(\frac{ik}{4\pi} \int_0^1 e^{ikdx} P_\nu(x) dx \right) 4\pi i^\nu j_\nu(kz) \sum_{\mu=-\nu}^{\nu} Y_\nu^\mu(\hat{\mathbf{z}}) Y_\nu^\mu(-\hat{\mathbf{q}})^* \\ &= \sum_{\nu=0}^{\infty} \left(\frac{ik}{4\pi} \int_0^1 e^{ikdx} P_\nu(x) dx \right) i^\nu j_\nu(kR_V)(2\nu+1) P_\nu(-\hat{\mathbf{q}}\cdot\hat{\mathbf{x}}) \end{aligned} \tag{6.56}$$

This result shows that the reproduced field can be interpreted as the field due to a plane wave traveling in the direction $\hat{\mathbf{q}}$ (again, see the Jacobi-Anger expansion (2.56)), whose Fourier coefficients have been modulated by the term in the brackets in the equation above.

Figure 6.15 represents the field due to an acoustic monopole located at $[r_q, \theta_q, \phi_q] = [1\text{ m}, 90°, 0°]$, in the interior of Λ. Figures 6.16-6.21 report the reproduced field and the normalized reproduction error (5.31) for a focused virtual source located at $\mathbf{q}$. The source strength functions have been calculated with the different methods discussed above, namely equations (6.39), (6.42) and (6.52). In all cases, the series were truncated to the order $N = 20$, although the smooth spectral damping solution can be regarded as truncated to the order $N = 10$ for the effect of the smoothing window (6.45). The boundary $\partial\Lambda$, reported in the figures, is a sphere with radius $R_\Lambda = 1.5$ m, while the wave number is $k = 12$ rad/m.

It can be observed that the simple spectral cut-off (figures 6.16 and 6.17) allow for a very accurate reproduction within the ball $B_q := \{\mathbf{z} \in \Lambda : z < q$, while the reproduction error

is very large in the exterior of this region. The large amplitude of the reproduced field indicates that the secondary sources generate a very large amount of acoustic energy. The smooth spectral damping (figures 6.18 and 6.19) allows for the computation of a much more stable solution, which also leads to a smaller error in the exterior of B_q. On the other hand, the normalized reproduction error is larger within B_q. Finally, figures 6.20 and 6.21 illustrate the performance of the method given by equation (6.52). The average error is small in the majority of the half space Γ_{-d}, but the reproduction is inaccurate in a long and narrow region through the center of the array. This result is in accordance with what has been discussed in section 6.2.2 and in [Men09].

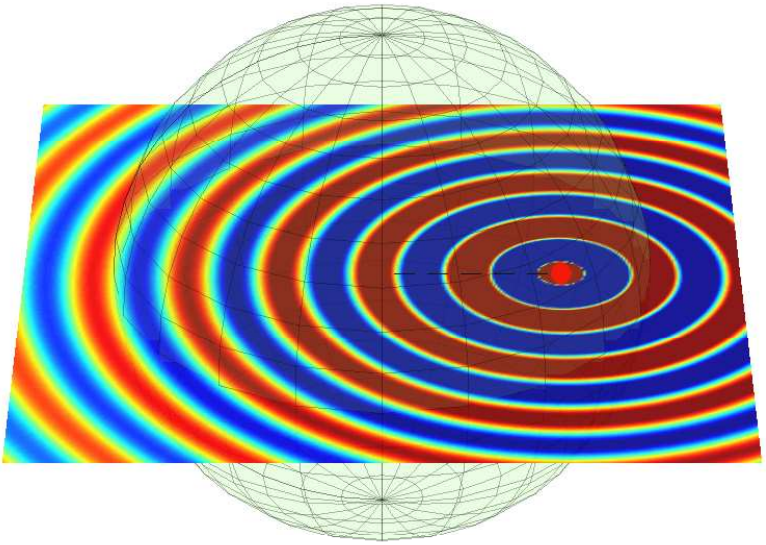

FIGURE 6.15: Horizontal cross-section of the field generated by an omnidirectional point source (red dot) located at $[r_q, \theta_q, \phi_q] = [1\,\text{m}, 90°, 0°]$. The wave number is $k = 12\,\text{rad/m}$. The sphere represents $\partial\Lambda$ and has a radius $R_\Lambda = 1.5$.

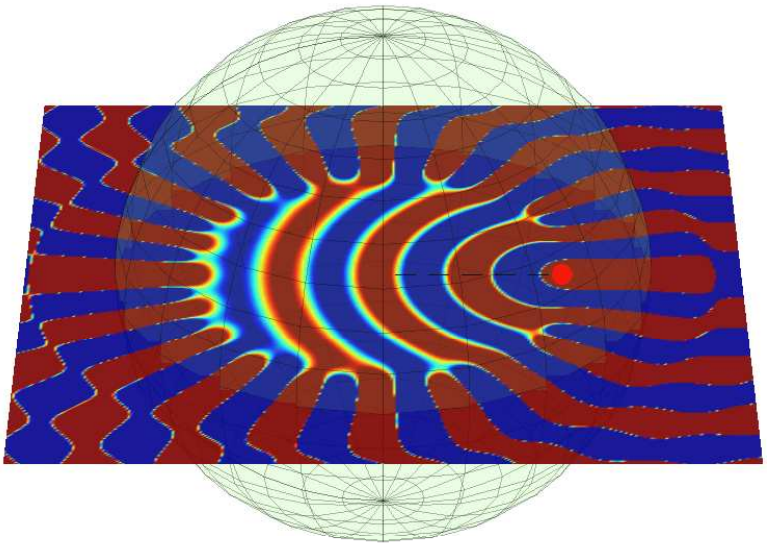

FIGURE 6.16: Horizontal cross-section of the reproduced field for a focused virtual source located at $[r_q, \theta_q, \phi_q] = [1\text{ m}, 90°, 0°]$. The source strength $a(\mathbf{y})$ was computed with equation (6.39).

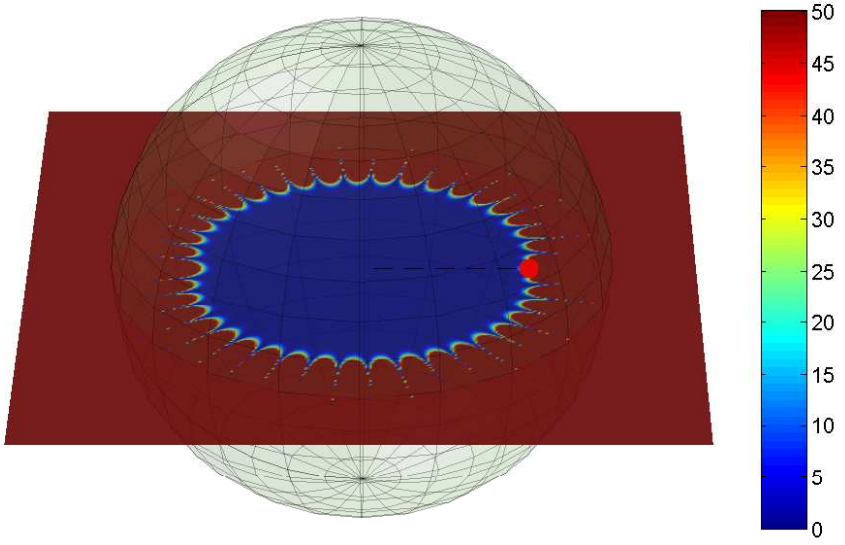

FIGURE 6.17: Horizontal cross-section of normalized reproduction error (%) for a virtual source located at $[r_q, \theta_q, \phi_q] = [1\text{ m}, 90°, 0°]$. The source strength $a(\mathbf{y})$ was computed with equation (6.39).

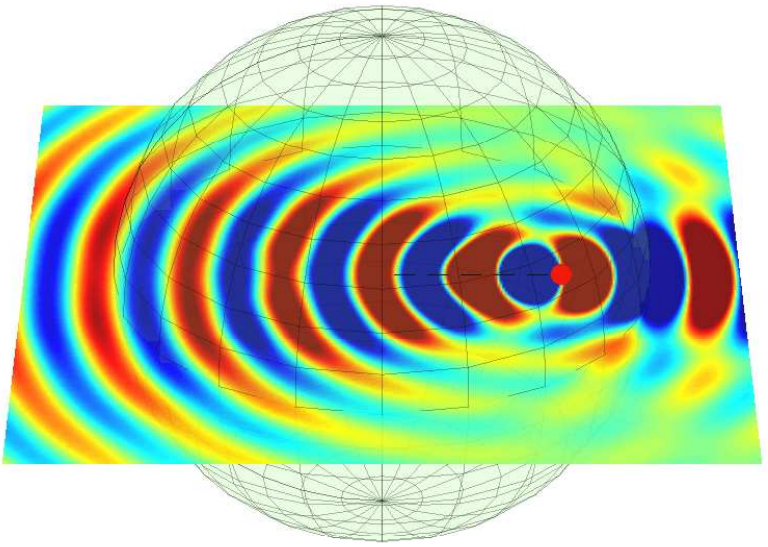

FIGURE 6.18: Horizontal cross-section of the reproduced field for a focused virtual source located at $[r_q, \theta_q, \phi_q] = [1\ \mathrm{m}, 90°, 0°]$. The source strength $a(\mathbf{y})$ was computed with equation (6.42).

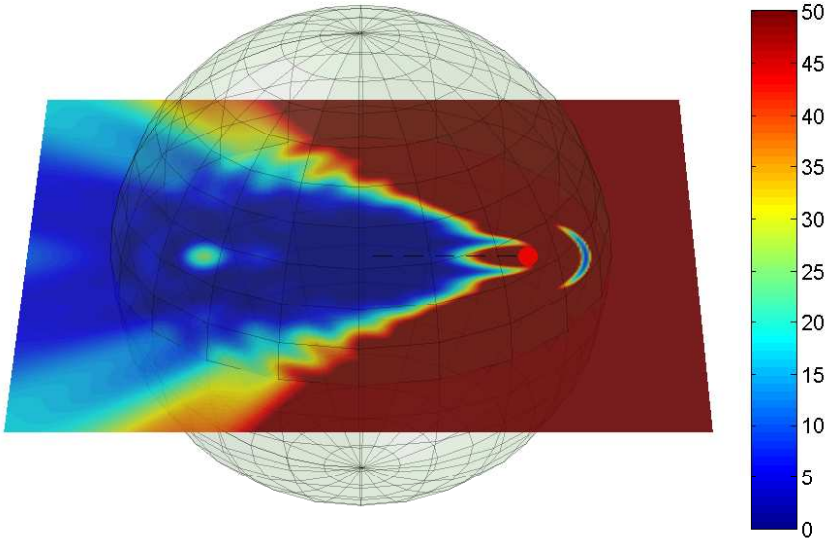

FIGURE 6.19: Horizontal cross-section of normalized reproduction error (%) for a virtual source located at $[r_q, \theta_q, \phi_q] = [1\ \mathrm{m}, 90°, 0°]$. The source strength $a(\mathbf{y})$ was computed with equation (6.42).

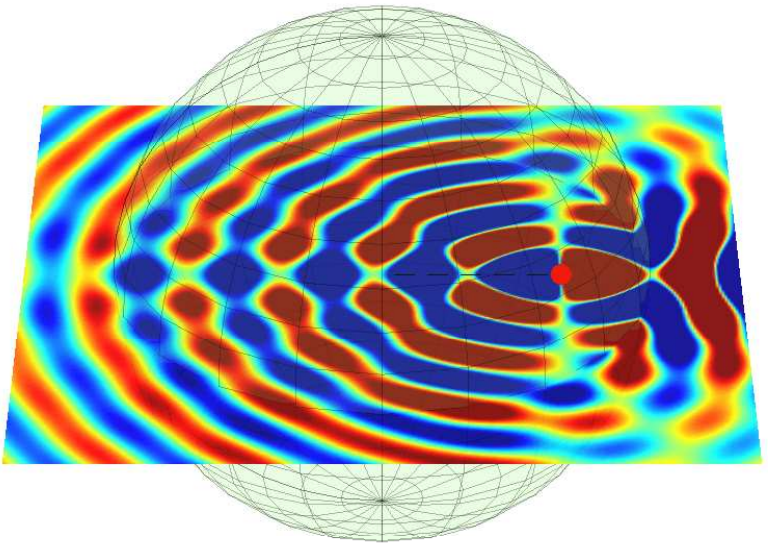

FIGURE 6.20: Horizontal cross-section of the reproduced field for a focused virtual source located at $[r_q, \theta_q, \phi_q] = [1\ \mathrm{m}, 90°, 0°]$. The source strength $a(\mathbf{y})$ was computed with equation (6.52).

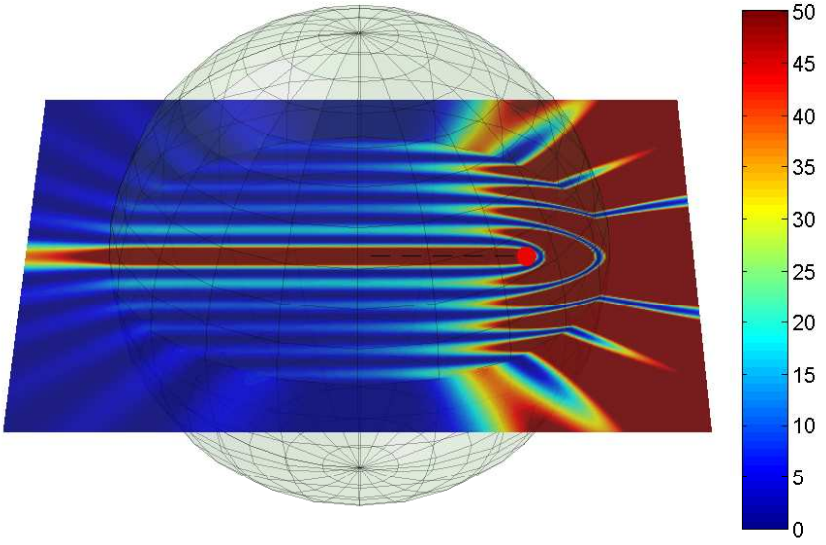

FIGURE 6.21: Horizontal cross-section of normalized reproduction error (%) for a virtual source located at $[r_q, \theta_q, \phi_q] = [1\ \mathrm{m}, 90°, 0°]$. The source strength $a(\mathbf{y})$ was computed with equation (6.52).

6.3 Strategies for overcoming the nonuniqueness of the solution

In Section 5.5 we have studied the problem of nonuniqueness of the solution, which might arise when solving the integral equation (3.19). We have seen that this problem arises when the operating wave number k corresponds to one of the Dirichlet eigenvalues k_n of the control region V (not of the reproduction region Λ). In fact, it has been shown that in this case the nullspace of S is non-trivial, and given a solution $a(\mathbf{y})$ of the integral equation under consideration, the function $a(\mathbf{y}) + a_0(\mathbf{y})$ is also a solution, where $a_0(\mathbf{y})$ can be any function belonging to the nullspace of S. On the other hand, only one of these solution allows for the reproduction of the target field in the *interior* of V (recall that, in view of the uniqueness of the interior Dirichlet problem discussed in Section 3.3, the sound control effort has been restricted to the boundary of the control region).

In what follows, several strategies are briefly presented, which allow the uniqueness problem to be overcome. As an example, we will consider the simple case of spherical geometry (the control region is a sphere of radius R_V) and the wave number equal to the Dirichlet eigenvalue k_0, that is $k = k_0$ and $j_0(k_0 R_V) = 0$. In view of the results presented in Section 5.6.1.4, we see that all functions of the form

$$a(\mathbf{y}) = \sum_{\nu=1}^{\infty} \sum_{\mu=-\nu}^{\nu} \frac{Y_\nu^\mu(\hat{\mathbf{y}})}{ikR_V^2 R_\Lambda^2 h_\nu^{(1)}(kR_\Lambda) j_\nu(kR_V)} \langle Y_\nu^\mu | p \rangle_{\partial V} + \alpha Y_0^0(\hat{\mathbf{y}}), \ \alpha \in \mathbb{C} \tag{6.57}$$

are solutions of the integral equation under consideration, but the reproduced field equals the target field in the interior of V for only one choice of the parameter α.

6.3.1 Changing the shape of the control region

Since the nonuniqueness problem is associated with the Dirichlet eigenvalues of V, and since these depend in turn on the shape of V, it is reasonable to change the shape of this region in order to overcome the nonuniqueness issue (see [BR07] for related method applied to spherical microphone arrays). Clearly, this technique can be applied only in a limited number of cases, namely when the shape of the control region is not imposed by physical constraints (such as the shape of a microphone array). On the other hand, this simple strategy proves to be very effective when the solution of the problem is computed from numerically simulated data.

In the example above, we can modify the control region and choose a sphere of radius $\tilde{R}_V \neq R_V$, such that $j_0(k\tilde{R}_V) \neq 0$. With this modification, the solution can be computed

with the usual formula (4.19), reported here in the form

$$a(\mathbf{y}) = \sum_{\nu=0}^{\infty} \sum_{\mu=-\nu}^{\nu} \frac{Y_\nu^\mu(\hat{\mathbf{y}})}{ik\tilde{R}_V^2 R_\Lambda^2 h_\nu^{(1)}(kR_\Lambda) j_\nu(k\tilde{R}_V)} \langle Y_\nu^\mu | p \rangle_{\partial V} \tag{6.58}$$

6.3.2 CHIEF points

Another method, frequently used in applications of the Boundary Element Method, consists of including some additional control points in the interior of V. The determination of the number and location of these so-called *CHIEF points* depend on the problem under consideration. This method was introduced by Schenck, who proposed in 1967 the so-called *Combined Helmholtz Integral Equation Formulation (CHIEF)* for the solution of radiation problems [Sch68].

In the case of the example above, an additional control point is introduced at the center of the coordinate systems, and the target field has at this location the value $p(0)$. Using the results presented in Chapter 4 and especially equation (4.4), it can be shown that

$$p(0) = ikj_0(0)h_0(kR_\Lambda)\langle Y_0^0 | a \rangle_{\partial\Lambda} \tag{6.59}$$

Recall that $j_\nu(0) = 0$ if $\nu \neq 0$. Combining this result with the expression (6.57) for the solution $a(\mathbf{y})$, we have that

$$\alpha = \frac{p(0)}{ikR_\Lambda^2 j_0(0)h_0(kR_\Lambda)Y_0^0(0)} \tag{6.60}$$

6.3.3 Scattering object

A further strategy is given by introducing (physically or by simulation) a scattering object in the interior of the control region, and by formulating the inverse problem using the sum of the target and scattered field (namely, the total field) in place of the target field only. This leads to the following equation

$$p_T(\mathbf{x}) = (Sa)(\mathbf{x}) + p_s(\mathbf{x}), \ \mathbf{x} \in \partial V \tag{6.61}$$

where $p_s(\mathbf{x})$ is the field scattered by the object in the interior of V and measured on ∂V, and $p_T(\mathbf{x}) = p(\mathbf{x}) + p_s(\mathbf{x})$ is the total field. If this object is such that we can compute the scattered field for a given incident field, it is possible to calculate the source strength $a(\mathbf{y})$ from the equation above.

We assume that, in the case of the example above, we introduce a rigid (sound-hard) sphere of radius $R_s \leq R_V$ n the interior of V. Using equation (4.4) it is possible to show

that the reproduced field $\hat{p}(\mathbf{x}) = (Sa)(\mathbf{x})$ can be expressed by the form

$$\begin{aligned}(Sa)(\mathbf{x}) &= \sum_{\nu=0}^{\infty} ikh_\nu^{(1)}(kR_\Lambda)j_\nu(kR_V)\sum_{\mu=-\nu}^{\nu} Y_\nu^\mu(\hat{\mathbf{x}})\langle Y_\nu^\mu|a\rangle_{\partial\Lambda} \\ &= \sum_{\nu=0}^{\infty} j_\nu(kR_V)\sum_{\mu=-\nu}^{\nu} A_{\mu\nu}Y_\nu^\mu(\hat{\mathbf{x}})\end{aligned} \tag{6.62}$$

With the manipulations presented in [Wil99], analogous to those reported in Appendix C for the sound-soft sphere, it can be shown that the scattered field is given by

$$p_s(\mathbf{x}) = \sum_{\nu=0}^{\infty} -\frac{j_\nu'(kR_s)}{h_\nu'(kR_s)}h_\nu(kR_V)\sum_{\mu=-\nu}^{\nu} A_{\mu\nu}(\omega)Y_\nu^\mu(\hat{\mathbf{x}}) \tag{6.63}$$

Combining the three equations above, the inverse problem under consideration is reformulated by

$$\begin{aligned}p_T(\mathbf{x}) &= \sum_{\nu=0}^{\infty}\left(j_\nu(kR_V) - \frac{j_\nu'(kR_s)}{h_\nu'(kR_s)}h_\nu(kR_V)\right)\sum_{\mu=-\nu}^{\nu} A_{\mu\nu}(\omega)Y_\nu^\mu(\hat{\mathbf{x}}) \\ &= \sum_{\nu=0}^{\infty} ik\left(j_\nu(kR_V)h_\nu'(kR_s) - j_\nu'(kR_s)h_\nu(kR_V)\right)\frac{h_\nu(kR_\Lambda)}{h_\nu'(kR_s)}\sum_{\mu=-\nu}^{\nu}\langle Y_\nu^\mu|a\rangle_{\partial\Lambda}Y_\nu^\mu(\hat{\mathbf{x}})\end{aligned} \tag{6.64}$$

Following mathematical manipulations analogous to those presented in Chapter 4, we obtain the following expression for the solution

$$a(\mathbf{y}) = \sum_{\nu=0}^{\infty}\sum_{\mu=-\nu}^{\nu}\frac{h_\nu'(kR_s)Y_\nu^\mu(\hat{\mathbf{y}})\langle Y_\nu^\mu|p_T\rangle_{\partial V}}{ikR_V^2R_\Lambda^2\left(j_\nu(kR_V)h_\nu'(kR_s) - j_\nu'(kR_s)h_\nu(kR_V)\right)h_\nu(kR_\Lambda)} \tag{6.65}$$

It can be observe that despite $j_0(kR_V) = 0$, the denominator of the fraction above does not equal zero for $\nu = 0$.

In the special case when $R_s = R_V$, we can apply the Wronskian relation (2.38) to equation (6.65), thus obtaining

$$a(\mathbf{y}) = \sum_{\nu=0}^{\infty}\sum_{\mu=-\nu}^{\nu} -\frac{k\,h_\nu'(kR_V)Y_\nu^\mu(\hat{\mathbf{y}})}{R_\Lambda^2 h_\nu(kR_\Lambda)}\langle Y_\nu^\mu|p_T\rangle_{\partial V} \tag{6.66}$$

This technique is often used for microphone arrays, in which the capsules are flush mounted on a rigid structure. A typical case is represented by spherical microphone arrays mounted on rigid spheres (see for example [Pol05]).

The method presented above can be also applied to scattering objects with different boundary conditions (such as sound soft objects or with impedance boundary conditions [CK92]).

6.3.4 Impedance boundary condition

It is also possible to describe the target sound field on ∂V by a linear combination of the pressure field $p(\mathbf{x})$ and of its normal derivative $\nabla_{\mathbf{n}} p(\mathbf{x})$. This represents an impedance boundary condition [CK83, p.97]. The inverse problem under consideration becomes

$$f(\mathbf{x}) = p(\mathbf{x}) + i\eta \nabla_{\mathbf{n}} p(\mathbf{x}) = (Sa)(\mathbf{x}) + i\eta \frac{\partial (Sa)(\mathbf{x})}{\partial \hat{\mathbf{n}}(\mathbf{x})}, \ \mathbf{x} \in \partial V \tag{6.67}$$

In view of the definition (3.16) of the operator S, the equation above is rewritten by

$$f(\mathbf{x}) = \int_{\partial \Lambda} \left[G(\mathbf{x}, \mathbf{y}) + i\eta \frac{\partial G(\mathbf{x}, \mathbf{y})}{\partial \hat{\mathbf{n}}(\mathbf{x})} \right] a(\mathbf{y}) dS(\mathbf{y}), \ \mathbf{x} \in \partial V \tag{6.68}$$

It can be easily understood that the function $p(\mathbf{x})$ can be interpreted, in practical terms, as the target field measured by a continuous distribution of ideal omnidirectional microphones arranged on ∂V. Analogously, the function $f(\mathbf{x}) = p(\mathbf{x}) + i\eta \nabla_{\mathbf{n}} p(\mathbf{x})$ can be regarded as the measurement of the target field with a continuous distribution of ideal *directional* microphones. In fact, directional microphones can be regarded as devices capable of measuring a combination of the pressure field and of its spatial derivative in a given direction.

For the example with spherical geometry considered above, using equation (4.4) we can rewrite equation (6.68) as

$$f(\mathbf{x}) = \sum_{\nu=0}^{\infty} ikh_{\nu}^{(1)}(kR_{\Lambda}) (j_{\nu}(kR_V) + i\eta k j_{\nu}'(kR_V)) \sum_{\mu=-\nu}^{\nu} Y_{\nu}^{\mu}(\hat{\mathbf{x}}) \langle Y_{\nu}^{\mu} | a \rangle_{\partial \Lambda}, \ \mathbf{x} \in \partial V \tag{6.69}$$

Applying again manipulations analogous to those presented in Chapter 4, we obtain the following expression for the solution

$$a(\mathbf{y}) = \sum_{\nu=0}^{\infty} \sum_{\mu=-\nu}^{\nu} \frac{Y_{\nu}^{\mu}(\hat{\mathbf{y}})}{ikR_V^2 R_{\Lambda}^2 \left(j_{\nu}(kR_V) + i\eta k j_{\nu}'(kR_V) \right) h_{\nu}(kR_{\Lambda})} \langle Y_{\nu}^{\mu} | f \rangle_{\partial V} \tag{6.70}$$

As in the previous case, although $j_0(kR_V) = 0$, the denominator of the fraction above does not equal zero for any ν.

6.4 Analogy with NAH and with the theory of acoustic scattering

6.4.1 Sound field reproduction and Near-Field Acoustical Holography

In Section 5.7 it has been argued that the stability of the solution $a(\mathbf{y})$ depends also upon the distance between the boundaries ∂V and $\partial\Lambda$. More precisely, the larger is the distance between the two surfaces (or contours for the 2D problem), the steeper is the decay of the singular values σ_n of the integral operator S.

A further insight into this phenomenon is provided by an analogy with Near-Field Acoustical Holography (NAH). We assume that we want to determine the normal particle velocity $\dot{w}(\mathbf{y})$ of the acoustic field on $\partial\Lambda$ from a set of measurement of the field $p(\mathbf{x})$ on ∂V. It is assumed here that a continuous measurement of the pressure field on ∂V is provided. As described by Williams [Wil99], this operation can be achieved by constructing an *inverse velocity propagator*. This operation is expressed explicitly for the spherical and planar geometry respectively by [2] :

$$\dot{w}(\mathbf{y}) = \frac{1}{i\rho_0 ck}\sum_{\nu=0}^{\infty}\frac{kj'_\nu(kR_\Lambda)}{R_V^2 j_\nu(kR_V)}\sum_{\mu=-\nu}^{\nu}Y_\nu^\mu(\hat{\mathbf{y}})\langle Y_\nu^\mu|p\rangle_{\partial V} \tag{6.71}$$

$$\dot{w}(\mathbf{y}) = \frac{1}{i\rho_0 ck}\mathcal{F}^{-1}\left[(\mathcal{F}p)\frac{i\zeta(\cdot)}{e^{i\zeta(\cdot)d}}\right] \tag{6.72}$$

We want to compare now these equations with the expression for the solution $a(\mathbf{y})$ provided by (4.19) and (4.85), respectively. It can be observed that, apart from the term $i\rho_0 ck$ arising from the Euler's equation (see, for example, [Wil99, p.19]), equations (4.85) and (6.72) differ only for the factor 2 (which hides, as we will see later, a very important meaning).

The term $(ikR_\Lambda^2 h_\nu(kR_\Lambda))^{-1}$ in equation (4.19) is substituted in equation (6.71) by the term $kj'_\nu(kR_\Lambda)$. Considering the high order expansion of spherical Bessel and Hankel functions given by equations (2.39) and (2.40), respectively, we observe that

$$kj'_\nu(kR_\Lambda) = k\frac{d}{d(kR_\Lambda)}\left(\frac{(kR_\Lambda)^\nu}{(2\nu+1)!!}\right) = \nu\frac{(kR_\Lambda)^\nu}{R_\Lambda(2\nu+1)!!}, \quad \nu\to\infty \tag{6.73}$$

$$\frac{1}{ikR_\Lambda^2 h_\nu^{(1)}(kR_\Lambda)} = \frac{1}{ikR_\Lambda^2}\frac{i(kR_\Lambda)^{\nu+1}}{(2\nu-1)!!} = (2\nu+1)\frac{(kR_\Lambda)^\nu}{R_\Lambda(2\nu+1)!!}, \quad \nu\to\infty \tag{6.74}$$

[2] In comparison with Equation (7.13) in [Wil99], the factor R_V^2 in the denominator of (6.71) has been added, as $\langle\cdot|\cdot\rangle_\Omega = \langle\cdot|\cdot\rangle_{\partial V}/R_V^2$, where Ω is the unitary sphere. Also, the factor k_z appearing in Equation (3.4) in [Wil99] has been substituted by $\zeta(\kappa)$ and the argument of the exponential $ik_z(z-z_h)$ has been substituted by $-i\zeta(\kappa)d$.

We observe that the asymptotic expression for the radial term in equation (6.71), after having removed the singular functions normalization factor$(R_\Lambda R_V)^{-1}$, is given by

$$\frac{kj'_\nu(kR_\Lambda)}{R_V^2 j_\nu(kR_V)} = \frac{\nu}{R_V}\left(\frac{R_\Lambda}{R_V}\right)^\nu \quad \nu \to \infty \tag{6.75}$$

This compares well (although it is not identical!) with the inverse of the large order approximation of the singular values given by equation (4.15) and that is repeated here:

$$\frac{1}{\sigma_n} = \frac{2\nu+1}{R_V}\left(\frac{R_\Lambda}{R_V}\right)^\nu \quad \nu \to \infty \tag{6.76}$$

These considerations shows that the ill-conditioning of the sound field reproduction problem addressed here, determined by the decay of the singular values of S, is analogous, though not identical, to the ill-conditioning of the Near-Field Acoustical Holography problem of determining the normal particle velocity on $\partial\Lambda$ from measurements on ∂V. More specifically, if we consider the forward velocity propagator to be an operator, we can observe that its singular values exhibit an exponential decay identical to the singular values of the inverse operator S^{-1}, and this exponential decay is governed by the distance between ∂V and $\partial\Lambda$. It should be noticed that the linear part of the two decays is different: in the spherical geometry, we have $1/\nu$ for the velocity propagator and $1/(2\nu+1)$ for S, while for the planar geometry we have $|\zeta(\kappa)|$ and $2|\zeta(\kappa)|$, respectively.

In view of these considerations, it is reasonable to address the following problem: what happens when the control region and the reproduction region are the same ($V = \Lambda$)? In this case, the asymptotic decay of the singular values is dominated by a linear factor, and the problem is therefore said to be *mildly ill-posed*. As is clear from the holography problem discussed above, the linear decay of the singular values is due to the operation of taking the derivative of the field in order to obtain its normal derivative.

At this point, it could be intuitively argued that the source strength $a(\mathbf{y})$ and the normal derivative of the field on $\partial\Lambda$ are strictly related. This is not surprising, if we consider the first Rayleigh integral (see equation (6.88) or [Wil99]). We will see that a relation actually exists, but it is not an identity.

6.4.2 Jump relation and simple source formulation

We consider the case when $V = \Lambda$. In chapter 5 it has been shown that any sound field due to a source outside the reproduction region can be reproduced exactly, or in other words it can be represented by the single layer potential (3.15) in $\partial\Lambda$. We define the sound field generated by the potential in Λ the *interior field* $p_i(\mathbf{z})$, and the field in the

region $\mathbb{R}^m \backslash \overline{\Lambda}$, $m = 2, 3$ the *exterior field* $p_e(\mathbf{z})$. In mathematical terms this reads

$$p_i(\mathbf{z}) := (Sa)(\mathbf{z}), \quad \mathbf{z} \in \Lambda \tag{6.77}$$

$$p_e(\mathbf{z}) := (Sa)(\mathbf{z}), \quad \mathbf{z} \in \mathbb{R}^3 \backslash \overline{\Lambda} \tag{6.78}$$

If the density $a(\mathbf{y})$ is continuous, the single layer potential (3.15) is continuous throughout $\mathbb{R}^m$, $m = 2, 3$ [CK92], implying that

$$p_i(\mathbf{y}) = p_e(\mathbf{y}), \quad \mathbf{y} \in \partial\Lambda \tag{6.79}$$

p_i and p_e represent two different fields, defined on different domains and each with a different physical nature. Even though the two fields have the same value on $\partial\Lambda$, the values of their normal derivatives $\nabla_{\mathbf{n}} p_i$ and $\nabla_{\mathbf{n}} p_e$ are in general different. The difference, or *jump*, between the normal derivatives is physically due to the presence of the layer of secondary sources on $\partial\Lambda$, which determine a discontinuity in the gradient of the single layer potential (3.15). This difference is given by the jump relation (2.102), which is reported again here in the form

$$a(\mathbf{y}) = \nabla_{\mathbf{n}} p_i(\mathbf{y}) - \nabla_{\mathbf{n}} p_e(\mathbf{y}), \quad \mathbf{y} \in \partial\Lambda \tag{6.80}$$

If we choose the interior field $p_i(\mathbf{z})$ to be equal to the desired sound field $p(\mathbf{z})$ in Λ, then the jump relation provides the expression for the secondary source strength function $a(\mathbf{y})$, which allows a perfect reproduction of the desired field in Λ. It is therefore possible to write the following expression

$$p(\mathbf{z}) = \int_{\partial\Lambda} G(\mathbf{z}, \mathbf{y}) [\nabla_{\mathbf{n}} p_i(\mathbf{y}) - \nabla_{\mathbf{n}} p_e(\mathbf{y})] dS(\mathbf{y}), \quad \mathbf{z} \in \Lambda \tag{6.81}$$

This result is perfectly consistent with the *Simple Source Formulation* presented in [Wil99]. The arguments presented here represent a different method for obtaining the same result. In order to obtain the source strength from the complete knowledge of the desired sound field, we need to compute the normal derivative of the exterior field, $\nabla_{\mathbf{n}} p_e(\mathbf{y})$.

6.4.3 Equivalent scattering problem

We assume now that $\partial\Lambda$ does not represent anymore the secondary source layer, but it represents instead the boundary of an impenetrable scattering object. If the desired sound field $p(\mathbf{z})$ impinges on this scattering object, a *scattered sound field* $p_s(\mathbf{z})$ is generated. This field is a radiating solution of the Helmholtz equation [CK92], thus

representing the solution to an exterior problem. The sum of the (incident) field $p(\mathbf{z})$ and of the scattered field $p_s(\mathbf{z})$ gives the *total field* $p_T(\mathbf{z})$.

The scattering object Λ is assumed to be a *sound soft object*, or in other words an idealized object with pressure release boundaries. In mathematical terms, this corresponds to the following boundary condition:

$$p_T(\mathbf{y}) = 0, \quad \mathbf{y} \in \partial\Lambda \tag{6.82}$$

This means that the acoustic pressure of the total sound field equals zero on the boundary of the scattering object. As we have seen, this condition is referred to as the *homogeneous Dirichlet boundary condition*.

Under these assumptions and given a target/incident field $p(\mathbf{z})$, it can be easily seen that

$$p_s(\mathbf{y}) = -p(\mathbf{y}), \quad \mathbf{y} \in \partial\Lambda \tag{6.83}$$

Recalling the definition of the exterior field given above, in view of equation (6.79) and of the uniqueness of the exterior Dirichlet problem [CK83], it can be easily seen that

$$p_s(\mathbf{z}) = -p_e(\mathbf{z}), \quad \mathbf{x} \in \mathbb{R}^m \backslash \Lambda, \ m = 2, 3 \tag{6.84}$$

In view of this result and of the definition of $p_T(\mathbf{z})$ given above, it is possible to rewrite equation (6.81) as follows

$$\int_{\partial\Lambda} G(\mathbf{z}, \mathbf{y}) \nabla_{\mathbf{n}} p_T(\mathbf{y}) dS(\mathbf{y}) = \begin{cases} p(\mathbf{z}), & \mathbf{x} \in \overline{\Lambda} \\ -p_s(\mathbf{z}), & \mathbf{x} \in \mathbb{R}^3 \backslash \Lambda \end{cases} \tag{6.85}$$

This meaningful result can be summarized by the following sentence:

Given a desired field $p(\mathbf{x})$ and a continuous distribution of monopole-like sources on $\partial\Lambda$, we wish to compute the function $a(\mathbf{y})$, representing the strength of these sources, which allows for an exact reproduction of the desired field in Λ. This function is equal to the normal derivative of the total field $p_T(\mathbf{y})$ on $\partial\Lambda$, which is generated by the scattering of the desired field by a sound soft object with the shape of Λ.

This result completes the discussion on the analogy with Near-Field Acoustical Holography, since it shows that the source strength $a(\mathbf{y})$ is not exactly equal to the normal derivative of the target field on Λ, but it is rather equal to the normal derivative of the *total* field (incident+scattered) on Λ.

Equation (6.85) represents also an important result with respect to the exterior field:

The sound field generated by the layer of secondary sources in the exterior region $\mathbb{R}^m \backslash \Lambda, \ m = 2, 3$ equals to the scattered field, with phase shifted of 180°.

For the case of Λ being a sphere with radius R_Λ, the total scattered field on $\partial\Lambda$ is derived in appendix C and is given by

$$\nabla_{\mathbf{n}} p_T(\mathbf{y}) = \sum_{\nu=0}^{\infty} \sum_{\mu=-\nu}^{\nu} \frac{A_{\mu\nu}}{ikR_\Lambda^2 h_\nu(kr)} Y_\nu^\mu(\hat{\mathbf{y}}) \tag{6.86}$$

where, assuming that $j_\nu(kR_\Lambda) \neq 0$ (namely, k in not one of the Dirichlet eigenvalues for V), $A_{\mu\nu}$ is given by [Wil99]

$$A_{\mu\nu} = \frac{\langle Y_\nu^\mu | p \rangle_{\partial\Lambda}}{R_\Lambda^2 j_\nu(kR_\Lambda)} \tag{6.87}$$

As expected, this expression coincides with the expression for $a(\mathbf{y})$ given by equation (4.19) for the case of $R_V = R_\Lambda$.

We consider the case of $\partial\Lambda$ being an infinite plane and we study the acoustic scattering by a pressure release infinite plane $\partial\Lambda$. We assume that the incident field is due to a monopole source with strength $\ddot{m}$ at a distance d, say, from the plane. It can be seen that the scattered sound field is equivalent to that generated by a mirror source, specular in respect to the scattering plane to the monopole source generating the incident field, but with phase-reversed strength $-\ddot{m}$. This scattered field satisfies the pressure release boundary condition $p_T = 0$ on the scattering plane. From simple geometrical considerations it follows that the normal derivative of the scattered acoustic field equals the normal derivative of the incident field. Therefore, the normal derivative of the total pressure field, $\nabla_{\mathbf{n}} p_T$, equals twice the normal derivative of the incident field. This argument can be extended to any sound field of interest. If this result is substituted into the jump relation (6.80), we see that the single layer potential reduces to the first Rayleigh integral formula [Wil99]:

$$p(\mathbf{x}) = \int_{\partial\Lambda} G(\mathbf{x}, \mathbf{y}) 2\nabla_{\mathbf{n}} p(\mathbf{y}) dS(\mathbf{y}) \tag{6.88}$$

This result is perfectly consistent with the expression of $a(\mathbf{y})$ given by equation(4.85). In view of equation (6.72) and assuming that $\hat{\mathbf{n}} = [\,0,\ 0, -1]$, we can indeed observe that

$$2\nabla_{\mathbf{n}} p(\mathbf{y}) = -2(i\rho_0 ck)\dot{w}(\mathbf{y}) = -2\mathcal{F}^{-1}\left[(\mathcal{F}p)\frac{i\zeta(\cdot)}{e^{i\zeta(\cdot)d}}\right](\mathbf{y}) = a(\mathbf{y}) \tag{6.89}$$

where the last equality is due to equation (4.85).

6.4.4 High frequency scattering and the Kirchhoff approximation

The result derived for the infinite plane proves to be useful also for different geometries involving a compact and convex set Λ when the wave length considered, $\lambda = 2\pi/k$, is much smaller than the characteristic dimension of Λ. The characteristic dimension can be thought as the radius of the smallest sphere that fully encloses Λ.

In this high frequency case, as suggested by Colton and Kress [CK92, p.54], it is possible to solve the scattering problem using the *Kirchhoff approximation* of the total field. As a first step, we divide the boundary $\partial\Lambda$ into the so called *illuminated region* $\partial\Lambda_-$ and the *shadow region* $\partial\Lambda_+$. They correspond to the portions of $\partial\Lambda$ which are illuminated and not illuminated, respectively, by the incident field. For example, in the case of an incident plane wave traveling in the direction $\mathbf{k}$, these two regions correspond respectively to [CK92]

$$\partial\Lambda_- = \{\mathbf{y} \in \partial\Lambda : \mathbf{y} \cdot \mathbf{k} < 0\} \tag{6.90}$$

$$\partial\Lambda_+ = \{\mathbf{y} \in \partial\Lambda : \mathbf{y} \cdot \mathbf{k} \geq 0\} \tag{6.91}$$

In the specific case of Λ being a sphere, these two regions correspond to two hemispheres.

Two relevant approximation are made:

- In the shadow region $\partial\Lambda_+$, the total field $p_T(\mathbf{y})$ and its normal derivative $\nabla_{\mathbf{n}} p_T(\mathbf{y})$ equal zero.
- In the illuminated area $\partial\Lambda_-$, the scattering object can be considered locally as a plane. Therefore, as shown in Section 6.4.3, the normal derivative of the total field $\nabla_{\mathbf{n}} p_T(\mathbf{y})$ equals twice the normal derivative of the incident field $\nabla_{\mathbf{n}} p_i(\mathbf{y})$.

These approximations can be expressed mathematically as follows:

$$\nabla_{\mathbf{n}} p_T(\mathbf{y}) = \begin{cases} 2\nabla_{\mathbf{n}} p(\mathbf{y}), & \mathbf{y} \in \partial\Lambda_- \\ 0, & \mathbf{y} \in \partial\Lambda_+ \end{cases} \tag{6.92}$$

Inserting these formulae in equation 6.85, we obtain the following result:

$$p(\mathbf{x}) \approx \int_{\partial\Lambda_-} G(\mathbf{x}, \mathbf{y}) 2\nabla_{\mathbf{n}} p(\mathbf{y}) dS(\mathbf{y}), \quad \mathbf{x} \in \Lambda \tag{6.93}$$

In practical terms, this meaningful result implies that:

If the wavelength is much smaller than the size of the reproduction region, the solution of the sound field reproduction problem can be computed by applying the Kirchhoff approximation. This implies that only the secondary sources in the illuminated region are active, and that their strength equals twice the normal derivative of the target field.

This result is analogous to the Wave Field Synthesis approach with an analytical secondary source selection criterion, proposed by Spors [Spo07], derived from the Kirchhoff-Helmholtz integral.

As mentioned above, this result is a high frequency approximation of the more general result given by equation (6.85), and does not produce an accurate reproduction of the

desired field when the wavelength considered is comparable to the size of Λ. On the other hand, this approach allows for an explicit and simple computation of the source strength function $a(\mathbf{y})$ in terms of the normal derivative of the incident field, with no need to solve a (usually non trivial) scattering problem.

Chapter 7

Towards the practical realization of a sound field reproduction system

The theoretical results presented in the previous chapters have been derived under two relevant assumptions, namely:

- An infinite number of secondary sources is continuously distributed on the boundary of the reproduction area.
- The operating frequency ω and therefore the wave number k are fixed.

Although these two assumptions have proved useful for deriving the results shown in the previous chapters, they need to be removed when these theoretical results are applied to real multi-channel audio systems. Such systems clearly include a finite number of secondary sources, and they usually operate on a broad range of audio frequencies.

In the first section of this chapter the consequences are studied of the discretization of the secondary source distribution. It is clear that the use of a finite number of secondary sources instead of a continuous distribution generates reproduction artifacts. These artifacts are studied in detail, with special attention to the problem of spatial aliasing. This and other phenomena described below are well-known and discussed also in the literature dedicated to sampling theory (see for example, [Hig96] and [Mar01]). The cases of spherical and linear geometry are analyzed with a greater level of detail.

The second section of this chapter is dedicated to an alternative method for solving the sound field reproduction problem under consideration. This technique may be regarded as a Boundary Element Method and involves directly the discretization of the single layer potential S, which assumes the form of a matrix, and of both the source strength $a(\mathbf{y})$ and the pressure profile $p(\mathbf{x})$, which are therefore represented by vectors. The solution of the problem involves a matrix inversion. It is demonstrated that in the limiting case

of a continuous distribution of sampling points on ∂V and $\partial\Lambda$, this method is equivalent to the solution of the integral equation discussed in the previous chapters of this thesis.

The last section of this chapter is concerned with the extension of the sound field reproduction problem to sound fields characterized by a broad-band frequency content rather than by a single frequency. This analysis leads to the formulation of time domain functions, corresponding to the signals driving the loudspeakers of a real sound field reproduction system. In some special cases, such as the reproduction of the field generated by a single motionless source, these signals can be obtained by convolving a single signal with a set of FIR filters, one for each loudspeaker. Explicit expressions for these filters are derived for the special cases of spherical, circular, linear and planar geometry.

7.1 Discretization of the driving function

We assume now that the continuous distribution of secondary sources on $\partial\Lambda$ is substituted by an array of $L < \infty$ secondary sources on $\partial\Lambda$. This passage implies that the single layer potential (3.15) is substituted by the following sum

$$\hat{p}(\mathbf{z}) = \sum_{\ell=1}^{L} G(\mathbf{z}, \mathbf{y}_\ell)\, \ddot{m}_\ell, \quad \mathbf{z} \in \mathbb{R}^{2,3} \tag{7.1}$$

Recalling the definition of $\ddot{m}$ given in Section 3.2, we observe that the $\ddot{m}_\ell$ is the strength of the ℓ-th secondary source, located at $\mathbf{y}_\ell \in \partial\Lambda$, and plays here the role that $a(\mathbf{y})dS(\mathbf{y})$ plays in the single layer potential (it is recalled that $a(\mathbf{y})$ is actually defined as the source strength *density*). Equation (7.1) clearly represents the linear superposition of the sound field generated by the L secondary sources.

7.1.1 Sampling scheme

We refer to the arrangement of the L secondary sources on $\partial\Lambda$, that is the set of locations $\mathbf{y}_\ell$, as the *sampling scheme*. Assuming $\partial\Lambda$ bounded, it is possible to associate to the sampling scheme a partitioning of $\partial\Lambda$ into Dirichlet (or Voronoi) cells D_ℓ. These are defined by [SK97]

$$D_\ell := \{\mathbf{y} \in \partial\Lambda : ||\mathbf{y} - \mathbf{y}_\ell||_{\partial\Lambda} = \min_{1 \le j \le L} ||\mathbf{y} - \mathbf{y}_j||_{\partial\Lambda}\}, \quad \ell = 1, 2, ...L \tag{7.2}$$

where $||\mathbf{y} - \mathbf{y}_\ell||_{\partial\Lambda}$ defines the distance on $\partial\Lambda$ between $\mathbf{y}$ and $\mathbf{y}_\ell$. It holds that [SK97]

$$\bigcup_{\ell=1}^{L} D_\ell = \partial\Lambda$$

$$D_\ell \cup D_{\ell'} \qquad \text{has empty interior.}$$

These expressions mean that the regions D_ℓ cover all $\partial\Lambda$ and that they do not overlap.

Each D_ℓ has a surface (or length, for the 2D problem) equal to ΔS_ℓ. It is clear that

$$\sum_{\ell=1}^{L} \Delta S_\ell = \int_{\partial\Lambda} dS \tag{7.3}$$

This formula represents the area or length of $\partial\Lambda$.

7.1.2 Quadrature of S and sampling of $a(\mathbf{y})$

Expression (7.1) can be interpreted as a quadrature formula of the integral representing the single layer potential. In order to show this, we subdivide the surface $\partial\Lambda$ into the L Dirichlet cells defined above. We then assume that

$$\int_{D_\ell} G(\mathbf{z},\mathbf{y})a(\mathbf{y})dS(\mathbf{y}) \approx G(\mathbf{z},\mathbf{y}_\ell)a(\mathbf{y}_\ell)\Delta S_\ell, \quad \ell = 1,2,...L, \quad \mathbf{z}\in\Lambda \tag{7.4}$$

If this approximation is accurate, we see that the single layer potential (3.15) can be rewritten in the following form:

$$(Sa)(\mathbf{z}) = \int_{\partial\Lambda} G(\mathbf{z},\mathbf{y})a(\mathbf{y})dS(\mathbf{y}) \approx \sum_{\ell=1}^{L} G(\mathbf{z},\mathbf{y}_\ell)a(\mathbf{y}_\ell)\Delta S_\ell \tag{7.5}$$

A comparison of this expression with equation (7.1) leads to the following result:

$$\ddot{m}_\ell = a(\mathbf{y}_\ell)\Delta S_\ell \tag{7.6}$$

which shows a possible expression of the source strength $\ddot{m}_\ell$ as a function of the source strength density $a(\mathbf{y})$ and of the sampling scheme adopted.

We can derive the same expression using the single layer potential (3.15), but substituting the density $a(\mathbf{y})$ with the sampled density $a_s(\mathbf{y})$ given by

$$a_s(\mathbf{y}) = \sum_{\ell=1}^{L} a(\mathbf{y})\delta_{\partial\Lambda}(\mathbf{y}-\mathbf{y}_\ell)\Delta S_\ell \tag{7.7}$$

Using this formula as the density of the single layer potential S and in view of the property (2.29) of the Dirac delta function we obtain the following result:

$$(Sa_s)(\mathbf{z}) = \int_{\partial\Lambda} G(\mathbf{z},\mathbf{y})a_s(\mathbf{y})dS(\mathbf{y}) = \sum_{\ell=1}^{L} G(\mathbf{z},\mathbf{y}_\ell)a(\mathbf{y}_\ell)\Delta S_\ell \tag{7.8}$$

This shows that substituting the density $a(\mathbf{y})$ with its sampled version $a_s(\mathbf{y})$ is equivalent to applying the quadrature method given by equation (7.5).

If the single layer potential Sa with continuous density provides an exact reproduction of the desired field, this is generally not the case for the single layer potential Sa_s, with sampled density. As we have seen, the accuracy of the reproduction depends on the accuracy of the approximation given by equation (7.4). This is a very critical step of the quadrature method, which might or might not lead to a sensible approximation of the target field. The validity of the approximation (7.4) depends clearly on the functions $a(\mathbf{y})$ and $G(\mathbf{z}, \mathbf{y})$ and on the sampling scheme adopted. It is possible that the approximation is accurate for some cells D_ℓ and/or for some locations $\mathbf{z} \in \Lambda$, while it might not be accurate for others (this is usually the case for strongly non-uniform sampling schemes). If this approximation is very inaccurate, serious reproduction artifacts might occur.

The approximation given by equation (7.4) can be justified by arguments analogous to those presented, for example, by Rayleigh [Ray97]: if the characteristic dimension of D_ℓ is small in comparison to the operating wave length $\lambda = 2\pi/k$ and in comparison to the distance $|\mathbf{y}_\ell - \mathbf{z}|$, then the kernel of the integral in the left hand side of (7.4) can be taken out of the integral, thus obtaining

$$\int_{D_\ell} G(\mathbf{z}, \mathbf{y}) a(\mathbf{y}) dS(\mathbf{y}) \approx G(\mathbf{z}, \mathbf{y}_\ell) \int_{D_\ell} a(\mathbf{y}) dS(\mathbf{y}) \tag{7.9}$$

where $\mathbf{y}_\ell$ is assumed to coincide with the centroid of the cell D_ℓ (this assumption is accurate for a uniform sampling scheme). This expression can be further reduced to (7.4) under the assumption that $a(\mathbf{y})$ is almost uniform over D_ℓ. This clearly depends on the smoothness of the function $a(\mathbf{y})$, which is in turn related to the wave number k (and hence to ω) and to the characteristics of the target field - as it has been observed in Section 5.6, $a(\mathbf{y})$ is smoother the farther is the location $\mathbf{q}$ of the virtual source. These considerations lead to the intuitive consequence that the accuracy of the approximation depends largely on the operating frequency ω as well as on the denseness of the sampling scheme adopted (that is the number of cells per unit of area or length).

7.1.3 Spatial aliasing and sampling reproduction error.

We have seen that the discretization of the single layer potential, or equivalently the sampling of its density, might lead to reproduction artifacts. In what follows, the analysis of these errors is presented.

We define the sampling reproduction error $\epsilon_s(\mathbf{z})$ as the difference between the target and reproduced sound field:

$$\epsilon_s(\mathbf{z}) = p(\mathbf{z}) - \hat{p}(\mathbf{z}) = (Sa)(\mathbf{z}) - (Sa_s)(\mathbf{z}), \quad \mathbf{z} \in \Lambda \tag{7.10}$$

We want to express this error by means of the singular system $\sigma_n, a_n(\mathbf{y}), p_n(\mathbf{x})$ of the operator S. In Section 3.5.3 it has been shown that the representation

$$(Sa)(\mathbf{x}) = \sum_{n=1}^{\infty} p_n(\mathbf{x}) \sigma_n \langle a_n | a \rangle_{\partial\Lambda} \tag{7.11}$$

(corresponding to equation (3.24)) is generally valid only for $\mathbf{x} \in \partial V$. It can however be extended to Λ for arrangements including separable geometries, such as those discussed in Chapter 4, for which the Helmholtz equation can be solved by separation of variables. We will consequently limit the error analysis to the pressure profile $p(\mathbf{x})$, $\mathbf{x} \in \partial V$ for the general case, and will extend the study to the entire reproduction region Λ for some special geometries.

As a first step, we consider the sampled version of the solution given by equation (3.28), which is given by

$$a_s(\mathbf{y}) = \sum_{\ell=1}^{L} \delta_{\partial\Lambda}(\mathbf{y} - \mathbf{y}_\ell) \left(\sum_{n=1}^{\infty} a_n(\mathbf{y}) \frac{1}{\sigma_n} \langle p_n | p \rangle_{\partial V} \right) \Delta S_\ell \tag{7.12}$$

We are assuming that a continuous description of the target pressure profile is provided ($p(\mathbf{x})$ is not sampled). The scalar product of a_s with the singular function a_n is therefore given by

$$\begin{aligned} \langle a_n | a_s \rangle_{\partial\Lambda} &= \int_{\partial\Lambda} a_n(\mathbf{y})^* a_s(\mathbf{y}) dS(\mathbf{y}) \\ &= \sum_{m=1}^{\infty} \frac{1}{\sigma_m} \langle p_m | p \rangle_{\partial V} \sum_{\ell=1}^{L} \left(\int_{\partial\Lambda} \delta_{\partial\Lambda}(\mathbf{y} - \mathbf{y}_\ell) a_n(\mathbf{y})^* a_m(\mathbf{y}) dS(\mathbf{y}) \right) \Delta S_\ell \\ &= \sum_{m=1}^{\infty} \frac{1}{\sigma_m} \langle p_m | p \rangle_{\partial V} \sum_{\ell=1}^{L} a_n(\mathbf{y}_\ell)^* a_m(\mathbf{y}_\ell) \Delta S_\ell \end{aligned} \tag{7.13}$$

where the last equality has been derived by applying the property (2.29) of the Dirac delta function.

7.1.3.1 Orthogonality matrix

We define the *orthogonality matrix* $\mathbf{R}$ as follows:

$$R_{n,m} := \sum_{\ell=1}^{L} a_n(\mathbf{y}_\ell)^* a_m(\mathbf{y}_\ell) \Delta S_\ell \tag{7.14}$$

It can be noticed that this formula is the discretized version of the orthogonality relation (2.111) of the singular functions, that is $\langle a_n | a_m \rangle_{\partial\Lambda} = \delta_{n,m}$. We can observe that $\mathbf{R}$ is Hermitian, since $R_{n,m} = R^*_{m,n}$, and that both of its dimensions are infinite. This matrix contains the information on whether the sampled singular functions preserve

their orthogonality or not. More specifically, the elements of $\mathbf{R}$ can be interpreted as the scalar products of one sampled mode $a_{m,s}$ with a non-sampled mode a_n. In fact, we observe that

$$a_{m,s}(\mathbf{y}) = \sum_{\ell=1}^{L} a_m(\mathbf{y})\delta_{\partial\Lambda}(\mathbf{y}-\mathbf{y}_\ell)\Delta S_\ell \tag{7.15}$$

$$\begin{aligned}\langle a_n|a_{m,s}\rangle_{\partial\Lambda} &= \int_{\partial\Lambda} a_n(\mathbf{y})^* \sum_{\ell=1}^{L} a_m(\mathbf{y})\delta_{\partial\Lambda}(\mathbf{y}-\mathbf{y}_\ell)\Delta S_\ell \, dS(\mathbf{y}) \\ &= \sum_{\ell=1}^{L} a_n(\mathbf{y}_\ell)^* a_m(\mathbf{y}_\ell)\Delta S_\ell = R_{n,m}\end{aligned} \tag{7.16}$$

If $\mathbf{R}$ is an identity matrix, then the orthogonality of the modes is preserved. On the contrary, the presence of non-zero off-diagonal terms $R_{n,m} \neq 0,\ n \neq m$ indicates the lack of orthogonality between sampled modes. In simple terms, the modes can no longer be controlled independently of one another. This phenomenon is hereafter referred to as *modal leakage*. As we will see soon, this is strictly connected with the phenomenon known as spatial aliasing. The matrix $\mathbf{R}$ is sometimes referred to as the *modal correlation matrix*. Clearly, $\mathbf{R}$ depends strongly on the sampling scheme adopted.

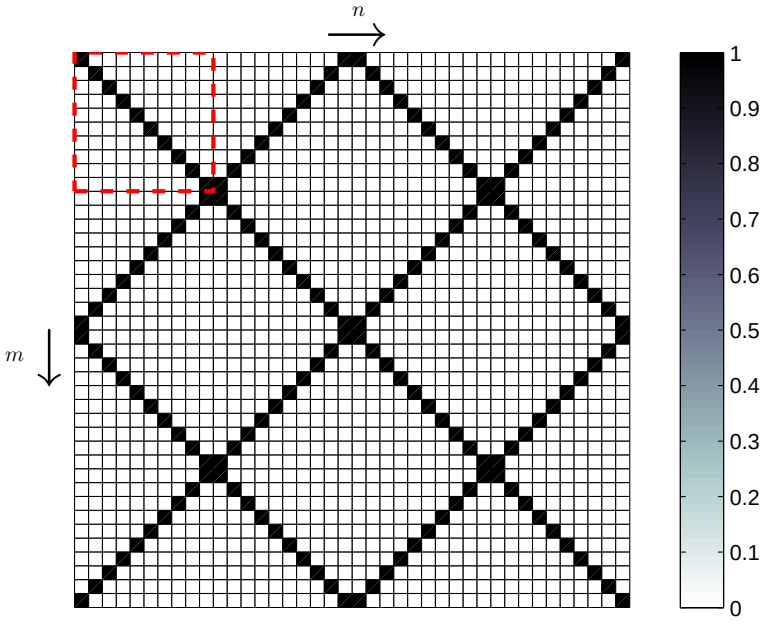

FIGURE 7.1: First 40x40 elements of the orthogonality matrix. $\partial\Lambda$ is a circle sampled at 10 uniformly arranged locations and $kR_V < 1.35$.

Figure 7.1 represents the example of an orthogonality matrix, with $\partial\Lambda$ being a circle sampled at 20 uniformly distributed samples, and $kR_V < 1.35$ (without this condition, the singular values and functions may need to be re-ordered). The singular functions are

given by equation (4.38), that is

$$a_n(\mathbf{y}) = \frac{e^{i\nu_n\hat{\mathbf{y}}}}{R_\Lambda\sqrt{2\pi}} \tag{7.17}$$

$$\nu_n = (-1)^{n-1}\left\lceil\frac{n-1}{2}\right\rceil \tag{7.18}$$

The very regular pattern of $\mathbf{R}$ suggests that some sampled modes have a unitary orthogonal projections on a given set of different modes. This can be seen by inserting the definition (7.17) of the singular functions into the definition (7.14) of $\mathbf{R}$ and observing that $\Delta S_\ell = 2\pi R_\Lambda/L$ and $\mathbf{y}_\ell = [R_\Lambda\cos\phi_\ell, R_\Lambda\sin\phi_\ell]$, where $\phi_\ell = (\ell-1)2\pi/L$. This yields

$$R_{n,m} = \frac{1}{2\pi R_\Lambda}\sum_{\ell=1}^{L} e^{i(\nu_m-\nu_n)\hat{\mathbf{y}}_\ell}\Delta S_\ell = \frac{1}{L}\sum_{\ell=0}^{L-1} e^{i(\nu_m-\nu_n)\frac{2\pi}{L}\ell} \tag{7.19}$$

This is a geometric series, whose sum gives

$$R_{n,m} = \frac{1}{L}\frac{1-e^{i(\nu_m-\nu_n)2\pi}}{1-e^{i(\nu_m-\nu_n)\frac{2\pi}{L}}} = \frac{1}{L}\frac{1-e^{i(\nu_m-\nu_n)2\pi}}{1-e^{i(\nu_m-\nu_n+aL)\frac{2\pi}{L}}} \tag{7.20}$$

$$= \begin{cases} 1, & \nu_n = \nu_m + aL \\ 0, & \nu_n \neq \nu_m + aL \end{cases}, \quad a\in\mathbb{Z} \tag{7.21}$$

The same arguments can be used in order to prove the well-known periodicity of the Discrete Fourier Transform, which clearly shares with the problem considered here the very same mathematics. In view of (7.18), we observe that

$$\nu_n = \begin{cases} \frac{n-1}{2}, & n \text{ is odd} \\ -\frac{n}{2}, & n \text{ is even} \end{cases} \tag{7.22}$$

The combination of the results above leads to

$$R_{n,m} = \begin{cases} 1, & n = m+2aL \text{ or } n = -m+2aL+1, \ a\in\mathbb{Z} \\ 0, & \text{otherwise} \end{cases} \tag{7.23}$$

This relation describes the regular aliasing pattern shown in Figure 7.1.

Figure 7.2 represents the absolute values of the elements of the orthogonality matrix for a spherical surface and a sampling scheme given by the 20 vertices of a regular dodecahedron. The singular functions $a_n(\mathbf{y})$ are given by equation (4.8) and are proportional to spherical harmonics. The condition $kR_V < 1.9$ is imposed, in order to avoid reordering the singular values. In this case, no simple derivation of the values of the matrix element is derived. Indeed, the sampling theory for functions defined on a sphere is a complex topic, whose detailed presentation lies beyond the scope of this thesis. Much research effort has been dedicated to the determination of sampling schemes for a sphere, with the aim of obtaining the largest number of independent modes for a given number of

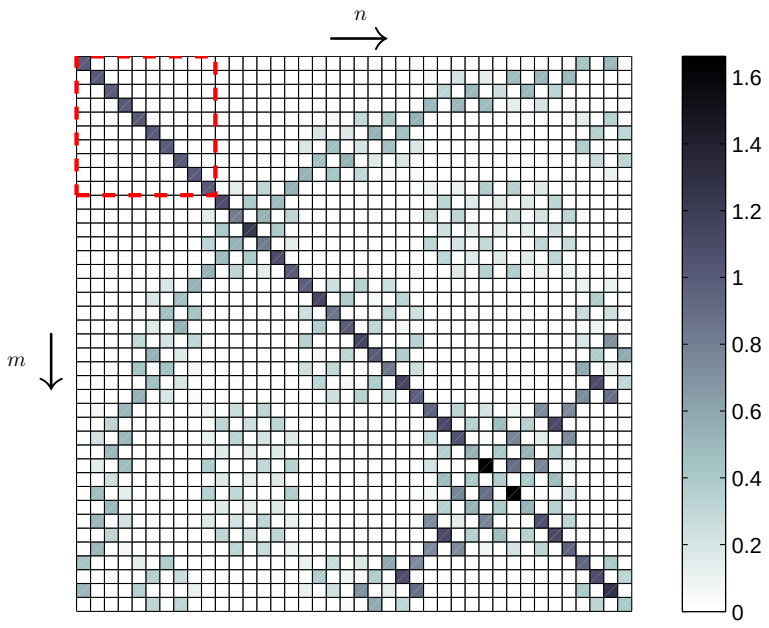

FIGURE 7.2: Absolute values of the first 40x40 elements of the orthogonality matrix. $\partial\Lambda$ is a spherical surface and the sampling scheme adopted corresponds to the 20 vertices of a regular dodecahedron, and $kR_V < 1.9$.

sampling points. The reader can refer, for example, to [SK97], [RWB07], [Raf05] and [Zot09] for a greater insight into this subject.

We can observe that in the orthogonality matrices of both the circle and the sphere there is a square sub-matrix which equals an identity matrix. This is identified by the red dashed contour line and corresponds to low orders n, m. This indicates that no modal leakage occurs between low order modes, which are therefore independent of one another (but they are not orthogonal to higher order modes). This situation is usual for regular or almost regular sampling schemes. The number of independent modes is related to the number of sampling points. We observe that for the circle, the number of independent modes equals the number L of the secondary sources. For the spherical geometry we have that the number of independent modes is less than the number of secondary sources.

7.1.3.2 Modal cross-efficiency

We go back to the expression of the sampling reproduction error ϵ_s and we insert equation (7.13) in the expression (7.11) of S with sampled density a_s, thus obtaining

$$(Sa_s)(\mathbf{x}) = \sum_{n=1}^{\infty}\sum_{m=1}^{\infty} p_n(\mathbf{x})\langle p_m|p\rangle_{\partial V}\frac{\sigma_n}{\sigma_m}R_{n,m} \tag{7.24}$$

Given the expression (7.11) of Sa with continuous density, and assuming that $(Sa)(\mathbf{x}) = p(\mathbf{x})$, we obtain the following expression for the reproduction error:

$$\epsilon_s(\mathbf{x}) = \sum_{n=1}^{\infty} \sum_{m=1}^{\infty} p_n(\mathbf{x}) \langle p_m | p \rangle_{\partial V} \frac{\sigma_n}{\sigma_m} (\delta_{n,m} - R_{n,m}) \tag{7.25}$$

The term σ_n/σ_m represents the ratio between the efficiency of the mode $a_n(\mathbf{y})$ and the mode $a_m(\mathbf{y})$, and is thus referred to as *modal cross-efficiency*. This ratio modulates the energy of the modal leakage, given by matrix $\mathbf{R}$. As the singular values are ordered with decreasing magnitude, we see that the contributions which are most likely to generate large errors correspond to those elements of the series with small index n and large index m.

The modal cross-efficiency does not depend on the sampling scheme adopted, but on the geometrical arrangement. We see that the spread of the singular values σ_n, which is the reason for the generation of a large modal cross-efficiency, is also responsible of the ill-conditioning of the problem. In light of the results presented in Chapter 6, it can be argued that the values of σ_n/σ_m are closer to unity when Λ and V coincide and the problem is mildly ill-conditioned. For example, in the spherical geometrical arrangement (Section 4.1), the modal cross-efficiency has the following asymptotic value (see equation (4.15))

$$\frac{\sigma_n}{\sigma_m} = \frac{2\nu_m + 1}{2\nu_n + 1} \left(\frac{R_\Lambda}{R_V} \right)^{\nu_m - \nu_n}, \quad \nu_n, \nu_m \to \infty \tag{7.26}$$

When the control and reproduction region coincide ($R_V = R_\Lambda$), this approximation reduces to ν_m/ν_n: in this case the modal cross efficiency is large for large ν_m and small ν_n (although the singular values may need to be reordered with decreasing magnitude). Analogously, in the case of planar and linear geometry (sections 4.3 and 4.4), in view of equation (4.57) we observe that

$$\frac{\sigma_\kappa}{\sigma_{\kappa'}} = \left| \frac{\zeta(\kappa')}{\zeta(\kappa)} \right| e^{[\mathrm{Im}(\zeta(\kappa')) - \mathrm{Im}(\zeta(\kappa))]d} \tag{7.27}$$

This is the exact value (not asymptotic). If $V = \Lambda$ and therefore $d = 0$, the above expression clearly reduces to $|\zeta(\kappa')| \,/\, |\zeta(\kappa)|$.

The modal cross-efficiency is therefore representative of a given choice of $\partial\Lambda$ *and* ∂V. Its value does not describe the reproduction error in the interior of Λ, but only on the boundary ∂V, also in the case of separable geometries.

7.1.3.3 Spatial aliasing

The loss of orthogonality of the sampled modes discussed above is known as *spatial aliasing*, from the Latin word *alius* (*other*, among many). As we have seen, the aliasing

error (used here as an equivalent term for the sampling error) actually represent the fact that, when attempting the reproduction of a given pressure mode p_ν, several modes other than the desired mode are unintentionally reproduced.

The expression for the sampling reproduction error can be reformulated after having introduced the *aliasing matrix* $\mathbf{E}$, defined by

$$E_{n,m} := \frac{\sigma_n}{\sigma_m} \left(\delta_{n,m} - R_{n,m} \right) \tag{7.28}$$

As for matrix $\mathbf{R}$, the dimensions of $\mathbf{E}$ are both infinite, but in contrast to $\mathbf{R}$, matrix $\mathbf{E}$ is not Hermitian.

An alternative definition of the aliasing matrix might not include the factor σ_n/σ_m, in which case the aliasing matrix would correspond to the difference between the identity matrix and the orthogonality matrix $\mathbf{R}$.

Equation (7.25) can therefore be rewritten as follows:

$$\epsilon_s(\mathbf{x}) = \sum_{n=1}^{\infty} \sum_{m=1}^{\infty} p_n(\mathbf{x}) \langle p_m | p \rangle_{\partial V} E_{n,m} \tag{7.29}$$

Figure 7.3 represents the absolute values of the aliasing matrix, in a logarithmic scale (dB), for the same spherical geometry and sampling scheme adopted for Figure 7.2. The radii of the reproduction and control regions are $R_\Lambda = 1.5$ m and $R_V = 0.1$ m, respectively, while the wave number $k = 6$ rad/m. It can be noticed that the elements with larger magnitude correspond to small values of the index n and large value of m, as mentioned above. Clearly, this configuration of the aliasing matrix depends upon the given choice of R_V, R_Λ and k.

7.1.4 Spectral truncation and truncation error

A common strategy to limit artifacts due to spatial aliasing lies in the exclusion of the high orders modes from the computation of the secondary source strength. This can be achieved by truncating the series of Fourier coefficients $\langle p_m | p \rangle_{\partial V}$, representing the pressure profile, to a given order M. The mode truncated version of the target profile is therefore given by

$$p_{s.t.}(\mathbf{x}) = \sum_{m=1}^{M} p_m(\mathbf{x}) \langle p_m | p \rangle_{\partial V} \tag{7.30}$$

The truncation error, that is the difference between the target pressure profile and its mode truncated version, is clearly given by

$$\epsilon_{s.t.}(\mathbf{x}) = \sum_{m=M+1}^{\infty} p_m(\mathbf{x}) \langle p_m | p \rangle_{\partial V} \tag{7.31}$$

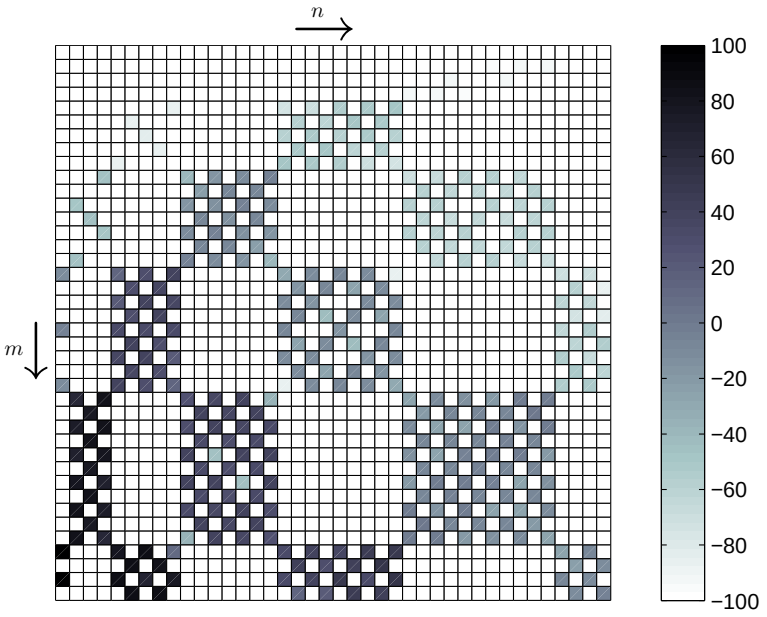

FIGURE 7.3: First 40x40 elements of matrix $\mathbf{E}$ (dB scale). $\partial\Lambda$ and ∂V are spheres with radii $R_\Lambda = 1.5$ m and $R_V = 0.1$ m, respectively, while $k = 6$ rad/m. The sampling scheme adopted corresponds to the 20 vertices of a regular dodecahedron.

It can be observed that this expression is identical to equation (6.8), which describes the reconstruction error associated to the application of the spectral cut-off. Indeed, this regularization technique discussed in Section 6.1 (and equivalently the spectral damping) is an effective method for reducing the reproduction artifacts caused by both spatial aliasing and ill-conditioning.

When we operate the truncation we are actually trading the sampling error with the truncation error. The truncation should be therefore applied once we are sure that, in the region where an accurate reproduction is desirable, the consequent truncation error will be smaller than the aliasing error we are going to avoid. The orthogonality matrix is often such that its first N rows and columns define an identity matrix, as shown for example by the red dashed lines in figures 7.1 and 7.2. Choosing this N as the truncation order appears therefore to be a sensible option, although it is not necessarily the best one for every situation.

7.1.5 Pre-aliasing and post-aliasing

The application of the spectral truncation described above implies that the order of *one* of the two series in the expression (7.29) of the sampling reproduction error (corresponding to *one* of the dimensions of matrices $\mathbf{R}$ and $\mathbf{E}$) is M instead of infinity. As discussed previously, this method corresponds to the exclusion of the high order modes from the computation of the density $a(\mathbf{y})$. This strategy can be regarded as a *pre-aliasing* filtering.

Pre-aliasing error can be avoided by a simple modal truncation of the solution, provided that the latter has been computed from a continuous description of the pressure profile. If $p(\mathbf{x})$ was sampled, as in the case when it is measured by an array of real or virtual microphones, much care should be taken in order to avoid artifacts caused by pre-aliasing (see discussion in Section 7.2.1).

In any case, the order of the second series in (7.29) is still infinite. This is due to a physical reason, namely that the finite number of secondary sources is generating all pressure modes $p_n(\mathbf{x})$, including modes of order higher than the truncation order M (see for example the expansion of a monopole field provided by equation (4.2)). This happens in spite of the fact that no attempt is made to control the high order modes and that they are excluded from the computation of the secondary source strengths. Ideally, this could be avoided by constructing an arrangement of secondary sources (in practice, a loudspeaker array) which does not generate high order pressure modes. In a way, this effect is implicitly generated by the physical distance between $\partial\Lambda$ and ∂V, when these do not coincide.

The reproduction artifacts due to the projection of the modes of order $m < M$ onto the higher modes is referred to as *post-aliasing* error, and is given by

$$\epsilon_{s,post} := \sum_{n=M+1}^{\infty} \sum_{m=1}^{M} p_n(\mathbf{z}) \langle p_m | p \rangle_{\partial V} E_{n,m} \tag{7.32}$$

Analogously, the pre-aliasing error is given by

$$\epsilon_{s,pre} := \sum_{n=1}^{M} \sum_{m=1}^{M} p_n(\mathbf{z}) \langle p_m | p \rangle_{\partial V} E_{n,m} \tag{7.33}$$

Although the post-aliasing can not be controlled by applying signal processing strategies, its effect is limited by the decay of the singular values σ_n representing the nominator of the fraction σ_n/σ_m, included in equation (7.28). The effect of pre-aliasing might also be limited by the fact that the orthogonality matrix $\mathbf{R}$ is often likely to be diagonal (or close to diagonal) for low orders n, m and almost uniform sampling schemes.

7.1.6 Reproduced field and total reproduction error

In light of the results presented, we are now able to derive an expression for the reproduced field and for the total reproduction error. The expression for the reproduced field reported below includes the effects of both spatial sampling and spectral truncation:

$$(Sa_{s+s.t.})(\mathbf{x}) = \sum_{n=1}^{\infty} \sum_{m=1}^{M} p_n(\mathbf{x}) \langle p_m | p \rangle_{\partial V} \frac{\sigma_n}{\sigma_m} R_{n,m} \tag{7.34}$$

The total reproduction error, including both aliasing and truncation errors, is given by

$$\begin{aligned} \epsilon_{s+s.t.}(\mathbf{z}) &= \sum_{n=1}^{\infty}\sum_{m=1}^{M} p_n(\mathbf{z})\langle p_m|p\rangle_{\partial V} E_{n,m} + \sum_{j=M+1}^{\infty} p_j(\mathbf{x})\langle p_j|p\rangle_{\partial V} \\ &= \sum_{n=1}^{\infty}\sum_{m=1}^{\infty} p_n(\mathbf{z})\langle p_m|p\rangle_{\partial V} \tilde{E}_{n,m} \end{aligned} \tag{7.35}$$

The last expression is analogous to equation (7.29), with the difference that the terms $E_{n,m}$ have been substituted by the elements of the modified aliasing matrix $\tilde{\mathbf{E}}$, defined by

$$\tilde{E}_{n,m} := \frac{\sigma_n}{\sigma_m}\Big(\delta_{n,m} - R_{n,m}\tilde{H}(m-M)\Big) \tag{7.36}$$

where the function $\tilde{H}(\cdot)$, similar to the discrete Heaviside (step) function, is given by

$$\tilde{H}(m-M) = \begin{cases} 1\,, & m \leq M \\ 0\,, & m > M \end{cases} \tag{7.37}$$

Figure 7.4 illustrates a diagrammatic representation of equation (7.35) and of matrix $\tilde{\mathbf{E}}$. The geometrical arrangement is the same as that used for Figure 7.3. The regions shaded with blue, green and yellow identify the elements contributing to the pre-aliasing, post-aliasing and truncation errors, respectively. The gray scale represents the absolute values of $\tilde{\mathbf{E}}$ in dB scale.

7.1.7 Separable geometries

The results presented in Chapter 4 indicate that, in the case of the separable geometries considered, the singular functions and singular values corresponding to different choices of control volume V are related by simple mathematical formulae. More specifically, it has been shown that the singular functions corresponding to different choices of V may differ by a complex factor of unitary magnitude (γ_ν, γ_κ) and by a normalization factor ($R_{V,\Lambda}^{-1,-1/2}$). The singular values for different V are given by identical functions with different arguments, and may also differ by a normalization factor.

Using these relations, it is possible to extend the expression for the reproduction error from ∂V to the entire reproduction region Λ. It should be considered that the expression for the modal cross-efficiency σ_n/σ_m includes in the numerator the singular value related to the estimation point $\mathbf{z} \in \Lambda$, and in the denominator the singular value related to the control boundary ∂V. Consequently, the aliasing matrix becomes a function of $\mathbf{z}$. In the light of these considerations we can write the following expression, valid for separable

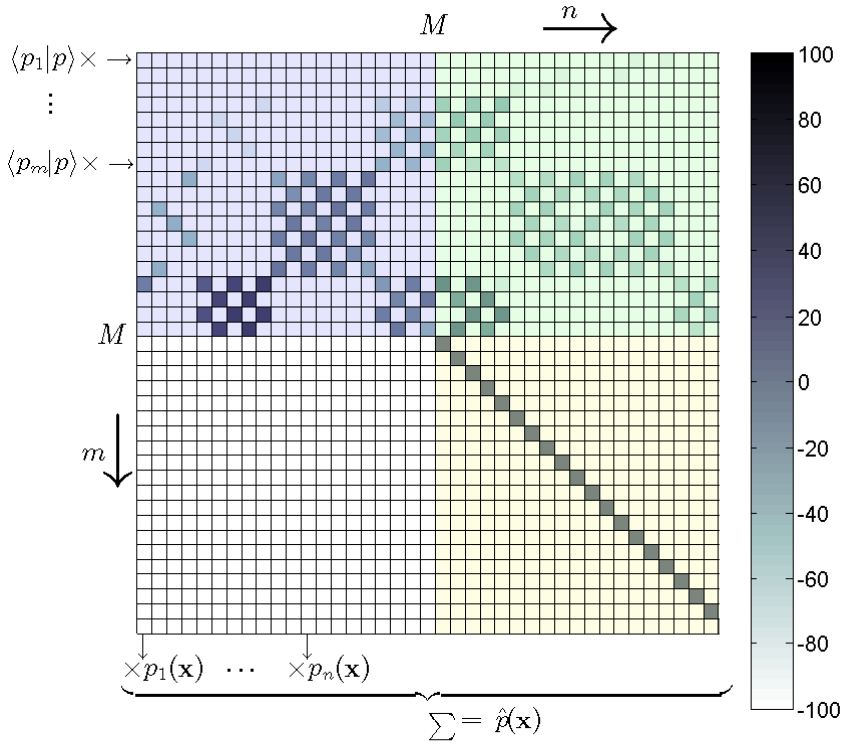

FIGURE 7.4: Diagrammatic representation of equation (7.35) and of the first 40x40 elements of matrix $\tilde{\mathbf{E}}$. $\partial\Lambda$ and ∂V are spheres with radii $R_\Lambda = 1.5$ m and $R_V = 0.1$ m, respectively, while $k = 6$ rad/m. The sampling scheme adopted corresponds to the 20 vertices of a regular dodecahedron. The gray scale represents the absolute values of $\tilde{\mathbf{E}}$ in dB. The regions shaded with blue, green and yellow identify the elements contributing to the pre-aliasing, post-aliasing and truncation errors, respectively.

geometries:

$$\begin{aligned} \epsilon_{s+s.t.}(\mathbf{z}) &= \sum_{n=1}^{\infty}\sum_{m=1}^{\infty} p_n(\mathbf{z})\langle p_m|p\rangle_{\partial V}\tilde{E}_{n,m}(\mathbf{z}) \qquad (7.38)\\ &= \sum_{n=1}^{\infty}\sum_{m=1}^{\infty} p_n(\mathbf{z})\langle p_m|p\rangle_{\partial V}\frac{\sigma_n(\mathbf{z})}{\sigma_m(\mathbf{x})}\left(\delta_{n,m} - R_{n,m}\tilde{H}(m-M)\right), \quad \mathbf{z}\in\Lambda,\ \mathbf{x}\in\partial V \end{aligned}$$

7.1.8 Reproduction error for spherical geometry

The results presented above are now calculated for an arrangement including concentric spheres, with reference to the results presented in Section 4.1, and more specifically with reference to the expressions (4.7)-(4.11) of the singular system.

The relevant fact is highlighted that the relation (4.11) between the index n of the singular values/functions and the indices ν, μ of the spherical harmonics, Bessel and Hankel functions, namely $\nu = \lceil\sqrt{n} - 1\rceil$, $\mu = n - 1 - \nu - \nu^2$ [1] , is valid only for small

[1] It is recalled that the symbol $\lceil\cdot\rceil$ indicates the ceiling operator (rounding up to the next integer).

values of the product kR_V. For higher frequencies or larger radii of the control region, this relation is no longer valid as a consequence of the oscillating behavior of the Bessel functions (see Figure 4.2) Hence, the singular functions and values should be reordered according to the magnitude of the latter. This would in turn require a permutation of the rows and columns of the orthogonality matrix $\mathbf{R}$, which would therefore have an irregular pattern. The independent modes, identified by the red dashed contour line in Figure 7.2, would in this case no longer correspond to the lower order modes. This would make the choice of the truncation order more complicated. For these reasons, the choice was made not to reorder the singular values and functions, but rather to keep them ordered consistent with the indices ν and μ, as indicated above. Analogous considerations hold also for the concentric circle geometry.

Given a generic sampling scheme $\{\mathbf{y}_\ell\}$ of the surface $\partial\Lambda$ and considering equation (7.34), we derive the following expression for the reproduced field:

$$\begin{aligned}(Sa_{s+s.t.})(\mathbf{z}) &= \sum_{\nu=0}^{\infty}\sum_{\mu=-\nu}^{\nu}\sum_{n=0}^{N}\sum_{m=-n}^{n} Y_\nu^\mu(\hat{\mathbf{z}})\int_{\partial V} Y_n^m(\hat{\mathbf{x}})^* p(\mathbf{x})\frac{dS(\mathbf{x})}{R_V^2} \\ &\cdot \frac{j_\nu(kz)h_\nu(kR_\Lambda)}{j_n(kR_V)h_n(kR_\Lambda)}\sum_{\ell=1}^{L} Y_\nu^\mu(\hat{\mathbf{y}}_\ell)^* Y_n^m(\hat{\mathbf{y}}_\ell)\frac{\Delta S_\ell}{R_\Lambda^2}, \quad \mathbf{z}\in\Lambda\end{aligned} \tag{7.39}$$

where $N=\sqrt{M}-1$, so the total number of singular functions is M (see the discussion on the degeneracy of the singular functions in Section 4.1). This expression takes into consideration the effects of both sampling and spectral truncation. The sampling reproduction error in Λ is derived from equation (7.29), including only the first M terms of the second series (with variable m). This leads to

$$\begin{aligned}\epsilon_s(\mathbf{z}) &= \sum_{\nu=0}^{\infty}\sum_{\mu=-\nu}^{\nu}\sum_{n=0}^{N}\sum_{m=-n}^{n} Y_\nu^\mu(\hat{\mathbf{z}})\int_{\partial V} Y_n^m(\hat{\mathbf{x}})^* p(\mathbf{x})\frac{dS(\mathbf{x})}{R_V^2} \\ &\cdot \frac{j_\nu(kz)h_\nu(kR_\Lambda)}{j_n(kR_V)h_n(kR_\Lambda)}\left(\delta_{n,\nu}\delta_{m,\mu}-\sum_{\ell=1}^{L} Y_\nu^\mu(\hat{\mathbf{y}}_\ell)^* Y_n^m(\hat{\mathbf{y}}_\ell)\frac{\Delta S_\ell}{R_\Lambda^2}\right), \quad \mathbf{z}\in\Lambda\end{aligned} \tag{7.40}$$

The terms of the first series with $0\le\nu\le N$ give the pre-aliasing error, while the terms with $N+1\le\nu<\infty$ give the post-aliasing error. The truncation error is calculated from equation (7.31) and is given by the following expression:

$$\begin{aligned}\epsilon_{s.t.}(\mathbf{z}) &= \sum_{\nu=N+1}^{\infty}\sum_{\mu=-\nu}^{\nu} Y_\nu^\mu(\hat{\mathbf{z}})\frac{j_\nu(kz)}{j_\nu(kR_V)}\int_{\partial V} Y_\nu^\mu(\hat{\mathbf{x}})^* p(\mathbf{x})\frac{dS(\mathbf{x})}{R_V^2} \\ &= \sum_{\nu=N+1}^{\infty}\sum_{\mu=-\nu}^{\nu} Y_\nu^\mu(\hat{\mathbf{z}})\int_{\Omega_z} Y_\nu^\mu(\hat{\mathbf{x}})^* p(\mathbf{x})\frac{dS(\mathbf{x})}{z^2}, \quad \mathbf{z}\in\Lambda\end{aligned} \tag{7.41}$$

In what follows, the example is provided of a spherical array of 40 secondary sources, having a radius of 1.8 m. This is the same array used for the experiments presented in

Chapter 8. The locations of the secondary sources, which define the sampling scheme adopted, are reported in Appendix E.

Figure 7.5 shows the orthogonality matrix for this configuration (with $R_V = 0.1$ m and $k = 6$ rad/m). As the sampling scheme is only approximatively uniform, almost all modes are not orthogonal one to another . Though many of the elements of the orthogonality matrix have small values, the large majority of them differs from zero.

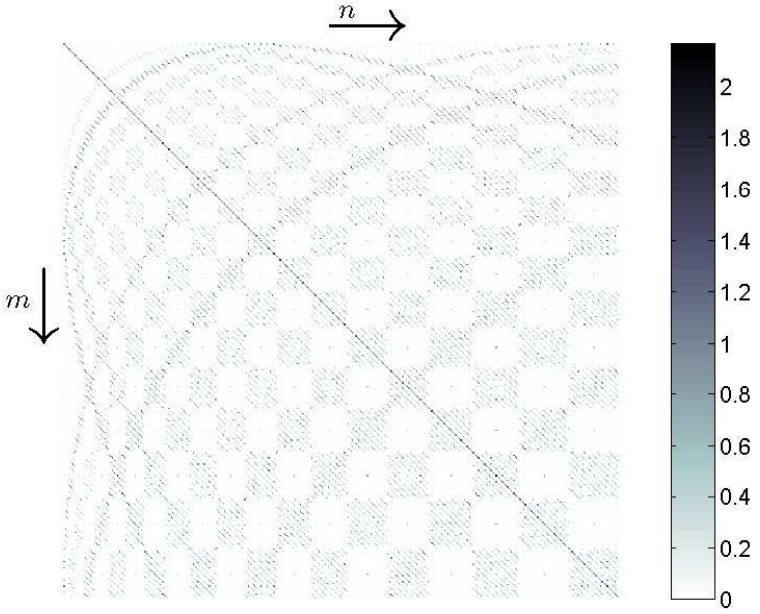

FIGURE 7.5: Absolute values of the first 100x100 elements of the orthogonality matrix. $\partial\Lambda$ and ∂V are spheres with radii $R_\Lambda = 1.8$ m and $R_V = 0.1$ m, respectively, while $k = 6$ rad/m. The sampling scheme adopted corresponds to that reported in Appendix E.

Figure 7.6 reports the absolute values of the elements of matrix $\tilde{\mathbf{E}}$ (dB), for two different choices of R_V and for the truncation order $N = 5$ (corresponding to $(N+1)^2 = 36$ modes). Figure 7.7 reports the absolute values of matrix $\tilde{\mathbf{E}}$ for the same two values of R_V but for the truncation order $N = 15$ (corresponding to $(N+1)^2 = 256$ modes).

The attempt is made to reproduce the sound field due to a virtual source located at $[r_q, \theta_q, \phi_q] = [2.5\text{ m}, 80°, 140°]$ and wave number $k = 6$ rad/m. The target sound field is reported in Figure 5.2. Figures 7.12 to 7.17 represent respectively the reproduced field (equation (7.39)), the normalized reproduction error (equation (5.31)), the pre- and post-aliasing errors (equation (7.40)) and the truncation error (equation (7.41)) in the region of the space given by

$$\Lambda_0 := \{\mathbf{z} \in \Lambda : z_3 = 0\} \tag{7.42}$$

that is the horizontal cross-section of the reproduction region. Two different orders of truncation $N = 5$ and $N = 15$ have been used, while all the infinite series have been

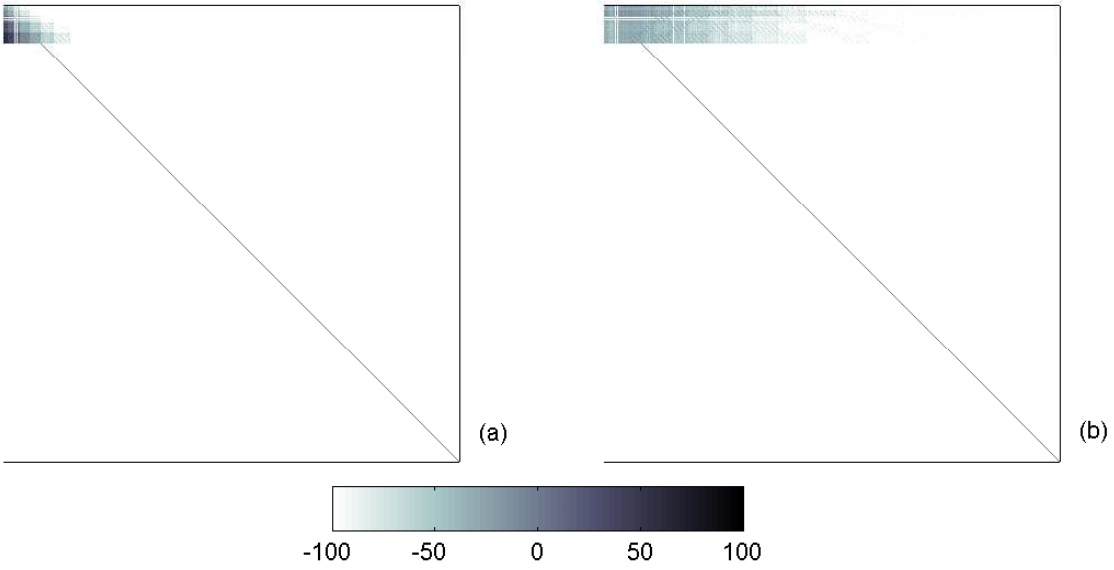

FIGURE 7.6: Absolute values of the first 440x440 elements of matrix $\tilde{\mathbf{E}}$ (dB scale), with truncation order $N = 5$. $\partial\Lambda$ and ∂V are spheres with radii $R_\Lambda = 1.5$ m, $R_V = 0.1$ m (a) and $R_V = 1$ m (b), respectively, while $k = 6$ rad/m. The sampling scheme adopted is reported in Appendix E.

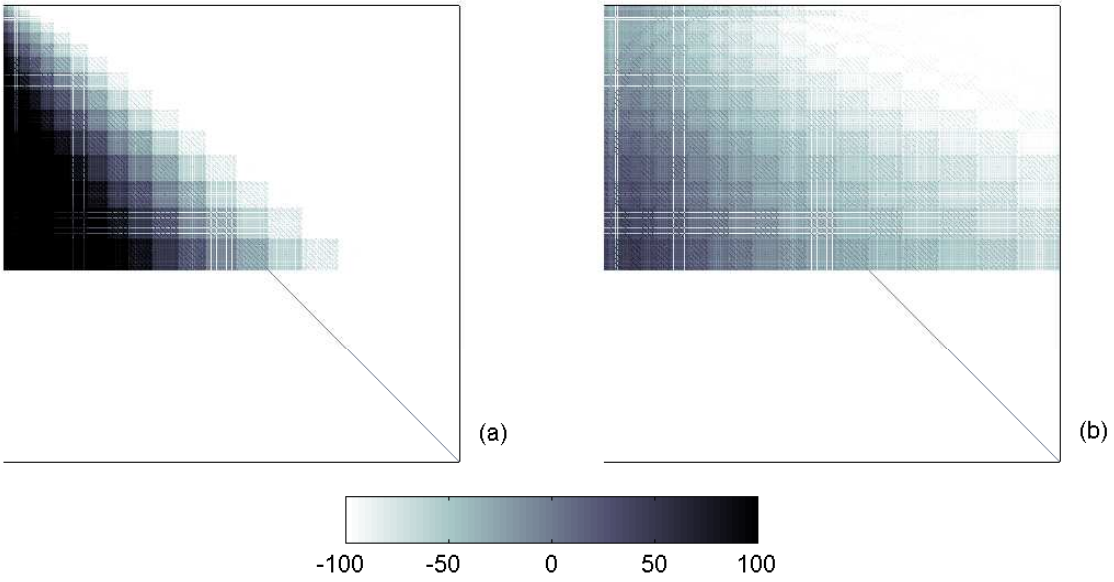

FIGURE 7.7: Absolute values of the first 440x440 elements of matrix $\tilde{\mathbf{E}}$ (dB scale), with truncation order $N = 15$. $\partial\Lambda$ and ∂V are spheres with radii $R_\Lambda = 1.5$ m, $R_V = 0.1$ m (a) and $R_V = 1$ m (b), respectively, while $k = 6$ rad/m. The sampling scheme adopted is reported in Appendix E.

approximated with finite summations up to the order $N = 20$ (corresponding to a total of 441 terms).

A further proof of the validity of the calculation was provided by the fact that the sum of the sampling and truncation errors on Λ_0 proves to be equal to the difference between the target field and the reproduced field (namely $\epsilon_{s,pre}(\mathbf{z}) + \epsilon_{s,post}(\mathbf{z}) + \epsilon_{s.t.}(\mathbf{z}) = p(\mathbf{z}) - \hat{p}(\mathbf{z}),\ \mathbf{z} \in \Lambda_0$).

The dashed circles in figures 7.14 and 7.16 identify the boundaries of the ball $B_{N/k}$ defined

$$B_{N/k} := \{\mathbf{z} \in \mathbb{R}^3 : z < N/k\} \tag{7.43}$$

It can be observed that, in the case of $N = 5$, the post-aliasing and truncation errors are approximatively confined to the exterior of this region. Recall that these errors are generated by the contributions of pressure modes of orders higher than N. This result is consistent with the "rule of thumb" proposed by Ward and Abhayapala [WA01], which suggest a truncation order $N \geq kR$ for an accurate reproduction within a sphere of radius R. An identical relation was proposed by Rafaely [RWB07], [Raf05] in the framework of spherical microphone arrays. This is a consequence of the fact that the closer $\mathbf{z}$ is to the origin, the smaller is the contribution of high order modes to the reproduced sound field $\hat{p}(\mathbf{z})$. This is clearly related to the interpretation of the operator S as a spatial low pass filter, proposed in Chapter 4.

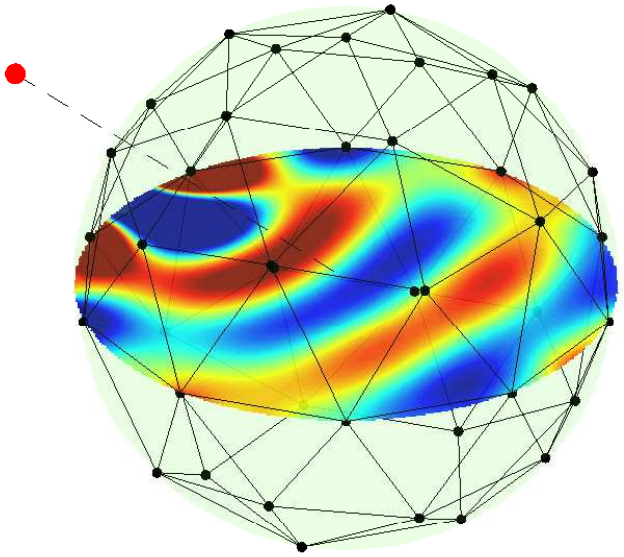

FIGURE 7.8: Reproduced sound field of a virtual source located at $[r_q, \theta_q, \phi_q] = [2.5\text{ m}, 80°, 140°]$ and $k = 6$ rad/m with a discrete array of 40 secondary sources. The field was computed from equation (7.39) with the order of truncation $N = 5$.

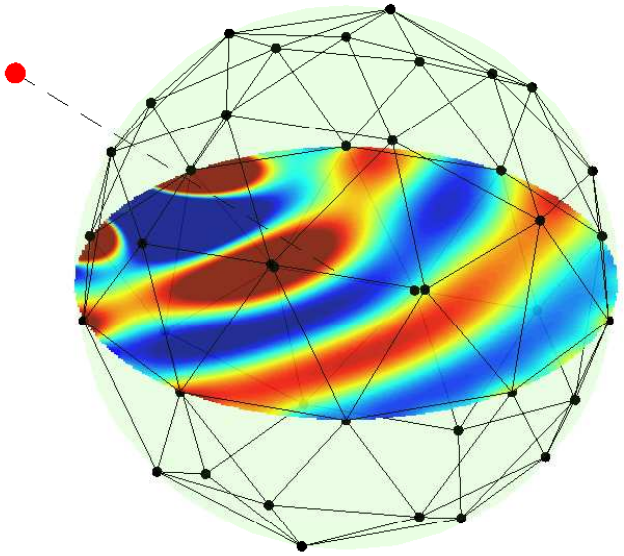

FIGURE 7.9: Reproduced sound field of a virtual source located at $[r_q, \theta_q, \phi_q] = [2.5\text{ m}, 80°, 140°]$ and $k = 6$ rad/m with a discrete array of 40 secondary sources. The field was computed from equation (7.39) with the order of truncation $N = 15$.

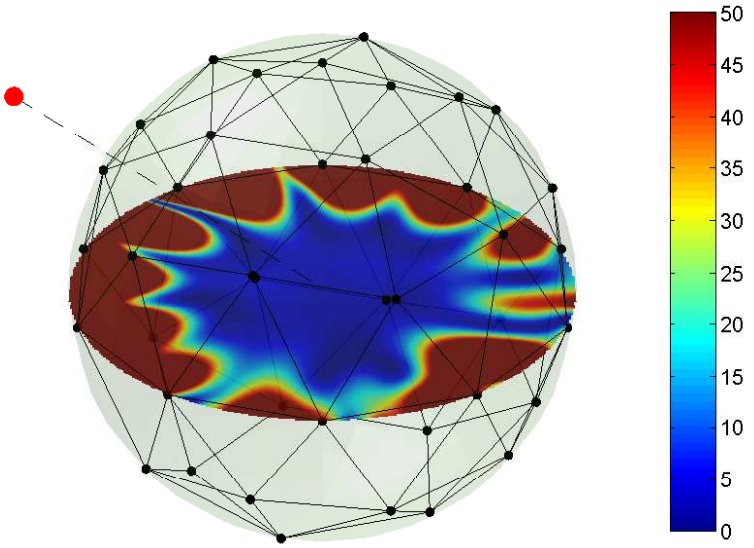

FIGURE 7.10: Normalized reproduction error (%) computed from equation (5.31) and $N = 5$.

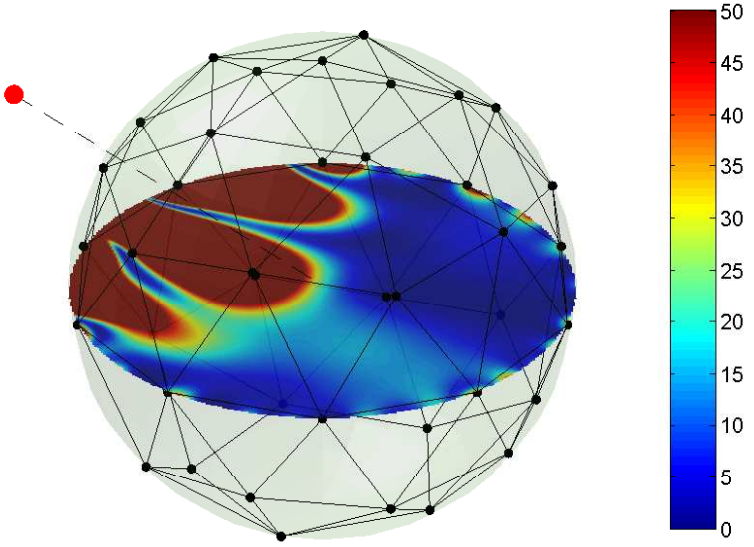

FIGURE 7.11: Normalized reproduction error (%) computed from equation (5.31) and $N = 15$.

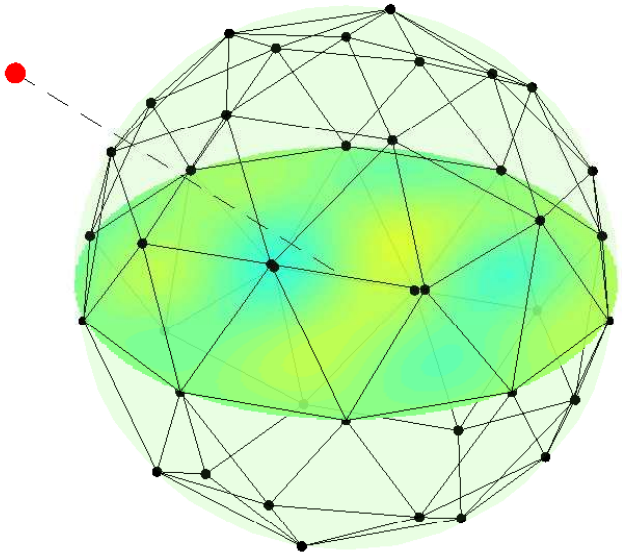

FIGURE 7.12: Pre-aliasing error computed from equation (7.40) and $N = 5$.

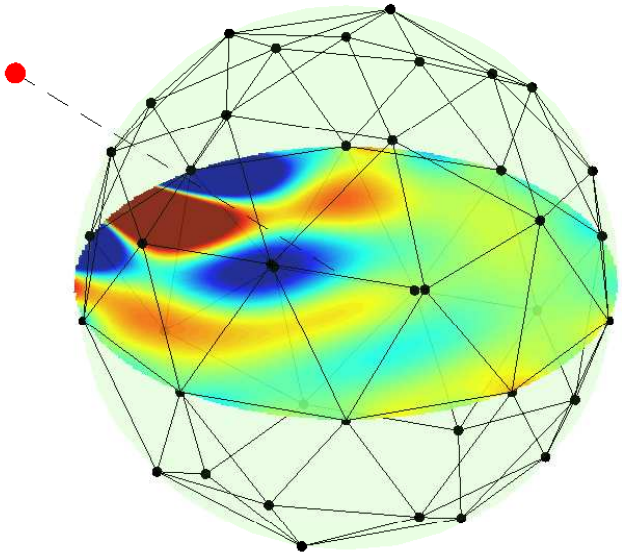

FIGURE 7.13: Pre-aliasing error computed from equation (7.40) and $N = 15$.

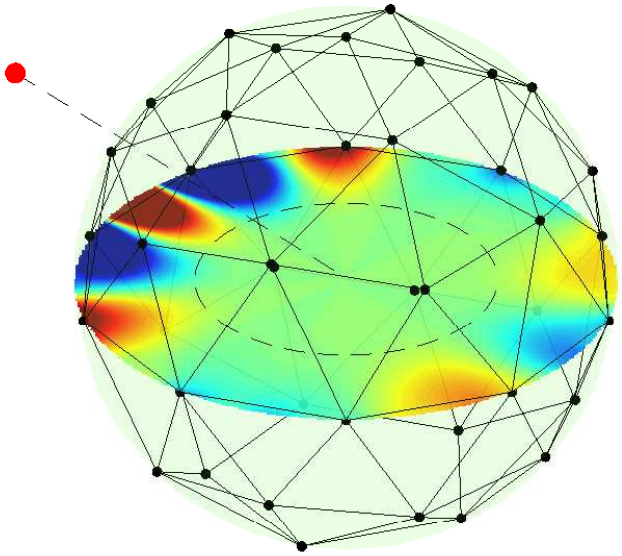

FIGURE 7.14: Post-aliasing error computed from equation (7.40) and $N = 5$.

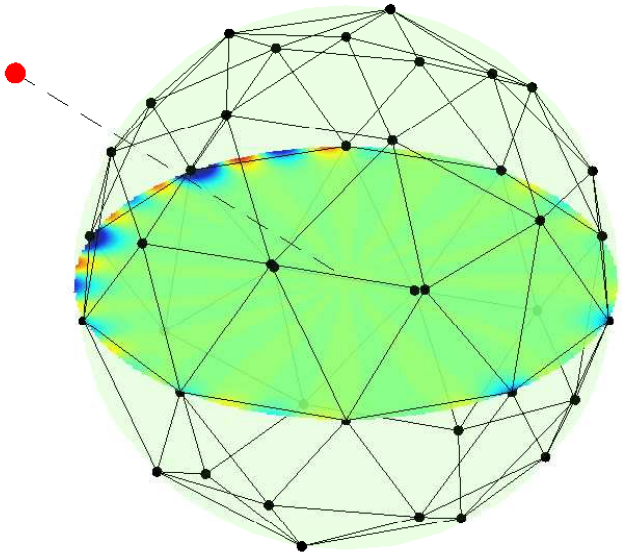

FIGURE 7.15: Post-aliasing error computed from equation (7.40) and $N = 15$.

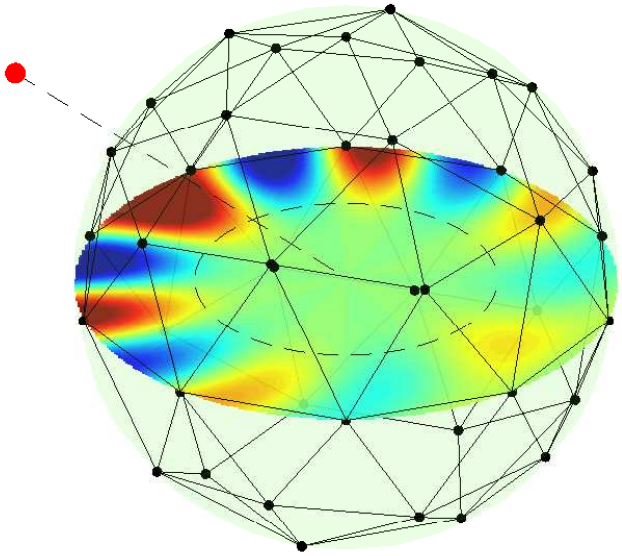

FIGURE 7.16: Truncation error computed from equation (7.41) and $N = 5$.

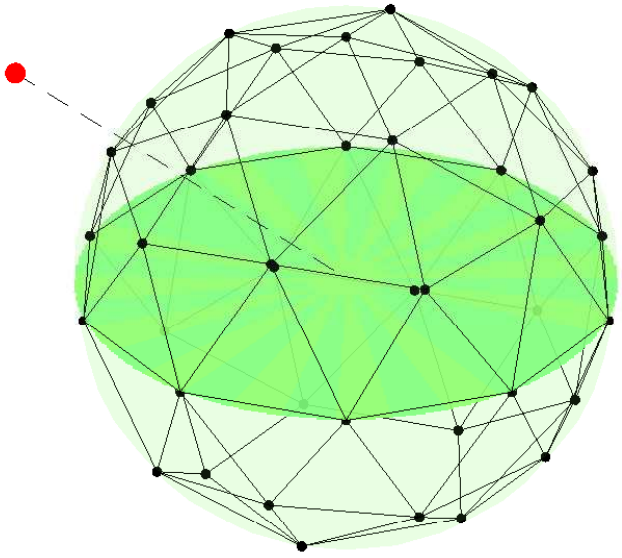

FIGURE 7.17: Truncation error computed from equation (7.41) and $N = 15$.

The L^1 norm of a function $f(\mathbf{x})$ on a subset D of its domain is defined by:

$$||f||_{1,D} = \int_D |f(\mathbf{x})| dS(\mathbf{x}) \tag{7.44}$$

This measure, applied to the reproduction error, provides the value of the average of the absolute value of the error (multiplied by the area of D). For this reason, it is used here instead of the usual L^2 norm. Figure 7.18 reports the L^1 norms (on Λ_0) of the different errors, normalized by the norm $||p||_{1,\Lambda_0}$ of the desired field.

It can be observed that for $N = 5$ the pre-aliasing error is low, while the post-aliasing and truncation errors are large. The opposite holds for the case of $N = 15$. This fact, in combination with the considerations on the spatial distribution of the truncation and post-aliasing errors mentioned above, provides a greater insight into the different spatial distributions of the normalized reproduction error depicted in figures 7.10 and 7.11.

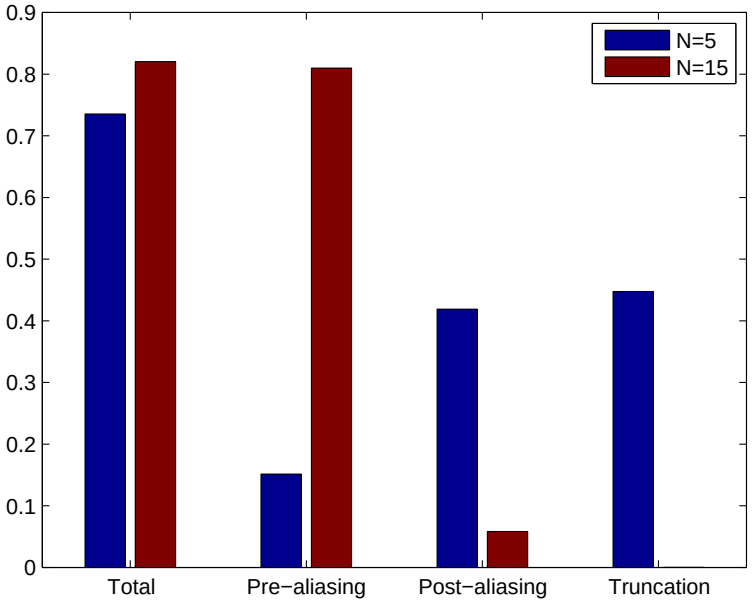

FIGURE 7.18: L^1 norm of the different reproduction errors on Λ_0, for $N = 5$ and $N = 15$. The values represent the norm of the errors on Λ_0, normalized by $||p||_{1,\Lambda_0}$

In order to better understand the effect of the order of truncation N, we present a brief analysis of the behavior of the source strength density function $a(\mathbf{y})$ for the two different choices of N reported above. Figure 7.19 shows the plots of $|a(\mathbf{y})|$ calculated from the series (5.30) truncated to $N = 5$ and $N = 15$, respectively, and as a function of the angle $\varphi_{\mathbf{qy}}$ between the vectors $\mathbf{q}$ (the location of the virtual source) and $\mathbf{y}$ (the location of the secondary source). The virtual source location is always $[r_q, \theta_q, \phi_q] = [2.5\text{ m}, 80°, 140°]$ and $k = 6$. It can be clearly noticed that the amplitude of the solution with $N = 15$ (red line in the figure) has a broad, large main lobe in the direction of the virtual source ($\varphi_{\mathbf{qy}} = 0°$), while the solution with $N = 5$ (blue line in the figure) is characterized by a

narrower main lobe with smaller amplitude, and side lobes with considerable magnitude. These side lobes are caused by the truncation of the infinite series (analogous plots for the case of $N = \infty$ is shown in Figure 5.6). A large lobe of less than 20 dB smaller than the main lobe appears at $\varphi_{\mathbf{qy}} = 180°$. This has the remarkable consequence that acoustic energy is generated by the secondary sources arranged in the direction opposite to the virtual source. This might result in an unwanted effect if the field reproduction is performed, for example, for audio purposes.

The width of the main lobes is controlled by the distance of the virtual source and by the order of truncation. When $N = \infty$, as it has been discussed in Section 5.6.1, only the main lobe is present and it becomes progressively narrow when the virtual source gets closer to $\partial\Lambda$ (if $\mathbf{q} \in \partial\Lambda$, $a(\mathbf{y})$ is a Dirac delta function). On the other hand, the narrower is the lobe, the larger is the magnitude of the high order terms in the generalized Fourier series representing $a(\mathbf{y})$. It can be argued that, when the virtual source is far away, the shape of the truncated solution resembles of the solution computed with an infinite series. When the virtual source gets closer, the width of the main lobe gets narrower, and when the width of the lobe is too narrow for being represented with the finite number of terms N, side lobes begin to appear.

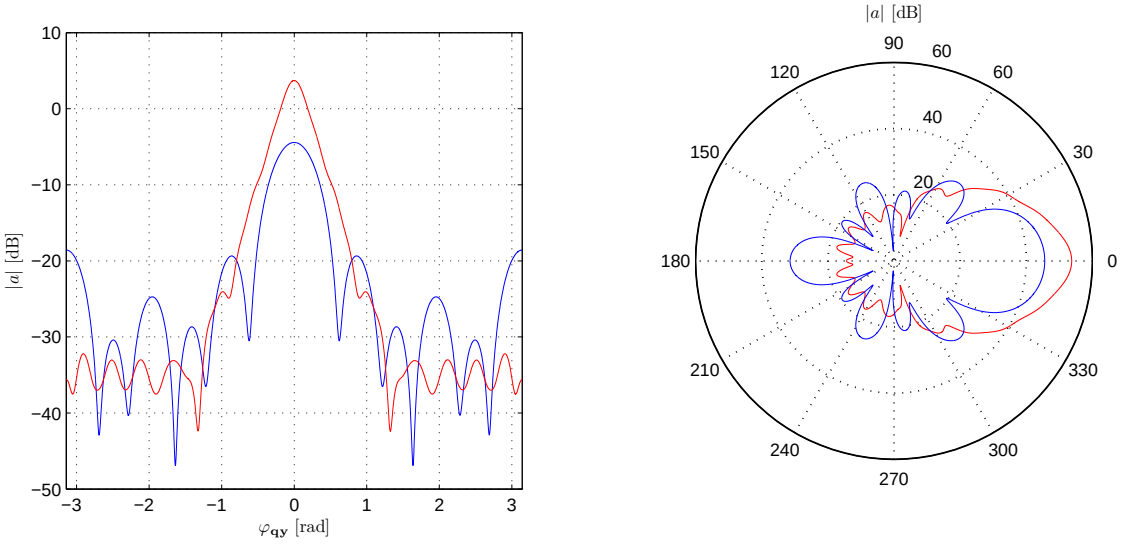

FIGURE 7.19: Absolute value of the secondary source density $a(\mathbf{y})$, given by series (5.30) truncated to $N = 5$ (blue line) and $N = 15$ (red line). The left hand side of the figure shows a plot with Cartesian axes, while the right hand side shows a polar plot.

7.1.9 Reproduction error for linear geometry

Results analogous to those presented in the previous sections can be extended also to the cases of linear and planar geometry for which, as has been mentioned more than once, the integral operator S is not compact. In this section, the reproduction error for linear geometry is analyzed.

The case is considered of $\partial\Lambda$ and ∂V being two parallel lines, as described in Section 4.4. In order to keep the notation simple, since all $\mathbf{y} \in \partial\Lambda$ are such that $\mathbf{y} = [y_1,\ 0,\ 0]$, we substitute here the vector $\mathbf{y} \in \partial\Lambda$ with the scalar $y = y_1$ (which can also be negative and does not represent in this case the absolute value of $\mathbf{y}$). A sampling scheme $\{y_\ell\}$ is defined on $\partial\Lambda$, with Dirichlet cells of length ΔS_ℓ. The sampled density $a_s(y)$ is therefore given by

$$a_s(y) = a(y) \sum_{\ell=1}^{L} \delta(y - y_\ell) \Delta S_\ell \tag{7.45}$$

where the continuous density is assumed to exist and is given by equation 4.102, reported here

$$a(y) = \mathcal{F}^{-1} \left[\frac{2\zeta}{i e^{i\zeta d}} (\mathcal{F}p) \right] (y) \tag{7.46}$$

where $\zeta = \zeta(\kappa) = \sqrt{k^2 - \kappa^2}$ and d is the distance between the two lines $\partial\Lambda$ and ∂V.

The reproduced field $\hat{p}(\mathbf{z}) = (Sa)(\mathbf{z})$, $\mathbf{z} \in \mathbb{R}^2$ can be derived from the extension of equation (4.69) to $\mathbb{R}^2$, namely

$$\begin{aligned}
(Sa_s)(\mathbf{z}) &= \left[\mathcal{F}^{-1} \frac{i e^{i\zeta |z_3|}}{2\zeta} (\mathcal{F}a_s) \right] (\mathbf{z}) \qquad (7.47) \\
&= \int_{\mathbb{R}} \frac{e^{i\kappa z_1}}{\sqrt{2\pi}} \frac{i e^{i\zeta(\kappa)|z_3|}}{2\zeta(\kappa)} \left[\int_{\mathbb{R}} \frac{e^{-i\kappa y}}{\sqrt{2\pi}} \sum_{\ell=1}^{L} \delta(y - y_\ell) \Delta y_\ell \left(\int_{\mathbb{R}} \frac{2\zeta(\kappa')}{i e^{i\zeta(\kappa')d}} \frac{e^{i\kappa' y}}{\sqrt{2\pi}} (\mathcal{F}p)(\kappa') d\kappa' \right) dy \right] d\kappa \\
&= \int_{\mathbb{R}} \int_{\mathbb{R}} \frac{e^{i\kappa z_1}}{\sqrt{2\pi}} \frac{\zeta(\kappa')\ e^{i\zeta(\kappa)|z_3|}}{\zeta(\kappa)\ e^{i\zeta(\kappa')d}} (\mathcal{F}p)(\kappa') \left(\sum_{\ell=1}^{L} e^{i(\kappa' - \kappa) y_\ell} \frac{\Delta y_\ell}{2\pi} \right) d\kappa' d\kappa
\end{aligned}$$

Recalling the definition of σ_κ and γ_κ, given by equations (4.94) and (4.95), respectively, and having defined the function $R(\kappa' - \kappa)$ similarly to matrix $\mathbf{R}$ by

$$R(\kappa' - \kappa) := \sum_{\ell=1}^{L} e^{i(\kappa' - \kappa) y_\ell} \frac{\Delta y_\ell}{2\pi} \tag{7.48}$$

we can rewrite equation (7.47) as follows:

$$(Sa_s)(\mathbf{z}) = \int_{\mathbb{R}} \int_{\mathbb{R}} \frac{e^{i\kappa z_1}}{\sqrt{2\pi}} (\mathcal{F}p)(\kappa') \frac{\sigma_\kappa(z_3)\gamma_\kappa(z_3)}{\sigma_{\kappa'}(d)\gamma_{\kappa'}(d)} R(\kappa' - \kappa)\, d\kappa' d\kappa \tag{7.49}$$

This expression can be interpreted as an extension of equation (7.24), in which the two sums have been substituted by integrals.

In view of the definition of convolution (2.92) and of the identity $R(\kappa - \kappa') = R(\kappa' - \kappa)^*$, the equation above can be expressed as follows:

$$(Sa_s)(\mathbf{z}) = \int_{\mathbb{R}} \frac{e^{i\kappa z_1}}{\sqrt{2\pi}} \sigma_\kappa(z_3)\gamma_\kappa(z_3) \left[\frac{(\mathcal{F}p)(\kappa)}{\sigma_\kappa(d)\gamma_\kappa(d)} \otimes R(\kappa)^* \right] d\kappa \tag{7.50}$$

7.1.9.1 Uniform sampling

The special case is considered of a uniform sampling scheme, that is to say $\Delta S_\ell = \Delta y$ and $y_\ell = \Delta y(\ell - 1 - (L-1)/2)$, where the number of secondary sources L is assumed to be odd (this implies that $y_1 = -\Delta y(L-1)/2$ and $y_L = \Delta y(L-1)/2$). In view of the definition of the rectangle function Π and of the comb function Ш given by equations (2.62) and (2.30), respectively, we observe that

$$\text{Ш}\left(\frac{y}{\Delta y}\right)\ \Pi\left(\frac{y}{L\Delta y}\right) = \sum_{\ell=-\frac{L-1}{2}}^{\frac{L-1}{2}} \delta(y - \ell\Delta y)\ \Delta y \tag{7.51}$$

The comb function represents the effect of sampling, while the multiplication by the rectangular function implies truncation of the series above to a finite sum. The sampled density (7.45) can be therefore expressed by

$$a_s(y) = \mathcal{F}^{-1}\left[\frac{\mathcal{F}p}{\sigma_\kappa \gamma_\kappa}\right](y)\ \text{Ш}\left(\frac{y}{\Delta y}\right)\ \Pi\left(\frac{y}{L\Delta y}\right) \tag{7.52}$$

The Fourier transform of this function can be computed from the convolution theorem (2.94) and from equations (2.31) and (2.63) and is given by

$$\begin{aligned}(\mathcal{F}a_s)(\kappa) &= \frac{(\mathcal{F}p)(\kappa)}{\sigma_\kappa \gamma_\kappa} \otimes \sum_{n=-\infty}^{\infty} \delta\left(\kappa - \frac{2\pi n}{\Delta y}\right) \otimes L\frac{\Delta y}{2\pi}\ \text{sinc}\left(L\Delta y\frac{\kappa}{2}\right) \\ &= \frac{(\mathcal{F}p)(\kappa)}{\sigma_\kappa \gamma_\kappa} \otimes L\frac{\Delta y}{2\pi} \sum_{n=-\infty}^{\infty} \text{sinc}\left(L\left(\frac{\kappa}{2}\Delta y - n\pi\right)\right)\end{aligned} \tag{7.53}$$

Equation (2.61) shows that

$$L\sum_{n=-\infty}^{\infty} \text{sinc}\left(L\left(\frac{\kappa}{2}\Delta y - n\pi\right)\right) = \frac{\sin(L\Delta y\ \kappa/2)}{\sin(\Delta y\ \kappa\ /2)} = \text{csinc}_L\left(\Delta y\ \kappa\right) \tag{7.54}$$

In view of this result, equation (7.50) is rewritten as follows:

$$(Sa_s)(\mathbf{z}) = \int_{\mathbb{R}} \frac{e^{i\kappa z_1}}{\sqrt{2\pi}}\ \sigma_\kappa(z_3)\gamma_\kappa(z_3)\left[\frac{(\mathcal{F}p)(\kappa)}{\sigma_\kappa(d)\gamma_\kappa(d)} \otimes \frac{\Delta y}{2\pi}\ \text{csinc}_L\left(\Delta y\ \kappa\right)\right] d\kappa \tag{7.55}$$

It is now clear that, in the case of uniform sampling,

$$R(\kappa) = \frac{\Delta y}{2\pi}\ \text{csinc}_L\left(\Delta y\ \kappa\right) = \frac{1}{\sqrt{2\pi}}\left[\mathcal{F}\ \text{Ш}\left(\frac{\cdot}{\Delta y}\right)\ \Pi\left(\frac{\cdot}{L\Delta y}\right)\right](\kappa) \tag{7.56}$$

This result can be simply derived also by applying the property (2.59) of the circular sinc function to equation (7.48).

It can be observed that $R(\kappa)$ is a real valued, even and periodic function, with period $\kappa_a = 2\pi/(\Delta y)$, with zeros at $\kappa = \pm\kappa_a n/L,\ n/L \notin \mathbb{N}$. $R(\kappa)$ depends on the number of

secondary sources L and on their spacing Δy, but it is independent of the wave number k. More specifically, the distance Δy between the secondary sources determines the period of $R(\kappa)$, while the width of the lobes at $\kappa = \pm n\kappa_a$ is inversely proportional to the product $L\Delta y$, that is the *aperture* of the array. Figure 7.20 shows a plot of the function $R(\kappa)$ for $L = 11$ and $\Delta y = 0.1$ m (the array aperture is $L\Delta y = 1.1$ m).

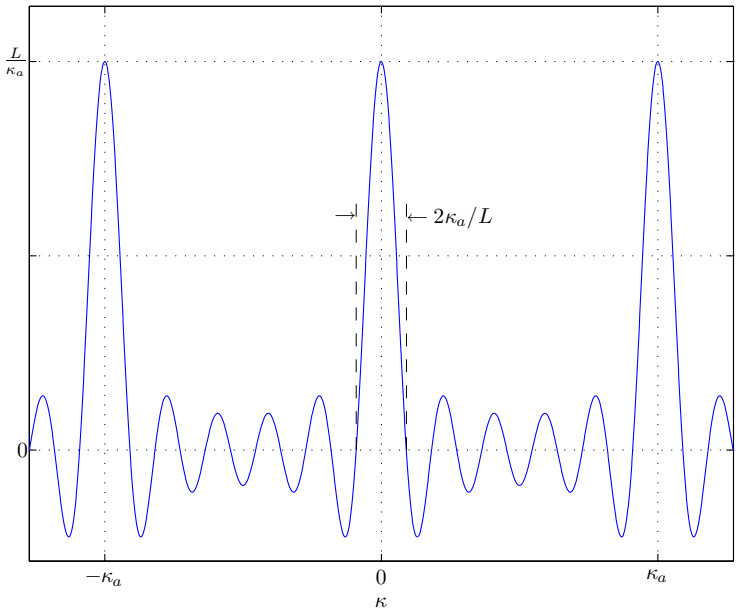

FIGURE 7.20: Function $R(\kappa)$ for $L = 11$ and $\Delta y = 0.1$ m.

Using formulae (2.60), (2.32) and (2.57) the following relations can be derived:

$$\lim_{L\to\infty} R(\kappa) = \sum_{n=-\infty}^{\infty} \delta(\kappa - n\kappa_a) = \sum_{\ell=-\infty}^{\infty} e^{i\kappa\ell\Delta y} \frac{\Delta y}{2\pi} \tag{7.57}$$

$$\lim_{\substack{\Delta y\to 0 \\ L\Delta y\to S_{\partial\Lambda}}} R(\kappa) = \frac{\Delta y}{2\pi} \frac{\sin(S_{\partial\Lambda}\kappa/2)}{\Delta y\,\kappa/2} = \frac{S_{\partial\Lambda}}{2\pi} \operatorname{sinc}\left(S_{\partial\Lambda}\frac{\kappa}{2}\right) \tag{7.58}$$

The second of these formulae represents the case of a continuous distribution of sources on a finite segment of length $S_{\partial\Lambda}$. It indicates that the restriction of the continuous source distribution to a finite subset of $\partial\Lambda$ introduces smearing of the spectrum of the reproduced field (a Dirac delta function becomes a sinc function).

The first formula above clearly resembles equation (7.48) and involves an infinite number of secondary sources, with spacing Δy between one another. This result demonstrates the well known phenomenon that the sampling of the continuous density $a(\mathbf{y})$ generates

periodic repetitions of the spectrum of the reproduced field, namely

$$\begin{aligned}\hat{p}(\mathbf{z}) &= \int_{\partial\Lambda} G(\mathbf{z},y)\left[a(y)\sum_{\ell=-\infty}^{\infty}\delta(y-\ell\Delta y)\Delta y\right]\,dy \\ &= \sum_{n=-\infty}^{\infty}\int_{\mathbb{R}}\frac{e^{i\kappa z_1}}{\sqrt{2\pi}}\left[\frac{\zeta(\kappa-n\kappa_a)\;e^{i\zeta(\kappa)|z_3|}}{\zeta(\kappa)\;e^{i\zeta(\kappa-n\kappa_a)d}}\right](\mathcal{F}p)(\kappa-n\kappa_a)\;\;d\kappa\end{aligned} \tag{7.59}$$

It should be noticed that these are not simple periodic repetition, as they are modulated by the ratio $\sigma_\kappa/\sigma_{\kappa+n\kappa_a}$ (the term within square brackets), analogous to the modal cross efficiency defined previously.

7.1.9.2 Example with plane waves

We consider now the case of a target field given by a single plane wave (either evanescent or propagating) of the form

$$p(\mathbf{z}) = e^{i\mathbf{z}\cdot\mathbf{k}} = e^{i[z_1\tilde{\kappa}+z_3\zeta(\tilde{\kappa})]},\quad \mathbf{z}\in\mathbb{R}^2,\ \tilde{\kappa}\in\mathbb{R} \tag{7.60}$$

We observe that, for $\mathbf{z}\in\partial V$ (namely $z_3 = d$)

$$(\mathcal{F}p)(\kappa) = \int_{\mathbb{R}}\frac{e^{-i\kappa z_1}}{\sqrt{2\pi}}e^{i[z_1\tilde{\kappa}+d\zeta(\tilde{\kappa})]}dz_1 = \sqrt{2\pi}\;e^{id\zeta(\tilde{\kappa})}\;\delta(\kappa-\tilde{\kappa}) \tag{7.61}$$

Meaning that the spatial spectrum of the target field is a single Dirac delta function. From equation (4.101) we have that

$$a(y) = -i2\zeta(\tilde{\kappa})e^{i\kappa y} \tag{7.62}$$

The reproduction is attempted initially with an array including an infinite number of uniformly arranged secondary sources. Inserting (7.61) in equation (7.59) and applying the usual properties of the Dirac delta function, we obtain

$$\hat{p}(\mathbf{z}) = \sum_{n=-\infty}^{\infty}\frac{\zeta(\tilde{\kappa})}{\zeta(\tilde{\kappa}+n\kappa_a)}\;e^{i[z_1(\tilde{\kappa}+n\kappa_a)+|z_3|\zeta(\tilde{\kappa}+n\kappa_a)]},\quad \mathbf{z}\in\mathbb{R}^2 \tag{7.63}$$

Since $\zeta(\tilde{\kappa}+n\kappa_a)$ could be either a real number or a purely imaginary number, the reproduced field is a superposition of an infinite number of evanescent waves ($|\tilde{\kappa}+n\kappa_a| > k$) and potentially also propagating waves ($|\tilde{\kappa}+n\kappa_a| < k$). We will refer to the elements of the series above such that $n \neq 0$ as *aliased waves*. Each aliased wave is modulated by a factor given by the fraction in the formula above (analogous to the modal cross-efficiency).

It is reasonable to consider the propagating aliased waves to be the most dangerous reproduction artifacts, since their effect is not limited to the near field of the array. Such

waves are generated when the condition $|\tilde{\kappa} + n\kappa_a| < k$ is verified. This happens when at least one $n \in \{\pm 1, \pm 2, \pm 3, \cdots\}$ exists such that

$$(n\kappa_a - k) < \tilde{\kappa} < (n\kappa_a + k) \tag{7.64}$$

Figure 7.21 shows a diagrammatic representation of this condition, for $\kappa_a = \pi k$. If the spectral line $\delta(\kappa - \tilde{\kappa})$ lies within one of the regions shadowed in yellow, then the aliased field generated by the discrete array will include propagating plane waves. The red and green arrows in the figure represent two target fields consisting of a single evanescent wave ($\tilde{\kappa} = -\kappa_a 4/5 \approx -2.51\ k$) and of a propagating plane wave ($\tilde{\kappa} = \kappa_a/4 \approx 0.79\ k$), respectively, for which the aliased field includes (red arrow) or does not include (green arrow) propagating waves. In the first case, the fact is remarkable that, in spite of the target field being an evanescent wave, the reproduced field might include propagating waves.

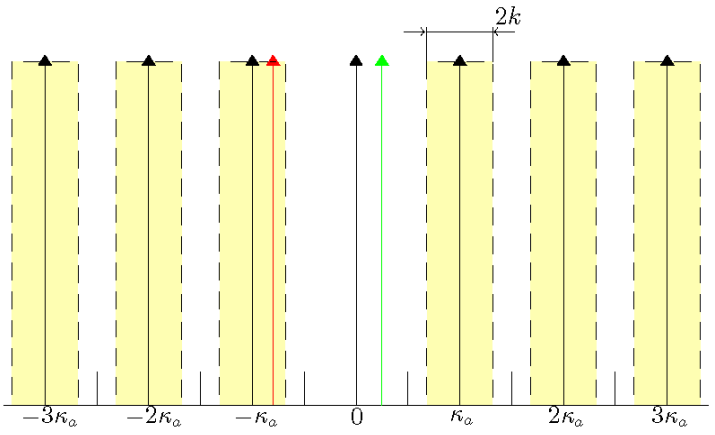

FIGURE 7.21: Diagrammatic representation of equation (7.64), for $\kappa_a = \pi k$. The red arrow represents an evanescent wave ($\tilde{\kappa} \approx -2.51\ k$), the reproduction of which generates both propagating and evanescent aliased waves. The green arrow represents a propagating plane wave ($\tilde{\kappa} \approx 0.79\ k$), whose reproduced field does not include propagating aliased waves.

Observing Figure 7.21 it can be noticed that, when both k and $|\tilde{\kappa}|$ are smaller than $\kappa_a/2$, all aliased waves are evanescent, regardless of the target field being a propagating or an evanescent wave. When either $|\tilde{\kappa}| > \kappa_a/2$ or $\kappa_a/2 < k < \kappa_a$ the aliased field might or might not include one or more propagating waves. If both k and $|\tilde{\kappa}|$ are larger than $\kappa_a/2$ or if $k > \kappa_a$ then at least one propagating aliased wave is generated. The worst situation occurs when $\kappa/2 < k < |\tilde{\kappa}|$: in this case the target field is an evanescent wave, while the reproduced field includes propagating components, which are aliased waves with a potentially large amplitude factor $\zeta(\tilde{\kappa})/\zeta(\tilde{\kappa} + n\kappa_a)$.

The number of secondary sources is now limited to the finite number L. The expression for the reproduced field is given by inserting (7.60) into equation (7.55), thus obtaining

$$\hat{p}(\mathbf{z}) \quad = \quad \int_{\mathbb{R}} e^{i[\kappa z_1 + \zeta(\kappa)|z_3|]} \left(\frac{\zeta(\tilde{\kappa})}{\zeta(\kappa)} \frac{\Delta y}{2\pi} \operatorname{csinc}_L \left(\Delta y \left(\kappa - \tilde{\kappa} \right) \right) \right) d\kappa \tag{7.65}$$

Note that when $L \to \infty$ this equation coincides with (7.63) for the relation (2.60). The formula above can be regarded as a linear superposition of an infinite number of evanescent and propagating plane waves, with the amplitude of each wave given by the function within brackets.

The magnitude of the Fourier transform of the reproduced field $\hat{p}(\mathbf{z})$, $z_3 = 0.01$ m, computed with formula (7.65), is shown in Figure 7.22. The following choices of the parameters have been made: $L = 201$, $k = 20$ rad/m, $\Delta y = 0.1$ m (hence $\kappa_a = \pi k$). The target fields are the two plane waves illustrated by Figure 7.21, with $\tilde{\kappa} = \kappa_a/4$ (Figure 7.22 a) and $\tilde{\kappa} = \kappa_a\ 4/5$ (Figure 7.22 b). The area highlighted in yellow corresponds to $|\kappa| < k$, that is the region of propagating waves. It can be observed that, in the second case (b), the peak associated with the aliased propagating wave ($\kappa = 4/5\kappa_a + \kappa_a$) is larger in magnitude than the peak corresponding to the target evanescent wave, even though the reproduced field is measured at just 1 cm away from the array of secondary sources.

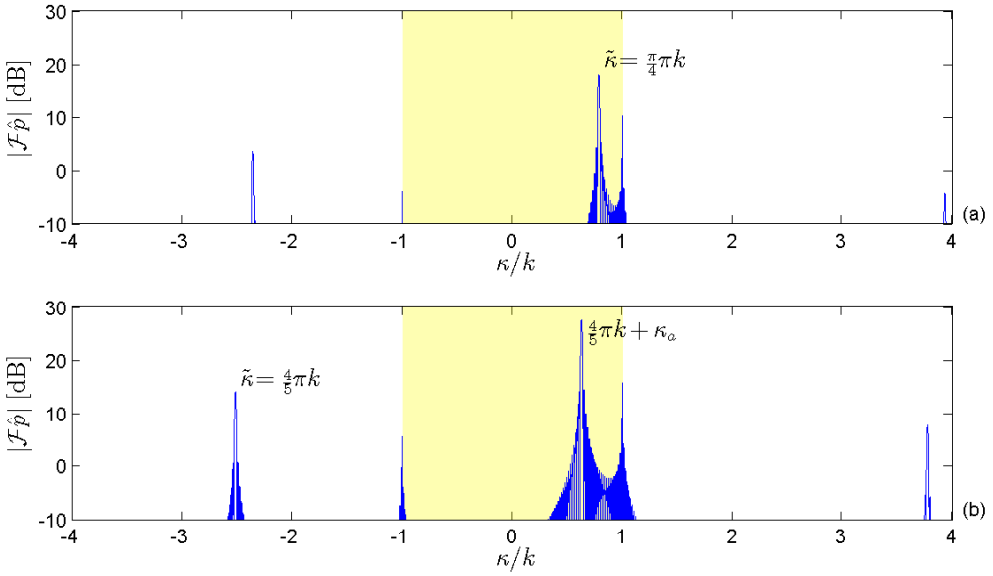

FIGURE 7.22: Absolute vale (dB scale) of the Fourier transform of the reproduced field $\hat{p}(\mathbf{z})$, $z_3 = 0.01$ m. The target fields are a single propagating wave with $\tilde{\kappa} = \kappa_a\ 4/5$ (a) and an evanescent wave with $\tilde{\kappa} = \kappa_a/4$ (b). The area highlighted in yellow represents the propagating wave region.

The target and reproduced fields discussed above are shown in figures 7.23 and 7.24 (for $\tilde{\kappa} = \kappa_a/4$) and in figures 7.25 and 7.26 (for $\tilde{\kappa} = -\kappa_a 5/4$). The total plotted area spans a square region of 2x2 m^2, while the aperture of the array is $L\Delta y = 20.1$ m. In both

figures 7.24 and 7.26 the reproduced field is generated by the 201 infinite line sources (a limited number of them are represented by the vertical lines) and is computed applying directly formula (7.1) with source strength $\ddot{m}_\ell$ computed with equation (7.6).

The target field represented in Figure 7.23 is a propagating wave of the form given by equation (7.60), with $\tilde{\kappa} = k\pi/4$. The corresponding reproduced field, shown in Figure 7.24, is accurate and does not include large energy propagating aliased waves. Propagating aliased waves with small energy, mainly traveling in a direction parallel to $\partial\Lambda$ (that is with $\kappa = k$, as illustrated in Figure 7.22 b), are present due to the limited aperture of the array.

The target field in Figure 7.25 is an evanescent wave. The field in the region $z_3 > 0$, although very small in magnitude, is not zero. The corresponding reproduced field, reported in Figure 7.26 clearly shows the high energy aliased propagating wave, with $\kappa = \tilde{\kappa} + \kappa_a$ (see Figure 7.22).

These considerations lead to the following conclusions: the reproduction of the pseudo-evanescent component of the target field (see Section 6.2.1) is a risky task, since spatial aliasing might determine the occurrence of aliased propagating waves. To be on the safe side, it is possible to limit the spatial spectrum of the target field to $|\kappa| < \kappa_a - k$, provided that $k < \kappa_a$ (if this is not the case, propagating aliasing components can not be avoided). This condition avoids the generation of propagating aliased waves, but on the other hand, it does not allow for the reproduction of the pseudo-evanescent component of the target field and allows for the reproduction of only part of its pseudo-propagating component. In Section 4.3 we have seen that, for $|\kappa| < k$, the direction of propagation of a plane wave of the form (7.60) in respect to the perpendicular to $\partial\Lambda$ is given by $\sin^{-1}(\kappa/k)$. In light of this, we observe that the condition $|\kappa| < \kappa_a - k$ requires the direction ϑ of the intensity vector of the reproduced field to be constrained by $|\vartheta| < \sin^{-1}(\kappa_a/k - 1)$. This condition could sometimes represent a serious limitation, and it might be preferable to substitute it with the milder condition $|\kappa| < k$, obviously at the cost of generating propagating aliased waves.

In the literature on Wave Field Synthesis, the two anti-aliasing conditions $k \leq \kappa_a/2 = \pi/(\Delta y)$ [DNM03] and $|\kappa| \leq \kappa_a/2$ [Sta97] are often reported. Both are a direct application of the well known Shannon sampling theorem [Mar01], and are clearly different from the requirement $|\kappa| < \kappa_a - k$ above. In fact, the condition $k \leq \kappa_a/2$ is too stringent since it does not take into consideration the fact that no aliasing artifacts are present in the far field also for the component of the target field with $|\kappa| < \kappa_a - k < \kappa_a/2 < k$ (Figure 7.21 might help visualizing this situation). On the other hand, the condition $|\kappa| \leq \kappa_a/2$ may prove too loose in the case of $\kappa_a - k < |\kappa| < \kappa_a/2 < k$, or too strict when $k < \kappa_a/2 < |\kappa| < \kappa_a - k$ (although in this case only the reproduction of the pseudo-evanescent component of the target field is penalized).

Finally, it is important to remark that, under any of these conditions, the field reproduced with a discrete linear array does always include aliasing artifacts. In the best of cases, these artifacts include only evanescent waves and their effect is limited to the near field of the array of secondary sources.

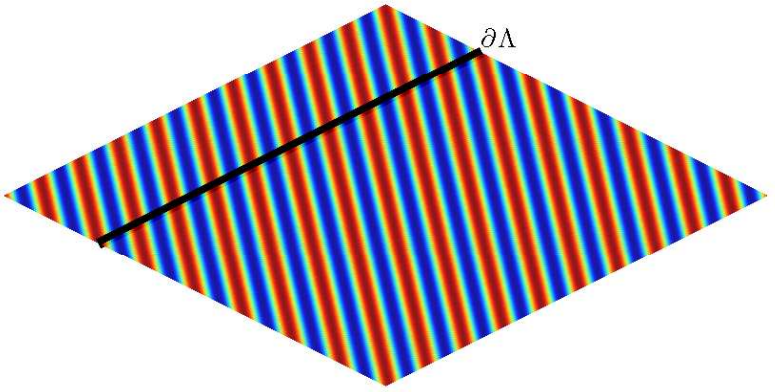

FIGURE 7.23: Sound field due to a propagating plane wave with $k = 20$ rad/m and $\tilde{\kappa} = \pi k/4$.

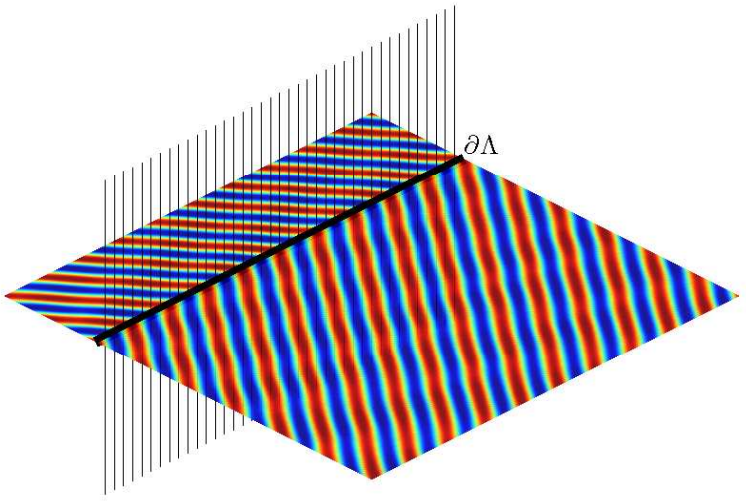

FIGURE 7.24: The field of a propagating plane wave with $k = 20$ rad/m and $\tilde{\kappa} = \pi k/4$ reproduced by an array of 210 vertical line sources with spacing $\Delta y = 0.1$ m. The vertical lines represents a portion of the secondary sources.

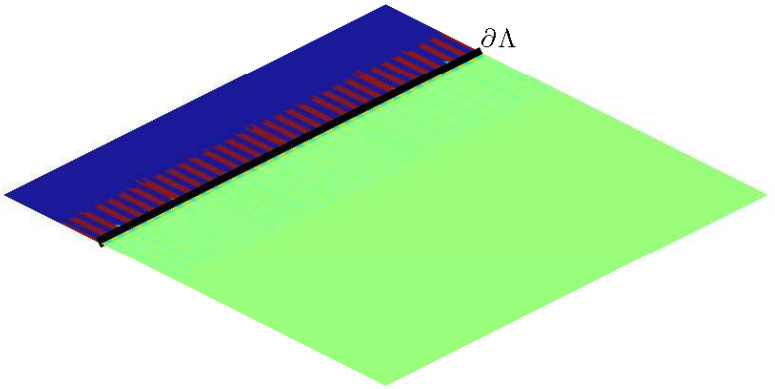

FIGURE 7.25: Sound field due to an evanescent wave with $k = 20\,\text{rad/m}$ and $\tilde{\kappa} = -\pi k 4/5$. Although very small in magnitude, the field in the region with $z_3 > 0$ is not zero.

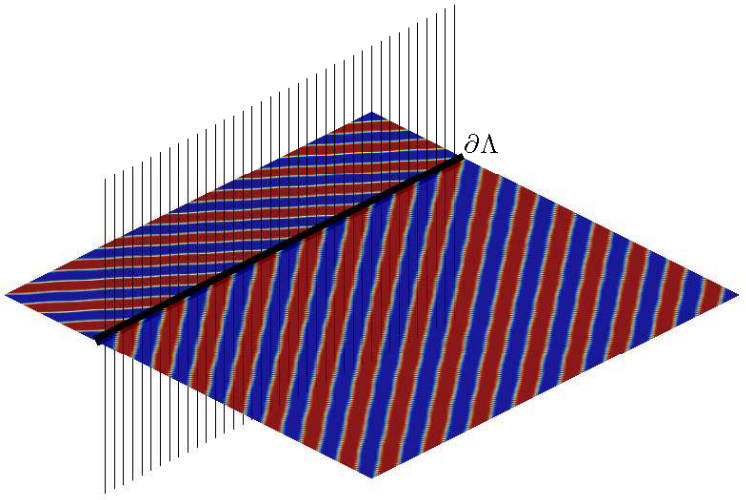

FIGURE 7.26: The field of an evanescent wave with $k = 20\,\text{rad/m}$ and $\tilde{\kappa} = -\pi k 4/5$ reproduced by an array of 210 vertical line sources with spacing $\Delta y = 0.1\,\text{m}$. The vertical lines represents a portion of the secondary sources. The field is dominated by the propagating aliased wave with $\kappa = \tilde{\kappa} + \kappa_a$.

7.2 Numerical solution of the integral equation

In Chapter 3 the sound field reproduction problem has been formulated as an integral equation of the first kind (equation (3.19)). Its solution has been derived by means of the singular value decomposition of the integral operator involved. We have seen that this approach provides a powerful method to derive analytically an explicit expression of the solution $a(\mathbf{y})$ once the singular system of the operator is known. The singular value decomposition (or, more generally, the spectral decomposition of the integral operator) is clearly not the only method available for the solution of the integral equation (3.19). A widely used approach is provided by the numerical solution. This involves the discretization of the single layer potential (3.15), which is represented by a matrix, and of the two functions $p(\mathbf{x})$ (the pressure profile) and $a(\mathbf{y})$ (the source strength density), which are represented by vectors. This technique can be by all means regarded as a Boundary Element Method (BEM), seeking the solution of an interior problem (since $V \subseteq \Lambda$) and using an indirect-implicit formulation (following the classification suggested by Valdivia and Williams [VW04]). For the case under consideration, the boundaries $\partial\Lambda$ and ∂V are generally not coincident. This has the advantage of avoiding the singularity of the Green function (equations (3.6) and (3.7) with $\mathbf{z} = \mathbf{y}$). On the other hand, the solution can not be derived by direct application of the jump relation (6.80), as discussed in Section 6.4.

Boundary element methods have been widely studied, and the interested reader can refer to the extensive literature on this subject (see, for example, [CZ92]). In what follows, a brief presentation of the simple technique introduced above is given. It should be made clear that this method is not the only method available, nor it claims to be the most accurate. Most of the points on the discretization process brought in Section 7.1 are of relevance for this subject too.

As a first step, we define two sampling schemes $\{\mathbf{y}_\ell\}$, $\ell = 1, 2, ...L$ and $\{\mathbf{x}_k\}$, $k = 1, 2, ...K$ for the boundaries $\partial\Lambda$ and ∂V, respectively, with the corresponding Dirichlet cells of area/length ΔS_ℓ, $\tilde{\Delta} S_k$. Then we approximate equation (3.19), that is

$$p(\mathbf{x}) = (Sa)(\mathbf{x}) = \int_{\partial\Lambda} G(\mathbf{x}, \mathbf{y}) a(\mathbf{y}) dS(\mathbf{y}), \quad \mathbf{x} \in \partial V \tag{7.66}$$

using the following discretized version [2]

$$\mathbf{p} = \mathbf{S}\boldsymbol{\Delta}\mathbf{a} \tag{7.67}$$

or equivalently

$$p_k = \sum_{\ell=1}^{L} S_{k,\ell}\, a_\ell\, \Delta_{\ell,\ell}, \quad k = 1, 2, ...K \tag{7.68}$$

[2] An alternative definition would include matrix $\boldsymbol{\Delta}$ into the definition of matrix $\mathbf{S}$, and matrix $\tilde{\boldsymbol{\Delta}}$ into matrix $\mathbf{S}_{inv}$. This would lead equations (7.67) and (7.70) to become $\mathbf{p} = \mathbf{S}\mathbf{a}$ and $\mathbf{a} = \mathbf{S}_{inv}\mathbf{p}$, respectively.

where the matrices $\mathbf{S}$ and Δ and the vectors $\mathbf{p}$ and $\mathbf{a}$ are given respectively by

$$\begin{array}{lll} S_{k,\ell} := & G(\mathbf{x}_k, \mathbf{y}_\ell), & 1 \leq k \leq K,\ 1 \leq \ell \leq L \\ p_k := & p(\mathbf{x}_k), & 1 \leq k \leq K \\ a_\ell := & a(\mathbf{y}_\ell), & 1 \leq \ell \leq L \\ \mathbf{\Delta} := & \mathrm{diag}\{\Delta \mathrm{S}_1, \Delta \mathrm{S}_1, ... \Delta \mathrm{S}_\mathrm{L}\} & \end{array} \tag{7.69}$$

We want to compute the matrix $\mathbf{S}_{inv}$ such that

$$\mathbf{a} = \mathbf{S}_{inv} \tilde{\mathbf{\Delta}} \mathbf{p} \tag{7.70}$$

where $\tilde{\mathbf{\Delta}}$ is defined by

$$\tilde{\mathbf{\Delta}} := \mathrm{diag}\{\tilde{\Delta} \mathrm{S}_1, \tilde{\Delta} \mathrm{S}_1, ... \tilde{\Delta} \mathrm{S}_\mathrm{K}\} \tag{7.71}$$

Note that $\mathbf{S}_{inv}$ is not the inverse of $\mathbf{S}$, but is simply related to the latter by the following relation

$$\mathbf{S}_{inv} = \left(\tilde{\mathbf{\Delta}} \mathbf{S} \mathbf{\Delta}\right)^{-1} = \mathbf{\Delta^{-1}} \mathbf{S^{-1}} \tilde{\mathbf{\Delta}}^{\mathbf{-1}} \tag{7.72}$$

obtained by multiplying both sides of (7.67) by $\tilde{\mathbf{\Delta}}$. This holds when the inverse matrix $\mathbf{S}^{-1}$ exists. If this is not the case, it is possible to substitute $\mathbf{S}^{-1}$ in the equation above with the Moore-Penrose pseudoinverse matrix $\mathbf{S}^\dagger$ given by

$$\mathbf{S}^\dagger = \left(\mathbf{S}^* \mathbf{S}\right)^{-1} \mathbf{S}^*, \quad \text{if the columns of } \mathbf{S} \text{ are linearly independent} \tag{7.73}$$

$$\mathbf{S}^\dagger = \mathbf{S}^* \left(\mathbf{S}\mathbf{S}^*\right)^{-1}, \quad \text{if the rows of } \mathbf{S} \text{ are linearly independent} \tag{7.74}$$

The first of these equations provides a least squares solution of the inverse problem, that is the approximate solution $\mathbf{a}$ that minimizes $|\mathbf{S}\mathbf{\Delta}\mathbf{a} - \mathbf{p}|$ (analogous to the L^2 norm $||Sa - p||$), and is typically used when $K > L$. The second equation is generally used when $L > K$ and the inverse problem has multiple exact solutions. Formula (7.74) gives the solution with minimum norm. If an exact inverse of $\mathbf{S}$ does not exist, equation (7.70) provides an approximate solution $\mathbf{a}$.

It is possible to choose a sampling scheme for $\partial\Lambda$, which is consistent with the discrete distribution of the secondary sources. In this case, once $\mathbf{S}_{inv}$ has been determined, it is possible to define the strength of the secondary sources $\ddot{m}_\ell$ as follows

$$\ddot{m}_\ell = \sum_{k=1}^{K} S_{inv,k,\ell}\ p_k\ \tilde{\Delta}_{k,k}, \quad \ell = 1, 2, ... L \tag{7.75}$$

It is clear that the reproduced field is then given by equation (7.1).

This approach is analogous to the sound field reproduction method proposed by Kirkeby and Nelson [KN93], with the relevant difference that the target field is sampled only on the boundary of the control region instead of on its interior. This difference leads to a considerable reduction of the computational effort.

The numerical solution of the integral clearly coincides with the analytical solution when both L and K tend to infinity and consequently ΔS_ℓ and ΔS_k tend to zero. The ill-posedness of the inverse problem discussed in Chapter 5 is still an issue. More specifically, matrix $\mathbf{S}$ is generally ill-conditioned, and the problem of non-uniqueness might arise at the Dirichlet eigenvalues of the control region. The nonexistence issue for focused sources appears to be removed for the fact that $\mathbf{S}$ has finite dimensions and therefore has a finite number of singular values. This is in practice analogous to the regularization of the integral operator S by spectral truncation, as discussed in Section 6.1. Other regularization techniques for matrix inversion, such as the Tikhonov method, can of course be applied.

7.2.1 Sampling of ∂V, spatial aliasing and geometry of the control volume

The discretization of the integral equation (3.19) involves the sampling of both $\partial\Lambda$ and ∂V. This in turns implies, as we have seen in Section 7.1, that the reproduced field is only an approximation of the desired field. As *both* functions $a(\mathbf{y})$ *and* $p(\mathbf{x})$ have been substituted by their sampled versions, the artifacts in the field reproduction are caused not only by the finite number L of secondary sources, connected to the sampling scheme $\{\mathbf{y}_\ell\}$, but also by the finite number K of sampling points of $p(\mathbf{x})$, related the sampling scheme $\{\mathbf{x}_k\}$. We have discussed in Section 7.1 that the sampling of $a(\mathbf{y})$ causes aliasing artifacts, which may potentially severely degrade the accuracy of the field reproduction. Analogous considerations may be done for the sampling of $p(\mathbf{x})$. In order to avoid the occurrence of aliasing artifacts, we need to make sure that the sampling scheme $\{\mathbf{x}_k\}$ is such that $p(\mathbf{x})$ is unambiguously represented by its sampled values $\{p(\mathbf{x}_k)\}$. This corresponds to a generalization of the well known *Shannon theorem*. We require that the pressure profile can be expressed (at least with good approximation) by a *finite* sum of pressure modes $p_n(\mathbf{x})$, generally the low order modes. In other words, we want $p(\mathbf{x})$ to be spatially band-limited. If this is the case, a finite number of properly arranged sampling points is enough to describe accurately all relevant pressure modes, thus providing an accurate representation of $p(\mathbf{x})$ and avoiding aliasing artifacts.

What has been said implies that, for a given sampling scheme, we need to make sure that the target pressure profile is represented only by those modes, which we can observe without ambiguity. If this is not the case, no signal processing strategy can avoid the occurrence of aliasing. This problem is simply overcome for sampling of functions of time by the use of analog low-pass filters (known as anti-aliasing filters), applied to the signal before it is sampled. The design of spatial low-pass, anti-aliasing filters is not trivial, if not impossible. On the other hand, in practical cases, the Fourier coefficients $\langle p_n|p\rangle_{\partial V}$ of the pressure profile are very small in magnitude for n larger than a given value N (which of course depends on the given target field). As a matter of fact, we

have seen that acoustic propagation in space acts as a low pass filter itself. This suggests that, in the case of a point-like virtual source, the further V is from the source, the smaller is the presence of high order modes in the pressure profile. This in turn suggests that the distance of V from the virtual source would act as a low-pass spatial filter for $p(\mathbf{x})$. This phenomenon can be easily observed in the geometrical arrangements including parallel planes or lines: the pressure modes $p_\kappa(\mathbf{x})$ that have more rapid spatial variation correspond to large values of κ. When $\kappa > k$, these modes are evanescent and decay exponentially with the distance d of ∂V from $\partial\Lambda$. We can therefore choose d to be such that the energy of all modes corresponding to a κ larger than a given value is, in practice, negligible on ∂V. A similar analysis of the spherical and circular geometries leads to the conclusion that high order modes are attenuated by making the radius R_V small (for a given radius R_Λ). It is therefore possible to avoid spatial aliasing artifacts determined by the sampling of $p(\mathbf{x})$ by wisely choosing in combination the number of samples K and the control region V. These considerations clearly hold provided that all virtual sources lie in the exterior of Λ.

It is evident that the mechanisms that determine the decay of the high order modes is the very same one that is responsible for the ill-conditioning of the inverse problem. For this reason, it is important to apply in combination strategies for avoiding spatial aliasing *and* ill-conditioning. A sensible strategy may be the following: given a number of samples K (usually determined by the computational capabilities of the system), and given a sampling scheme for ∂V, which is as uniform as possible, we can determine the number N of pressure modes, which are unambiguously described by the given sampling scheme. This can be performed by observing the orthogonality matrix given by equation (7.14). We may then define the appropriate parameter of V (d for planar and linear arrangements, R_V for spherical and circular arrangements), for which the energy of modes of order larger than N is small. Finally, we may apply a regularization strategy (typically spectral damping) in odder to avoid the ill-conditioning artifacts caused by the inversion of the singular values σ_n, with $n > N$. The choice of the 'anti-aliasing' parameter of V depends generally on the operating frequency ω. It is therefore a sensible option to choose a *frequency dependent control volume*, when this is possible.

As a final remark, the fact is recalled that the aliasing issues arising from the sampling of $p(\mathbf{x})$ may occur only if the integral equation (3.19) is solved numerically, or in general if no continuous description of the pressure profile is available (as in the case of measurement with a microphone array). These issues are therefore not relevant in the case when the solution $a(\mathbf{y})$ is computed by the analytical singular value decomposition discussed in Chapter 3. It is also worth mentioning that, if the sampling schemes $\{\mathbf{y}_\ell\}$ and $\{\mathbf{x}_k\}$ are uniform (or almost uniform) and no significant spatial aliasing effect occur for the sampling of $p(\mathbf{x})$, simulations show that the computations of the source strengths $\ddot{m}_\ell$ with the analytical and numerical solution of the integral equation give nearly identical results.

7.2.2 Singular Value Decomposition of matrix S

It is possible to calculate the numerical Singular Value Decomposition of $\mathbf{S}$. It is expected that, in the limit of $K, L \to \infty$, the discrete singular system $\mathbf{U}, \mathbf{\Sigma}, \mathbf{V}$, such that $\mathbf{S} = \mathbf{U}\mathbf{\Sigma}\mathbf{V}^{\mathrm{H}}$ (see Appendix A), can be expressed in terms of the singular functions and values $\sigma_n, a_n(\mathbf{y}), p_n(\mathbf{x})$. In [FN07c] the authors have shown that this is the case for spherical geometry. Considering the singular system (4.7)-(4.11) and assuming a regular sampling, such that $\Delta S = 4\pi R_\Lambda^2/L, \forall \ell$ and $\tilde{\Delta} S = 4\pi R_V^2/K, \forall k$, in the limit of $K, L, N \to \infty$ we have that

$$\begin{aligned}
\Sigma_{n,n} &= \frac{\sqrt{KL}}{4\pi} k |j_\nu(kR_V) h_\nu(kR_\Lambda)| = \frac{\sigma_n}{\sqrt{\Delta S \tilde{\Delta} S}} && (7.76)\\
V_{\ell,n} &= \sqrt{\frac{4\pi}{L}} Y_\nu^\mu(\hat{\mathbf{y}}_\ell) = \sqrt{\Delta S} a_n(\mathbf{y}_\ell) && (7.77)\\
U_{k,n} &= \sqrt{\frac{4\pi}{K}} \gamma_\nu Y_\nu^\mu(\hat{\mathbf{x}}_k) = \sqrt{\tilde{\Delta} S} p_n(\mathbf{x}_k) && (7.78)\\
\gamma_\nu &= \exp\left[i \left(\arg\left(h_\nu(kR_\Lambda) j_\nu(kR_V) \right) + \frac{\pi}{2} \right) \right] \\
\nu &= \lceil \sqrt{n} - 1 \rceil, \qquad \mu = n - 1 - \nu - \nu^2
\end{aligned}$$

This is proven by the following relations:

$$\begin{aligned}
\lim_{N\to\infty} \left(\mathbf{U}\mathbf{\Sigma}\mathbf{V}^{\mathrm{H}} \right)_{k,\ell} &= \lim_{N\to\infty} \sum_{n=1}^{N} \sum_{\mu=-\nu}^{\nu} \gamma_\nu Y_\nu^\mu(\hat{\mathbf{x}}_k) k |j_\nu(kR_V) h_\nu(kR_\Lambda)| Y_\nu^\mu(\hat{\mathbf{y}}_\ell)^* = G(\mathbf{x}_k, \mathbf{y}_\ell) \\
\lim_{K\to\infty} \left(\mathbf{U}^{\mathrm{H}}\mathbf{U} \right)_{n,n'} &= \lim_{K\to\infty} \sum_{k=1}^{K} \gamma_\nu^* Y_\nu^\mu(\hat{\mathbf{x}}_k)^* \gamma_{\nu'} Y_{\nu'}^{\mu'}(\hat{\mathbf{x}}_k) \frac{4\pi}{K} = \delta_{\nu,\nu'} \delta_{\mu,\mu'} = \delta_{n,n'} \\
\lim_{N,K\to\infty} \left(\mathbf{U}\mathbf{U}^{\mathrm{H}} \right)_{k,k'} &= \lim_{N,K\to\infty} \sum_{\nu=1}^{N} \sum_{\mu=-\nu}^{\nu} \gamma_\nu Y_\nu^\mu(\hat{\mathbf{x}}_k) \gamma_\nu^* Y_\nu^\mu(\hat{\mathbf{x}}_{k'})^* \frac{4\pi}{K} = \lim_{K\to\infty} \delta_\Omega(\mathbf{x}_k - \mathbf{x}_{k'}) \frac{4\pi}{K} \\
\lim_{L\to\infty} \left(\mathbf{V}^{\mathrm{H}}\mathbf{V} \right)_{n,n'} &= \lim_{L\to\infty} \sum_{\ell=1}^{L} Y_\nu^\mu(\hat{\mathbf{y}}_\ell)^* Y_{\nu'}^{\mu'}(\hat{\mathbf{y}}_\ell) \frac{4\pi}{L} = \delta_{\nu,\nu'} \delta_{\mu,\mu'} = \delta_{n,n'} \\
\lim_{N,L\to\infty} \left(\mathbf{V}\mathbf{V}^{\mathrm{H}} \right)_{\ell,\ell'} &= \lim_{N,L\to\infty} \sum_{\nu=1}^{N} \sum_{\mu=-\nu}^{\nu} Y_\nu^\mu(\hat{\mathbf{y}}_\ell) Y_\nu^\mu(\hat{\mathbf{y}}_{\ell'})^* \frac{4\pi}{L} = \lim_{L\to\infty} \delta_\Omega(\mathbf{y}_\ell - \mathbf{y}_{\ell'}) \frac{4\pi}{L}
\end{aligned}$$

The first of these results is due to equation (4.2), the second one and fourth one to the orthonormality relation of the spherical harmonics (2.52) and the third and fifth results are derived from the completeness relation of the spherical harmonics (2.55) and from definition of the Dirac delta function.

7.3 Sound fields with broadband frequency content and filter design

Up to this point we have considered that the wave number k and consequently the frequency ω are fixed. This assumption has proved to be useful for the derivation simple expression of the solution $a(\mathbf{y})$. In the general case, however, the desired acoustic field is not monochromatic, meaning that it does not include the contribution of a single frequency, but it is rather a function of ω. We restore therefore the dependency of the field $p(\mathbf{z}, \omega)$ on the frequency ω, which we had removed at the beginning of Chapter 3 in order to keep the notation simple. This dependency holds also for the source strength density $a(\mathbf{y}, \omega)$, for the source strengths $\ddot{m}_\ell(\omega)$, for the Green function $G(\mathbf{x}, \mathbf{y}, \omega)$ and also for the singular system $\sigma_n(\omega)$, $a_n(\mathbf{y}, \omega)$, $p_n(\mathbf{x}, \omega)$. It is clear that any function $f(k)$ can be equivalently expressed as $f(\omega/c)$, as long as the speed of sound c is uniform on $\mathbb{R}^m$, $m = 2, 3$, namely, if the sound propagates in a non-dispersive medium.

The expression of all functions above can be derived by performing the Fourier transform (2.89), reported here:

$$p(\omega) = (\mathcal{F}_t P)(\omega) = \frac{1}{\sqrt{2\pi}} \int_{-\infty}^{\infty} P(t) e^{i\omega t} dt \tag{7.79}$$

The time-domain transformed function is here represented by the upper-case of the corresponding lower-case letter representing the frequency domain function, when this does not lead to any ambiguity (as for example in the case of the Bessel functions). In particular, in view of the results presented previously, we have that time domain source strength $\ddot{M}_\ell(t)$ is given by the following expression:

$$\ddot{M}_\ell(t) = \Delta S_\ell \int_{\mathbb{R}} \frac{e^{-i\omega t}}{\sqrt{2\pi}} \left[\sum_{n=1}^{\infty} \frac{a_n(\mathbf{y}_\ell, \omega)}{\sigma_n(\omega)} \int_{\partial V} p_n(\mathbf{x}, \omega) (\mathcal{F}_t P)(\mathbf{x}, \omega) dS(\mathbf{x}) \right] d\omega \tag{7.80}$$

Clearly the application of regularization techniques discussed in Chapter 6 can be included in the expression above. The latter corresponds to the signal driving the secondary source located at $\mathbf{y}_\ell$, which in practical cases corresponds to the electrical signal driving a loudspeaker. Therefore we will also refer to $\ddot{M}_\ell(t)$ as the *secondary source signal*. The determination of these signals is the final goal of the digital signal processing of a practical sound field reproduction system. The equation above provides a very general formula which can be applied to an arbitrary arrangement (provided, clearly, that an expression for the singular system is given). In this section we determine the expression of these signals for some of the special arrangements introduced in Chapter 4.

7.3.1 Digital filters for a virtual point source

In a large number of cases of practical interest, the pressure profile $P(\mathbf{x}, t)$ is such that it can be expressed by the form

$$P(\mathbf{x}, t) = P_\delta(\mathbf{x}, t) \otimes V(t) \tag{7.81}$$

and henceforth

$$(\mathcal{F}_t P)(\mathbf{x}, \omega) = \sqrt{2\pi}(\mathcal{F}_t P_\delta)(\omega)(\mathcal{F}_t V)(\omega) = \sqrt{2\pi} p_\delta(\mathbf{x}, \omega) v(\omega) \tag{7.82}$$

This is the case, for example, of the field due to a motionless point source located at $\mathbf{q}$, either in the free field or in a reverberant environment. In this example, $P_\delta(\mathbf{x}, t)$ is the impulse response of the point source in the given environment, evaluated on the control boundary ∂V. This function can be either expressed analytically, computed numerically or directly measured. The source signal $\ddot{M}_\ell(t)$ can be therefore computed from

$$\ddot{M}_\ell(t) = F_\ell(t) \otimes V(t) \tag{7.83}$$

where the function $F_\ell(t)$ is a filter, depending only on the location $\mathbf{y}_\ell$ of the corresponding secondary source and on the location $\mathbf{q}$ of the virtual source.

Using a general approach, valid for an arbitrary geometrical arrangement, the filters can be computed in the frequency domain by substituting $P(\mathbf{x}, t)$ with $P_\delta(\mathbf{x}, t)$ in equation (7.80), which yields (in the frequency domain)

$$f_\ell(\omega) = \Delta S_\ell \sum_{n=1}^{\infty} \frac{a_n(\mathbf{y}_\ell, \omega)}{\sigma_n(\omega)} \int_{\partial V} p_n(\mathbf{x}, \omega)(\mathcal{F}_t P_\delta)(\mathbf{x}, \omega) dS(\mathbf{x}) \tag{7.84}$$

These filters can be implemented as digital FIR filters. The calculation can be performed for a discrete set of frequencies $\{n_\omega \Delta\omega\}$, where $n_\omega = 0, 1, 2...N_\omega$ and $\Delta\omega$ is the frequency resolution. The upper frequency $N_\omega \Delta\omega$ is determined by the given practical application and by the sampling frequency of the digital converters. For audio purposes, we usually have that $N_\omega \Delta\omega \geq 20000$ Hz. The optimal resolution $\Delta\omega$ depends on the smoothness of $f_\ell(\omega)$. As the latter is inversely proportional to the length T of the support of $(\mathcal{F}_t^{-1} f_\ell)(t)$, which we assume to be finite (namely $T > 0$ exists such that $(\mathcal{F}_t^{-1} f_\ell)(t) = 0, |t - \xi| > T/2$ for some $\xi \in \mathbb{R}$), a good estimate of $\Delta\omega$ is given by

$$\Delta\omega \leq \frac{2\pi}{T} \tag{7.85}$$

This relation is directly related to the well known Heisenberg uncertainty principle. The values $f_\ell(n_\omega \Delta\omega)$ define the coefficients of the digital filter for the secondary source located at $\mathbf{y}_\ell$, defined in the frequency domain.

This calculation requires a considerable computational effort since, in the general case, all functions involved in equation (7.84) depend on ω and should therefore be recalculated for each n_ω. In what follows, we will see that simpler relation can be derived for separable geometries, leading to considerable reduction of the computational cost.

In order to guarantee the causality of the filters, it is recommended to include an extra delay to the filters (in the experiments presented in the next chapter, a delay equal to 1/4 of the total length of the filter has been included in the calculation of the filters).

7.3.2 Source signals and digital filters for spherical geometry

Equation (4.19), providing the solution $a(\mathbf{y})$ for the spherical geometry arrangement, is reported here:

$$a(\mathbf{y}) = \sum_{\nu=0}^{\infty} \sum_{\mu=-\nu}^{\nu} \frac{Y_\nu^\mu(\hat{\mathbf{y}})}{ikR_V^2 R_\Lambda^2 h_\nu^{(1)}(kR_\Lambda) j_\nu(kR_V)} \langle Y_\nu^\mu | p \rangle_{\partial V} \tag{7.86}$$

From the definition of the spherical harmonics (2.51), it can be observed that these functions do not depend on the frequency. The fact that they are complex valued functions may appear as a problem, but it can be simply overcome by redefining the spherical harmonics after having substituted the complex exponential with sines and cosines (the Legendre associated functions considered here are real valued functions). This is accomplished by defining [3]

$$\begin{aligned} \tilde{Y}_\nu^\mu(\hat{\mathbf{x}}) = \tilde{Y}_\nu^\mu(\theta_x, \phi_x) &:= \frac{\mathrm{sgn}(\mu + \delta_{\nu,0})^\mu}{\sqrt{2 - \delta_{\nu,0}}} \left(\mathrm{sgn}(\mu) \mathrm{Y}_\nu^\mu(\hat{\mathbf{x}}) + (-1)^\mu \mathrm{Y}_\nu^{-\mu}(\hat{\mathbf{x}}) \right) \\ &= \sqrt{\frac{(2\nu+1)(\nu-|\mu|)!}{4\pi(\nu+|\mu|)!}} P_\nu^{|\mu|}(\cos\theta_x) \times \begin{cases} \sqrt{2}\cos(\mu\phi_x), & \mu > 0 \\ 1, & \mu = 0 \\ \sqrt{2}\sin(|\mu|\phi_x), & \mu < 0 \end{cases} \end{aligned} \tag{7.87}$$

where the relation $Y_\nu^{-\mu}(\hat{\mathbf{x}}) = (-1)^\mu Y_\nu^\mu(\hat{\mathbf{x}})^*$ [Wil99] has been used and $\mathrm{sgn}(\cdot)$ is the sign function defined by

$$\mathrm{sgn}(\mu) = \begin{cases} 1, & \mu > 0 \\ 0, & \mu = 0 \\ -1, & \mu < 0 \end{cases}$$

It can be shown that the real valued spherical harmonics $\tilde{Y}_\nu^\mu(\hat{\mathbf{x}})$ define a complete orthonormal set for $L^2(\Omega)$. This substitution of the basis functions is actually not mandatory, as the choice of real valued or complex valued spherical harmonics does not affect the solution that, as we have seen, is generally unique. Despite that, the use of real valued spherical harmonics $\tilde{Y}_\nu^\mu$ might prove useful for DSP implementation and is preferred

[3] Alternative definitions of real spherical harmonics are also given in the literature (see for example [DNM03]).

by some authors, especially in the literature on Ambisonics [Ger73], [Dan00], [DNM03], [AE98].

The secondary source strengths $\ddot{m}_\ell(\omega)$ can be therefore simply computed from equations (7.86) by

$$\ddot{m}_\ell(\omega) = \frac{\Delta S_\ell}{4\pi R_\Lambda^2} \sum_{\nu=0}^{N} \sum_{\mu=-\nu}^{\nu} \tilde{Y}_\nu^\mu(\hat{\mathbf{y}}_\ell) \left[\frac{4\pi}{i\frac{\omega}{c} h_\nu^{(1)}\left(\frac{\omega}{c}R_\Lambda\right) j_\nu\left(\frac{\omega}{c}R_V\right)} \right] \int_\Omega \tilde{Y}_\nu^\mu(\hat{\mathbf{x}}) (\mathcal{F}_t P)(\hat{\mathbf{x}}, \omega) dS(\hat{\mathbf{x}}) \tag{7.88}$$

where the order N of the series can be either infinity or a finite number, if a spectral cut-off of the operator has been applied. In the time domain, after having applied the convolution theorem (2.94) this expression becomes

$$\ddot{M}_\ell(t) = \frac{\Delta S_\ell}{4\pi R_\Lambda^2} \sum_{\nu=0}^{N} \sum_{\mu=-\nu}^{\nu} \tilde{Y}_\nu^\mu(\hat{\mathbf{y}}_\ell) \ \langle \tilde{Y}_\nu^\mu | \eta_\nu(t) \otimes P(\cdot, t) \rangle_\Omega \tag{7.89}$$

where

$$\eta_\nu(t) := \frac{1}{\sqrt{2\pi}} \left[\mathcal{F}_t^{-1} \frac{4\pi}{i\frac{\cdot}{c} h_\nu^{(1)}\left(\frac{\cdot}{c}R_\Lambda\right) j_\nu\left(\frac{\cdot}{c}R_V\right)} \right](t) \tag{7.90}$$

The fact is relevant that the filter $\eta_\nu(t)$ depends only on the parameter ν and does not depend on the angular location of the secondary source considered. The terms $\langle \tilde{Y}_\nu^\mu | \eta_\nu(t) \otimes P(\cdot, t) \rangle$ in (7.89) can be therefore computed once for all secondary sources. On the other hand, the only term depending on $\hat{\mathbf{y}}_\ell$ is a simple scalar (a gain) given by $\Delta S_\ell \tilde{Y}_\nu^\mu(\hat{\mathbf{y}}_\ell)$. This is a very simple and powerful method to compute the filters. Its simplicity derives from the fact that the wave equation (3.1), expressed in spherical coordinates, can be solved by separation of variables [Wil99].

The filter $\eta_\nu(t)$ can be simplified under the assumption that the region of interest for the reconstruction lies in the far field of the secondary sources. This is usually valid for frequencies associated with a wavelength much smaller than the array radius R_Λ. With this assumption we can insert the large argument approximation (2.43) for the Hankel function, thus obtaining

$$\begin{aligned} \eta_\nu(t) &= \frac{1}{\sqrt{2\pi}} \left[\mathcal{F}_t^{-1} \frac{i^\nu 4\pi R_\Lambda}{j_\nu\left(\frac{\cdot}{c}R_V\right)} e^{-i\frac{\cdot}{c}R_\Lambda} \right](t) \\ &= \frac{1}{\sqrt{2\pi}} \left[\mathcal{F}_t^{-1} \frac{i^\nu 4\pi}{j_\nu\left(\frac{\cdot}{c}R_V\right)} \right](t) \otimes R_\Lambda \delta\left(t + \frac{R_\Lambda}{c}\right) \end{aligned} \tag{7.91}$$

While the first term in the convolution above is a filter depending on R_V, the second term is a combination of a simple delay and a gain, which compensate for the radius of the array. In many circumstances of practical interest, this term can be neglected.

7.3.2.1 Digital filters for virtual point source in the free field

The filters $f_\ell(\omega)$ introduced above can be computed by inserting the impulse response $P_\delta(\mathbf{x},t)$ in place of the target field $P(\mathbf{x},t)$ in equation (7.88) (or in equation (7.89) for the time domain). In the case of a virtual source in the free field located at $\mathbf{q}\in\mathbb{R}^3\backslash\Lambda$, the solution $a(\mathbf{y})$ is given by equation (5.30) and the filters are therefore

$$f_\ell(\omega)=\frac{\Delta S_\ell}{4\pi R_\Lambda^2}\sum_{\nu=0}^{N}(2\nu+1)\Xi_\nu(\omega)P_\nu(\hat{\mathbf{q}}\cdot\hat{\mathbf{y}}_\ell) \tag{7.92}$$

where $\Xi_\nu(\omega)$ is the spatial filter defined by equation (5.35), namely

$$\Xi_\nu(\omega):=\frac{h_\nu\left(\frac{\omega}{c}q\right)}{h_\nu\left(\frac{\omega}{c}R_\Lambda\right)} \tag{7.93}$$

This filter could be expressed also in a different form, having considered the following expansion of the spherical Hankel functions, derived from [GR65, p.925 eq.8.466.1]

$$h_n(x)=i^{-n-1}\frac{e^{ix}}{x}\sum_{j=0}^{n}\left(\frac{i}{2}\right)^j\frac{(n+j)!}{j!(n-j)!}\frac{1}{x^j} \tag{7.94}$$

This result yields

$$\Xi_\nu(\omega) \;=\; \Xi_0(\omega)\,\tilde{\Xi}_\nu(\omega) \tag{7.95}$$

where

$$\Xi_0(\omega) \;=\; \frac{R_\Lambda}{q}\,e^{i\frac{\omega}{c}(q-R_\Lambda)} \tag{7.96}$$

$$\tilde{\Xi}_\nu(\omega) \;:=\; \frac{\sum_{j=0}^{\nu}\xi_{\nu,j}/(\omega q)^j}{\sum_{j=0}^{\nu}\xi_{\nu,j}/(\omega R_\Lambda)^j} \tag{7.97}$$

$$\xi_{\nu,j} \;:=\; \left(\frac{i}{2}\right)^j\frac{(\nu+j)!}{j!(\nu-j)!}c^j \tag{7.98}$$

The results above imply that the filter $\Xi_\nu(\omega)$ can be implemented as a simple gain R_Λ/q and a simple delay $\delta(t-(q-R_\Lambda)/c)$, both depending on the distance of the virtual source from $\partial\Lambda$, combined with the more complicated function $\tilde{\Xi}_\nu(\omega)$ (the latter reduces to unity in the far field, that is when $q,R_\Lambda\gg N/\omega$). In light of the convolution theorem (2.94), we obtain

$$(\mathcal{F}_t^{-1}\Xi_\nu)(t)=\frac{R_\Lambda}{q}\,\delta\left(t-\frac{q-R_\Lambda}{c}\right)\otimes\left(\mathcal{F}_t^{-1}\tilde{\Xi}_\nu\right)(t) \tag{7.99}$$

and

$$f_\ell(\omega)=\Xi_0(\omega)\,\frac{\Delta S_\ell}{4\pi R_\Lambda^2}\sum_{\nu=0}^{N}(2\nu+1)\tilde{\Xi}_\nu(\omega)P_\nu(\hat{\mathbf{q}}\cdot\hat{\mathbf{y}}_\ell) \tag{7.100}$$

The secondary source signals are given by the following expression:

$$\ddot{M}_\ell(t) = \frac{\Delta S_\ell}{4\pi R_\Lambda^2} \sum_{n=0}^{N} P_\nu(\hat{\mathbf{q}} \cdot \hat{\mathbf{y}}_\ell) \left[(2\nu+1)(\mathcal{F}_t^{-1}\tilde{\Xi}_\nu)(t) \otimes \frac{R_\Lambda}{q}\, \delta\left(t - \frac{q - R_\Lambda}{c}\right) \otimes V(t) \right] \tag{7.101}$$

where the term in square brackets is independent from ℓ and can be calculated once for all secondary sources. In many practical applications it is possible to neglect the convolution by $R_\Lambda/q \;\; \delta\big(t - (q - R_\Lambda)/c\big)$. It can be observed that the summation above includes only $N+1$ terms, while the summation (7.88) includes $(N+1)^2$ terms.

The expression above can be further simplified under the assumption that the control region is in the far field of both the virtual source and the secondary sources. This hypothesis is usually satisfied at high frequencies and is identical to the assumption that $q = R_\Lambda$, that is the virtual source is on $\partial\Lambda$. In these circumstances, as discussed in Section 5.6.1, $\Xi_\nu = 1$ for the large argument approximation of the Hankel functions (2.43) and f_ℓ corresponds to a Dirac delta function $\delta(\mathbf{y} - \mathbf{q})$ (up to a multiplication factor) when the series (7.92) is not truncated. This would imply that, if the location of the virtual source does not coincide with the location of one of the secondary sources, the reproduced field is zero. This effect could be possibly regarded as an extreme consequence of spatial aliasing. However, if the spherical harmonic series is truncated to the order $N < \infty$, chosen in accordance with the considerations discussed in Section 7.1, the expression for the filter is

$$f_\ell = \frac{\Delta S_\ell}{4\pi R_\Lambda^2} \sum_{\nu=0}^{N} (2\nu+1) P_\nu(\hat{\mathbf{q}} \cdot \hat{\mathbf{y}}_\ell) = \frac{\Delta S_\ell}{4\pi R_\Lambda^2} (N+1) \frac{P_N(\hat{\mathbf{q}} \cdot \hat{\mathbf{y}}_\ell) - P_{N+1}(\hat{\mathbf{q}} \cdot \hat{\mathbf{y}}_\ell)}{1 - \hat{\mathbf{q}} \cdot \hat{\mathbf{y}}_\ell} \tag{7.102}$$

where the Christoffel summation formula (2.48) has been used. It can be observed that this expression of f_ℓ gives a real valued function, which is independent of frequency, and can be therefore implemented by a simple gain rather than as a digital filter. This formula can be expressed as a function $f_\ell(\varphi_{\mathbf{q}\mathbf{y}_\ell})$ of the angle $\varphi_{\mathbf{q}\mathbf{y}_\ell}$ between the vectors $\mathbf{q}$ and $\mathbf{y}_\ell$. This function is referred to as a *panning function*.

In light of these results, we have that

$$\ddot{M}_\ell(t) = \left[\frac{\Delta S_\ell}{4\pi R_\Lambda^2} (N+1) \frac{P_\nu(\hat{\mathbf{q}} \cdot \hat{\mathbf{y}}_\ell) - P_{\nu+1}(\hat{\mathbf{q}} \cdot \hat{\mathbf{y}}_\ell)}{1 - \hat{\mathbf{q}} \cdot \hat{\mathbf{y}}_\ell} \right] V(t) \tag{7.103}$$

It is recalled that if the sampling scheme of $\partial\Lambda$ is uniform (or almost uniform), the term $\Delta S_\ell/(4\pi R_\Lambda^2)$ in all the expressions above can be simply substituted by $1/L$ (where L is the number of secondary sources).

Figure 7.27 shows a plot of the panning function above for different truncation orders $N = 3, 5, 8$. In order to normalize this function, the assumption is made that $\Delta S_\ell/(4\pi R_\Lambda^2) = 1/(N+1)^2$, corresponding to a number of secondary sources $L = (N+1)^2$ in the case

of ideal uniform sampling. It can be noticed that the larger the truncation order N, the narrower is the width of the main lobe, and that the panning functions has $2N$ zeros.

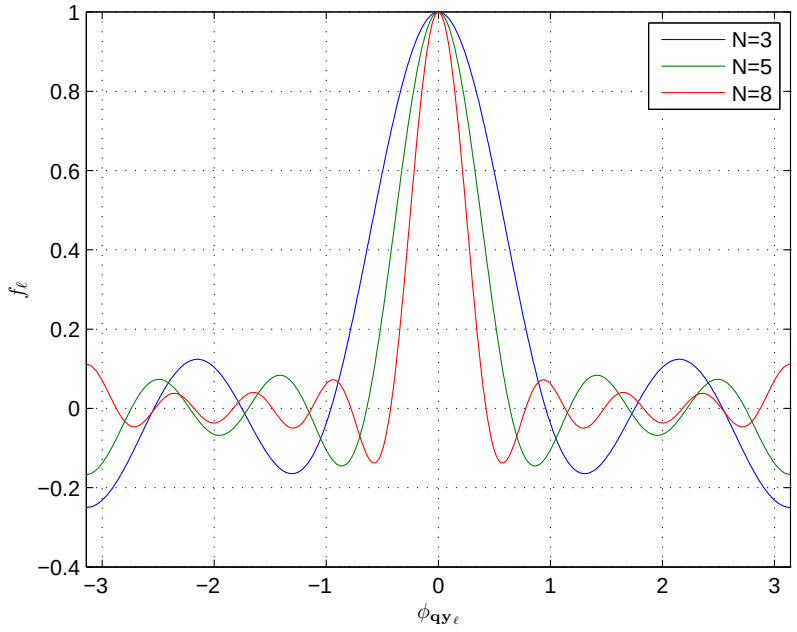

FIGURE 7.27: Panning function $f_\ell(\phi_{\mathbf{q}\mathbf{y}_\ell})$ for spherical geometry, provided by equation (7.102), for different truncation orders N. In order to normalize this function, the assumption is made that $\Delta S_\ell/(4\pi R_\Lambda^2) = 1/(N+1)^2$.

We now remove the far-field assumption which has been introduced above and we study the behavior of the filters $f_\ell(\omega)$ with the aid graphical representations. Figure 7.28 and Figure 7.29 represent the magnitude (dB) and the phase, respectively, of the filters $f_\ell(\omega)$ as a function of both the frequency ω and the angle $\varphi_{\mathbf{q}\mathbf{y}_\ell}$ between the vectors $\mathbf{q}$ and $\mathbf{y}_\ell$. The filters have been computed from equation (7.100), but without including the factor $\Xi_0(\omega)$ in the calculation. The series has been truncated to the order $N = 5$, and the assumption is made that $\Delta S/(4\pi R_\Lambda^2) = 1/(N+1)^2$ (that would be the ideal case of 36 uniformly arranged secondary sources). The secondary sources are assumed to be arranged on a sphere of radius $R_\Lambda = 1.5$ m. The filters have been computed for various distances q of the virtual source, namely 100 m, 3 m, 1.5 m and 1 m, the latter corresponding to the case of a focused source (see Section 6.2). The magnitude and phase of the filters for $\varphi_{\mathbf{q}\mathbf{y}_\ell} = 0$ rad and $\varphi_{\mathbf{q}\mathbf{y}_\ell} = \pi/2$ rad, identified respectively by the continuous and dashed horizontal black lines in figures 7.28 and 7.29 are reported in Figure 7.30.

Figure 7.31 reports the filters $\mathcal{F}_\ell(t)$ in the time domain, for $\varphi_{\mathbf{q}\mathbf{y}_\ell} = 0$ rad and $\varphi_{\mathbf{q}\mathbf{y}_\ell} = \pi/2$ rad and for various distances of the virtual source. The impulse responses of the filters have been calculated from an inverse discrete Fourier transform of the filters computed in the frequency domain. The FFT size is 1999 points with frequency interval

$df = 20.02$ Hz (the symmetry of the filters has been deployed and the computation has been performed for half of the FFT points).

The filter coefficients for 53.37 Hz and 533.7 Hz as a function of the angle $\varphi_{\mathbf{qy}_\ell}$ are identified respectively by the continuous and dashed vertical line in figures 7.28 and 7.29 and are reported in figures 7.32 and 7.33.

Figures 7.34 to 7.39 illustrate the same data as in the figures 7.28 to 7.33, with the difference that the filter computation has been carried out with a truncation order $N = 10$.

We observe now the behavior of the filters for a large distance $q > R_\Lambda$ of the virtual source. At low frequencies, the filters exhibit smooth variations of both amplitude and phase with respect to the variation of the angle $\varphi_{\mathbf{qy}_\ell}$, since they are dominated by the low order terms of the series (7.100) (see also the considerations presented in Section 5.6.1). When the frequency ω increases, the contribution of high orders of the series becomes progressively more relevant, and the number of phase oscillations from π to $-\pi$ with varying $\varphi_{\mathbf{qy}_\ell}$ increases, up to the limit of $2N$ oscillations imposed by the truncation order N. This limit determines the generation of the $2N$ *lobes* clearly shown in figures 7.32, 7.33, 7.38 and 7.39. In the high frequencies limits, the filters exhibit a constant behavior, which is given by the panning function (7.102).

Considering now the effect of the virtual source distance q, we observe that the latter does not affect the filters at high frequencies, apart from the factor $\Xi_0(\omega)$ not considered here. On the contrary, at low frequencies, the filters are largely influenced by the distance of the virtual source: we have seen that for large q the secondary sources signals are characterized by smooth variations with $\varphi_{\mathbf{qy}_\ell}$. When the virtual source gets closer, the contribution of the high order terms of the series becomes larger, and the number of phase oscillations of the filters with $\varphi_{\mathbf{qy}_\ell}$ increases progressively, up to the limit of $2N$ oscillation, which is reached when $q = R_\Lambda$. It has been observed that for this distance q the filters are independent of the frequency. When q decreases further we observe that, while the phase oscillations with $\varphi_{\mathbf{qy}_\ell}$ are limited by the truncation order, the magnitude of the filters increases progressively, as a consequence of the *high order explosion* responsible for the nonexistence or the instability of the solution, widely discussed in Chapter 5).

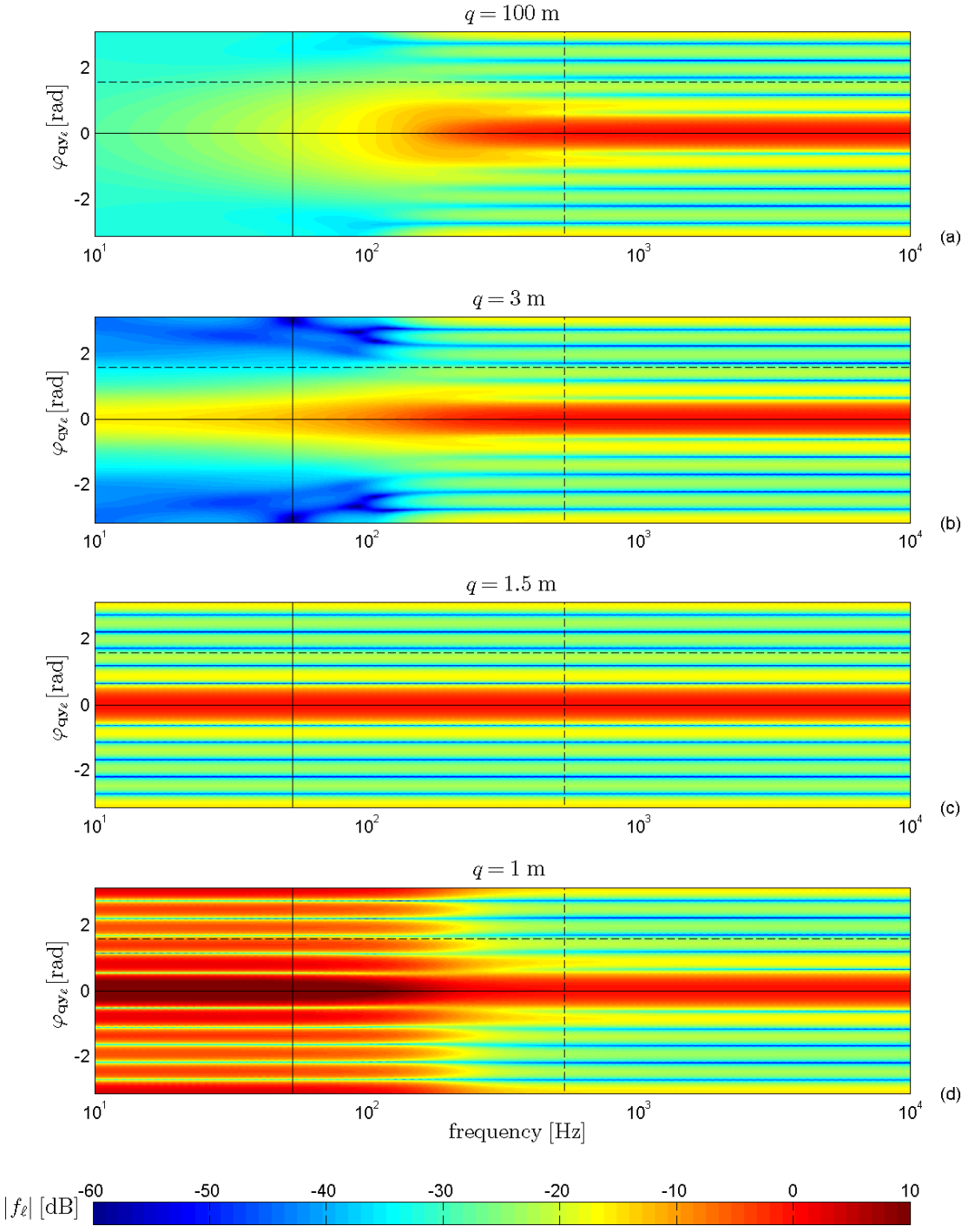

FIGURE 7.28: Magnitude (dB) of the filters f_ℓ, as a function of the frequency and of the angle $\varphi_{\mathbf{qy}_\ell}$. The filters have been computed from equation (7.100), without the term $\Xi_0(\omega)$ and for several values of the distance q of the virtual source, while the radial distance of the secondary sources is $R_\Lambda = 1.5$ m. The series has been truncated to the order $N = 5$.

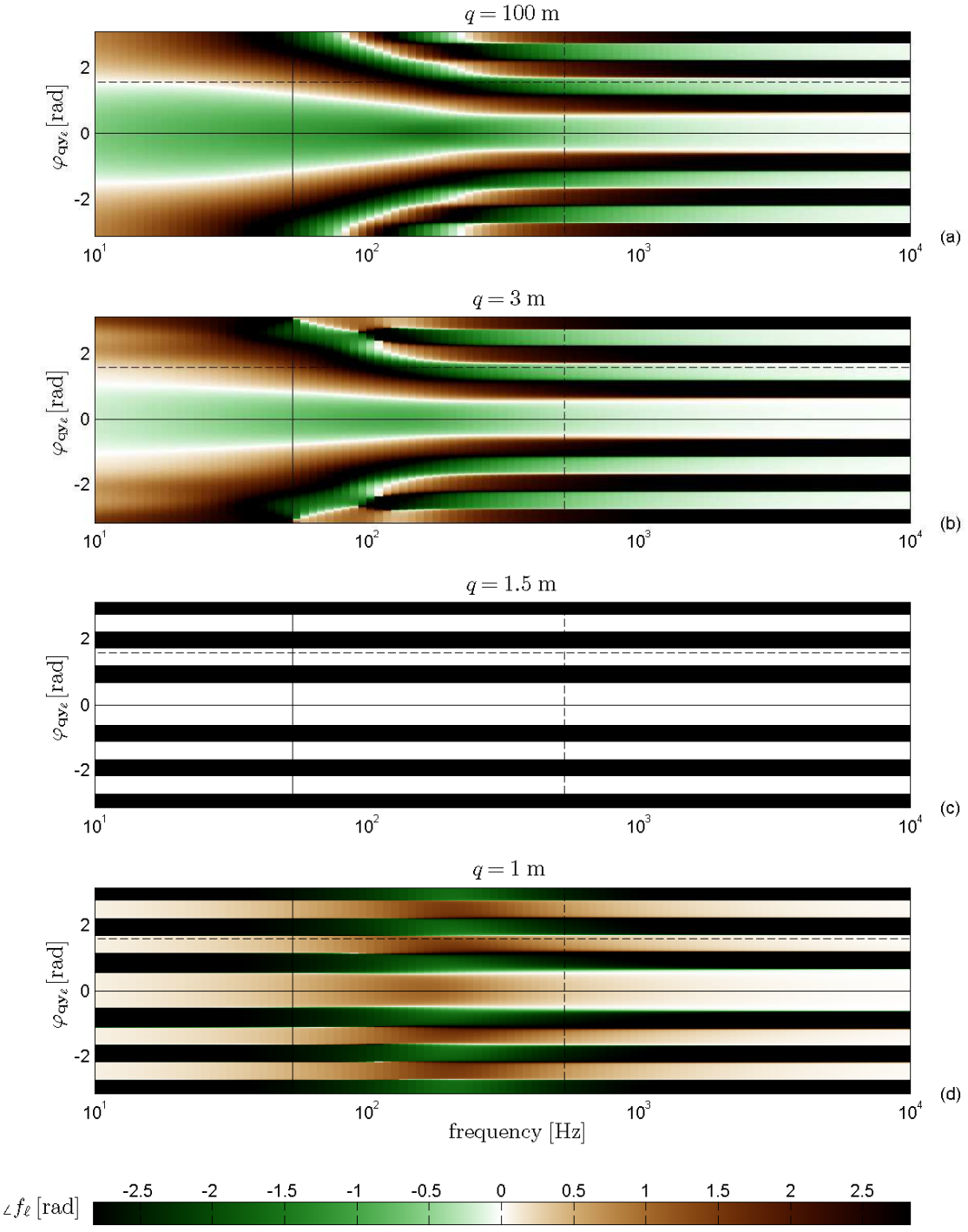

FIGURE 7.29: Phase of the filters f_ℓ, as a function of the frequency and of the angle $\varphi_{\mathbf{q}\mathbf{y}_\ell}$. The filters have been computed from equation (7.100), without the term $\Xi_0(\omega)$ and for several values of the distance q of the virtual source, while the radial distance of the secondary sources is $R_\Lambda = 1.5$ m. The series has been truncated to the order $N = 5$.

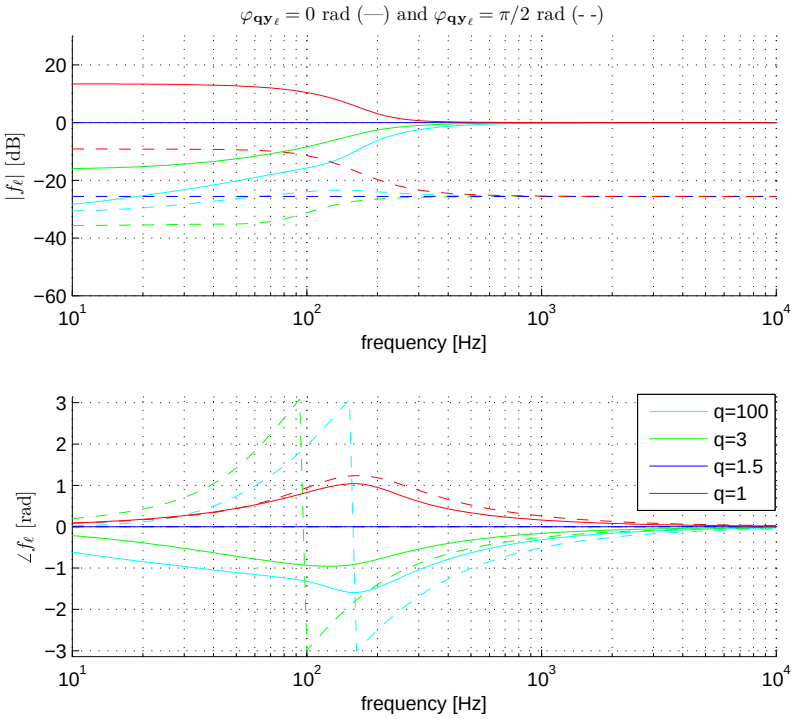

FIGURE 7.30: Magnitude and phase of the filters $f_\ell(\omega)$ for $\varphi_{\mathbf{qy}_\ell} = 0$ rad (continuous line) and $\varphi_{\mathbf{qy}_\ell} = \pi/2$ rad (dashed line). The truncation order is $N = 5$.

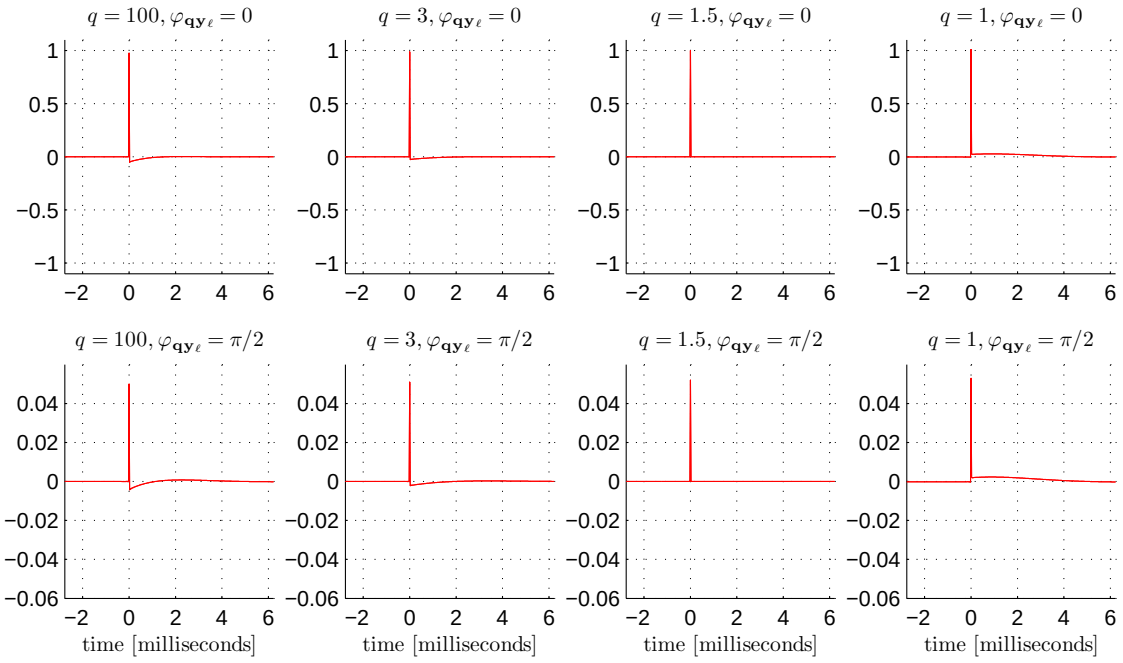

FIGURE 7.31: Filters $\mathcal{F}_\ell(t)$ (time domain) for $\varphi_{\mathbf{qy}_\ell} = 0$ rad and $\varphi_{\mathbf{qy}_\ell} = \pi/2$ rad. The truncation order is $N = 5$.

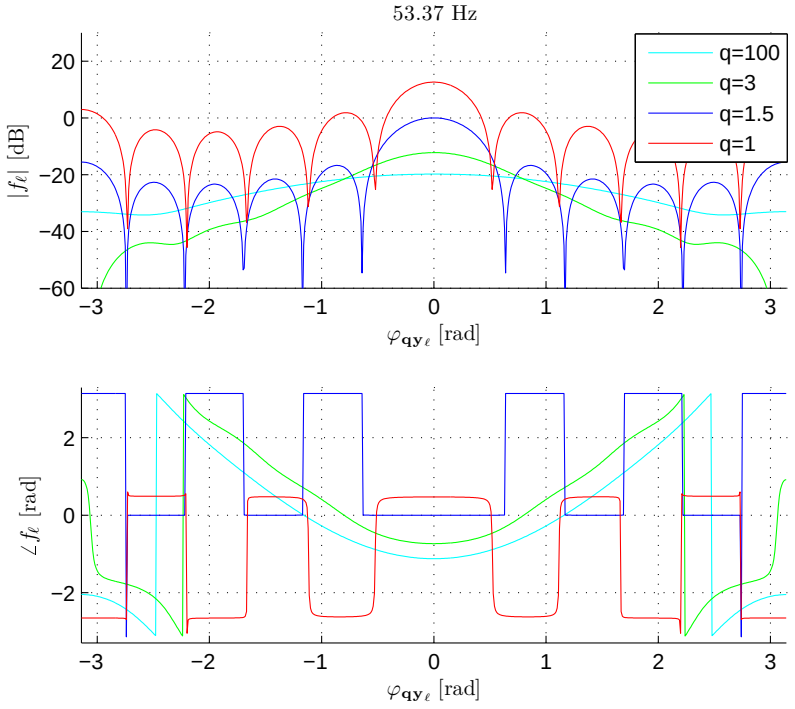

FIGURE 7.32: Magnitude and phase of the filter f_ℓ at 53.37 Hz as a function of the angle $\varphi_{\mathbf{q}\mathbf{y}_\ell}$. The truncation order is $N = 5$.

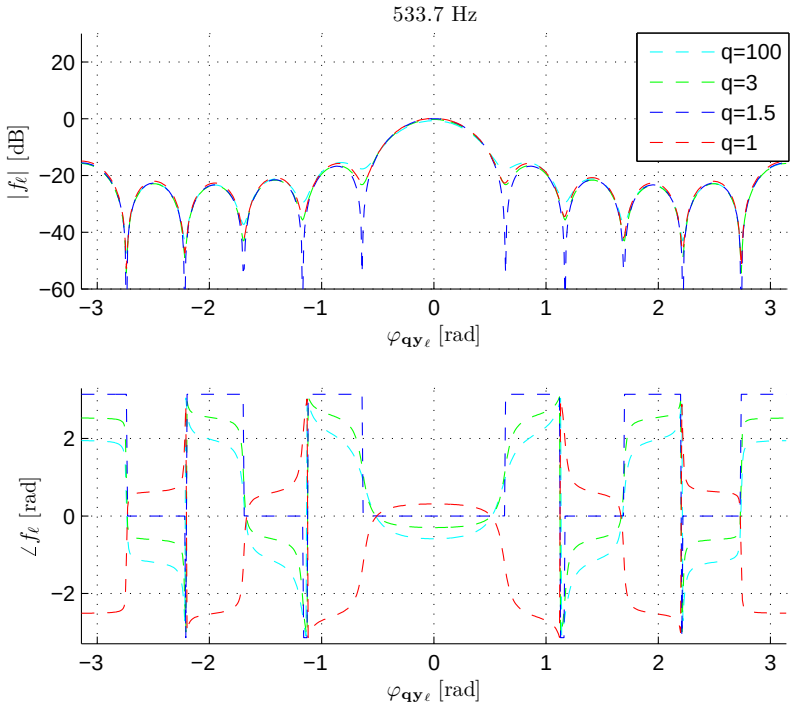

FIGURE 7.33: Magnitude and phase of the filter f_ℓ at 533.7 Hz as a function of the angle $\varphi_{\mathbf{q}\mathbf{y}_\ell}$. The truncation order is $N = 5$.

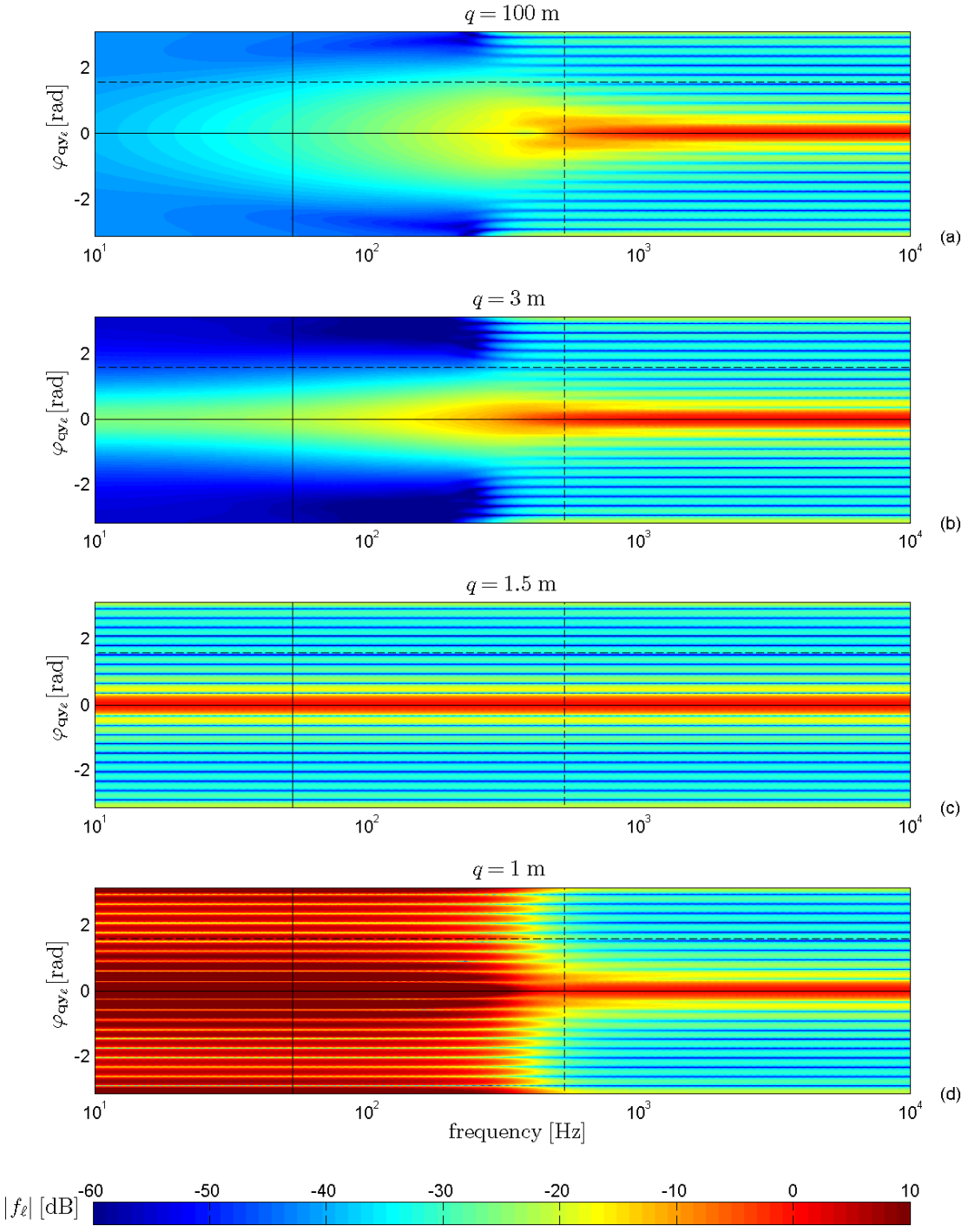

FIGURE 7.34: Magnitude (dB) of the filters f_ℓ, as a function of the frequency and of the angle $\varphi_{\mathbf{qy}_\ell}$. The filters have been computed from equation (7.100), without the term $\Xi_0(\omega)$ and for several values of the distance q of the virtual source, while the radial distance of the secondary sources is $R_\Lambda = 1.5$ m. The series has been truncated to the order $N = 10$.

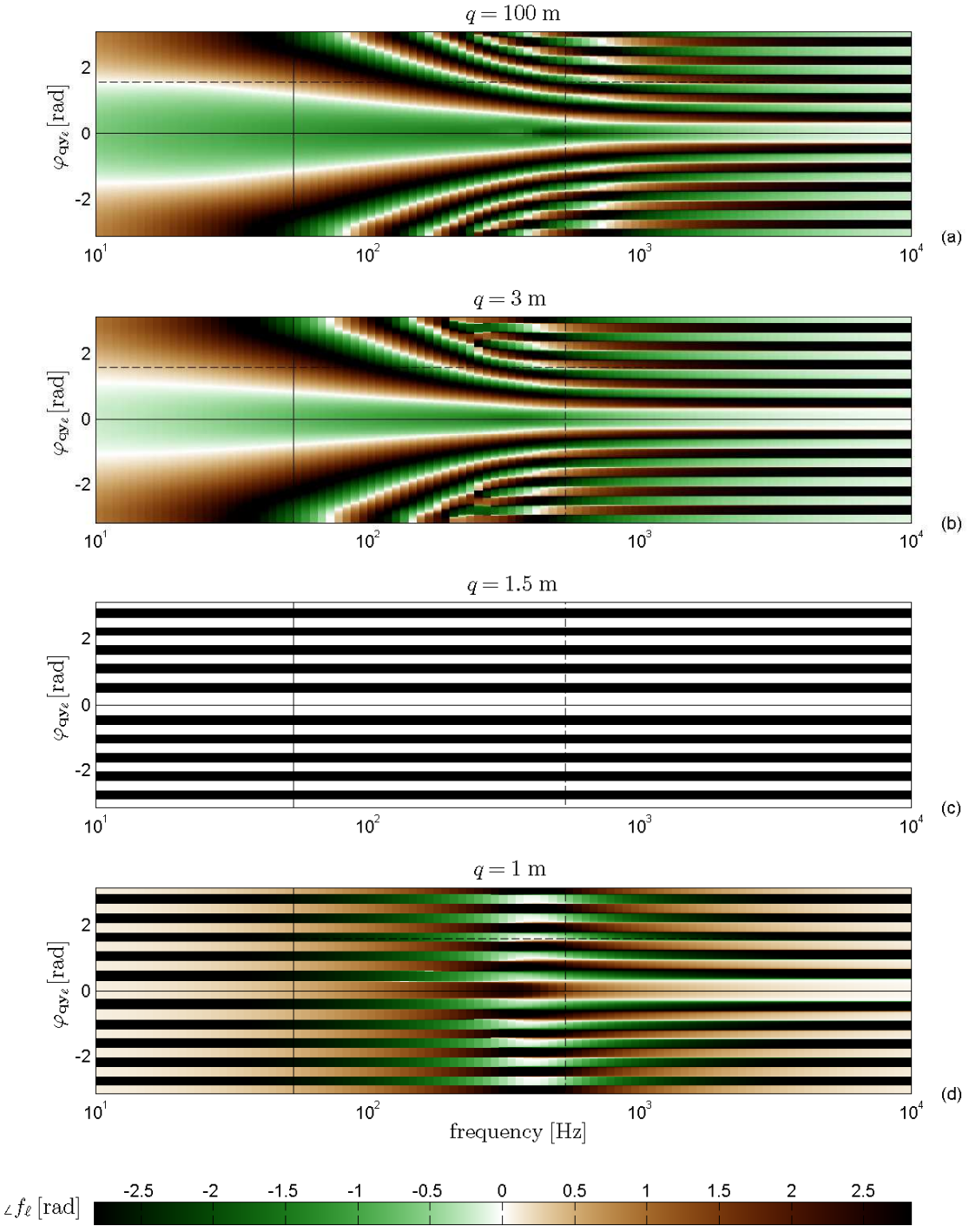

FIGURE 7.35: Phase of the filters f_ℓ, as a function of the frequency and of the angle $\varphi_{\mathbf{qy}_\ell}$. The filters have been computed from equation (7.100), without the term $\Xi_0(\omega)$ and for several values of the distance q of the virtual source, while the radial distance of the secondary sources is $R_\Lambda = 1.5$ m. The series has been truncated to the order $N = 10$.

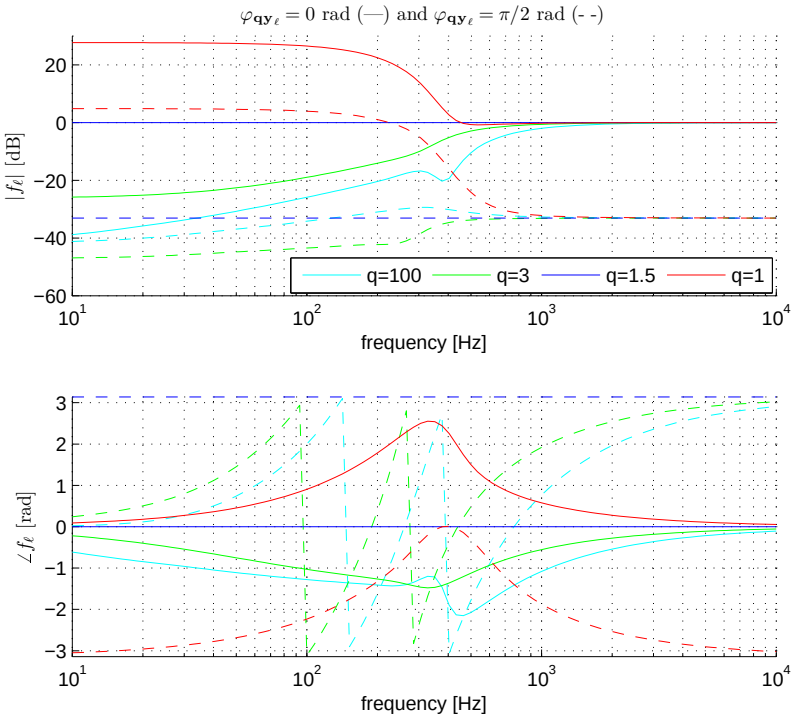

FIGURE 7.36: Magnitude and phase of the filters $f_\ell(\omega)$ for $\varphi_{\mathbf{qy}_\ell} = 0$ rad (continuous line) and $\varphi_{\mathbf{qy}_\ell} = \pi/2$ rad (dashed line). The truncation order is $N = 10$.

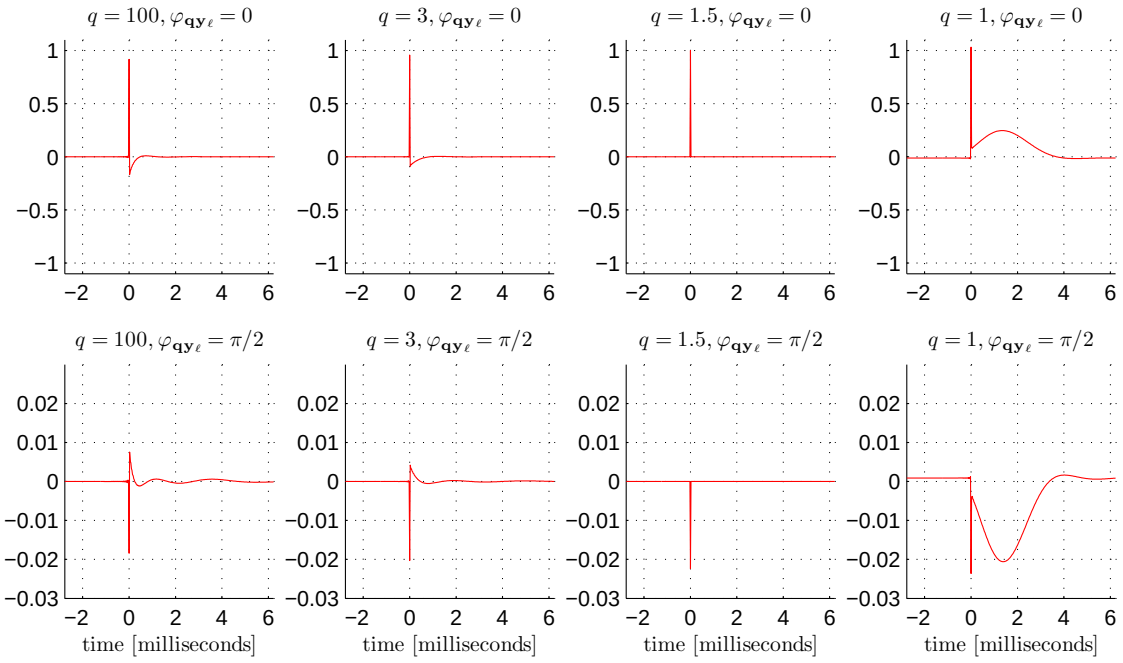

FIGURE 7.37: Filters $\mathcal{F}_\ell(t)$ (time domain) for $\varphi_{\mathbf{qy}_\ell} = 0$ rad and $\varphi_{\mathbf{qy}_\ell} = \pi/2$ rad. The truncation order is $N = 10$.

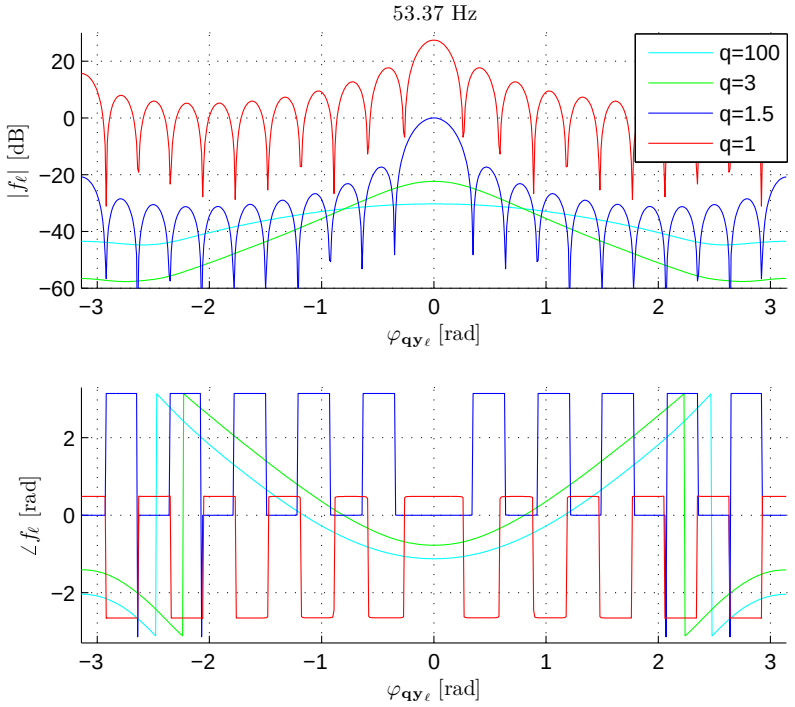

FIGURE 7.38: Magnitude and phase of the filter f_ℓ at 53.37 Hz as a function of the angle $\varphi_{\mathbf{q}\mathbf{y}_\ell}$. The truncation order is $N = 10$.

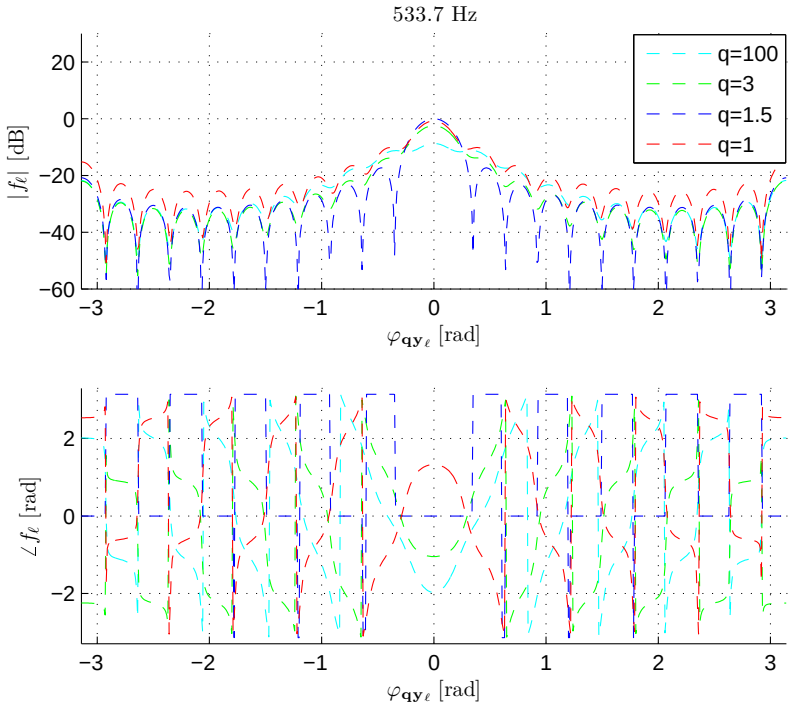

FIGURE 7.39: Magnitude and phase of the filter f_ℓ at 533.7 Hz as a function of the angle $\varphi_{\mathbf{q}\mathbf{y}_\ell}$. The truncation order is $N = 10$.

7.3.3 Source signals and filters for circular geometry

The expression of the secondary source signals $\ddot{M}_\ell(t)$ for the circular geometry can be obtained through mathematical manipulations analogous to those discussed above. In view of the results presented in Section 4.2, and especially of equation (4.42), reported here

$$a(\mathbf{y}) = \sum_{\nu=-N}^{N} \frac{e^{i\nu\hat{\mathbf{y}}}}{i\pi^2 R_V R_\Lambda H^{(1)}_{|\nu|}(kR_\Lambda) J_{|\nu|}(kR_V)} \langle e^{i\nu\hat{\mathbf{x}}} | p \rangle_{\partial V} \tag{7.104}$$

we can derive the following result:

$$\ddot{m}_\ell(\omega) = \frac{\Delta S_\ell}{2\pi R_\Lambda} \sum_{\nu=-N}^{N} e^{i\nu\phi_\ell} \left[\frac{2}{i\pi H^{(1)}_{|\nu|}\left(\frac{\omega}{c}R_\Lambda\right) J_{|\nu|}\left(\frac{\omega}{c}R_V\right)} \right] \int_0^{2\pi} e^{-i\nu\phi_x} (\mathcal{F}_t P)(\phi_x, \omega) d\phi_x \tag{7.105}$$

$$\ddot{M}_\ell(t) = \frac{\Delta S_\ell}{2\pi R_\Lambda} \sum_{\nu=-N}^{N} e^{i\nu\phi_\ell} \langle e^{i\nu\cdot} | \tilde{\eta}(t) \otimes P(\phi_x, t) \rangle_{\Omega^1} \tag{7.106}$$

$$\tilde{\eta}_\nu(t) := \frac{1}{\sqrt{2\pi}} \left[\mathcal{F}_t^{-1} \frac{2}{i\pi H^{(1)}_{|\nu|}\left(\frac{\cdot}{c}R_\Lambda\right) J_{|\nu|}\left(\frac{\cdot}{c}R_V\right)} \right](t) \tag{7.107}$$

where $\mathbf{y}_\ell = [R_\Lambda \cos\phi_\ell, R_\Lambda \sin\phi_\ell]$ and Ω^1 is the circle with unitary radius, which can be also regarded as the one-dimensional unitary sphere. As in the case of the spherical harmonics, in order to deal with real valued basis functions, it is possible to substitute the complex exponentials above with sines and cosines (real valued functions), multiplied by a normalization factor.

For a virtual line source orthogonal to the plane on which Λ lies at $\mathbf{q} \in \mathbb{R}^2 \backslash \Lambda$ and in the free field, following again passages analogous to those presented in Section 5.6.1 and in the previous section we obtain the following expression of the filters

$$f_\ell(\omega) = \frac{\Delta S_\ell}{2\pi R_\Lambda} \sum_{\nu=-N}^{N} \left[\frac{H^{(1)}_{|\nu|}\left(\frac{\omega}{c}q\right)}{H^{(1)}_{|\nu|}\left(\frac{\omega}{c}R_\Lambda\right)} \right] e^{i\nu(\phi_\ell - \phi_q)} \tag{7.108}$$

In the far field assumption or equivalently if $q = R_\Lambda$ and considering $N = \infty$ and the Poisson sum formula (2.32), we have that

$$f_\ell = \frac{\Delta S_\ell}{2\pi R_\Lambda} \sum_{\nu=-\infty}^{\infty} e^{i\nu(\phi_\ell - \phi_q)} = \frac{\Delta S_\ell}{R_\Lambda} \delta(\phi_\ell - \phi_q) \tag{7.109}$$

These coefficients are independent of the frequency, and can be therefore implemented by simple gains. The function $f_\ell(\phi_\ell - \phi_q)$ can be referred to as a *panning function*. If the sampling is uniform, we have that $\Delta S_\ell/(2\pi R_\Lambda) = 1/L$, where L is the number of secondary sources. If the series above is truncated to the order $N = (L-1)/2$ (assuming

L even), from equation (2.59) we obtain

$$f_\ell = \frac{1}{L}\frac{\sin\left(\frac{L}{2}(\phi_\ell - \phi_q)\right)}{\sin\left(\frac{1}{2}(\phi_\ell - \phi_q)\right)} = \frac{1}{L}\,\mathrm{csinc}_L(\phi_\ell - \phi_q) \tag{7.110}$$

An analogous result has been derived by Poletti, who presented strategies for the design of encoding functions for two-dimensional surround sound systems [Pol96] (in this Paper panning functions also for an even number L of secondary sources are discussed). Figure 7.40 shows a plot of f_ℓ, given by the formula above, as a function of the angle $\phi_\ell - \phi_q$ with $L = 11$. The angle $\Delta\phi = 2\pi/L$ defines the angular spacing between neighboring secondary sources.

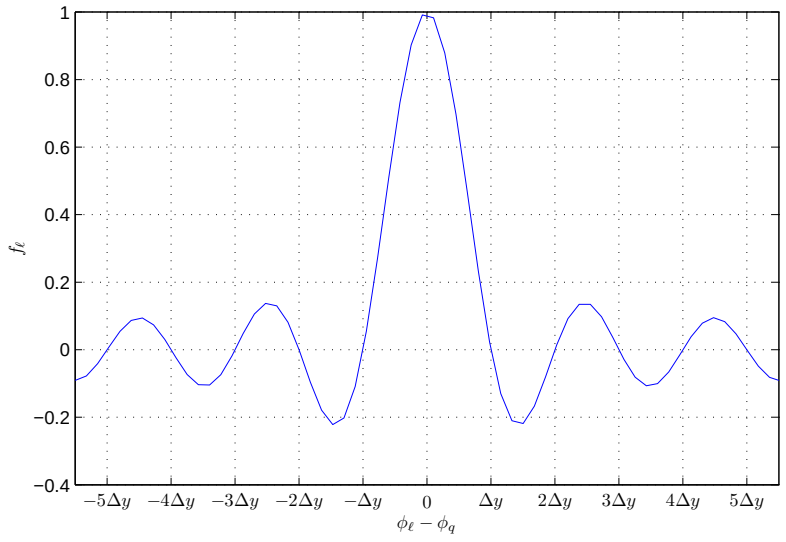

FIGURE 7.40: Panning function $f_\ell(\phi_\ell - \phi_q)$ for circular geometry. The number of secondary sources is $L = 11$ and these are uniformly arranged on the circle, with angular spacing $\Delta\phi = 2\pi/L$. The x-axis of the graph includes values in the interval $[-\pi, \pi]$.

It is interesting to notice that the zeros of the function $f_\ell(\phi_\ell - \phi_q)$, the latter corresponding to the secondary source arranged at ϕ_ℓ, are equally spaced (this is not the case for the spherical geometry) and correspond to the location of the other secondary sources, when these are arranged uniformly. In fact, as suggested by Poletti [Pol96], the panning function acts as an *interpolant* between the sampling points defined by the secondary source locations. This implies that if the angular coordinate of the virtual source ϕ_q coincides with the location of one of the secondary sources, only that secondary source will be active and the strength of all the other sources will be zero. On the other hand, if ϕ_q does not coincide with any of the secondary source locations, all secondary sources will be active and will contribute to the reproduced field. Nevertheless, the signals of the secondary sources arranged in the vicinity of the location of the virtual source will have larger amplitude than the other secondary source signals.

It may be possible to regard also the spherical panning function (7.102) as an interpolant for an ideally uniformly sampled function on a sphere (see for example [Hig96, p.37], where a function analogous to (7.102) is regarded as a *reproducing kernel*). It should be noticed, however, that apart from the case of $N = 1$, the zeros of the spherical panning function do not occur at constant angular spacing. This can be observed qualitatively in Figure 7.27.

7.3.4 Source signals and filters for linear and planar geometry

The expression of the secondary source signals $\ddot{M}(t)$ for planar and linear geometry can be derived from the results presented in sections 4.3 and 4.4. Formula (4.85), which gives the expression of the source strength density $a(\mathbf{y})$, is reported below:

$$a(\mathbf{y}) = \mathcal{F}^{-1}\left[\frac{2\zeta}{ie^{i\zeta d}}(\mathcal{F}p)\right](\mathbf{y}) \tag{7.111}$$

$$\zeta(\kappa) = \sqrt{k^2 - \kappa^2} \tag{7.112}$$

The source strengths $\ddot{m}_\ell(\omega)$ can be calculated by discretizing the source strength density function, namely

$$\ddot{m}_\ell(\omega) = \frac{\Delta S_\ell}{2\pi} \int_{\mathbb{R}^2} \frac{2\zeta(\kappa,\omega)}{ie^{i\zeta(\kappa,\omega)d}}\, e^{i\boldsymbol{\kappa}\cdot\mathbf{y}_\ell}\, (\tilde{\mathcal{F}}P)(\boldsymbol{\kappa},\omega)\, dS(\boldsymbol{\kappa}) \tag{7.113}$$

where the operator $\tilde{\mathcal{F}}$ defines the Fourier transform for both domains of space and time and is given by:

$$(\tilde{\mathcal{F}}P)(\boldsymbol{\kappa},\omega) := \left(\frac{1}{2\pi}\right)^{\frac{3}{2}} \int_{\mathbb{R}^3} P(\mathbf{x},t)\, e^{-i\,[\boldsymbol{\kappa}\cdot\mathbf{x}-\omega t]}\, dS(\mathbf{x})\, dt \tag{7.114}$$

For uniform sampling, ΔS_ℓ equals the distance between two consecutive secondary sources for a two dimensional problem, or the square of this distance for the three dimensional problem.

As for the previous cases, an expression of the digital filters $f(\omega)$ for a motionless virtual source can be obtained by substituting $P(\mathbf{x},t)$ in the equation above with the impulse response $P_\delta(\mathbf{x},t)$ of the virtual source, measured on the control boundary ∂V.

In order to gain a better understanding of formula (7.113), we study the simple case of a propagating impulse with planar wavefront of the form

$$P_{\delta,\hat{\mathbf{k}}}(\mathbf{z},t) = \delta\left(t - \frac{\hat{\mathbf{k}}\cdot\mathbf{z}}{c}\right) \tag{7.115}$$

where the real valued vector $\hat{\mathbf{k}} = [\cos\phi_k \sin\theta_k, \sin\phi_k \sin\theta_k, \cos\theta_k]$ has unitary magnitude and identifies the direction of propagation of the pulse-wave. We make also the following

simplifying assumptions:

$$\Lambda = \{\mathbf{z} \in \mathbb{R}^3 : z_3 > 0\} \tag{7.116}$$

$$V = \{\mathbf{z} \in \mathbb{R}^3 : z_3 > d\} \tag{7.117}$$

For the usual properties of the Dirac delta function we observe that

$$\begin{aligned}
(\tilde{\mathcal{F}} P_{\delta,\hat{\mathbf{k}}})(\boldsymbol{\kappa},\omega) &= \left(\frac{1}{2\pi}\right)^{\frac{3}{2}} \int_{\mathbb{R}^3} \delta\left(t - \frac{\hat{\mathbf{k}}\cdot\mathbf{x} + \cos\theta_k d}{c}\right) e^{-i[\boldsymbol{\kappa}\cdot\mathbf{x} - \omega t]}\, dS(\mathbf{x})\, dt \\
&= \left(\frac{1}{2\pi}\right)^{\frac{3}{2}} \int_{\mathbb{R}^2} e^{i\frac{\omega}{c}\cos\theta_k d}\, e^{i\frac{\omega}{c}\hat{\mathbf{k}}\cdot\mathbf{x}}\, e^{-i\boldsymbol{\kappa}\cdot\mathbf{x}}\, dS(\mathbf{x}) \\
&= \sqrt{2\pi}\, e^{i\frac{\omega}{c}\cos\theta_k d}\, \delta\left(\boldsymbol{\kappa} - \frac{\omega}{c}\tilde{\mathbf{k}}\right)
\end{aligned} \tag{7.118}$$

where $\tilde{\mathbf{k}} = \sin\theta_k[\cos\phi_k, \sin\phi_k,\ 0]$, implying that $\hat{\mathbf{k}}\cdot\mathbf{x} = \tilde{\mathbf{k}}\cdot\mathbf{x}, \quad \mathbf{x} \in \partial V$ and $\hat{\mathbf{k}}\cdot\mathbf{y} = \tilde{\mathbf{k}}\cdot\mathbf{y}, \quad \mathbf{y} \in \partial\Lambda$. In view of these results and considering the relation

$$\zeta\left(\frac{\omega}{c}\tilde{k}, \omega\right) = \frac{\omega}{c}\sqrt{1 - \sin^2\theta_k} = \frac{\omega}{c}\cos\theta_k$$

the expression for the filters $f_\ell(\omega)$ given by equation (7.113) becomes

$$f_\ell(\omega) = \Delta S_\ell \left(-i\omega\frac{2}{c}\cos\theta_k\right) \frac{e^{i\frac{\omega}{c}\hat{\mathbf{k}}\cdot\mathbf{y}_\ell}}{\sqrt{2\pi}} \tag{7.119}$$

This formula provides a fairly simple expression for the filter, which as expected is independent of the distance d between $\partial\Lambda$ and ∂V. Taking a closer look at this expression, we observe that the latter can be divided into two parts: the term in the brackets arises from the operation of taking the normal derivative of the target field, as we have seen in Section 6.4. It includes a real factor $2\cos\theta_k/c$, which depends on the direction of the plane wave, and the linear high-frequency boost filter $-i\omega$, corresponding in the time domain to the operation of taking the time derivative (see formula (2.80) and Section 2.3 - the minus sign is due to the time convention chosen). The second part is the complex exponential, which represents a simple time delay of Δt_ℓ sec given by

$$\Delta t_\ell = \frac{1}{c}\,\hat{\mathbf{k}}\cdot\mathbf{y}_\ell \tag{7.120}$$

The fact should be highlighted, that this is the only part of the filter that depends on the location $\mathbf{y}_\ell$ of the secondary source considered. The filter can be therefore split into a first filter which applies to all secondary sources, and then a delay that applies to the single secondary source considered. Consequently, the secondary source signals for a target field of the form $P(\mathbf{z},t) = V(t) \otimes P_{\delta,\hat{\mathbf{k}}}(\mathbf{z},t) = V(t - \hat{\mathbf{k}}\cdot\mathbf{z}/c)$ can be computed

using the convolution theorem (2.94), which yields

$$\begin{aligned}\ddot{M}(t) &= \Delta S_\ell \left[\mathcal{F}_t^{-1}\frac{e^{i\frac{\cdot}{c}\hat{\mathbf{k}}\cdot\mathbf{y}_\ell}}{\sqrt{2\pi}}\right](t) \otimes \frac{2}{c}\cos\theta_k \frac{\left[\mathcal{F}_t^{-1}(-i\,\cdot)\right](t)}{\sqrt{2\pi}} \otimes V(t) \\ &= \Delta S_\ell\, \delta\left(t-\Delta t_\ell\right) \otimes \left[\frac{2}{c}\cos\theta_k \frac{d}{dt}V(t)\right] \end{aligned} \tag{7.121}$$

The term between square brackets in the right hand side is independent of the source index ℓ and can be computed once for all secondary sources, thus simplifying the signal processing.

We consider now the slightly more complex case of an impulse-like wave with spherical wavefront, with center in $\mathbf{q} \in \mathbb{R}^3 \backslash \Lambda$, outside of the reproduction region Λ. This has the form

$$P_{\delta,\mathbf{q}}(\mathbf{z},t) = \frac{1}{4\pi|\mathbf{q}-\mathbf{z}|}\delta\left(t-\frac{|\mathbf{q}-\mathbf{z}|}{c}\right) \tag{7.122}$$

The filters $f_\ell(\omega)$ can again be derived by inserting $P_{\delta,\mathbf{q}}(\mathbf{z},t)$ into equation (7.113). We observe that

$$\begin{aligned}(\tilde{\mathcal{F}}P_{\delta,\mathbf{q}})(\boldsymbol{\kappa},\omega) &= \left(\frac{1}{2\pi}\right)^{\frac{3}{2}} \int_{\mathbb{R}^3} \frac{1}{4\pi|\mathbf{q}-\mathbf{x}|}\delta\left(t-\frac{|\mathbf{q}-\mathbf{x}|}{c}\right) e^{-i[\boldsymbol{\kappa}\cdot\mathbf{x}-\omega t]}\, dS(\mathbf{x})\, dt \\ &= \frac{1}{\sqrt{2\pi}}\int_{\mathbb{R}^2} \frac{e^{i\frac{\omega}{c}|\mathbf{q}-\mathbf{x}|}}{4\pi|\mathbf{q}-\mathbf{x}|}\frac{e^{-i\boldsymbol{\kappa}\cdot\mathbf{x}}}{2\pi}\, dS(\mathbf{x}) = \frac{1}{\sqrt{2\pi}}\frac{ie^{i\zeta(\kappa,\omega)(d-q_3)}}{2\zeta(\kappa,\omega)}\frac{e^{-i\boldsymbol{\kappa}\cdot\mathbf{q}}}{2\pi}\end{aligned}$$

where the last passage has been obtained from the Weyl integral (4.55). Substituting this result into (7.113) we obtain

$$f_\ell(\omega) = \frac{\Delta S_\ell}{\sqrt{2\pi}}\frac{1}{4\pi^2}\int_{\mathbb{R}^2} e^{-i\zeta(\kappa,\omega)q_3}\, e^{\boldsymbol{\kappa}\cdot(\mathbf{y}_\ell-\mathbf{q})}\, dS(\boldsymbol{\kappa}) \tag{7.123}$$

This result is analogous to equation (6.35), with the difference that the pseudo-evanescent component of the target field is included in the calculation here. Assuming that $q_3 < 0$ (since $\mathbf{q} \notin \Lambda$) and in light of (4.55) the following relations hold true:

$$\begin{aligned}\frac{1}{4\pi^2}\int_{\mathbb{R}^2} e^{-i\zeta(\kappa)q_3}e^{i\boldsymbol{\kappa}\cdot(\mathbf{y}-\mathbf{q})} &= -2\frac{\partial}{\partial y_3}\left[\int_{\mathbb{R}^2}\frac{ie^{i\zeta(\kappa)(y_3-q_3)}}{2\zeta(\kappa)}\frac{e^{i\boldsymbol{\kappa}\cdot(\mathbf{y}-\mathbf{q})}}{4\pi^2}dS(\boldsymbol{\kappa})\right]_{y_3=0} \\ &= -2\frac{\partial}{\partial y_3}\left[\frac{e^{ik|\mathbf{y}-\mathbf{q}|}}{4\pi|\mathbf{y}-\mathbf{q}|}\right]_{y_3=0} \\ &= -2\frac{\partial}{\partial y_3}\left[\frac{e^{ik\sqrt{(y_1-q_1)^2+(y_2-q_2)^2+(y_3-q_3)^2}}}{4\pi\sqrt{(y_1-q_1)^2+(y_2-q_2)^2+(y_3-q_3)^2}}\right]_{y_3=0} \\ &= -\frac{1}{2\pi}\frac{e^{ik|\mathbf{y}-\mathbf{q}|}}{|\mathbf{y}-\mathbf{q}|}\frac{-q_3}{|\mathbf{y}-\mathbf{q}|}\left[ik-\frac{1}{|\mathbf{y}-\mathbf{q}|}\right]\end{aligned}$$

We observe that $-q_3/|\mathbf{y}-\mathbf{q}|$ corresponds to $\sin\vartheta_{\mathbf{qy}}$, where $\vartheta_{\mathbf{qy}}$ is the angle between the segment joining the points $\mathbf{q}$ and $\mathbf{y}$ and its projection on $\partial\Lambda$. In light of these formulae we obtain the following expression of the filters

$$f_\ell(\omega) = \frac{\Delta S_\ell}{\sqrt{2\pi}}\ 2\sin\vartheta_{\mathbf{qy}_\ell}\ \frac{e^{i\frac{\omega}{c}|\mathbf{y}_\ell-\mathbf{q}|}}{4\pi|\mathbf{y}_\ell-\mathbf{q}|}\left[-i\frac{\omega}{c}+\frac{1}{|\mathbf{y}_\ell-\mathbf{q}|}\right] \tag{7.124}$$

We observe that the filter for the secondary source located at $\mathbf{y}_\ell$ includes a delay $\Delta t_\ell = |\mathbf{y}_\ell-\mathbf{q}|/c$ and an attenuation factor $1/(4\pi|\mathbf{y}_\ell-\mathbf{q}|)$, both proportional to the distance between the virtual source and the secondary source under consideration. This is not surprising if we take into consideration the Huygens-Fresnel principle [Huy66]. The filter includes also a gain factor $2\sin\vartheta_{\mathbf{qy}_\ell}$, which depends on the angle between the virtual source and secondary source. This factor is strictly related to the spatial normal derivative of the target field $\nabla_{\mathbf{n}}p(\mathbf{y})$ arising in the Rayleigh first integral formula (6.88) discussed in Section 6.4.3.

Given the target field $P(t) = V(t)\otimes P_{\delta,\mathbf{q}}(\mathbf{z},t) = V(t-|\mathbf{q}-\mathbf{z}|/c)/(4\pi|\mathbf{q}-\mathbf{z}|)$, recalling that $\ddot{M}_\ell(t) = [\mathcal{F}_t^{-1}(\sqrt{2\pi}\ v\ f_\ell)](t)$, we obtain the source signals

$$\ddot{M}_\ell(t) = \Delta S_\ell\ \frac{2\sin\vartheta_{\mathbf{qy}_\ell}}{4\pi|\mathbf{y}_\ell-\mathbf{q}|}\ \delta\left(t-\frac{|\mathbf{y}_\ell-\mathbf{q}|}{c}\right)\otimes\left[\frac{1}{c}\frac{d}{dt}V(t)+\frac{V(t)}{|\mathbf{y}_\ell-\mathbf{q}|}\right] \tag{7.125}$$

Observing the term within square brackets we can distinguish two terms: the first is given by the time derivative of the signal, while the second term is the signal attenuated by a factor given by the distance between the virtual and the secondary source.

When the distance of the virtual source is very large and we neglect in (7.125) the attenuation factor $1/(4\pi|\mathbf{y}_\ell-\mathbf{q}|)$ and the delay $\delta(t-|\mathbf{y}_\ell-\mathbf{q}|/c)$, we have that $\sin\vartheta_{\mathbf{qy}_\ell}=1$ and the second term in square brackets can be neglected. Consequently, equation (7.125) becomes identical to equation (7.121), with $\theta_k = 0$. In fact, the spherical wave reduces to a plane wave propagating in the direction perpendicular to the planar secondary source layer $\partial\Lambda$.

Results analogous to equations (7.119), (7.121), (7.124) and (7.125) are reported in the literature on Wave Field Synthesis (see, for example, [SRA08]) and are generally derived from a straightforward application of the Rayleigh first integral (6.88) or of the Huygens-Fresnel principle (see, for example, [Sta97]).

Chapter 8

Experiments

Some of the theoretical results presented in the previous chapters have been validated experimentally. A loudspeaker array, including 40 transducers arranged on a sphere, has been designed, manufactured and assembled in the large anechoic chamber of the Institute of Sound and Vibration Research.

The spherical geometry has been chosen for several reasons. Firstly, the chosen arrangement allows for a full three dimensional control of the reproduced field (rather than the 2D reproduction). Secondly, the single layer potential (3.15) introduced in Chapter 3.1 on the bounded spherical boundary $\partial\Lambda$ is a compact operator. This allows for the rigorous application of the singular value decomposition of the integral operator, introduced in Chapter 3.1. The singular system for spherical geometry has been explicitly derived in Chapter 4. The analytical expressions for the singular values and singular functions involve some relatively simple functions, which simplifies the design of the digital filters included in the signal processing apparatus of the system, as discussed in Chapter 7.3.

The system included 40 loudspeakers, used as secondary sources. The important assumption has been made that the radiation pattern of the speakers is omnidirectional and that their electroacoustical transfer function in the free field could be represented by a three dimensional free field Green function, as expressed by equation (3.6). The choice of the loudspeakers was therefore restricted to transducers which can satisfy this assumption with reasonable accuracy within the frequency range of interest. We will come back to this point later in this chapter.

The scope of the experiment was to reproduce a target sound field with the loudspeaker array and evaluate the accuracy of the reproduced field in comparison to the target field. The reproduction region was clearly the interior of the sphere on which the loudspeakers were arranged. The target field was chosen to be the acoustic field generated by an omnidirectional point source, located in the exterior of the reproduction region. In spite of the fact that the analytical expression of the target field is given by the three

dimensional free field Green function, the choice was made to generate and measure also the target field. The latter was originated by a single loudspeaker (not included in the array) arranged in the location of the virtual point source. This procedure would help compensate for inaccuracies of the measurement system, such as errors in microphone arrangement and microphone phase mismatch (although the microphones underwent a calibration procedure), since both target and reproduced field were measured with the same device.

The measurement apparatus was a translating linear array of microphones, which could span the horizontal cross section of the reproduction region and sample the acoustic field on a two dimensional uniform lattice.

In what follows, the experimental arrangement is described in detail [1] . Then, the digital signal processing steps adopted for the measurement are presented. Finally, the experimental results are illustrated and discussed.

8.1 Experimental arrangement

Among the different items of experimental equipment, three main elements can be identified:

Loudspeaker array (Figure8.8): includes the supporting structure, the speakers, the power amplifiers and the cables carrying the amplified signals driving the loudspeakers.

Microphone array : includes the supporting structure, the microphones, the microphone amplifiers and the cables carrying the microphone signals;

DSP and control unit : includes the digital signal converters (DAC/ADC), a computer equipped with PCI card for interfacing with the converters and several software packages used for the generation, acquisition, processing and analysis of the signals.

8.1.1 The anechoic chamber

The entire experiment had been carried out in the large anechoic chamber of the Institute of Sound and Vibration Research (ISVR), at the University of Southampton. All the experimental equipment was arranged in the chamber, with the only exception of the control PC, located in the adjacent control room. Figure 8.1 shows a picture of the chamber.

[1] The majority of the photos in this chapter were taken by Jens E.N. Christensen, to whom the author is much obliged.

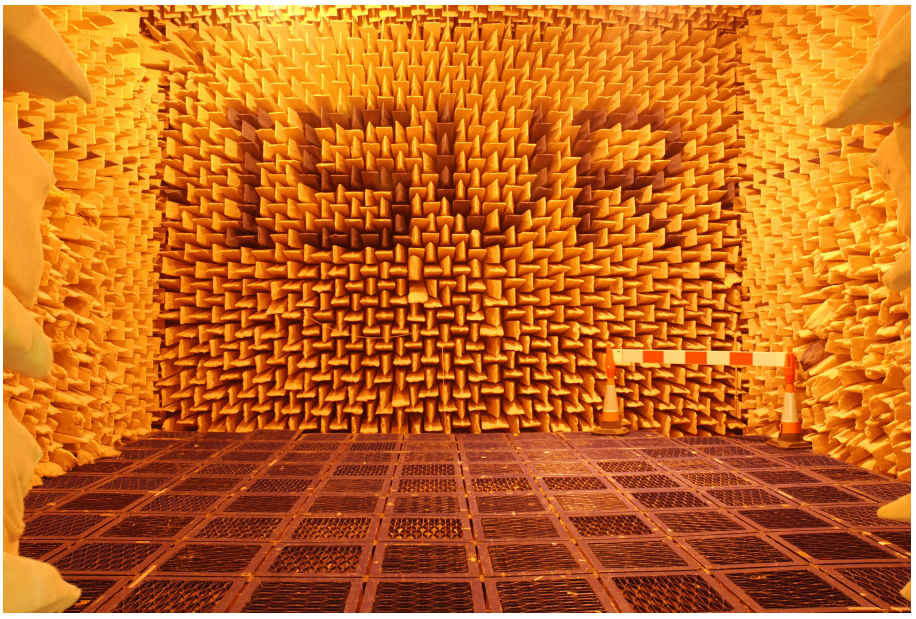

FIGURE 8.1: Large anechoic chamber of the Institute of Sound and Vibration Research.

The following list of specification has been taken from the ISVR website [ISV].

The Large Anechoic Room at ISVR is one of the largest in the country. It was extensively refurbished during 1995/96 and the original polyurethane foam wedges were replaced with glass fibre wedges.

Construction Built as a box within a box, it is acoustically isolated from the rest of the building and adjacent chambers by an air gap all around and is supported on vibration isolation mounts. The reinforced concrete walls are 305 mm thick.

Wall Lining There are over 8,000 non-flammable glass-fibre cored wedges, extending 910 mm from the walls, floor and ceiling. Free-field conditions exist at frequencies above 80 Hz.

Dimensions Without wedges the bare chamber is 9.15 m x 9.15 m x 7.32 m, volume 611 cubic metres. The usable space between the wedges is 7.33 m x 7.33 m x 5.50 m, giving a usable volume of 295 cubic meters.

Access Double doors 2.0 m wide x 2.4 m high.

Flooring A grid of removable floor panels can support a spread load of several tons with a minimum of interference with the anechoic nature of the chamber. An optional floor of varnished chipboard is available for measurements requiring a free field above a reflecting plane (hemi-anechoic conditions).

8.1.2 The loudspeakers

The 40 loudspeakers included in the array are KEF HTS3001. Table 8.1 reports some technical characteristics of these units. The data have been taken from the product user manual [KEF]. Figure 8.2 shows a picture of one of the loudspeaker array units.

Model	**HTS3001**	**HTC3001**
Design	Bass reflex two-way	Closed box three-way
Driver Unit Array	115mm Uni-Q® 19mm aluminium HF	115mm UniQ 19mm aluminium HF 2 x 75mm LF
Frequency Range	70Hz - 55kHz	60Hz- 55kHz
Amplifier Requirement	10 - 100 Watts	10 - 100 Watts
Sensitivity (2.83V/1m)	88dB	90dB
Maximum Output (SPL)	104dB SPL @1m	106dB SPL @ 1m
Impedance	8Ω	8Ω
Internal volume	1.75 litres	2.4 litres
Weight	3kg	6kg
Dimensions (H x W x D)	198 x 130 x 150 mm	198 x 130 x 150 mm
Finish	High Gloss Black & High Gloss Silver	High Gloss Black & High Gloss Silver
Dispersion	Over 90° arc within 2dB reference response, both horizontal and vertical	Over 90° arc within 2dB reference response, both horizontal and vertical
Harmonic Distortion	TBA	TBA
Crossover Frequency	2.2kHz	2.2kHz / 500Hz

TABLE 8.1: Technical specifications of the loudspeakers included in the array (HTS3001) and used for generating the reference field (HTC3001). The data have been taken from the product user manual [KEF]

These transducers are two-way units (2.2kHz crossover frequency) equipped with concentric drivers (implementing UNI-Q® technology). Figure 8.3 (courtesy of KEF AUDIO) shows an exploded view of the graphic model of the concentric drivers. This technical solution reduces the variation with frequency of the location the acoustic center of the

device, and minimizes the presence of destructive interference between the drivers in the region of the cross-over frequency. The loudspeakers include a port on their back, but this had been closed with sound absorbing material in order to maximize the uniformity of radiation.

FIGURE 8.2: Picture of one KEF HTS3001 mounted on the supporting structure of the array.

FIGURE 8.3: Exploded view of the concentric drivers (courtesy of KEF AUDIO).

The theoretical results presented in this thesis have been developed on the assumption that the secondary sources radiate sound as omnidirectional point sources (acoustic monopoles). Therefore, as mentioned above, the loudspeakers should exhibit a radiation pattern which is as omnidirectional as possible across the frequency range of interest. The choice of the HST3001 was taken in light of a series of experimental measurements of

the radiation patterns of several loudspeaker models. This work was carried out by Vincent Brunel together with the author and other researchers and is presented in [Bru08], [FBN+08] and [FBN07]. The aim of the experiment was to achieve a numerical reconstruction of the sound field radiated by the transducer from a set of measured transfer functions between the loudspeaker and a set of omnidirectional microphones arranged on the surface of a 1.15 m radius hemisphere, at the center of which the loudspeaker had been arranged (the data on the second half of the sphere were derived from symmetry assumptions on the radiated field). The field was then reconstructed by applying a holographic method as shown in [FBN+08] and [Wil99]. In Figure 8.4 (taken from [Bru08]) the radiation pattern of one HTS3001 is shown, for various frequencies. This was computed by interpolating the absolute value of the Fourier transform of the pressure impulse responses of the loudspeaker measured by the microphones arranged as described above. The interpolation was achieved from the computation of the spherical spectrum (2.73) of the radiated field, sampled on the hemisphere, and then synthesizing the radiation pattern by computing a truncated spherical harmonic series (2.72). For the sake of scientific rigor, it should be mentioned that the radiation patterns were not obtained from a far field propagation of the measured field but rather from a direct interpolation of the field measured at 1.15m. This implies that some near-field components might be included in the plots of the radiation pattern, which might be relevant at low frequencies but negligible at high frequencies. It can be observed that the radiation pattern in the front of the transducer is quite uniform up to relatively high frequencies (4kHz). Though smooth decay of energy can be observed (from 0dB on axis up to around -10dB or more at 90°), no sharp discontinuities in the radiation pattern, such as those generated by destructive interference between two drivers at the cross-over frequency, are visible at any frequencies.

The signals driving the loudspeakers were amplified by a set of five eight-channel custom made power amplifiers, a picture of which is shown in Figure 8.6.

The level of the amplifiers was calibrated as follows. A measurement microphone was placed in the center of the array and for each loudspeaker, a reference signal was played back by the transducer and the gain of the corresponding amplifier was adjusted. The reference signal adopted was white noise filtered with a band-pass filter (100 Hz-1500 Hz) in order to reduce the effect of directionality of the microphone at high frequencies.

The frequency response functions of three loudspeakers, namely units 23, 24 and 26, were measured and reported in Figure 8.5. Note that the loudspeakers 23 and 24 and the loudspeaker 26 are driven by two different 8-channel amplification modules. The delay of the signals have been compensated for in order to better visualize the phase plots. The measurement were performed on axis at a distance of 1 m from the driver. It can be clearly observed that the differences of phase and amplitude between the different units are very small. For this reason, individual calibration filters for the single units of the loudspeaker array were not used.

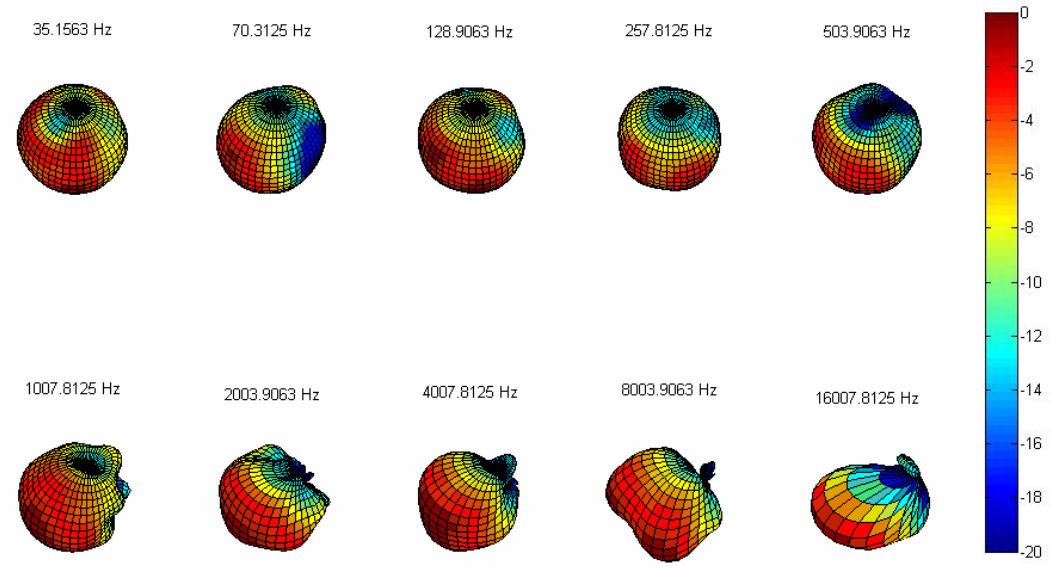

FIGURE 8.4: Radiation pattern of one KEF HTS3001, measured at 1.12m. The color scale and the radial coordinate of the spheroids represent the magnitude of the radiated pressure (dB scale, with range -20 dB to 0 dB), for various frequencies. The IR is normalized in respect to the on-axis response of the loudspeaker (0 dB)

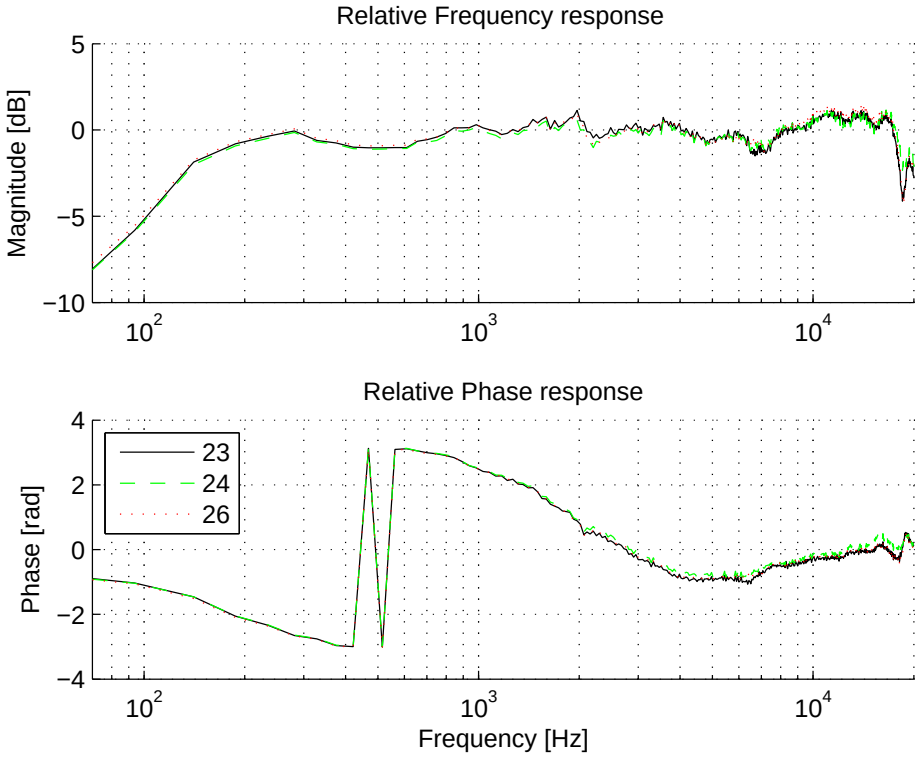

FIGURE 8.5: Frequency response function of unit 23, 24 and 26 of the loudspeaker array.

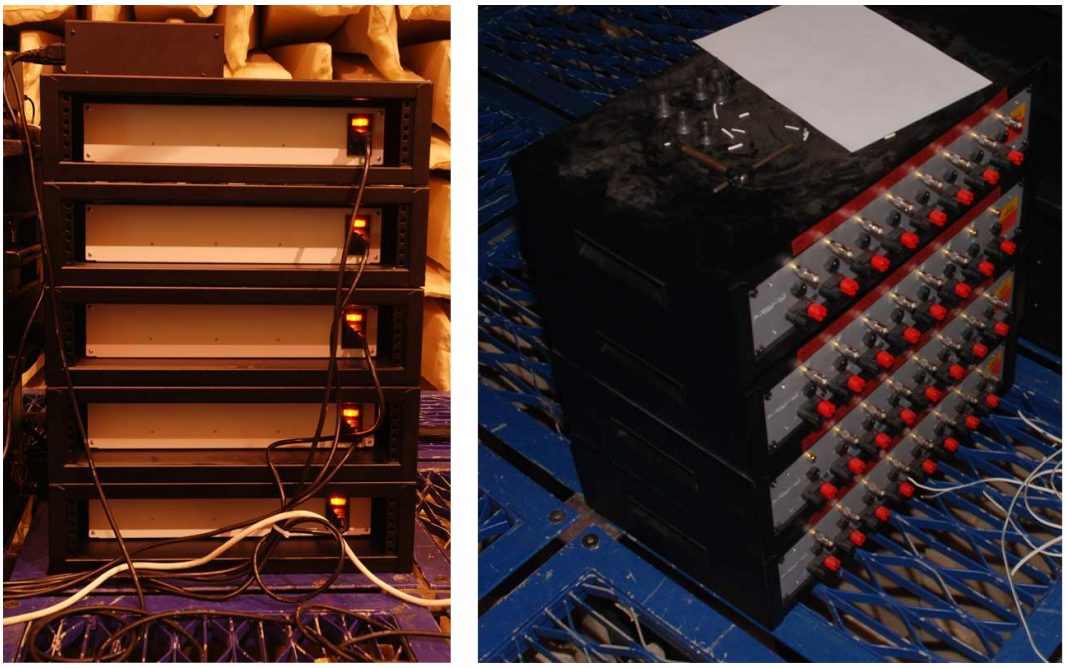

FIGURE 8.6: The eight-channels amplifiers driving the loudspeakers (note that in the right hand side picture, only four units are shown).

8.1.3 The supporting structure

The loudspeakers were arranged on the surface of a sphere of 1.8 m radius (which defines the secondary source layer $\partial\Lambda$ discussed in the previous chapters of this thesis). The loudspeaker arrangement was defined as follows: some of the locations are defined by the vertices of a regular icosahedron. The other locations are defined by the middle points of the thirty-two edges of the icosahedron projected onto the circumscribed sphere of the icosahedron. This arrangement defines an almost regular sampling scheme, with angle between neighboring points of either 36° or 32°. The coordinates of the loudspeaker layout are reported in Appendix E, while a diagram is reported in Figure 8.7. As shown in the figure, loudspeakers were not arranged at two of the locations defined above, corresponding to the base and the entrance of the array, respectively.

The loudspeakers were mounted on a large spherical supporting structure of 4 m diameter, a picture of which is shown in Figure 8.8. The structure was designed jointly with and manufactured by The Dome Company [2]. The structure included a number of curved, zinc plated, steel tubes, with external and internal nominal diameter of 26.9 mm and 18.84 mm, respectively, and length of either 1.26 m or 1.12 m.

The tubes were joined by steel connectors, consisting of six or five machined sockets radiating from a central boss, as shown in Figure 8.9. The loudspeakers were mounted on these connectors, with the aid of two rubber mounts acting as vibration isolators between

[2]The Dome Company, Unit 4, Station Yard, Halesworth, Suffolk, IP19 8BZ, UK - T:01986 872175 - M:07966514046

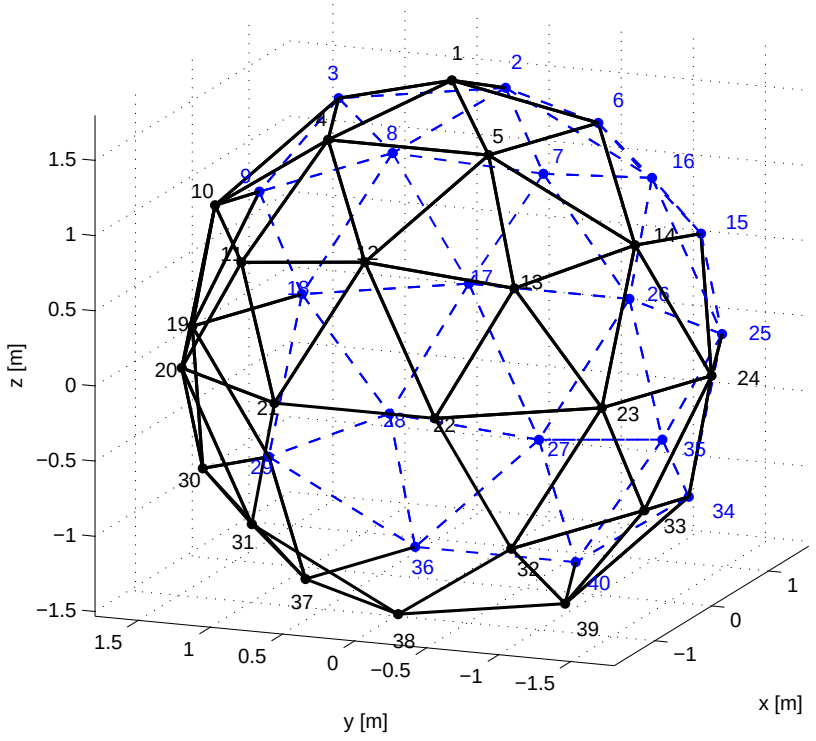

FIGURE 8.7: Diagram of the loudspeaker layout. In order to facilitate visualization, the locations with cartesian coordinate $x_\ell \leq 0$ are represented in black, while those with $x_\ell > 0$ are in blue.

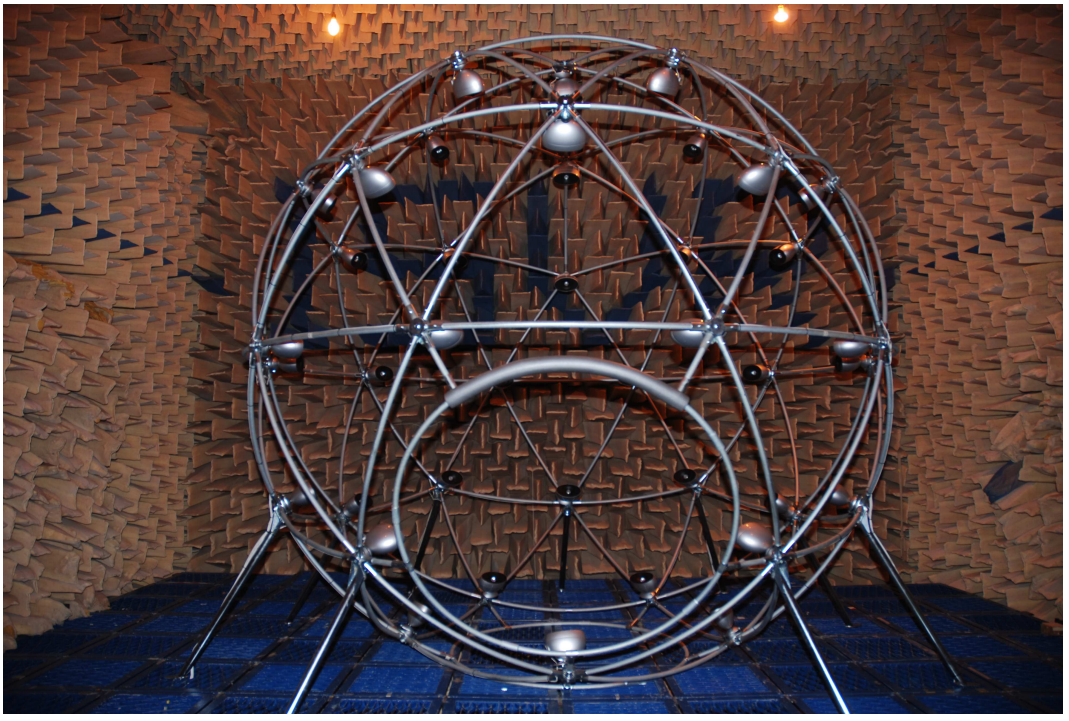

FIGURE 8.8: Picture of the loudspeaker atty in the ISVR large anechoic chamber.

FIGURE 8.9: Detail of the loudspeaker mounts.

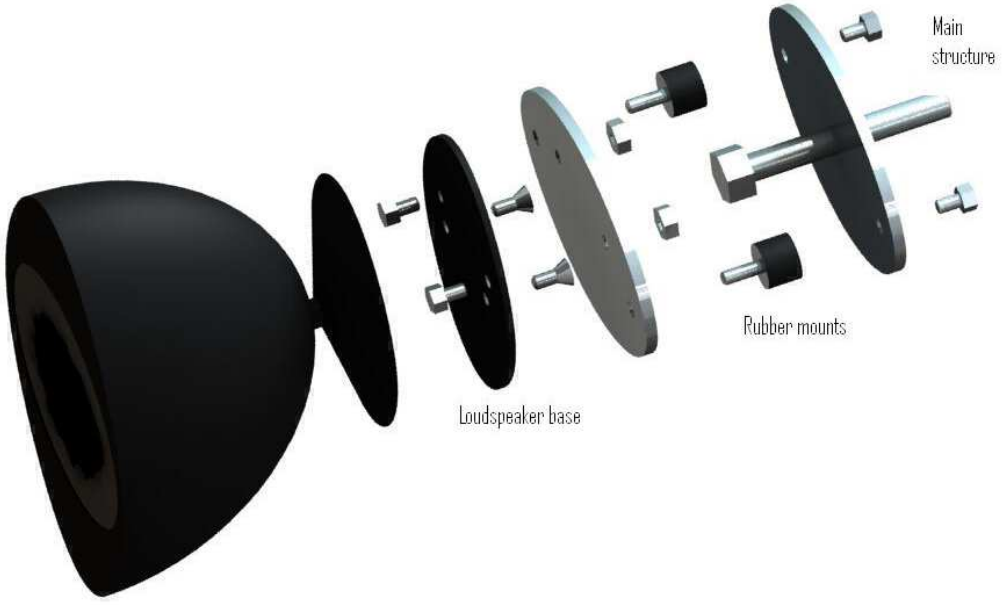

FIGURE 8.10: Diagram of the loudspeaker mounts.

the transducers and the metal structure. A diagram of the loudspeaker mounting sketch is shown in Figure 8.10. Some extra isolating material was added while assembling the array in order to make the speaker mounts more stable,(see Figure 8.9).

As shown in Figure 8.8, the structure was sitting on the ring at its base, and nine steel feet were used for better stability of the structure.

8.1.4 Acoustic source for the reference field

The reference sound field was chosen to be the field generated by an acoustic monopole, located in the exterior of the reproduction volume, that is in the exterior of the loudspeaker array. This field was generated by a loudspeaker, namely a KEF HTC3001, arranged as shown in Figure 8.11 at the location of the virtual source. The latter was, in Cartesian coordinates, $[x_q, y_q, z_q] = [0\text{ m}, -2.36\text{ m}, 0.64\text{ m}]$. The loudspeaker adopted is very similar, though not identical, to those included in the array, and its technical characteristic are reported in Table 8.1.

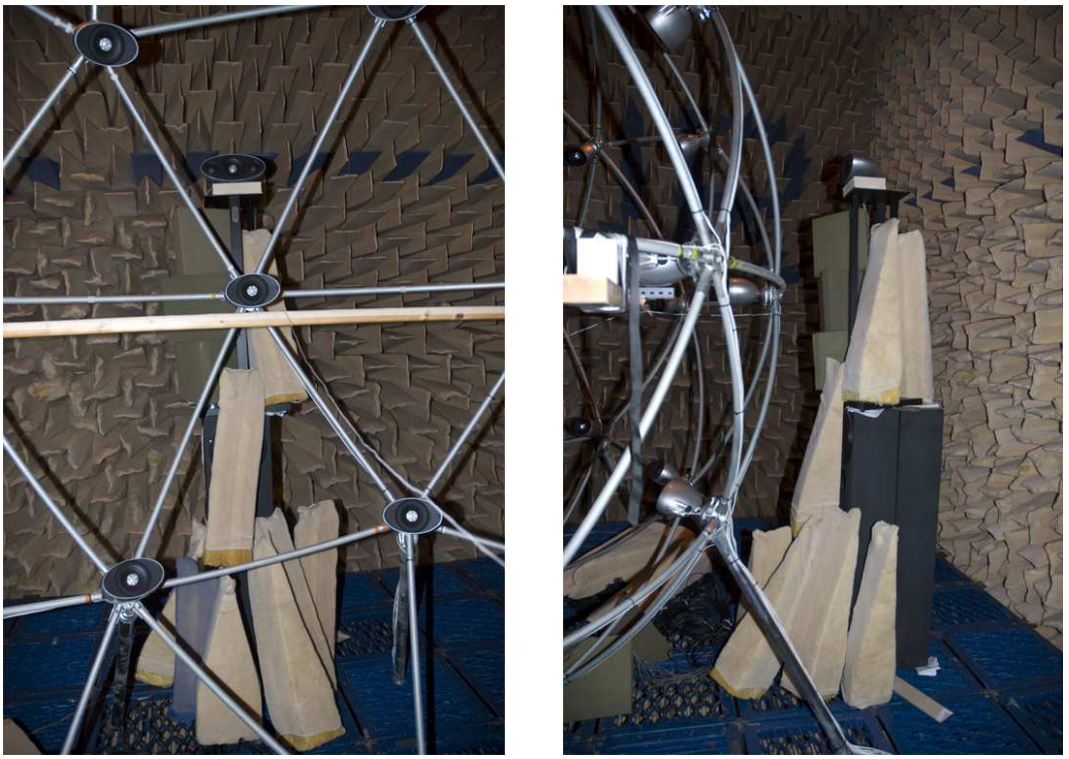

FIGURE 8.11: Arrangement of the acoustic source generating the reference sound field.

8.1.5 The microphone array

The microphone array included a set of forty measurement microphones, evenly arranged on a linear segment with spacing between neighboring transducers of 51 mm. The microphone used pre-polarized free-field Brüel and Kjær microphones, with half-inch capsules,

Type 4189. The microphones were fixed, with cable ties, on a supporting structure. The latter included a length of *Dexion*, supported by two wooden guides as shown in figures 8.12 and 8.13. The linear array could slide on the guides, thus allowing for the sampling of the acoustic field on the locations defined by a regular lattice. The construction of the array was such that all microphone diaphragms were lying on the plane $z = 0$, with some degree of approximation due to mechanical tolerances. As mentioned above, the latter were compensated for by measuring not only the reproduced field but also the target field.

The spacing between the microphone and the translation steps of the array on the wooden guide were both equal to 51 mm. Considering the usual limit of at least two sampling points per wavelength and assuming the speed of sound to be equal to 343 m/s, this spacing allowed for a higher frequency limit of about 3400 Hz. Above this frequency limit, the measurement could be contaminated by spatial aliasing artifacts.

For limitations of the electronic hardware (probably due limited speed of writing on the hard drive the data acquired from multi-channel recordings) a subset of 28 microphones was used. The array was then translated 28 times and the same sound field was measured, thus allowing for a total measured region of about 1.4 m x 1.4 m, lying on the equatorial plane of the loudspeaker array, with geometrical center coinciding with the center of the spherical loudspeaker array. A diagram of the measured region and of the microphone positions is reported in Figure 8.14.

Two custom-made multi-channel amplifiers, one of which is shown in Figure 8.15, were used for supplying power to the microphones and to amplify the acquired signals before these were routed to the analog to digital converters (ADC).

The microphone array underwent a calibration procedure. A custom made calibration apparatus was built. The latter included the chassis of a broken pistonphone, inside which a small loudspeaker was mounted. The calibration apparatus was placed on each microphone, the latter being connected to the corresponding amplifier and ADC. Figure 8.16 shows this step of the calibration process, performed by Dr. Mincheol Shin. A reference signal (white noise) was played back by the loudspeaker in the calibration device, and was acquired by the microphone under test and recorded. The procedure was repeated for each ensemble of microphone, amplifier and ADC. A set of inverse filters was then created by inverting the transfer function between each microphone and a reference microphone, the latter being one of the microphones of the array. Figure 8.17 shows the calibration filters (in the frequency domain, magnitude and phase) for all the 40 units of the array. It can be observed that the variations in magnitude are in the range of ± 2 dB up to 8 kHz, and are probably caused by the tolerances of the amplifier gains. In the same frequency range, the phase variations are negligible. Beyond 8 kHz, some larger variations and a more erratic behavior of the filters can be observed for both magnitude and phase. It is believed that these deviations are due to limits of

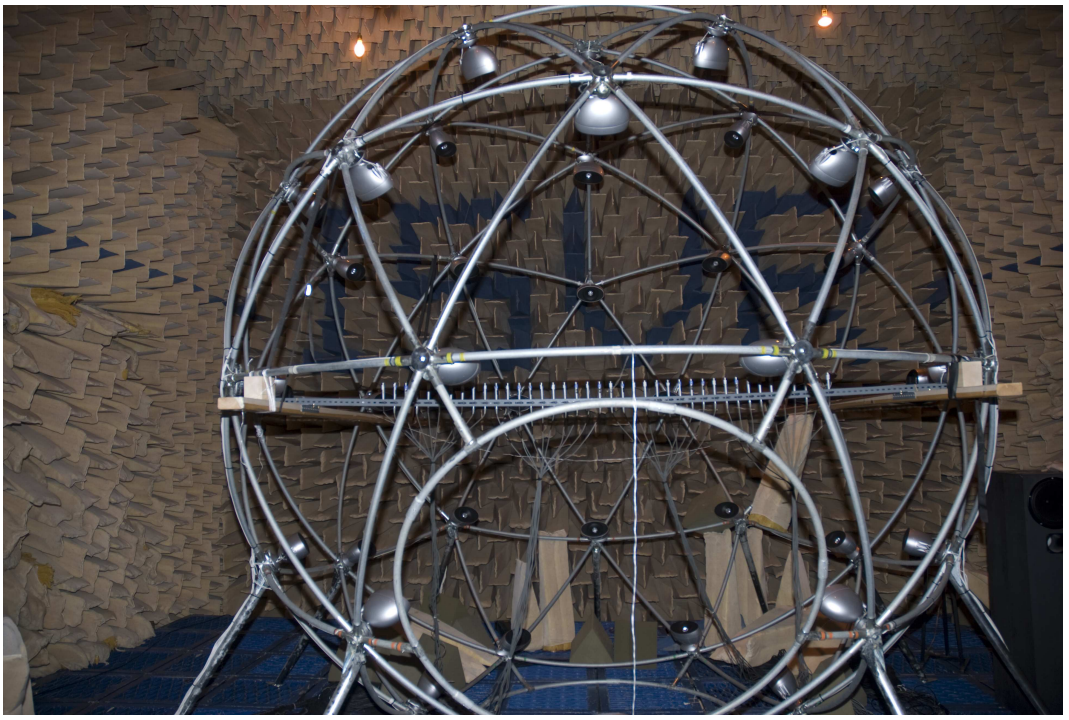

FIGURE 8.12: Microphone array and loudspeaker array.

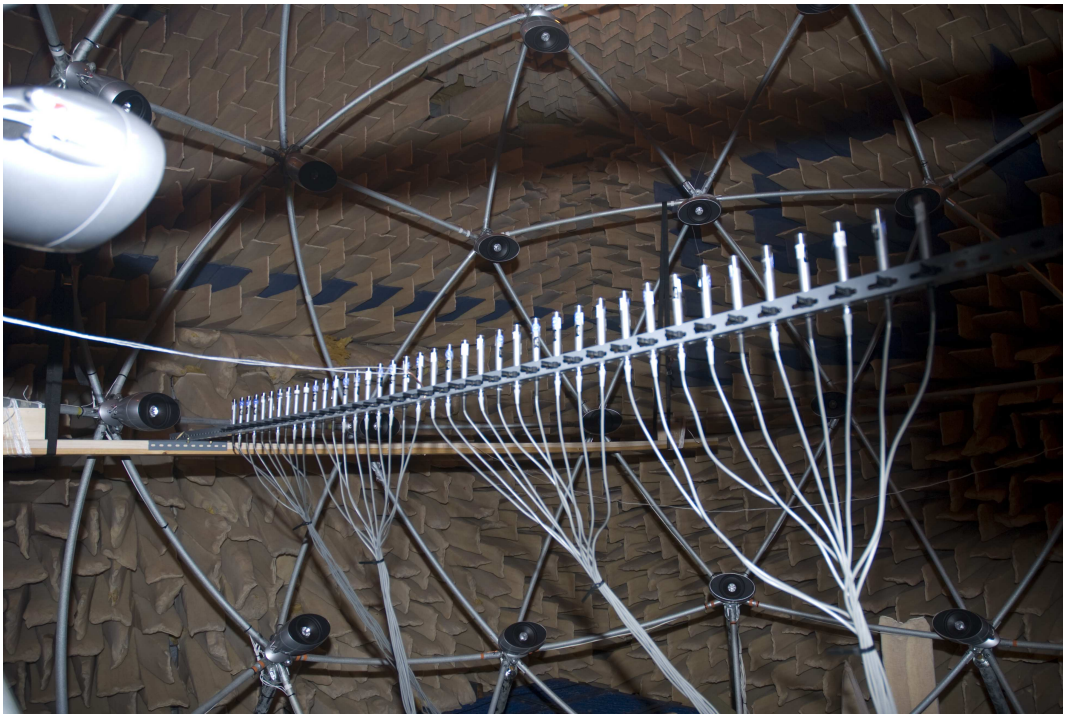

FIGURE 8.13: Microphone array.

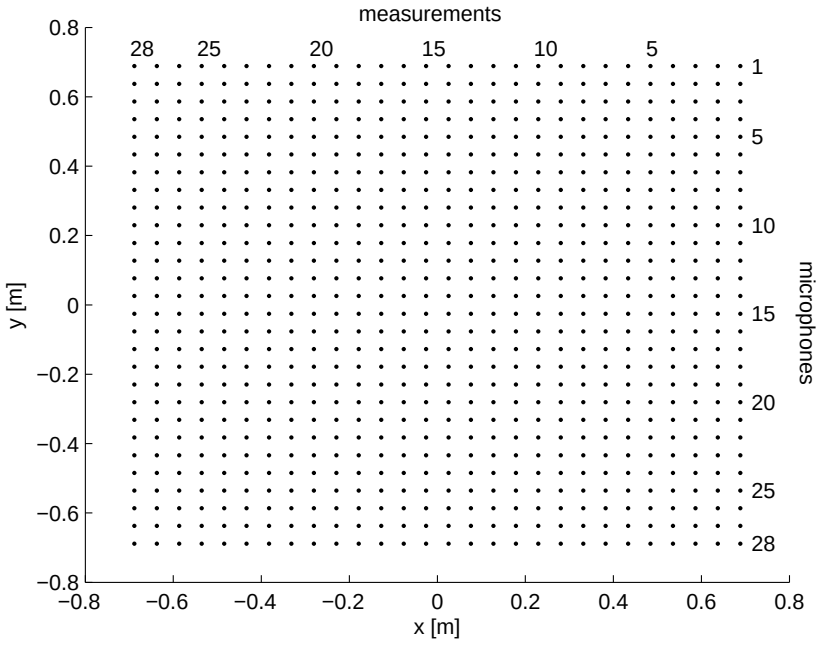

FIGURE 8.14: Diagram of the measured region. The black dots indicate the microphone positions, for all translation steps of the linear array.

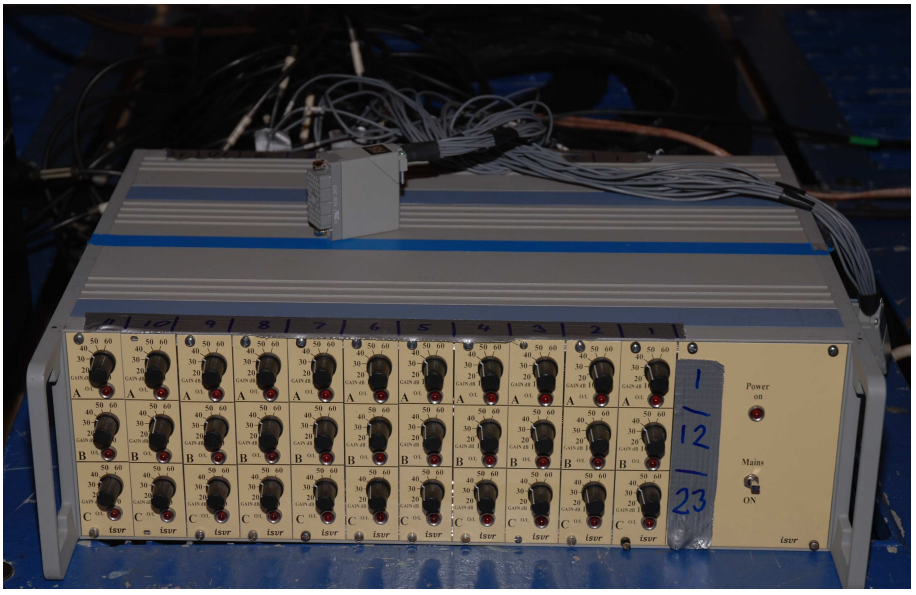

FIGURE 8.15: One of the two multi-channel microphone amplifiers.

accuracy of the calibration apparatus. In fact, phenomena such as acoustics modes of the cavity of the calibrator and non ideal radiation of the little driver enclosed may affect the repeatability and accuracy of the calibration method at high frequencies. However, these supposed limits of the calibration procedure have a significant effect at frequencies well beyond the spatial aliasing limit of the array (3.4 kHz), and are therefore not influential for the proposed experiment.

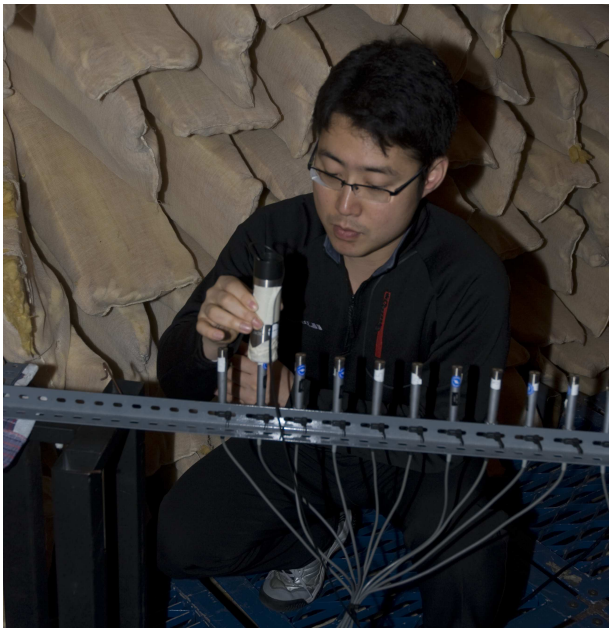

FIGURE 8.16: Microphone array calibration, performed by Dr. Mincheol Shin.

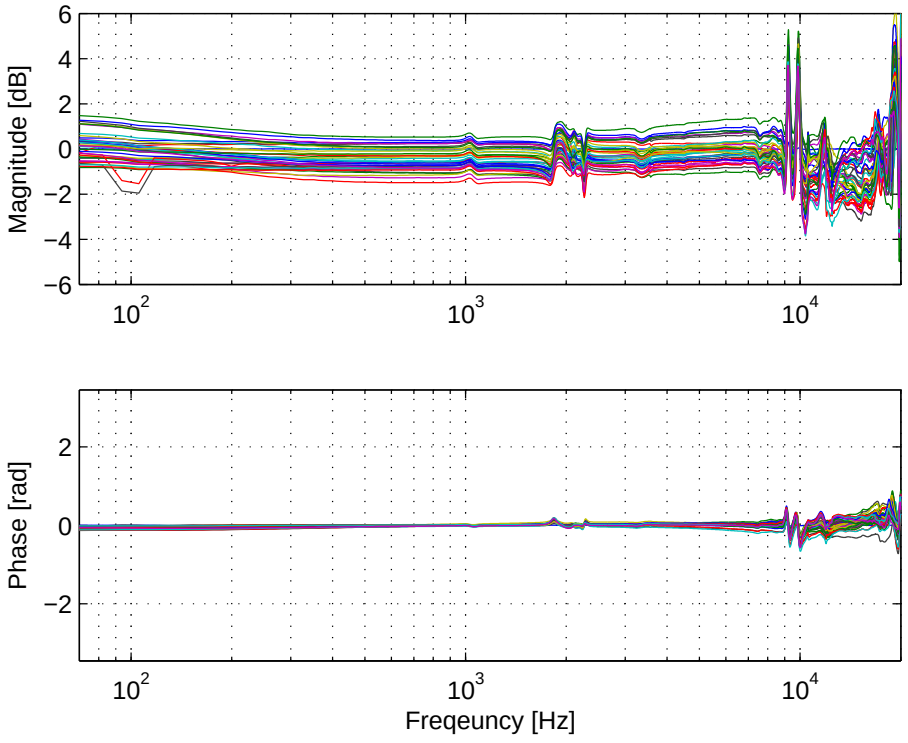

FIGURE 8.17: Calibration filters for the 40 units of the microphone array.

8.1.6 The signal processing apparatus

The analog signals feeding the amplifiers of the loudspeaker array and the signals acquired by the microphone array were converted from and into digital format by a set of five eight-channel RME ADI-8 DS DAC/ADC converters. The sampling frequency of the system was 48 kHz, and one of the ADI-8 DS was operating as master clock. The digital input and output of these devices was carried into ADAT optical cables, capable of carrying up to eight digital signals at 48 kHz on a single optic fiber cable. These signals were in turn converted into 2 MADI data streams by a RME ADI-648 ADAT to MADI and MADI to ADAT converter. Each MADI optical cable is capable of carrying up to 64 channels at 48 kHz. Figure 8.18 report a picture of the rack including the five RME ADI-8 DS and the RME ADI-648. Observing the rear side of the rack, we can see the two orange cables that are the MADI optical cables, while the thin black cables are ADAT optical cables. The thicker, black, numbered cables on the left hand side carry the analog signals feeding the loudspeaker array, while the thick, black, numbered cables on the right hand side carry the analog signals acquired by the microphone array.

The two MADI optical cables (one for all the loudspeaker array signals and one for all the microphone array signals) were connected to a standard PC desktop, equipped via an RME Hammerfall DSP (HDSP) MADI PCI card.

The entire digital signal processing was performed in post- or pre-processing with a PC, using MATLAB software package. The real-time signal reproduction and acquisition was controlled by Adobe Audition software package.

FIGURE 8.18: DAC/ADC conversion system, including the five RME ADI-8 DS and of the RME ADI-648.

8.2 Measurement procedure and digital signal processing

The target of the experiment was to generate the target acoustic field with the dedicated acoustic source and to measure it, and then to reproduced and measure the same field with the loudspeaker array. Figure 8.19 reports a diagram of the reciprocal arrangement of the loudspeaker array, of the area spanned by the microphone array and of the source generating the target sound field.

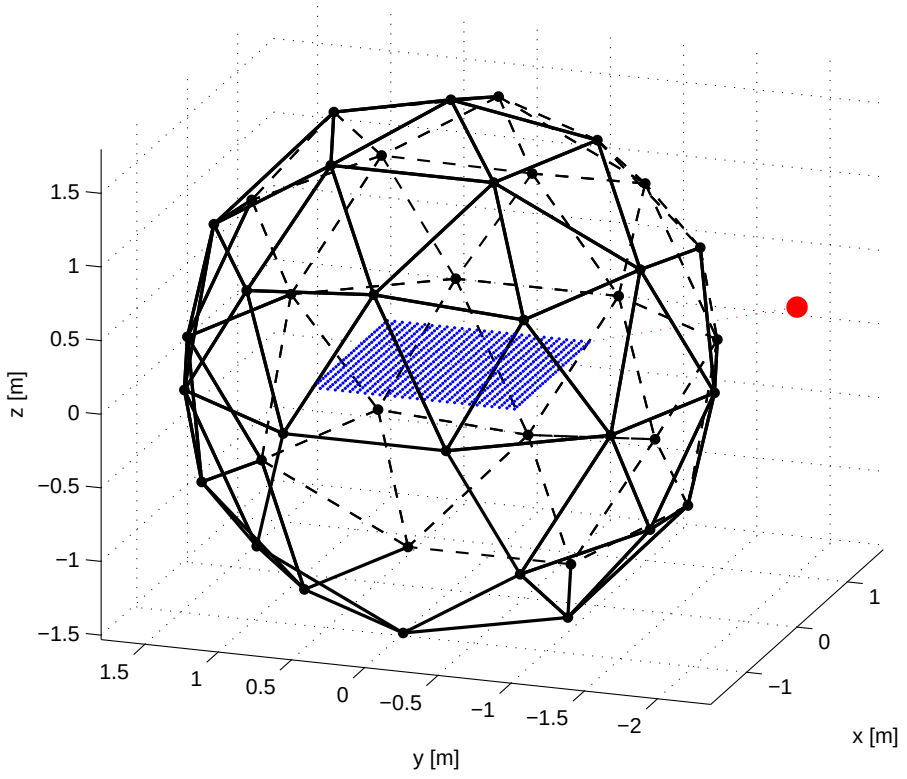

FIGURE 8.19: Diagram of the arrangement of the loudspeaker array, of the area spanned by the microphone array and of the virtual source. The location of the latter is indicated by a red dot, while the black and blue dots represent the location of the loudspeakers and of the microphones, respectively.

Both the target and the reproduced field were generated using the same reference signal in the time domain. The ideal signal would be a single pulse (a Dirac delta function in the time domain). However, for experimental purposes, a sinusoidal chirp with exponentially varying instantaneous frequency was used, and then convolved with its inverse filter in order to retrieve the desired impulse response. This technique is presented in detail in [Far07]. The so-called deconvolution was performed using the Aurora plug-in of Adobe Audition. The chirp was 10 seconds long and spanned a frequency interval from 50 Hz to 15 kHz. The time series and spectrograms (computed with 16384 FFT points and using a Blackmann-Harris window) of the chirp, of its inverse filter and of a sample impulse response are reported in Figure 8.20. This impulse response measurement technique was

chosen for its capability of rejecting the nonlinearities of the measurement system, such as the harmonic distortion of the loudspeakers, as discussed in [Far07].

The measurement of the target field was performed by reproducing the chirp signal with the dedicated loudspeaker, acquiring the signals measured by the microphone array and saving them in the hard drive of the PC. This procedure was repeated for each translation step of the microphone array.

The measurement of the reproduced field was performed by playing back forty previously prepared signals with the corresponding loudspeakers of the array, and by measuring the reproduced acoustic field with the microphone array.

The signals above were obtained by filtering the chirp signal with a set of FIR filters, one for each loudspeaker. These FIR filters were computed numerically in the frequency domain following the steps presented in the previous chapters of this thesis and are discussed further below. Clearly, the filter coefficients depend on the location of the virtual source and on the location of the loudspeaker associated to the filter.

The fact should be emphasized that for each translation step of the linear microphone array, the measurement of the target and reproduced field were taken consecutively, and then the array was translated to the next measurement position. This procedure was undertaken in order to compensate for the array position and to minimize the measurement effort and time.

All the acquired signals were then convolved with the same inverse filter of the exponential sweep, thus retrieving the desired impulse responses. The latter contained all the required information about the target and reproduced field, and could be analyzed in different ways, as discussed later in this chapter.

8.2.1 Digital filter design

The filter design technique used in this experiment is based on equation (7.100) truncated to the order $N = 5$ and with coordinates of the virtual source being $\mathbf{q} = [0\text{ m}, -2.36\text{ m}, 0.64\text{ m}]$. The filters adopted were not designed following a straightforward application of this equation but some modifications were introduced for practical purposes.

The first modification is that the delay $\delta(t-(q-R_\Lambda)/c)$ appearing in equation (7.101) was removed from the filter computation. This delay corresponds to the difference between the distances of the virtual and of the secondary sources from the center of the array. This simple delay does not influence the scope of this experiment. A plot of these digital filters is reported in Figure 8.21 (note that these are not the final version of the filter used for this experiment).

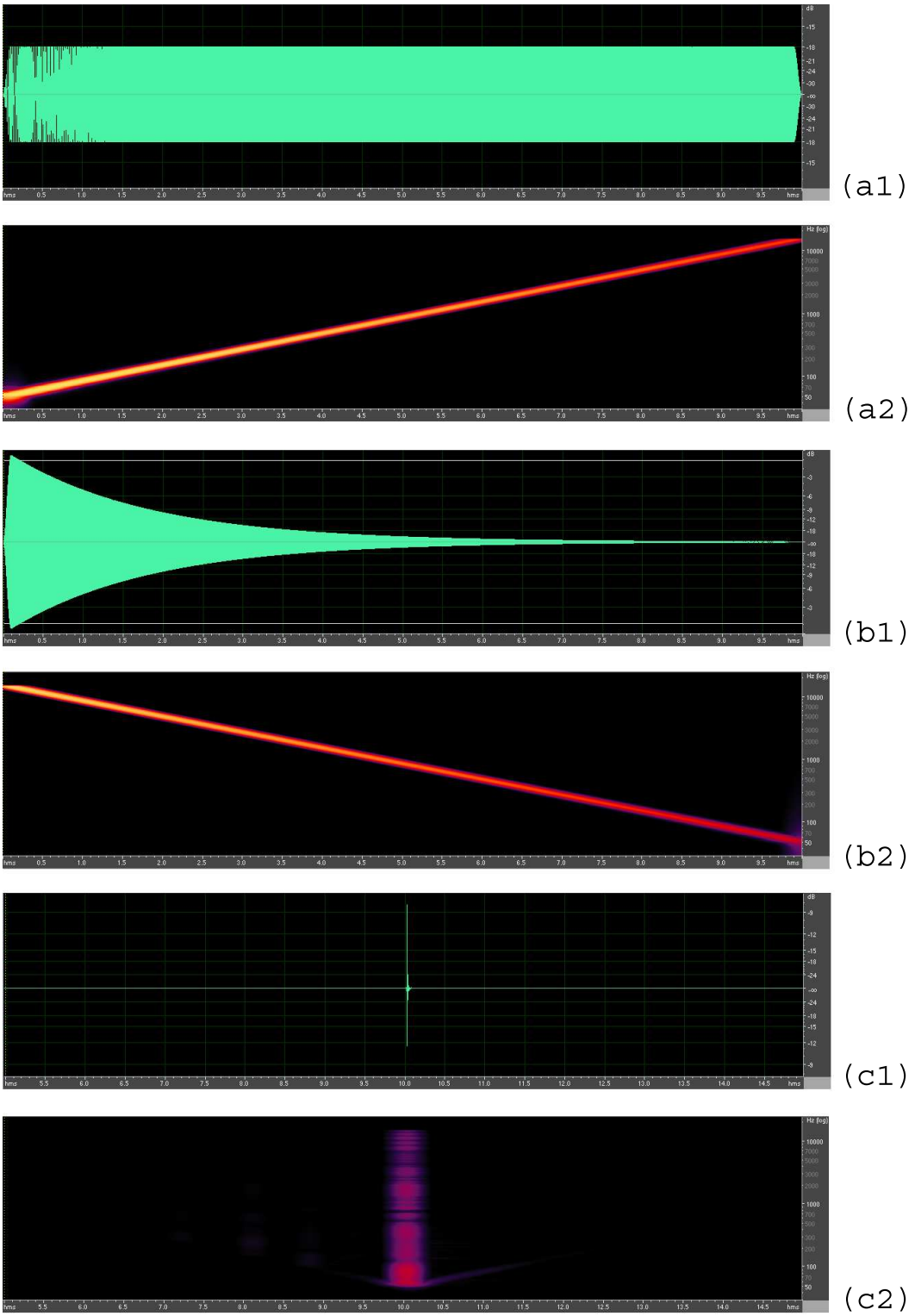

FIGURE 8.20: Time series and spectrogram of the exponential chirp (a1-a2), of its inverse filter (b1-b2) and of a sample impulse response obtained from measurement (c1-c2). Note that the frequency axis (vertical) of the spectrogram has a logarithmic scale.

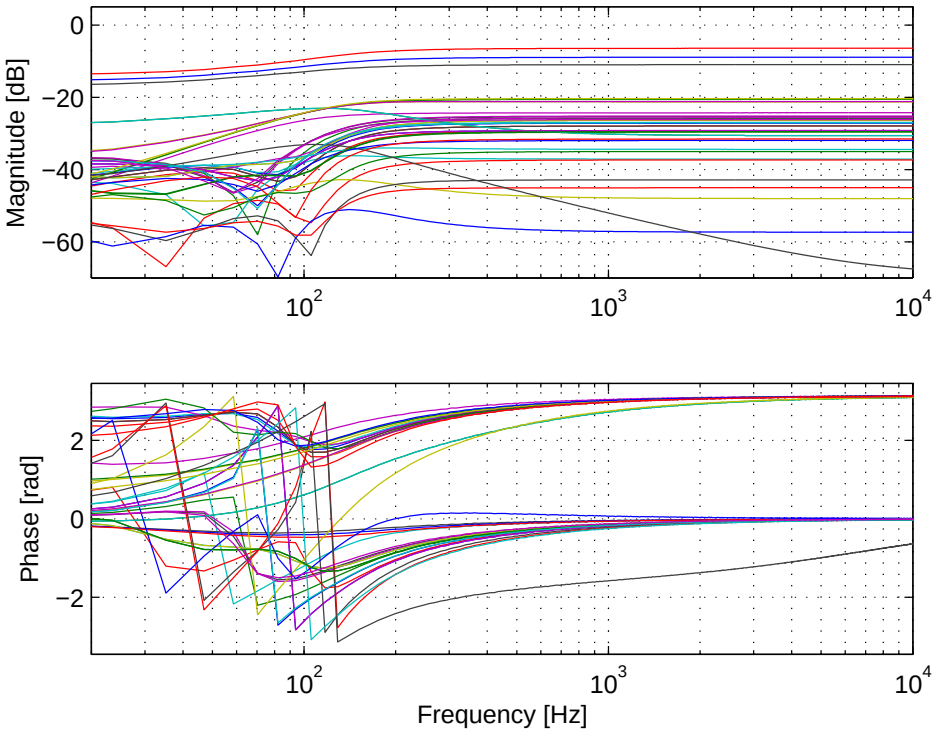

FIGURE 8.21: Digital filters (represented in the frequency domain) obtained by direct application of equation (7.100). Each filter corresponds to a single loudspeaker of the array.

A second, more relevant, difference involves dedicated processing for low, middle and high frequencies. In order to achieve this task, the test signal was pre-filtered using three filters, more specifically a low-pass filter, a band-pass filter and a high-pass filter. These did not apply any phase shift to the signal, which means that their coefficients in the frequency domain are real numbers. These filters are reported in Figure 8.22. The cross-over frequencies are 100 Hz for low-middle frequencies, and 1.5 kHz for middle-high frequencies. It can be noticed that the filters exhibit very steep roll-off.

The low frequency component of the signal was delivered equally to all forty loudspeakers of the array. In this way, only the array mode corresponding to the spherical harmonic $Y_0^0(\mathbf{y})$ was reproduced (refer to chapters 3 and 4 for more detail) . At low frequencies, this is the most efficient mode. This technique had therefore the consequence of compensating the low-frequency roll off of the transfer function of the loudspeakers adopted (see Figure 8.5), thus maximizing the sound level at low frequencies at the price of reducing the accuracy of reproduction of the field. This choice was motivated by the fact that the system used for this experiment was optimized for audio reproduction, which requires good performance at all frequencies of the audible range. As a matter of fact, the application of this technique produced an excess of acoustic energy at low frequencies. For this reason, the low pass filter shown in Figure 8.22 includes an attenuation of 6 dB. This value was chosen after subjective evaluation.

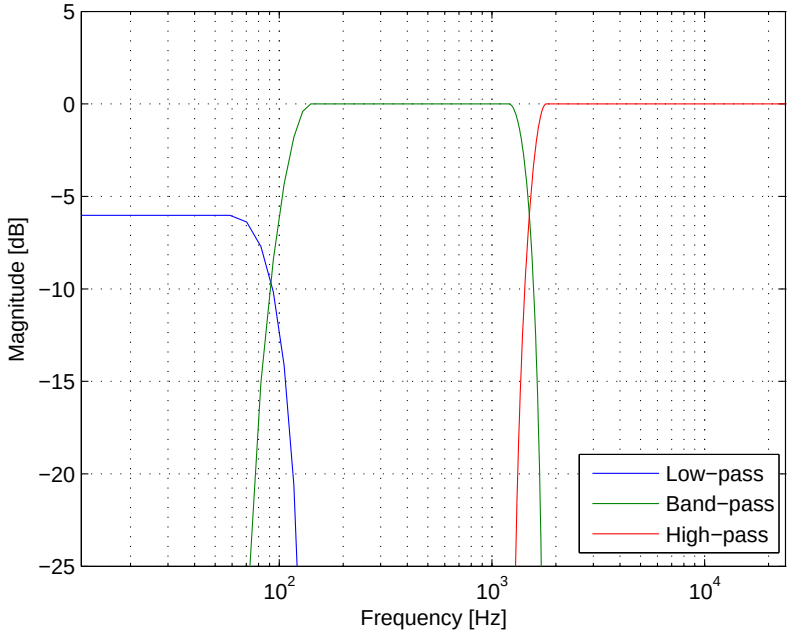

FIGURE 8.22: Low-pass filter, band-pass filter and high-pass filter. The phase of the filters is identically zero for all frequencies.

This technique had also another relevant consequence. In Section 5.5.1 we have seen that a given array mode $a_n(\mathbf{y})$ does not radiate any energy in the exterior of Λ if the operating frequency corresponds to one of the Dirichlet eigenvalues of Λ, which is related to that given mode. For spherical geometry, the Dirichlet eigenvalues of Λ related to the mode $Y_0^0(\mathbf{y})$ are identified by the zeros of the spherical Bessel function $j_n(R_\Lambda \omega/c)$. For the spherical array of radius $R_\Lambda = 1.8$ m, such as that under consideration, this occurs in the vicinity of the frequency $\omega/(2\pi) = 96$ Hz. Since at low frequency only the array mode $Y_0^0(\mathbf{y})$ is reproduced, only little or no acoustic energy is radiated outside of the array at all frequencies in the vicinity of 96 Hz. This phenomenon was not measured but was clearly noticeable.

The output signal of the band-pass filter was filtered by a set of forty FIR filters designed following a straightforward application of equation (7.100) (removing the delay mentioned above).

The processing of the output of the high-pass filter was engineered in view of the following considerations. As discussed previously, for the case under consideration the linear superposition of the fields generated by the secondary sources is intended to reproduce the target field with good accuracy over a region, whose volume reduces progressively with increasing frequency. As suggested in [WA01], the radius of this region is $r = N/k$. Therefore, outside the region of good reproduction, which is very small at high frequencies, the superposition of the loudspeaker fields generates undesired artifacts. Furthermore, at high frequencies small errors in the arrangement of the array units may lead to major alteration of the desired interference pattern, resulting in severe reproduction

errors. It is therefore believed that, at least for audio purposes and for high frequencies, it is preferable to allow only few loudspeakers to be active, which are in the vicinity of the direction of the virtual source and which operate in-phase.

In Section 7.3.2 it has been observed that the high frequency asymptotic limit of the filters designed following equation (7.100) coincides with the panning function (7.102) (apart from a constant factor and a delay). It has also been observed that this panning function exhibits a main lobe in the direction of the virtual source and $2N-1$ side lobes. This implies that loudspeakers arranged far from the direction of the virtual source are active, and they may operate with opposite phase to that of the loudspeakers in the vicinity of the virtual source, lying within the aperture of the main lobe.

In view of these considerations, the choice was made to deliberately eliminate the high frequency components of the signals feeding the speakers outside of the main lobe of the panning function (7.102). The angular half-width of the main lobe of the panning function computed for a truncation order $N = 5$, equals 36.6° (cfr. Figure 7.27), while the angle between neighboring loudspeakers is, for the case under consideration, either 36° or 32°. The application of this technique implies that, when the direction of the virtual source coincides with one of the loudspeakers, six or seven units of the array are active at high frequencies, but most of the energy is produced by the unit aligned with the virtual source. When, on the contrary, the virtual source direction does not coincide with any secondary source, usually only three loudspeakers are active at high frequencies. This technique produced the desired effect that only few speakers, arranged in the vicinity of the direction of the virtual source and acting in-phase, generated the high frequency components of the field. Though developed on different basis, this technique shares some practical similarities with the Vector Based Amplitude Panning (VBAP), proposed by Pulkki [Pul97].

The combination of the filters shown in Figure 8.22 and of the signal processing strategies presented above can be condensed into a unique set of forty digital filters. These are illustrated in Figure 8.23. The apparent discontinuity of the phase is actually due to the high frequency attenuation involved in the high frequency processing technique discussed above. All filters which would exhibit a high frequency asymptotic phase of π (opposition of phase in respect to 0 phase) undergo the aforementioned high frequency attenuation.

It can be easily deduced that the reproduced field was dominated by the contribution of three loudspeakers. These are the units lying within the main lobe of the panning function and are numbered 14, 15 and 24 in Figure 8.7. Figure 8.24 reports only the digital filters associated with these three loudspeakers. It can be noticed that both phase and amplitude remain almost unvaried throughout the frequency spectrum. The smooth discontinuity in the vicinity of 100 Hz and the boost of lower frequencies are a consequence of the low frequency processing technique discussed above.

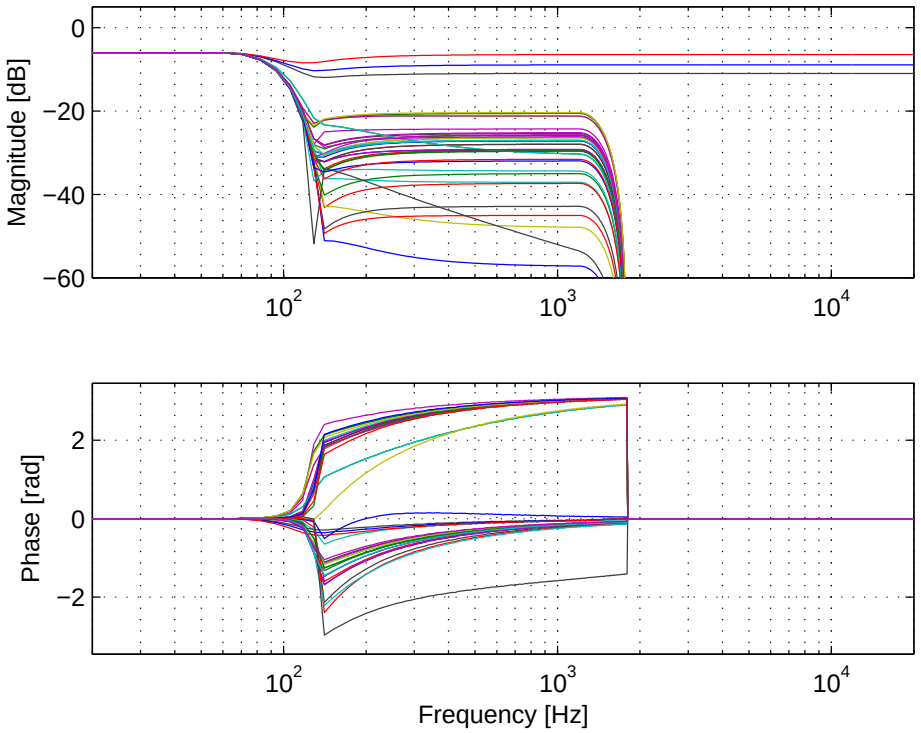

FIGURE 8.23: Digital filters (represented in the frequency domain) used for processing the test signal. Each filter corresponds to a single loudspeaker of the array.

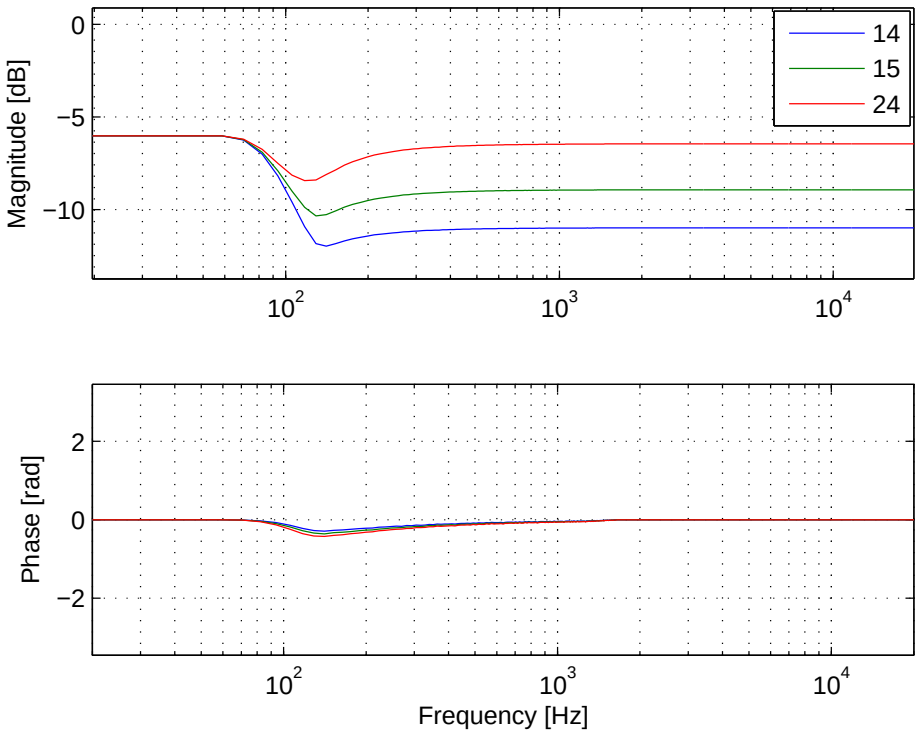

FIGURE 8.24: Digital filters the corresponding to the three loudspeaker (number 14, 15 and 24) lying within the angular aperture of the main lobe of the panning function.

8.3 Experimental results

In what follows, the measured reference pressure field is compared with the reproduced pressure field. The comparison is performed for monochromatic fields, for a set of different operating frequencies. These data have been extracted from the measured impulse responses, acquired with the method discussed above. In order to provide a comparison with the expected results, analogous data obtained from numerical simulations are reported. Figures 8.25 to 8.38 show these results. Each figure reports the reference and reproduced pressure field (the real part of a complex valued function), both simulated and measured, in the region of the space scanned by the microphone array. A plot of the normalized reproduction error is also reported for both simulated and real case. This error has been computed with equation (5.31), reported here

$$\epsilon_N(\mathbf{z}) := \frac{|p(\mathbf{z}) - \hat{p}(\mathbf{z})|^2}{|p(\mathbf{z})|^2} 100 \tag{8.1}$$

The color scale represents the percentage value of the error. In several plots of the normalized reproduction error, a circle of radius $r = N/k \approx 5 \cdot 54.66/f$ is represented, in order to indicate the region where an accurate reproduction is to be expected. When this circle is not visible, it means that its radius is larger than the dimension of the plotting area.

It should be mentioned that all the data acquired with two microphones, numbered 13 and 20 in Figure 8.14, resulted in being unusable. These missing measurements have been replaced with data obtained by linear interpolation of the data measured with neighboring microphones. This fact has the implication that the spatial aliasing limit of 3400 Hz is locally reduced to half of that value (1700 Hz).

Figures 8.25 to 8.38 report plots of the measured horizontal components of the intensity (plotted using the MATLAB function *streamslice*), for a set of different frequencies. The intensity component in the direction perpendicular to area scanned by the microphone array has been imposed to be zero, since these could not be computed from the measured data. The colored plot of the measured pressure has been superimposed. These intensity plots are useful in order to gain a better understanding of the direction of the flow of acoustic energy in the different locations of the measured area. The time averaged intensity $\mathbf{I}(\mathbf{z})$ was computed from equation (3.12), reported here

$$\mathbf{I}(\mathbf{z}) \quad = \quad \frac{1}{2}\mathrm{Re}\left[p(\mathbf{z})\mathbf{v}(\mathbf{z})^*\right] \tag{8.2}$$

The two horizontal components of the velocity $\mathbf{v}(\mathbf{z})$ have been computed by applying the Euler equation (3.9), reported here

$$\nabla p(\mathbf{z}) = i\omega\rho_0\mathbf{v}(\mathbf{z}) \tag{8.3}$$

where the horizontal components of the gradient $\nabla p(\mathbf{z})$ have been replaced by a finite difference between the pressure measured at two neighboring microphone locations, divided by their distance.

8.3.1 Discussion

A general overview of the results shows a good agreement between the simulated and measured results in the frequency range considered. For most of the frequencies a difference of phase can be observed between the simulated and measured field. This is due to the non linear phase of the frequency response function of the loudspeakers HTS3001 of the array, shown in Figure 8.5, while the simulated data have been computed under the assumption of ideal sources (unitary magnitude and zero phase across the entire frequency range). The accuracy of the reproduced field suggests that the frequency response of the loudspeaker HTC3001, used for generating the reference field, exhibits a phase response identical to the HTS3001.

The reproduced field at frequencies in the vicinity of 100 Hz is dissimilar from the reference field. In fact, as discussed above, the signal processing applied to the low frequency components of the signal was not aimed at achieving an accurate reproduction of the reference field. Figure 8.25 indicates the prevalence of the mode corresponding to the zero order spherical harmonic (compare this with Figure 4.5).

The frequency range from 200 Hz to 400 Hz is characterized by an accurate reproduction of the target field over the entire measured region. This is the case also for the intensity diagrams.

In the frequency range between 400 and 800 Hz, it is evident that an accurate reproduction of the desired field is achieved only on the area within the dashed circle with radius r=N/k. The measured error is slightly larger that the simulated one, but measured and simulated results are still in good agreement.

At 1000 Hz a large reproduction error is measured within the dashed circle, but at 1250 Hz we observe again a reasonably good agreement between simulated and measured data. This error is unexpected, but does not affect dramatically the direction of the intensity field within the $r = N/k$ circle.

The intensity plots show that the direction of the reproduced intensity field is still in good agreement with the target over almost all the measured area. However, at 600 and 800 Hz it can be observed that the direction of the flux lines in the exterior of the circle starts deviating from the reference. This phenomenon is very evident at 1000 and 1200 Hz, and is believed to be caused by the acoustic field generated by the loudspeakers located far from the direction of the virtual source. This hypothesis is confirmed by the fact that at higher frequencies, when the signal processing technique dedicated to

high frequencies presented above is applied, the direction of the intensity field appears to be more consistent with the target. It is recalled that the high frequency processing technique involves the use of only those loudspeakers which are located in the vicinity of the direction of the virtual source.

Starting from 1600 Hz and beyond, a progressively increasing disagreement between simulated and measured data is observed. A large reproduction error is present in many locations of the measured region. This effect is much less dramatic in the intensity plots, which still do not differ too severely from the target field plots. The two apparent horizontal discontinuities in the intensity plots are actually due to the local reduction of spatial aliasing threshold caused by the replacement of the data of the microphones 13 and 20 with data obtained from interpolation. This phenomenon is partially observable also in the pressure field plots.

At 2500 Hz it is evident that we are approaching the accuracy limit of the system, and the target and reproduced field differ visibly.

Note on the following figures

In Figure 8.25 to Figure 8.38, the plots on the left hand column represent the simulated data, while those on the right-hand column represent the measured data.

The first row of plots shows the reference field, while the second row represents the reproduced field. The colors represents the real part of the complex scalar field describing the acoustic pressure for the given operating frequency (reported at the top of each figure). Red and yellow represent positive values, blue and turquoise negative values and green is zero.

The plots in the last row report the normalized reproduction error defined by equation (8.1). The color bar at the bottom of the figures indicates the relation between colors and percentage value of the error (the color bar does not refer to the reference and reproduced field plots). The dashed circle, when visible, has a radius $r = N/k \approx 5 \cdot 54.66/f$ (the region of expected accurate reproduction).

Figures 8.25 to 8.38 represent the measured horizontal components of the intensity, with the plot of the measured pressure superimposed. The reference field is on the left-hand side, while the reproduced field is on the right-hand side.

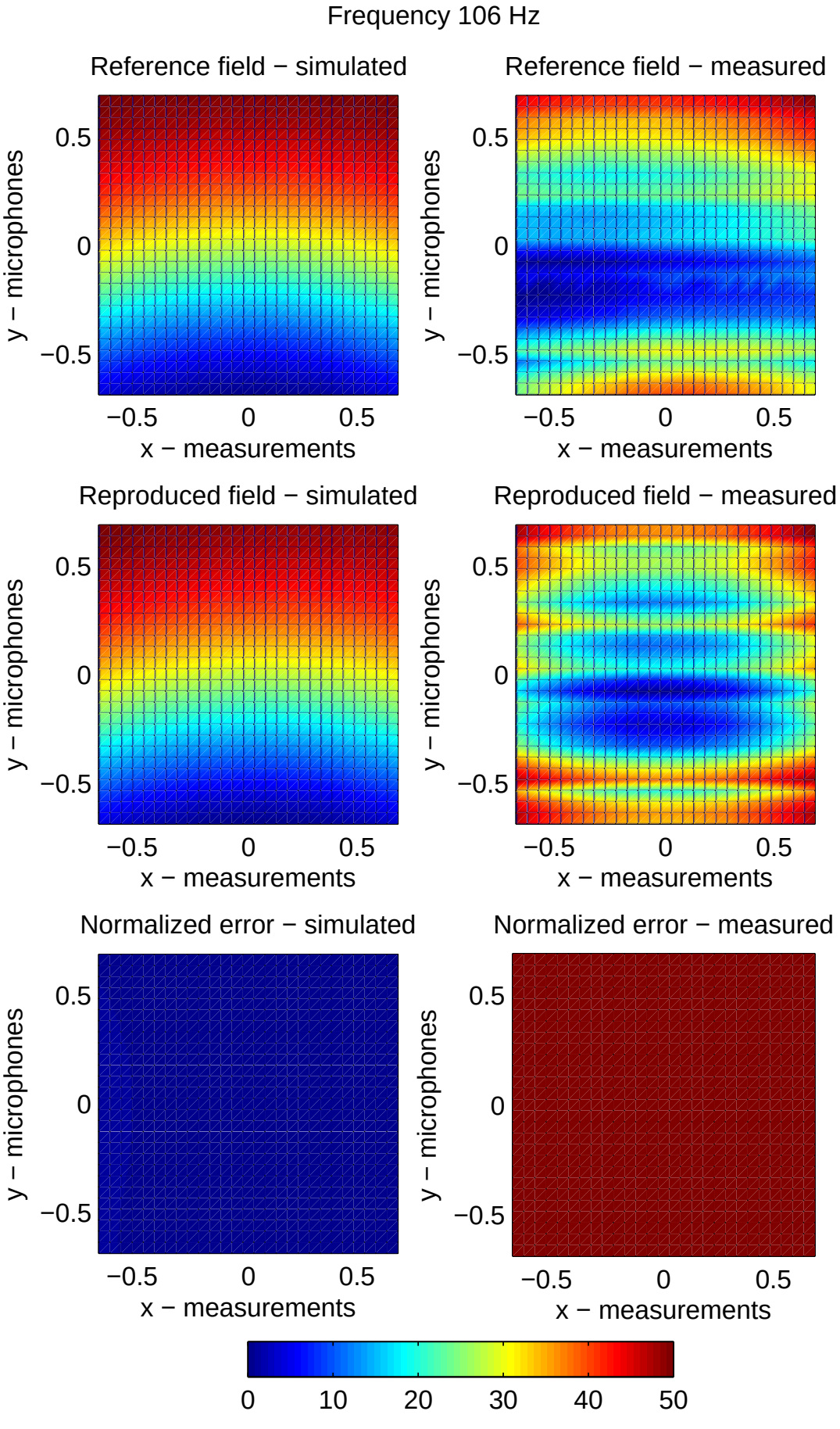

FIGURE 8.25: Reference field, reproduced field and normalized reproduction error. The color bar refers to the error plots. The operating frequency is 106 Hz.

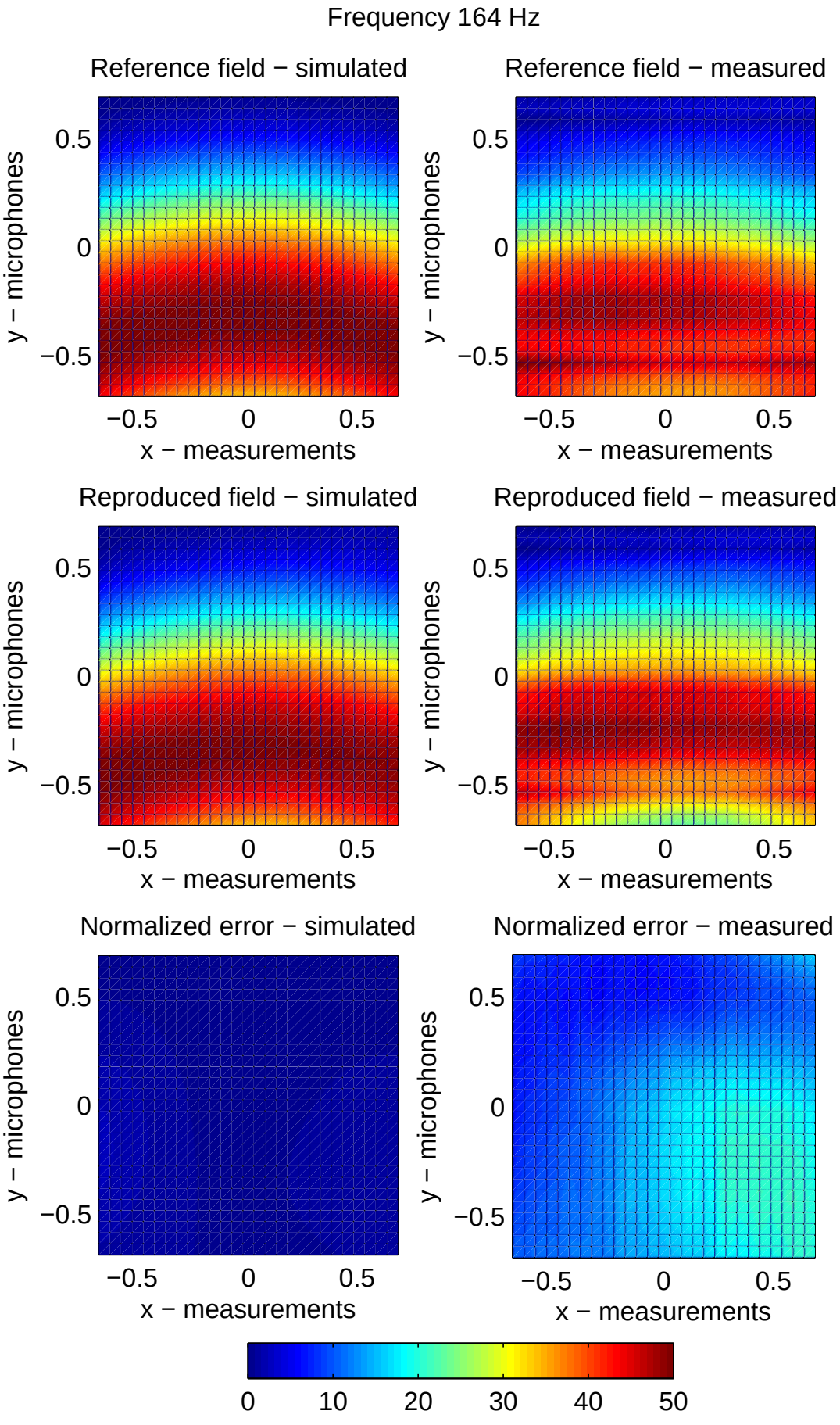

FIGURE 8.26: Reference field, reproduced field and normalized reproduction error. The color bar refers to the error plots. The operating frequency is 164 Hz.

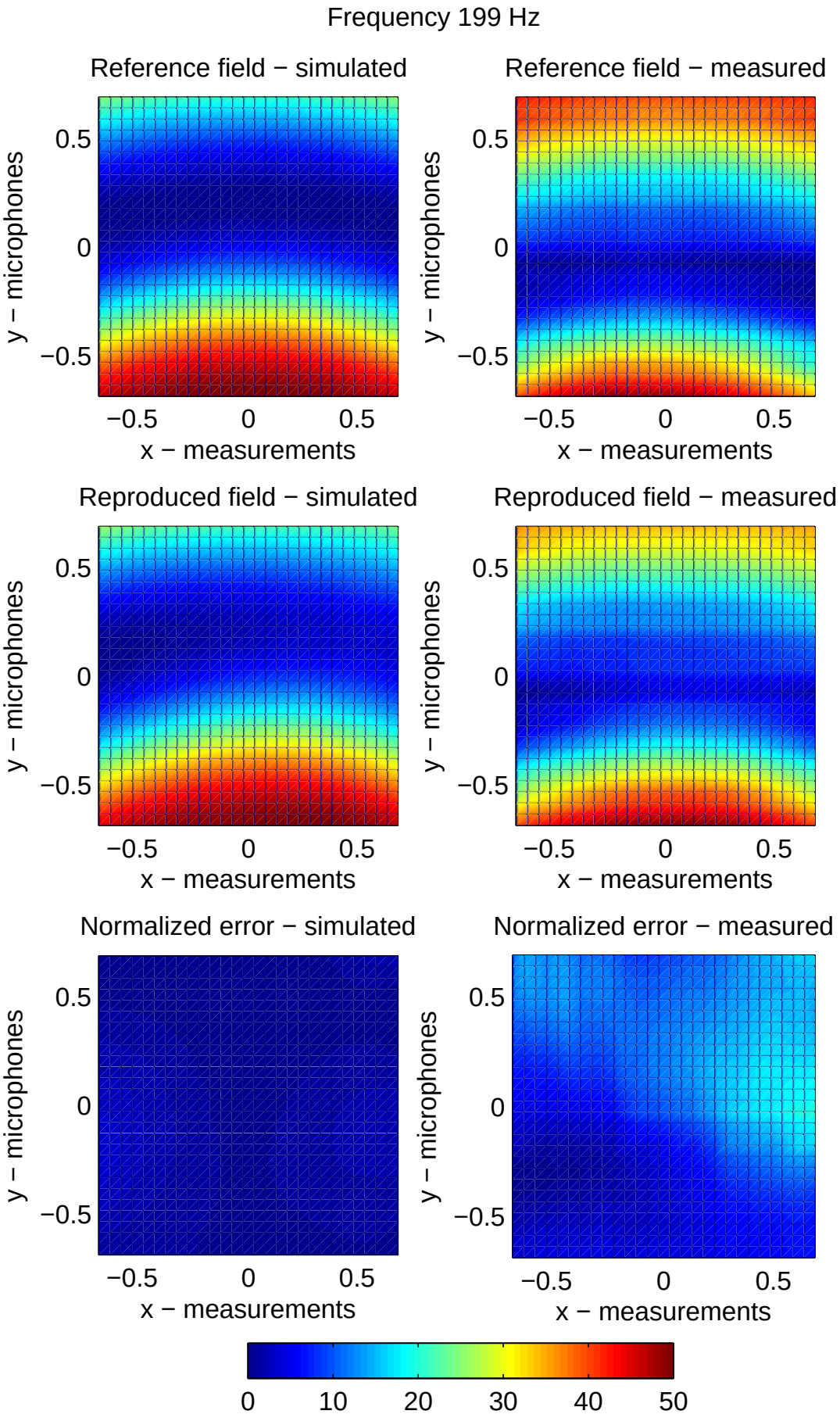

FIGURE 8.27: Reference field, reproduced field and normalized reproduction error. The color bar refers to the error plots. The operating frequency is 199 Hz.

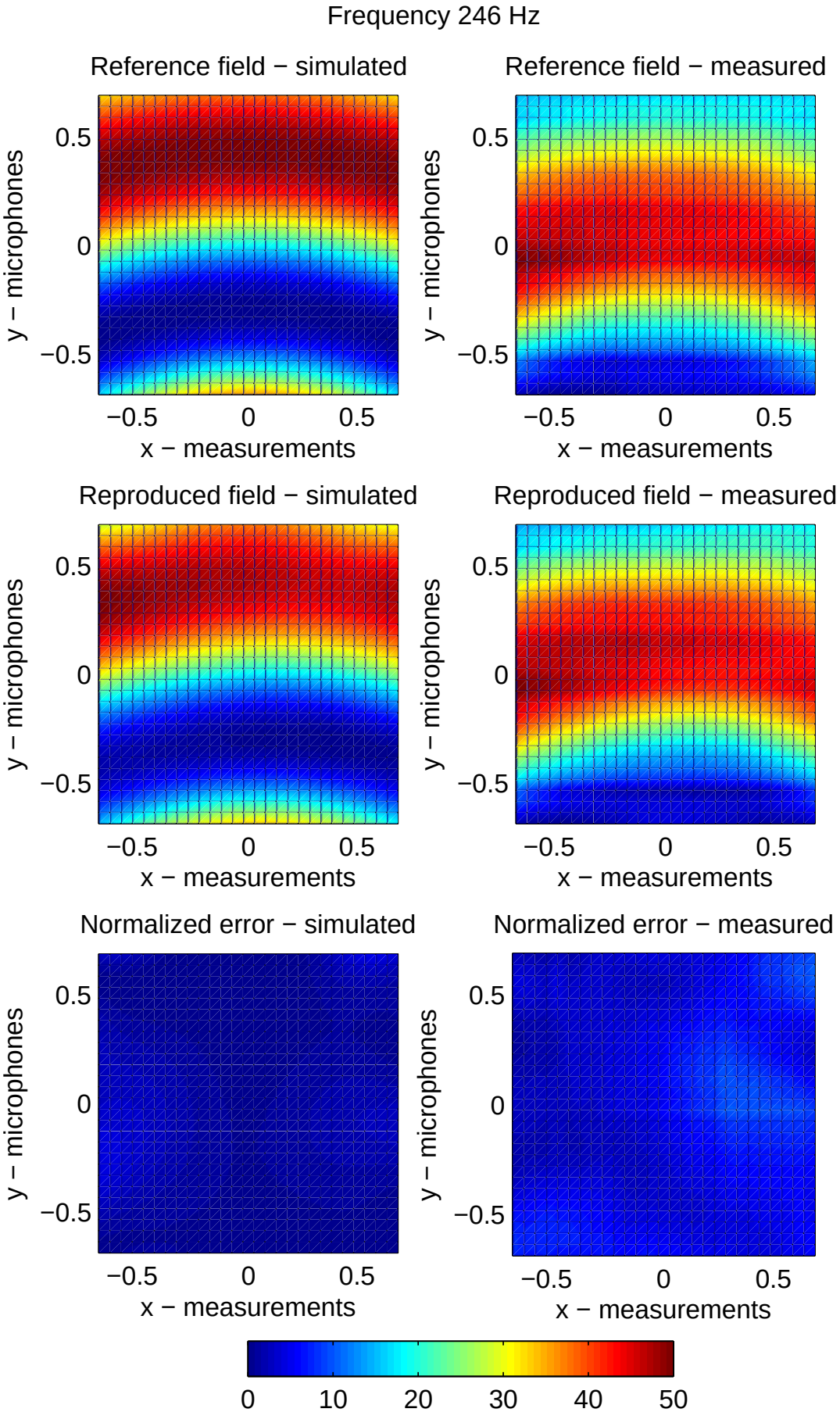

FIGURE 8.28: Reference field, reproduced field and normalized reproduction error. The color bar refers to the error plots. The operating frequency is 246 Hz.

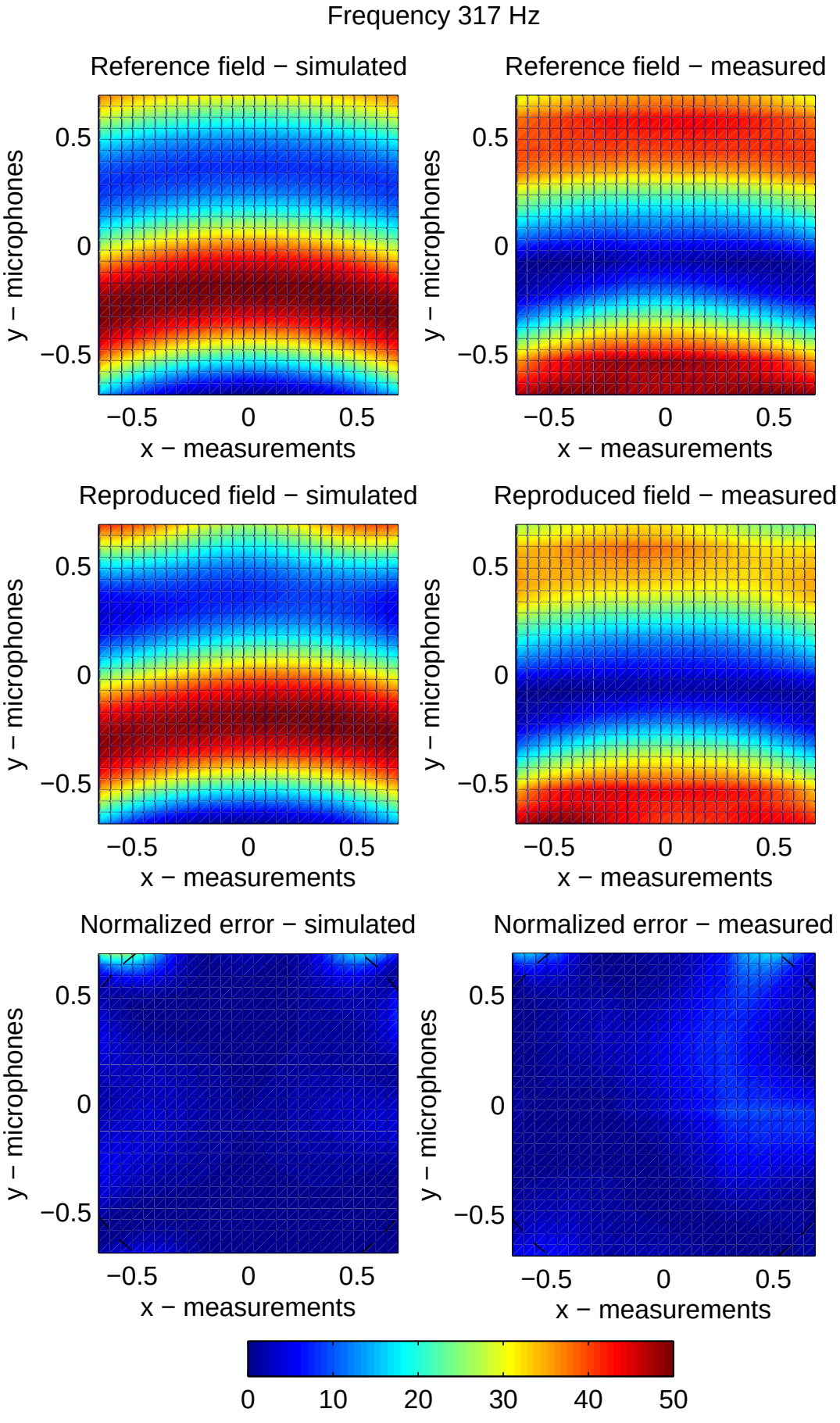

FIGURE 8.29: Reference field, reproduced field and normalized reproduction error. The color bar refers to the error plots. The operating frequency is 317 Hz.

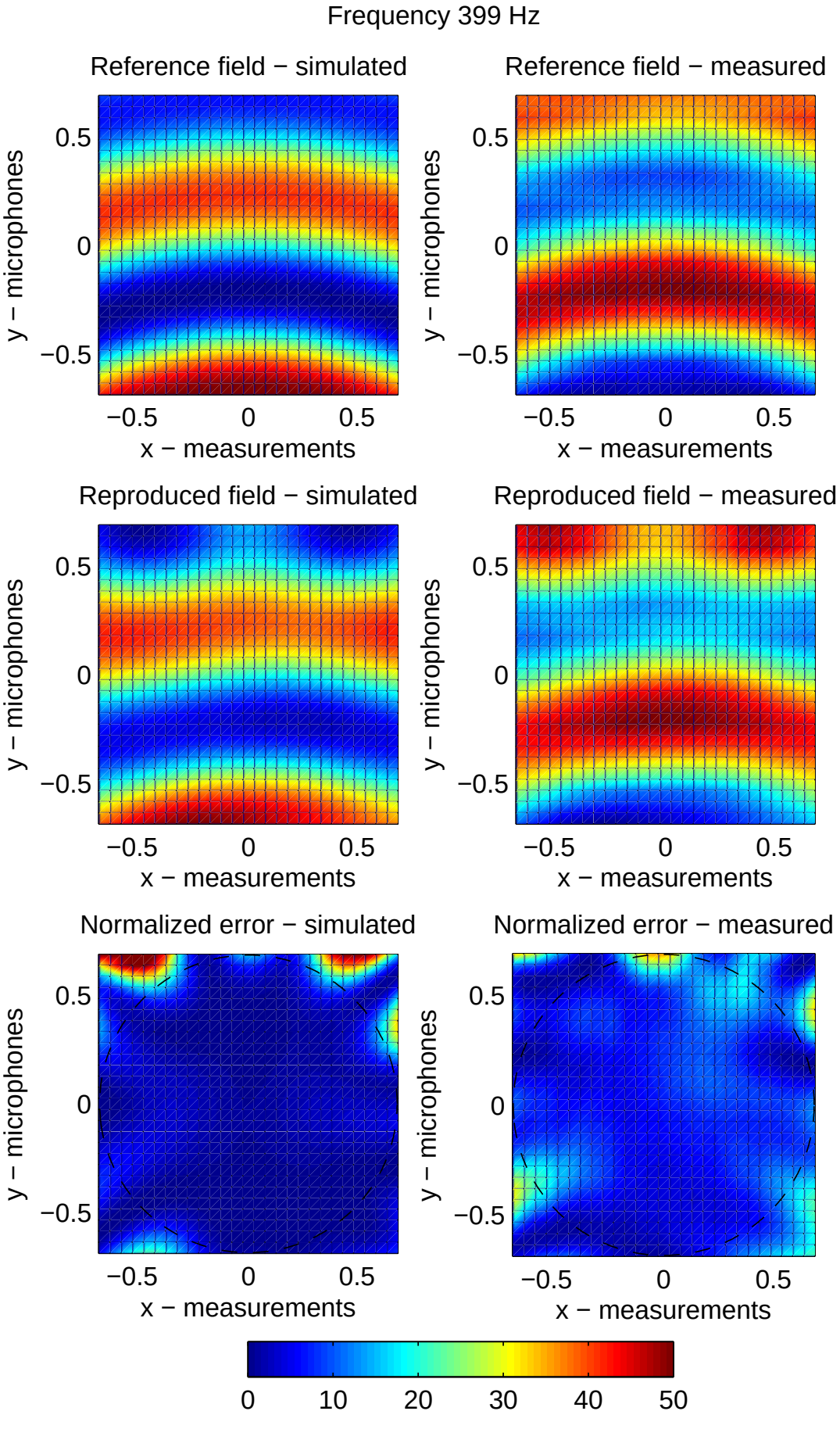

FIGURE 8.30: Reference field, reproduced field and normalized reproduction error. The color bar refers to the error plots. The operating frequency is 399 Hz.

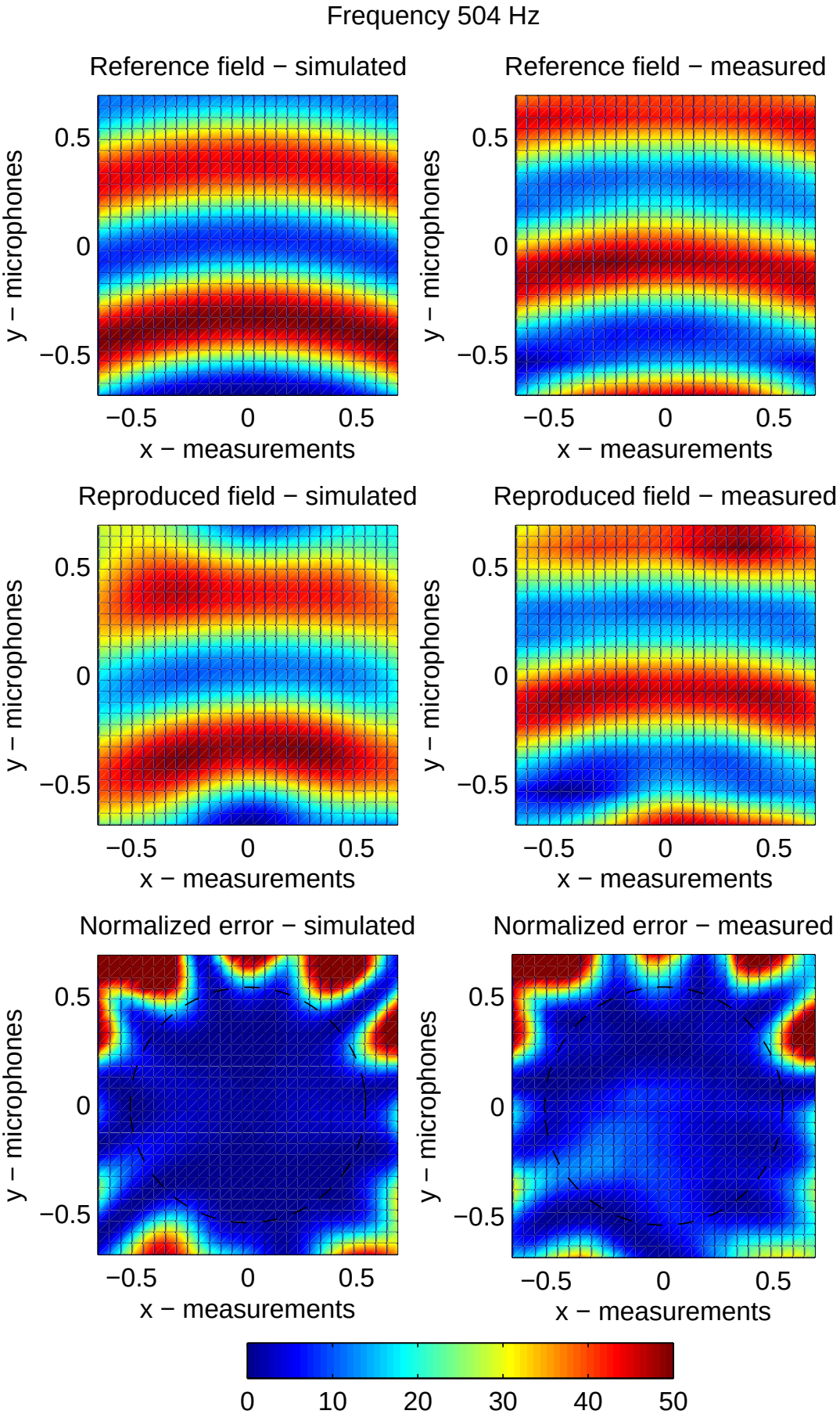

FIGURE 8.31: Reference field, reproduced field and normalized reproduction error. The color bar refers to the error plots. The operating frequency is 504 Hz.

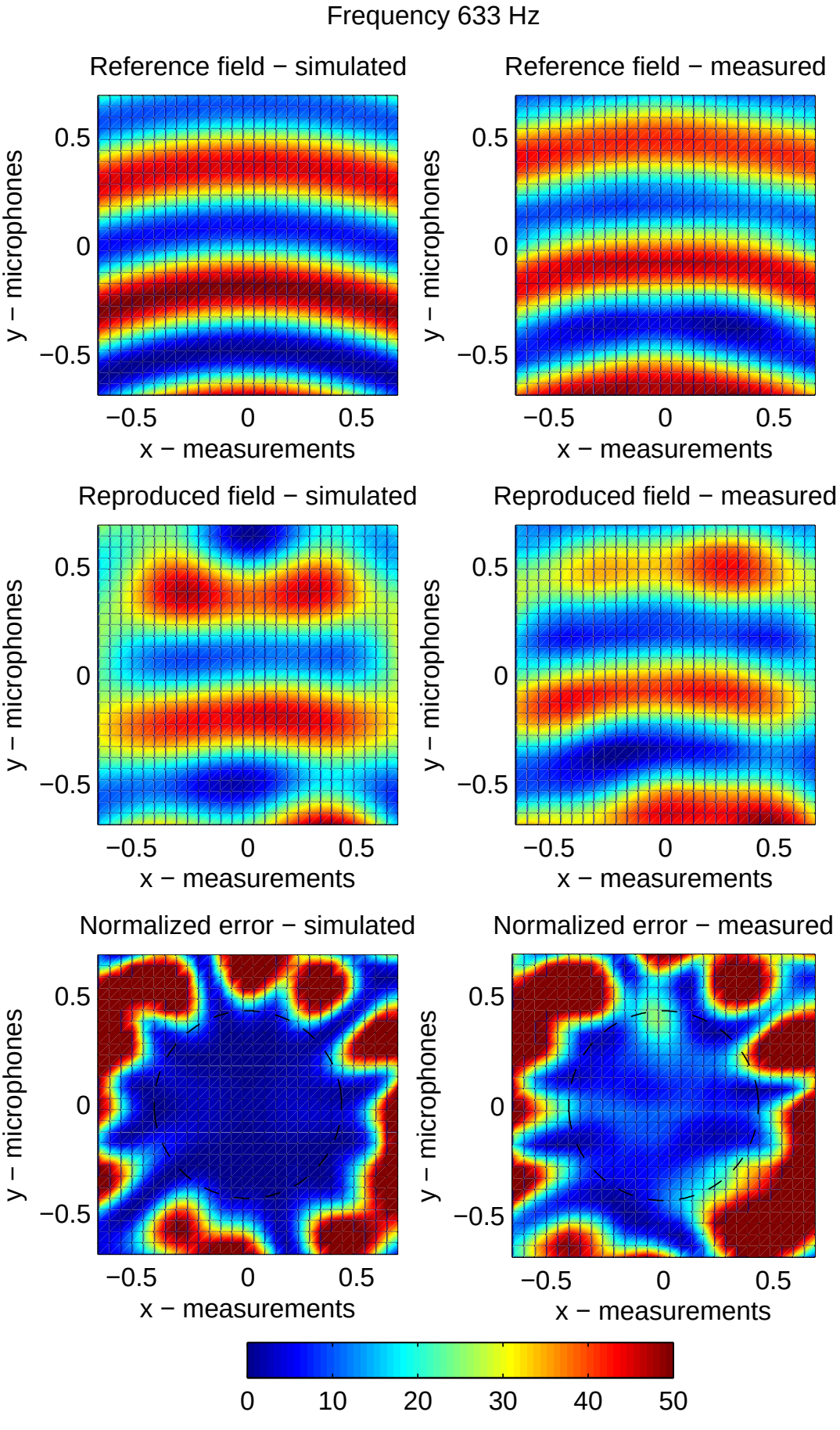

FIGURE 8.32: Reference field, reproduced field and normalized reproduction error. The color bar refers to the error plots. The operating frequency is 633 Hz.

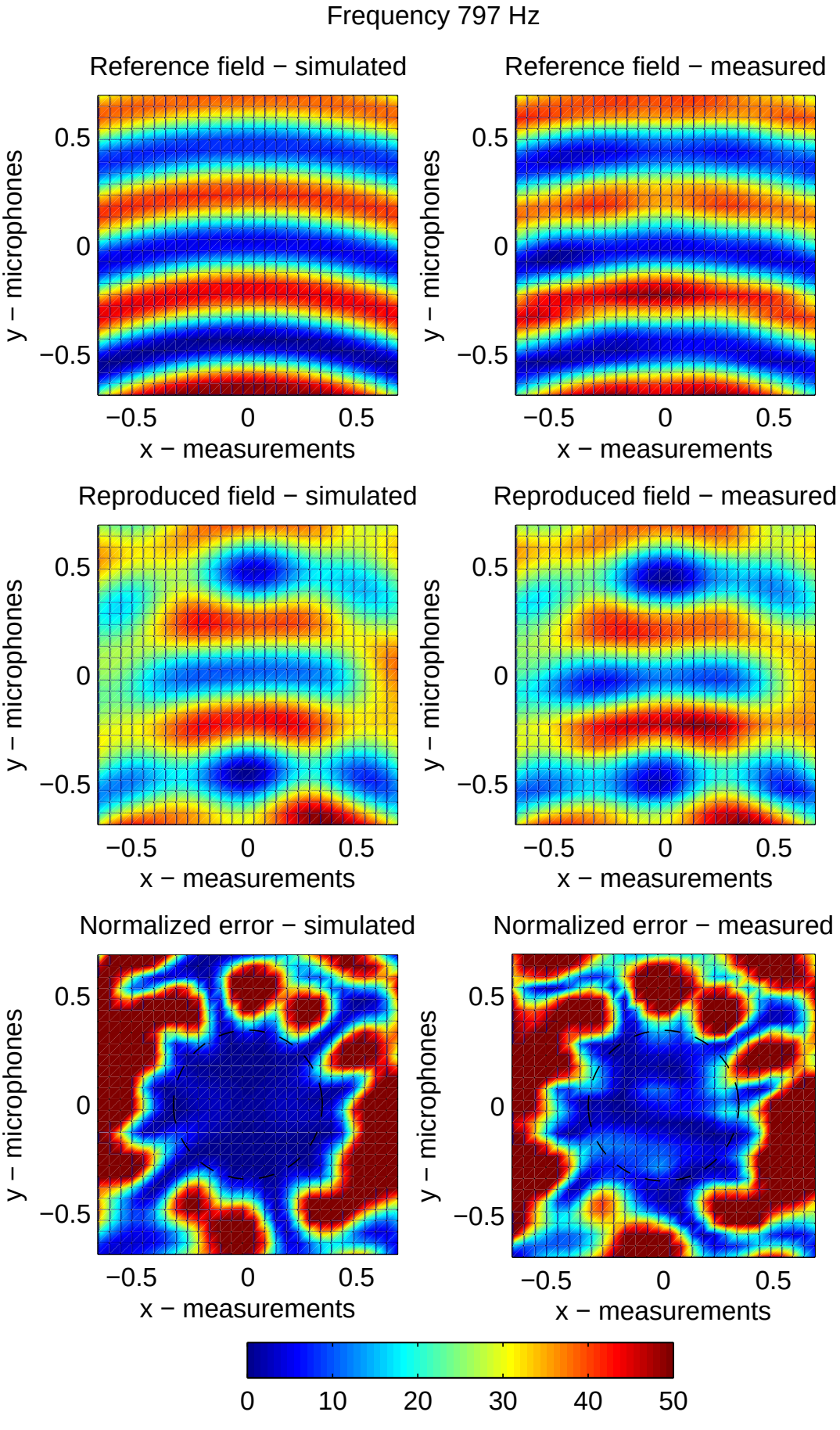

FIGURE 8.33: Reference field, reproduced field and normalized reproduction error. The color bar refers to the error plots. The operating frequency is 797 Hz.

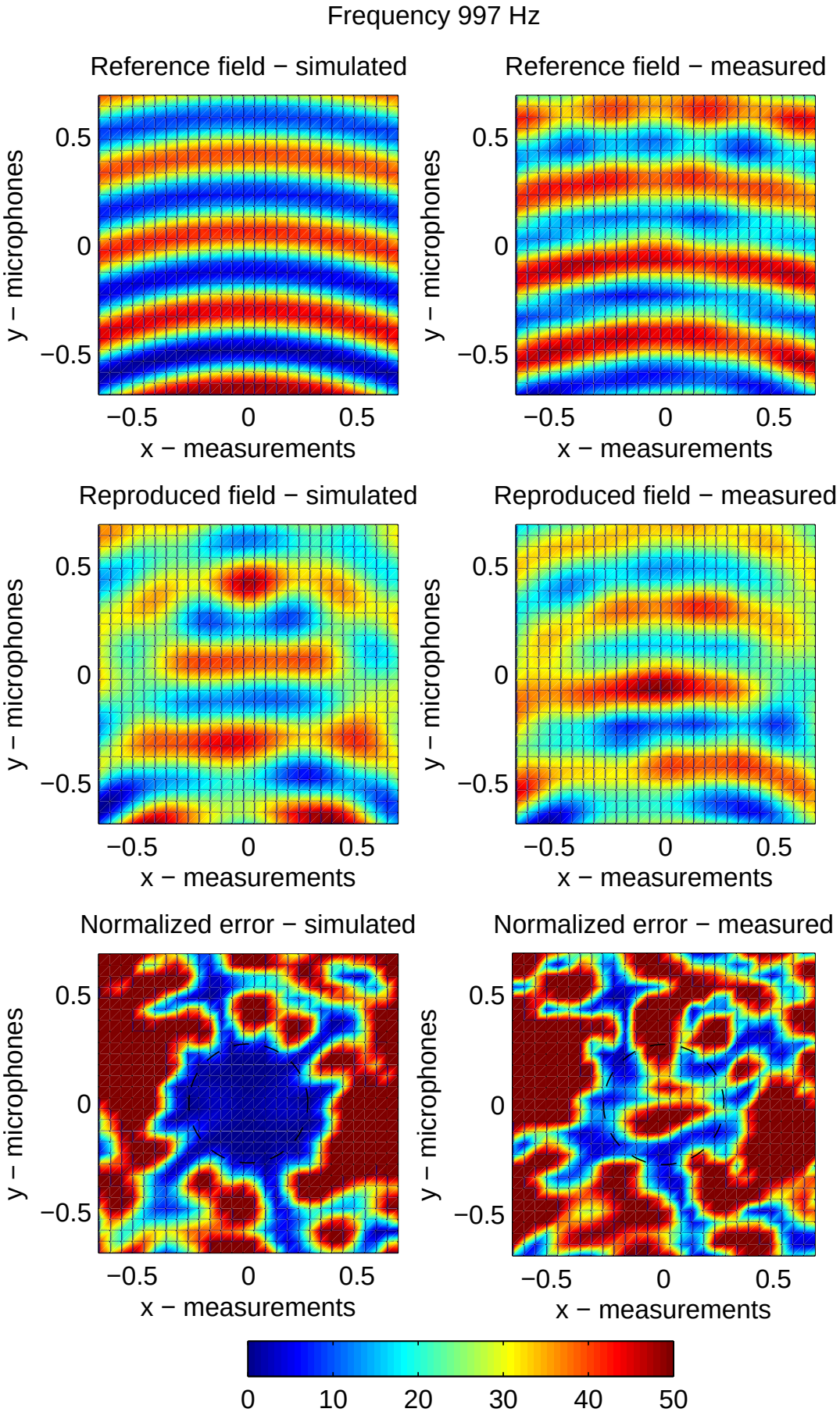

FIGURE 8.34: Reference field, reproduced field and normalized reproduction error. The color bar refers to the error plots. The operating frequency is 997 Hz.

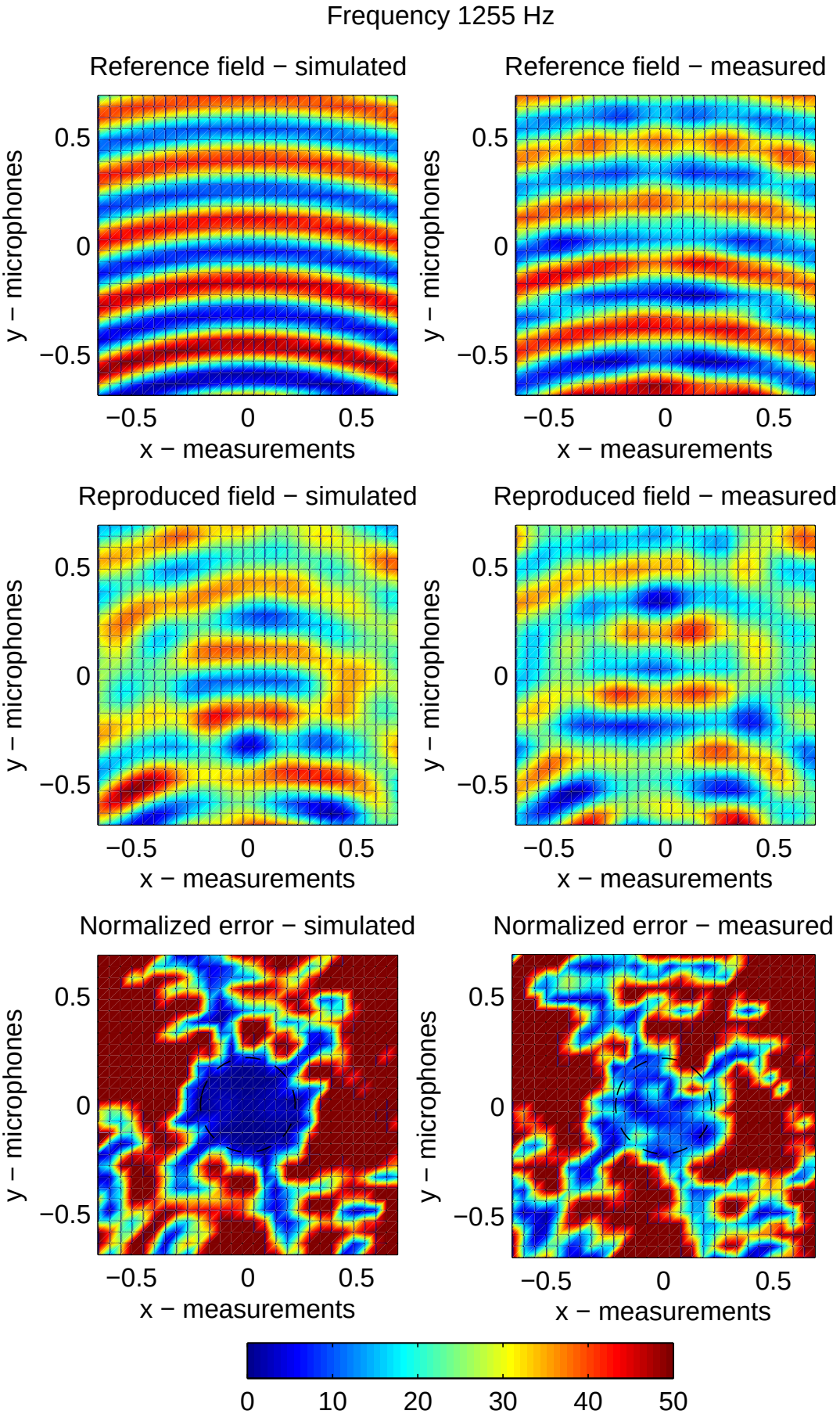

FIGURE 8.35: Reference field, reproduced field and normalized reproduction error. The color bar refers to the error plots. The operating frequency is 1255 Hz.

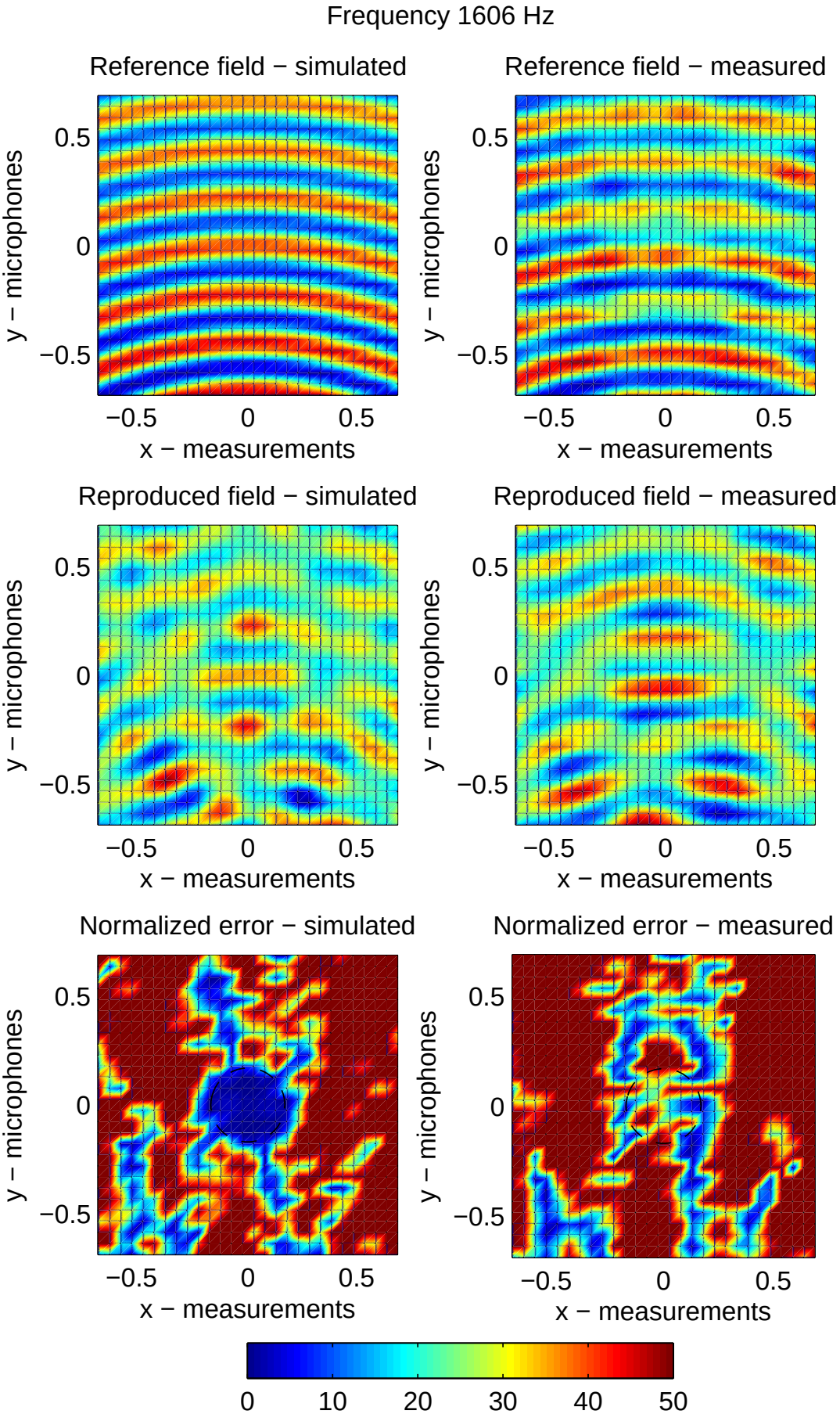

FIGURE 8.36: Reference field, reproduced field and normalized reproduction error. The color bar refers to the error plots. The operating frequency is 1606 Hz.

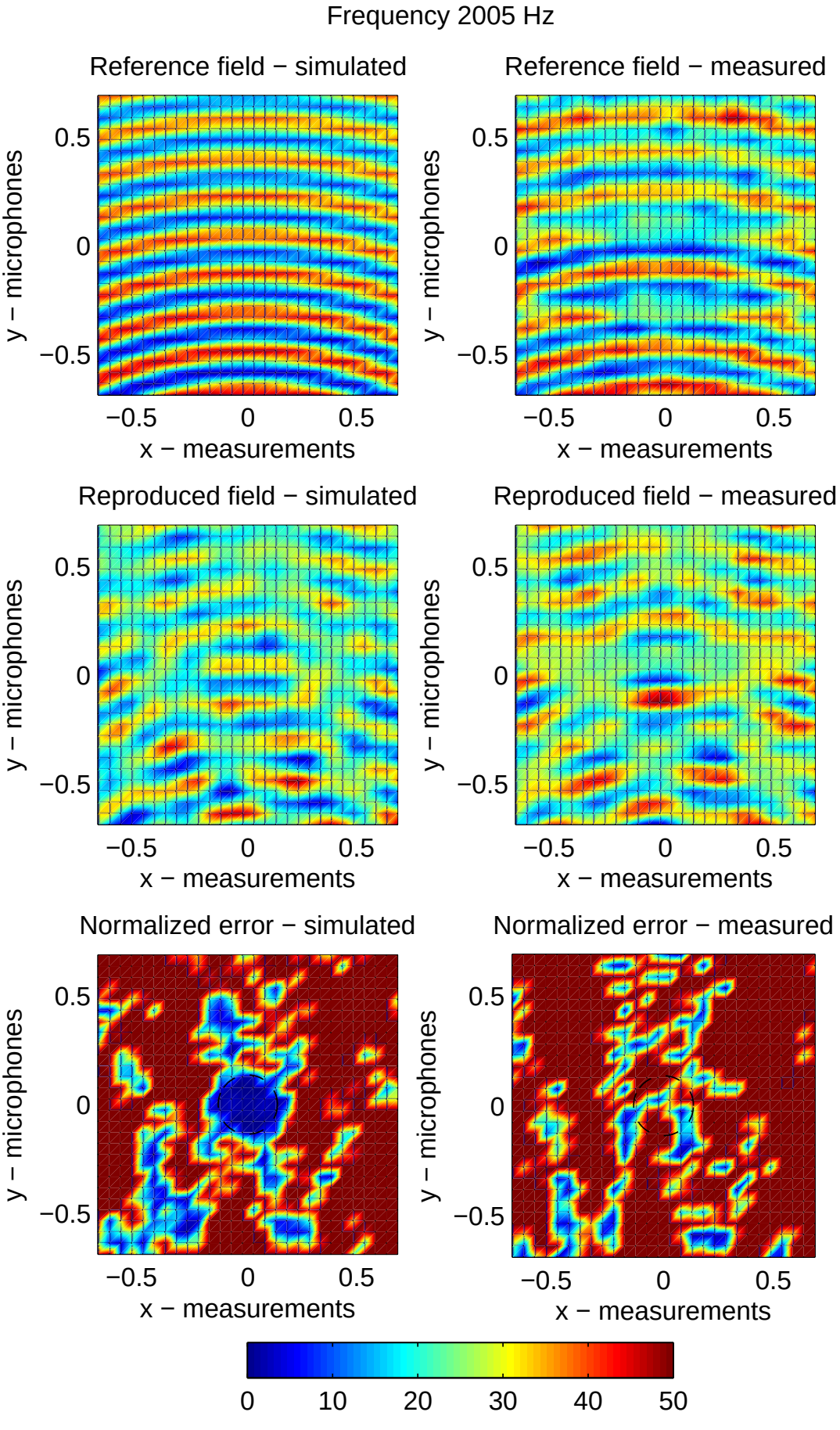

FIGURE 8.37: Reference field, reproduced field and normalized reproduction error. The color bar refers to the error plots. The operating frequency is 2005 Hz.

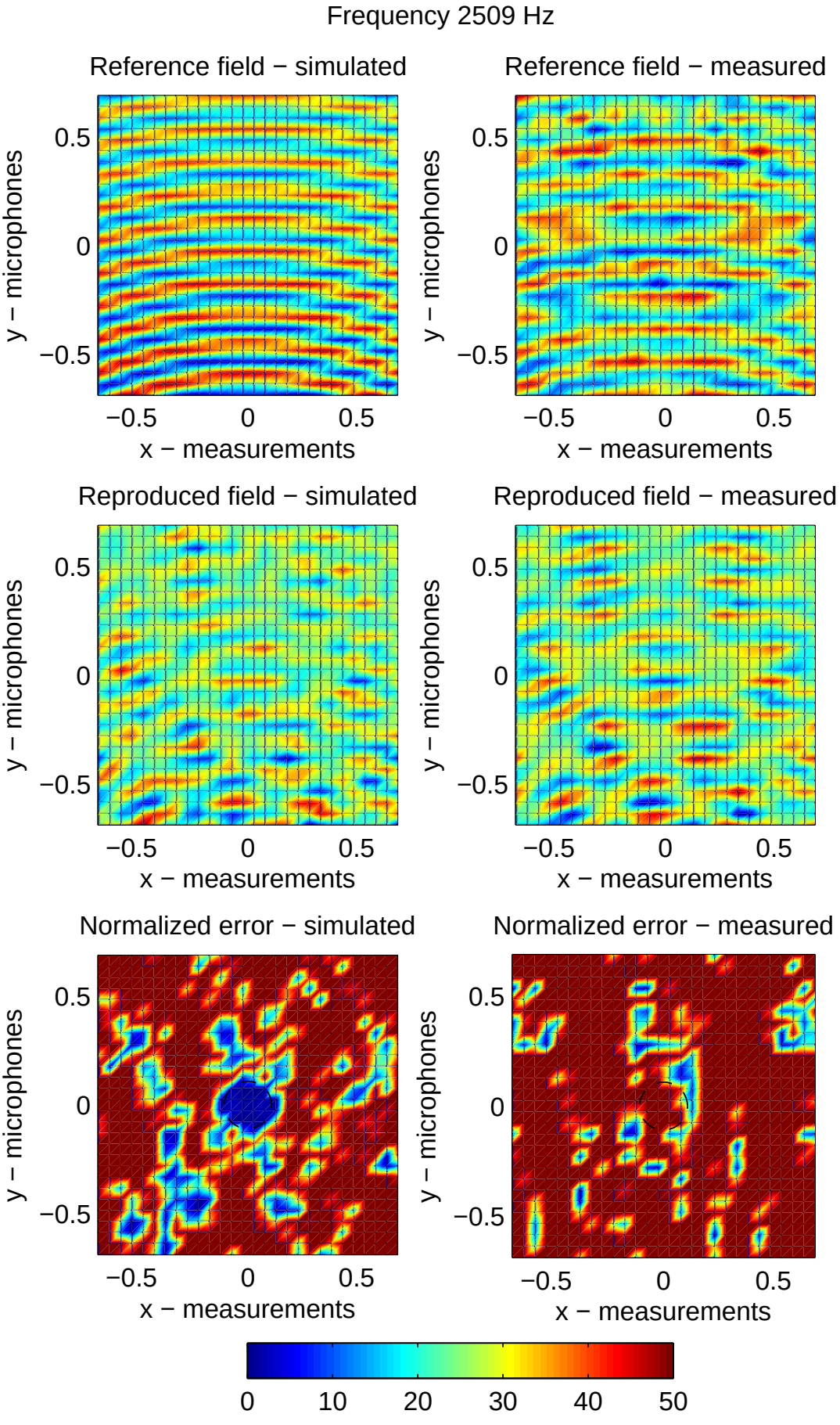

FIGURE 8.38: Reference field, reproduced field and normalized reproduction error. The color bar refers to the error plots. The operating frequency is 2509 Hz.

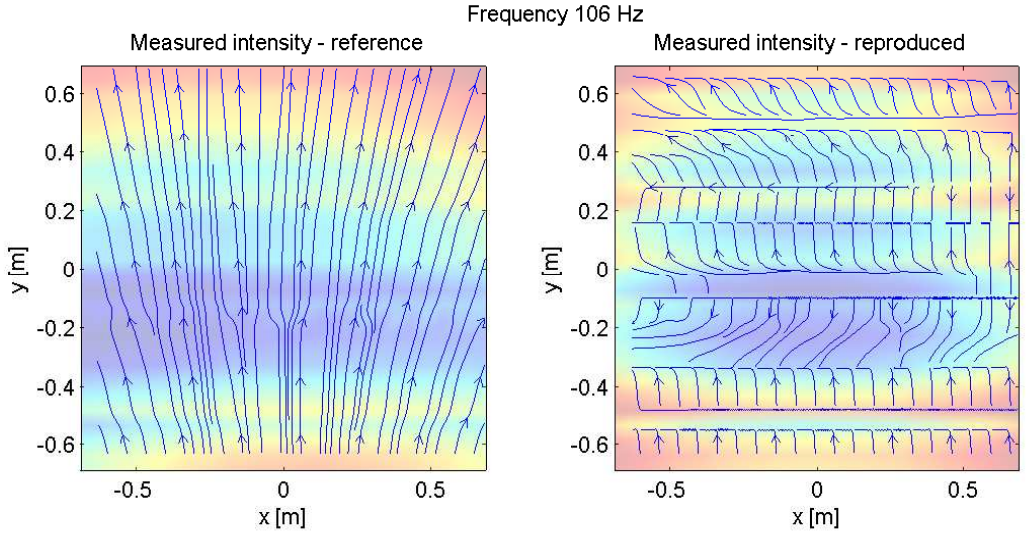

FIGURE 8.39: Intensity plot. The operating frequency is 106 Hz.

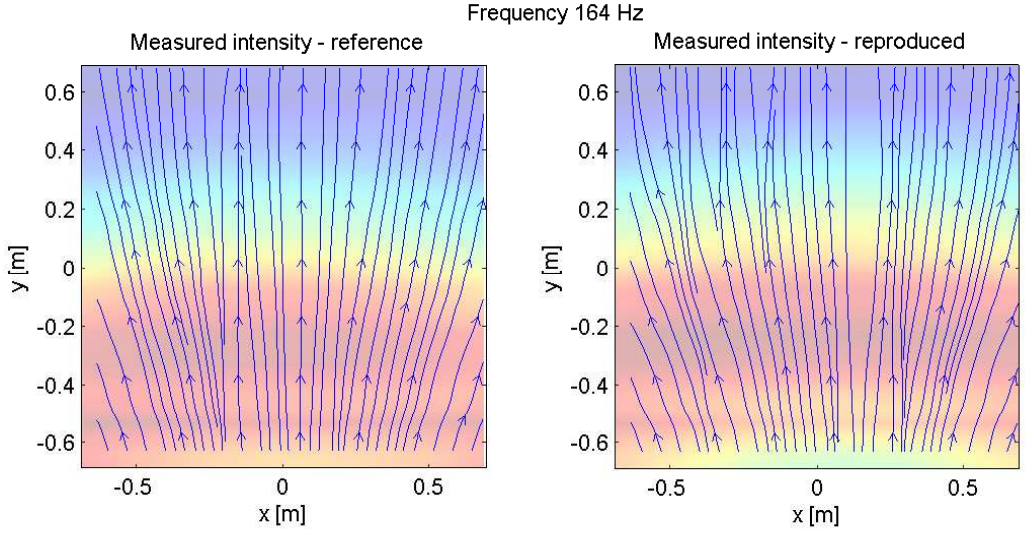

FIGURE 8.40: Intensity plot. The operating frequency is 164 Hz.

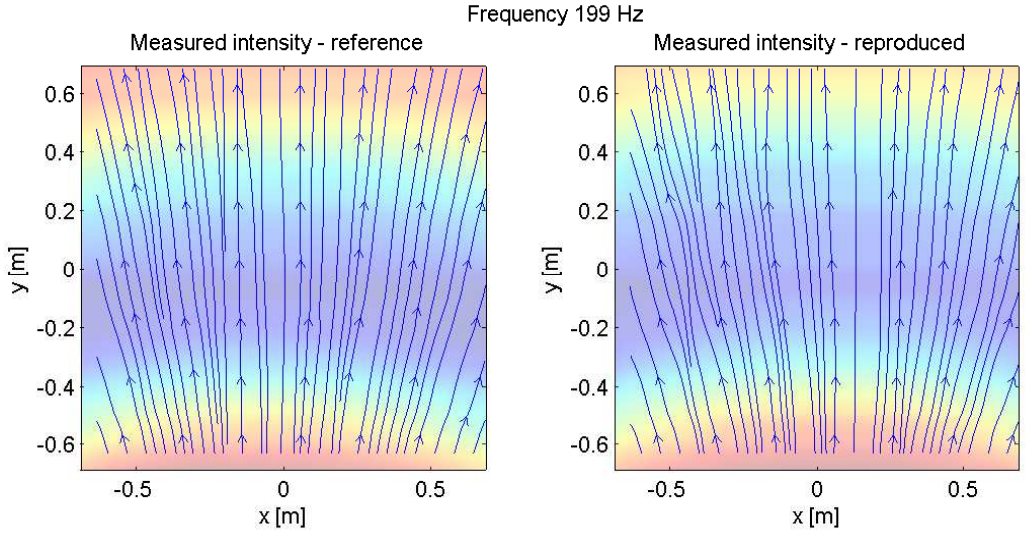

FIGURE 8.41: Intensity plot. The operating frequency is 199 Hz.

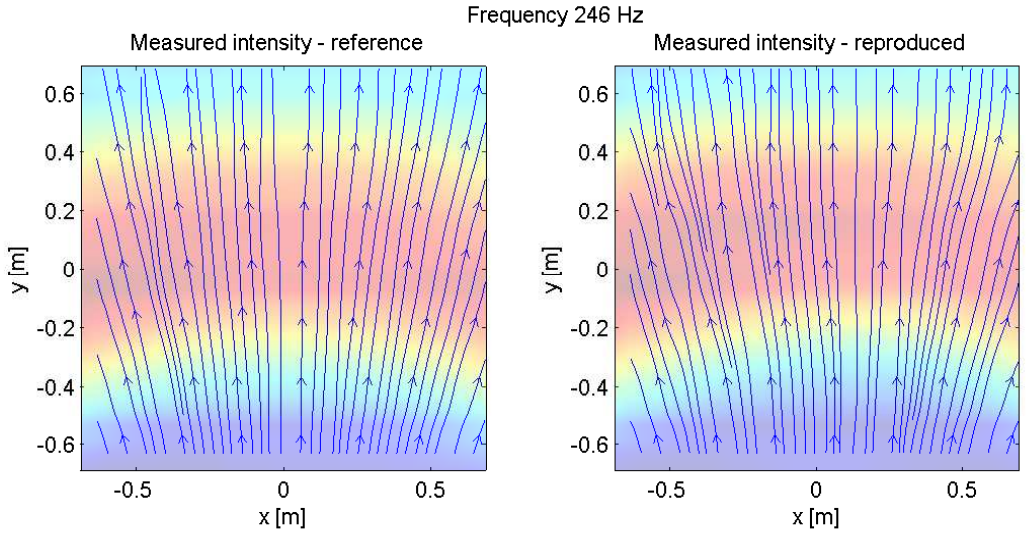

FIGURE 8.42: Intensity plot. The operating frequency is 246 Hz.

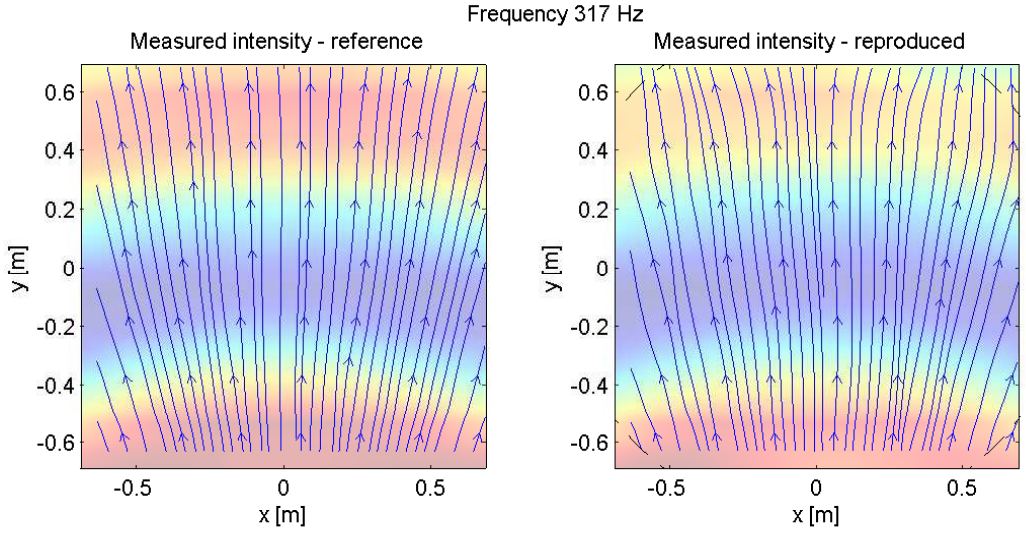

FIGURE 8.43: Intensity plot. The operating frequency is 317 Hz.

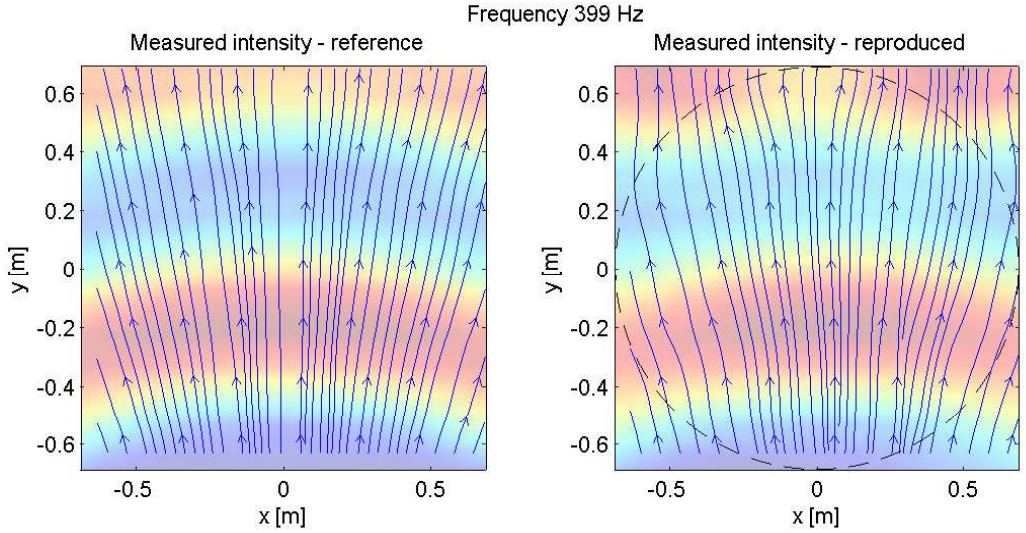

FIGURE 8.44: Intensity plot. The operating frequency is 399 Hz.

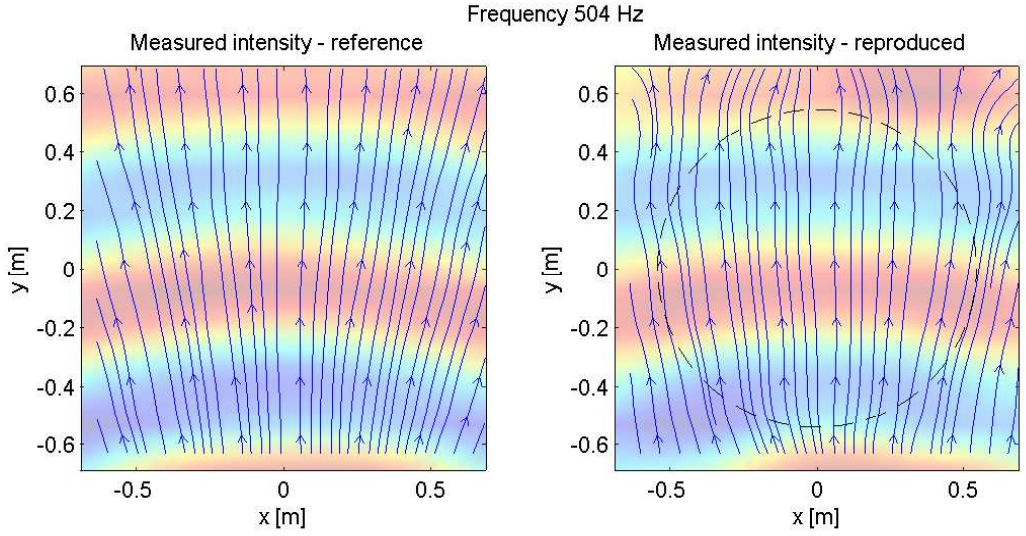

FIGURE 8.45: Intensity plot. The operating frequency is 504 Hz.

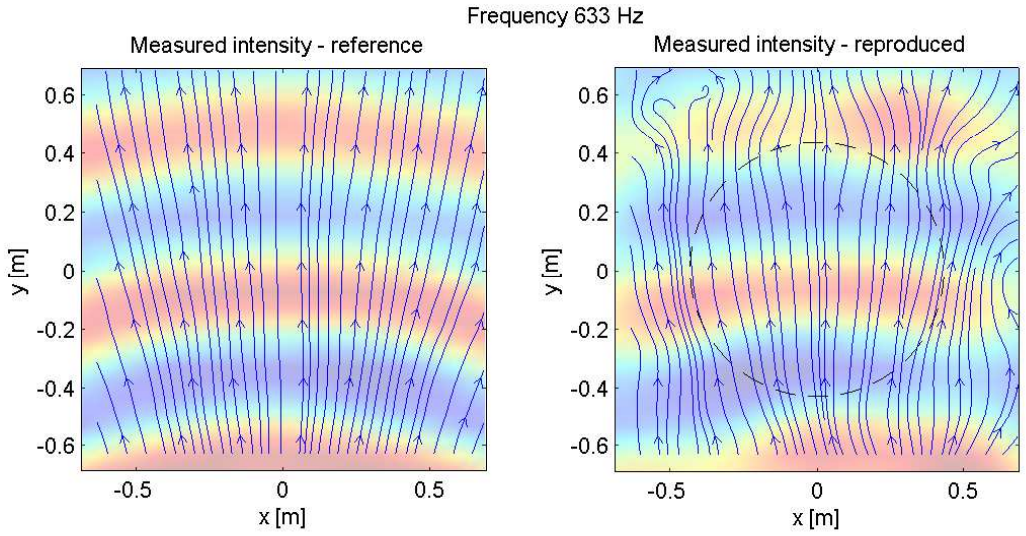

FIGURE 8.46: Intensity plot. The operating frequency is 633 Hz.

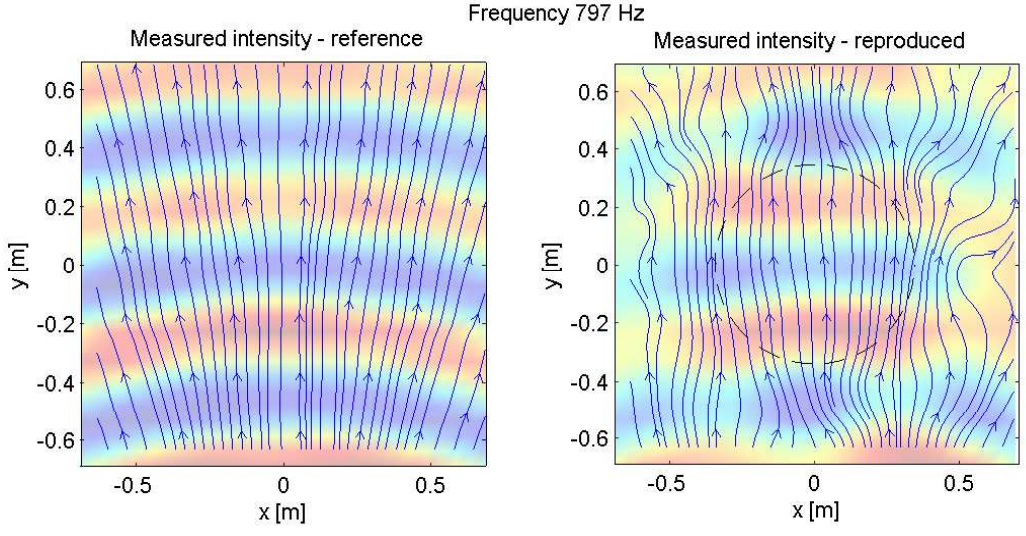

FIGURE 8.47: Intensity plot. The operating frequency is 797 Hz.

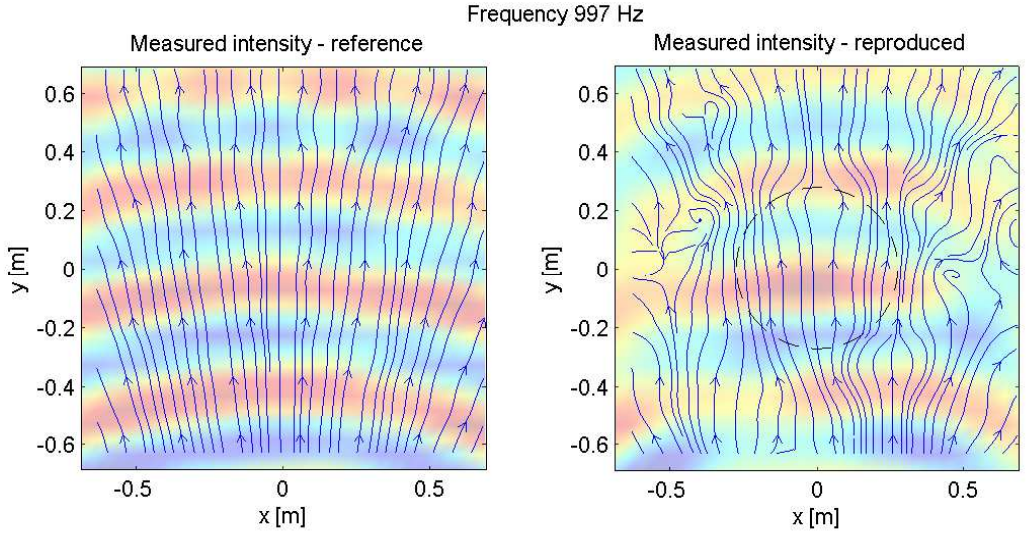

FIGURE 8.48: Intensity plot. The operating frequency is 997 Hz.

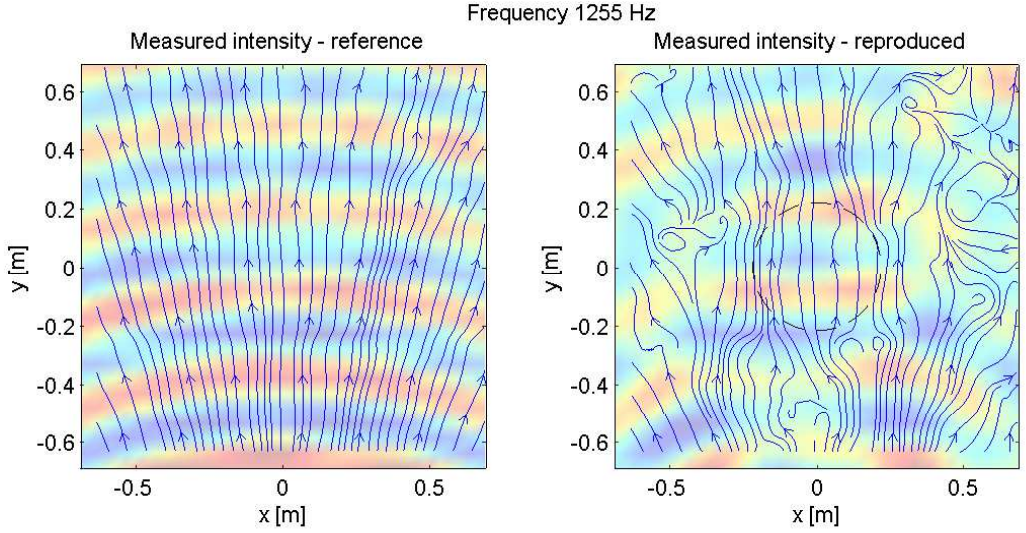

FIGURE 8.49: Intensity plot. The operating frequency is 1255 Hz.

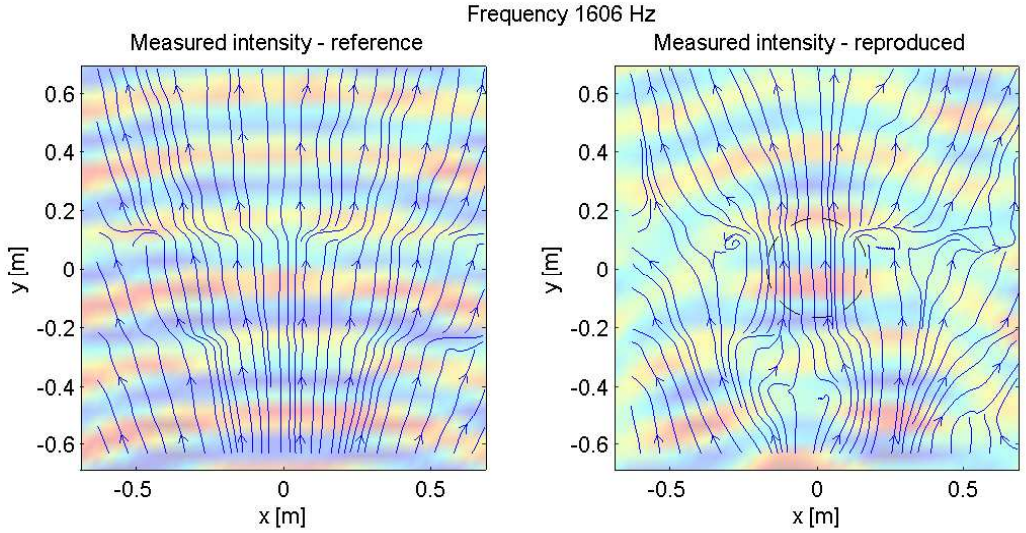

FIGURE 8.50: Intensity plot. The operating frequency is 1606 Hz.

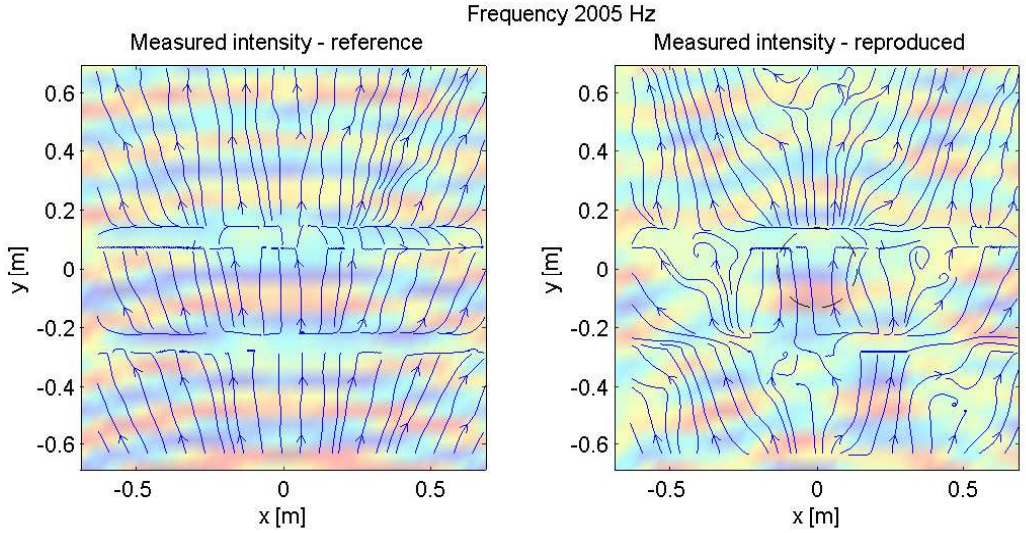

FIGURE 8.51: Intensity plot. The operating frequency is 2005 Hz.

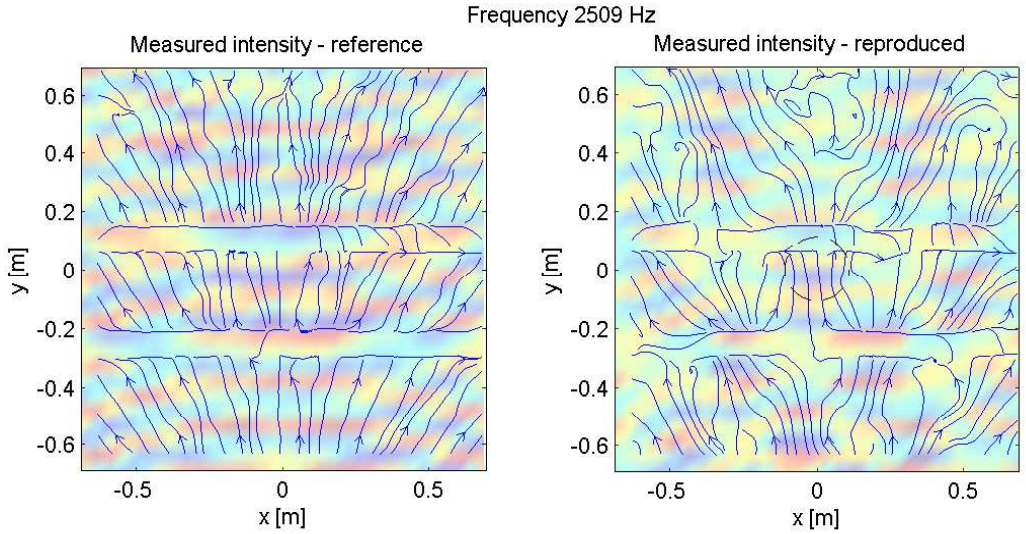

FIGURE 8.52: Intensity plot. The operating frequency is 2509 Hz.

Chapter 9

Conclusions

A general theory has been presented for studying the problem of sound field reproduction with an array of loudspeakers. Starting with the assumption of a continuous distribution of monopole-like secondary sources arranged on the boundary of the control region, we have seen that the problem can be formulated mathematically as an integral equation of the first kind.

The singular value decomposition of the integral operator involved has been used for the computation of the solution of the problem, the latter corresponding to the strength density function of the secondary sources. Closed form expressions for the singular system have been derived for some geometries, and the method of solution has been extended also to the case of unbounded planar and linear geometry, for which the operator involved is not compact.

We have seen that the problem under consideration is in general ill-posed, but it has been shown that in many cases of practical interest an exact solution exists and is unique, though it can be unstable. The parameters of the problem that are the responsible of the different kind of ill-posedness have been identified and discussed. The cases of target sound fields that do not allow for an exact solution or a unique solution have been discussed, and strategies have been proposed for overcoming these problems. Special attention has been dedicated to the reproduction of focussed sources.

An important analogy between the problem of sound field reproduction and the theory of acoustic scattering has been drawn. It has been shown that, when the control region and the reproduction region coincide, the reproduction problem is mildly ill-posed and can be reformulated as an equivalent scattering problem. It has been shown that the Kirchhoff approximation can be used for solving the reproduction problem at high frequencies.

The effects have been described, which arise from the discretization of the ideally continuous distribution of secondary sources, and have been studied especially in relation to the singular system of the integral operator. More specifically, the phenomenon of

spatial aliasing has been analyzed, and some guidance has been proposed for limiting the effects of this phenomenon.

An alternative solution method has been presented, which involves the discretization of the boundaries of both the reproduction region and of the control region, and which can be regarded as a boundary element method.

The problem, initially studied for a single-frequency field, has been extended to sound fields with broad band frequency content. This has led to the computation of the secondary source signals for the reproduction of virtual sources. Close form expression for these signals have been derived for some geometries.

The experiments undertaken to validate some of the theoretical results presented have been described in detail. The experimental setup included a loudspeaker array with 40 transducers and a translating linear microphone array. These experiments involved the reproduction of the field generated by a single virtual source located in the exterior of the reproduction region (the loudspeaker array). Different digital signal processing strategies for three different frequency bands have been presented and used in the experiment. The experimental results are in very good agreement with the theoretical results, up to about 2000 Hz.

Several of the results presented in this thesis arise also in other methods for sound field reproduction, especially Wave Field Synthesis and High Order Ambisonics, and also in the theory of microphone arrays and antennas. It is the hope of the author that this work sheds some light on the theoretical link between these techniques and contributes to laying the basis for a generalized theory of sound field reproduction.

Some of the outcomes of this work might also be of use in other physical problems and engineering applications. As a matter of fact, we have seen how acoustical problems, such acoustic scattering, acoustic radiation and acoustic holography, have some fundamental similarities with the reproduction problem considered here, and may benefit from some of the results presented in this thesis.

Further work might involve the study of the reproduction problem for other geometrical arrangements of practical interest. This would involve the derivation of the singular system of the operator involved. Prolate and oblate spheroids, as well as hemispheres, are geometries which have been widely studied and might prove useful in many practical applications. Maury et al. [ME05], [MB08] have recently derived the expressions for the singular system of a similar integral operator and for the case of bounded planar and linear geometry (namely a rectangle and a segment, respectively). These works pave the way to the extension of the approach proposed here to the geometries above.

The theory discussed in this work can be improved for the case of unbounded sets. In fact, the results presented here for integral operators defined over unbounded sets are simple extensions of analogous results derived for the simpler case of compact operators.

However, a more rigorous and possibly more general approach could be defined, which allows for a rigorous formulation of the problem with milder assumptions relating to the operator (non necessarily compact) and regards the case of compact operators as a specific case.

Further work can also involve the study of the same reproduction problem addressed here, but with more general assumption on the characteristics of the secondary sources, here assumed to be omnidirectional and linear sound sources. The development of the theory presented here to the case of directional source with first order directivity includes the use of a combined layer potential (single and double layer) and is a subject of current research for the author.

Relatively similar to the above is the use of different boundary conditions in the formulation of the reproduction problem. Here we have considered the data of the problem to be the value of the field on the control boundary (Dirichlet problem) but it is possible to include different boundary conditions such as the Neumann or impedance (Robin) boundary conditions [CK92], as suggested in Section 6.3 of this thesis.

Most of the effort in this work has been dedicated to the problem of the reproduction of a field, assuming that the latter was known on the boundary of the control region. Little attention was dedicated to the subject of measurement and analysis of an unknown sound field. This is an obvious application of microphone arrays, and the extension of the results presented in this thesis to the study of microphone arrays and related DSP strategies might lead to novel results and applications.

Finally, as mentioned in the outline of this work, it is recalled that the L^2 metric has been used throughout this thesis as a measure of accuracy of the reproduction of the field. However, sound field reproduction systems are often intended for audio application, and the L^2 metric used here might not be the most appropriate measure of the effectiveness with which a reproduction system is capable of rendering the spatial attributes of a given sound scene. It would be therefore of great scientific and commercial interest the study of a new metric, based on both acoustical and psychoacoustics parameters, and which can suit better the problem of spatial audio reproduction. The reproduction problem could be therefore reformulated in light of this new metric, and a new reproduction method might be formulated.

Appendix A

Singular value decomposition of a matrix

A simple parallel between the SVD of an operator and the SVD of a matrix can be drawn as follows. Let $\mathbf{H}$ be a matrix, transforming a vector $\mathbf{a}$ defined on $\mathbb{C}^N$ into a vector $\mathbf{p}$ defined in $\mathbb{C}^M$ ($\mathbf{b} = \mathbf{Ha}$). $\mathbf{H}$ can be expressed as

$$\mathbf{H} = \mathbf{U}\mathbf{\Sigma}\mathbf{V}^{\mathrm{H}} \tag{A.1}$$

where $\mathbf{U}$ and $\mathbf{V}$ are unitary matrices and $\mathbf{\Sigma}$ is a diagonal, real valued matrix. $\mathbf{U}$ and $\mathbf{V}$ represent rotations or reflections in a Cartesian space and their columns, the left and right singular vectors $\mathbf{u_n}$ and $\mathbf{v_n}$, respectively, are orthogonal to each other in respect to the scalar product (2.4). This means that

$$\begin{aligned} \langle \mathbf{u_n} | \mathbf{u_m} \rangle &= \delta_{n,m} \\ \langle \mathbf{v_n} | \mathbf{v_m} \rangle &= \delta_{n,m} \end{aligned} \tag{A.2}$$

$$\begin{aligned} \mathbf{U}^{\mathrm{H}}\mathbf{U} &= \mathbf{I} \\ \mathbf{V}^{\mathrm{H}}\mathbf{V} &= \mathbf{I} \end{aligned} \tag{A.3}$$

The vectors $\mathbf{u_n}$ and $\mathbf{v_n}$ are orthonormal, meaning that they are orthogonal and that their norm is unitary. The vectors $\mathbf{a}$ and $\mathbf{b}$ can describe the state of N and M degrees of freedom of two systems, respectively. As in the example with sound field reproduction described in [FN07b], $\mathbf{a}$ can represent the signals of an array of N loudspeakers and $\mathbf{p}$ the signals of an array of M microphones. In this case the columns of the matrices $\mathbf{U}$ and $\mathbf{V}$ can be interpreted as *modes* of the two systems. $\mathbf{v_1}$, the first *loudspeaker array mode*, is often constituted by identical elements, thus corresponding to all loudspeakers acting in phase and with the same amplitude. Following this approach, the operation $\mathbf{V}^{\mathrm{H}}\mathbf{a}$ can

be interpreted as a modal decomposition of the vector $\mathbf{a}$. The coefficients obtained from the product (or orthogonal projection) $\langle \mathbf{u_n} | \mathbf{a} \rangle$ shows "how much of the array mode $\mathbf{v_n}$ is present in $\mathbf{a}$".

The power of the SVD originates from the fact that each mode $\mathbf{v_n}$ is transformed by $\mathbf{H}$ into the mode $\mathbf{u_n}$. This, together with the mutual orthogonality of the modes, implies that the mode $\mathbf{u_n}$ depends on the mode $\mathbf{v_n}$ and on this mode only. It holds that

$$\mathbf{H}\mathbf{v_n} = \sigma_n \mathbf{u_n} \tag{A.4}$$

The singular values σ_n , real and positive scalars, are the elements of the diagonal matrix $\mathbf{\Sigma}$. In our framework, they represent the amount of *amplification* or *attenuation* that each mode $\mathbf{v_n}$ (of unitary norm) undergoes for the transformation $\mathbf{H}$. If the singular value σ_n is large, then the mode $\mathbf{v_n}$ is efficient, in energetic terms, and it is non efficient if σ_n is small.

Appendix B

Proofs of some theorems

Proof of Theorem 5.1

Let $S : L^2(\partial\Lambda) \to L^2(\partial V)$ be the integral operator defined by (3.16) and S^* its adjoint operator , given by (3.20). Let D_V be the set of functions defined by (5.4), namely

$$D_V := \left\{ \nabla_{\mathbf{n}} u(\mathbf{x})|_{\partial V} : \nabla^2 u(\mathbf{z}) + k^2 u(\mathbf{z}) = 0 \quad \mathbf{z} \in V, \quad u(\mathbf{x}) = 0 \;\; \mathbf{x} \in \partial V \right\} \tag{B.1}$$

We want to prove that the nullspace of the operator S^* coincides with the set D_V, that is

$$N(S^*) = D_V$$

Proof. Considerations about the definition of D_V and about the Helmholtz equation lead to the fact that if $\nabla_{\mathbf{n}} u(\mathbf{x})$ is in D_V, then also its complex conjugate $\nabla_{\mathbf{n}} u(\mathbf{x})^*$ is in D_V.

$(\phi \in N(S^*) \to \phi \in D_V)$
Assume that $\phi \in N(S^*)$. The single layer potential $S_{\partial V}$ is defined by

$$(S_{\partial V}\phi^*)(\mathbf{z}) := \int_{\partial V} G(\mathbf{z}, \mathbf{x})\phi(\mathbf{x})^* dS(\mathbf{x}), \quad \mathbf{z} \in \mathbb{R}^m \;\; m = 2, 3 \tag{B.2}$$

and let u_+ and u_- be its restrictions to the exterior and interior of V (including the boundary), respectively, namely

$$u_+(\mathbf{z}) : \;\; = \;\; (S_{\partial V}\phi^*)(\mathbf{z})|_{\mathbb{R}^m \setminus V} \tag{B.3}$$

$$u_-(\mathbf{z}) : \;\; = \;\; (S_{\partial V}\phi^*)(\mathbf{z})|_{\overline{V}} \tag{B.4}$$

Equation (2.99) shows that $S_{\partial V}$ is continuous throughout $\mathbb{R}^m$ and that it satisfies the homogeneous Helmholtz equation (2.95) in $\mathbb{R}^m \setminus \partial V$. This implies that $u_+(\mathbf{x}) = u_-(\mathbf{x})$

on the boundary ∂V and

$$\nabla^2 u_+(\mathbf{z}) + k^2 u_+(\mathbf{z}) = 0, \quad \mathbf{z} \in \mathbb{R}^m \backslash \overline{V} \tag{B.5}$$

$$\nabla^2 u_-(\mathbf{z}) + k^2 u_-(\mathbf{z}) = 0, \quad \mathbf{z} \in V \tag{B.6}$$

In other terms, $u_+(\mathbf{z})$ and $u_-(\mathbf{z})$ are solutions of an exterior and interior problem, respectively [Wil99].

For the results above and from the definition of nullspace (2.23), it holds that

$$0 = (S^*\phi)(\mathbf{y})^* = (S_{\partial V}\phi^*)(\mathbf{y}) = u_+(\mathbf{y}) \quad \mathbf{y} \in \partial\Lambda \tag{B.7}$$

The analyticity of $u_+(\mathbf{z})$ [CK83, p.72] and the uniqueness of the exterior Dirichlet problem [CK83, p.85] imply that, if $u_+ = 0$ on $\partial\Lambda$, then it is zero also in all of the exterior of V. Hence

$$u_+(\mathbf{z}) = 0 \quad \mathbf{z} \in \mathbb{R}^m \backslash V \tag{B.8}$$

$$\nabla_{\mathbf{n}} u_+(\mathbf{z}) = 0 \quad \mathbf{z} \in \mathbb{R}^m \backslash \overline{V} \tag{B.9}$$

where the normal derivative $\nabla_{\mathbf{n}} u_+$ on the boundary ∂V is defined similarly to equation (2.100).

u_- is a solution (in general not unique) of the homogeneous Dirichlet problem in V. Using the jump relation (2.102) for the normal derivative of $S_{\partial V}$ we obtain that

$$\phi(\mathbf{x})^* = \nabla_{\mathbf{n}} u_-(\mathbf{x}) - \nabla_{\mathbf{n}} u_+(\mathbf{x}), \quad \mathbf{x} \in \partial V \tag{B.10}$$

and for (B.9) it holds that

$$\phi(\mathbf{x})^* = \nabla_{\mathbf{n}} u_-(\mathbf{x}), \quad \mathbf{x} \in \partial V \tag{B.11}$$

Henceforth, $\phi(\mathbf{x})^*$ is the normal derivative of one solution of the interior Dirichlet problem on V, and so $\phi(\mathbf{x})^*$ and $\phi(\mathbf{x})$ are in D_V.

$(\phi \in D_V \rightarrow \phi \in N(S^*))$
Conversely, if $\phi(\mathbf{x}) = \nabla_{\mathbf{n}} u(\mathbf{x}) \in D_V$, then $u(\mathbf{x}) = 0$ on ∂V and the Kirchhoff-Helmholtz integral (2.105) implies that

$$\begin{aligned} 0 &= \int_{\partial V} G(\mathbf{z},\mathbf{x})\nabla_{\mathbf{n}} u(\mathbf{x}) - \nabla_{\mathbf{n}} G(\mathbf{z},\mathbf{x}) u(\mathbf{x}) dS(\mathbf{x}) = \\ &= \int_{\partial V} G(\mathbf{z},\mathbf{x})\nabla_{\mathbf{n}} u(\mathbf{x}) dS(\mathbf{x}) = (S_{\partial V}\nabla_{\mathbf{n}} u)(\mathbf{z}), \quad \mathbf{z} \in \mathbb{R}^m \backslash V \end{aligned} \tag{B.12}$$

This obviously leads to

$$0 = (S_{\partial V} \nabla_{\mathbf{n}} u)(\mathbf{y})^* = (S^* \nabla_{\mathbf{n}} u^*)(\mathbf{y}), \quad \mathbf{y} \in \partial\Lambda \tag{B.13}$$

Therefore, $\phi \in D_V$ implies that $\phi^* \in N(S^*)$. As mentioned above, if ϕ^* belongs to $N(S^*)$ then the same holds also for ϕ. This completes the proof.

Proof of Theorem 5.4

The proof is given that any pressure profile $p(\mathbf{x}) \in \Psi_V$ is in the closure of the range of S, where Ψ_V is given by (3.3) and S by (3.16).

Proof. Let $\nabla_{\mathbf{n}} u(\mathbf{x}) \in D_V$, defined by (5.4). The Green second formula (2.104) states that

$$\int_V u(\mathbf{x}) \nabla^2 p(\mathbf{x}) - p(\mathbf{x}) \nabla^2 u(\mathbf{x}) dV(\mathbf{x}) = \int_{\partial V} u(\mathbf{x}) \nabla_{\mathbf{n}} p(\mathbf{x}) - p(\mathbf{x}) \nabla_{\mathbf{n}} u(\mathbf{x}) dS(\mathbf{x}) \tag{B.14}$$

Because both $u(\mathbf{x})$ and $p(\mathbf{x})$ are solutions of the homogeneous Helmholtz equation in V, it holds that

$$\nabla^2 p(\mathbf{x}) = -k^2 p(\mathbf{x}), \quad \mathbf{x} \in \overline{V} \tag{B.15}$$

$$\nabla^2 u(\mathbf{x}) = -k^2 u(\mathbf{x}), \quad \mathbf{x} \in V \tag{B.16}$$

As a consequence the left hand side of (B.14) equals zero. The field $u(\mathbf{x})$ is a solution of the homogeneous interior Dirichlet problem in V, and it is therefore identically equal to zero on ∂V. In view of these considerations, equation (B.14) can be rewritten as

$$\int_{\partial V} p(\mathbf{x}) \nabla_{\mathbf{n}} u(\mathbf{x}) dS(\mathbf{x}) = \langle \nabla_{\mathbf{n}} u^* | p \rangle_{\partial V} = 0 \tag{B.17}$$

Corollary 5.2 completes the proof.

Proof of Theorem 5.5

We want to prove that, if the wave number k is not one of the Dirichlet eigenvalues for V (see Section 3.3), then the solution of the inverse problem $Sa = p$ is unique, when this exists.

Let the function $a(\mathbf{y})$ belong to the nullspace of S. Then $(Sa)(\mathbf{x}) = 0$, $\forall \mathbf{x} \in \partial V$ and the function

$$u_-(\mathbf{z}) := (Sa)(\mathbf{z}) \quad \mathbf{z} \in V \tag{B.18}$$

is a solution of the homogeneous interior Dirichlet problem for V. If the wave number k is not one of the Dirichlet eigenvalues for V, then the only solution of the homogeneous interior Dirichlet problem is $u_-(\mathbf{z}) = 0,\ \forall \mathbf{z} \in V$. This implies that, given a subset $W \subset V$, all derivatives of $u(\mathbf{z}),\ \mathbf{z} \in \partial W$ are zero. Hence, for analytical continuation, $(Sa)(\mathbf{z}) = 0,\ \forall \mathbf{z} \in \Lambda$. The continuity of the single layer potential (2.99) implies that $(Sa)(\mathbf{z}) = 0,\ \forall \mathbf{z} \in \partial\Lambda$. As a consequence of the uniqueness of the exterior Dirichlet problem, we have that $(Sa)(\mathbf{z}) = 0,\ \forall \mathbf{z} \in R^m$. This leads to

$$\lim_{h \to 0} \hat{\mathbf{n}}(\mathbf{z}) \cdot \nabla (Sa)(\mathbf{z} + h\hat{\mathbf{n}}(\mathbf{z})) = 0, \quad \mathbf{z} \in \partial\Lambda \tag{B.19}$$

for both $h > 0$ and $h < 0$. Using the jump relation (2.102) of the single layer potential, we have that $a(\mathbf{y}) = 0,\ \forall \mathbf{y} \in \partial\Lambda$. This proves that, under the conditions mentioned above, S is injective.

Appendix C

Spherical cavity and scattering by a sound soft sphere

Solution of the homogeneous Dirichlet problem for the sphere

Let B_R be the three-dimensional ball defined by

$$B_R := \{\mathbf{z} \in R^3 : |\mathbf{z}| < R\} \tag{C.1}$$

whose boundary Ω_R is the sphere of radius R.

It can be easily proven that given the wave number k_n such that $j_n(k_n R) = 0$, all functions of the kind

$$u_n(\mathbf{z}) = a j_\nu(k_n z) Y_n^m(\hat{\mathbf{z}}), \quad \mathbf{z} \in B_R, \quad |m| \leq n, \quad a \in \mathbb{R} \tag{C.2}$$

are solutions of the homogeneous Dirichlet problem (3.18), with boundary condition $f(\mathbf{x}) = 0$. Using arguments analogous to [Wil99, p.218], it can be shown that u_n satisfies the homogeneous Helmholtz equation in B_R. It can be simply verified also that $u_n(\mathbf{z}) = 0 \; \forall \mathbf{z} \in \Omega_R$, which indicates that u_n satisfies the homogeneous Dirichlet boundary condition.

The frequencies $\omega_n = k_n/c$ identify the resonance frequencies of a spherical cavity with radius R and pressure release boundary conditions.

Scattering by a sound soft sphere

As shown in [Wil99], the incident and scattered sound field can be expressed by means of spherical harmonics and spherical Bessel functions:

$$p_i(\mathbf{z}) = \sum_{\nu=0}^{\infty} \sum_{\mu=-\nu}^{\nu} A_{\mu\nu}(\omega) j_\nu(kz) Y_\nu^\mu(\hat{\mathbf{z}}) \tag{C.3}$$

$$p_s(\mathbf{z}) = \sum_{\nu=0}^{\infty} \sum_{\mu=-\nu}^{\nu} C_{\mu\nu}(\omega) h_\nu(kz) Y_\nu^\mu(\hat{\mathbf{z}}) \tag{C.4}$$

The two equations above can be used for the representation of the field generated by the single layer potential (6.85). Equation (C.3) can be used for the representation of the target sound field $p(\mathbf{z})$, corresponding to the field in the interior region Λ, while equation (C.4) can be used for the representation of the field in the exterior region $\mathbb{R}^3 \backslash \overline{\Lambda}$. It is clear that, in general, $A_{\mu\nu} \neq C_{\mu\nu}$. The homogeneous Dirichlet boundary condition implies that

$$p_i(\mathbf{y}) + p_s(\mathbf{y}) = 0, \quad \mathbf{y} \in \partial\Lambda \tag{C.5}$$

Combining this condition with equations (C.3) and (C.4), and in view of equation (6.79) that represents the continuity of the single layer potential over the boundary $\partial\Lambda$, leads to the following relation:

$$\sum_{\nu=0}^{\infty} \sum_{\mu=-\nu}^{\nu} A_{\mu\nu}(\omega) j_\nu(kR_\Lambda) Y_\nu^\mu(\hat{\mathbf{y}}) = -\sum_{\nu=0}^{\infty} \sum_{\mu=-\nu}^{\nu} C_{\mu\nu}(\omega) h_\nu(kR_\Lambda) Y_\nu^\mu(\hat{\mathbf{y}}), \quad \mathbf{y} \in \partial\Lambda \tag{C.6}$$

In view of the orthogonality relation of the spherical harmonics (4.3), the previous equation leads to

$$C_{\mu\nu}(\omega) = -\frac{j_\nu(kR_\Lambda)}{h_n(kR_\Lambda)} A_{\mu\nu}(\omega) \tag{C.7}$$

This is the boundary condition of a sound-soft sphere (sometimes referred to as the *Dirichlet sphere*). The total field is given by the sum of the incident and scattered field and is given by

$$p_T(\mathbf{z}) = \sum_{\nu=0}^{\infty} \sum_{\mu=-\nu}^{\nu} A_{\mu\nu}(\omega) \left(j_\nu(kz) - \frac{j_\nu(kR_\Lambda)}{h_\nu(kR_\Lambda)} h_\nu(kz) \right) Y_\nu^\mu(\hat{\mathbf{z}}) \tag{C.8}$$

Its radial derivative is given by

$$\nabla_{\mathbf{n}} p_T(\mathbf{z}) = \sum_{\nu=0}^{\infty} \sum_{\mu=-\nu}^{\nu} k A_{\mu\nu}(\omega) \left(j_\nu'(kz) - \frac{j_\nu(kR_\Lambda)}{h_\nu(kR_\Lambda)} h_\nu'(kz) \right) Y_\nu^\mu(\hat{\mathbf{z}}) \tag{C.9}$$

For $z = R_\Lambda$, applying the Wronskian relation (2.38) we obtain

$$\nabla_{\mathbf{n}} p_T(\mathbf{y}) = \sum_{\nu=0}^{\infty} \sum_{\mu=-\nu}^{\nu} \frac{A_{\mu\nu}(\omega)}{ikR_\Lambda^2 h_\nu(kr)} Y_\nu^\mu(\hat{\mathbf{y}}) \tag{C.10}$$

Appendix D

Solution for a focused source in the concentric sphere geometry

Given the source location $\mathbf{q} = [0, 0, -d]$, we consider the Weyl integral limited to a ball $B_k := \{\boldsymbol{\kappa} \in \mathbb{R}^2 : |\boldsymbol{\kappa}| \leq k\}$ given by equation (6.48) and repeated here:

$$\tilde{G}(\mathbf{z}, \mathbf{q}) = \frac{i}{8\pi^2} \int_{B_k} \frac{e^{i\zeta(\kappa)(z_3+d)}}{\zeta(\kappa)} e^{i\boldsymbol{\kappa}\cdot\mathbf{z}} dS(\boldsymbol{\kappa}), \quad z_3 \geq -d \tag{D.1}$$

We define

$$\mathbf{k} := [\kappa_1, \kappa_2, \zeta(\kappa)] \tag{D.2}$$

and change the integration variables as shown in [MW95, p.120], namely

$$\begin{aligned} \kappa_1 &= k\cos(\phi_k)\sin(\theta_k) \\ \kappa_2 &= k\sin(\phi_k)\sin(\theta_k) \\ \zeta(\kappa) &= k\cos(\theta_k) \\ \frac{dS(\boldsymbol{\kappa})}{\zeta(\kappa)} &= k\sin(\theta_k) d\phi_k d\theta_k \end{aligned}$$

The integral (D.1) becomes

$$\tilde{G}(\mathbf{z}, \mathbf{q}) = \frac{i}{8\pi^2} \int_0^{2\pi} d\phi_k \int_0^{\frac{\pi}{2}} e^{ik\cos\theta_k d} e^{i\mathbf{k}\cdot\mathbf{z}} k\sin(\theta_k) d\theta_k \tag{D.3}$$

This expression can be interpreted as an infinite superposition of propagating plane waves $e^{i[\kappa_1 z_1 + \kappa_2 z_2 + \zeta(\kappa)(z_3+d)]}$, whose directions span a hemisphere of radius $\sqrt{(}k)$.

The field due to a propagating plane wave $e^{i\mathbf{k}\cdot\mathbf{z}}$ can be expressed by the Jacobi-Anger expansion (2.56), reported again here as

$$e^{i\mathbf{k}\cdot\mathbf{z}} = \sum_{n=0}^{\infty} i^n (2n+1) j_n(kz) P_n(\hat{\mathbf{z}}\cdot\hat{\mathbf{k}}) \tag{D.4}$$

where $\hat{\mathbf{z}}\cdot\hat{\mathbf{k}} = (\mathbf{z}\cdot\mathbf{k})/(kz)$. Analogously, we have that

$$e^{ik\cos\theta_k d} = \sum_{n=0}^{\infty} i^n (2n+1) j_n(kd) P_n(\cos\theta_k) \tag{D.5}$$

Considering equation (D.4) and following the passages illustrated in Section 4.1, it can be shown that the plane wave $e^{i\mathbf{k}\cdot\mathbf{z}}$ can be represented in the form of a single layer potential of the form

$$e^{i\mathbf{k}\cdot\mathbf{z}} = \int_{\partial\Lambda} G(\mathbf{z},\mathbf{y}) \left(\sum_{\nu=0}^{\infty} \sum_{\mu=-\nu}^{\nu} \frac{i^\nu 4\pi}{ikR_\Lambda^2 h_\nu(kR_\Lambda)} Y_\nu^\mu(\hat{\mathbf{y}}) Y_\nu^\mu(\hat{\mathbf{k}})^* \right) dS(\mathbf{y}) \tag{D.6}$$

where $\partial\Lambda$ is a sphere of radius R_Λ and centered in the origin, which defines the surface on which the secondary sources are arranged. Inserting this result in (D.3) and rearranging the order of integration and summation we obtain the following result:

$$\tilde{G}(\mathbf{z},\mathbf{q}) = (Sa)(\mathbf{z}), \quad z_3 > -d, \; z < R_\Lambda \tag{D.7}$$

$$\begin{aligned} a(\mathbf{y}) &= \sum_{\nu=0}^{\infty} \sum_{\mu=-\nu}^{\nu} \frac{i^\nu}{R_\Lambda^2 h_\nu(kR_\Lambda)} Y_\nu^\mu(\hat{\mathbf{y}}) \sum_{n=0}^{\infty} i^n (2n+1) j_n(kd) \\ &\cdot \int_0^{\frac{\pi}{2}} \left[\frac{1}{2\pi} \int_0^{2\pi} Y_\nu^\mu(\hat{\mathbf{k}})^* d\phi_k \right] P_n(\cos\theta_k) \sin(\theta_k) d\theta_k \end{aligned} \tag{D.8}$$

Recalling the definition of the spherical harmonics (2.51)

$$Y_\nu^\mu(\hat{\mathbf{k}})^* = Y_\nu^\mu(\theta_k,\phi_k) := \sqrt{\frac{(2\nu+1)(\nu-\mu)!}{4\pi(\nu+\mu)!}} P_\nu^\mu(\cos\theta_k)\, e^{i\mu\phi_k} \tag{D.9}$$

we observe that

$$\frac{1}{2\pi} \int_0^{2\pi} e^{-i\mu\phi_k} d\phi_k = \delta_{\mu,0} \tag{D.10}$$

and that

$$\begin{aligned} \breve{P}_{n\nu} &:= \int_0^{\frac{\pi}{2}} \left[\frac{1}{2\pi} \int_0^{2\pi} Y_\nu^\mu(\hat{\mathbf{k}})^* d\phi_k \right] P_n(\cos\theta_k) \sin(\theta_k) d\theta_k \\ &= \int_0^{\frac{\pi}{2}} P_\nu(\cos\theta_k) P_n(\cos\theta_k) \sin(\theta_k) d\theta_k \end{aligned} \tag{D.11}$$

Applying the following substitution of variables in the integral above

$$\begin{aligned} \cos\theta_k &= \alpha \\ -\sin\theta_k d\theta_k &= d\alpha \end{aligned} \tag{D.12}$$

we obtain [GR65, p.789], equation 7.221.2

$$\breve{P}_{n\nu} := \int_0^1 P_\nu(\alpha)P_n(\alpha)d\alpha = \begin{cases} \frac{1}{2\nu+1} & [\nu = n] \\ 0 & [\nu - n \text{ is even}, \nu \neq \text{n}] \\ \frac{(-1)^{\frac{1}{2}(\nu+n-1)}\nu!n!}{2^{\nu+n-1}(\nu-n)(n+\nu+1)\left[\left(\frac{n}{2}\right)!\left(\frac{\nu-1}{2}\right)!\right]^2} & [n \text{ even}, \nu \text{ odd}] \end{cases} \tag{D.13}$$

Finally, inserting these results in equation (D.8), we obtain

$$a(\mathbf{y}) = \sum_{\nu=0}^{\infty}\sum_{n=0}^{\infty} i^{n+\nu}\frac{j_n(kd)}{h_\nu(kR_\Lambda)}\frac{(2\nu+1)(2n+1)}{4\pi R_\Lambda^2}P_\nu(\cos\theta_y)\breve{P}_{n\nu} \tag{D.14}$$

This equation can be reformulated using the Jacobi-Anger expansion (D.4), thus obtaining the following formula:

$$\begin{aligned} a(\mathbf{y}) &= \sum_{\nu=0}^{\infty}\left(\int_0^1\sum_{n=0}^{\infty} i^n j_n(kd)(2n+1)P_n(x)P_\nu(x)dx\right)\frac{i^\nu(2\nu+1)}{4\pi R_\Lambda^2 h_\nu(kR_\Lambda)}P_\nu(\cos\theta_y) \\ &= \sum_{\nu=0}^{\infty}\left(\frac{ik}{4\pi}\int_0^1 e^{ikdx}P_\nu(x)dx\right)\frac{i^\nu(2\nu+1)}{R_\Lambda^2 ikh_\nu(kR_\Lambda)}P_\nu(\cos\theta_y) \end{aligned} \tag{D.15}$$

In the special case when $d = 0$, that is the source location $\mathbf{q}$ coincides with the origin of the coordinate system, we observe that $j_n(0) = \delta_{0,n}$ and therefore obtain the following simpler result:

$$a(\mathbf{y}) = \sum_{\nu=0}^{\infty}\left(\int_0^1 P_\nu(x)dx\right)\frac{i^\nu(2\nu+1)}{R_\Lambda^2 ikh_\nu(kR_\Lambda)}P_\nu(\cos\theta_y) \tag{D.16}$$

From (D.13) and considering that $P_0(x) = 1,\ x \in [-1, 1]$ we have that

$$\int_0^1 P_\nu(x)dx = \begin{cases} 1 & [\nu = 0] \\ 0 & [\nu \text{ is even}, \nu \neq 0] \\ \frac{(-1)^{\frac{1}{2}(\nu-1)}\nu!}{2^{\nu-1}\nu(\nu+1)\left[\left(\frac{\nu-1}{2}\right)!\right]^2} & [\nu \text{ odd}] \end{cases} \tag{D.17}$$

Given the following relations

$$\nu = 2n+1, \quad n = 0, 1, 2... \tag{D.18}$$

$$(2n+1)!! := 1 \cdot 3 \cdot ... \cdot (2n-1) \cdot (2n+1) \tag{D.19}$$

$$(2n+1)!! = \frac{(2n+1)!}{2^n n!} \tag{D.20}$$

$$(2n)!! := 2 \cdot 4 \cdot ... \cdot 2(n-1) \cdot 2n \tag{D.21}$$

$$(2n)!! = 2^n n! \tag{D.22}$$

the expression above can be rewritten as follows:

$$\int_0^1 P_\nu(x)dx = \begin{cases} 1 & [\nu = 0] \\ 0 & [\nu \text{ is even}, \nu \neq 0] \\ \frac{(-1)^{\frac{1}{2}(\nu-1)}\nu!!}{\nu(\nu+1)(\nu-1)!!} & [\nu \text{ odd}] \end{cases} \tag{D.23}$$

Appendix E

Coordinates of the loudspeaker layout

Number	x	y	z	Number	x	y	z
1	0	0	1.8	21	-1.7119	0.5562	0
2	0.9463	0	1.5312	22	-1.7119	-0.5562	0
3	0.2924	0.9	1.5312	23	-1.058	-1.4562	0
4	-0.7656	0.5562	1.5312	24	0	-1.8	0
5	-0.7656	-0.5562	1.5312	25	1.058	-1.4562	0
6	0.2924	-0.9	1.5312	26	1.7119	-0.5562	0
7	1.61	0	0.805	27	1.5312	0	-0.9463
8	1.2387	0.9	0.9463	28	1.3025	0.9463	-0.805
9	0.4975	1.5312	0.805	29	0.4732	1.4562	-0.9463
10	-0.4732	1.4562	0.9463	30	-0.4975	1.5312	-0.805
11	-1.3025	0.9463	0.805	31	-1.2387	0.9	-0.9463
12	-1.5312	0	0.9463	32	-1.2387	-0.9	-0.9463
13	-1.3025	-0.9463	0.805	33	-0.4975	-1.5312	-0.805
14	-0.4732	-1.4562	0.9463	34	0.4732	-1.4562	-0.9463
15	0.4975	-1.5312	0.805	35	1.3025	-0.9463	-0.805
16	1.2387	-0.9	0.9463	36	0.7656	0.5562	-1.5312
17	1.7119	0.5562	0	37	-0.2924	0.9	-1.5312
18	1.058	1.4562	0	38	-0.9463	0	-1.5312
19	0	1.8	0	39	-0.2924	-0.9	-1.5312
20	-1.058	1.4562	0	40	0.7656	-0.5562	-1.5312

TABLE E.1: Cartesian coordinates of the loudspeaker layout used for the experiments presented in Chapter 8

Bibliography

[AE98] James A. S. Angus and Michael J. Evans. Loudspeaker polar pattern measurement and representation with surface spherical harmonics. In *104th International Convention of the Audio Engineering Society*, Amsterdam, 1998.

[AS07] Jens Ahrens and Sascha Spors. Implementation of directional sources in wave field synthesis. *2007 Ieee Workshop on Applications of Signal Processing to Audio and Acoustics*, pages 205–208 350, 2007.

[AS08a] Jens Ahrens and Sascha Spors. An analytical approach to sound field reproduction using circular and spherical loudspeaker distributions. *Acta Acustica United with Acustica*, 94(6):988–999, 2008.

[AS08b] Jens Ahrens and Sascha Spors. Analytical driving functions for higher order ambisonics. *2008 Ieee International Conference on Acoustics, Speech and Signal Processing, Vols 1-12*, pages 373–376 5407, 2008.

[AS08c] Jens Ahrens and Sascha Spors. Focusing of virtual sound sources in higher order ambisonics. In *124th International Convention of the Audio Engineering Society*, 2008.

[AS08d] Jens Ahrens and Sascha Spors. Reproduction of a plane-wave sound field using planar and linear arrays of loudspeakers. *2008 3rd International Symposium on Communications, Control and Signal Processing, Vols 1-3*, pages 1486–1491 1599, 2008.

[BA05] Terence Betlehem and Thushara D. Abhayapala. Theory and design of sound field reproduction in reverberant rooms. *Journal of the Acoustical Society of America*, 117(4):2100–2111, 2005.

[Bam95] Jeffery S. Bamford. *An Analysis of Ambisonics Sound Systems of First and Second Order*. M.sc. thesis, 1995.

[BdS97] A. J. Berkhout, D. deVries, and J. J. Sonke. Array technology for acoustic wave field analysis in enclosures. *Journal of the Acoustical Society of America*, 102(5):2757–2770, 1997.

[BDV93] A. J. Berkhout, D. Devries, and P. Vogel. Acoustic control by wave field synthesis. *Journal of the Acoustical Society of America*, 93(5):2764–2778, 1993.

[Ber88] A. J. Berkhout. A holographic approach to acoustic control. *Journal of the Audio Engineering Society*, 36(12):977–995, 1988.

[BJ93] Giorgio V. Borgiotti and Kenneth E. Jones. The determination of the acoustic far-field of a radiating body in an acoustic fluid from boundary measurements. *Journal of the Acoustical Society of America*, 93(5):2788–2797, 1993.

[Boo04] M. M. Boone. Multi-actuator panels (maps) as loudspeaker arrays for wave field synthesis. *Journal of the Audio Engineering Society*, 52(7-8):712–723, 2004.

[Bor90] Giorgio V. Borgiotti. The power radiated by a vibrating body in an acoustic fluid and its determination from boundary measurements. *Journal of the Acoustical Society of America*, 88(4):1884–1893, 1990.

[BR07] I. Balmages and B. Rafaely. Open-sphere designs for spherical microphone arrays. *Ieee Transactions on Audio Speech and Language Processing*, 15(2):727–732, 2007.

[Bru08] Vincent Brunel. *Measurement and spherical harmonic representation of loudspeaker radiation patterns.* Master thesis, 2008.

[BSWS90] Giorgio V. Borgiotti, Angie Sarkissian, Earl G. Williams, and Luise Schuetz. Conformal generalized near-field acoustic holography for axisymmetric geometries. *Journal of the Acoustical Society of America*, 88(1):199–209, 1990.

[BV95] Jeffery S. Bamford and John Vanderkooy. Ambisonic sound for us. In *99th International Convention of the Audio Engineering Society*, 1995.

[BVv94] Marinus M. Boone, Edwin N. G. Verheijen, and Peter F. vanTol. The wave field synthesis concept applied to sound reproduction. *Aes 96th Convention Preprints, Pts 1 and 2*, pages 437–446 1223, 1994.

[CBG10] Israel Cohen, Jacob Benesty, and Sharon Gannot. *Speech Processing in Modern Communication*, volume 3 of *Springer Topics in Signal Processing.* Springer, Berlin, 2010.

[CG77] Peter G. Craven and Michael A. Gerzon. Coincident microphone simulation covering three dimensional space and yielding various directional outputs. US patent 4042779, 1977.

[CIB08] Wan-Ho Cho, Jeong-Guon Ih, and Marinus M. Boone. Holographic design of a source array for achieving a desired sound field. In *124th International Convention of the Audio Engineering Society*, Amsterdam, 2008.

[CK83] David L. Colton and Rainer Kress. *Integral Equation Methods in Scattering Theory*. Wiley, New York, 1983.

[CK92] David L. Colton and Rainer Kress. *Inverse acoustic and electromagnetic scattering theory*. Applied mathematical sciences. Springer, Berlin, 1992.

[CK02] J. W. Choi and Y. H. Kim. Generation of an acoustically bright zone with an illuminated region using multiple sources. *Journal of the Acoustical Society of America*, 111(4):1695–1700, 2002.

[Cop68] L. G. Copley. Fundamental results concerning integral representations in acoustic radiation. *Journal of the Acoustical Society of America*, 44(1):28–32, 1968.

[Cor06] Etienne Corteel. Equalization in an extended area using multichannel inversion and wave field synthesis. *Journal of the Audio Engineering Society*, 54(12):1140–1161, 2006.

[Cor07] Etienne Corteel. Synthesis of directional sources using wave field synthesis, possibilities, and limitations. *Eurasip Journal on Advances in Signal Processing*, 2007.

[Cot02] Philip S. Cotterell. *On the Theory of the Second-Order Soundfield Microphone*. PhD thesis, 2002.

[CPKR08] Etienne Corteel, Renato Pellegrini, and Clemens Kuhn-Rahloff. Wave field synthesis with increased aliasing frequency. In *124th International Convention of the Audio Engineering Society*, Amsterdam, 2008.

[CWHP06] Simon N. Chandler-Wilde, Eric Heinemeyer, and Roland Potthast. Acoustic scattering by mildly rough unbounded surfaces in three dimensions. *Siam Journal on Applied Mathematics*, 66(3):1002–1026, 2006.

[CZ92] Goong Chen and Jingmin Zhou. *Boundary Element Method*. Academic Press, London, 1992.

[Dan00] Jerome Daniel. *Représentation de Champs Acoustiques, Application à la Transmission et à la Reproduction de Scènes Sonores Complexes dans un Contexte Multimédia*. Phd thesis, 2000.

[Dan03] Jerome Daniel. Spatial sound encoding including near field effect: Introducing distance coding filters and a viable, new ambisonic format. In *23rd International Conferece of the Audio Engineering Society*, Helsingør, Denmark, 2003.

[Dav63] Harry F. Davis. *Fourier series and orthogonal functions.* Allyn and Bacon, Boston, 1963.

[DC72] Deschamp.Ga and H. S. Cabayan. Antenna synthesis and solution of inverse problems by regularization methods. *Ieee Transactions on Antennas and Propagation*, Ap20(3):268–274, 1972.

[DNM03] Jerome Daniel, Rozenn Nicol, and Sebastien Moureau. Further investigations of high-order ambisonics and wavefield synthesis for holophonic sound imaging. In *114th International Convention of the Audio Engineering Society*, 2003.

[DRP98] Jerome Daniel, Jean-Bernard Rault, and Jean-Dominique Polack. Ambisonics encoding of other audio formats for multiple listening conditions. In *105th International Convention of the Audio Engineering Society*, 1998.

[dV96] Diemer de Vries. Sound reinforcement by wavefield synthesis: Adaptation of the synthesis operator to the loudspeaker directivity characteristics. *Journal of the Audio Engineering Society*, 44:1120–1131, 1996.

[EF07] N. Epain and E. Friot. Active control of sound inside a sphere via control of the acoustic pressure at the boundary surface. *Journal of Sound and Vibration*, 299(3):587–604, 2007.

[Far07] Angelo Farina. Advancements in impulse response measurements by sine sweeps. In *122nd International Convention of the Audio Engineering Society*, Vienna, Austria, 2007.

[FBN07] Filippo M. Fazi, Vincent Brunel, and Philip A. Nelson. Misura e ricostruzione olografica del campo acustico generato da un altoparlante. In *AES Italian Section Annual Meeting*, Parma, Italy, 2007.

[FBN+08] Filippo M. Fazi, Vincent Brunel, Philip A. Nelson, Lars Hörchens, and Jeongil Seo. Measurement and fourier-bessel analysis of loudspeaker radiation patterns using a spherical array of microphones. In *124th International Convention of the Audio Engineering Society*, Amsterdam, 2008.

[Fel75] Peter B. Fellgett. Ambisonics. part one: General system description. *Studio Sound*, pages 20–40, 1975.

[FGAT01] Angelo Farina, Ralph Glasgal, Enrico Armelloni, and Anders Torger. Ambiophonic principles for the recording and reproduction of surround sound for music. In *19th International Conference of the Audio Engineering Society*, Schloss Elmau, Germany, 2001.

[Fin92] Mathias Fink. Time-reversal of ultrasonic fields .1. basic principles. *Ieee Transactions on Ultrasonics Ferroelectrics and Frequency Control*, 39(5):555–566, 1992.

[Fli] Jörg Fliege. http://www.personal.soton.ac.uk/jf1w07/nodes/nodes.html.

[FM96] Jörg Fliege and Ulrike Maier. A two-stage approach for computing cubature formulae for the sphere. Technical report, Mathematik 139T, Universität Dortmund, Fachbereich Mathematik, Dortmund, 1996.

[FN07a] Filippo M. Fazi and Philip A. Nelson. Application of functional analysis to the sound field reconstruction. In *23rd Conference on Reproduced Sound of the Institute of Acoustics*, Newcastle, 2007.

[FN07b] Filippo M. Fazi and Philip A. Nelson. The ill-conditioning problem in sound field reconstruction. In *123rd International Convention of the Audio Engineering Society*, New York, 2007.

[FN07c] Filippo M. Fazi and Philip A. Nelson. A theoretical study of sound field reconstruction techniques. In *19th International Congress on Acoustics*, Madrid, 2007.

[FNCS08] Filippo M. Fazi, Philip A. Nelson, Jens E. N. Christensen, and Jeongil Seo. Surround system based on three-dimensional sound field reconstruction. In *125th International Convention of the Audio Engineering Society*, San Francisco, USA, 2008.

[FNP09] Filippo M. Fazi, Philip A. Nelson, and Roland Potthast. Analogies and differences between three methods for sound field reproduction. In *Ambisonics Symposium 2009*, Graz, Austria, 2009.

[FNPS08a] F. M. Fazi, P. A. Nelson, R. Potthast, and J. Seo. Application of the theory of integral equations to the design of a multi-channel reverberation simulator. In *35o Convegno Nazionale dell'Associazione Italiana di Acustica*, Milano, Italy, 2008.

[FNPS08b] Filippo M. Fazi, Philip A. Nelson, Roland Potthast, and Jeongil Seo. An introduction to a generalised theory for sound field reproduction. In *24th Conference on Reproduced Sound of the Institute of Acoustics*, Brighton, 2008.

[FNPS08c] Filippo M. Fazi, Philip A. Nelson, Roland Potthast, and Jeongil Seo. The study of sound field reconstruction as an inverse problem. In *Institute of Acoustics Spring Conference*, Reading, 2008.

[FU98] Angelo Farina and Emanuele Ugolotti. Software implementation of b-format encoding and decoding. In *104th International Convention of the Audio Engineering Society*, Amsterdam, 1998.

[GB92] Michael A. Gerzon and Geoffrey J. Barton. Ambisonic decoders for hdtv. In *92nd International Convention of the Audio Engineering Society*, Vienna, 1992.

[GB98] Michael A. Gerzon and Geoffrey J. Barton. Surround sound apparatus: US patent 5757927, 1998.

[GB06] Philippe-Aubert Gauthier and Alain Berry. Adaptive wave field synthesis with independent radiation mode control for active sound field reproduction: Theory. *Journal of the Acoustical Society of America*, 119(5):2721–2737, 2006.

[GB08a] Philippe-Aubert Gauthier and Alain Berry. Adaptive wave field synthesis for active sound field reproduction: Experimental results. *Journal of the Acoustical Society of America*, 123(4):1991–2002, 2008.

[GB08b] Philippe-Aubert Gauthier and Alain Berry. Adaptive wave field synthesis for broadband active sound field reproduction: Signal processing. *Journal of the Acoustical Society of America*, 123(4):2003–2016, 2008.

[GBW05] Philippe-Aubert Gauthier, Alain Berry, and Wieslaw Woszczyk. Sound-field reproduction in-room using optimal control techniques: Simulations in the frequency domain. *Journal of the Acoustical Society of America*, 117(2):662–678, 2005.

[Ger72] Michael A. Gerzon. Periphony (with-height sound reproduction). In *2nd Central Europe Convention of the Audio Engineering Society*, Munich, Germany, 1972.

[Ger73] Michael A. Gerzon. Periphony - with-height sound reproduction. *Journal of the Audio Engineering Society*, 21(1):2–10, 1973.

[Ger74] Michael A. Gerzon. Surround-sound psychoacoustics - criteria for design of matrix and discrete surround-sound systems. *Wireless World*, 80(1468):483–486, 1974.

[Ger75] Michael A. Gerzon. The design of precisely coincident microphone arrays for stereo and surround sound. In *50th International Convention of the Audio Engineering Society*, London, 1975.

[Ger77a] M. Gerzon. Surround sound decoders .7. multi-system ambisonic decoder .2. main decoder circuits. *Wireless World*, 83(1500):69–73, 1977.

[Ger77b] Michael A. Gerzon. Multi-system ambisonic decoder .1. basic design philosophy. *Wireless World*, 83(1499):43–47, 1977.

[Ger77c] Michael A. Gerzon. Nrdc surround-sound system. *Wireless World*, 83(1496):36–39, 1977.

[Ger80] Michael A. Gerzon. Practical periphony - the reproduction of full-sphere sound. *Journal of the Audio Engineering Society*, 28(5):364–364, 1980.

[Ger85] Michael A. Gerzon. Ambisonics in multichannel broadcasting and video. *Journal of the Audio Engineering Society*, 33(11):859–871, 1985.

[Ger92] Micahel A. Gerzon. General metatheory of auditory localisation. In *92nd International Convention of the Audio Engineering Society*, Vienna, 1992.

[Ger97] Michael A. Gerzon. Sound reproduction system having a matrix converter. US patent 5594800, 1997.

[GR65] I. S. Gradshteyn and I. M. Ryzhik. *Table of integrals, series and products*. Academic Press, New York, NY, 1965.

[Had23] Jacques Hadamard. *Lectures on Cauchy's problem in Linear Partial Differential Equations*. Yale University Press, New Haven, 1923.

[Hal09] J. Hald. Basic theory and properties of statistically optimized near-field acoustical holography. *Journal of the Acoustical Society of America*, 125(4):2105–2120, 2009.

[Har78] F. J. Harris. Use of windows for harmonic-analysis with discrete fourier-transform. *Proceedings of the Ieee*, 66(1):51–83, 1978.

[HD08] Jens Hannemann and Kevin D. Donohue. Virtual sound source rendering using a multipole-expansion and method-of-moments approach. *Journal of the Audio Engineering Society*, 56(6):473–481, 2008.

[Hig96] John R. Higgins. *Sampling theory in Fourier and signal analysis: foundations*, volume 1. Oxford University Press, Oxford, 1996.

[HLB08] Aaron J. Heller, Richard Lee, and Eric M. Benjamin. Is my decoder ambisonic? In *125th International Convention of the Audio Engineering Society*, San Francisco, California, 2008.

[HS09] Eric Hellerud and U. Peter Svensson. Lossless compression of spherical microphone array recordings. In *126th International Convention of the Audio Engineering Society*, Munich, Germany, 2009.

[Huy66] Christiaan Huygens. *TraitÃľ de la lumiÃĺre : avec, Un discours de la cause da la pesanteur, 1690*. Dawson, London, 1966.

[Ise99] Shiro Ise. A principle of sound field control based on the kirchhoff-fâĂŞhelmholtz integral equation and the theory on inverse systems. *Acustica-Acta Acustica*, 85:78–87, 1999.

[ISV] http://www.isvr.co.uk/faciliti/lg_anech.htm, last access 15 october 2009.

[KEF] KEF. Home theatre 3000 series, model HTS3001 satellite speaker & model HTC3001 centre speaker, installation manual.

[KF62] Lawrence E. Kinsler and Austin R. Frey. *Fundamentals of acoustics*. Wiley, London, 2nd edition, 1962.

[KN93] Ole Kirkeby and Philip A. Nelson. Reproduction of plane-wave sound fields. *Journal of the Acoustical Society of America*, 94(5):2992–3000, 1993.

[KN03] Y. Kim and P. A. Nelson. Spatial resolution limits for the reconstruction of acoustic source strength by inverse methods. *Journal of Sound and Vibration*, 265(3):583–608, 2003.

[KNHOB98] O. Kirkeby, P. A. Nelson, H. Hamada, and F. Orduna-Bustamante. Fast deconvolution of multichannel systems using regularization (reprinted from ieice transactions on fundamentals of electronics, communications, and computer sciences, vol e80-a, pg 809-820, 1997). *Ieee Transactions on Speech and Audio Processing*, 6(2):189–194, 1998.

[Kre78] Erwin Kreyszig. *Introductory functional analysis with applications*. Wiley, New York, 1978.

[Kre99] Rainer Kress. *Linear integral equations*. Applied mathematical sciences. Springer, New York, 2nd edition, 1999.

[MAA07] Dylan Menzies and Marwan Al-Akaidi. Ambisonic synthesis of complex sources. *Journal of the Audio Engineering Society*, 55(10):864–876, 2007.

[Mal99] Dave Malham. Higher order ambisonic systems for the spatialisation of sound. In *ICMC99*, Beijing, 1999.

[Mar01] Farokh Marvasti. *Nonuniform Sampling: Theory and Practice*. Kluwer Academic / Plenum, New York, 2001.

[MB08] Cedric Maury and Teresa Bravo. Analytic solutions to the acoustic source reconstruction problem. *Proceedings of the Royal Society a-Mathematical Physical and Engineering Sciences*, 464(2095):1697–1718, 2008.

[ME05] Cedric Maury and Steve J. Elliott. Analytic solutions of the radiation modes problem and the active control of sound power. *Proceedings of the Royal Society of London Series a-Mathematical Physical and Engineering Sciences*, 461(2053):55–78, 2005.

[Men09] Dylan Menzies. Calculation of near-field head related transfer functions using point source representations. In *Ambisonics Symposium 2009*, Graz, Austria, 2009.

[MF53] Philip M. Morse and Herman Feshbach. *Methods of theoretical physics. Part I : chapters 1 to 8*. McGraw Hill Book Co, 1953.

[MLdV05] F. Melchior, T. Laubach, and D. de Vries. Authoring and user interaction for the production of wave field synthesis content in an augmented reality system. *International Symposium on Mixed and Augmented Reality, Proceedings*, pages 48–51 219, 2005.

[Mor06] S. Moreau. *ÃĽtude et rÃľalisation dâĂŹoutils avancÃľs dâĂŹencodage spatial pour la technique de spatialisation sonore Higher Order Ambisonics : microphone 3D et contrÃŧle de distance*. PhD thesis, 2006.

[MW95] Leonard Mandel and Emil Wolf. *Optical coherence and quantum optics*. C.U.P., Cambridge, 1995.

[MWL85] J. D. Maynard, E. G. Williams, and Y. Lee. Nearfield acoustic holography .1. theory of generalized holography and the development of nah. *Journal of the Acoustical Society of America*, 78(4):1395–1413, 1985.

[NE92] Philip A. Nelson and Steve J. Elliott. *Active control of sound*. Academic Press, London, 1992.

[NE98] Rozenn Nicol and Marc Emerit. Reproducing 3d-sound for videoconferencing: a comparison between holophony and ambisonic. In *DAFX98*, pages 17–20, Barcelona, Spain, 1998.

[NE99] Rozenn Nicol and Marc Emerit. 3d-sound reproduction over an extensive listening area: A hybrid method derived from holophony and ambisonic. In *16th International Conference of the Audio Engineering Society*, Rovaniemi, Finland, 1999.

[Nic99] Rozenn Nicol. *Restitution Sonore SpatialisÃľe sur une Zone Etendue : Application Ãă la TÃŧlÃľprÃľsence*. Ph. d. thesis, 1999.

[NMSH03] M. Noisternig, T. Musil, A. Sontacchi, and R. Holdrich. 3d binaural sound reproduction using a virtual ambisonic approach. *Vecims'03: 2003 Ieee International Symposium on Virtual Environments, Human-Computer Interfaces and Measurement Systems*, pages 174–178 217, 2003.

[NOBH96] Philip A. Nelson, Felipe Orduna-Bustamante, and Hareo Hamada. Multichannel signal processing techniques in the reproduction of sound. *Journal of the Audio Engineering Society*, 44:973–989, 1996.

[Now81] J. L. Nowinski. *Applications of Functional Analysis in Engineering*. Mathematical Concepts and Methods in Sceince and Engineering. Plenum Press, New York, 1981.

[NY00] Philip A. Nelson and Seong-Ho Yoon. Estimation of acoustic source strength by inverse methods: Part i, conditioning of the inverse problem. *Journal of Sound and Vibration*, 233(4):643–668, 2000.

[Pol96] Mark A. Poletti. The design of encoding functions for stereophonic and polyphonic sound systems. *Journal of the Audio Engineering Society*, 44(11):948–963, 1996.

[Pol00] Mark A. Poletti. A unified theory of horizontal holographic sound systems. *Journal of the Audio Engineering Society*, 48:1155–1182, 2000.

[Pol05] Mark A. Poletti. Three-dimensional surround sound systems based on spherical harmonics. *Journal of the Audio Engineering Society*, 53(11):1004–1025, 2005.

[Pol07] Mark A. Poletti. Robust two-dimensional surround sound reproduction for nonuniform loudspeaker layouts. *Journal of the Audio Engineering Society*, 55(7/8):598–610, 2007.

[Pot01] Roland Potthast. *Point-sources and Multipoles in Inverse Scattering*. Chapman & Hall, London, 2001.

[Pot07] Roland Potthast. Introduction to functional analysis and inverse problems, lecture notes, 2007.

[PRP+08] Paolo Peretti, Laura Romoli, Lorenzo Palestini, Stefania Checchi, and Francesco Piazza. Wave field synthesis: Practical implementation and application to sound beam digital pointing. In *125th International Convention of the Audio Engineering Society*, San Francisco, California, 2008.

[Pul97] Ville Pulkki. Virtual sound source positioning using vector base amplitude panning. *Journal of the Audio Engineering Society*, 45(6):456–466, 1997.

[Raf04] Boaz Rafaely. Plane-wave decomposition of the sound field on a sphere by spherical convolution. *Journal of the Acoustical Society of America*, 116(4):2149–2157, 2004.

[Raf05] Boaz Rafaely. Analysis and design of spherical microphone arrays. *Ieee Transactions on Speech and Audio Processing*, 13(1):135–143, 2005.

[Ray97] John W. S. Rayleigh. On the passage of waves through apertures in plane screens, and allied problems. *Philosophical Magazine*, 43:259–272, 1897.

[RWB07] Boaz Rafaely, B. Weiss, and E. Bachmat. Spatial aliasing in spherical microphone arrays. *Ieee Transactions on Signal Processing*, 55(3):1003–1010, 2007.

[SA08] Sascha Spors and Jens Ahrens. A comparison of wave field synthesis and higher-order ambisonics with respect to physical properties and spatial sampling. In *125th International Convention of the Audio Engineering Society*, San Francisco, CA, 2008.

[SA09] S. Spors and J. Ahrens. Spatial sampling artifacts of wave field synthesis for the reproduction of virtual point sources. In *126th International Convention of the Audio Engineering Society*, Munich, Germany, 2009.

[Sar05] A. Sarkissian. Method of superposition applied to patch near-field acoustic holography. *Journal of the Acoustical Society of America*, 118(2):671–678, 2005.

[SBRH07] S. Spors, H. Buchner, R. Rabenstein, and W. Herbordt. Active listening room compensation for massive multichannel sound reproduction systems using wave-domain adaptive filtering. *Journal of the Acoustical Society of America*, 122(1):354–369, 2007.

[Sch07] Erhard Schmidt. Zur theorie der linearen und nichtlinearen integralgleicungen. i teil. entwicklung willkürlichen funktionen nach system vorgeschriebener. *Mathematische Annalen*, 63:433–476, 1907.

[Sch68] H. A. Schenck. Improved integral formulation for acoustic radiation problems. *Journal of the Acoustical Society of America*, 44(1):41–58, 1968.

[SH01] Alois Sontacchi and Robert Höldrich. Further investigations on 3d sound fields using distance coding. In Ireland Limerick, editor, *2001*, 2001.

[SK97] E. B. Saff and A. B. J. Kuijlaars. Distributing many points on a sphere. *Mathematical Intelligencer*, 19(1):5–11, 1997.

[Sol08] Audun Solvang. Spectral impairment for two-dimensional higher order ambisonics. *Journal of the Audio Engineering Society*, 56(4):267–279, 2008.

[Spo06] Sasha Spors. *Active Listening Room Compensation for Spatial Sound Reproduction Systems.* Phd thesis, 2006.

[Spo07] Sascha Spors. Extension of analytic secondary source selection criterion for wave field synthesis. In *123rd International Convention of the Audio Engineering Society*, New York, 2007.

[SR06] Sascha Spors and Rudolf Rabenstein. Spatial aliasing artifacts produced by linear and circular loudspeaker arrays used for wave field synthesis. In *120th International Convention of the Audio Engineering Society*, Paris, France, 2006.

[SRA08] Sascha Spors, Rudolf Rabenstein, and Jens Ahrens. The theory of wave field synthesis revisited. In *124th International Convention of the Audio Engineering Society*, Amsterdam, The Netherlands, 2008.

[SS06] B. Stofringsdal and U. P. Svensson. Conversion of discretely sampled sound field data to auralization formats. *Journal of the Audio Engineering Society*, 54(5):380–400, 2006.

[Sta97] Evert W. Start. *Direct Sound Enhancement by Wave Field Synthesis.* Phd thesis, 1997.

[Ste93] G. W. Stewart. On the early history of the singular-value decomposition. *Siam Review*, 35(4):551–566, 1993.

[TAG+01] M. Tanter, J. F. Aubry, J. Gerber, J. L. Thomas, and M. Fink. Optimal focusing by spatio-temporal inverse filter. i. basic principles. *Journal of the Acoustical Society of America*, 110(1):37–47, 2001.

[Ver97] Edwin N.G. Verheijen. *Sound Reproduction by Wave Field Synthesis.* Phd thesis, 1997.

[VM89] W. A. Veronesi and J. D. Maynard. Digital holographic reconstruction of sources with arbitrarily shaped surfaces. *Journal of the Acoustical Society of America*, 85(2):588–598, 1989.

[Vog93] P. Vogel. *Application of Wave Field Synthesis in Room Acoustics.* Phd thesis, 1993.

[VW04] Nicolas P. Valdivia and Earl G. Williams. Implicit methods of solution to integral formulations in boundary element method based nearfield acoustic holography. *Journal of the Acoustical Society of America*, 116(3):1559–1572, 2004.

[WA79] G. Weinreich and E. B. Arnold. Measuring system for the radiation-field of a violin. *Journal of the Acoustical Society of America*, 65:S72–S72, 1979.

[WA01] Darren B. Ward and Thushara D. Abhayapala. Reproduction of a plane-wave sound field using an array of loudspeakers. *Ieee Transactions on Speech and Audio Processing*, 9(6):697–707, 2001.

[WA09] Yan J. Wu and Thushara D. Abhayapala. Theory and design of soundfield reproduction using continuous loudspeaker concept. *Ieee Transactions on Audio Speech and Language Processing*, 17(1):107–116, 2009.

[WHH03] E. G. Williams, B. H. Houston, and P. C. Herdic. Fast fourier transform and singular value decomposition formulations for patch near-field acoustical holography. *Journal of the Acoustical Society of America*, 114(3):1322–1333, 2003.

[Wig04] Bruce Wiggins. *An investigation into the real-time manipulation and control of three-dimensional sound fields.* PhD thesis, 2004.

[Wil99] Earl G. Williams. *Fourier acoustics : sound radiation and nearfield acoustical holography.* Academic, San Diego, 1999.

[WTF92] F. Wu, J. L. Thomas, and M. Fink. Time-reversal of ultrasonic fields .2. experimental results. *Ieee Transactions on Ultrasonics Ferroelectrics and Frequency Control*, 39(5):567–578, 1992.

[WW27] E. Whittaker and G. N. Watson. *A Course of modern analysis. (4th edition)*. Cambridge University Press, Cambridge, 1927.

[WW97] Z. X. Wang and S. F. Wu. Helmholtz equation least-squares method for reconstructing the acoustic pressure field. *Journal of the Acoustical Society of America*, 102(4):2020–2032, 1997.

[WY98] S. F. Wu and J. Y. Yu. Reconstructing interior acoustic pressure fields via helmholtz equation least-squares method. *Journal of the Acoustical Society of America*, 104(4):2054–2060, 1998.

[YN00] Seong-Ho Yoon and Philip A. Nelson. Estimation of acoustic source strength by inverse methods: Part ii, experimental investigation of methods for choosing regularization parameters. *Journal of Sound and Vibration*, 233(4):669–705, 2000.

[YTF03a] S. Yon, M. Tanter, and M. Fink. Sound focusing in rooms. ii. the spatio-temporal inverse filter. *Journal of the Acoustical Society of America*, 114(6):3044–3052, 2003.

[YTF03b] S. Yon, M. Tanter, and M. Fink. Sound focusing in rooms: The time-reversal approach. *Journal of the Acoustical Society of America*, 113(3):1533–1543, 2003.

[Zot09] Franz Zotter. Sampling strategies for acoustic holography/holophony on the sphere. In *NAG-DAGA*, Rotterdam, 2009.

[ZPF09] Franz Zotter, Hannes Pomberger, and Matthias Frank. An alternative ambisonics formulation: Modal source strength matching and the effect of spatial aliasing. In *126th International Conference of the Audio Engineering Society*, Munich, Germany, 2009.

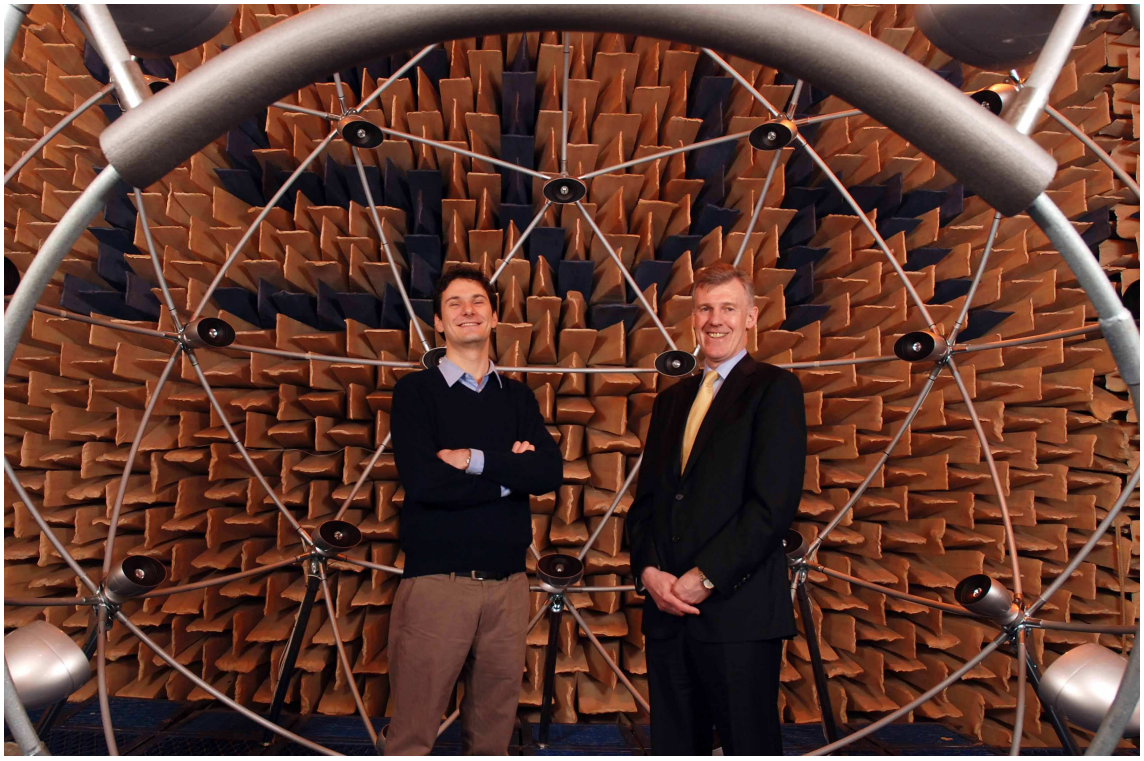

Goodbye!